

An International
Forum For
The AE Science
and Technology

JOURNAL OF ACOUSTIC EMISSION

Vol.30/January-December 2012



EWGAE30 - ICAE7 Granada, Spain

Endorsed by
AEWG
and
EWGAE

Published by
Acoustic Emission Group
Encino, CA USA

Journal of Acoustic Emission, Volume 30, 2012

CONTENTS

- 30-001** -Analysis of AE Signals during Scratch Test on the Coated Paperboard
Hiroyuki Kishi, Akio Matudoe, Ken Yamashita, Shigeru Nagasawa and Yasushi Fukuzawa
- 30-011** Acoustic Emission Related to Drought Stress Response of Four Deciduous Broad-Leaved Woody Species
Sabine Rosner
- 30-021** Micro-mechanical Damage in Tool Steels Analyzed by Acoustic Emission Technique
Ingrid Picas, Eva Martinez-Gonzalez, Daniel Casellas and Jordi Romeu
- 30-029** Viable Precursors of Paroxysmal Phenomena as Detected by Applying RQA to Acoustic Emission Time Series
Maurizio Poscolieri, Claudio Rafanelli and Giovanna Zimatore
- 30-040** Artificial Neural Network Analyses of AE Data during Long-Term Corrosion Monitoring of a Post-Tensioned Concrete Beam
Lucio Bonaccorsi, Luigi Calabrese, Giuseppe Campanella and Edoardo Proverbio
- 30-054** On the Use of the Acoustic Emission Technique for In-situ Monitoring of the Pulverization of Battery Electrodes
Aurélien Etiemble, Hassane Idrissi and Lionel Roué
- 30-064** AE Wavelet Processing in Dynamical Tests of a Reinforced Concrete Slab
Miguel E. Zitto, Rosa Piotrkowski, Antolino Gallego and Francisco Sagasta³
- 30-076** Recent Advances of AE Technology for Damage Assessment of Infrastructures
Tomoki Shiotani
- 30-100** Preliminary Investigations of Acoustics Emission Signal from Snow and its Wavelet Transform
Karmjeet Singh, Yogesh C. Nagar, Jagdish C. Kapil, Pramod K. Satyawali and Ashwagosh Ganju
- 30-109** Attenuation of Lamb Waves in CFRP Plates
Kanji Ono and Antolino Gallego
- 30-124** Application of ICI Principle for AE Data Processing
Vera Barat, Sergey Elizarov, Irina Bolokhova and Evgeniy Bolokhov
- 30-137** Modeling of the Far-field Acoustic Emission from a Crack under Stress
Warida Ben Khalifa, Karim Jezzine, Sébastien Grondel, Gaëtan Hello and Alain Lhémery
- 30-152** Primary Calibration of Acoustic Emission Sensors by the Method of Reciprocity, Theoretical and Experimental Considerations
Thomas Monnier, Seydou Dia, Nathalie Godin and Fan Zhang
- 30-167** Neural Network Burst Pressure Prediction In Tall Graphite-Epoxy Pressure Vessels From Acoustic Emission Data
Eric v. K. Hill, Christopher J. Foti, Ning Y. Leung and Andrea E. Palacios

30-180 Research and Applications of AE on Advanced Composites
Kanji Ono and Antolino Gallego

Contents30	Contents of Volume 30 (2012)	I-1 – I-2
	Meeting Calendar - AE Activity (EWGAE30/ICAE7)	I-2
	Announcement	I-2
AUindex30	Authors Index of Volume 30	I-3
AusNotes	Policy/Author's Notes	I-4 – I-5
In Memoriam	Professor Steve Carpenter	I-6
Cover illustration	From EWGAE30-ICAE7, Granada, Spain.	
JAE Index Folder*	Cumulative Indices of J. of Acoustic Emission, 1982 – 2012	
	JAE-Contents1-30	Contents of Volumes 1-30
	JAE-Authors Index 1-30	Authors Index Volumes 1-30
	Comprehensive Authors Index (2012) is also included.	

* indicates the availability in CD-ROM only. Indices are also available for download from www.aewg.org.

Meeting Calendar

AEWG 55

The 55th Meeting on Acoustic Emission Working Group will be held on June 11-12, 2013 at Garden Grove, CA. The host is Dr. Jerry Huang of Boeing (jerry.q.huang@boeing.com). More information is available at www.aewg.org. For accommodation, contact Crowne Plaza Anaheim Resort at <http://www.anaheim.crowneplaza.com/>

AE Activity

EWGAE30-International Conf. on AE 7, 2012

Information on this successful conference is available at www.ewgae.es, including Program and Proceedings in downloadable pdf file. See also a report on the conference at <http://www.ndt.net/search/docs.php3?id=13636&content=1>

Announcement

With the publication of this volume, this Journal will shift to the open-access mode, terminating the paper/CD distribution and subscription services. I wish to thank all of you, authors, reviewers, co-editors, book agencies and readers, who have supported this Journal for the past 32 years. Some of the reasons for the founding of this publication have faded as there are so many venues for quality publications. In particular, academic authors require impact factors, which are incompatible with our goals. We will continue providing a forum in timely manner with web-based distribution, rather than annual basis, with rigorous review as in the past to maintain the quality we have sustained. We hope future contributors and readers keep the confidence in Journal of Acoustic Emission in the new approach for disseminating the information useful to the global AE community.

Kanji Ono, Editor and Publisher

Authors Index, Volume 30, 2012

Vera Barat	30-124
Evgeniy Bolokhov	30-124
Irina Bolokhova	30-124
Luigi Calabrese	30-040
Giuseppe Campanella	30-040
Daniel Casellas	30-021
Seydou Dia	30-152
Sergey Elizarov	30-124
Aurélien Etiemble	30-054
Christopher J. Foti	30-167
Yasushi Fukuzawa	30-001
Antolino Gallego	30-064, 30-109, 30-180
Ashwagoshha Ganju	30-100
Nathalie Godin	30-152
Sébastien Grondel	30-137
Gaëtan Hello	30-137
Eric v. K. Hill	30-167
Hassane Idrissi	30-054
Karim Jezzine	30-137
Jagdish C. Kapil	30-100
Warida Ben Khalifa	30-137
Hiroyuki Kishi	30-001
Ning Y. Leung	30-167
Alain Lhémercy	30-137
Eva Martinez-Gonzalez	30-021
Akio Matudoe	30-001
Thomas Monnier	30-152
Yogesh C. Nagar	30-100
Shigeru Nagasawa	30-001
Kanji Ono	30-109, 30-180
Andrea E. Palacios	30-167
Ingrid Picas	30-021
Rosa Piotrkowski	30-064
Maurizio Poscolieri	30-029
Edoardo Proverbio	30-040
Claudio Rafanelli	30-029
Jordi Romeu	30-021
Sabine Rosner	30-011
Lionel Roué	30-054
Francisco Sagasta	30-064
Pramod K. Satyawali	30-100
Tomoki Shiotani	30-076
Karmjeet Singh	30-100
Ken Yamashita	30-001
Fan Zhang	30-152
Giovanna Zimatore	30-029
Miguel E. Zitto	30-064

JOURNAL OF ACOUSTIC EMISSION

Editor: Kanji Ono

Associate Editors: A. G. Beattie, T. F. Drouillard, M. Ohtsu and W. H. Prosser

1. Aims and Scope of the Journal

Journal of Acoustic Emission is an international journal designed to be of broad interest and use to both researcher and practitioner of acoustic emission. It will publish original contributions of all aspects of research and significant engineering advances in the sciences and applications of acoustic emission. The journal will also publish reviews, the abstracts of papers presented at meetings, technical notes, communications and summaries of reports. Current news of interest to the acoustic emission communities, announcements of future conferences and working group meetings and new products will also be included.

Journal of Acoustic Emission includes the following classes of subject matters;

A. Research Articles: Manuscripts should represent completed original work embodying the results of extensive investigation. These will be judged for scientific and technical merit.

B. Applications: Articles must present significant advances in the engineering applications of acoustic emission. Material will be subject to reviews for adequate description of procedures, substantial database and objective interpretation.

C. Technical Notes and Communications: These allow publications of short items of current interest, new or improved experimental techniques and procedures, discussion of published articles and relevant applications.

D. AE Program and Data Files: Original program files and data files that can be read by others and analyzed will be distributed in CD-ROM.

Reviews, Tutorial Articles and Special Contributions will address the subjects of general interest. Nontechnical part will cover book reviews, significant personal and technical accomplishments, current news and new products.

2. Endorsement

Acoustic Emission Working Group (AEWG), European Working Group on Acoustic Emission (EWGAE), have endorsed the publication of Journal of Acoustic Emission.

3. Governing Body

The Editor and Associate Editors will implement the editorial policies described above. The Editorial Board will advise the editors on any major change. The Editor, Professor Kanji Ono, has the general responsibility for all the matters. Associate Editors assist the review processes as lead reviewers. The members of the Editorial Board are selected for their knowledge and experience on AE and will advise and assist the editors on the publication

policies and other aspects. The Board presently includes the following members:

A. Anastasopoulos	(Greece)
F.C. Beall	(USA)
J. Bohse	(Germany)
P. Cole	(UK)
M.A. Hamstad	(USA)
R. Hay	(Canada)
K.M. Holford	(UK)
O.Y. Kwon	(Korea)
J.C. Lenain	(France)
G. Manthei	(Germany)
P. Mazal	(Czech Republic)
C.R.L. Murthy	(India)
A.A. Pollock	(USA)
F. Rauscher	(Austria)
J. Schmidt	(Poland)
T. Shiotani	(Japan)
P. Tschliesnig	(Austria)
H. Vallen	(Germany)
M. Wevers	(Belgium)
B.R.A. Wood	(Australia)

4. Publication

Journal of Acoustic Emission is published annually in CD-ROM by Acoustic Emission Group, PMB 409, 4924 Balboa Blvd, Encino, CA 91316. It may also be reached at 2121H, Engr. V, University of California, Los Angeles, California 90095-1595 (USA). tel. 310-825-5233. FAX 310-206-7353. e-mail: aegroup7@gmail.com or ono@ucla.edu

5. Subscription

Subscription should be sent to Acoustic Emission Group. Annual rate for 2012 is US \$111.00 including CD-ROM delivery, by priority mail in the U.S. and by air for Canada and elsewhere. For additional print copy, add \$40-49. Overseas orders must be paid in US currencies with a check drawn on a US bank. PayPal payment accepted. Inquire for individual (with institutional order) and bookseller discounts.

6. Advertisement

No advertisement will be accepted, but announcements for books, training courses and future meetings on AE will be included without charge.

Notes for Contributors

1. General

The Journal will publish contributions from all parts of the world and manuscripts for publication should be submitted to the Editor. Send by e-mail or to:

Professor Kanji Ono, Editor - JAE
Rm. 2121H, Engr. V, MSE Dept.
University of California
420 Westwood Plaza,
Los Angeles, California 90095-1595 USA
e-mail: kanjiono1@gmail.com

Authors of any AE related publications are encouraged to send a copy to:

Acoustic Emission Collection
Grainger Engineering Library
University of Illinois at Urbana-Champaign.
c/o: Mary C. Schlembach, Engineering Physics &
Astronomy Librarian
154 Grainger Engineering Library Information Center
1301 West Springfield Ave. Urbana, IL 61801
Email: schlemba@illinois.edu

Only papers not previously published will be accepted. Authors must agree to transfer the copyright to the Journal and not to publish elsewhere, the same paper submitted to and accepted by the Journal. A paper is acceptable if it is a revision of a governmental or organizational report, or if it is based on a paper published with limited distribution.

The language of the Journal is English. All papers should be written concisely and clearly.

2. Page Charges

No page charge is levied. The contents of CD-ROM will be supplied to the authors free of charge via Internet site.

3. Manuscript for Review

Manuscripts for review need only to be typed legibly; preferably, double-spaced on only one side of the page with wide margins. The title should be brief. An abstract of 100-200 words is needed for articles. Except for short communications, descriptive heading should be used to divide the paper into its component parts. Use the International System of Units (SI).

References to published literature should be quoted in the text citing authors and the year of publication or consecutive numbers. These are to be grouped together

at the end of the paper. Journal references should be arranged as below. Titles for journal or book articles are helpful for readers, but may be omitted.

H.L. Dunegan, D.O. Harris and C.A. Tatro (1968), *Eng. Fract. Mech.*, 1, 105-122.

Y. Krampfner, A. Kawamoto, K. Ono and A.T. Green (1975), "Acoustic Emission Characteristics of Cu Alloys under Low-Cycle Fatigue Conditions," NASA CR-134766, University of California, Los Angeles and Acoustic Emission Tech. Corp., Sacramento, April.

A.E. Lord, Jr. (1975), *Physical Acoustics: Principles and Methods*, vol. 11, eds. W. P. Mason and R. N. Thurston, Academic Press, New York, pp. 289-353.

Abbreviations of journal titles should follow those used in the ASM Metals Abstracts. In every case, authors' initials, appropriate volume and page numbers should be included. The title of the cited journal reference is optional.

Illustrations and tables should be planned to fit a single page width (165 mm or 6.5"). For the reviewing processes, these need not be of high quality, but submit glossy prints or equivalent electronic files with the final manuscript. Lines and letters should be legible.

4. Review

All manuscripts will be judged by qualified reviewer(s). Each paper is reviewed by one of the editors and may be sent for review by members of the Editorial Board. The Board member may seek another independent review. In case of disputes, the author may request other reviewers.

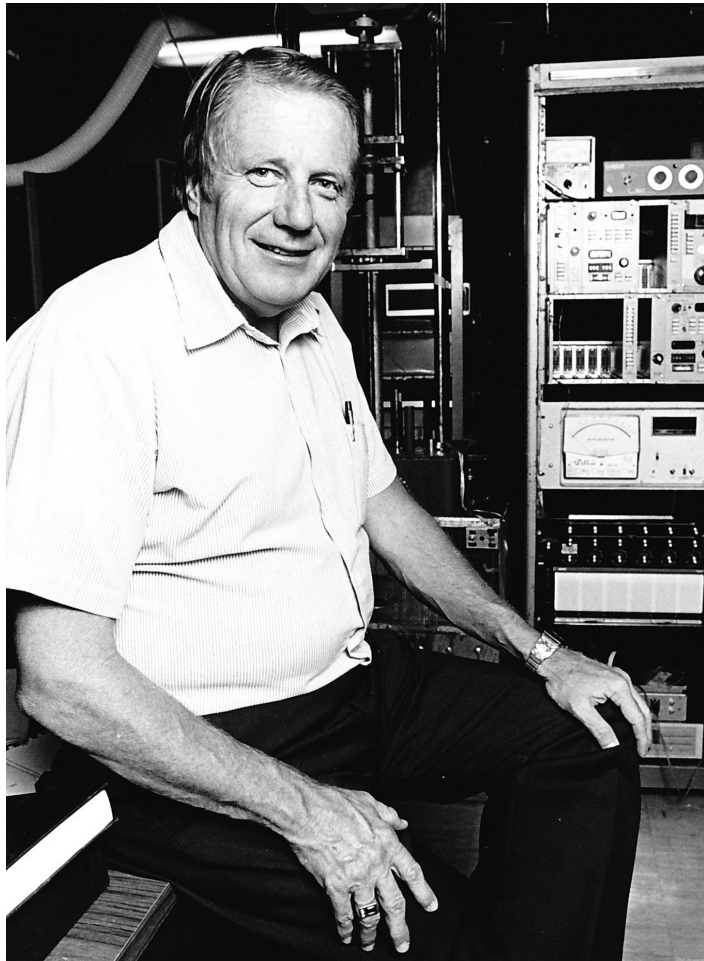
5. Electronic Media

This Journal will be primarily distributed electronically by CD-ROM. In order to expedite processing and minimize errors, the authors are requested to submit electronic files of the paper. On the INTERNET, you can send an MS Word file and the separate figure files (in JPEG or other formats) to "aegroup7@gmail.com".

6. Color Illustration

With the new format, authors are encouraged to use them.

In Memoriam



Steve H. Carpenter (1938 – 2012)

Steve H. Carpenter, John Evans Professor Emeritus, Department of Physics, University of Denver, of Littleton, CO, passed away June 10, 2012. He was 74. He was internationally known for his acoustic emission research, especially on the plastic deformation of metals and hydrogen effects and for resonance measurements of crack detection. He contributed over one hundred papers on AE alone. Born May 15, 1938, in Cedar City, UT, he has been an active member of the Church of Jesus Christ of Latter-day Saints and is survived by his wife, Marie, by his four children, Michelle, Kerri, Stephanie and Christopher, and 15 grandchildren.

After getting BS (1959) and PhD (1964) in Physics from University of Utah, Steve was at Aerojet General Corp. and joined the faculty of University of Denver in 1965, and has been full professor since 1974. From 1984, he also worked part time at Rocky Flats Plant. He gave 1987 University Lecture on AE entitled "Materials Cry when Stressed". He served as chairman of Physics Dept. and as head of DRI. Steve lectured in many countries as visiting professor/scientist, including New Zealand, Australia, Europe, USSR (now Belarus), China and Japan. He was a Fulbright-Hayes scholar and the recipient of the AEWG Achievement and Gold Medal Awards for outstanding contributions in scientific understanding of acoustic emission. Steve also received the AEWG Publication Award with Clint Heiple. He was a fellow of APS, a charter fellow of AEWG and also member of ASM International, TMS-AIME, and ASNT. Steve served as Chairman of AEWG in 1990-1992.

He will be dearly missed by his family, friends and colleagues from around the world.

Kanji Ono

Analysis of AE Signals during Scratch Test on the Coated Paperboard

Hiroyuki Kishi, Akio Matudoe, Ken Yamashita, Shigeru Nagasawa and Yasushi Fukuzawa

Department of Mechanical Engineering, Nagaoka University of Technology,
1603-1 Kamitomioka, Nagaoka, Niigata, 940-2188, Japan

Abstract

The deformation and fracture behavior of ink-printed layers on clay-coated paperboards were estimated using the scratch tester with the acoustic emission (AE) method. The designed scratch tester was custom-designed made for the paper. To investigate the boundary effects of coated and printed layers on the fiber matrix, two kinds of paperboards were prepared. Scratch tests were carried out using three types of machined spherical indenters with an AE transducer attached on the surface of the paperboard. The shape of compressed marks was observed by the laser microscopy. The measured AE signal was analyzed by amplitude and peak frequency and related to the deformation and fracture behaviors. The detected AE generation was divided into two zones: one corresponded to the micro-crack generation and the other was the generation of delamination. This AE generation behaviors varied with the indenter tip radius.

Keywords: Scratch test, paperboard, coated layer, micro-crack, delamination

Introduction

Paperboard has received much attention since it is easily and cheaply recycled. Further, in order to meet modern packaging needs, the coloring and texture have both been enhanced using different base papers and coating substances. Printed paperboard surfaces are damaged by scuffing and abrasions during careering operation in the shape forming and carton forming processes. The fracture behavior of printing surfaces needs to be easily quantified in order to evaluate their mechanical properties. Scratching tests are available to evaluate the mechanical properties of coating substances. These tests have been used to evaluate the strength of adhesion between a hard membrane and a matrix such as a deposited film or plating layer on a metallic surface [1]. It has also been reported that the scratching test is useful for evaluating the mechanical properties of paperboards [2, 3]. However limited results were obtained regarding the strength of a coated layer or paper substrate, based on the compressive load or width of scratching indent. These results could not be used to completely evaluate the adhesion strength of the printing layer. Furthermore, the relationship between the adhesion strength and the fracture behavior is not clear, and is insufficiently understood to confirm the effect of indenter shape on the fracture behavior during the scratching process.

Acoustic emission (AE) is useful in detecting fracture behavior in dynamically deformed materials. It reveals AE signals, which correspond to the deformation and fracture behaviors during the paperboard cutting process [4, 5]. AE signals during the cutting, ruling and embossing machining have been collected and analyzed in the same manner [6-9]. However, AE signals from surface fractures such as scuffs and abrasions have not been widely studied.

In this study, scratching tests were examined on two types of paperboards, a black-ink layer printed surface and a white-clay layer coated surface, with three scratching indenter diameters under constant scratching rates to investigate the abrasion phenomenon and the fracture behaviors within the very thin depth region of 50 μm . AE signals were detected in the respective

scratching tests, and the compressed traces were observed using microscopy. These signals and microscopic images were synchronized and verified to recognize the fracture behaviors of coated layers.

Experimental

Materials: The fundamental structure of the paperboard is displayed in Fig. 1. Paperboard is composed of a pulp fiber structure matrix and clay structured coated layer having a color printed layer and varnish. To investigate the boundary strength of the printed paperboard, two pattern paperboards were prepared for the scratch test. One was conventional coated paperboard of 230 g/m² nominal basis weight and 0.3 mm thickness. Specimens were cut to 100 mm in length and 15 mm in width. The second was printed paperboard of carbon black pigment with a varnish layer. It was the same size and weight of unprinted paperboard.

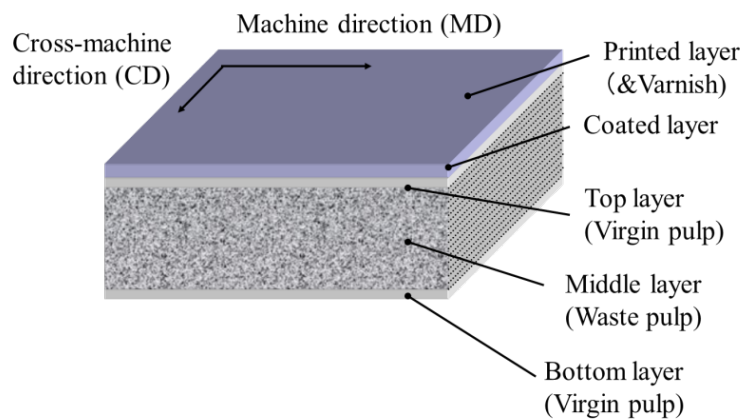


Fig. 1 Fundamental structure of the printed paperboard.

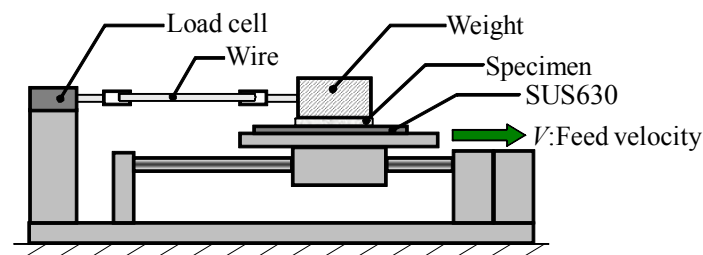


Fig. 2 Illustration of the dynamic friction test machine.

Estimation of mechanical properties: The machining strength of the base paperboard was examined using the tensile test along the machining direction (MD) and cross direction (CD) following the JIS P8113 specification. To estimate the friction coefficient between the surface of the paperboard and the indenter material, the dynamic friction test (horizontal method) was carried out with a specially designed machine. Figure 2 shows a schematic illustration of the frictional system.

Scratching test and AE detection system: Figure 3 shows a schematic illustration of scratching test configuration and AE system using the universal testing machine. The automatic X-stage was attached to the lower crosshead, and the specimen was placed upon the SUS630 steel faceplate embedded on the X-stage. Indenters were made of SKD tool steel and were shaped with

tip radii of 0.05, 0.1 and 0.5 mm. The spherical shaped indenters were attached below the upper crosshead with a load cell. The universal testing machine was operated by lowering the upper crosshead at a constant speed of 0.001 mm/s in the vertical direction and the X-stage was synchronized at a constant speed of 0.1 mm/s in the horizontal direction. The applied load was measured over the duration of indenter contacts with the surface for a penetration depth of 50 μm .

The AE waves were detected using AE sensors attached to the sides of the indenter. The AE detection and analysis system is shown in Fig. 4. The AE sensor has a resonance frequency of 220 kHz, and signal processing was operated with a 10 kHz high-pass filter and a 400 kHz low-pass filter. These examinations were performed at 296 K, 50% RH in the thermo-hygrostat room, and were repeated ten times. The scratching traces of the width and depth were observed using laser microscopy. The images of the scratching were synchronized to the time scale of the scratching and AE signals, and the elastic waves were related to the fracture behaviors. The scratching mark profiles were also traced from the surface texture measurements.

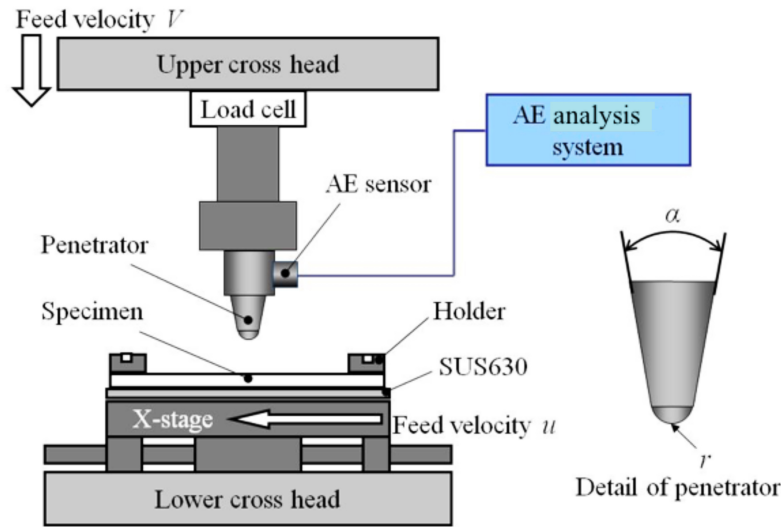


Fig. 3 Schematic illustration of the scratching test with the AE analysis system.

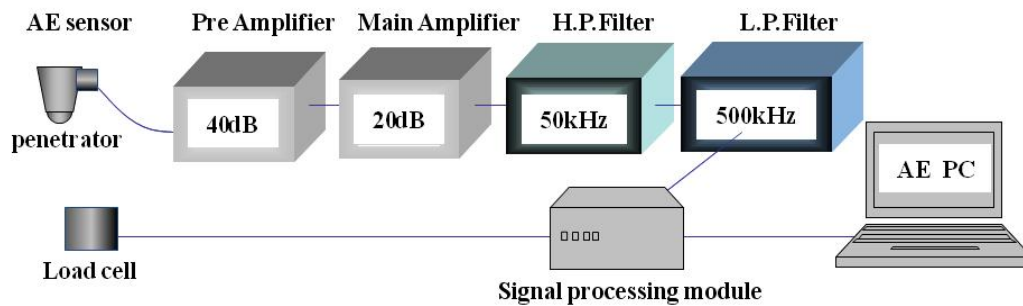


Fig. 4 Schematic illustration of the AE analysis system.

Results and Discussion

Characteristics of the paperboard: To evaluate the structure of the printed paperboard, the cross sectional view was observed using a laser microscope. The observed result is shown in Fig. 5. A paperboard is composed with a pulp fiber matrix, clay layer, printed ink layer and varnish. The clay is adhered on the pulp matrix with 10 to 20 μm thickness, and ink layer has a few μm thick-

ness. Figure 6 shows the surface conditions on each paperboard surface for (a) non-coated surface, (b) surface of the coated layer with clay and (c) printed surface with black ink (Carbon black) and adhered to the varnish on the ink layer. In this observation, the surface roughness could also be evaluated. The results are shown in Fig. 7. On the non-coated surface, many fibers are adhered and arrayed in one direction. The surface roughness became large. In the clay layer coated surface, as the space of the jointed fiber structure is filled with clay, the surface roughness become less than the non-coated surface. On the other hand, when the printed surfaces are covered with black carbon ink and varnish, the surface roughness depended on the printed ink elements, thickness and flatness. The surface roughness value of the printed paperboard improved much more than other surfaces. This indicates that, if the adhesion strength between the coated and printed ink layer could be estimated with some mechanical method, the printing condition could be evaluated on every printed paperboard. The scratch test and AE method was applied so this evaluation could be realized.

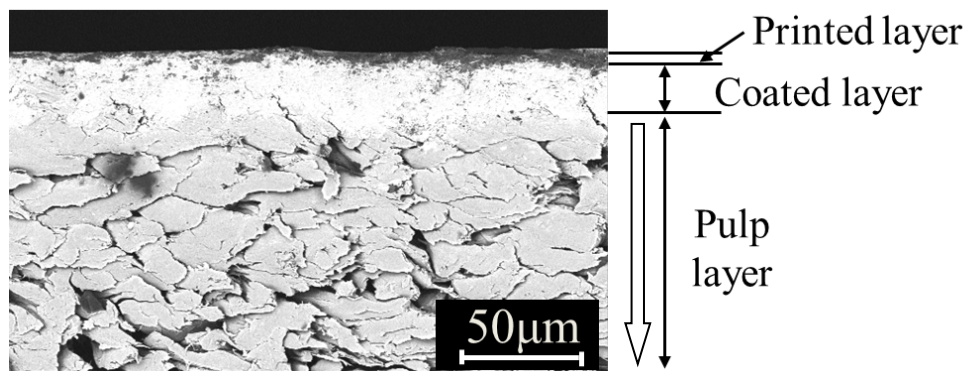
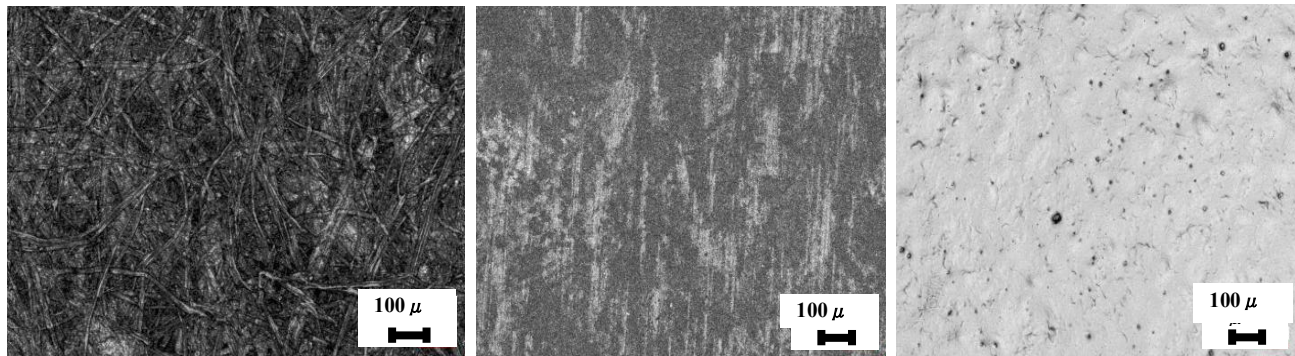


Fig. 5 Sectional view of the paperboard using a laser microscope.



(a) No coated surface,

(b) Coated surface,

(c) Printed surface,

Fig. 6 Observed top surface using a laser microscope.

Strength of paperboard: To evaluate the strength of the paperboard, the machine direction (MD) and cross-machine direction (CD) tensile tests were carried out on the coated and printed paperboard, using the tensile machine following the JIS-P8113 specification. The results are shown in Table 1. As the difference in tensile strength values between coated and printed paperboard for each tensile direction was small, the strength of the printed layer on the coating layer could not be evaluated using the tensile test.

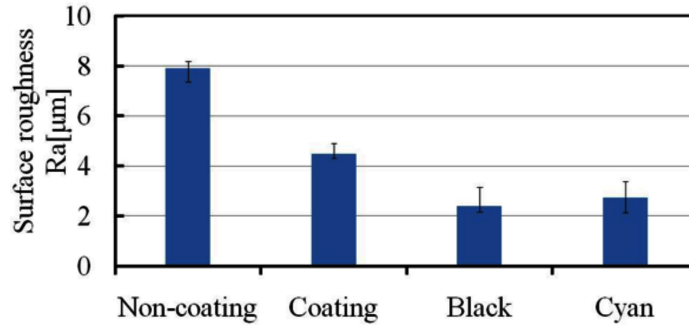


Fig. 7 Results of surface roughness of Ra.

Table 1. Tensile strength of coating and printed paperboard on MD and CD.

Material	Coated		Printed (black ink)	
	MD	CD	MD	CD
Tensile Strength (MPa)	36±3	19±1	36±2	19±1

Table 2 Results of friction test on coated and printed paperboard.

Material	Coating	Printed (black ink)
Dynamic friction coefficient	0.24 ~0.25	0.23 ~0.24

The results of the friction coefficient tests are shown in Table 2. The friction coefficient of printed paperboard is a little less than that of the coated paperboard. It was concluded that the surface roughness slightly affected the friction coefficient. As the scratch test could be carried out under small friction force, the deformed depth and width value seem to be almost independent to the surface conditions. Hence, when the indentation force is sufficiently small, the AE signal would be detected under a low noise level without any effects of compressed inside layer of paperboard.

Scratch test: Figure 8 shows a typical AE signal with the vertical forces on the same time scale. The corresponding scratching trace image on the clay layer is shown in Fig. 9 with an indenter radius of 0.1 mm.

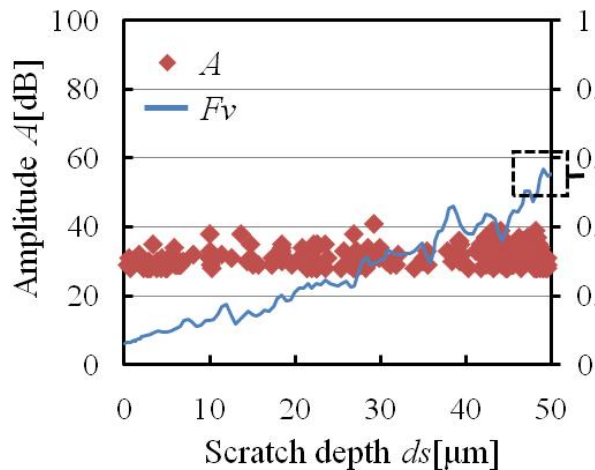


Fig. 8 Relation between AE amplitude, vertical force and scratch depth

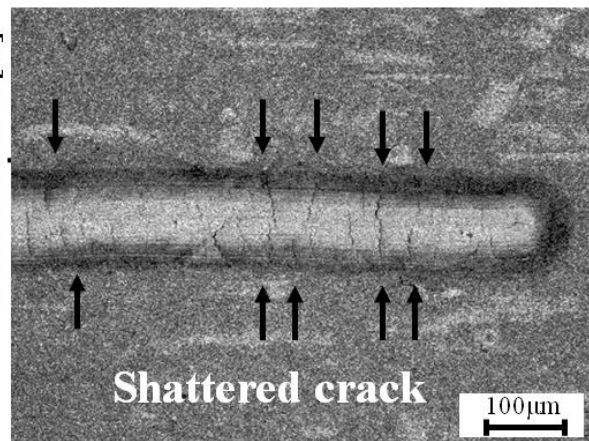


Fig. 9 Compressed figure of coating layer surface.

Coated paperboard: On the clay layer, AE signals were generated from the moment of indenter contact and continued during the scratching process. In the observed compressed surface, many cracks could be detected inside the scratched surface. This indicates that the AE signal resulted from the friction behavior of the clay layer surface and the flaking behavior of the boundary region of the fiber layer. To confirm the separation behavior of the coating layer from fiber matrix, a one-dimensional compression test was carried out with the same tensile machine on the printed layer. Figure 10 shows the penetrated hole shape after the compression test. Figure 10(a) and (b) respectively show the results when using a 0.5 and 0.1 mm radius tip. In Fig. 10(a), it is assumed that the hole surface was evenly deformed, but in case of the smaller tip radius, 10(b), some micro cracks could be detected on the hole wall. This shows that the printed and clay layer did not break during the compression process in the large tip. An AE signal could not be observed during these tests, but was detected during the scratch tests. Figure 11 shows the typical AE signal and vertical forces on the same time scale, and the corresponding scratching trace images on the printed layer are shown in Fig. 12 with an indenter radius of 0.1 mm.

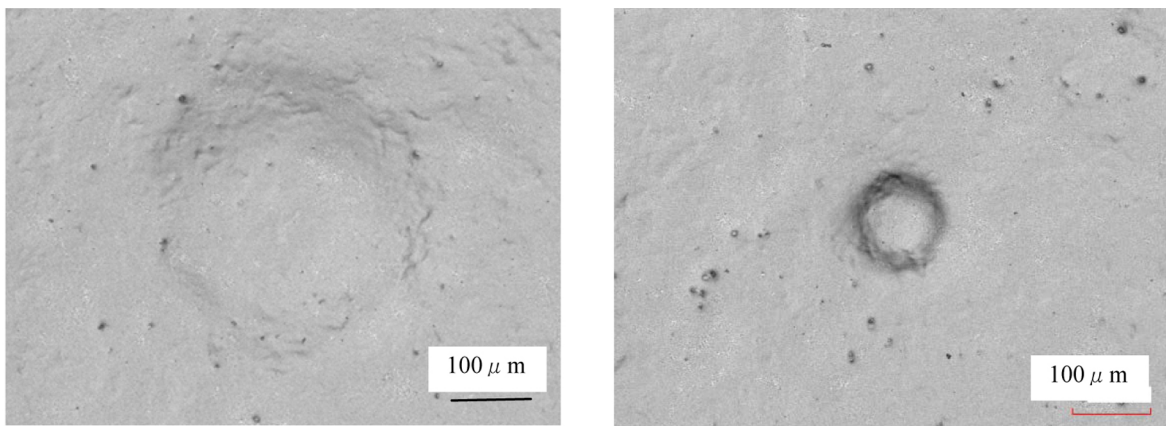


Fig. 10 Compressed hole with a tip radius of (a) 0.5 and (b) 0.1 mm.

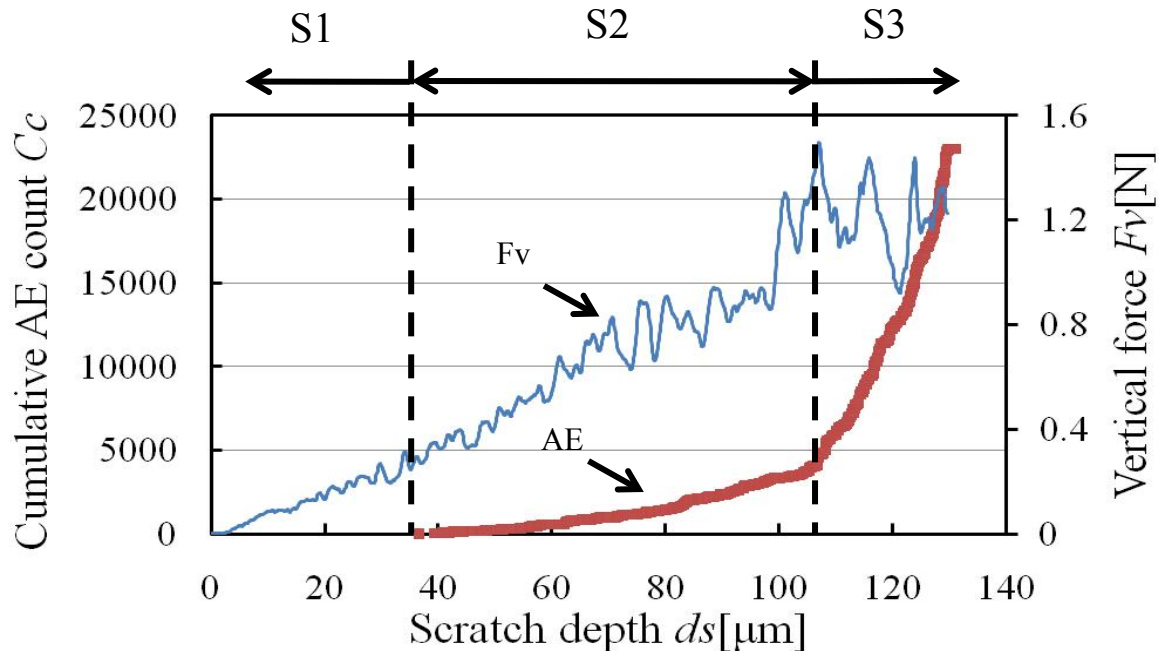


Fig. 11 Typical relation between AE generation and vertical forces during the scratch test on the printed paperboard. (tip radius of 0.1 mm)

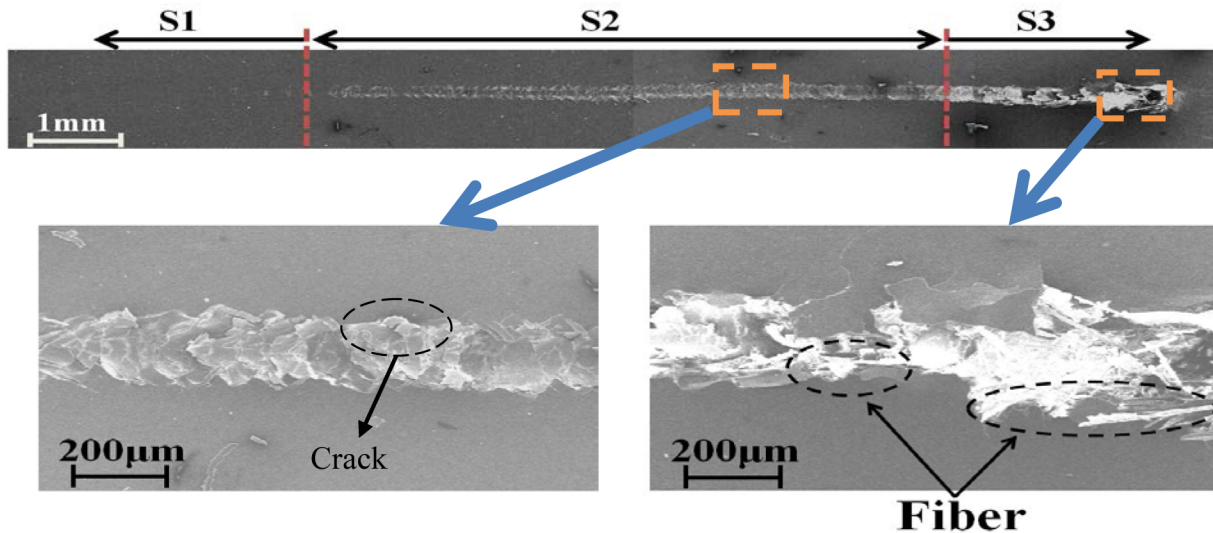


Fig. 12 Observed compressed trace image during scratch test on printed paperboard.

For indentation depth below $40\ \mu\text{m}$, no AE signal was observed (region S1). In the larger scratch depth region of 40 to $100\ \mu\text{m}$, AE was continuously generated (region S2). In this region many micro-cracks could be observed on the surface edge of the scratch mark, as shown in Fig. 12. When the scratched depth became larger than $100\ \mu\text{m}$ (region S3), AE signal generation increased abruptly. It is assumed that the AE behavior corresponded to the separation of the printed layer from the coating layer and the fracture of fibers.

Effects of indenter tip radius: The compressed trace shape of the scratched surface changed with the indenter tip radius. To investigate the effects of tip radius, three indenters were machined for this experiment, and they were compressed to a depth of $50\ \mu\text{m}$ (50 sec). The scratching tests were carried out on a printed surface with carbon black pigment ‘black’, using the indenters with a tip radius of (a) $0.5\ \text{mm}$, (b) $0.1\ \text{mm}$, and (c) $0.05\ \text{mm}$, respectively. Relationship between the scratch depth, AE amplitude, and vertical force, is shown in Fig. 13 for each indenter tip radius. Every vertical force increased proportionally with the penetrating depth, and values in the clay layer were always less than the printed layer. This indicates that the clay layer was harder and stronger than the printed layer. Figure 13(a) shows the result of the largest indenter radius ($0.5\ \text{mm}$). The AE signal could not be observed under this penetration depth, and only the compressed shape was impressed on the surface. On the compressed trace, no micro-cracks were observed by the estimation system. This indicated that the indenter penetrated into the printed layer smoothly in this large depth region.

In Fig. 13(b), when the indenter tip radius was $0.1\ \text{mm}$, the force curve increased with scratching depth more smoothly than the $0.5\ \text{mm}$ radius case. Further, the first AE signal detected, corresponding to micro-crack generation, could be observed around $40\ \mu\text{m}$, as shown in the SEM observation result. The observed AE amplitude existed between the region of 30 to $40\ \text{dB}$. In the smallest radius case ($0.05\ \text{mm}$), the force curve trended upwards, and AE signal was detected around a depth of $20\ \mu\text{m}$. The amplitude of the AE signals was observed in the wider region to be from 30 to $60\ \text{dB}$ (compared to the $0.1\ \text{mm}$ radius). Micro-cracks and delamination were detected in the same compressed region. Comparing the results of Fig. 13(b) and (c), the cracks are generated by a vertical force of over $0.3\ \text{N}$ and the corresponding AE signal could be observed in the amplitude range of 30 to $40\ \text{dB}$. On the other hand, delamination was also detected on the compressed trace surface. It appears that micro-cracks occurred during

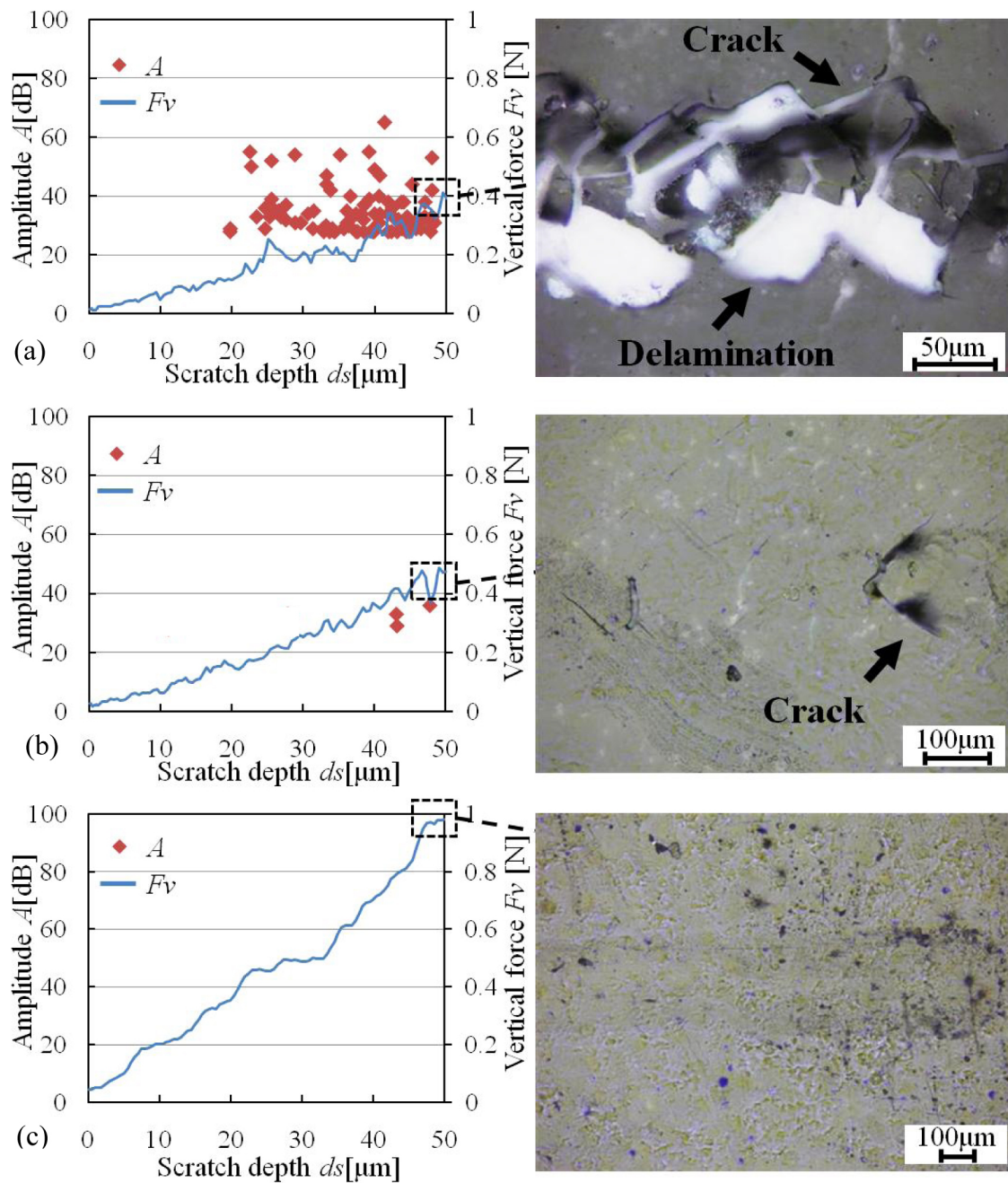


Fig. 13 AE signals and the vertical force in the scratching test and a typical image. (a) Black, $r=0.05\text{mm}$, (b) Black $r=0.1\text{mm}$, and (c) Black $r=0.5\text{mm}$.

delamination under this tip radius condition. Comparing Figs. 13(c) with (b), AE signals near 40 dB were not detected, and delamination did not occur in Fig. 13(b). It is obvious that the greater AE signals can be attributed to the occurrence of delamination. It was also confirmed that deformation without fracture could not be detected in the AE signals in Fig. 13(a). As a result, the AE signal amplitude on the coated paperboard can be classified into three ranges from the scratching test: elastic compressive deformation at less than 28 dB (A1), crack initiation in the range of 28 to 40 dB (A2) and the occurrence of delamination above 40 dB (A3).

It is assumed that the three deformation behaviors would be generated by:

1. Elastic deformation of the entire structure.

2. Plastic deformation of the printed surface layer after a yield point.
3. Break-down of the surface and clay layer.

The generation point of these deformation behaviors varied with indentation tip radius. The deformation behavior of advanced indentation surface area changed with the applied load surface area, which depended on the stress concentration. On the other hand, a notable number of AE signals are observed in Fig. 13(a). These AE signals can be classified by their amplitude, greater than 40 dB and less than 30 dB. In Fig. 13(b), the AE signals decreased drastically, and the upper level signals did not appear on this time scale. Despite the high vertical force, AE signals could not be detected, as shown in Fig. 13(c). The detected AE signal corresponded to accelerated motion phenomena such as brittle crack generation and delamination. As the results of AE generation behavior on Fig. 13(a), the AE signal generation level were divided into three region in comparison with the crack and delamination. The schematic AE generation behavior on small tip radius of 0.05 mm, is shown in Fig. 14. In the early stage (A1), there were no AE signals but only deformation was observed. Cracks generation occurred in the lower AE amplitude region (A2), and the delamination occurred higher amplitude region (A3), almost same indenter compressed depth area.

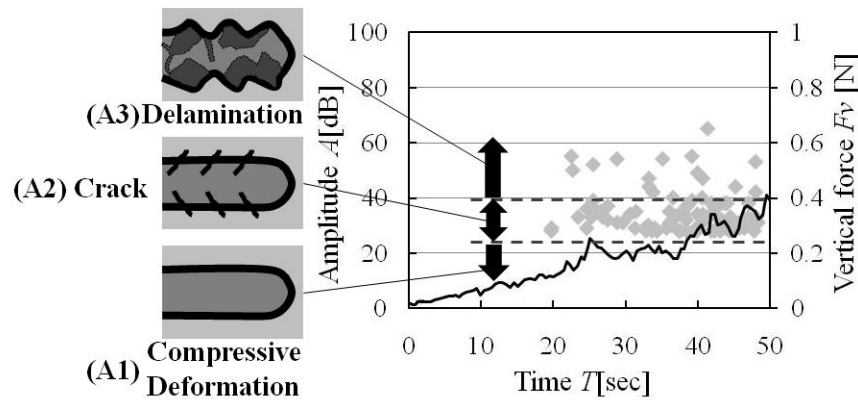


Fig. 14 The classification of the AE signals corresponding to fracture behaviors.

Summary

To evaluate the deformation and fracture behaviors of printed paperboard surfaces, the scratch test was carried out and the AE method was used simultaneously. The main results are summarized below.

1. The strength of the surface layer on the printed paperboard could not be evaluated using the normal mechanical method.
2. On the clay coating layer, many cracks occurred after a very low applied load, and many AE signal were detected at the same time.
3. During the compression test, micro-cracks were detected in the penetrated wall when a small indentation radius was used, but no AE signal was observed.
4. When an indentation radius of 0.1 mm was used AE signal generation began at 40 μm , which corresponded to the occurrence area of micro-cracks. Abrupt AE generation occurred over 100 μm , which was attributed to delamination.
5. The deformation and fracture behavior of surface printed layers changed with the indentation tip radius, and the generation of AE signals also varied with changes in fracture behavior. It was considered that stress concentration effects in the advanced deformation surface area, depended on the micro-crack occurrence phenomena.

6. The AE signals could be detected and categorized into three regions in order of amplitude, and on the same time scale corresponded to compressive deformation, crack initiation, and delamination. It was revealed that the AE method provides an effective evaluation of the printed layers on paperboards.

References

- [1] N. Shinke, A. Yonekura, M. Takuma, H. Yoshida, and S. Kawai, "Evaluation of Fracture Characteristics of TiN Ceramics Film with Scratch Testing", *JSME International Journal Series A*, **44** (1), 2001, 123-129.
- [2] D. Arai, "Adhesion Strength Evaluation Method for Thin Films Using Micro-Scratch Tester", *The Surface Finishing Society of Japan*, **58**, Feb. 1992, 295.
- [3] S. Suzuki, M. Murayama, S. Nagasawa, Y. Fukuzawa, I. Katayama, "Estimation of Mechanical Properties of White-Coated Paperboard by Scratch Test and Push Shear Test", *J. Jpn. Soc. Technol. Plast.*, **46**-530, Mar. 2005, 230-234.
- [4] S. Suzuki, Y. Fukuzawa, S. Nagasawa, I. Katayama and H. Iijima, "Acoustic Emission Characteristics on Variation of Cutter Tip Thickness during Cutter Indentation on Paperboard," *J. JSTP*, **46**, 2005, 1061-1065.
- [5] A. Sadamoto, T. Yamaguchi, S. Nagasawa, Y. Fukuzawa, D. Yamagushi, I. Katayama, "Sensing for Machining Using Sound Radiated by Paperboard Die Cutting," *J. Jpn. Soc. Precision Eng.*, **68** (12), 2002, 1554-1558.
- [6] H. Katayama, "Point of Paper Container Processing Technology," *Japan TAPPI Journal*, **62** 2008, 115-120.
- [7] S. Suzuki, Y. Fukuzawa, S. Nagasawa, H. Sakayori, I. Katayama, "Characterization of Paperboard Deformation by AE," *Progress in AE XI*, The Jpn. Soc. Non-Destructive Inspection, 2002, pp. 37-44.
- [8] S. Nagasawa, Y. Fukuzawa, T. Hine, I. Katayama, A. Yoshizawa, T. Furumi, "Effects of Edge Clearance and Board Thickness on Shearing Characteristic of Paperboard Diecutting," *J. Jpn. Soc. Technol. Plast.*, **41**-469, 2000, 126-130.
- [9] S. Nagasawa, Y. Fukuzawa, D. Yamaguchi, S. Nagae, I. Katayama, and A. Yoshizawa, "Deformation Characteristics on Creasing of Paperboard Under Shallow Indentation," *Advances in Fracture Research*, ICF100202OR(CD-ROM), Elsevier Science, 2001.

Acoustic Emission Related to Drought Stress Response of Four Deciduous Broad-Leaved Woody Species

Sabine Rosner

Institute of Botany, BOKU, Vienna, Austria

Abstract

The aim of the present study was to test if acoustic emission (AE) detected on leaves and stem surfaces of young trees gives information about stomatal closure and thus about a tree's performance under drought stress. Two diffuse-porous (conduit size shows little variation within an annual ring) and two ring-porous (conduits in earlywood are much bigger than in latewood) species were tested for their reaction to drought stress. In both diffuse (*Populus alba* L., *Fagus sylvatica* L.) and ring-porous (*Fraxinus excelsior* L., *Quercus pubescens* WILLD.) species, AE activity of leaves ceased when stomatal conductance reached minimum values. In some species, AE rate and amplitude distribution can be a useful parameter to discriminate between AE resulting from conductivity loss and from other processes such as shrinkage and wilting. AE activity of stem wood showed a clear pattern with two amplitude peaks in ring-porous species whereas no such pattern was found in diffuse-porous species. The results are discussed with respect to the species-specific reaction to drought stress.

Keywords: Drought stress, stomata response, stomatal closure, vulnerability to cavitation

1. Introduction

Knowledge about the hydraulic performance of long-living plants under drought stress is of high importance with respect to global change. Water is transported from the roots to the leaves of the crown in a metastable state (i.e. under tension) [1]. Due to this metastable state the water column inside the small conduits is likely to break when the water tension increases above a certain level. Breakage of the water columns (cavitation) produces acoustic emission (AE) in the high frequency range [2, 3]. Cavitation induces a reduction in the hydraulic conductivity of the plant, which impairs water supply of the transpiring leaves. Cavitation would result in total loss of hydraulic conductance in the absence of any regulative mechanisms of transpiration [4]. Plants therefore respond by closing their stomata, which should reduce transpiration and keep the water potential (i.e. tension) above the species-specific cavitation threshold value, preventing further loss of conductivity [1]. Limitation in gaseous exchange due to stomatal closure restricts, however, simultaneous carbon assimilation by the plant and thus growth [5].

Drought stress induced stomatal behavior differs widely among species and may be a critical factor in the regulation of survival and mortality during extended drought periods and thus for species distribution [6]. Plants fall into two categories according stomatal regulation of transpiration; "drought avoiders of the saving type" (isohydric plants) and "drought avoiders of the spending type" (anisohydric plants) [7]. Isohydric plants maintain high leaf water potentials during the day for extended periods of drought, thus preventing cavitation. Anisohydric species let midday leaf water potentials decline as soil water potential declines with drought. They can keep their stomata open because their xylem is either less prone to cavitation or they are able to compensate rapidly for water loss, due to a deep and large root system [6, 8]. Ring-porous woody species, with a band of wide vessels in earlywood followed by much narrower vessels in latewood should be successful if plants maintain similar water status throughout the season. This strategy would

however be less essential for diffuse-porous species, with narrower conduits, packed more densely per unit wood area [10].

The control of stomata under conditions of drought is achieved due to chemical or hydraulic signaling processes [4, 11]. ABA (abscisic acid) is the most likely candidate for chemical root-to-shoot signaling [12]. It might however also be possible that a combination of both hydraulic and chemical signaling is important in the stomatal regulation in plants [4, 9, 13]. Stomata have to respond directly to some component of the leaf water status because a lack of response to distal shoot water potentials would be dangerous and potentially fatal to plants. Moreover, ABA transport will be limited under severe drought by increased hydraulic resistance in the xylem [14]. Stomata might not respond to leaf water potential *per se* [15], but to factors affecting leaf water status, such as cavitation, which decreases the hydraulic conductivity in stems [13, 16] and leaves [17, 18]. The onset of stomatal closure is in some species reported to coincide well with the onset of cavitation [19-21], whereas in other species no such relationship was found [16]. AE counting combined with water potential measurements is a reliable method to detect cavitations in different plant organs, but provides little information on the loss in hydraulic conductance [16, 22]. If conductivity loss is a trigger for stomatal closure [13, 18-20], AE testing with subsequent feature analysis could give additional information on stomata's responses to drought stress [22].

Within this study, the response of stomata to drought stress induced cavitation in leaves and in stem wood was tested in two ring-porous and two diffuse-porous woody species with different demands on water availability. The aim was to test if AE testing combined with AE feature analysis gives information about the species-specific strategy to avoid severe losses in hydraulic conductivity.

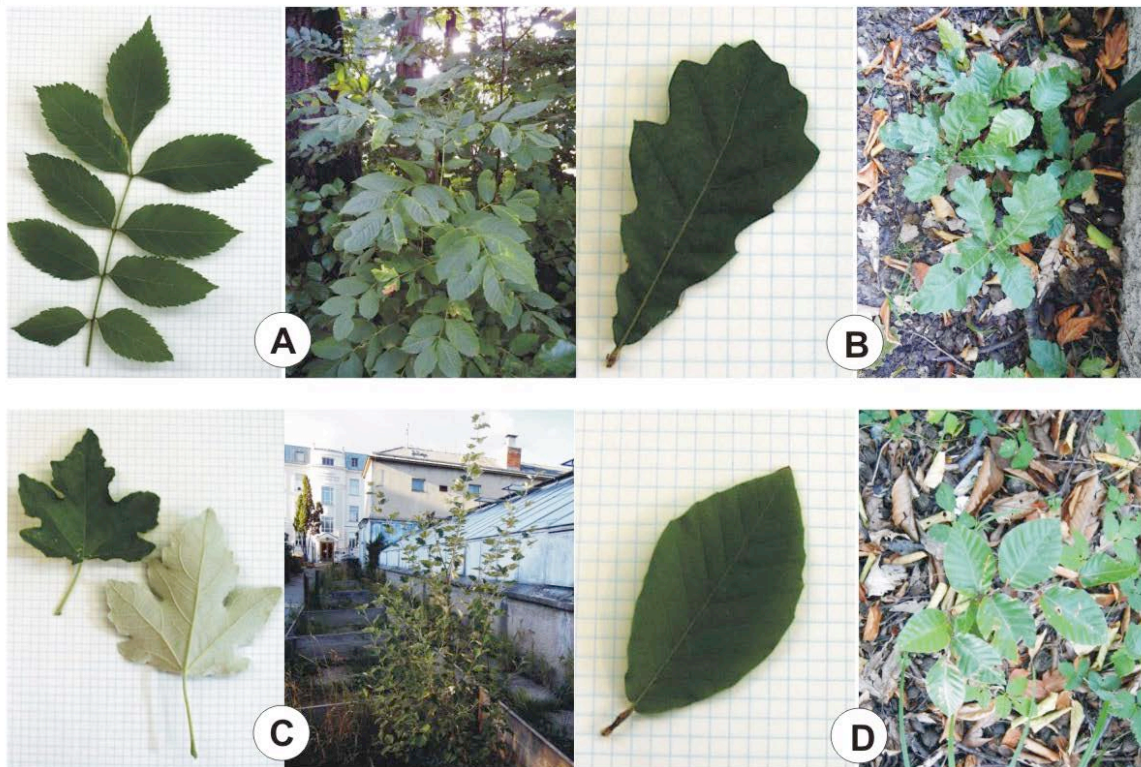


Fig. 1. Species investigated were European ash (*Fraxinus excelsior* L.) (A), Downey oak (*Quercus pubescens* WILLD.) (B), silver poplar (*Populus alba* L.) (C) and European beech (*Fagus sylvatica* L.) (D).

2. Experiment

2.1 Plant Material

Young trees (2-3 years) grown in the botanical garden at BOKU, Vienna, were harvested during the morning hours and re-hydrated for 24 hours in the dark in order to refill all sapwood conduits with free water (Fig. 1). Species used within this study were European (common) ash (*Fraxinus excelsior* L.), occurring in riparian mixed forests along big rivers in central Europe, Downey oak (*Quercus pubescens* WILLD.), a submediterranean species native to southern and eastern Europe, silver poplar (*Populus alba* L.), a relatively drought tolerant riparian pioneer species, and European (common) beech (*Fagus sylvatica* L.), which can be found in pure as well as in mixed stands across central and northern Europe [23]. Common ash and Downey oak are ring-porous woody species, whereas silver poplar and beech are diffuse-porous woody species. In ring-porous wood, wide conduits are produced in the early growing season and narrow conduits during the rest of the growing season. In diffuse-porous species, all water-conducting elements have quite similar diameters and are evenly spread across the annual ring.

2.2 Bench drying experiment

Whole above-ground biomass of young trees was dehydrated at the laboratory bench (“bench drying”) at ambient conditions (25°C, 50% r.h.) for 24 h. During dehydration, AE from leaves and the main trunk as well as changes in water potential and stomatal conductance of leaves were acquired. Prior to the dehydration experiment, cut ends of the small trees were tightly wrapped in Parafilm® (Pechiney Plastic Packaging, Chicago, IL, USA).



Fig. 2. Experimental setup: Drought stress experiment on silver poplar (*Populus alba* L.) shoot.

AE testing was performed with the μ DiSP™ digital AE system from Physical Acoustics Corporation (PAC, Princeton Jct, USA). Preamplifiers (40 dB) were used in connection with WD transducers (100 to 1000 kHz). One WD transducer was positioned on the upper side of the leaf, at the proximal third of the leaf midrib [24], except in common beech, where better results were obtained when the sensor was positioned on the lower side of the leaf. AE signals were recorded with a detection threshold of 32 dB (0 dB = 1 μ V input). Data analysis was done with Vallen VisualAE™ software (Vallen Systeme GmbH, Munich, Germany).

Bark was thereafter removed from the young stems and the second WD transducer was positioned directly on the wood surface (Fig. 2). Silicone grease served as a coupling agent (Wacker, Burghausen, Germany). Open cut faces, which were not covered by the transducer, were sealed

with Parafilm®. All preparation steps were performed while the main parts of the small trees were covered by dark polyethylene sheets in order to avoid moisture loss due to transpiration.

During dehydration, water potential was measured at intervals of 10-120 min by means of a plant water status console (“Scholander pressure bomb”, Soilmoisture Equipment Corp. Santa Barbara, CA, USA). Continuous changes in stomatal conductance in leaves were measured with the AP4 leaf porometer (Delta-T Devices Ltd, Cambridge, GB) in intervals of 1-20 min.

2.3 Anatomical investigations

Wood sections and sections from the midrib of leaves (20 µm) were produced on a sliding microtome (Jung Reichert, Germany). Sections were stained with Astrablue/Safranin dye and mounted in Entellan (Merck, Darmstadt, Germany). Microscopic views of tree stems and leaf midribs were produced by means of a Leica DM4000M microscope interfaced with a digital camera and Leica image analysis software (Leica Microsystems Wetzlar GmbH, Germany).

3. Results and Discussion

3.1 AE characteristics of tree stems

AE from tree stems of ring-porous species (ash and oak) showed different amplitude distribution compared to diffuse-porous species (poplar and beech) (Fig. 3). In ash and oak, a distinct amplitude cluster could be detected, whereas poplar and beech wood had a similar amplitude distribution throughout the whole dehydration experiment. The amplitude cluster of ring-porous species coincided with their first AE rate peak. A distinct rate peak was also found in poplar but not in common beech. It is suggested that AE of the first peak were produced from the breakage of the water columns in conducting elements, whereas AE detected thereafter represents sound produced from capillary action in wood fibers (non-water conducting wood elements), wood shrinkage or crack formation [25]. In Fig. 3, AE results are shown only for the first 10 hours of dehydration, since AE production thereafter is of no physiological relevance, meaning that most of the hydraulic conductivity was lost already by then.

Dehydration of whole plants on the laboratory bench simulates extreme drought stress. Out in the field, all these reactions will proceed much slower and plants will have the chance to refill emptied conduits during the nighttime provided that water availability from the ground is sufficient. Nevertheless, AE monitored from living, extremely drought stressed trees should show a similar pattern. If it is assumed that almost all hydraulic conductivity is lost when the AE rate reaches again very low values after the first AE rate peak, decreasing AE rates indicate a beginning of dramatic loss in hydraulic conductance. Common ash and especially silver poplar developed sufficient mechanisms to prevent further cavitation in stem wood, when most of the hydraulic conductivity was lost already, whereas Downey oak and common beech exhibited quite high AE rates after the first rate peak.

3.2 AE characteristics of leaves

Stomatal closure and cavitation started right from the beginning of the drought stress experiment [19-21]. AE rate of drought stressed leaves showed a distinct peak during the first two hours of dehydration [26], which coincided with a first AE amplitude cluster in both ring- and diffuse-porous species and the course of stomatal conductance (Figs. 4 and 5). At the AE rate peak, single hits with highest amplitudes were detected. Highest amplitudes were found in oak leaves, which might be explained either by bigger lumen diameters of the sound producing sources, the xylem conduits [22, 27, 28], or by less attenuation of the (denser) plant tissue.

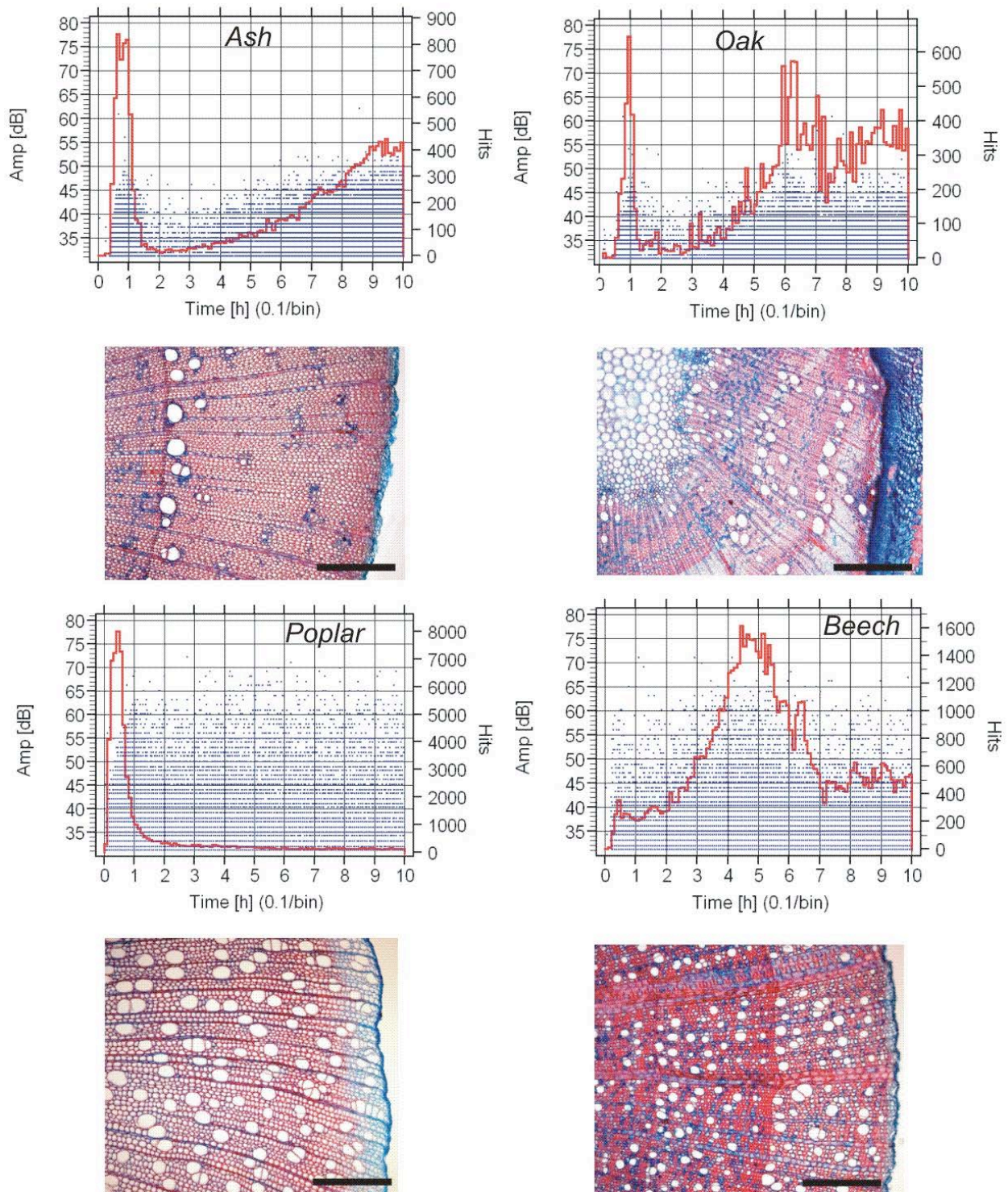


Fig. 3. AE amplitudes and AE rates/10 min (red lines) received from stems of different broad-leaved species (common ash, Downey oak, silver poplar, common beech) plotted against time. Microscopic views of transverse cuts (20 μ m) of the same stems where the AE transducers were positioned are shown below the AE plots. The reference bars represent 250 μ m.

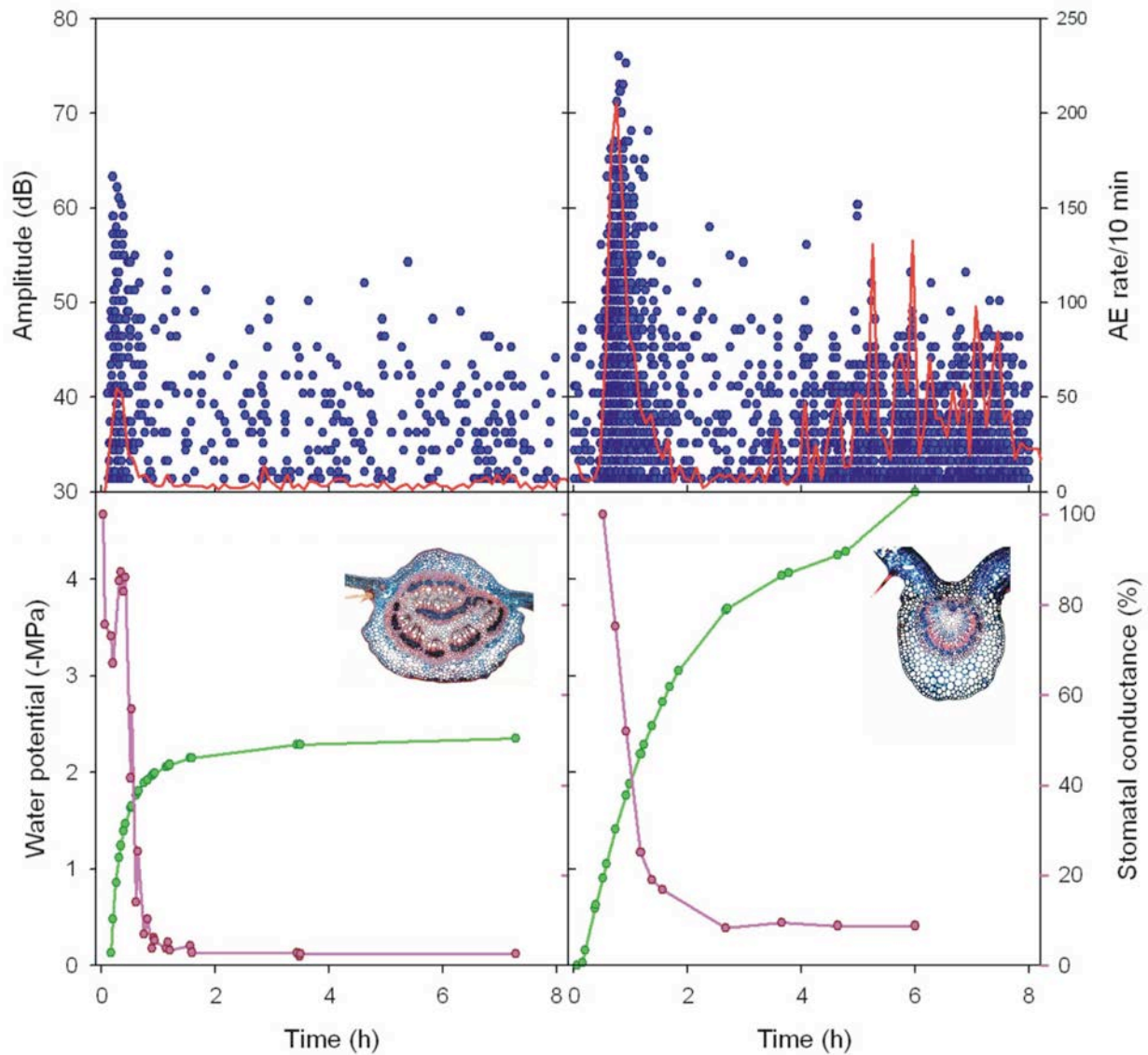


Fig. 4. AE amplitudes (blue dots) and AE rates/10 min (red lines) received from leaves of two different ring-porous species plotted against time. The courses of the water potential (green line) and the stomatal conductance (pink line, in % of the maximum value measured during dehydration) and a microscopic view of the leaf midrib (where the transducer was positioned) for each species are shown below the corresponding AE plots. On the left side, results for common ash (*Fraxinus excelsior* L.), and on the right side, results for Downey oak (*Quercus pubescens* WILLD.) are presented.

(Total) stomatal closure is reached when stomatal conductance approaches towards minimum percentage values. Thereafter, AE rate decreased rapidly, but increased again when leaves started to wilt. Most of the hydraulic conductivity was probably lost already by then. In common ash and silver poplar, stomatal closure proceeded very fast and was quite efficient; after the first peak, AE rate did not increase within the next 6 hours. In common beech and Downey oak, however, AE rate increased again after another hour of dehydration. These results coincided with the drop in the water potential: whereas Downey oak and common beech reached quite negative water potentials between -5 and -4 MPa, water potentials of silver poplar and common ash did not drop below -2.5 MPa, although leaves started to wilt already.

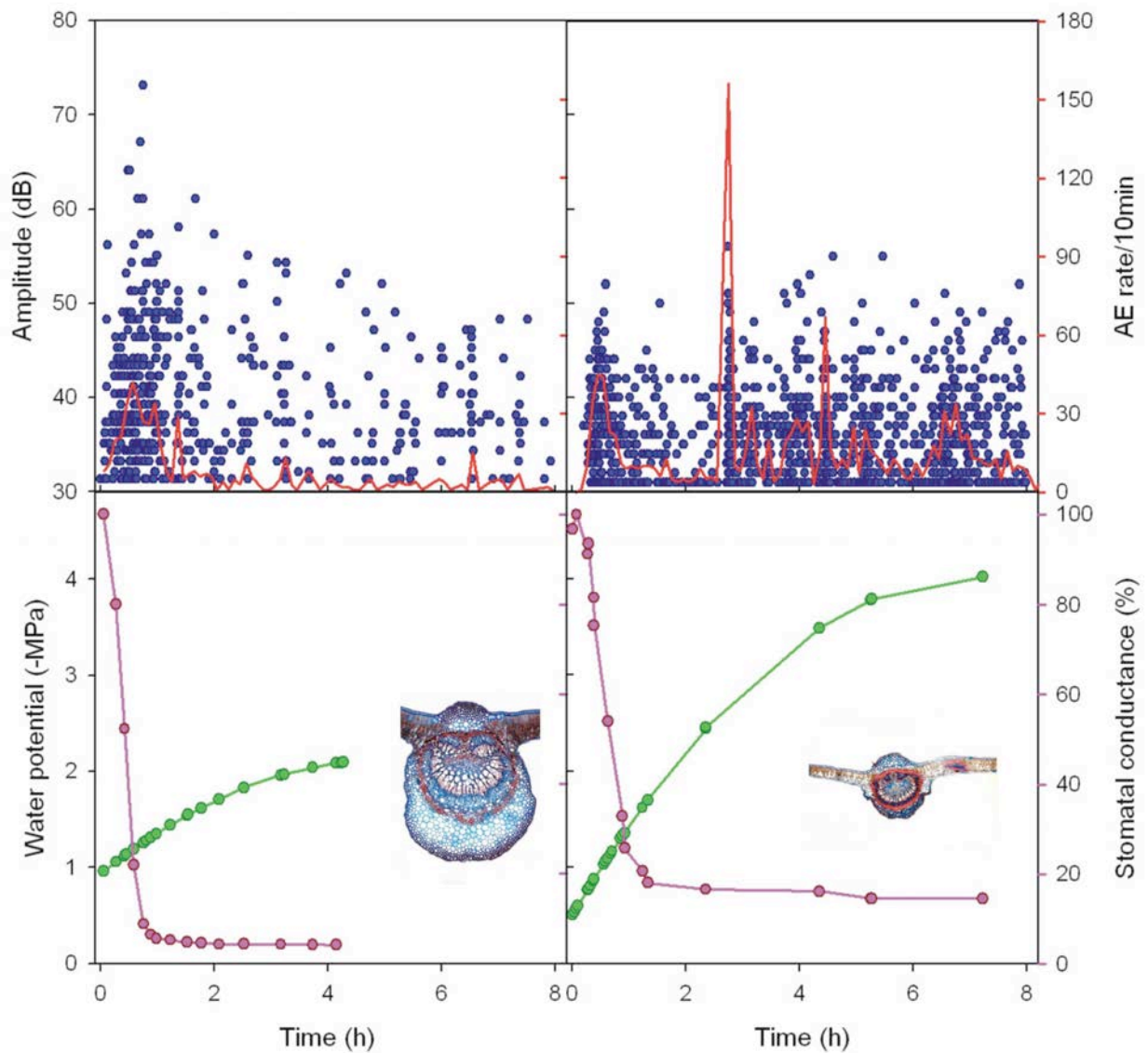


Fig. 5. AE amplitudes (blue dots) and AE rates/10 min (red lines) received from leaves of two different diffuse-porous species plotted against time. The courses of the water potential (green line) and the stomatal conductance (pink line, in % of the maximum value measured during dehydration) and a microscopic view of the leaf midrib (where the transducer was positioned) for each species are shown below the corresponding AE plots. On the left side results for silver poplar (*Populus alba* L.), and on the right side results for common beech (*Fagus sylvatica* L.) are presented.

Thus, a decline in the AE rate of leaves after a previous rise indicates that plants reacted to drought stress by closing their stomata. Common ash and silver poplar had the most efficient strategy to prevent transpiration, since water potential reached a quite stable high (less negative) value; furthermore, in silver poplar no increase in AE rate of stems could be detected after total stomatal closure.

3.3 Drought avoiders of the spending or of the saving type?

Based on these preliminary results, common ash and silver poplar would be classified as isohydric species; as “drought avoiders of the saving type”, whereas common beech and Downey oak as anisohydric species; as “drought avoiders of the spending type” [7].

Isohydric plants have a high degree of stomatal control enabling them to maintain high leaf water potentials during the day for extended periods of drought, thus preventing cavitation. Anisohydric plants can keep their stomata open because their conducting elements in the xylem are either less prone to cavitation or they compensate for water loss due to a deep and large root system [6, 8, 9]. A deep root system is typical for oak species [23]; however, ring-porous species, with a band of wide vessels in the earlywood followed by much narrower vessels in latewood, should show in theory isohydric behavior of stomatal control, i.e., a tighter stomatal regulation of transpiration to extremes in vapor pressure than diffuse-porous species and conifers [15, 29-32].

Although isohydry would be less beneficial in diffuse-porous species [10], silver poplar exhibited an efficient stomatal control, thus a near-isohydric behavior in order to avoid cavitation and keep the water potential at high (less negative) values. It has been reported in literature that diffuse-porous species with a tendency to half-ring-porosity, such as beech (*Fagus sylvatica* L.) and poplars (*Populus* spp.), might exhibit isohydric [33-35] as well as anisohydric behavior [30].

4. Conclusions

At least in some broad-leafed species, AE rate and amplitude distribution of dehydrating stems can be a useful parameter to discriminate between AE resulting from conductivity loss and from other processes such as cavitation from non-conducting wood elements, wood shrinkage and wilting. The pattern of AE activity of dehydrating stem wood was strongly related to wood anatomy, where ring-porous species show clear clusters, which can be separated by their amplitude characteristics. AE activity of dehydrating leaves gives information on the (a) onset of stomatal closure and (b) achievement of maximum stomatal closure. Together with water potential measurements, AE activity and peak amplitude analysis should give thus a quite good insight into the species-specific strategy to survive drought stress.

Acknowledgements

This study was financed by the Austrian Science Fund (FWF): V146-B16.

References

1. MT Tyree and MH Zimmermann. 2002. Xylem structure and the ascent of sap, 2nd edition., Berlin, Germany: Springer.
2. MT Tyree and JS Sperry. 1989a. Vulnerability of xylem to cavitation and embolism. Ann. Rev. Plant Physiol. Plant Molecular Biol. Vol.40, pp 19–38.
3. MT Tyree and JS Sperry. 1989b. Characterization and propagation of acoustic emission signals in woody plants: towards an improved acoustic emission counter. Plant Cell Environ. Vol. 12, pp 371-382.
4. JP Comstock. 2002. Hydraulic and chemical signalling in the control of stomatal conductance and transpiration. J. Exp. Bot. Vol. 53, pp 195-200.

5. DW Lawlor and G Cornic. 2002. Photosynthetic carbon assimilation and associated metabolism in relation to water deficits in higher plants. *Plant Cell Environ.* Vol.25, pp 275-294.
6. N McDowell, WT Pockaman, CD Allen, DD Breshears, N Cobb, T Kolb, J Plaut, J Sperry, A West, DG Williams, EA Ypez. 2008. Mechanisms of plant survival and mortality during drought: why do some plants survive while others succumb to drought? *New Phytol.* Vol. 178, pp 719-739.
7. J Levitt. 1980. Responses of plants to environmental stresses. Vol. II. Water, radiation, salt and other stresses. Academic Press, New York, 606 p.
8. MM Chaves. 1991. Effects of water deficits on carbon assimilation. *J. Exp. Bot.* Vol. 42, pp 1-16.
9. F Tardieu and WJ Davies. 1992. Stomatal response to abscisic acid is a function of current plant water status. *Plant Physiol.* Vol. 98, pp 540-545.
10. UG Hacke, JS Sperry, JK Wheeler and L Castro. 2006. Scaling of angiosperm xylem structure with safety and efficiency. *Tree Physiol.* Vol. 26, pp 689-701.
11. R Lössch and JD Tenhunen. 1981. Stomatal responses to humidity – phenomenon and mechanism. In: *Stomatal physiology*. Eds PG Jarvis and TA Mansfield. Cambridge Univ-Press, Cambridge, pp 137-161.
12. DP Schachtman and J.Q.D Goodger. 2008. Chemical root to shoot signaling under drought. *Trends Plant Sci.* Vol. 13, pp 281-287.
13. A Pou, J Flexas del Mar, M Alsina, J Bota, C Carambula, F de Herralde, J Galmés, C Levi-solo, M Jiménez, M Ribas-Carbó, D Rusjan, F Secchi, M Tomàs, Z Zsófi and H Medrano. 2008. Adjustment of water use efficiency by stomatal regulation during drought and recovery in the drought-adapted *Vitis* hybrid Richter-110 (*V. berlandieri* x *V. rupestris*). *Physiol. Plant.* Vol. 134, pp 313-323.
14. C Fort, F Muller, P Label, A Granier and E Dreyer. 1998. Stomatal conductance, growth and root signaling in *Betula pendula* seedlings subjected to partial soil drying. *Tree Physiol.* Vol. 18, pp 769-776.
15. H Cochard, L Coll, X Le Roux and T Améglio. 2002. Unraveling the effects of plant hydraulics on stomatal closure during water stress in walnut. *Plant Physiol.* Vol. 128, pp 282-290.
16. A Nardini and S Salleo. 2000. Limitation of stomatal conductance by hydraulic traits: sensing or preventing xylem cavitation? *Trees* Vol. 15, pp 14-24.
17. A Nardini, S Salleo and S Andri. 2005. Circadian regulation of leaf hydraulic conductance in sunflower (*Helianthus annuus*). *Plant Cell Environm.* Vol. 28, pp 750-759.
18. TJ Brodribb and H Cochard. 2009. Hydraulic failure defines the recovery and point of death in water-stressed conifers. *Plant Physiol.* Vol. 149, pp 575-584.
19. S Salleo, A Nardini, F Pitt and MA Lo Gullo. 2000. Xylem cavitation and hydraulic control of stomatal conductance in laurel (*Laurus nobilis* L.) *Plant Cell Environm.* Vol. 23, pp 71-79.
20. A Nardini, MT Tyree and S Salleo. 2001. Xylem cavitation in the leaf of *Prunus laurocerasus* and its impact on leaf hydraulics. *Plant Physiol.* Vol. 125, pp 1700-1709.
21. A Chouzouri and HR Schultz. 2006. Hydraulic anatomy, cavitation susceptibility and gas-exchange of several grapevine cultivars of different geographic origin. *Acta Hort.* Vol. 689, pp 325-332.
22. S Rosner, A Klein, R Wimmer and B Karlsson. 2006. Extraction of features from ultrasound acoustic emissions: a tool to assess the hydraulic vulnerability of Norway spruce trunkwood ? *New Phytol.* Vol. 171, pp 105-116.

23. H Mayer. 1984. *Waldbau auf soziologisch-ökologischer Grundlage*. Gustav Fischer Verlag, Stuttgart NY, 514pp.
24. SB Kikuta, MA LoGullo, MA Nardini, H Richter and S Salleo. 1997. Ultrasound acoustic emissions from dehydrating leaves of deciduous and evergreen trees. *Plant, Cell Environm.* Vol. 20, pp 1381-1390.
25. S Wolkerstorfer, S Rosner and P Hietz. 2012. An improved method and data analysis for ultrasound acoustic emissions and xylem vulnerability in conifer wood. *Physiologia Plant.* (*in press*: DOI: 10.1111/j.1399-3054.2012.01605.x)
26. HR Schultz. 2003. Differences in hydraulic architecture account for near-isohydric and anisohydric behaviour of two field-grown *Vitis vinifera* L. cultivars during drought. *Plant Cell Environ.* Vol. 26, pp 1393-1405.
27. DM Johnson, FC Meinzer, DR Woodruff and KA McCulloh. 2009. Leaf xylem embolism, detected acoustically and by cryo-SEM, corresponds to decreases in leaf hydraulic conductance in four evergreen species. *Plant Cell Environ.* Vol. 32, pp 828-836.
28. S. Mayr and S Rosner. 2011. Cavitation in dehydrating xylem of *Picea abies*: energy properties of ultrasonic emissions reflect tracheid dimensions. *Tree Physiol.* 31, pp 59-68.
29. P Trifilò, F Raimondo, A Nardini, MA Lo Gullo and S Salleo. 2004. Drought resistance of *Ailanthus altissima*: root hydraulics and water relations. *Tree Physiol.* Vol. 24, pp 107-114.
30. A Geßler, C Keitel, J Kreuzwieser, R Matyssek, W Seiler and H Rennenberg. 2007. Potential risks for European beech (*Fagus sylvatica* L.) in a changing climate. *Trees* Vol. 21, pp 1-11.
31. SE Bush, DE Pataki, AG Hultine, AG West, JS Sperry and JR Ehlinger. 2008. Wood anatomy constrain stomatal responses to atmospheric vapor pressure deficit in irrigated urban trees. *Oecologia* Vol. 156, pp 13-20.
32. H Taneda and JS Sperry. 2008. A case study of water transport in co-occurring ring- versus diffuse-porous trees: contrasts in water-status, conducting capacity, cavitation and vessel refilling. *Tree Physiol.* Vol. 28, pp 1641-1651.
33. U Hacke and JJ Sauter. 1995. Vulnerability of xylem to embolism in relation to leaf water potential and stomatal conductance in *Fagus sylvatica* f. *purpurea* and *Populus balsamifera*. *J. Exp. Bot.* Vol. 46, pp 1177-1183.
34. D Lemoine, H Cochard and A Granier. 2002. Within crown variation in hydraulic architecture in beech (*Fagus sylvatica* L.): evidence for a stomatal control of xylem embolism. *Ann. For. Sci.* Vol. 59, pp 19-27.
35. A Gallé and U Feller. 2007. Changes of photosynthetic traits in beech saplings (*Fagus sylvatica*) under severe drought stress and during recovery. *Physiologia Plant.* Vol. 131, pp 412-421.

Micro-mechanical Damage in Tool Steels Analyzed by Acoustic Emission Technique

Ingrid Picas¹, Eva Martinez-Gonzalez², Daniel Casellas¹ and Jordi Romeu²

¹ Fundació CTM Centre Tecnològic, Av. Bases de Manresa 1, 08242 Manresa, Spain

² Laboratori d'Enginyeria Acústica i Mecànica (LEAM), Departament d'Enginyeria Mecànica (DEM)m Universitat Politècnica de Catalunya (UPC), EUETIB, Urgell 187, 08036 Barcelona, Spain

Abstract

The carbides in tool steels act as hard particles and dictate the wear resistance. The origin of failure of these steels is mostly related with the carbide cracking, as a nucleation site of final cracks. This paper shows the acoustic emission (AE) signals related with the nucleation (carbide cracking) and the crack growth (in the metallic matrix) during a monotonic bending test of a tool steel obtained by ingot metallurgy routes (DIN 1.2379). The paper presents a relationship between the frequency spectrum of AE signals obtained and the microscopic images during the test.

Introduction

Understanding the fracture events of tools in the manufacturing process is crucial to foresee tool lifetime and develop tool steels with improved mechanical performance [1]. Failure detection helps in predicting premature failure of the tool, which directly affects the price of the manufactured part. The interaction between the two main constituents of the tool steel microstructures: the primary carbides and the metallic matrix, determines their mechanical properties and the performance of tools.

Carbides play an important role in the mechanical response of these steels, since they act as hard particles and dictate the wear resistance. The origin of fracture and fatigue cracking of cast tool steels is usually associated with the primary carbides, which break under the applied stress and act as initiation sites [2]. However, there is a lack of knowledge about the mechanical behavior of carbides in tool steels, mainly due to the experimental difficulties associated with its measurement [3]. With conventional non-destructive testing methods, it is difficult to identify the moment when carbides begin to break and even more difficult to identify when the crack starts to propagate in the metal matrix because it is necessary to stop the test and inspect the trial.

The acoustic emission (AE) technique “listens” what is happening within the material during the test; because the AE is based on the phenomenon of transient elastic-waves generated due to a rapid release of strain energy caused by a structural alteration in the solid material. So, it serves as a powerful method to monitor progressive damage accumulation in different materials [4-7].

Only scarce data exist in the literature concerning the application of AE for the analysis of micro-damage of tool steels. Fukaura et al. [8, 9] and Yokoi et al. [10] are amongst the few authors, who employed this technique to determine the progression of internal damage on tool steels. These authors successfully detected AE signals from carbide cracking; the signals started at a certain applied load and the event rates continually increased until reaching the fracture stress. No continuous AE signals existed (related with plastic deformation processes), but that numerous burst emissions at close intervals were recorded instead. Yamada and Wakayama [11]

observed a rapid increase in cumulative AE energy prior to the final fracture and attributed this phenomenon to the main crack formation. They also distinguished two types of AE signal: one was a burst-type signal with high frequency and the other was a low frequency and continuous-type signal. The former was considered to be emitted from micro-cracking while the latter was due to plastic deformation of the binder phase.

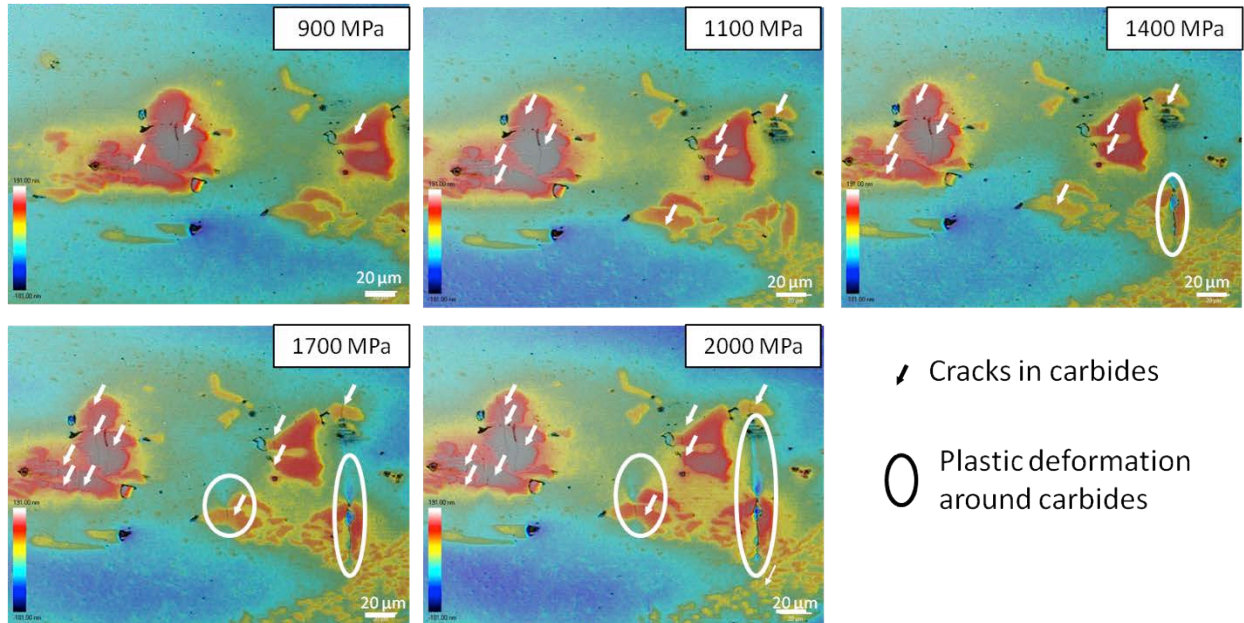


Fig. 1. Example of broken carbides observed by means of CM (Confocal Microscopy) in the tensile stressed surface of DIN 1.2379 specimens. [12]

In a previous work, Martinez et al. [12] applied AE in a three-point bending test. Three different zones were distinguished during a bending test in a tool steel sample with regard to the AE events, and the stress level at which cracking carbides start was also found (Fig. 1). This work dealt with real time detection of elastic waves signals generated during a monotonic mechanical test, a three-point bending test, in case of a tool steel named DIN 1.2379. The main aim is to cluster the recorded signals during the test, based on the spectral characteristics, and correlate the classification with the failure mechanism that generates the reference waveform, identified by microstructural inspection of the specimen.

Experimental Procedure

The material studied was a conventional ledeburitic high-carbon, high-chromium tool steel named DIN 1.2379 (AISI D2) obtained by ingot metallurgy routes. The main alloying elements found in their chemical composition are shown in Table 1.

Table 1. Main alloying elements in the chemical composition of DIN 1.2379 (in wt %).

Steel	C	Cr	Mo	W	V
1.2379	1.5-1.6	11.0-12.0	0.6-0.8	-	0.9-1.0

Prismatic samples were machined from forged and annealed commercial bars parallel to the forging direction. Heat treatment was applied to the sample material in order to get a hardness level of 60 – 62 HRC, as summarized in Table 2. The bending strength, σ^R , was reported by

Picas et al. [1], and the fracture toughness, K_{IC} , was determined as specified in the ASTM E 399-90 standard. These values are also shown in Table 2.

Table 2. Heat treatment and obtained hardness and bending strength.

Steel	Austenitizing (oil quench)	Tempering	HRC	σ^R [MPa] [1]	K_{IC} [MPa·m ^{1/2}]
1.2379	1050 °C for 30 min	550 °C for 2 h (x2)	60 - 62	2847 ± 96	28

Fracture tests were performed by means of three-point bending tests with a constant span length of 40 mm. Samples dimensions were 8 mm x 6 mm x 120 mm. Samples were mechanically ground and their corners were rounded to avoid stress magnifications and remove any defect introduced during sample preparation. Faces subject to tensile stress during three-point bending tests were carefully polished to mirror-like finish using colloidal silica particles with approximately 40 nm sizes.

Microstructural inspection of the samples was carried out using a FE-SEM (Field Emission Scanning Electron Microscope) and the fracture tests were performed in a universal testing machine using an articulated fixture to minimize torsion effects. The applied displacement rate was 0.01 mm/min.

The test was monitored using sensors of a fixed resonance frequency of 700 kHz (VS700D, Vallen System GmbH). Three pre-amplifiers with a 34 dB gain of the same brand were also used (AEP4). Acoustic Emission (AE) signals were recorded and analyzed using the Vallen Systeme GmbH AMSY5 analyzer. The experimental set-up is schematized in Fig. 2.

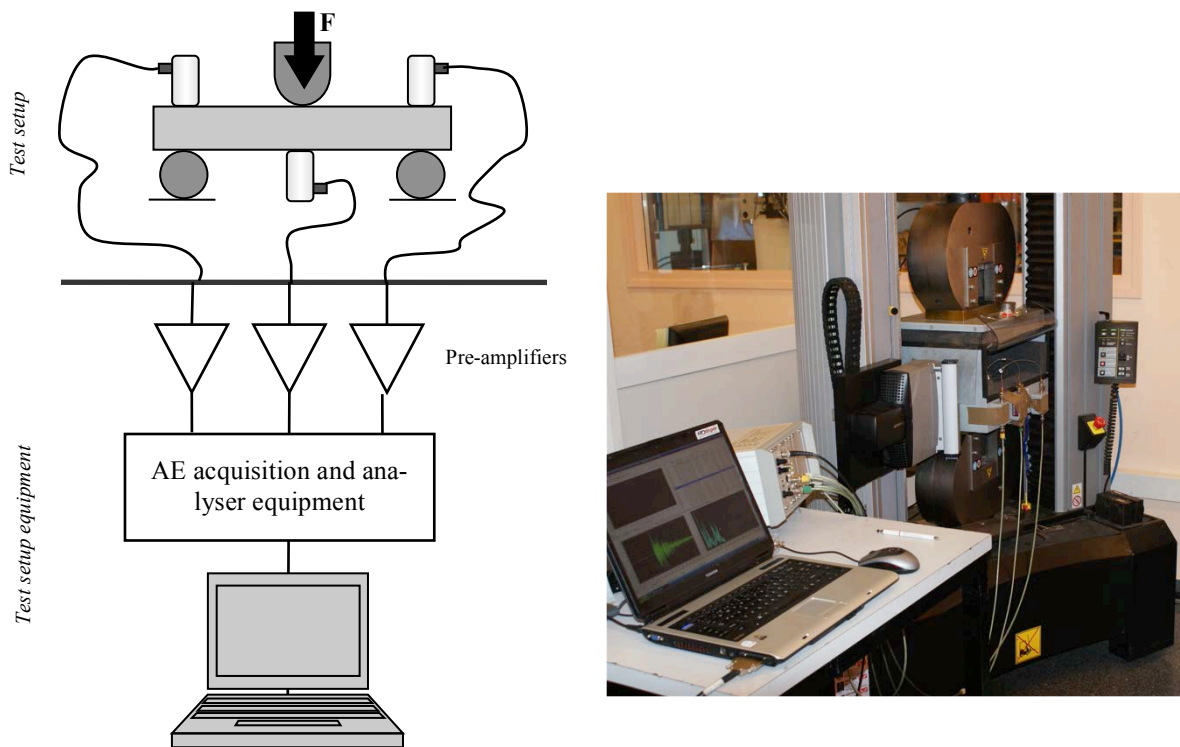


Fig. 2. Experimental set-up for the AE-monitored bending tests.

During the measurements, digital filters of 95-850 kHz were applied. In order to avoid the multiple reflections due the small dimensions of the specimen, only the first counts of each hit were analyzed as purely representative of micro-damage phenomena.

Using this set-up configuration, 3 to 5 samples of each material were monitored until final fracture. Later, 2 to 3 samples were analyzed by means of stepwise loading (Fig. 3a)) in order to relate each type of AE characteristic signal pattern to the generated damage in the microstructure. Surface inspection of samples was carried out after each load increment in a Confocal Microscope (CM) (Fig. 3b)).

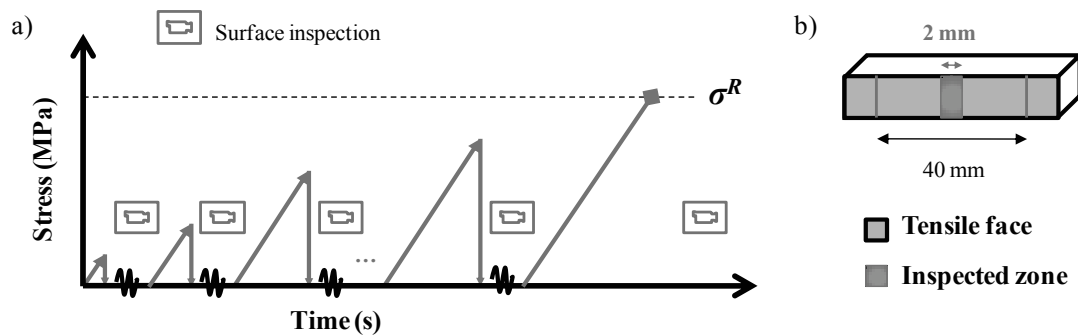


Fig. 3. a) Stepwise loading to final fracture of the sample, σ^R ; b) schema of the micrographically inspected zone of samples.

Results and Discussion

A. Microstructural Analysis.

In Fig. 4 the microstructure of the studied steel can be observed. The microstructure was markedly anisotropic, with large carbide stringers forming bands in the metallic matrix. The primary carbides of this steel were rather large and had irregular morphologies.

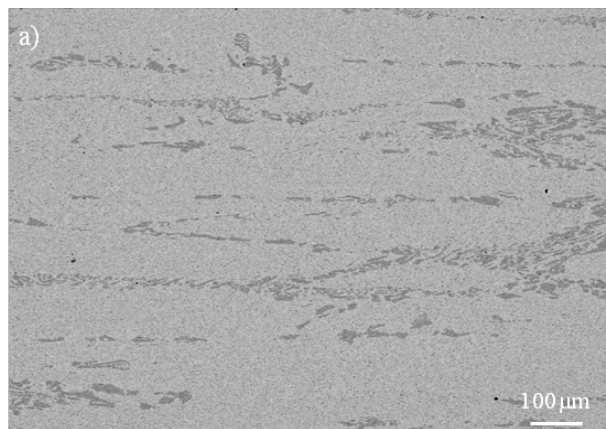


Fig. 4. Microstructure of tool steel, DIN 1.2379.

B.1. Identification of Characteristic AE Signal Patterns in Bending Tests of 1.2379 under Monotonic Loading.

Figure 5a) shows the results of the AE signals registered in bending tests under monotonic loading for 1.2379. This diagram plots the cumulative number of hits as a function of the stress applied and the location of each signal on the sample surface (with respect to the center of the sample). As it can be observed, the highest amount of signals was generated at the center of the

sample (X-Loc. = 0 in Fig. 5a), where the applied stress was the highest during the three-point bending test, and the quantity of emitted signal continuously increased with the applied stress. The Y axis refers to the applied stress and the Z axis to the cumulated number of hits registered).

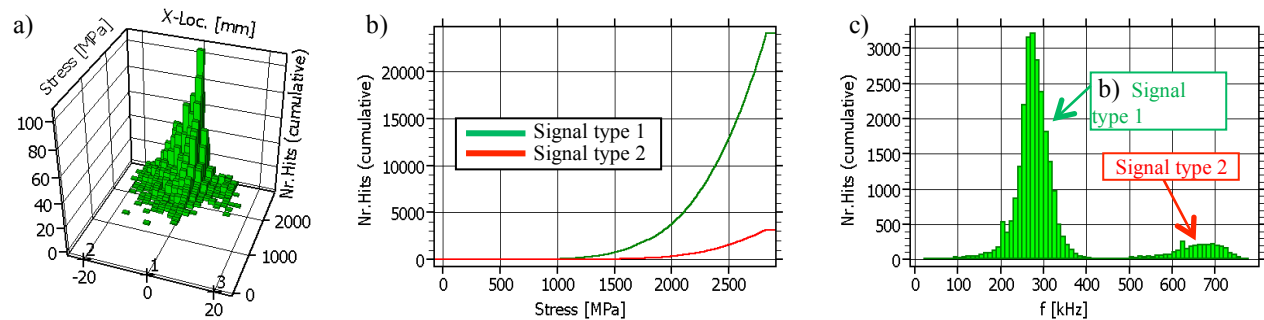


Fig. 5. a) Cumulative number of hits (Z) as a function of the stress applied during the bending test (Y) and the location of the signals (X). b) Cumulative number of hits vs. applied stress during a monotonic bending test in which two different types of AE signals could be identified; c) Cumulative number of hits vs. frequency for the two signals registered.

A closer look to the AE signals obtained allowed us to classify them into two categories depending on the frequency spectrum. As shown in Fig. 5b), at the beginning of the test, no AE signals were detected. At a certain applied stress level, a first type of AE signal started to be recorded (green line in Fig. 5b)). These signals were not continuous but they were emitted in a burst-like manner, and the quantity of hits registered increased along with the applied stress. Later as the stress increased, a second type of signal was distinguished (red line in Fig. 5b)). This signal also increased in number of hits together with the applied stress, but at the moment of final fracture it attained lower hit values than the first signal type.

These two signals identified not only differed because of the number of hits, but also they had very different characteristic frequencies and waveforms. As shown in Fig. 5c), the first type of signal had a main frequency of 280 kHz, while the frequency of the second type was around 650 kHz. These different frequency ranges of the two signals indicated that the responsible mechanisms for emitting them took place at different velocities in the microstructure, i.e. the second mechanism would be much faster than the first one.

B.2. Relationship between AE Signals and Micro-Damage during Bending Tests of 1.2379 a under Monotonic Loading.

Stepwise bending tests permitted to inspect the tensile surface of the samples at different increasing stress levels, and correlate the registered AE data (namely the two different identified signal types) to the micro-damage observed in the microstructure.

In Fig. 6a) the cumulative number of hits as a function of the stress applied at the first load step can be observed. This test was stopped at 800 MPa, when the first signals were detected. These signals indicated the same pattern as those of type 1 identified before. However, no damage could be observed at the sample surface, as shown in Fig. 7a); it is likely that something happened at the microstructure but it could not be detected yet by microscopy.

The next test was stopped at 2200 MPa, when a higher quantity of AE signal was detected. Practically all signals responded to the characteristics of the type 1 identified before, and a small number of hits of characteristic type 2 signals were first detected (Fig. 6b)). In this case, the first

cracks were observed in the microstructure and they were located at primary carbides (Fig. 6b) and c)). However, despite many carbides were broken, none of the cracks nucleated from them were observed to have started propagating through the metallic matrix surrounding the broken carbide. The last load step at 2600 MPa revealed a notable increase of the type 2 signal, even though the number of hits of the type 1 had not ceased to increase (Fig. 6c)), as well as the number of broken carbides in the sample. The inspection of the surface permitted to observe that some cracks had now propagated through the metallic matrix (Fig. 7d)).

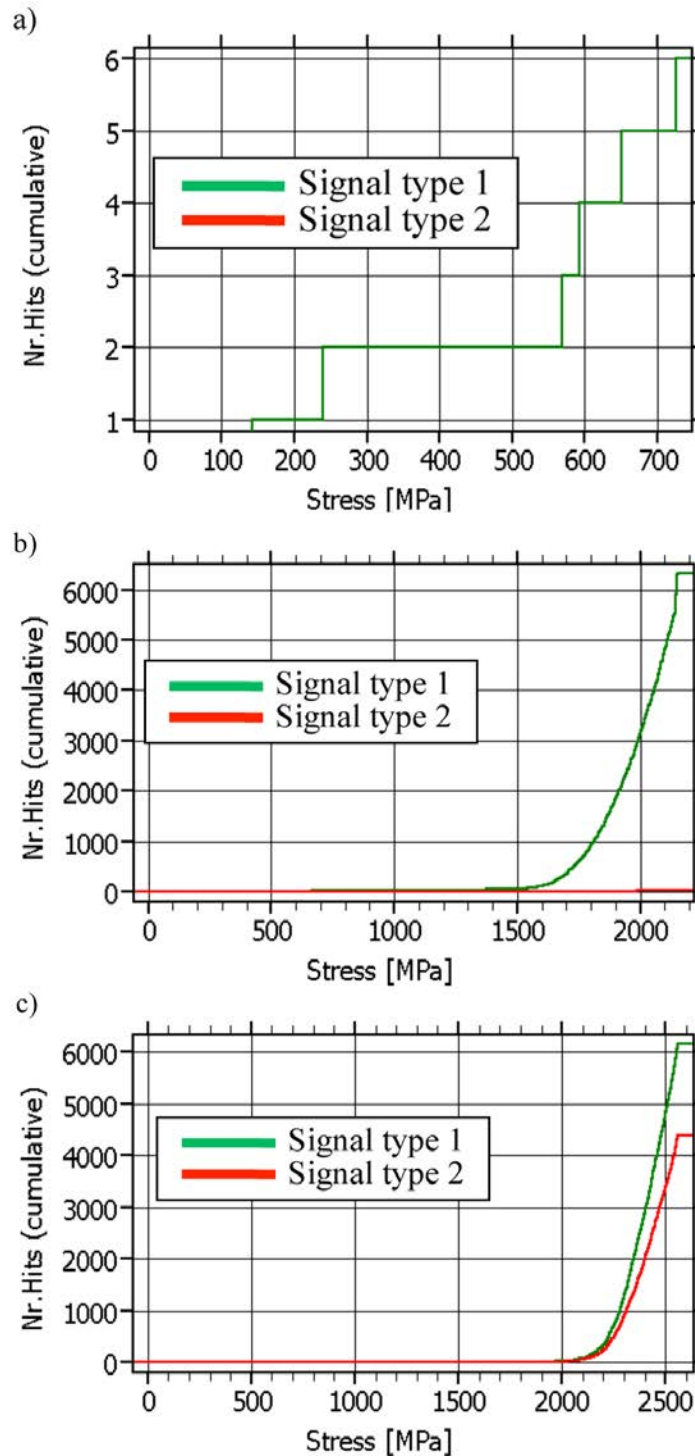


Fig. 6. AE signal results of monotonic stepwise tests in 1.2379 in terms of the cumulated number of hits vs applied stress to: a) 800 MPa; b) 2200 MPa and c) 2600 MPa.

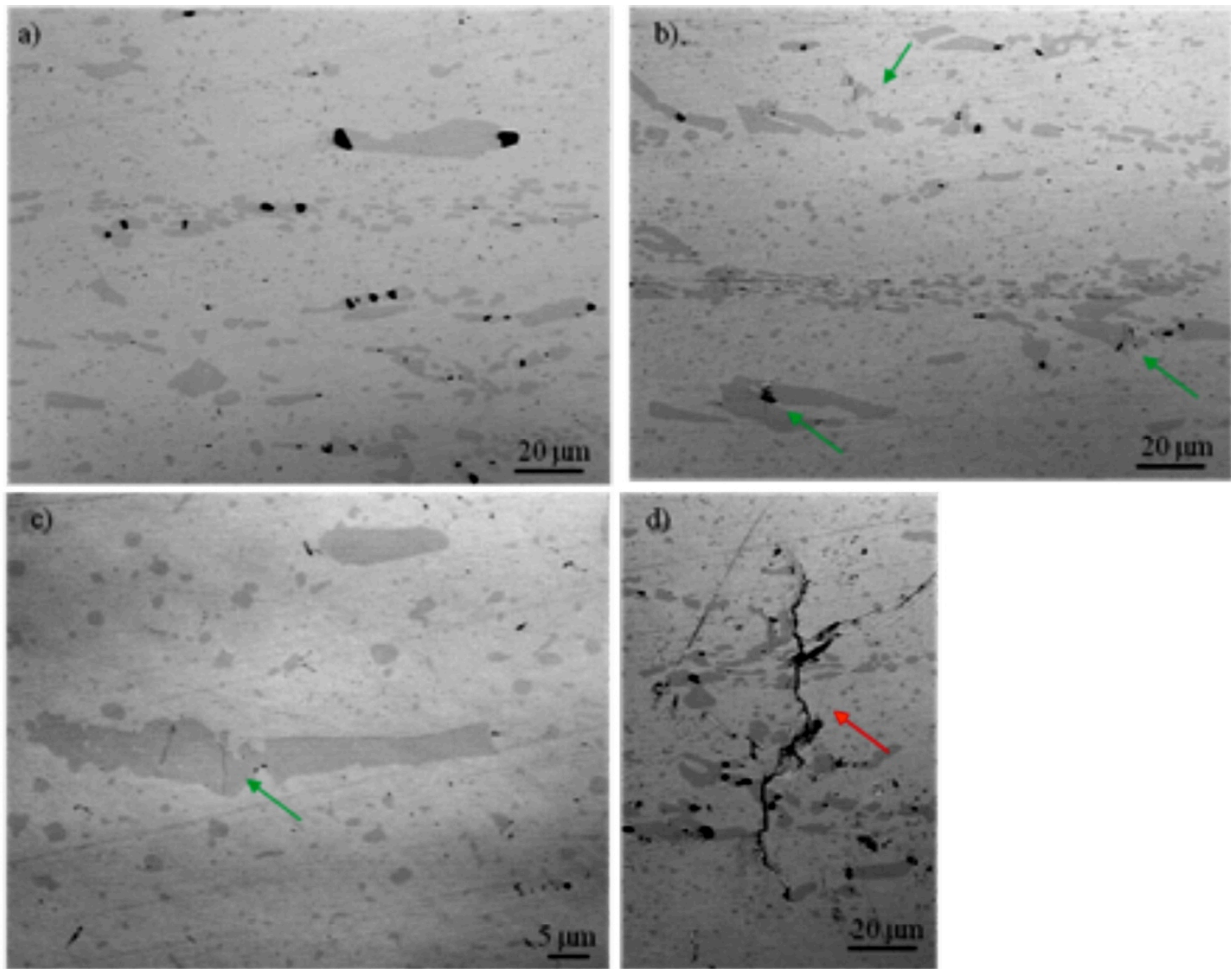


Fig. 7. Images of the microstructure of 1.2379 at: a) 800 MPa; b)-c) 2200 MPa and d) 2600 MPa.

As it followed from the obtained results, the first and the second AE signal types were related to different damage mechanisms occurring in 1.2379 samples as the applied stress increased. The first type of signal corresponded to the breakage of carbides in the microstructure, i.e. the nucleation of cracks, while the second type was emitted by the subsequent propagation of these cracks through the metallic matrix.

The data shown above demonstrate that the AE technique, coupled to the bending tests under monotonic conditions, was able to provide accurate information regarding the acting micro-mechanical and damaging mechanisms of 1.2379. In this case, the nucleation and propagation of cracks in the microstructure was well identified by means of two different types of AE signals reporting respectively, the breakage of carbides in the microstructure, i.e. the nucleation of cracks, and the moment when these cracks left the carbide and grew through the metallic matrix, i.e., the propagation of cracks. Therefore, this technique provided a unique and very accurate tool to determine the threshold stresses, at which carbides started to break and the stresses at which the first cracks were nucleated.

Summary

The method developed in this study by which bending fracture tests were coupled to AE techniques provided helpful results to understand in great detail the failure mechanisms of tool steels under such applied loading, as well as the interaction of their microstructural constituents.

In the 1.2379 steel studied, two different AE signal wave patterns were identified during a fracture test. These signals were respectively assigned to crack nucleation in primary carbides, and the propagation of these through the metallic matrix.

Acknowledgements

Authors from Fundació CTM Centre Tecnològic acknowledge the Catalan government for partially funding this work under grant TECCTA11-1-0006.

References

- [1] Picas, I., Hernández, R., Casellas, D., Valls, I.: 2010; Strategies to increase the tool performance in punching operations of UHSS; 50th IDDRG Conference (50th International Deep-Drawing Research Group), Graz, Austria; June 2010; p.325.
- [2] Picas I., Cuadrado N., Casellas D., Goetz A., Llanes L.; 2010; Microstructural effects on the fatigue crack nucleation in cold work tool steels. *Proc Eng* 2:1777-1785.
- [3] Casellas D., Caro J., Molas S., Prado J.M., Valls I.; 2007; Fracture toughness of carbides in tool steels evaluated by nanoindentation. *Acta Mater* 55:4277-4286
- [4] Waller J.M., Saulsberry R.L., Andrade E.; 2009; Use of acoustic emission to monitor progressive damage accumulation in Kevlar 49 composites. *AIP Conf Proc* 1211:1111-1118.
- [5] Lugo M., Jordon J.B., Horstemeyer M.F., Tschopp M.A., Harris J., Gokhale A.M.: 2011; Quantification of damage evolution in a 7075 aluminium alloy using an acoustic emission technique. *Mat Sci A* 528:6708-6714
- [6] Pollock A.A.; 2007; Some observations on acoustic emission – stress – time relationships. In: Carpinteri A, Lacidogna RG (ed) *Acoustic emission and critical phenomena: from structural mechanics to geophysics*. Boca Raton, London: CRC Press/Taylor&Francis, ISBN:9780415450829
- [7] Maillet E., Godin N., R'Mili M., Reynaud P., Lamon J., Fantozzi G.; 2012; Analysis of acoustic emission energy release during static fatigue test at intermediate temperatures on ceramic matrix composites: towards rupture time prediction. *Compos Sci Technol* 72:1001-1007.
- [8] Fukaura, K., Yokoyama, Y., Yokoi, D., Tsujii, N., Ono, K.; 2004; Fatigue of cold-work tool steels: effect of heat treatment and carbide morphology on fatigue life formation, life and fracture surface observations; *Metallurgical and materials transactions A*; vol.35A, April 2004, pp. 1289-1300.
- [9] Fukaura K. and Ono, K.; 2001; Acoustic emission analysis of carbide cracking in tool steels, *Journal of Acoustic Emission (JAE)*; vol.19, pp. 91-99.
- [10] Yokoi D., Tsujii N., Fukaura F.; 2003; Effects of tempering temperatures and stress amplitude on low-cycle fatigue behavior of a cold work tool steel. *Mater Sci Res Int.* 9: 216-222.
- [11] Yamada, K. and Wakayama, S.; 2009; AE Monitoring of microdamage during flexural fracture of cermets; In *Proceedings International Congress and Exhibition EURO PM2009*, Copenhagen, Denmark; October 2009; p. 247-252.
- [12] Martinez-Gonzalez, E.; Picas, I.; Casellas, D.; Romeu, J.; 2010; Analysis of fracture resistance of tool steels by means of acoustic emission; *Journal of acoustic emission (JAE)*; vol.28; pp.163-169.

Viability Precursors of Paroxysmal Phenomena as Detected by Applying RQA to Acoustic Emission Time Series

Maurizio Poscolieri, Claudio Rafanelli and Giovanna Zimatore

CNR-IDASC – Institute of Acoustics and Sensor "Orso Mario Corbino" – ICES Group
Area della Ricerca "Roma - Tor Vergata", via del Fosso del Cavaliere, 100, Rome, Italy

Abstract

Recurrence quantification analysis (RQA) represents a recent method for processing non-linear time series, already addressed to different topics concerning earth sciences and others. RQA is applied in this work to analyze time series of acoustic emission (AE) triggered by Earth's crust phenomena, so to detect feasible precursors of catastrophic events. The AE records of rms values were acquired at two different sites, placed close to the Peteroa volcano (Argentina) and at Valsinni (Matera, Italy), considering two ultrasound frequencies (25 and 150 kHz) with 30-sec sampling rate. The preliminary results of the application of RQA to the AE data of Valsinni with respect to the L'Aquila earthquake (Italy, on April 6, 2009), and to those related to the activity of the Peteroa volcano (Argentina) are described and appear suited to stress relationships with an impending catastrophic event.

Keywords: AE sensor, AE time series, signal analysis, RQA, precursors, paroxysmal events.

1. Introduction

Humankind often faces the hazard due to catastrophic natural phenomena, such as earthquakes and volcanic eruptions. They occur mostly with no feasible warning and cause often victims, serious damage to buildings and civil structures according to the involved energy. As regards the seismic events, the best protection is to plan earthquake-resistant dwellings, while against volcanic eruptions, especially for the explosive ones, the main safety suggestion is related to the definition of an appropriate escape strategy and of a land planning that foresees an urban development enough far away from the volcanic edifice.

Hence, reduction of danger for people, goods and structures should be a main task of society having available tools addressed to highlight impending earthquakes or volcanic eruptions. This is possible by identifying a so-called *precursor*, that is, a timely index providing a warning for approaching paroxysmal events. One of such parameters yielding suitable results is based on monitoring and analysing acoustic emission (AE) signals [1]. The AEs are elastic waves, in ultrasound frequencies (25 - 800 kHz), due to the energy release within natural or manmade structures affected by mechanical stress [2]. AE frequencies lower progressively almost up to the infrasound when the collapse occurs (Fig. 1).

The catastrophic stage is preceded (months, weeks, days, hours in advance) by the occurrence of ultrasonic AE according to the force that yields the structural stress and to its strength. A constant monitoring of AE signals and their time-series analysis allows to achieve anticipated information on the collapse risk choosing appropriate threshold values, defined on the basis of laboratory studies [3]. This way, the AE technique can be applied to geological structures, providing information about impending seismic, volcanic and hydrogeological (landslides, mudflows) events.

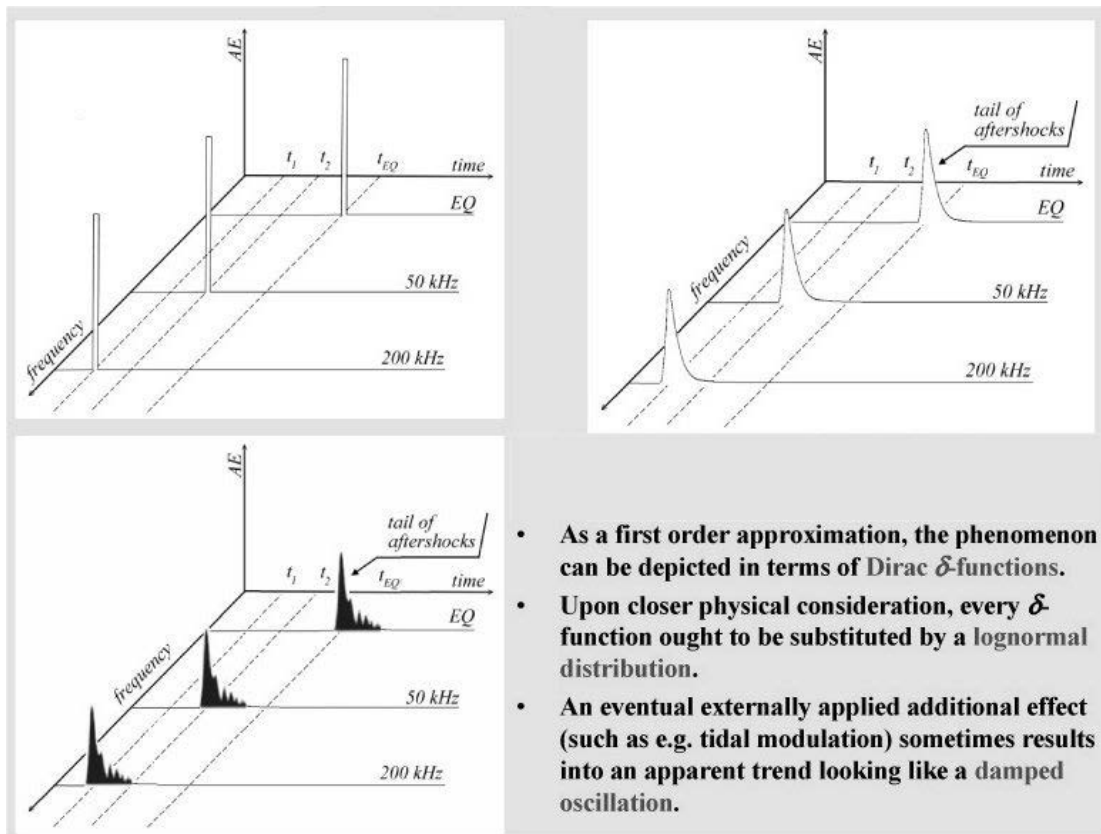


Fig. 1. The decrease of the frequencies sequence of the observed AE vs. time [1].

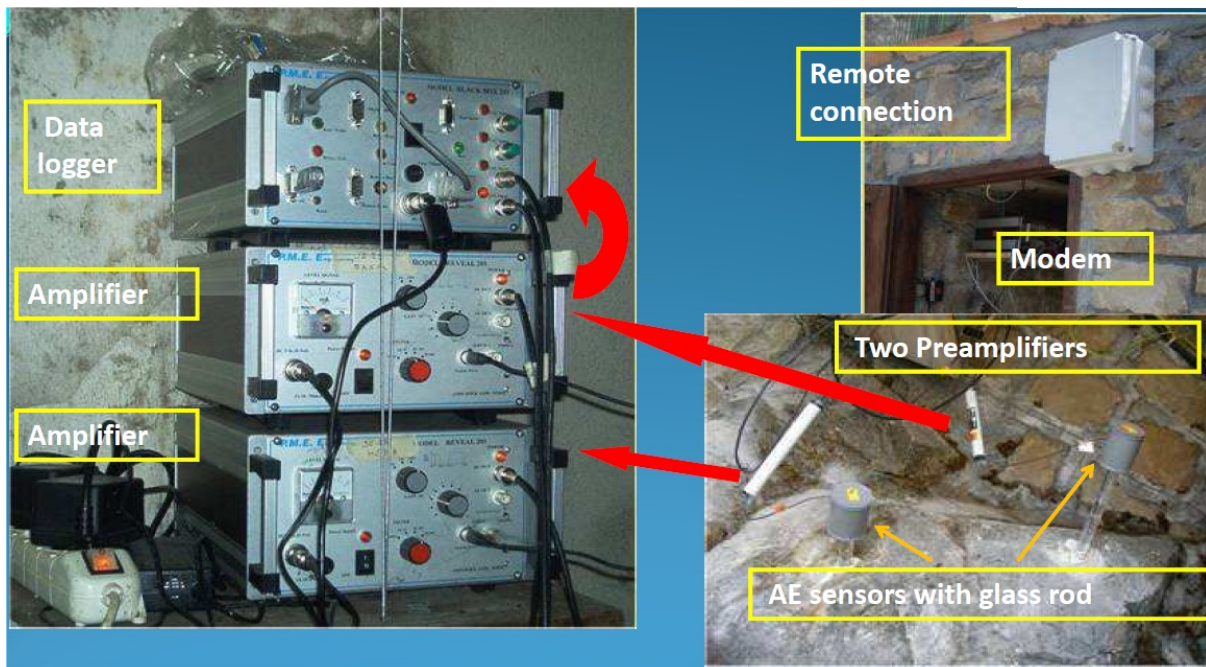


Fig. 2. Present configuration of an AE acquisition station.

Consequently, a suitable surveillance service for early warning handling can be provided by an AE recording equipment connected to an ICT network (Fig. 2), thus exhibiting AE as a challenging *precursor*. AE signal amplitude varies with the acoustic impedance, related to local rock stress conditions and particularly sensitive to fracture density and water content; therefore, the

application of a method such as *Recurrence Quantification Analysis* (RQA) [4-6] to the AE time series is particularly suited; in fact, RQA is focused on pinpointing peculiar recurrence pattern without taking into account the amplitude. RQA allows studying the change in correlation structure of the observed phenomenon; a relevant increase of correlation is known to precede the catastrophic event in many different systems ranging from physiology to economy [7].

This technique belongs to a category of recent methods of analysis of so-called *disordered systems*. Such methods show that many objects and processes that earlier were considered as completely random reveal clear evidence of having some ordered structure in both time and space [8]. Hence, this paper shows the absolutely new application of RQA to AE time series recorded in areas undergoing earthquakes and volcanic eruptions. The RQA method is applied to the non-stationary AE signals, in order to investigate the evolution features of the quiescence and activation status of the crustal system. Two case histories, recorded at Valsinni (Matera, Italy) and at Peteroa volcano (on the Argentina – Chile border), are presented.

2. RQA Method

2.1 RQA general description

In the study of the numerical series, among various statistical analysis techniques, the "dynamic" techniques are relatively new. They are generally based on representing, in a multi-dimensional space, a one-dimensional or time-dependent signal, through the technique of *embedding* [5]. This way, with the same analytical techniques, it is possible to identify in the numerical series members, i.e. the profile of hydrophobicity of the protein sequences or the variation over time of biopotentials such as the ECG (electrocardiogram), those 'hidden' variables, which are supposed to help define the dynamic characteristics of the system. These characteristics are analyzed individually, and this allows detecting subtle periodicities and recurrences not caught by the traditional methods (e.g. Fourier analysis or wavelet analysis [9]). A further advantage is that the reliability of the results is not conditioned by any assumptions of stationary or minimum length of the signal [5, 10].

Among these methods, the RQA includes an embedding procedure that allows expanding a mono-dimensional signal into multi-dimensional space, thus permitting the identification of fine peculiarities of the sampled series that in turn are described by few global parameters allowing for a synthetic description. RQA has been recently applied in medicine for the analysis of time series of oto-acoustic emissions [11, 12]. It introduces some parameters of the overall complexity of the signal, derived from the so-called "*Plot of Recurrence*" (RP). The trend of the original signal over time is represented by a set of n points equally spaced (e.g. $\{a_1 a_2 \dots a_n\}$, where a_i is the signal value at time i). Next, the series is copied into successive columns (the number of columns is defined as a dimension of *embedding*, N), each one shifted by a given number of points (*lag*): this way, the *embedding* matrix is created. Finally, the graph of recurrence is built by drawing a *dot* in the space that represents the distances between the corresponding rows if the distance between the j_{th} and the $(j + 1)_{th}$ rows of the *embedding* matrix is less than a fixed value (called *radius*), producing a graph pattern. In the so obtained plot, the horizontal and vertical axes represent the relative position of the n points of the time series. The presence of horizontal and vertical lines in the recurrence plot shows that part of the considered signal matches closely with a sequence farther along the time.

The RQA descriptors are calculated based on the number and location of *dots* on the plot. In particular, percent of recurrence (*%Rec*) is the percentage of recurrence points in a recurrent plot; percent of determinism (*%Det*) is the percentage of recurrence points, which form diagonal lines and it indicates the degree of deterministic structure of the signal. Entropy (*Ent*) is the Shannon entropy of the probability distribution of the diagonal line lengths and is linked to the richness of deterministic structure [11]. Laminarity (*LAM*) is the percentage of recurrent points that are included in line segments vertical to the upward diagonal and whose length meets or exceeds the minimum length threshold. It measures chaotic transitions and is related to the amount of laminar phases in the system (intermittency) [6, 10].

Within this framework, Chelidze's team applied RQA to study the dynamics of earthquakes' temporal distribution by considering the inter-arrival times between two events of Caucasian earthquakes with Magnitude 3 [13]. They calculated the correlation dimension of the integral time series (14,100 time intervals) for a large period of observations; the possible control of dynamics of a complex seismic process by strong electromagnetic impacts in the temporal domain was observed. The result obtained by Chelidze et al. was that the qualitative methods testify the presence of some non-random nonlinear structure in energetic, spatial and temporal distributions of earthquakes. The predictive potential of complexity analysis of seismological time series is recently considered in the review by Chelidze and Matcharashvili [8].

2.2 RQA input parameters for AE application

For this work an average on 120 points (1 hour) as a first smoothing of the recorded AE signals is reckoned, reminding that sampling rate was 30 seconds. Then, the optimization procedure suggested the following parameters: the delay (lag) is set to 1; the number of the embedding matrix columns (embedding dimension) is set to 10 and the cut-off distance (radius) is set to 15.

If RQA is carried out by the computation of many small distance matrices corresponding to consecutive and overlapping sliding windows (epochs) along the series, the changing values of RQA variables in the subsequent windows allow for the detection of abrupt changes in the dynamical regime of the signal. This procedure, *Recurrence Quantification over Epochs* (RQE) was used to test the presence of phase changes in AEs.

RQE analysis was carried out by adopting the same parameters setting as for the global mode (RQA), plus the definition of windows having length of 24, 150 and 300 points (1 point = 1 hour) and shifting of 24, 150 or 300 points between consecutive windows, respectively (to obtain non-superimposed windows).

3. Case Histories

Figure 1 shows how a quite extensive range of frequencies in the ultrasound spectrum must be monitored in order to collect a satisfactory AE data set. This is an enough hard task taking into account the difficulty of simultaneously handling different piezoelectric sensors in the natural world. However, the skill acquired on laboratory experiments has allowed to define the best selection of transducer frequencies in correspondence of 25 and 150 kHz that depict the crack evolution in different materials [14]. Figure 2 shows the instrument sequence for AE data collection as well as a typical installation case, at Valsinni site.

In the present configuration of an AE acquisition site the two sensors are connected to a rocky outcrop through a glass bar, transparent to ultrasonic signals; then, the AE acquisition apparatus' chain includes a pre-amplifier, an amplifier, a data logger and a remote connection module based on GPRS protocol. The incoming AE signals are sampled at 3 kHz, averaged and then recorded at 30-seconds time steps as rms values.

Within this context, two case studies of AE recording sites are described: one is Valsinni, Italy (Basilicata region; 40°10'05" Lat. and 16°26'35" Long.), a highly seismogenetic area, and the other, along the Argentina/Chile boundary, the Peteroa volcano (35°15' S Lat. and 70°35' W Long.), exhibiting either seismic events or explosive eruptions. By analyzing both AE time-series, quite remarkable anomalies of paroxysm precursors showed up. Henceforth, the AE data collected at 25 kHz will be termed as *LF AE*, while the AEs recorded at 150 kHz as *HF AE*.

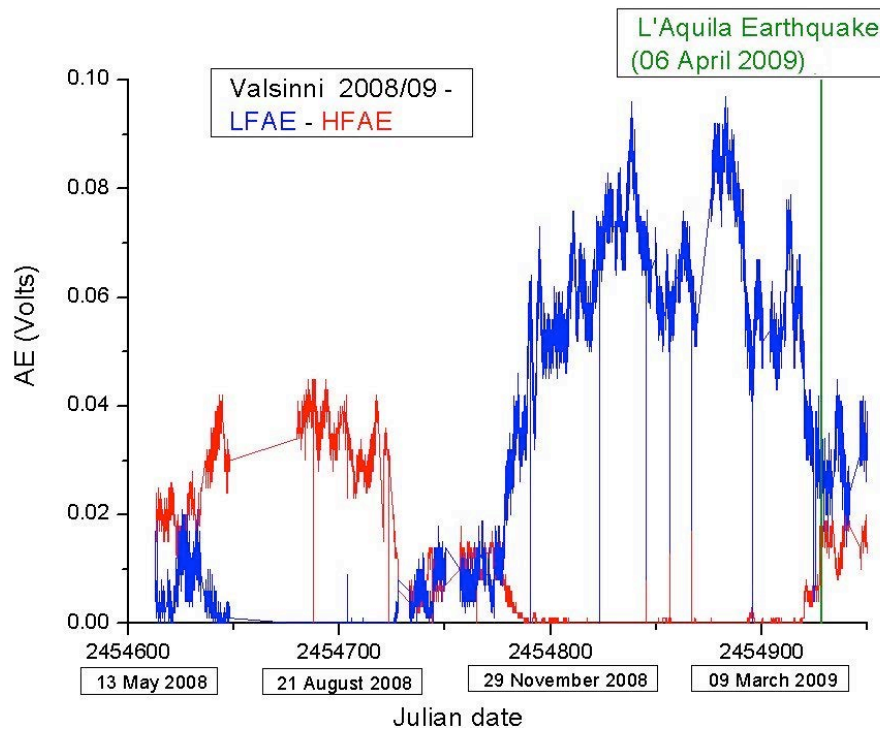


Fig. 3. Input AE signals recorded at Valsinni acquisition site during Springs 2008-2009 period. Blue line depicts LF AE data, while red one shows HF AE data. L'Aquila earthquake (Magnitude = 6.3) occurrence is also reported.

The AE time series acquired at Valsinni site between May 2008 and April 2009, just after the L'Aquila seismic event, are depicted in Fig. 3. In this plot the HF AEs (red line) show a considerable activity up to November 2008 and a subsequent depletion until March 2009, one month before L'Aquila earthquake; later, they start to increase again. Conversely, LF AEs exhibit evident activity from May to July 2008 and a following depletion up to the end of September 2008 when a rather remarkable activity begins, decreasing only when the seismic event comes up [15].

Next, the two AE time series acquired at the HF and LF frequencies on Peteroa volcano between April 2009 and March 2011 are depicted in Fig. 4. The plots show a periodic pattern of the LF AEs (right), as long as six months, perhaps related to Earth's tide force [16]. The HF AEs (left), instead, show a more subdued periodic trend, and exhibit, as main characteristic, an abrupt

increase on November 2011, in correspondence to the first eruption phase. Better pictures of the two whole AE temporal distributions are shown in the left panels of Figs. 5 and 6.

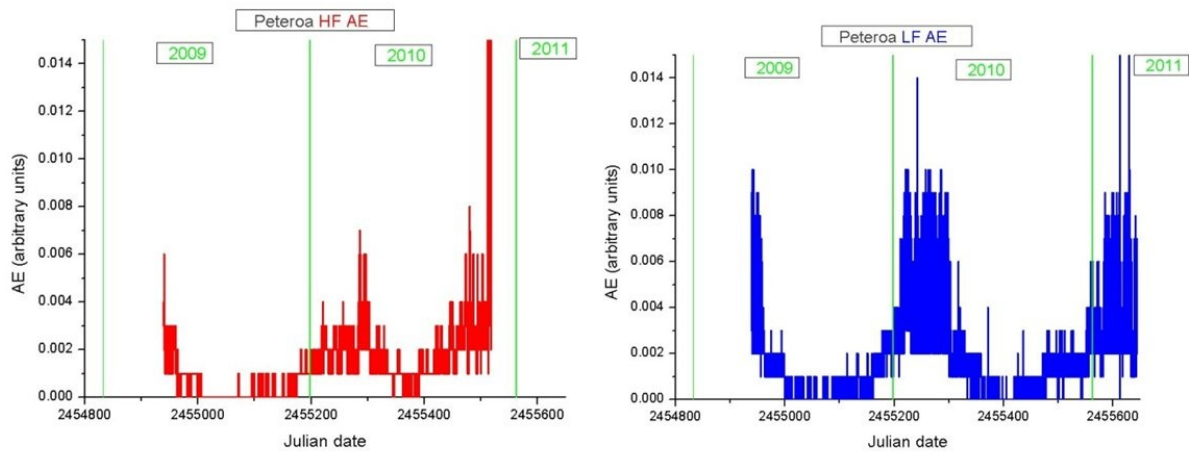


Fig. 4. The AE collected on Peteroa volcano between 17 April 2009 and 23 March 2011. (Left) HF AE; (Right) LF AE data. The green vertical lines point out the end of every year.

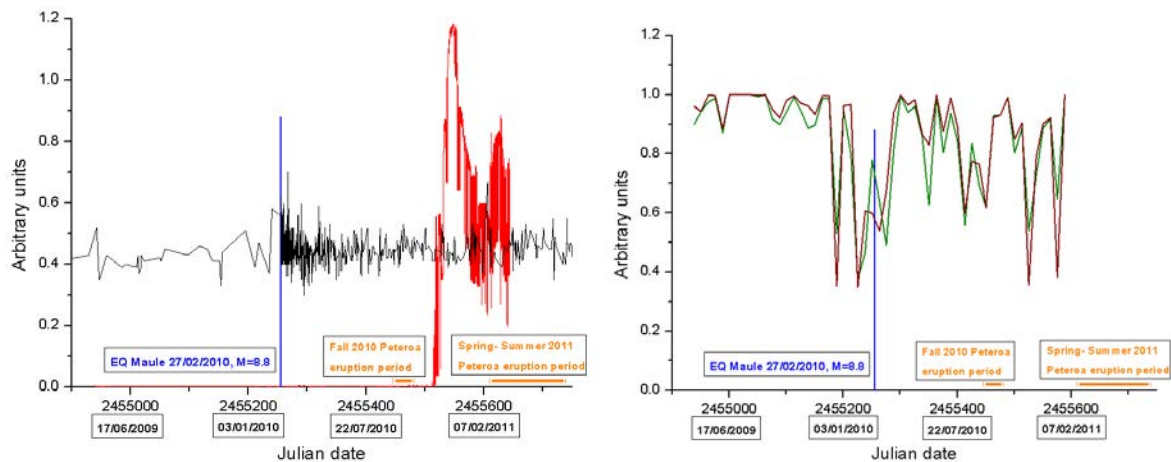


Fig. 5. (Left) Time-series of HF AE (red lines) collected on Peteroa volcano between Falls 2009 and 2011. Black lines point out the earthquakes (1/10 of Magnitude values larger than 0.3) occurred within 300 km from Peteroa volcano (USGS catalogue). Blue line refers to the very strong earthquake of Maule (Magnitude = 8.8), while the orange lines identify the explosive eruptions periods of Peteroa. (Right) RQA parameters calculated from the HF AE series: the green line points out the %DET descriptor, while the brown line the %LAM (51 non-overlapping epochs; 1 epoch=300 hours).

4. Results of the RQA Application to AE Data

4.1 Valsinni case history

The RQA application to LF AE data collected at Valsinni site during the Springs 2008-2009 period (see Fig. 3) has yielded four RP, depicted in Fig. 7, relative to four different time lags. The top-left and bottom right graphs score low values (%DET ~70) before, about six months, and just after the L'Aquila earthquake and, moreover, exhibit much similar patterns, which appear to resemble the one of a sinusoidal trend. On the contrary, the other two RP, related to a

$\%DET \sim 90$, exhibit quite complex patterns quite different from the other two. Thus, the incoming catastrophic event is observed in terms of a change in dynamic regime of AEs.

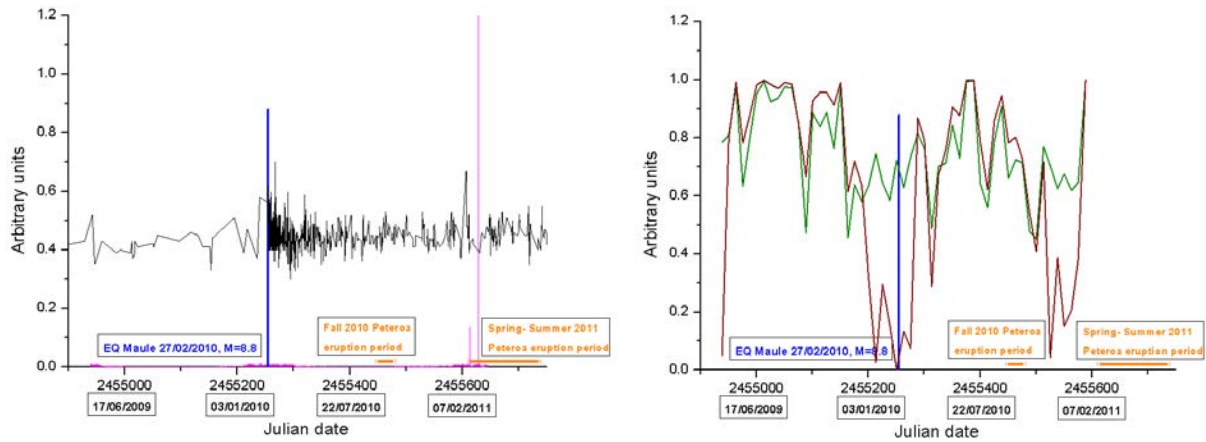


Fig. 6. (Left) Time-series of LF AE (magenta lines) acquired on Peteroa volcano between Falls 2009 and 2011. Black lines point out the seismic events (1/10 of Magnitude values larger than 0.3) recorded within 300 km from Peteroa volcano (USGS catalogue). Blue line is referring to the greatest earthquake of Maule (Magnitude = 8.8), while the orange lines define the explosive eruptions periods of Peteroa. (Right) RQA parameters calculated from the LF AE series: the green line points out the $\%DET$ descriptor, while the brown line the $\%LAM$ (51 non-overlapping epochs; 1 epoch= 300 hours).

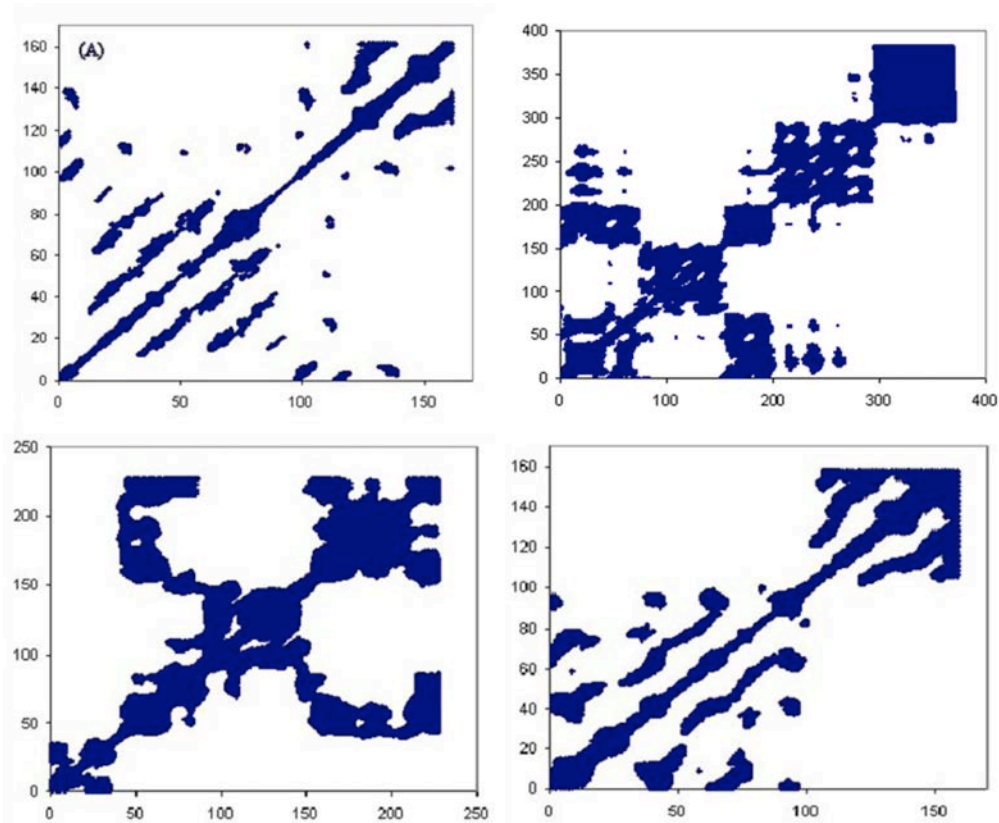


Fig. 7. Comparison of the RP of the LF AEs recorded at Valsinni site in four different time periods, between September 2008 and April 2009. (Top left) Sep. 26-Oct. 03, 2008; (Top right) Dec. 12-Dec. 28, 2008; (Bottom left) Feb. 27-Mar. 09, 2009; (Bottom right) Apr. 13-Apr. 19, 2009.

Modification in dynamic regime of AEs is observed in Fig. 8, where the trend of the %DET values since the installation of the Valsinni AE station (May 2008) is reported. It can be noted that there is an almost continuous raise of %DET values until the occurrence of L'Aquila earthquake (Apr. 6, 2009) and a successive sudden depletion afterward.

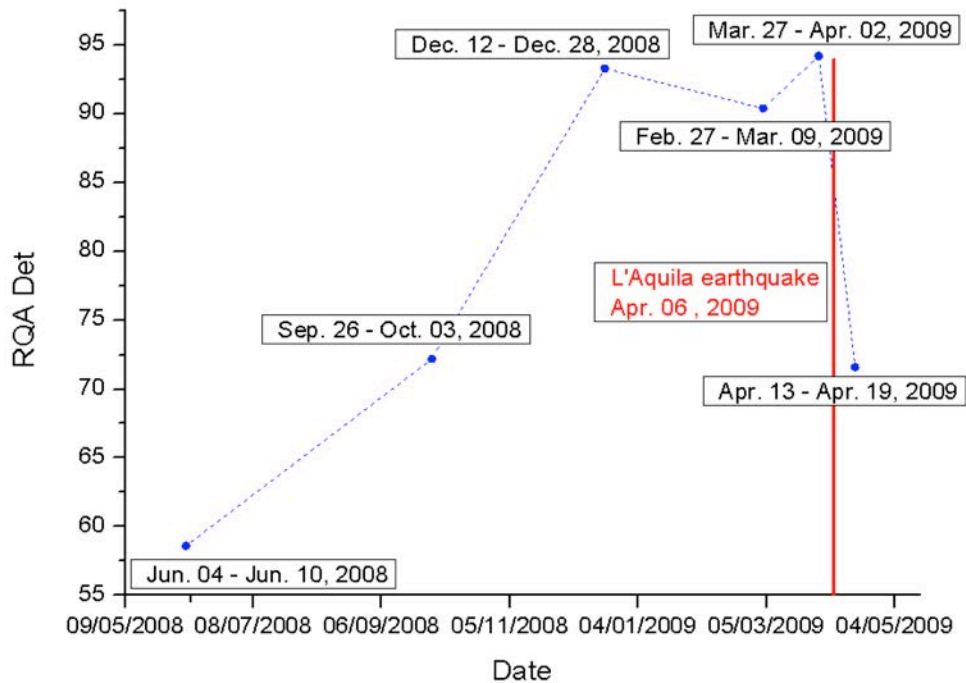


Fig. 8. Trend of the RQA %DET values for the LF AEs recorded at Valsinni station since June 2008 to middle April 2009. The red line indicates the occurrence of the L'Aquila earthquake. The time intervals reflect the different periods in which the %DET has been calculated.

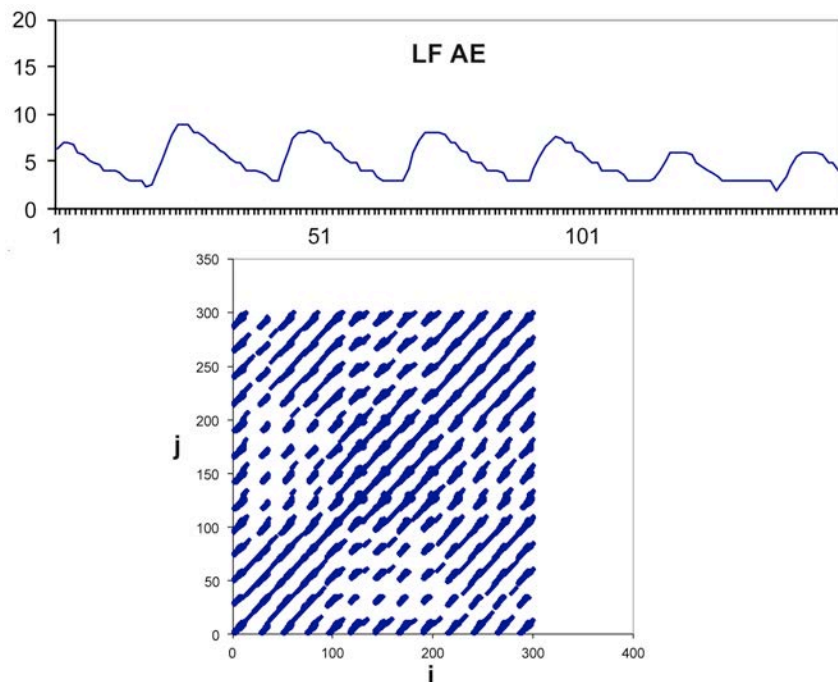


Fig. 9. Peteroa volcano. Top: An early record of LF AEs (150 hours: 17-23 April 2009). Bottom: Corresponding Recurrence plot (RP): the inset on 300 epochs (1 epoch=24 h=24 points). A periodic signal and the very regular pattern of RP can be observed.

4.2 Volcano Peteroa case history

As already mentioned in Sec. 2.2, the volcano Peteroa AE time series were analyzed in different time windows, in order to fine-tune its RQA parameters and to examine events at various time scales (Figs. 5, 6, 9, 10). In particular, the results obtained for the LF AE data with two different non-superimposed windows (termed *epochs*), of 24 and 300 points, are described. In the upper panel of Fig. 9, the pattern of the earlier record (the first 150 epochs corresponding to 6.25 days) of LF AEs is reported, while the upper panel of Fig. 10 shows the pattern of the entire recording period (16,146 points; corresponding to 2 years) of LF AEs. The lower panels of both Figs. 9 and 10 exhibit the corresponding RP.

Figure 9 points out a daily Earth's tide oscillation in the AEs while its RP shows the typical pattern of sinusoidal trend, well observed plotting only the first 150 points (top of Fig. 9). Conversely, Fig. 10 for the whole monitored period shows a seasonal fluctuation of the LF AE data. The corresponding RP (lower panel of Fig. 10) exhibits a blank area around the middle, placed between two complex patterns, probably reflecting some modification in the internal structure of the volcano. It could correspond to sharp transition of the regime, probably being a threshold value in the AE time series, quite coinciding with the Chile Maule earthquake (Magnitude = 8.8; Feb. 27, 2010).

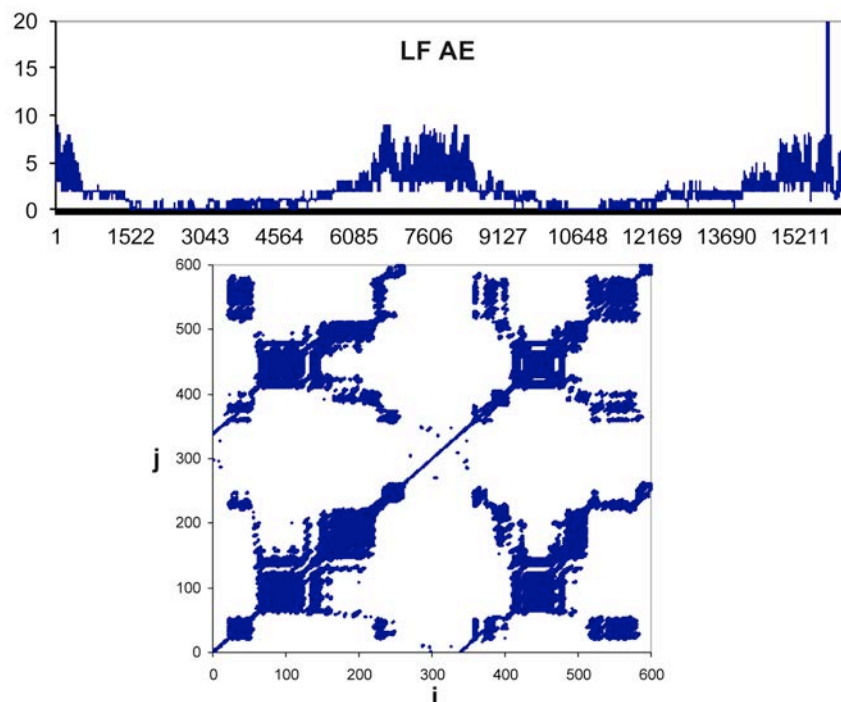


Fig. 10. Peteroa volcano, (Top) LF AEs recorded in the whole period between Apr. 17, 2009 and Mar. 23, 2011 (16,146 points). (Bottom) RP on 600 epochs (1 epoch = 24 points = 24 h).

A better interpretation of RQA results about Peteroa volcano has been obtained by overlapping the time distribution of the RQA descriptors $\%DET$ and $\%LAM$ to the original AE time series and to the earthquakes occurred in the neighborhood of the volcano within a radius of 300 km. In Figs. 5 and 6, respectively, these data for HF and LF AEs are shown with the date of the Maule seismic event and the volcanic eruption periods. The HF AEs (right panel of Fig. 5) exhibit three significant patterns of both $\%DET$ and $\%LAM$ for different periods. The first one, lasting about seven months, shows uniform patterns of high values for both parameters, in accord-

ance with the smoothed sequence of seismic events. Then, the $\%DET$ and $\%LAM$ trends, about after middle December 2009, drop suddenly until the Maule earthquake occurrence, followed by a subsequent increase of both parameters. Next, after the intense Maule aftershocks seismic series, the RQA parameters present both remarkable fluctuations, perhaps driven by the explosive eruption sequences occurred on Spring 2010 and Easter-Fall 2011.

The LF AEs (Fig. 6) show a less evident pattern. The $\%DET$ and $\%LAM$ trends before the occurrence of the Maule earthquake appear less uniform than those exhibited by the HF AEs with strong fluctuations; they show (particularly $\%LAM$) a remarkable decrease of values as the earthquake is approaching. Next, after the Maule earthquake, both RQA parameters exhibit a quite variable trend achieving a relative maximum during the Spring 2010 eruption period and a strong value depletion (especially the $\%LAM$) during the inter-period between the two eruption phases and a successive abrupt increase before the second eruption period.

These results seem to confirm the capabilities of RQA method to depict the modifications in the volcanic edifice due to the combined action of seismic and volcanic activities. Particular interest has to be devoted to the relations between the RQA parameters trends and the occurrence of the Maule earthquake (Magnitude = 8.8), while it is difficult to define peculiar relations with the volcanic explosive activity.

5. Concluding Remarks

The results of the application of RQA technique to AE time series within two frequencies (HF = 150 kHz and LF = 25 kHz) in seismogenetic and volcanic areas are given considering different time scales. The temporal distribution of the obtained RQA parameters (Figs. 5, 6, 8) exhibits remarkable variations as a paroxysmal event is approaching.

Despite any possible warning due to the uncertainty of the underlying relationships with volcanic activity and earthquakes and to the merely episodic nature of the observations (more case studies are to be analyzed to confirm the obtained results), the anomalies detected in the RQA parameters could represent a likely *signature* of an incoming catastrophic event in terms of AE dynamic regime modifications, possibly providing a remarkable finding. The arrangement of dynamical processes can be analyzed, so reckoning noteworthy “*predictive*” RQA parameters. The obtained results appear quite interesting, but a fine-tuning of the analysis and more data sets from different seismic and volcanic areas are needed to assess the impact.

Acknowledgements

The authors are very thankful to Dr. J. Ruzzante and his team of ICES-CNEA (Argentina) for providing the AE data collected on Peteroa volcano monitoring site within the framework of the project PICT 2007-2009 “*Emisión Acústica y precursors sísmicos*”. They also thank the Civil Protection of Basilicata for the financial support for the installation of the Valsinni AE monitoring station in the framework of the Research Agreement between Regional Civil Protection of Basilicata and CNR IDASC. They are grateful to G. Ventrice of the SME P.M.E. srl (Italy) for his contribution to the instrument development, installation and maintenance at Valsinni site.

References

- [1] G.P. Gregori, G. Paparo, M. Poscolieri, C. Rafanelli, G. Ventrice, ‘Acoustic Emission (AE) for monitoring stress and ageing in materials, including either manmade or natural structures, and assessing paroxysmal phases precursors’, in: Acoustic Emission, Intech Pub., Rijeka, Croatia, (2011), 365-398.
- [2] K. Ono, ‘Trends of recent acoustic emission literature’, *J. of Ac. Emission*, **12** (1993), 177-198.
- [3] G. Paparo and G.P. Gregori, ‘Multifrequency acoustic emissions (AE) for monitoring the time evolution of microprocesses within solids, reviews of quantitative nondestructive evaluation’, 22, AIP Conference Proceedings, D.O. Thompson, and D.E. Chimenti (eds.), (2003), pp. 1423-1430.
- [4] J.P. Eckmann, S.O. Kamphorst and D. Ruelle, ‘Recurrence plots of dynamical systems’, *Europhysics Letters*, **4** (1987), 973-977.
- [5] C.L. Webber and J.P. Zbilut., ‘Dynamical assessment of physiological systems and states using Recurrence Plots Strategy’, *J. Appl. Physiol.*, **76(2)** (1994), 965-973.
- [6] N. Marwan, N. Wessel, U. Meyerfeldt, A. Schirdewan and J. Kurths, ‘Recurrence plot based measures of complexity and its application to heart rate variability data’, *Phys. Rev. E*, **66(2)** (2002), 026702.1-026702.8.
- [7] A.N. Gorban, E.V. Smirnova and T.A. Tyukina, ‘Correlations, risk and crisis: from physiology to finance’, *Physica A*, **389** (2010), 3193-3217.
- [8] T. Chelidze and T. Matcharashvili, ‘Complexity of seismic process; measuring and applications - A review’, *Tectonophysics*, **431** (2007), 49-60.
- [9] M. Takemoto, H. Nishino and K. Ono, ‘Wavelet Transform - Applications to AE Signal Analysis’, in: Acoustic Emission - Beyond the Millennium, Elsevier, (2000), pp. 35-56.
- [10] <http://homepages.luc.edu/~cwebber/> (looked on Dec. 4, 2012)
- [11] G. Zimatore, A. Giuliani and A. Colosimo, ‘Revealing deterministic structures in click-evoked otoacoustic emissions’, *J. Appl. Physiol.*, **88(4)** (2000), 1431-1437.
- [12] G. Zimatore, A. R. Fetoni, G. Paludetti, M. Cavagnaro, M. V. Podda, and D. Troiani. ‘Early detection of hearing impairment by using transient-evoked otoacoustic emissions- a pilot study’, *Med. Sci. Monit.*, **17(6)** (2011), MT41-49.
- [13] T. Chelidze, T. Matcharashvili, ‘Electromagnetic control of earthquake dynamics?’ *Computers & Geosciences*, **29** (2003), 587-593.
- [14] G. P. Gregori and G. Paparo, G., ‘Acoustic emission (AE). A diagnostic tool for environmental sciences and for non destructive tests (with a potential application to gravitational antennas)’, in: Meteorological and Geophysical Fluid Dynamics (A Book to Commemorate the Centenary of the Birth of Hans Ertel), W. Schröder,(ed.), *Arbeitskreis Geschichte der Geophysik und Kosmische Physik*, W. Schröder/Science, Bremen, Ger., (2004), pp. 166–204.
- [15] G.P. Gregori, M. Poscolieri, G. Paparo, S. De Simone, C. Rafanelli, G. Ventrice, ‘“Storms of crustal stress” and AE earthquake precursors’, *Nat. Hazards Earth Syst. Sci.*, **10** (2010), 319-337.
- [16] J. Ruzzante, M.I. Lòpez Pumarega, M. Armeite, R. Piotrkowski, G.P. Gregori, I. Marson, G. Paparo, M. Poscolieri, A. C. Catellani, ‘Análisis sobre el comportamiento del volcán Peteroa (Argentina), por metodos de Emisión Acústica (EA)’, *Proceedings of the Workshop AAGG2009*, 1st ed., Buenos Aires (Arg), Asociación Argentina de Geofisicos y Geodestas, ISBN 978-987-25291-1-6, Ciencias de la Tierra. I (2009), 221-227.

Artificial Neural Network Analyses of AE Data during Long-Term Corrosion Monitoring of a Post-Tensioned Concrete Beam

Lucio Bonaccorsi¹, Luigi Calabrese¹, Giuseppe Campanella² and Edoardo Proverbio¹

¹ University of Messina, Dept. Industrial Chemistry and Material Engineering, Viale F. Stagno d'Alcontres 31, S. Agata di Messina, 98166 Messina, Italy

² NDT consultant, Via San Giuseppe 7 is. 297, 98122 Messina, Italy

Abstract

Acoustic emission (AE) technique is well suited for real-time control and detection of active defects within a structure. We used AE to monitor a post-tensioned concrete beam for about seven months, undergoing stress corrosion cracking (SCC) assisted by hydrogen embrittlement, activated by ammonium thiocyanate solution during a laboratory corrosion test. By multivariate analysis, three stages of damage mechanisms were identified: activation, propagation and rupture. An artificial neural self-organizing map (SOM) analysis was used to identify the relationship between the AE variables and to classify AE events. This methodology has in fact proved particularly powerful in identifying the evolution and extent of damage of the monitored post-tensioned concrete beam with the use of exemplified topological maps. The SOM analysis made it possible to correlate each AE stage, with unambiguous significant variables, to a specific degradation phase.

Keywords: Signal discrimination, corrosion, damage, prestressed concrete, principal component analysis, Kohonen map, SOM analysis

1. Introduction

Post-tensioning, as well as pre-stressing technology, is widely adopted in civil engineering, esp. in bridge engineering [1,2], since it allows to obtain slender but high performing structures. Although this technology is effective from a structural standpoint, it is sensitive, depending on environmental conditions, in which the structure operates, to corrosion damages. In particular, several cases have been described in the literature of premature failures of structures due to localized attack such as corrosion fatigue, wear-corrosion, but mainly stress corrosion cracking (SCC) [3-5]. This SCC mechanism is more critical than others because it induces a premature and unexpected rupture of the steel cables, affecting the mechanical integrity of the structure [6].

The development of reliable and affordable technique for monitoring and for damage evaluation of reinforced concrete structures, and in particular of prestressed concrete structures, is therefore becoming a pressing demand since the increasing age of the structures, the progression of deterioration processes and the ever increasing demanded performance. Acoustic emission (AE) technique is very promising in this field since it is not invasive, allows a volume evaluation and at the same time offers the possibility to locate discrete defects.

AE was widely used in studying corrosion phenomena and in particular SCC since the early stage of the development of the technique [7]. More recently AE technique was introduced in the civil engineering in evaluating SCC of reinforcing cables in prestressed concrete structure [8] as well as in the detection of corrosion of reinforcing bar, in the identification of corrosion processes [9] and for damage evaluation [10].

Concerning SCC phenomena it has to be underlined that in prestressing steel they evolve through complex and different mechanisms, where anodic metal dissolution and hydrogen embrittlement (HE) are not unique stages [11-12]. However, many mechanisms can be identified by AE [13-14]. AE signals are generated mainly by crack initiation and growth due to metal dissolution or HE. Furthermore the hydrogen evolution induced by cathodic reaction within the crack, the breakdown of thick surface-oxide films, the fracture or decohesion of phases (such as precipitates, second-phase particles and non-metallic inclusions), twin or slip deformation in the plastic zone at the crack tip are all mechanisms that can produce detectable AE signals [15].

By considering the above-mentioned aspects it is clear that traditional AE analysis techniques are not sufficient to discriminate the different stages of damage in a corroding structure. The adoption of new statistical methods of data analysis is necessary to find out the significant parameters capable of discriminating the different forms of damage. Pattern recognition techniques can be used with this aim [16], and signal processing is performed at the waveform level, either by applying digital filtering, Fourier transforms or other processing such as wavelet transform, or by extracting AE features as a mean to describe the shape and content of a detected AE waveform. However, waveform acquisition requires high data storage capacity and sophisticated equipment while feature analysis is based only on the evaluation of the main AE signal parameters such as energy, counts, amplitude, without the need of the waveform record and is carried out by mean of the cross evaluation of different “health indexes” related to AE signal intensity and to loading condition [17].

Aim of this work is to identify the different damage mechanisms in steel cables in a post-tensioned concrete beam due to hydrogen assisted cracking by means of AE technique. A self-organized map (SOM) procedure was applied in order to interpret the experimentally acquired data. It was possible to group events into sub-clusters, each being an identifier of a specific degradation condition. The topological neural map was implemented in identifying the temporal evolution of damage and its related structural risk.

2. Material and methods

2.1 Experimental set-up

Table 1: Steel wire composition and mechanical properties

Nominal chemical composition of eutectoid steel								
C	Si	S	P	Cr	Ni	Mn	Cu	Fe
0.81	0.24	0.002	0.008	0.12	0.04	0.65	0.1	Bal.
Mean mechanical properties of cold drawn steel								
Steel type	Yield stress $f_{p 0.1k}$ (MPa)			UTS f_{pk} (MPa)		Elongation (%)		
Cold drawn	1670			1860		3.5		

AE monitoring was carried out on a post-tensioned concrete beam during long-term hydrogen assisted stress corrosion cracking test (HASCC). The beam had a length of 6.30 m and a cross section of 0.40 x 0.25 m (Fig. 1a). It was made by a concrete mix with 430 kg/m³ of ordinary Portland cement (OPC) content having the characteristic compressive strength of $R_{ck} =$

55 MPa. It was reinforced with four 18-mm steel bars and post-tensioned with four 7-wire 6/10” strands (Fig. 1b). Steel wire composition and mechanical properties are reported in Table 1.

Post-tensioning force induced a stress level on the strand of about 60% of the UTS, of about 52% UTS after deducing losses due to elastic shortening, creep and shrinkage in the concrete and relaxation in the steel. The tendon was completely grouted with the exception of a small corrosion cell of 25 cm in length in the middle of the beam [18] (Fig. 1c). The corrosive solution used was composed with 250 g/l of ammonium thiocyanate (NH_4CNS) in accordance to ISO 15630 [19]. The solution was kept at room temperature, and with constant liquid re-circulation from an external reservoir by a pump.

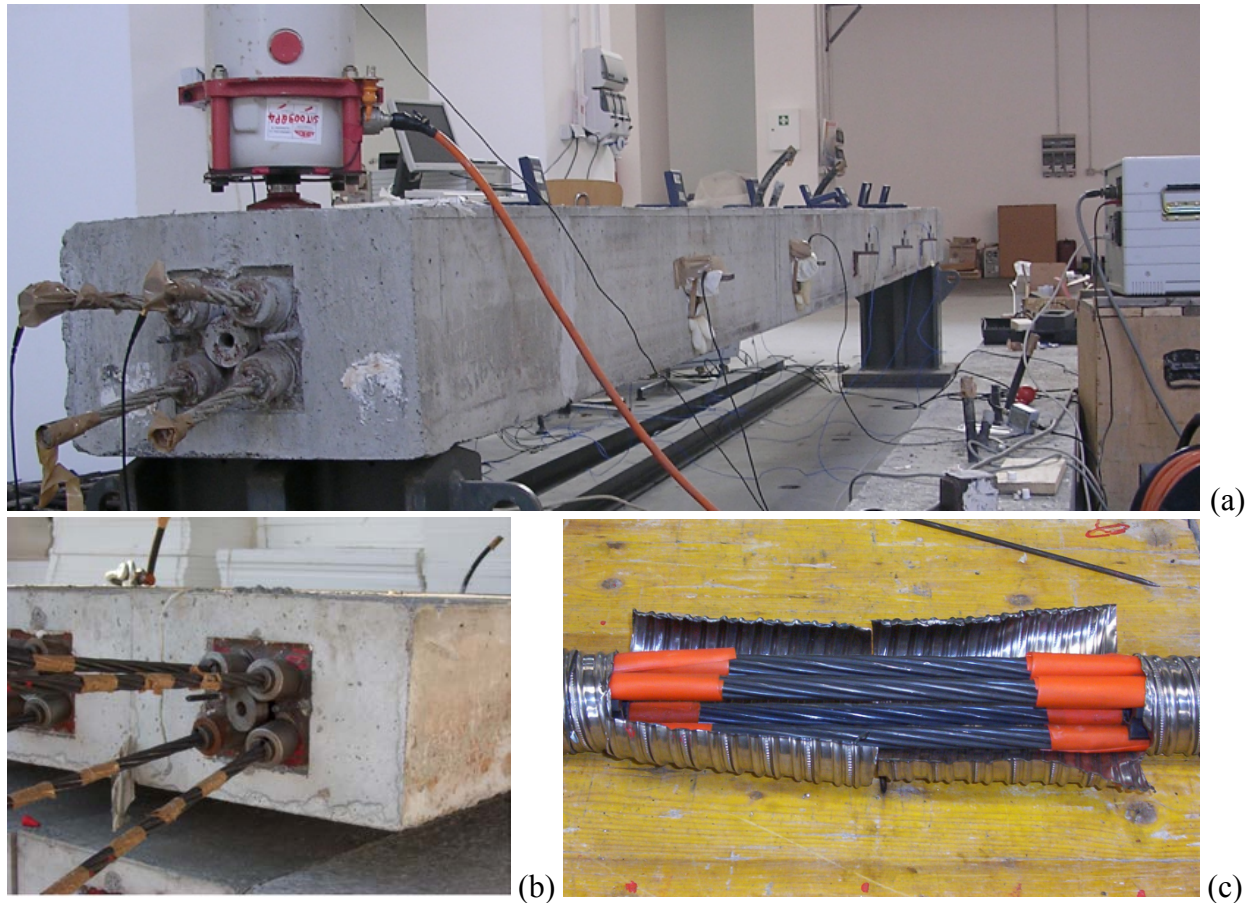


Fig. 1: a) View of test setup used for corrosion test. b) Close-up view of strands anchorage. c) Corrosion cell obtained in the metal duct.

AE signals were recorded by a 10-channel Vallen AMSY-5 measurement system. It was used with 8 piezoelectric transducers for steel, VS150-M type that worked in 100-450 kHz frequency range with resonance at 150 kHz. The sensors were positioned on ends of steel wires (Figure 1c). The AE acquisition covered a period approximately of 7 months, with a daily 24h monitoring. Before analysis, raw data were de-noised as reported in a previous work [20]. The neural network analysis has been proposed to provide meaningful information on the quality of acquired signals and their interpretation on the status of the structure and damage evolution. In particular a self-organizing map (SOM) was constructed. It allowed to homogenize the acquired data and to interpret them in explicit form with a topological map that exemplifies the damage evolution of the structure during the acquisition time.

All specific algorithms proposed to analyze AE data were written by using Matlab 7.5 software. The SOM analysis was carried out by using 6 uncorrelated variables (i.e. average frequency, amplitude, duration, energy, time and event frequency) extrapolated from the acquired AE signal, as resulted by correlation matrix analysis.

2.2 Self Organizing Map

Self-organizing map (SOM) or Kohonen's map is a neural network used in the classification of complex multi-dimensional data [21]. The algorithm could be unsupervised, requiring no user intervention. The self-organizing map (SOM) is one of the most prominent artificial neural network models adhering to the unsupervised learning paradigm. The model consists of a number of neural processing elements, i.e. units. Each of the units i is assigned an n -dimensional weight vector m_i , $m_i \in R_m$. The training process of self-organizing map may be described in terms of input pattern presentation and weight vector adaptation. Each training iteration t starts with the random selection of one input pattern $x(t)$. This input pattern is presented to the self-organizing map and each unit determines its activation. Euclidean distance between the weight vector and the input pattern was used to calculate a unit's activation. In this particular case, the unit with the lowest activation is referred to as the winner, c , of the training iteration, as given in equation 1.

$$c:m_c(t) = \min_i \|x(t) - m_i(t)\| \quad (1)$$

Subsequently, the weight vector of the winner as well as the weight vectors of selected units in the vicinity of the winner are adapted. This adaptation is implemented as a gradual reduction of the difference between corresponding components of the input pattern and the weight vector, as shown in equation 2.

$$m_i(t+1) = m_i(t) + \alpha(t) * h_{ci}(t) * [x(t) - m_i(t)] \quad (2)$$

Geometrically speaking, the weight vectors of the adapted units are moved slightly towards the input pattern. The amount of weight vector movement is guided by a so-called learning rate, α , decreasing in time. The number of units that are affected by adaptation as well as the strength of adaptation is determined by a so-called neighborhood function h_{ci} . This number of units decreases in time. Typically, the neighborhood function is a unimodal function, which is symmetric around the location of the winner and monotonically decreasing with increasing distance from the winner. A Gaussian is used to model the neighborhood function. At the beginning of training a wide area of output space is subject to adaptation. The special width of units affected by adaptation is reduced gradually during the training process. Such a strategy allows the formation of large clusters at the beginning and a fine-grained input discrimination towards the end of training process. The training process of the self-organizing map leads to a spatial arrangement of the input pattern such that alike input are ordered in a topological map (U-matrix) [21,22]. Training has enabled the convergence of the system towards a model clustering the internal nature of data (Fig. 2).

The default training algorithm in SOM script is this batch algorithm; this because it needs a much smaller number of iterations than the classic one, and each iteration uses a large number of input data points. The whole training set is gone through at once and only after this the map is updated with the net effect of all the samples. Actually, the updating is done by simply replacing the prototype vector with a weighted average over the samples where the weighting factors are the neighborhood function values.

$$m_i(t+1) = \frac{\sum_{j=1}^n h_{ic(j)}(t)x_j}{\sum_{j=1}^n h_{ic(j)}(t)} \quad (3)$$

where $c(j)$ is the BMU of sample vector x_j , $h_{i,c(j)}$ is the neighborhood function (the weighting factor), and n is the number of sample vectors.

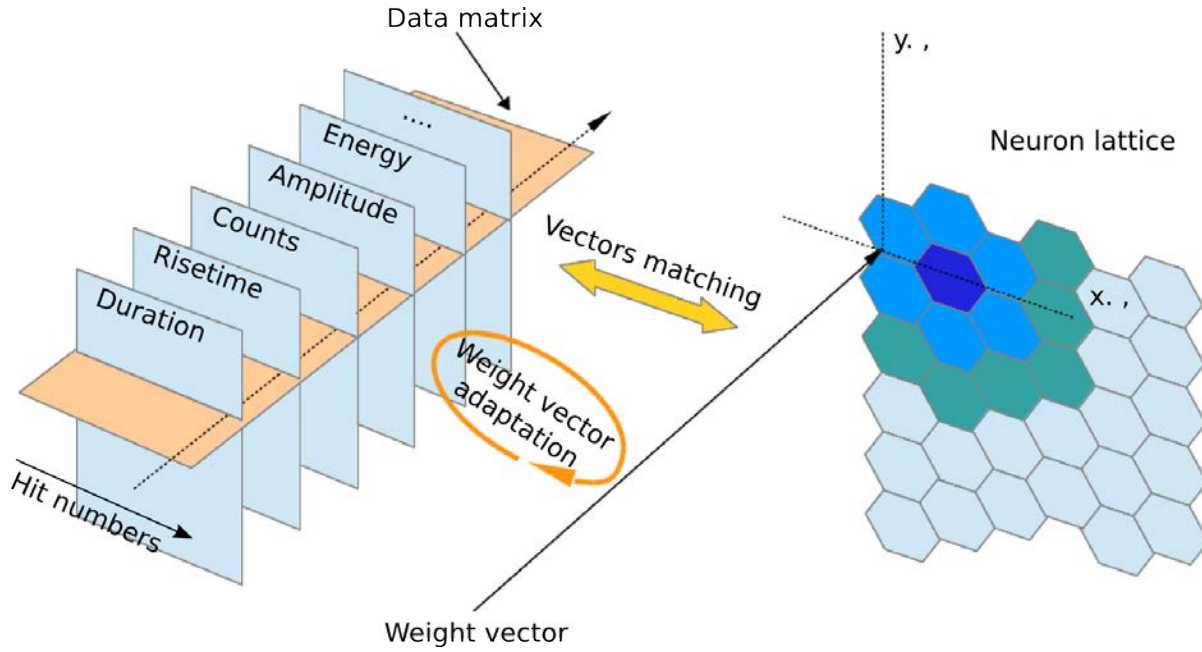


Fig. 2: Scheme of SOM training operation.

Additional information can be obtained by plotting the hit histogram U-matrix. This map shows the projection of data samples into map. The data are calculated by finding the BMU (Best Matching Unit) of each data sample from the map, and increasing a counter in the map unit each time it is the BMU. The colors are related to a specific level of a variable and hexagon size is related to the numbers of AE hits related to that cluster point.

3. Results and discussion

Figure 3 shows the cumulative hits plot against acquisition time, with the purpose to indicate the AE activity evolution with time. We can identify three relevant steps that could be related to specific damage evolution of the steel.

Region I: During the early stages of the test there was a significant AE activity due to initial electrochemical interaction between the steel wires and the electrolyte solution. This period of activity is characterized by several sub-steps due to the activation and stabilization of different corrosive phenomena. At first the AE activity is related to the homogenization and stabilization of reactions at the metal surface in the corrosive solution [23]. Region I is characterized by events in a wide range of amplitude (in the range 40-70 dB) and usually medium-high rise-time ($> 30 \mu s$). The low amplitude events could be attributed mainly to hydrogen formation at the steel surface [24,25]. As reported in literature, AE with amplitudes in the range of 40-50 dB with high rise-

time can be induced by hydrogen evolution phenomenon [26]. Besides, the presence of hydrogen favors the breakdown mechanism of a pseudo-passive layer at the metal surface of the strand and the beginning of hydrogen diffusion inside the metal, inducing a strong AE activity [27]. During this incubation period, corrosion mechanisms are activated, as random pit formation on the surface of the metal [28]. The localized corrosion is however not sufficiently energetic to be detected by AE, but it could also favor the energetically more relevant SCC [29]. The SCC initiation phenomenon induces events with low duration, counts and rise-time and amplitude in the same range of hydrogen evolution events (30-50 dB) [30]. The crack initiation is followed by short crack propagation, identified with AE at higher amplitude (in the range 60-70 dB) [30].

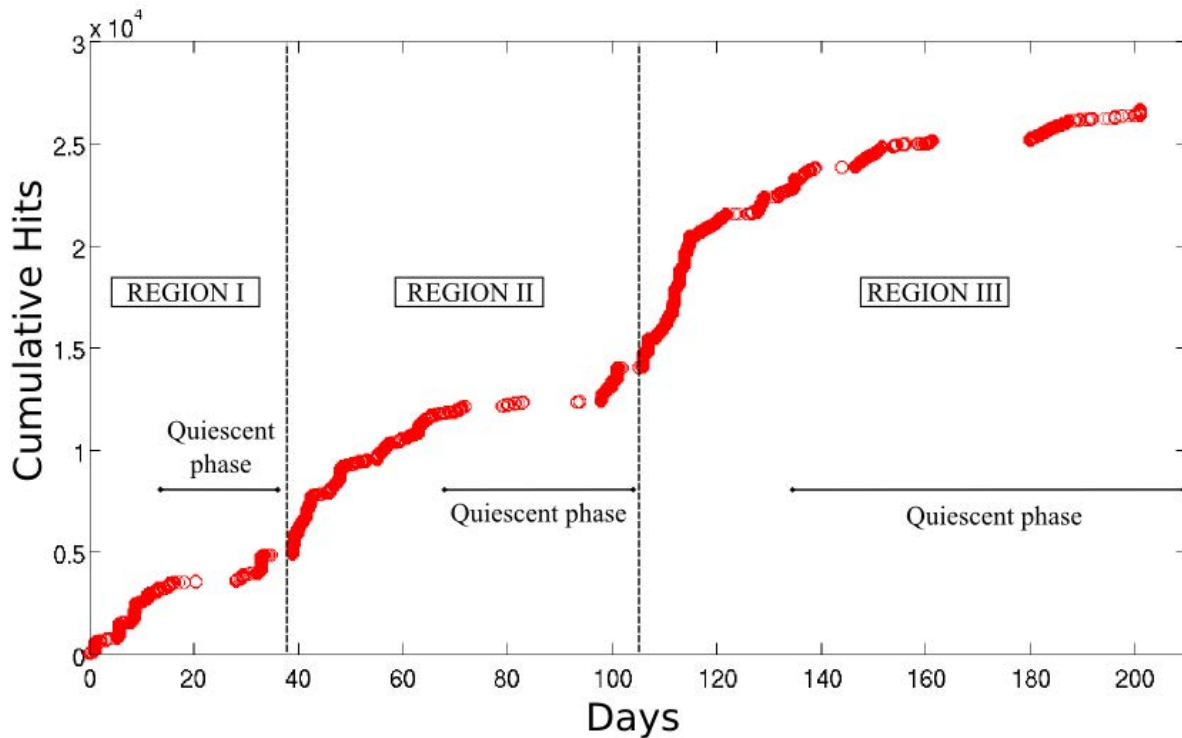


Fig. 3: Cumulative hits plot versus time.

Region II: After 35 days a new swarm of significant events in a short period occurred (in about 15 days over 5000 hits were observed) and the cumulative AE hit curve increases significantly. Afterwards the structure has a new quiescent phase where the increase of AE hits is very low. At this stage, at the strand surface, micro-cracks gradually initiate, increase and coalesce [14,31,32]. This phase is the evolution stage concerning hydrogen embrittlement and propagation of cracks [23]. This is confirmed by the relevant amount of events in the range amplitude of 40-50 dB with the rise-time about 100 μ s. The hydrogen diffusion through the metal lattice occurs. When the hydrogen uptake is sufficient for the steel to overcome its threshold stress intensity factor a new AE activity will take place, due to initiation and propagation of cracks [23]. In region II the time period between two AE events increases significantly; this phenomenon could be related with the formation of plastic zone at the crack tip during the crack propagation stages [26]. With increasing the crack length an increase of stress concentration occurs, which induces larger plastic zone ahead of the crack tips. This results in a greater blunting of the crack tip. Larger plastic zone implies that a longer

time is needed for crack to resharpen by dissolution for further crack propagation. The period of time between two AE events corresponds to the period of material dissolution that induced the crack growth [26]. This could explain the larger time gaps between two AE events during later stages of crack growth.

Region III: High-intensity AE events were recorded after four months. Some steel wires were approaching final rupture and the post-tensioned concrete beam was undergoing a stabilization phase due to a new redistribution state of stress levels. This phase of reassessment was the prelude to new damaging phases progressively much more destructive. After this period we acquired about 25,000 AE events for a total of about 800,000 cumulative counts. In this phase the AE were mainly generated by crack propagation. However, corresponding to wire failure, the intense AE activity was probably generated due to rapid reduction of the cross-section during its rupture [28]. The large burst of activity characterized by very high energy and amplitude up to 90 dB is symptomatic of final ductile fracture of a strand [30].

These considerations are summarized in Fig. 4 that shows the rise time versus amplitude distribution of the data discriminated according to the three steps identified in Fig. 3. In Region I, it is possible to identify the AE phenomena related with corrosion activation and crack initiation (oxide breakdown, hydrogen evolution, SCC initiation). In Region II the acoustic events, characterized by low amplitude and medium risetime, were associated to hydrogen embrittlement mechanisms. Finally in Region III we have a large amount of data at medium amplitude related with crack propagation and few AE events with very high amplitude due to the final fracture of the strand.

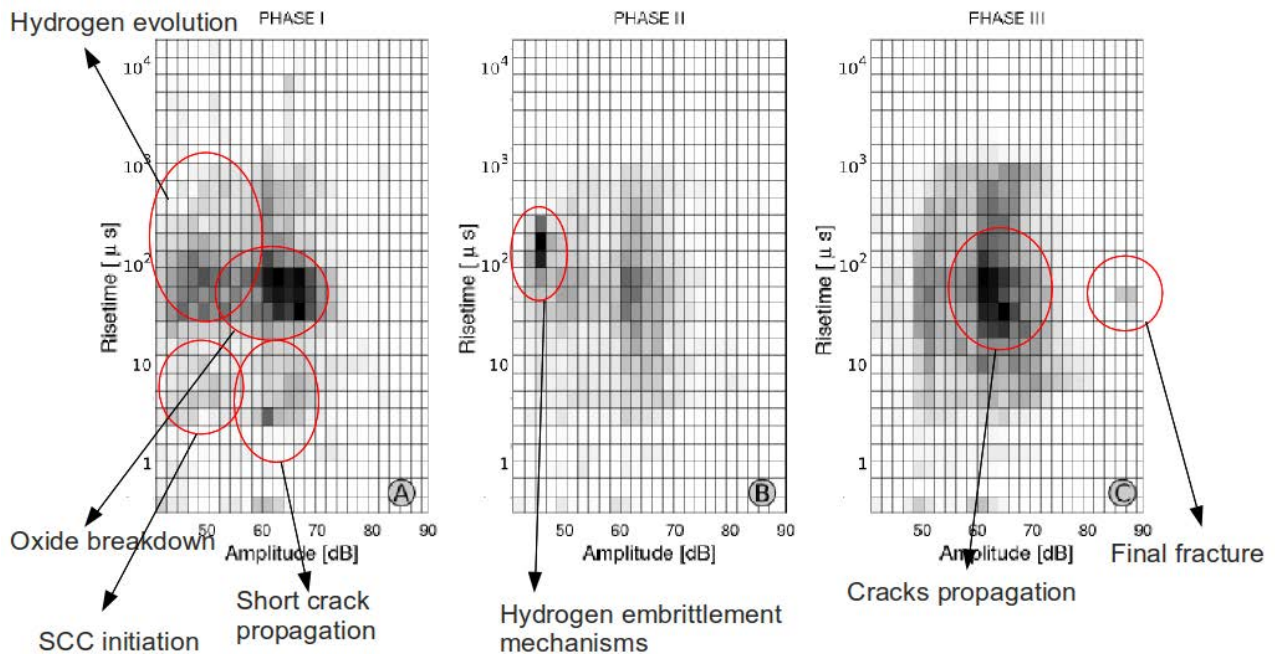


Fig. 4: Amplitude vs. risetime grid maps; corrosion mechanisms identification was done following literature data.

The Kohonen's self-organizing map algorithm was applied to the uncorrelated variables resulting from the analysis of the correlation matrix, i.e. average frequency, amplitude, duration, energy, time and event frequency. In Fig. 5 the U-matrix map resulting from SOM analysis is reported. The U-matrix map shows distances from map units and their nearest neighborhood,

evaluated by Euclidean method. High values of U-matrix map (red and yellow pixels) mean large distances between neighboring map units. Elements belonging to the same cluster are, therefore, identified by uniform areas of low value (blue pixels). In this specific case, we identified many homogeneous areas associated with cluster areas. It is interesting to note that using the topological maps of the variables (reported in Fig. 6) it should be possible, on the basis of variable magnitude distribution, to relate data cluster to local area of specific variables. In particular, according with the regions identified in Fig. 3 and on the basis of time variable maps we defined three regions on the U-matrix map. The definition of the area associated to the first region is heavily influenced by the event frequency distribution as can be observed in the topological map (Fig. 6).

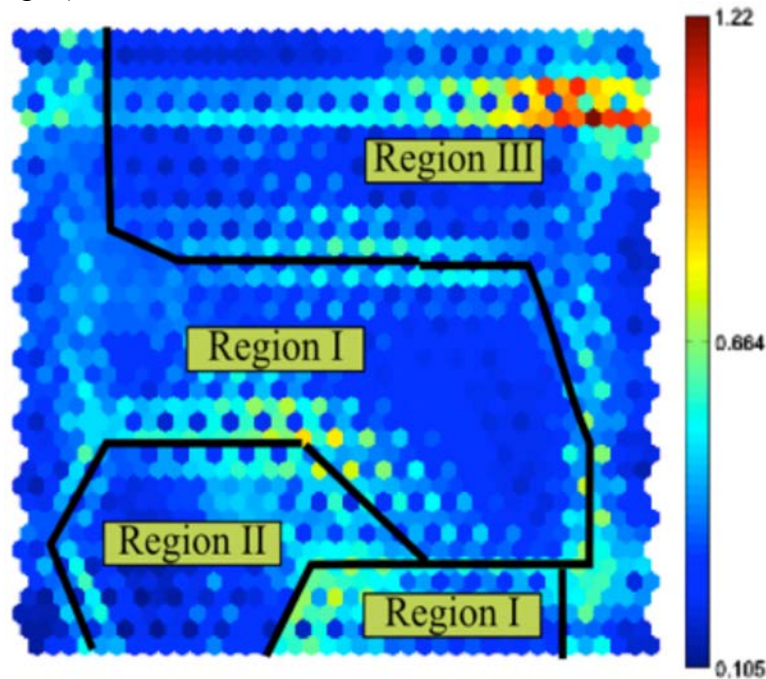


Fig. 5:U-matrix resulting from the application of the Kohonen self-organizing map algorithm.

In fact, the events characterized by high event frequency (red and yellow pixels in the event frequency topological map) are grouped in the right and central area of the map. The second region is a left bottom area in the U-matrix map. The events grouped there have a low event frequency and middle/average frequency and duration. The third region includes the top and right areas of the map. These events are characterized by energy and amplitude variables. In particular the AE events with highest energy are grouped in the top-right corner of the map. Furthermore, a large variation of duration and average frequency can be observed. In particular on the top of the map AE events with high duration and low average frequency are grouped; vice versa AE events with low duration and high average frequency are grouped in the right side of the U-matrix map.

Based on these considerations it is possible to say that the U-matrix identifies some clusters related to the damage evolution of the steel strand. But further investigation are necessary to better clarify the discrimination of that damage phenomena and its time evolution. With this purpose a so-called hits-U-matrix (Fig. 7) was performed using the data collected in the regions identified in Fig. 3. This graph shows the projection of data samples into the U-map. The projection is obtained by finding the BMU (best matching unit) of each data sample from the map, and increasing a counter in the map unit each time it is the BMU. The colors are related to a

specific event group (activation or quiescence phase as defined in Fig. 3) and colored hexagon size is related to the numbers of AE hits related to that cluster point. Figure 7 shows that the interpretation of the U-matrix map could be much more complex than the previous analysis.

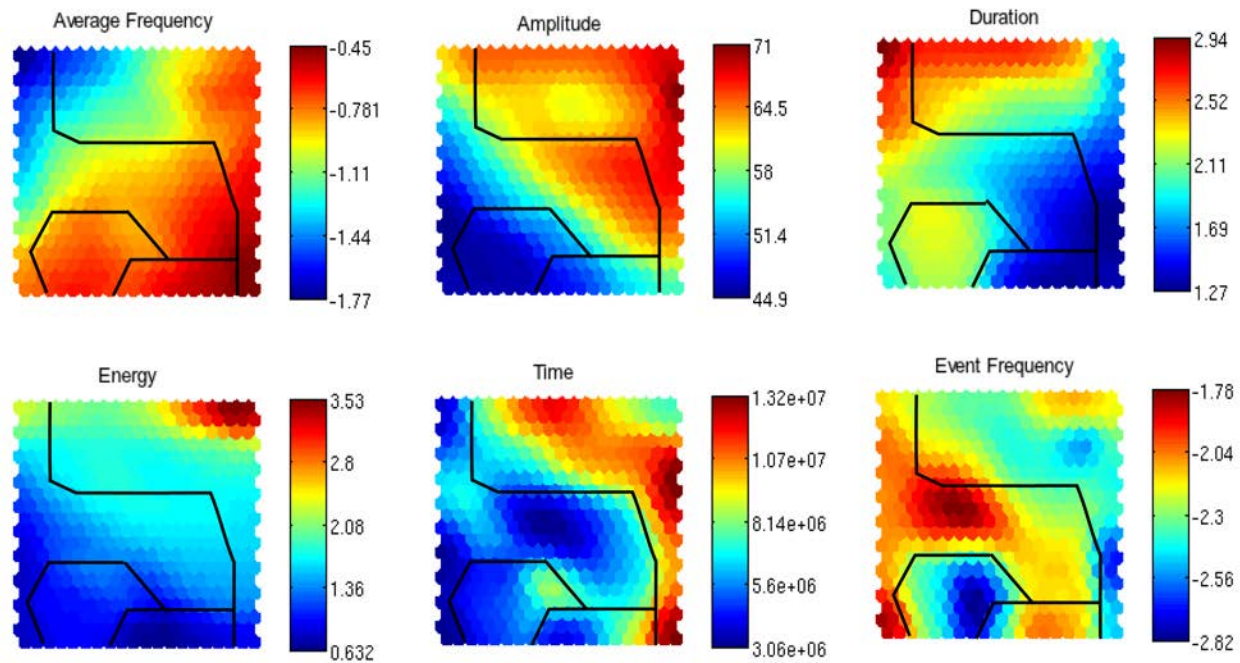


Fig. 6: Topological maps of the variables as resulted from the application of the Kohonen's self-organizing map algorithm.

The clusters associated with the regions *I*, *II* and *III* are characterized by several events, which could create internal sub-cluster or interference regions where multiple families of events coexist.

Region I: About the data collected in region *I*, the activation AE are located mainly in the zone *Ia* (characterized by high energy and high duration) and *Ib* (characterized by low energy and low amplitude); in contrast, the quiescence data are not well identifiable in a specific area, although a group of hits of these events is identifiable in the zone *Ic* and *Id*. The area *Ic* includes AE events of the region I characterized by low energy, medium low amplitude and high average frequency. The area *Id* is related mainly with quiescence AE with high amplitude and relatively high average and event frequency.

Region II: Other considerations can be extrapolated analyzing the hits distribution for region II data. A large amount of activation AE are located in *Ila* and *Ilb* region, with the former related with lower event frequency than the latter one. The zone *Ilc* could be related with the quiescence phase of region II.

Region III: The analysis of the hits map for region III data confirms that the AEs of this region are located in the top of the map. In particular a large amount of activation data are located in the top corner. The AE with very high energy, generated during the activation of region III, are located on the top-right corner of the map (area *IIIa*). The quiescence phase is located in peripheral region of this section of the map. In particular in the quiescence phase two sub-cluster can be identified. Events with high duration and low average frequency are mainly grouped in area *IIIb*, while events with high amplitude and low duration are predominant in area *IIIc*.

With the purpose to verify the hits distribution and to better clarify the discriminating performances of the SOM analysis about the event evolution on SCC tests on post-tensioned strands, a hits validation map was analyzed by using a fuzzy response parameter to show the relative goodness of each map unit in representing the data. The fuzzy response was calculated by summing a function of quantization error as follow [33]:

$$g(x, u_i) = \frac{1}{(1 + (q_i/a)^2)} \quad (4)$$

where $q_i = |x - u_i|$ is the quantization error (i.e. the distance between the sample x and map unit u_i). The scaling factor a is the average distance between each training data sample and its BMU. Consequently, a high value of the fuzzy response is related to high affordability of the previsioned hits.

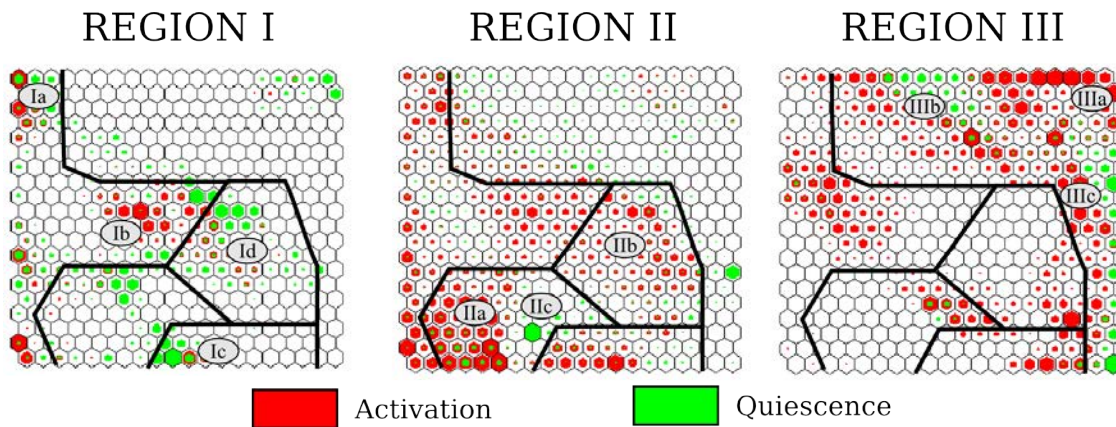


Fig. 7: Hits U-matrix for the data regions identified in Fig. 3.

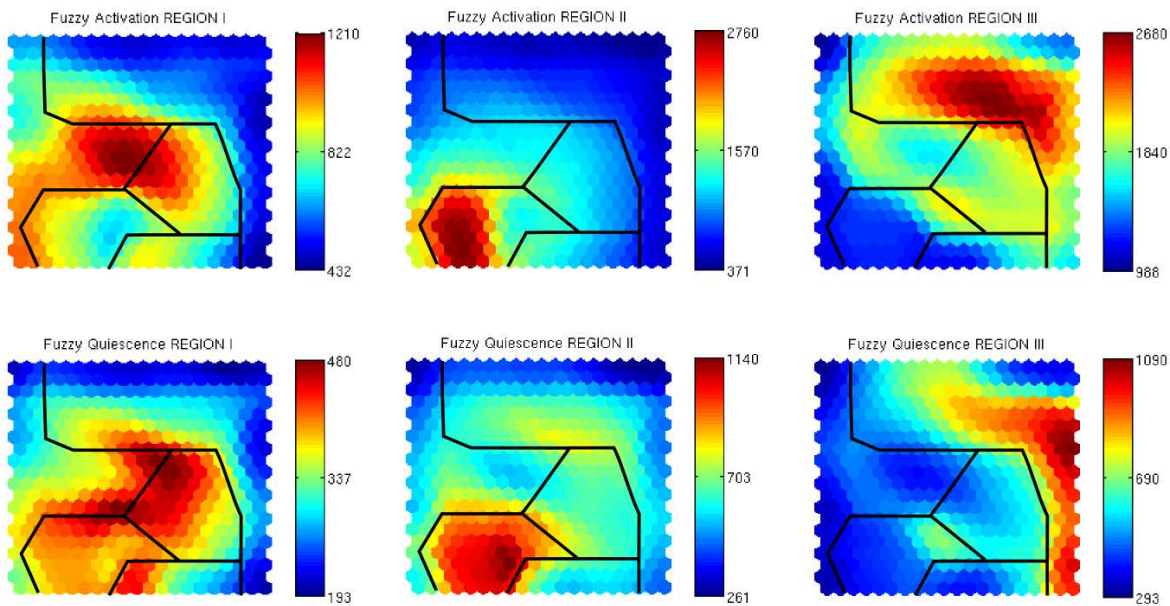


Fig. 8: Fuzzy response index distribution for data regions identified in Fig. 3.

Figure 8 confirm that the SOM analysis identified the damage phase of the SCC strand well as reported in Fig. 7. The activation and propagation data for each region are well clustered in local areas on the U-matrix map. All configurations showed a high fuzzy response index, related

with high accuracy of the numerical analysis. A higher uncertainty was observed only for region II quiescence data, where we observe a low fuzzy response value (maximum value is only 480).

Consequently, only for this dataset, we believe that not enough information was available to discriminate with good affordability their location on the U-matrix map. Furthermore this investigation showed that in the middle of the U-matrix map an interference area generated by AE of region I and II was present.

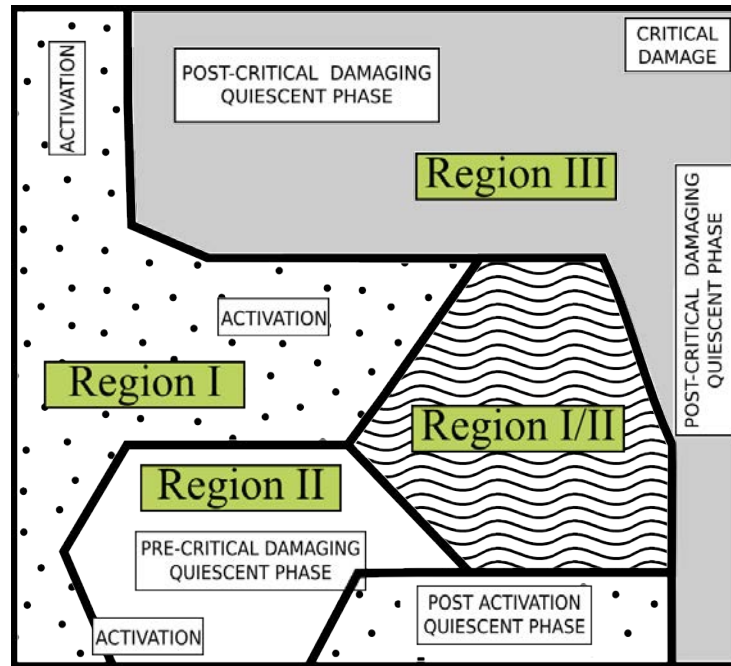


Fig. 9: Scheme of damage detection areas by SOM.

On the basis of the above reported considerations it is possible to divide the U-matrix map into specific damage mechanism areas, according to the schematic representation shown in Fig. 9. Here, we can distinguish the activation, propagation and critical damage areas, respectively, related with areas *Ia* and *Ib*, *IIa* and *IIb* and finally *IIIa*. The peripheral regions, not directly related with a specific variable (and characterized by multiple sub-clusters) represent the quiescence areas. In particular, the peripheral area *Ic* includes quiescent events that occurred after the electrochemical activation of steel surface characterized by high level of average frequency. The so-called pre-critical damaging quiescent area (*IIc*) was instead characterized by low event frequency and middle duration events. Consequently, the lower peripheral region in the map is related with the quiescent phase events before the critical damaging of the structure, while the peripheral regions at the top and right of the map (*IIIb* and *IIIc*) are related to the quiescent phase following the critical damaging and characterized mainly by high amplitude values.

The changes in waveform patterns of AE hits during the above described damage evolution are well visualized in Fig. 10. Starting from the activation phase (*Ia*) where AE hits are characterized by low average frequency, medium amplitude and high duration, in region II (*IIa*) we can observe an AE hit population defined by medium-high average frequency, low amplitude and medium duration, while the final damage step (post critical quiescent phase in region III, i.e. *IIIc*) is characterized by very high average frequency, medium high amplitude and very low duration.

Globally, the authors believe that the self-organizing map algorithms and the related U-matrix maps are powerful instruments for analyzing multivariate data set. In the specific cases their application allowed not only to validate preliminary hypotheses formulated on the basis of the interpretation of cumulative hit curve but permitted to discriminate between different damage mechanisms occurring over time on steel strands on the basis of the correlation between specific AE wave attributes.

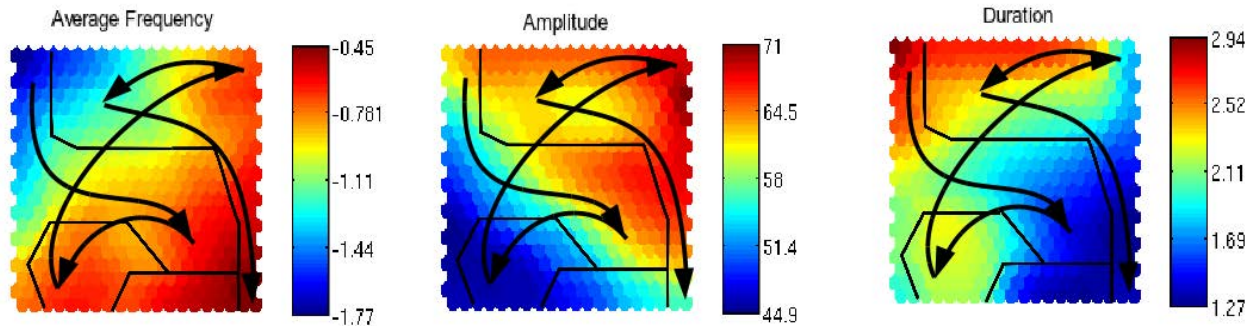


Fig. 10: Trajectory plots of some AE hit patterns during damage evolution.

4. Conclusions

Acoustic emission (AE) technique was used to monitor hydrogen-assisted stress corrosion cracking of post-tensioned strands stimulated by using accelerated test with an ammonium thiocyanate solution. Three damage phases were clearly distinguished from the cumulative hit plot, but a more detailed interpretation of the damage mechanisms occurring on steel wires during aging time was obtained by using a self-organizing map (SOM) methodology. The numerical results show that it is possible to integrate in an effective and synergistic way by using SOM with the traditional univariate analysis. Moreover this methodology has proved particularly effective in identifying, using exemplified topological maps, the evolution and intensity of corrosion damage on steel wires in the monitored post-tensioned concrete beam. Initiation, propagation and critical rupture phases were clearly identified and associated to specific features of the AE events. Such results allow, also on the basis of further refining of the methodology, to hypothesize the use of such a procedure for *in situ* recognition of damage processes.

References

- 1 R. Benaim, 'The design of prestressed concrete bridges: concepts and principles', Taylor & Francis, New York, 2008.
- 2 N.R. Hewson, 'Prestressed Concrete Bridges: Design and Construction', Thomas Telford London, 2003.
- 3 J.S. West, C.J. Larosche, B.D. Koester, J.E. Breen, M.E. Kreger, 'State-of-the-Art. Report about Durability of Post-Tensioned Bridge substructures', Centre for Transportation Research Bureau of Engineering Research, University of Texas at Austin, Research Report 1405-1, 1999.
- 4 ACI 222.2R-01. 'Corrosion of prestressing steels' – ACI Committee 222; 2001.
- 5 R.M. Salas, A.J. Schokker, J.S. West, J.E. Breen, M.E. Kreger, 'Conclusions, Recommendations and Design Guidelines for Corrosion Protection of Post-Tensioned Bridges', Center for Transportation Research, The University of Texas at Austin, Research Report 1405-9, 2005.

- 6 C.L. Freyermuth, 'Durability of Post-Tensioned Concrete Structures', *Concrete International*, Vol 13, pp 58-65, 1991.
- 7 R.C. Newman, K. Sieradzki, 'Correlation of Acoustic and Electrochemical Noise in the Stress-Corrosion Cracking of Alpha Brass', *Scripta Metallurgica* Vol 17, No 5, pp 621-624, 1983.
- 8 S. Ramadan, L. Gaillet, C. Tessier, H. Idrissi, '*Detection* of stress corrosion cracking of high-strength steel used in prestressed concrete structures by acoustic emission technique', *Applied Surface Science*, Vol 254, No 8, pp 2255-2261, 2008.
- 9 M. Ohtsu, Y. Tomoda, 'Acoustic Emission Techniques for Rebar Corrosion in Reinforced Concrete', in *Advances in Construction Materials*, Grosse, Christian U. ed., Springer Netherlands, Dordrecht, The Netherland, pp.615-621, 2007.
- 10 A. Nair, C.S. Cai, 'Acoustic emission monitoring of bridges: Review and case studies', *Engineering Structures* Vol 32, No 6, pp1704-1714, 2010.
- 11 J. Toribio, A.M. Lancha, 'Anisotropic stress corrosion cracking behaviour of prestressing steel', *Materials and Corrosion* Vol 49, pp 34-38, 1998.
- 12 D.G. Enos, J.R. Scully, 'A Critical-Strain Criterion for Hydrogen Embrittlement of Cold-Drawn, Ultrafine Pearlitic Steel', *Metallurgical and Materials Transactions A Volume 33A*, pp 1151, April 2002.
- 13 M.G. Alvarez, P. Lapitz, J. Ruzzante, 'Analysis of acoustic emission signals generated from SCC propagation', *Corrosion Science*, Vol 55, pp 5-9, 2012.
- 14 S. Yuyama, T. Kishi, Y. Hisamatsu, 'AE analysis during corrosion, stress corrosion cracking and corrosion fatigue processes', *Journal of Acoustic Emission* 2 (1983) 71–93.
- 15 S. Yuyama, 'Fundamental aspects of acoustic emission applications to the problems caused by corrosion'. In: Moran G.C. , Labine P., '*Corrosion Monitoring in Industrial Plants Using Nondestructive Testing and Electrochemical Methods*', ASTM STP 908, American Society for Testing and Materials, Philadelphia , pp. 43–74, 1986.
- 16 A.A. Anastasopoulos, 'Signal processing and pattern recognition of AE signatures, in *Experimental Analysis of Nano and Engineering Materials and Structures*', Springer Netherlands, Dordrecht, The Netherland, 929, 2007.
- 17 E. Proverbio, 'Evaluation of deterioration in reinforced concrete structures by AE technique,' *Materials and Corrosion*, Vol 62, No 2, pp 161-169, 2011.
- 18 E. Proverbio, G. Campanella, V. Venturi , 'Evaluation of damage evolution under repeated loading of post tensioned concrete beams by acoustic emission', 12th International Conference on Structural Faults and Repair, University of Edinburgh U.K., 10 - 12 June 2008.
- 19 ISO 15630 – 3:2002, 'Steel for Reinforcement and Pre-stressing of Concrete – Test Methods – Part 3: Pre-stressing Steel,' Int. Org., Geneva, Switzerland, 2002.
- 20 L. Calabrese, G. Campanella, E. Proverbio, 'Noise removal by cluster analysis after long time AE corrosion monitoring of steel reinforcement in concrete', *Construction and Building Materials* Vol 34, pp 362–371, 2012.
- 21 T. Kohonen, 'Self-organized formation of topologically correct feature maps', *Biological Cybernetics*, Vol 43, pp 59-69, 1982.
- 22 N. Godin, S. Huguet, R. Gaertner, L. Salmon, 'Clustering of Acoustic Emission Signals Collected during Tensile Tests on Unidirectional Glass/Polyester Composite Using Supervised and Unsupervised Classifiers', *NDT&E Int*, Vol 37, pp 253-264, 2004.
- 23 M. Perrin, L. Gaillet, C. Tessier, H. Idrissi, 'Assessment of stress corrosion cracking in prestressing strands using AE technique', *Journal of Acoustic Emission*, Vol 26, pp 32-39, 2008.
- 24 S. Ramadan, H. Idrissi, 'In situ monitoring of deposition and dissolution of calcium

- carbonate by acoustic emission techniques associated to electrochemical measurements', *Desalination*, Vol 219, pp 358-366, 2008.
- 25 M. Fregonese, H. Idrissi, H. Mazille, Y. Cetre , L. Renaud, 'Initiation and propagation steps in pitting corrosion of austenitic stainless steels: monitoring by acoustic emission', *Corrosion Science*, Vol 43, No 4, 627-641, 2001.
- 26 H. Shaikh, R. Amirhalingam, T. Anita, N. Sivaibharasi, T.Jaykumar , P. Manohar, H.S. Khatak, 'Evaluation of stress corrosion cracking phenomenon in an AISI type 316LN stainless steel using acoustic emission technique', *Corrosion Science* Vol 49, No 2, pp 740-765, 2007.
- 27 C. Jomdecha, A. Prateepasen, P. Kaewtrakulpong, 'A study on source location using acoustic emission system on various type of corrosion in industry', *NDT&E International*, Vol 40, pp 584-593, 2007.
- 28 J. Kovac, M. Leban, A. Legat, 'Detection of SCC on prestressing steel wire by the simultaneous use of electrochemical noise and acoustic emission measurements', *Electrochimica Acta*, Vol 52, pp 7607-7616, 2007.
- 29 S. Ramadan, L. Gaillet, C. Tessier, H. Idrissi, 'Contribution of acoustic emission to evaluate cable stress corrosion cracking in simulated concrete pore solution', *Journal of Acoustic Emission*, Vol 27, pp 254-262, 2009.
- 30 J. Kovac, C. Alaux, T.J. Marrow, E. Govekar, A. Legat, 'Correlations of electrochemical noise, acoustic emission and complementary monitoring techniques during intergranular stress-corrosion cracking of austenitic stainless steel', *Corrosion Science*, Vol 52, pp 2015-2025, 2010.
- 31 S. Ramadan, L. Gaillet, C. Tessier, H. Idrissi, 'Detection of stress corrosion cracking of high-strength steel used in prestressed concrete structures by acoustic emission technique', *Applied surface science* Vol 254, pp 2255–2262, 2008.
- 32 S. Ramadan, L. Gaillet, C. Tessier, H. Idrissi, 'Assessment of the stress corrosion cracking in a chloride medium of cables used in prestressed concrete structures by the acoustic emission technique', *Measurement Science and Technology* Vol 19, pp 115702-115710, 2008.
- 33 J. Himberg, J. Ahola, E. Alhoniemi, J. Vesanto, O. Simula, 'The Self-Organizing Map as a Tool in Knowledge Engineering, in *Pattern Recognition in Soft Computing Paradigm*', by N.R. Pal, World Scientific, Singapore 2001.

On the Use of the Acoustic Emission Technique for In-situ Monitoring of the Pulverization of Battery Electrodes

Aurélien Etienneble^{1,2}, Hassane Idrissi² and Lionel Roué¹

¹ INRS-Énergie, Matériaux et Télécommunications, 1650, bd. Lionel Boulet, Varennes, Québec, J3X1S2 Canada.

² INSA-Lyon MATEIS CNRS UMR5510, F-69621 Villeurbanne, France

Abstract

Acoustic emission coupled with electrochemical measurements have been successfully applied for the *in situ* monitoring of the cracking upon cycling of metal hydride electrodes for Ni-MH batteries and Si-based electrode for Li-ion batteries. This method offers the possibility to characterize the electrode disintegration process depending on the electrode composition and cycling conditions and then, it would become a powerful tool in the evaluation/optimization of new electrode materials for different types of batteries.

Keywords: particle cracking, metal hydride, silicon, Ni-MH battery, Li-ion battery

1. Introduction

In various batteries, the electrode cracking due to the volume variation of the active materials with cycling has a negative effect on the battery durability by accelerating the electrode corrosion by the electrolyte and/or by inducing a loss of electronic connectivity. For instance, for LaNi₅-based alloys used as metal hydride materials in commercial Ni-MH batteries, the pulverization phenomenon induces the breaking of the native surface oxide layer and increases the effective surface area of the electrode. This favors the hydriding reaction but it also decreases the MH cycle life by increasing the alloy corrosion rate [1, 2]. For Mg-based alloys, which present higher hydrogen storage capacities than the conventional LaNi₅-based alloys, the pulverization process intensifies the irreversible oxidation of the active material by the KOH electrolyte. For instance, amorphous MgNi and crystalline MgTi-10%_w Pd alloys obtained by high-energy ball milling have a maximum discharge capacity close to 500 mAh g⁻¹, but retain less than 50 % and 70 % of it after only 10 cycles, respectively [3, 4].

For Li-ion batteries, silicon-based anode appears as an attractive candidate to replaced carbon-based anode, thanks to a ten-times higher capacity (3572 mAh g⁻¹) and safer behavior than that of graphite electrodes [5]. However, the cracking of the silicon-based anodes due to the important volume variation of the Si particles (up to ~300 %) with lithiation has a negative effect on their cycle life by inducing a loss of electronic connectivity within the composite electrode in addition to be unfavorable to the formation of a stable solid electrolyte interface (SEI) resulting in severe electrolyte degradation at the surface of the Si particles.

To date, the study of the electrode cracking in batteries is generally limited to a post mortem examination of the electrode by microscopy. This does not allow a detailed analysis of the cracking process, which can significantly vary depending on the electrode composition and processing, and the charge/discharge conditions. However, we have recently shown that the acoustic emission (AE) technique is a relevant tool for *in situ* monitoring of the cracking of MgNi and LaNi₅-based electrodes for Ni-MH batteries [6, 7]. We have demonstrated that MgNi

and LaNi₅-based alloys present different pulverization mechanisms. It was also shown that the cracking of MgNi increases with the particle size and the charge rate [7]. A new experimental set-up constituted of an electrochemical cell connected to a compression load cell and an AE equipment was also used to characterize the force and the cracking of LaNi₅-based and MgNi electrodes generated by their volume expansion/contraction during their cycling [8].

In the present paper, acoustic emission coupled with electrochemical measurements is performed on different metal-hydride electrodes for Ni-MH batteries and on a Si-based anode for Li-ion batteries. It will be shown that this methodology is very effective for determining the main process responsible of their decrepitation.

2. Experimental

2.1 Metal hydride electrodes

A commercial LaNi₅-based alloy (MmNi_{13.68}Co_{0.78}Mn_{0.36}Al_{0.28}) powder from Japan Metals & Chemicals Co, MgNi and MgTi-10%_w Pd alloy powders obtained by high energy ball milling [3, 4] were studied as active materials. 0.2 g of active material was manually mixed with 0.2 g of copper powder. The mixture was then cold pressed on 2 g of copper powder at 6 tons cm⁻² for 10 minutes in a stainless steel die to form a pellet (16 mm in diameter, ~2 mm in thickness), which is used as working electrode.

The experimental set-up coupling AE and electrochemical measurements has been described elsewhere [6]. The reference electrode and the counter electrode were respectively an Hg/HgO electrode and a nickel wire. The three-electrode cell was monitored by a Voltalab PGZ 301 galvanostat/potentiostat. The working electrode was charged at -100 mA g⁻¹ for 3 h for the LaNi₅-based alloy and 5 h for MgNi and MgTi-10%_w Pd. It was discharged at 20 mA g⁻¹ until reaching -0.6 V vs. Hg/HgO for the LaNi₅-based and MgNi alloys and -0.5 V vs. Hg/HgO for MgTi. All the experiments were carried out at room temperature in a 6 mol l⁻¹ KOH solution. Before the first charge, the potential of the working electrode was maintained at -0.85 V vs. Hg/HgO for a few minutes to reduce the native oxide layer present on the Cu and active material powders.

The AE signals were recorded during cycling by a wide band sensor EPA micro 80 (frequency range 100-1000 kHz) and transmitted via an EPA USB Node acquisition card to the computer. For all the experiments, the gain G and the threshold S were fixed at 40 dB and 27 dB, respectively. The recorded AE signals were treated and the waveforms were obtained with AEWIn software (EPA). The AE signals are separated in two classes using Noesis software (EPA). The first one, labelled P1, is attributed to cracking of MH particles and the second one, labelled P2, is due to the release of H₂ bubbles [6, 7]. The temporal and energetic characteristics of the P1 and P2 classes were described in detail in ref. [6].

2.2 Silicon electrode

Pure Si (99.999%, 20 mesh) ball milled for 20 h with a ball-to-powder ratio of 5:1 using a SPEX 8000 mixer was used as active material, Super P carbon black (CB) as the conductive agent and carboxymethyl cellulose (CMC) as the binder. A mixture of 200 mg of active material + CB + CMC in a weight ratio of 80:12:8 with 0.5 ml of citric acid + KOH buffer solution at pH

3 was mixed at 500 rpm for 1 h using a Fritsch Pulverisette 7 mixer. The slurry was tape cast onto a 25 μm thick copper foil and dried for 12 h at room temperature and then 2 h at 100°C in vacuum. Structural and morphological characteristics of the Si powder and electrochemical behavior of the Si/CB/CMC anode were described in detail in ref. [9].

Two-electrode Swagelok cells were used for the cycling tests performed at room temperature using a VMP3 potentiostat/galvanostat. The cells were assembled in a glove box under argon atmosphere and comprised (i) a 1 cm^2 disc of composite working electrode containing 0.7 mg $\pm 10\%$ of active material, (ii) a Whatman GF/D borosilicate glass-fiber sheet saturated with the electrolyte (1M LiPF_6 dissolved in 1:1 dimethyl carbonate/ethylene carbonate and (iii) a 1 cm^2 Li metal disc as the negative and reference electrode. Cycling tests were performed in galvanostatic mode between 1 and 0.005V versus Li^+/Li at a current density of 400 mA g^{-1} . The AE signals were obtained and treated as before using AEWIn and Noesis softwares (EPA).

3. Results and discussion

3.1 Metal hydride electrodes for Ni-MH batteries

3.1.1 Electrochemical behaviour

The evolution of the discharge capacity with cycling for LaNi_5 -based, MgNi and MgTi-10%_w Pd electrodes is shown in Fig. 1. In the case of the LaNi_5 -based electrode, a slight increase of the discharge capacity is observed during the two first cycles. This increase can be attributed to the particle cracking due their volume expansion with hydriding, leading to their activation by breaking the native surface oxide layer and by increasing the effective surface area of the electrode [1]. For the MgNi electrode, the discharge capacity decreases strongly with cycling. This is related to the irreversible oxidation of the active material by the KOH electrolyte (i.e., formation of $\text{Mg}(\text{OH})_2$), which is intensified by the creation of new surfaces with the particle cracking [3]. For the MgTi-10%_w Pd electrode, the discharge capacity increases during the two first cycles. This activation is associated with the phase transition from a bcc+hcp initial structure to an fcc phase induced by the hydriding reaction [4]. After the third cycle, the

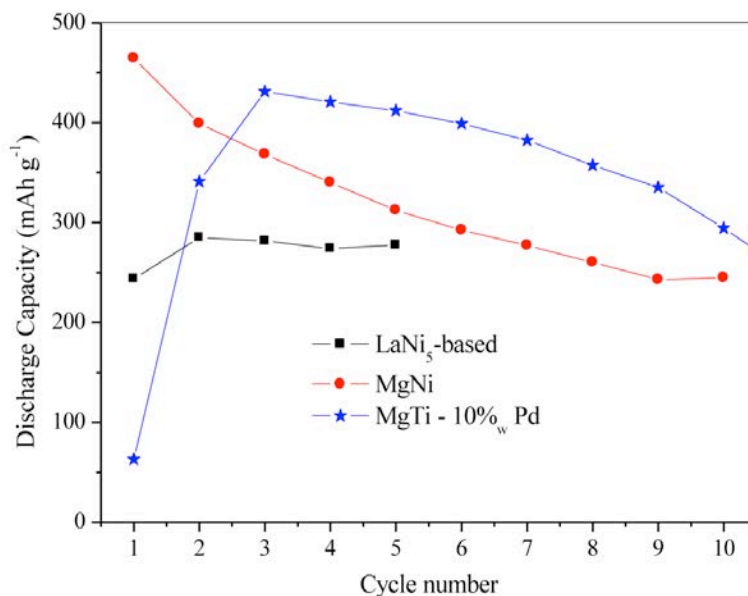


Fig. 1 Evolution of the discharge capacity with cycling for LaNi_5 -based, MgNi and MgTi 10%_w Pd electrodes.

discharge capacity decreases with cycling due to the irreversible oxidation of the active material by the KOH electrolyte as observed for the MgNi electrode.

3.1.2. AE Measurements

The evolution of the P1-type normalized AE activity (related to the particle cracking) and P2-type normalized AE activity (related to the formation of H₂ bubbles) during the first charge on LaNi₅-based, MgNi and MgTi-10%_wPd electrodes are shown in Figs. 2a and 2b, respectively. Note that no significant acoustic activity was observed during the discharge step (not shown).

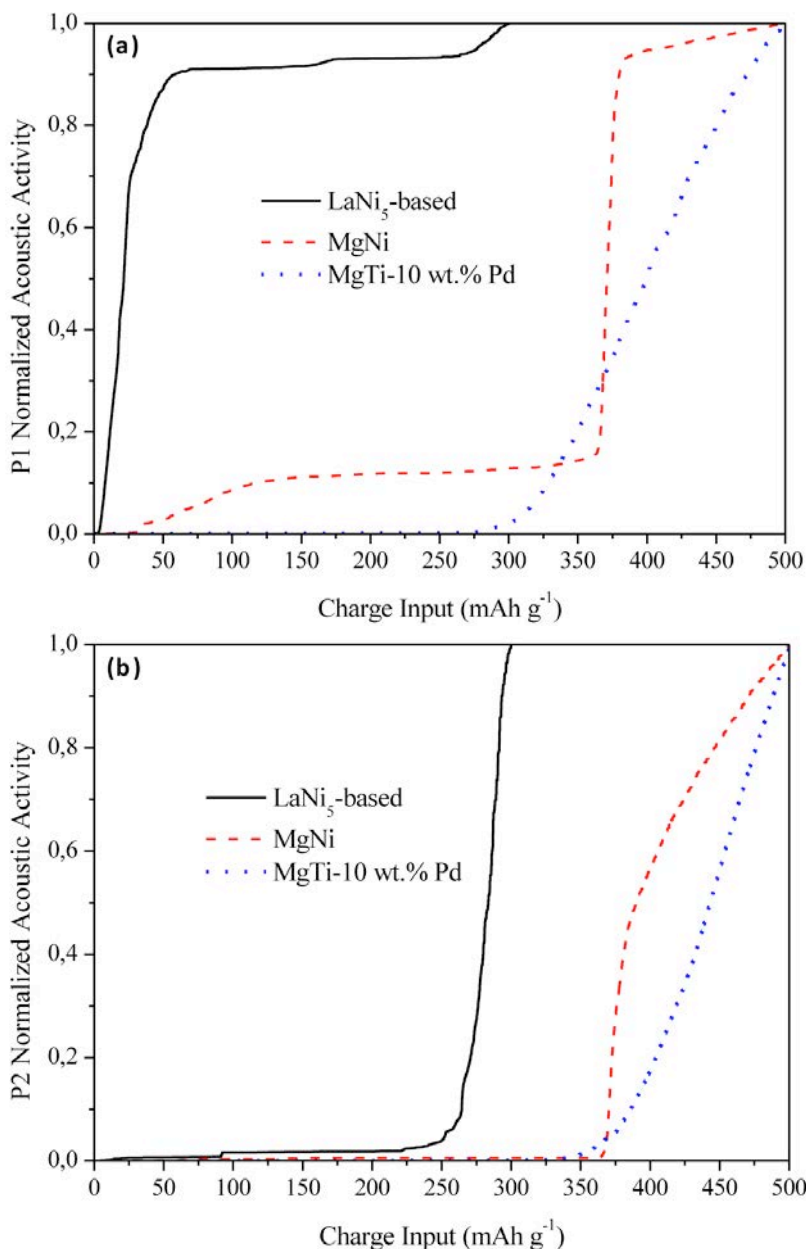


Fig. 2 Evolution of the P1-type (a) and P2-type (b) normalized acoustic activities as a function of the charge input on LaNi₅-based, MgNi and MgTi-10%_w Pd electrodes.

For the LaNi₅-based electrode, an abrupt increase of the P1-type acoustic activity is observed from ~5 to 25 mAh g⁻¹ (Fig. 2a). Almost no additional P1 events are observed during the rest of

the charge period, except at the end of the charge (*i.e.*, from $\sim 260 \text{ mAh g}^{-1}$) where a small increase in P1 activity is again observed. This indicates that the mechanical stress inducing the cracking of the LaNi₅-based alloy is concentrated at the beginning of the charge, *i.e.* in the α -to- β phase transition region. This is in accordance with in situ generated stress measurements [8] and in situ XRD investigations [1] on LaNi₅-based alloys showing that the volume expansion does not increase linearly with the H-content in the alloy but occurs abruptly when the α -to- β phase transition is initiated.

For the MgNi electrode, the evolution of the P1 activity with the charge input differs notably from that observed for the LaNi₅-based electrode. Indeed, a small increase of the P1 activity is observed from ~ 25 to 100 mAh g^{-1} . Then, no P1 activity is detected before reaching a charge input of $\sim 365 \text{ mAh g}^{-1}$ where an abrupt and large rise of the P1 activity is observed. At the same time, an important increase of the P2 acoustic activity related to the release of H₂ bubbles through the hydrogen evolution reaction (HER) is detected as shown in Fig. 2b. These observations demonstrate that the MgNi particle cracking is mainly induced by the HER rather than by the α - β lattice expansion in contrast to that was previously observed for the LaNi₅-based electrode. It can be explained by the fact that the MgNi alloy produced by ball milling has an amorphous structure, which results in the absence of abrupt volume expansion during the hydrogen absorption reaction (HAR) [8]. On the other hand, ball-milled MgNi powder is constituted of porous agglomerates made up of many particles cold-welded together (Fig. 3a) whereas LaNi₅-based powders appear much denser (Fig. 3c). These agglomerates are likely to be broken down by the mechanical stress induced by the accumulation of H₂ bubbles into the agglomerate pores during the HER.

For the MgTi-10%_w Pd electrode, no P1 activity is detected before reaching a charge input of $\sim 300 \text{ mAh g}^{-1}$ where an abrupt and large rise of the P1 activity is observed (Fig. 2a). At the same time, an important increase of the P2 acoustic activity related to the release of H₂ bubbles is detected (Fig. 2b). These observations suggest that the MgTi-10%_w Pd electrode pulverization is mainly induced by the mechanical action of the H₂ bubbles as observed for the MgNi electrode. This is not surprising since both materials are elaborated by ball-milling and present the same porous agglomerate morphology (Fig. 3b).

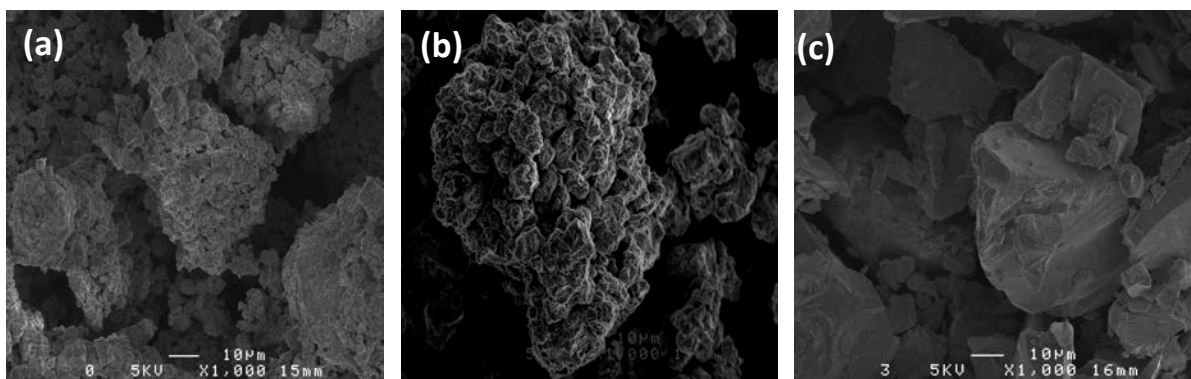


Fig. 3 SEM images of the MgNi (a), MgTi-10%_w Pd (b) and LaNi₅-based alloy (c) powders.

The evolution of the P1 acoustic activity with cycling on LaNi₅-based, MgNi and MgTi-10%_w Pd electrodes is shown in Fig. 4. On the three electrodes, the P1 activity is maximum during the first charge. This clearly indicates that the pulverization of the LaNi₅-based, MgNi

and MgTi-10%_w Pd electrodes mainly occurs during the first charge. Note that the P1 activity is lower for the MgTi-10%_w Pd electrode, which may indicate that this alloy is less sensitive to cracking. In addition, the fact that its P1 activity is maximum at the first cycle despite its low H-storage capacity (60 mAh g⁻¹, see Fig. 1) tends to confirm that its pulverization is mainly related to HER and not to the HAR.

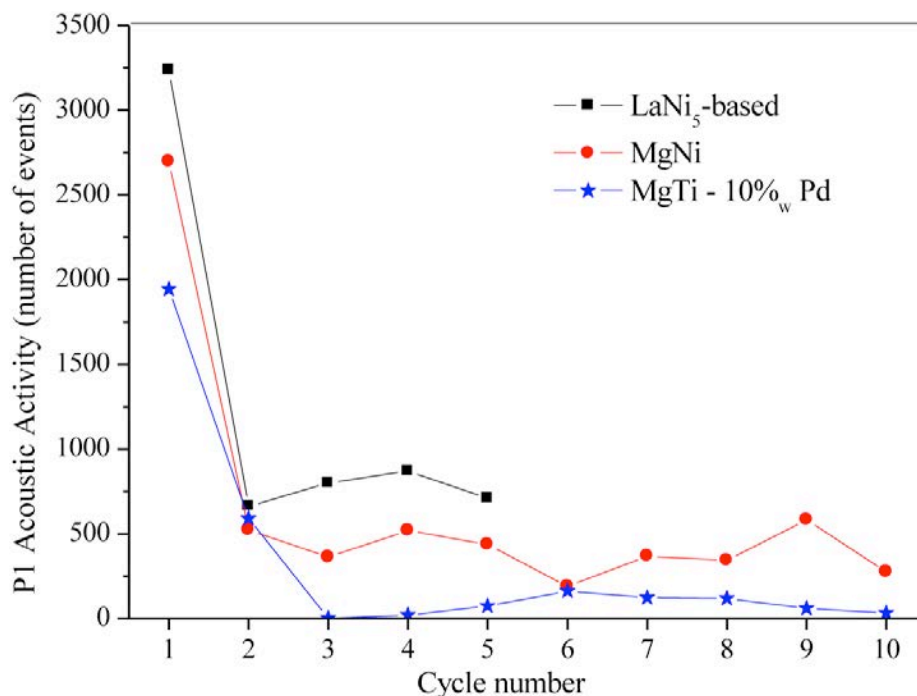


Fig. 4 Evolution of the P1 AE activity with cycling for LaNi₅-based, MgNi and MgTi-10%_w Pd electrodes.

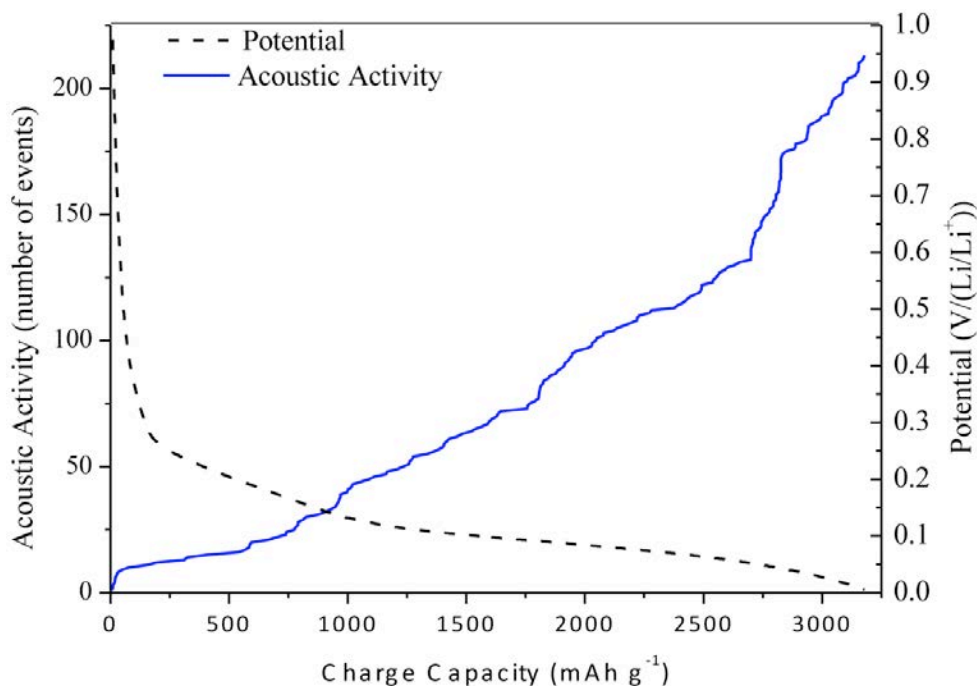


Fig. 5 Evolution of the electrode potential and AE activity as a function of the charge capacity during the first lithiation of the silicon electrode.

3.2 Silicon electrode for Li-ion batteries

3.2.1. Evolution of the acoustic activity during the first charge (lithiation)

The evolution of the electrode potential and the acoustic activity as a function of the charge capacity during the first lithiation of the silicon electrode are shown in Fig. 5. During the first lithiation, the electrode potential first decreases quickly up to reach a sloping plateau between ~ 0.15 and ~ 0.05 V. During this stage, the crystalline Si reacts with lithium to form amorphous SiLi_x [10]. At the end of the charge (i.e., below ~ 0.05 V), the crystalline $\text{Li}_{15}\text{Si}_4$ phase is formed [10]. Regarding the acoustic activity, a small increase is observed at the beginning of the charge and may be related to surface reactions such as the reduction of the native Si oxides and/or the formation of the solid electrolyte interface (SEI). Then, from a charge capacity of ~ 600 mAh g^{-1} to ~ 2700 mAh g^{-1} , the AE activity increases almost linearly and could be associated with the Si particle cracking induced by their volume expansion with lithiation. Then, at the end of the discharge (i.e., at ~ 0.05 V), a abrupt increase of the acoustic activity is observed, which can be correlated to the formation of the crystalline $\text{Li}_{15}\text{Si}_4$ phase [10].

3.2.2. Evolution of the acoustic activity during the first discharge (delithiation)

The evolution of the electrode potential and the acoustic activity as a function of the discharge capacity during the first delithiation of the silicon anode is shown in Fig. 6. An abrupt increase of the acoustic activity attributed to the particle cracking is observed when the electrode potential reaches 0.4 V, corresponding to a discharge capacity of 1100 mAh g^{-1} . At this potential, the phase change from crystalline $\text{Li}_{15}\text{Si}_4$ to amorphous silicon occurs [10]. This tends to confirm that the electrode decrepitation is mainly induced by the abrupt volume variation related to the formation/disappearance of the $\text{Li}_{15}\text{Si}_4$ phase.

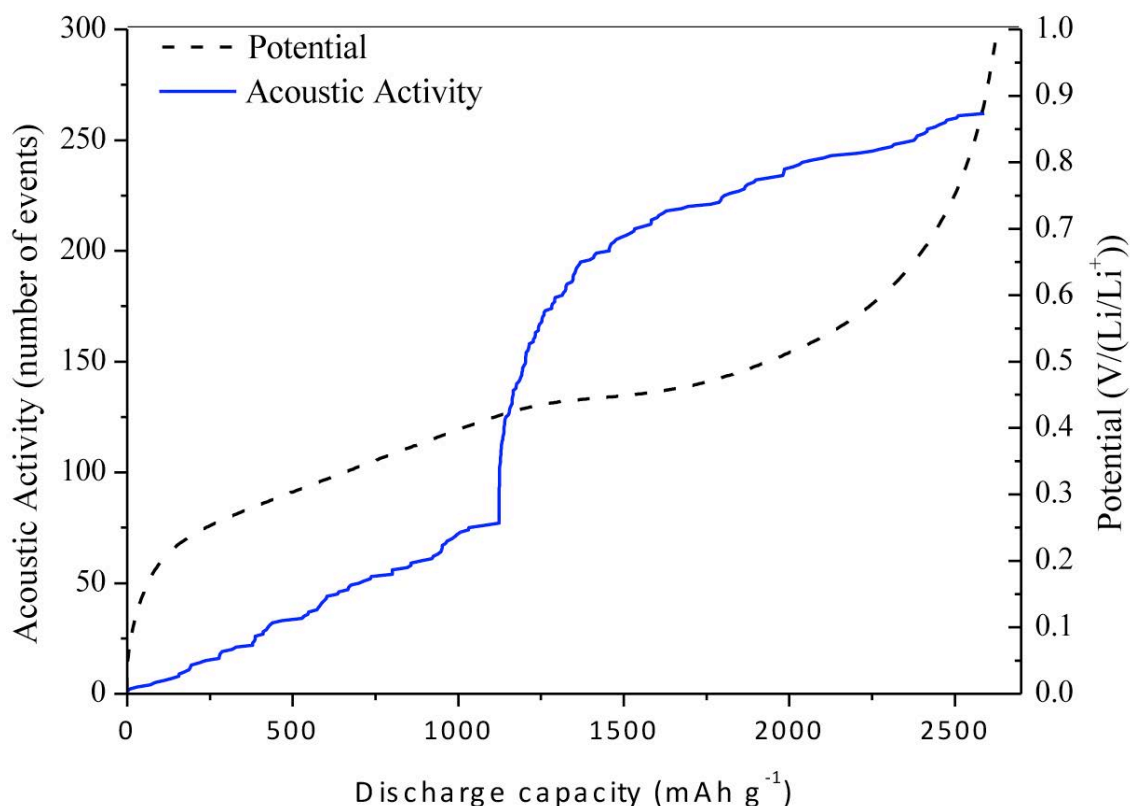


Fig. 6 Evolution of the electrode potential and the AE activity as a function of the discharge capacity during the first delithiation of the silicon anode.

3.2.3. Evolution of the acoustic activity and charge capacity with cycling

The evolution of the acoustic activity with cycling is shown in Fig. 7a. The acoustic activity is maximum during the first charge (lithiation) and discharge (delithiation). Then, the acoustic activity decreases rapidly with cycling to reach less than 50 events per cycle after the third cycle. Similar evolution with cycling is observed for the electrode charge capacity as shown in Fig. 7b. This clearly indicates that the decrepitation of the silicon electrode mainly occurs during the first three cycles and greatly affects the electrode cycle life. After the third cycle, it is assumed that Si particles have reached a critical size, which limits further particle cracking. Additional AE study about the influence of the initial Si particle size on their cracking sensitivity will be performed to confirm this issue.

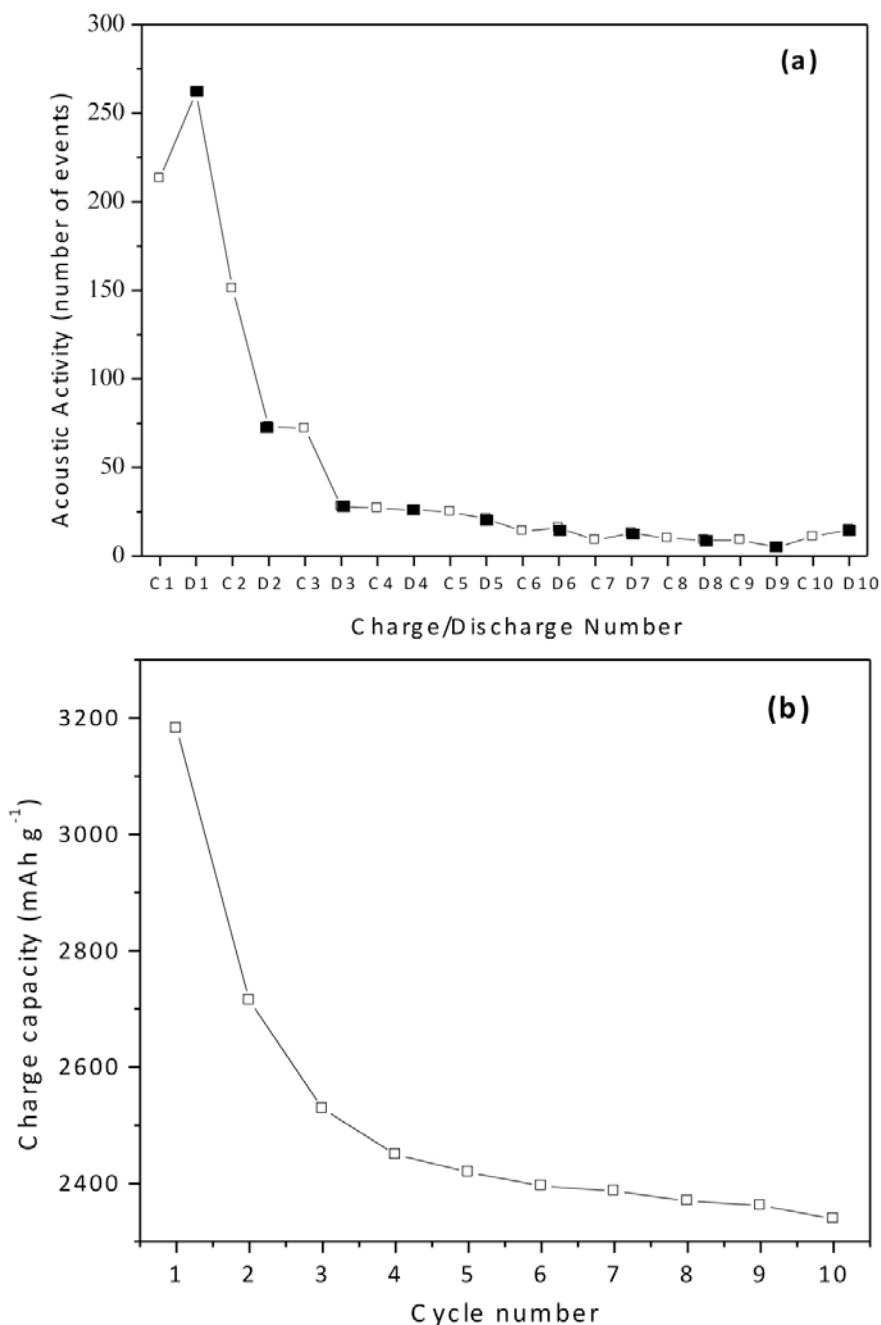


Fig. 7 Evolution with cycling of the AE activity (a) and charge capacity (b) of the Si electrode.

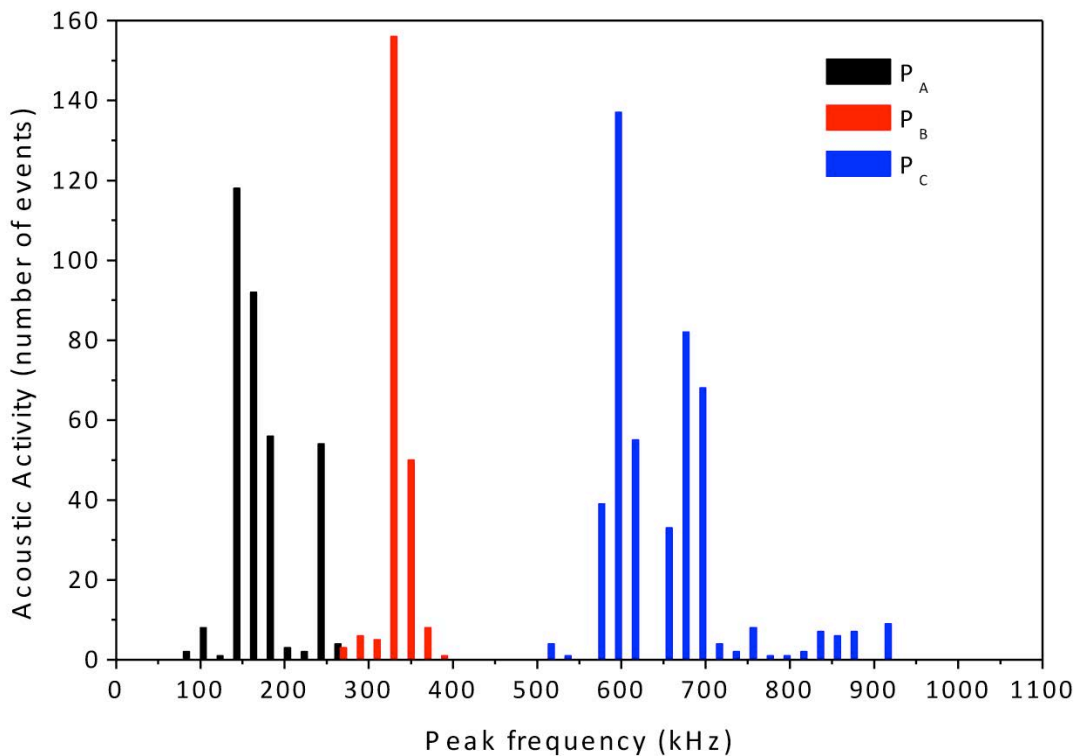


Fig. 8 Peak frequency histogram of the AE signals detected during the ten first cycles of the silicon electrode.

3.2.4. Characterization of the AE classes

From the analysis of the AE signals performed using Noesis software, the peak frequency appears as the most discriminate acoustic parameter. The peak frequency histogram of the AE signals detected during the ten first cycles on the Si electrode is shown in Fig. 8. Three classes of AE signals can be distinguished. The first one, labeled P_A, exhibits peak frequencies between 80 and 250 kHz with a maximum number of events at ~150 kHz. The second one, labelled P_B, is characterized by peak frequencies between 250 and 400 kHz with a maximum number of events at ~330 kHz. These P_B-type signals also exhibit short duration and high energy. This is characteristic of AE signals related to cracking phenomenon, as observed on metal hydride electrodes [6] and during aluminium exfoliation corrosion [11] or hydrogen embrittlement process [12]. The third AE class, labelled P_C, exhibits high peak frequencies, between 500 and 950 kHz. Further investigation using different electrode materials, electrolytes, particle morphology, etc. are planned in order to identify the main sources of these three AE classes and to evaluate their respective influence of the electrode cycle life.

4. Conclusion

The study confirms that acoustic emission techniques coupled with electrochemical measurements is an effective *in situ* method for studying the pulverization of electrodes for Ni-MH and Li-ion batteries. With metal hydride electrodes for Ni-MH batteries, it was demonstrated that the process inducing the pulverization of MgNi and MgTi-10%_wPd produced by ball milling differs notably from that of LaNi₅-based material. The pulverization of this latter occurs at the beginning of the charge step and can be related to the abrupt volume change in the α -to- β phase transition zone whereas for MgNi and MgTi-10%_wPd, it is mainly due to the mechanical action of the H₂ bubbles produced at the end of the charge step. On silicon electrode

for Li-ion batteries, the AE measurements tends to indicate that the electrode decrepitation is mainly due to the abrupt volume variation related to the formation (in charge) and disappearance (in discharge) of the crystalline $\text{Li}_{15}\text{Si}_4$ phase.

References

1. J.J.G. Willems, 'Metal hydrides electrodes stability of LaNi_5 -related compounds', *Philips J. Res*, **39**, 1-94, 1984.
2. P.H.L. Notten, J.L.C. Daams and R.E.F. Einerhand, 'On the nature of the electrochemical cycling stability of non-stoichiometric LaNi_5 -based hydride-forming compounds Part II. In situ x-ray diffractometry', *J. Alloys Compd.*, **210**, (1-2), 233-241, 1994
3. S. Ruggeri and L. Roué, 'Correlation between charge input and cycle life of MgNi electrode for Ni-MH batteries'. *J. Power Sources*, **117**, (1-2), 260-66, 2003
4. S. Rousselot, M.-P. Bichat, D. Guay and L. Roué, 'Structural and Electrochemical Hydriding Characteristics of Mg-Ti-Based Alloys Prepared by High Energy Ballmilling', *J. Electrochem. Soc.*, **156**, (12), A967-A973, 2009
5. U. Kasavajjula, C. Wang and A.J. Appleby, 'Nano- and bulk-silicon-based insertion anodes for lithium-ion secondary cells', *J. Power Sources*, **163**, (2), 1003-1039.
6. S. Didier-Laurent, H. Idrissi and L. Roué, 'In-situ study of the cracking of metal hydride electrodes by acoustic emission technique', *J. Power Sources*, **179**, (1), 412-416, 2008.
7. A. Etiemble, H. Idrissi and L. Roué, 'On the decrepitation mechanism of MgNi and LaNi_5 -based electrodes studied by in situ acoustic emission', *J. Power Sources*, **196**, (11), 5168-5173, 2011.
8. A. Etiemble, H. Idrissi and L. Roué, 'In situ investigation of the volume change and pulverization of hydride materials for Ni-MH batteries by concomitant generated force and acoustic emission measurements', *J. Power Sources*, **205**, 500-505, 2012.
9. S. Rousselot, M. Gauthier, D. Mazouzi, B. Lestriez, D. Guyomard and L. Roué, 'Synthesis of boron-doped Si particles by ball milling and application in Li-ion batteries', *J. Power Sources*, **202**, 262-268, 2012.
10. J. Li and J.R. Dahn, 'An In Situ X-Ray Diffraction Study of the Reaction of Li with Crystalline Si', *J. Electrochem. Soc.*, **154**, (3), A156-A161, 2007.
11. F. Bellenger, H. Mazille and H. Idrissi, 'Use of acoustic emission technique for the early detection of aluminum alloys exfoliation corrosion', *NDT & E International*, **35**, (6), 385-392, 2002.
12. M. Perrin, L. Gaillet, C. Tessier and H. Idrissi, 'Hydrogen embrittlement of prestressing cables', *Corr. Sc.*, **52**, (6), 1915-1926, 2010.

AE Wavelet Processing in Dynamical Tests of a Reinforced Concrete Slab

Miguel E. Zitto¹, Rosa Piotrkowski^{1,2}, Antolino Gallego³
and Francisco Sagasta³

¹ Mathematics Department, Engineering Faculty, University of Buenos Aires, Argentina.

² School of Science and Technology, University of San Martin, Argentina

³ Department of Applied Physics, University of Granada, Spain

Abstract

Different processing techniques have been previously applied to AE signals coming from dynamic tests of reinforced concrete structures on a shaking table. The dynamic test simulated the earthquake of Campano-Lucano recorded in Calitri, Italy. After the test, the recorded AE had been classified into fracture and noise hits according to various parameters: autocorrelation, power wavelet in different frequency bands, kurtosis, RMS from different parts of the signal and approximate entropy value. The results of comparing the classifications of the hits according to different parameters encouraged the convenience of using the filtered AE signals to obtain damage indices in RC structures subjected to earthquake loads. Values of the parameters thus obtained are used in the present paper as guidelines of our work, but the philosophy of the processing is now different. The hits are not already classified into fracture or noise hits according to different parameters, but instead relevant information is extracted from each hit by adequate processing and filtering. Continuous wavelet transform, most suitable for non-stationary phenomena, was applied to each hit; various wavelet bases were tested in order to improve scale resolution. Different scale (frequency) bands could be ascribed to different AE sources; the bands were separated using statistical clustering methods. The comparison with the cumulative dissipated energy related to damage permitted to clearly identify the band, which corresponds to concrete fracture. The proposed algorithm is automatic and direct and it improves previous procedures, besides providing a deeper physical understanding.

Keywords: Dynamical tests, continuous wavelet transform, signal processing, modeling.

1. Introduction

The applicability of acoustic emission (AE) to assess the damage in reinforced concrete (RC) structures subjected to earthquake loading was investigated in previous papers [1-3]. One of the main challenges in applying the AE technique to measurements obtained from such complex dynamic loading is to remove the spurious information not related to concrete damage. A procedure was applied in [1-3] to the measured AE signals obtained from dynamic shaking table tests conducted on a RC slab supported on four steel columns. The proposed procedure consisted in applying two filters; one of them was a polygonal filter over the Amplitude-Duration diagram, and the other one was based on the calculation of the RMS of the AE signal in different temporal windows. The filters were applied in order to separate the short-duration signals (associated with concrete fracture and, thus, with cumulative damage to the structure) and the long-duration signals (corresponding to other noisy mechanisms). A quite good correlation between the cumulative AE energy thus calculated and the cumulative damage on the concrete measured in terms of cumulative dissipated energy was obtained.

In the present paper we intend to achieve the same or better results applying algorithms that involve straight, automatic and physically grounded procedures to each AE signal. In this way

we hope to obtain at the same time more efficient codes to assess damage and a deeper understanding of the basic phenomena connected with damage generation in RC structures subjected to earthquake loads.

In the line of previous work [4,5] performed on scratch-tests on coatings, specific frequency bands were intended to be assigned to different failure mechanisms applying the Continuous Wavelet Transform (CWT) to AE signals.

2. Modeling and experimental background

Modeling and experimental details are fully explained in [1-3], and the AE signals processed in the present work are some of those used in previous work. A brief description is provided for clarity.

The objective of our work is to calculate the cumulative AE energy (named *AE* in what follows for simplicity) and to perform the comparison with the cumulative dissipated energy related to damage (named *DE*) that was previously obtained in [1,2] and was named *WP* in those works.

From basic principles of dynamics, and assuming that the inherent damping of the structure is of the viscous type, in a one-dimensional model, the equilibrium equation can be expressed by

$$m \ddot{x}' + c\dot{x}' + F_r = 0 \quad (1)$$

where x is the relative horizontal displacement between the shake table and the slab, \ddot{x}' is the absolute acceleration of the slab, c is the viscous damping coefficient ($c = 4\pi\xi m/T$), m is the structure mass, T is the vibration period, ξ is the viscous damping fraction of the structure (see Table 1) and F_r is the restoring force opposed by the tested structure against the relative displacement x . Solving Eq. (1) for F_r the corresponding F_r - x curves were obtained, and then, the cumulative energy *DE* dissipated by the test model was calculated by integration.

2.1 Experimental setup and seismic simulation

Here, the experimental acquisition of parameters is described. The experimental setup was a one-story (2.8m height) and one-bay (4.8m length) prototype structure consisting of an RC slab supported on four box-type steel columns. It was designed following current Spanish codes NCSE-02 and EHE-08. From the prototype structure, the corresponding test model was derived by applying the following similarity laws: $\lambda_l=1/2$, $\lambda_a=1$ and $\lambda_\sigma=1$, where λ_l , λ_a and λ_σ are the scaling factors by which the geometry, the acceleration and the stress in the prototype must be multiplied to obtain the corresponding dimensions in the test model. The thickness of the slab was 125 mm and it was reinforced with steel meshes, one on the top made with 6 mm diameter bars spaced 100 mm, and another on the bottom consisting of 10 mm diameter bars spaced 75 mm. The test model was prepared in the laboratory. The average yield stress f_s of the reinforcing steel was 467 MPa, and the average concrete strength f_c was 23.5 MPa.

The test model was tried with the uniaxial MTS 3×3 m² shaking table of the University of Granada (Spain). The bottom ends of the columns were fixed to the table by bolts. Similitude requirements between prototype and test model and the dead and live gravity load were satisfied by attaching additional steel blocks on the top of the RC slab. The total mass of the slab including the added steel blocks was $m = 7390$ kg. The acceleration record used for the shake

table tests reproduced the NS component of the 1980 Campano-Lucano earthquake recorded at Calitri (Italy).

Two series of seismic simulations were applied to the test model. The same accelerogram was used in all simulations, the scaling factor of the peak accelerations (PA) being the only difference (Table 1). The first series consisted of eight simulations with PA increasing progressively from 0.08g to 0.58g (g : gravity of acceleration). The second series consisted of six simulations with PA increasing from 0.19g to 0.95g. The second series started with values of PA smaller than the maximum obtained in the first series, that is, in several simulations of the second series the test model was subjected to load levels smaller than those it had been previously exposed to. This was intentionally done so that the simulations reproduced two types of situations on the structure: (i) that in which the AE energy and the dissipated energy related to damage are dominated by the new damage associated with the opening and extension of cracks; and (ii) the situation in which AE energy and hysteretic energy are dominated by friction generated from existing damage. Both situations are realistic scenarios that the structure may experience over its lifetime. During the seismic simulations the test model was driven very close to the limit commonly acceptable on an RC structure subjected to moderate earthquakes. The measurements of the strain gages attached to the reinforcing bars indicated two facts: the maximum strain in the reinforcing bars $\varepsilon_{max, reinf}$ closely reached the yield strain (2200 $\mu\epsilon$); slip occurred between the longitudinal reinforcing bars and the surrounding concrete. The variables ξ (damping fraction) and T (vibration period) of Table 1 were determined in free vibration tests.

Table 1: Seismic simulations

Test series		PA (g)	T (s)	ξ (%)	$\varepsilon_{max, reinf}$ ($\mu\epsilon$)
1	2				
Simulation (in order of application)					
A1		0.08	0.26	1.10	497
B1		0.10	0.29	1.14	568
C1		0.12	0.30	1.20	638
D1		0.19	0.31	1.26	909
E1		0.29	0.31	1.30	1150
F1		0.38	0.31	1.42	1361
G1		0.44	0.31	1.48	1537
H1		0.58	0.31	1.60	1670
	A2	0.19	0.32	1.66	836
	B2	0.38	0.32	2.11	1295
	C2	0.58	0.32	2.55	1350
	D2	0.66	0.32	3.16	1460
	E2	0.74	0.32	3.24	1540
	F2	0.95	0.32	3.50	1800

2.2 Monitoring

2.2.1 Displacement, strains and acceleration monitoring

Displacement, strain and acceleration were simultaneously acquired during each seismic simulation. The relative horizontal displacement x between the shake table and the slab was measured by displacement transducers. Electrical resistance strain gages were attached to nineteen (top and bottom) longitudinal reinforcing bars near the corner of the slab prior to casting the concrete. Strain gages were also attached at the upper and lower ends of the columns.

Accelerometers were fixed to the shake table and to the slab, which measured the absolute acceleration of the table and the absolute response acceleration of the slab, in the direction of shaking. All data were collected continuously with a sampling rate of 200 Hz by a data acquisition system. In addition to the electronic data, detailed visual inspections of the slab were made after each seismic simulation to identify the propagation of the cracks.

2.2.2. *AE monitoring*

A Vallen Systeme ASMY-5 was used to measure the AE signals during the tests. Eight low-frequency AE sensors, type VS30 set in the range 20-100 kHz, were placed on the test model; four positions were chosen along the four lateral sides of the specimen, while the other four positions were on the bottom of the specimen. In all channels, the 25-180 kHz frequency band was used during signal acquisition. During acquisition, a sample period of 1.6 μ s and 1024 data were used for signal recording (200 of them, before the arrival time). Thus, the entire duration of the record window was $t_{\max}=1318 \mu$ s. Silicone adhesive bonding agent was used for the coupling of sensors on concrete. Before testing, the electric noise in the laboratory was measured and a calibration test by breaking pencil leads (AE Hsu-Nielsen source) along the specimen was carried out. Thus, it was established that using 45 dB as the threshold of detection, pencil leads broken at any place of the specimen could be recorded by all the sensors. Also to prevent undesired noise generated by the contact between the base plate of the columns and the shake table, four guard sensors were placed near the bottom end of the columns.

Attenuation tests were carried out by breaking pencil leads along the specimen and measuring the signals in all the 8 sensors. Five leads were broken at each position, and the mean value was calculated. Thus, it was established that 0.11 dB/cm was the mean attenuation. Then, keeping in mind that the point farthest from an AE sensor (the center of slab) is 94 cm away, the maximum attenuation of a source located at that point would be 10.3 dB. Since a threshold of 45 dB was used, it can be stated that all the sources producing AE signals with amplitude higher than 55.3 dB could be recorded by at least one sensor. Note, however, that the center of the slab is the place where less cracking is expected, since the bending moment under lateral loads is approximately zero.

In general, different modes of propagation can be expected in the AE waves generated by the cracking of a concrete slab (i.e. longitudinal waves, transversal waves, Rayleigh waves). These modes of propagation superpose and are influenced by many factors such as the mechanics of the damaging process in concrete. Under earthquake-type cyclic loadings, the concrete experiences both damage associated with the opening (new cracks) and extension of cracks, and damage due to friction between the planes of fracture of previous cracks. Other factors such as the orientation of the cracks, the geometry of the specimen, the type of sensor, the multiple reflections occurring along the wave path between the source and the sensor etc., play an important role. Most of these factors are random and they can hardly be controlled. All these factors make the signal very cumbersome and modify the vibration modes. The analysis of a complex material such as concrete or of a reinforced concrete structure based on the study of the vibration modes is meaningless, since it is very difficult to identify the different vibration modes.

For the depth of the slab tested in this study (125 mm), the frequency of the propagation modes corresponding to the Lamb waves is below 20 kHz, that is, outside the frequency range of sensitivity of the two types of sensors used. Therefore, it can be concluded that the recorded waves are a mixture of longitudinal and transversal waves. Besides, the velocity of propagation of the longitudinal waves was measured by breaking pencil leads, giving an average value

(obtained with six measurements in the longitudinal direction of a concrete bar made of the same material of the slab) of 3200 m/s.

Due to the complexity of the test and of this type of dynamic loading, a great quantity of undesired friction noise and mechanical noise was expected. For this reason, different precautions were taken to deal with such spurious signals before and after the test. Considerable mechanical noise coming from the oil flow in the actuator that moved the shaking table was detected. The level of this noise was above 100 dB in the actuator, and about 70 dB at the base of the four steel columns that formed the specimen. For this reason, one guard sensor was placed at the bottom of each column, in order to filter out this noise and the friction noise generated in the connection between the base plate of the columns and the surface of the shaking table.

3. AE signal processing

3.1 Continuous Wavelet Transform (CWT)

The wavelet transform is widely used to analyze time series that contain non-stationary power at many different frequencies. We next describe the method used for the wavelet analysis, including a discussion of different wavelet functions and details for the analysis of the wavelet power spectrum. The proposed equations, obtained from the continuous formulas, have been adapted to discrete notation according to results obtained by other authors [6, 7]. The CWT of a function $f(t)$ is defined as the integral transformation in Eq. (2)

$$(Wf)(s, b) = \int_{-\infty}^{\infty} f(t) \overline{\psi_{s,b}(t)} dt \quad s \neq 0 \quad (2)$$

with the wavelet function $\psi(t)$ and Eq. (3) has to be fulfilled.

$$\psi_{s,b}(t) = \frac{1}{\sqrt{|s|}} \psi\left(\frac{t-b}{s}\right) \quad (3)$$

In order that $\psi(t)$ is “admissible” as a wavelet, this function must have a zero mean value and it has to be localized both in time and frequency spaces. An example is the Morlet wavelet, consisting of a plane wave modulated by a Gaussian, i.e.

$$\psi(\eta) = \pi^{-1/4} e^{i\omega_0\eta} e^{-\eta^2/2} \quad (4)$$

where ω_0 is a non-dimensional frequency, here taken as 6 in order to satisfy the admissibility condition.

The CWT of a discrete sequence $x(n \cdot \delta t)$ is defined as the convolution of $x(n \cdot \delta t)$ with a scaled and translated version of $\psi(\eta)$ given in Eq. (5), (see [8])

$$(Wx)(s, n) = \sum_{n'=0}^{N-1} x(n' \delta t) \overline{\psi\left[\frac{(n'-n)\delta t}{s}\right]} \quad (5)$$

Although it is possible to calculate the wavelet transform using the given equations, it is considerably faster to do calculations in the Fourier space using a discrete Fourier transform (DFT). The DFT of a sequence x_n is given by

$$\hat{x}_k = \frac{1}{N} \sum_{n=0}^{N-1} x_n \exp(-i2\pi kn/N) \quad (6)$$

The following Eq. (7) was obtained by three steps: discretization of Eq. (2); DFT of Eq. (5); inverse DFT (IDFT).

$$(Wx)(s, n) = \sqrt{|s|} \sum_{k=0}^{N-1} \hat{x}_k \bar{\psi}_k(s \omega_k) \exp(i\omega_k n \delta t) \quad (7)$$

$$\text{where the angular frequency is } \omega_k = \begin{cases} \frac{2\pi k}{N\delta t} & k = 0, K, N/2 \\ \frac{-2\pi k}{N\delta t} & k = N/2 + 1, K, N-1 \end{cases} \quad (8)$$

We can calculate the CWT for a given s and for all n simultaneously using Eq. (7) and a standard Fourier transform routine. It is then possible to *reconstruct* the original time series from the CWT. This is straightforward for an orthogonal wavelet transform, but it is complicated for the CWT because of the redundancy in time and scale. However, this redundancy has the advantage of allowing the reconstruction of the time series using a completely different wavelet function, the simplest of which is a delta function [7]. For a real time series

$$x_n = \frac{\delta_j \cdot \delta t^{1/2}}{C_\delta \cdot \psi(0)} \sum_{j=0}^J \frac{\Re\{(Wx)(s_j, n)\}}{s_j^{1/2}} \quad (9)$$

where the index j is the one corresponding to the scale $s_j = s_0 2^{j\delta_j}$, with $j=0, 1, \dots, J$. The factor C_δ comes from the reconstruction of a δ function from its wavelet transform using the function $\psi(\eta)$. This factor is a constant, different for each wavelet function; for the Morlet wavelet it is $C_\delta=0.776$.

Summarizing, the calculation is essentially described in Scheme 1.

Scheme 1

1. Selection of the wavelet function
2. Discretization and scale selection
3. DFT calculation of the signal and the wavelet
4. IDFT calculation of the product of both Fourier transforms
5. Eventual reconstruction of the filtered signal

3.2 Statistical clustering (*K-means* algorithm)

A very popular approximate non-hierarchic method is the *K-means* method [9-11], which has been used in previous occasions [12-15] with very good results. The idea of this algorithm is to divide the n samples into k groups/clusters according to how far the sample is from certain mean values, which are found in an iterative procedure. In this way, the concept of metric is introduced and a distance definition is needed. In our case, we used the Euclidean distance. The number of clusters k should be selected from the beginning according to physical criteria.

For a given a set of samples, each one consisting of n samples $\{x_i\}$, the *K-means* algorithm will try to find the vector of k -means values $\{\mu_i\}$. The algorithm starts with random seeds for the $\{\mu_i\}$ values and from them all the samples are classified according to the nearest μ_i . Once it is done, the mean values are recomputed applying maximum-likelihood criteria until the difference with the previous set of $\{\mu_i\}$ is practically zero. The calculation is concisely described in Scheme 2.

Scheme 2

1. *begin*
2. *initialize variables $n, k, \mu_1, \mu_2, \dots, \mu_k$*
3. *do*
4. *classify n samples according to nearest μ_i*
5. *recomputed μ_i*
6. *until no change in μ_i*
7. *return $\mu_1, \mu_2, \dots, \mu_k$*
8. *End*

In the present work the selected number of clusters was 2, because we considered that relevant information related to concrete damage corresponded to a specific frequency band.

4. Results and Discussion

4.1 Wavelet selection

The seismic simulations B1, D1, F1, H1, D2, and F2 were selected from Table 1. The first step in the wavelet analysis was the selection of the wavelet function among different possibilities: *orthogonal* or *non-orthogonal*, *complex* or *real*, *shape*. We decided to use the non-orthogonal transform because we did not expect very sharp variations in the absolute values of the wavelet coefficients. Different wavelets were tested: Morlet, Paul of order 4, (both complex) and Derivative of a Gaussian (DOG) of order 2 (real). In all cases the wavelet power spectrum, defined as $|(W \times)(s, n)|^2$, was plotted on a time-scale mesh. Although similar results were obtained for the three wavelets, the Morlet wavelet was selected because of the best scale resolution.

Table 2. Morlet wavelet index and scale and Fourier period and frequency

Index (j)	Scale (s)	Period (μ s)	Frequency (kHz)
0	3.2	3.3	302
1	3.8	3.9	254
2	4.5	4.7	214
3	5.4	5.6	180
4	6.4	6.6	151
..
8	12.8	13.2	76
9	15.2	15.7	64
10	18.1	18.7	53
11	21.5	22.2	45
12	25.6	26.4	38
13	30.4	31.4	32
14	36.2	37.4	27
15	43.1	44.5	22
..

4.2 Wavelet scale and Fourier frequency

It is convenient, from the computational point of view, to express the scales as potential functions with fractional exponents and base 2. In all the cases the scales were taken as: $s_j = s_0 \cdot 2^{j\delta_j}$, with $j = 0, 1, \dots, J$, the lower scale being $s_0 = 2 \delta t$, where δt is the sampling period of the signal (1.6 μs) and $J = \delta_j^{-1} \log_2(N \delta t / s_0)$ is the index that allows to obtain as highest scale value $s_{\max} = N \cdot \delta t$. Table 2 shows the scales used for a sampling period of 1.6 μs that was the same for all the seismic simulation signals, and $\delta_j = 1/4$. To find the relationship between the wavelet scale and the period we performed the wavelet transform of a cosine wave of known frequency with a particular wavelet function (Eq. 7). Then, the scale at which the wavelet power spectrum reaches the maximum is calculated, and this period is known as the *equivalent Fourier period* [16]. Using the Morlet wavelet, with $\omega_0 = 6$, the scale has to be multiplied by 1.03 to obtain the period.

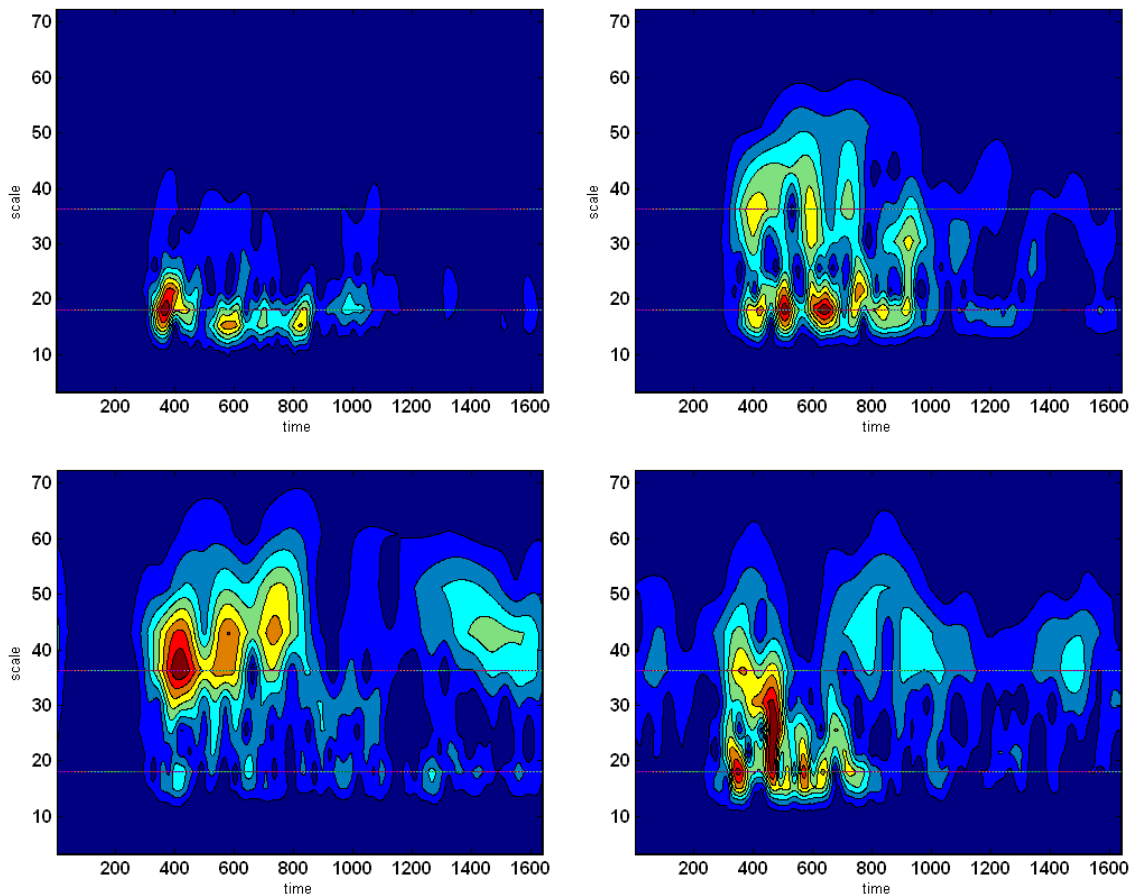


Fig. 1. Typical wavelet power spectra. Test D2. Time in microseconds.

Figure 1 shows typical wavelet power spectra from signals obtained in the seismic simulation D2. The highest values of absolute wavelet coefficient occur at characteristic scales. This was a general result.

4.3 Statistical clustering (*K-means Algorithm*)

In order to clearly recognize the wavelet scales related to different processes the highest value in each CWT matrix was considered. The wavelet scale location of these maxima was

defined as a component of the data vector, to which the one-dimensional (1D) K -means algorithm was applied [15]. We found that the maxima occurred at the scales: 12.8; 15.2; 18.1; 21.5; 25.6; 30.4; 36.2. Figure 2 displays a graph where the time (horizontal axis) refers to the hit occurrence and the wavelet scale (vertical axis) refers to the scale, for which the absolute value of the wavelet coefficient is highest for the given hit. We then applied the K -means algorithm with different number of centroids k , finding that for $k = 2$ the scales 36.2 and 18.1 (see Fig. 2) were the most significant. In fact, the centroids were located at these positions and they can be clearly seen as two horizontal lines in Fig. 2. From previous works [1-3], we knew that high scales are associated with noise. For this reason, the scale 18.1 was pre-assigned to concrete fracture. This result was validated in our work as it is explained in Section 4.4.

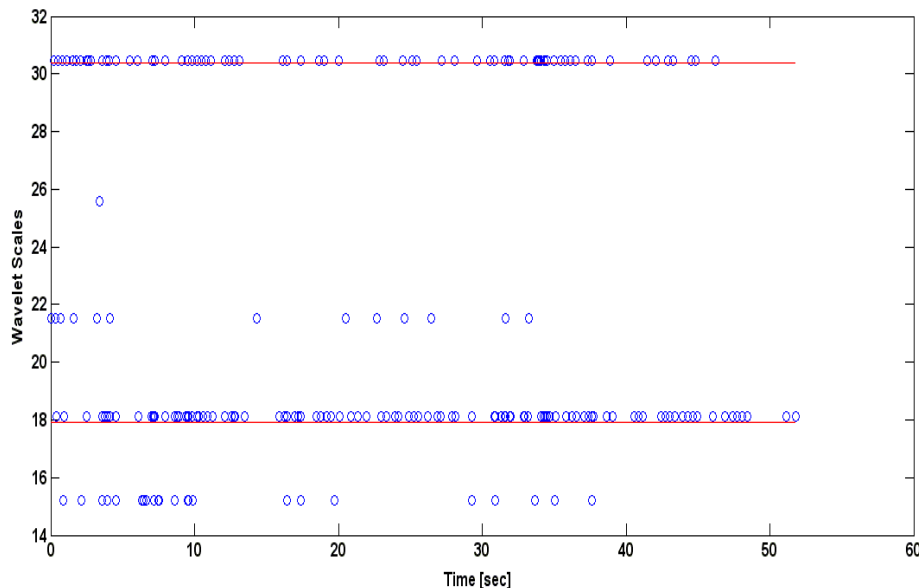


Fig. 2. 1D Clustering applied to the scale location of the maximum absolute values of CWT versus the time of hit occurrence. Test D1 in Table 1.

4.4 AE Energy (AE)

The cumulative dissipated energy in damage processes, obtained by integrating F_r over x , that is to say DE , is considered an appropriate parameter for characterizing low-cycle fatigue damage in RC components and is used for well-established RC damage indices [17]. Correlation between the AE energy obtained from filtered signals (AE) and DE was previously performed and demonstrated in [1,2]. Our objective is to perform the same correlation with signals filtered with the method proposed in the present work. For that, from the wavelet transform of the signal we picked up the coefficients of scales assigned to fracture and then reconstructed the filtered signal (Eq. 9). AE of the filtered signal was calculated; this procedure is necessary for non-orthogonal wavelet functions. For all the tests analyzed in this work the best correlation between cumulative AE and DE was obtained when the 18.1 scale-53 kHz band was considered. This result could not be improved with other bands or by adding different bands. Figure 3 shows as an example the evolution of cumulative AE and DE for test D1, considering for AE only the scale 18.1, only the scale 36.2 and the whole signal (not filtered signal).

Figure 4 shows the comparison of cumulative AE of the band 18.1 and cumulative DE for all the seismic simulation considered in the present work. It can be seen that both curves follow similar trends, like in paper [1,2]. The advantage of the present results is that they were obtained

with a more direct and faster procedure, which is implemented in a totally automatic way and a deeper understanding is possible.

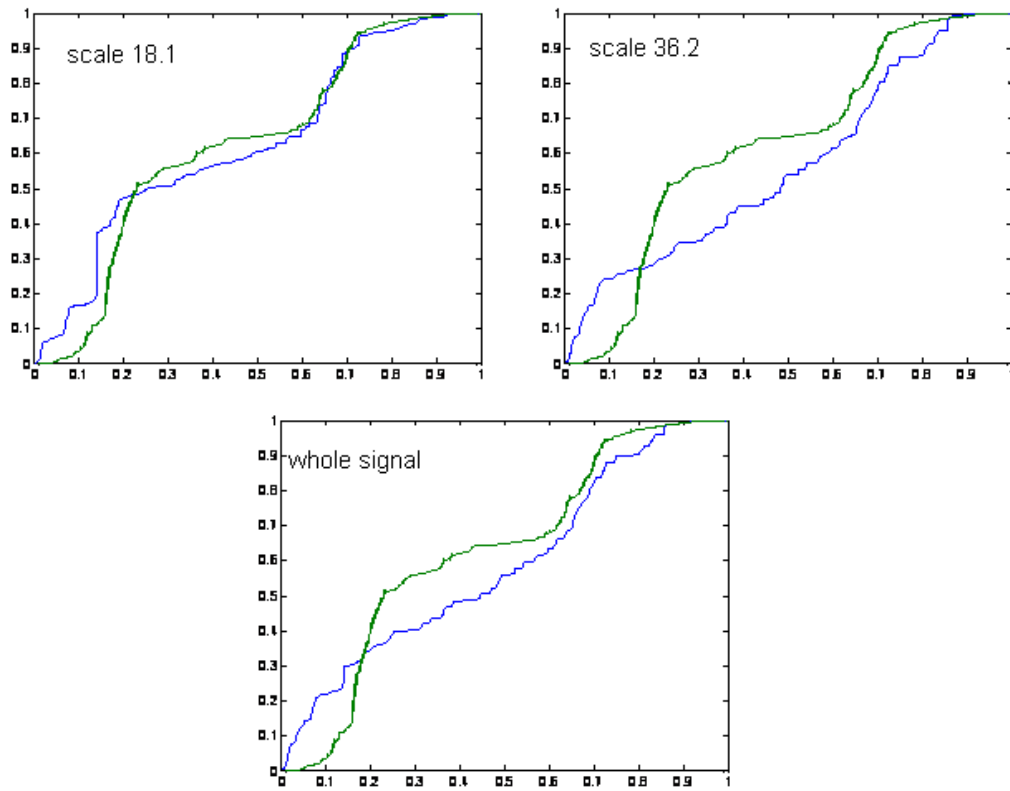


Fig. 3. Correlation between cumulative *AE* (blue) and cumulative *DE* (green) for test D1.

A portion of the mechanical energy provided by the actuator dissipates into heat; this portion can be obtained by integrating the viscous force over x . Another portion of the mechanical energy dissipates into damage; it can be obtained by integration of the restoring force over x . This dissipation occurs when irreversible microstructural changes take place: fracture processes in concrete and deformation processes in the reinforcing steel. These damage processes altogether contribute to *DE*. On the other hand, the cumulative acoustic energy *AE* is mainly due to the fracture of concrete and friction between faces of previous cracks. By comparing the blue and the green curves in Fig. 4, we can think that in the case that a jump in *DE* is not accompanied by a similar jump in *AE* it is because the deformation of reinforcing steel is prevalent. When a jump in *AE* occurs that is not accompanied by a jump in *DE*, this would indicate a process connected with previous fracturing; it could be ascribed to friction between the faces of previous fractures. In general we can infer from the graphs that concrete fracture is prevalent and/or fracture of concrete and deformation of reinforcing steel are correlated; this would explain the similar trends. These facts deserve to be quantitatively established in future work.

5. Conclusions

1. The wavelet power spectra obtained with the Morlet wavelet reaches maximum values mostly at certain scales (frequencies). This was observed visually and then fully automatically corroborated using the *K*-means algorithm.

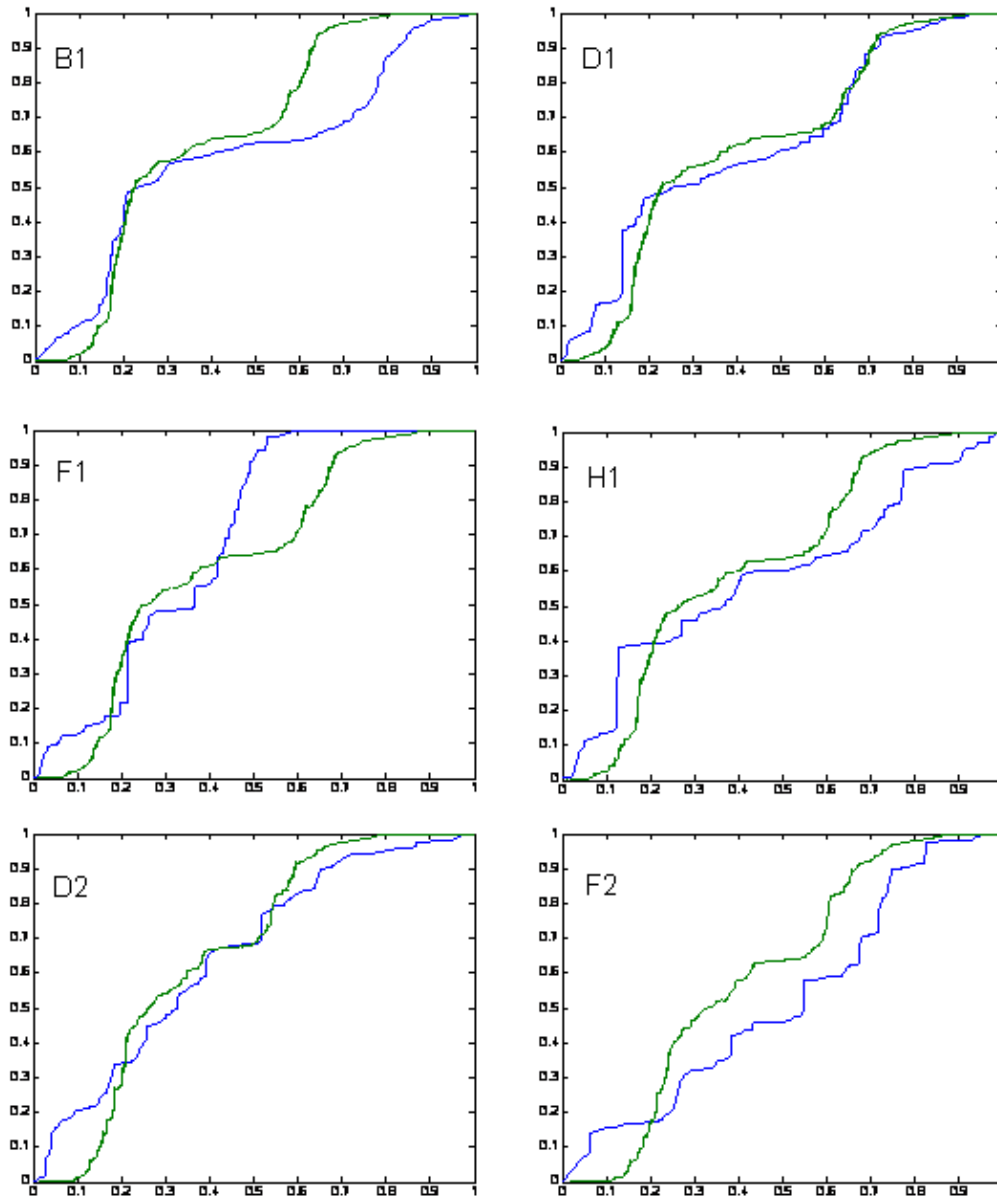


Fig. 4. Normalized *AE* (blue) reconstructed with scale 18.1 and *DE* (green). Curves show the evolution of cumulative energy.

2. We could identify the *AE* frequency band associated with concrete damage mechanisms (opening and extension of new cracks and friction of previous fracture faces) in reinforced structures submitted to load tests simulating moderate earthquakes.
3. We found that filtering the acoustic signals by the CWT and reconstructing the signal by taking the coefficients corresponding to the scale 18.1 (frequency 53.3 kHz) we obtained a quite good correlation between the cumulative *AE* and *DE* for all the seismic simulations considered in the present work.

Acknowledgements

This research received financial support the Education Ministry of Argentina (*Fortalecimiento De Redes Interuniversitarias V*), from the local government of Spain,

References

1. A. Benavent-Climent, A. Gallego and J.M. Vico (2012), “An acoustic emission energy index for damage evaluation of reinforced concrete slabs under seismic loads”, *Structural Health Monitoring (SHM)*, **11**, (1), 69-81.
2. A. Gallego, A. Benavent-Climent, J.M. Vico, C. Infantes and E. Castro (2010), “Health monitoring of reinforced concrete slabs during seismic tests using acoustic emission”, EWGAE 29, Vienna. www.ndt.net
3. E. Castro, R. Piotrkowski, A. Gallego (2010), “Discrimination of acoustic emission hits from dynamic tests of a reinforced concrete slab”, *Journal of Acoustic Emission*, **28**, 120-128.
4. R. Piotrkowski, E. Castro, A. Gallego (2009), “Wavelet power, entropy and bispectrum applied to AE signals for damage identification and evaluation of corroded galvanized steel”, *Mechanical Systems and Signal Processing*, **23**, (2), pp. 432-445.
5. R. Piotrkowski, A. Gallego, E. Castro, M.T. García-Hernández, J.E. Ruzzante (2005), “Ti and Cr nitride coating/steel adherence assessed by acoustic emission wavelet analysis”, *Non Destructive Testing and Evaluation (NDT and E) International*, **8**, (4), 260-267.
6. I. Daubechies (1992), “Ten lectures in wavelets”, *Society for Industrial and Applied Mathematics*, pp. 357.
7. M. Farge (1992), “Wavelet transforms and their applications to turbulence”, *Annual Review of Fluid Mechanics*, **24**, 395-458.
8. C. Torrence, G. Compo (1998), “A Practical Guide to Wavelet Analysis”, *Bulletin of the American Meteorological Society*, pp. 79.
9. R. Duda, P. Hart, D. Stork (1984), “Pattern Classification”, Second Edition, Wiley, 2001.
10. G. A. F. Seber, (1984), “Multivariate Observations”, John Wiley, Hoboken, NJ.
11. H. Spath, (1985), “Cluster Dissection and Analysis: Theory, FORTRAN Programs, Examples”, Translated by J. Goldschmidt. New York: Halsted Press.
12. J.I. Mieza, M.E. Oliveto, M.I. Lopez, M. Armeite, J.E. Ruzzante and R. Piotrkowski (2005), “Identification of AE Burst by Classification of Physical and Statistical Parameters”, *Review of Progress in Quantitative Nondestructive Evaluation*, Ed. D.O. Thompson and D.E. Chimenti, American Institute of Physics, USA, **24**, 1174-1181.
13. A. Sibil, N. Godin, M. R’Mili, E. Maillet and G. Fantozzi (2012), “Optimization of Acoustic Emission Data Clustering by a Genetic Algorithm Method”, *Journal of Nondestructive Evaluation*, **31**, (2), 169-180.
14. R. Gutkin, C.J. Green, S. Vangrattanachai, S.T. Pinho, P. Robinson, P.T. Curtis (May 2011), “On acoustic emission for failure investigation in CFRP: Pattern recognition and peak frequency analyses”, *Mechanical Systems and Signal Processing*, **25** (4), 1393-1407.
15. E. Zitto, M. Scaramal, F. Sagasta, R. Piotrkowski, A. Gallego, E. Castro, (2012), “AE Signal Processing in Dynamical Tests of Reinforced Concrete Structures”, EWGAE 30, Granada, Spain. www.ndt.net.
16. S. D. Meyers, B. G. Kelly and J. J. O’Brien (1993), “An introduction to wavelet analysis in oceanography and meteorology”, *Monthly Weather Review*, **121**, 2858-2866.
17. Y.J. Park, A.H.S. Ang, (1985), “Mechanistic seismic damage model for reinforced concrete”, *Journal of Structural Engineering, ASCE*, **111**, 722-739.

Recent Advances of AE Technology for Damage Assessment of Infrastructures

Tomoki Shiotani

Graduate School of Engineering and Graduate School of Business, Kyoto University
Nishikyo, Kyoto, Japan

Abstract

Acoustic emission is a powerful NDT to detect the internal cracking process of civil engineering materials qualitatively, which cannot be readily realized by other NDT methods. Identified AE sources through the AE measurement help reveal further information on fracturing behavior based on the energy-related AE parameters, slope of the waveform as well as frequency features of the waveform. From these experimental findings, several promising AE procedures may be applied for the damage assessment of actual infrastructures. These AE activities of in-situ applications are typically ‘secondary emission’ produced by friction among existent cracks or damage. Thus, fracture-originated AE activity, primary AE activity, is not applicable to the infrastructure damage assessment. In this paper, several AE findings toward in-situ infrastructural assessment for their current status are mainly described. Specifically AE parametric features useful for the damage assessment are summarized; elimination of ambient noise when utilizing active mobile loads is clarified; strategic AE monitoring procedure for a large structure is demonstrated; several promising AE waveform features are introduced with fatigue tests of concrete bridge deck; and the latest on-going studies for a global inspection over the whole of structures with AE technique are demonstrated.

Keywords: Damage assessment, infrastructures, secondary AE activity, transfer function, quantitative NDT

1. Introduction

Acoustic emission (AE) is an elastic wave generated due to crack occurrence or crack coalescence. As AE activity characterizes such fracture states as early, intermediate and final stage, it has been employed as a precursor alerting the impending failure of materials or structures. When the AE technique is applied for damage assessment in infrastructures, e.g., civil engineering structures, one shall pay his/her attention to other types of AE activity in distinction from the former AE activity, namely primary AE activity. In Fig. 1, schematic behavior of damage progress as a function of time is demonstrated, where the circles show the time of AE monitoring as in the most ideal case for an important infrastructures but in actual, AE monitoring has been conducted so far only for the experimental case or the case of crucially damaged important structures. As in the open circles of the chart, AE monitoring has sometimes been utilized as to expect a real time trace for the eventual failure. The author has been involved in the rock failure monitoring on the basis of this expectation, and reported that internal deformation of rock slope could be evaluated by several promising AE parameters, predicting resultant final failure [1-4]. Indeed this continuous AE monitoring is in demand for important infrastructures; however, it was for the limited number of infrastructures, and the actual requirement of AE monitoring lays in other purposes i.e., evaluation of current condition is the highest demand and which shall be conducted in such a short period as a couple hours or several days at the longest. In this monitoring, obtaining AE activity is not from newly crack occurrence but emerged due to reversible motion of existent damage. This is referred to as secondary AE activity while the other is defined as primary

AE activity as aforementioned. In this paper, with secondary AE activity, recent advances of AE technology for damage assessment in infrastructures are drawn. Specifically in the following: AE parametric features being useful for the damage assessment are summarized; elimination of ambient noise when utilizing active mobile loads is clarified; strategic AE monitoring procedure for a large structure is demonstrated; several promising AE waveform features are introduced with fatigue tests of concrete bridge deck; and the latest on-going study utilizing the transfer function of AE waveforms is demonstrated.

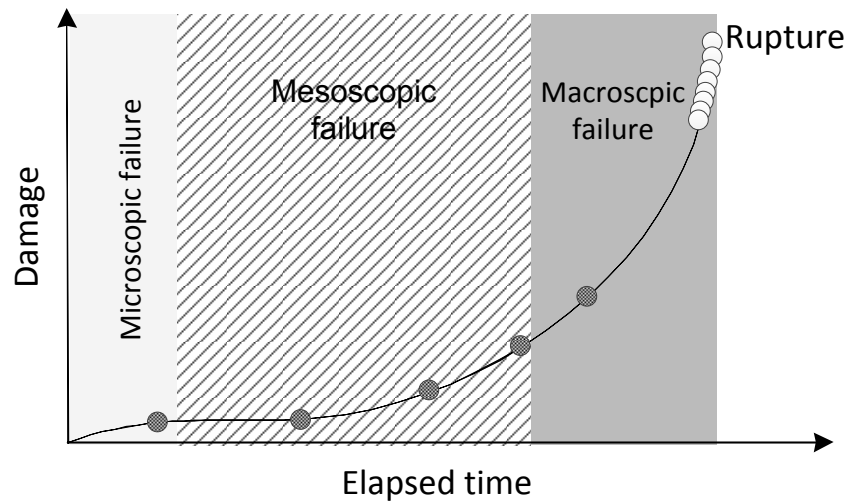


Fig. 1. General AE behavior approaching final failure.

2. AE based damage assessment parameters

2.1 Load ratio, Calm ratio, RTRI, i-Load ratio and i-Calm ratio derived from Kaiser effect

Under incremental cyclic load application to materials, AE activity can be represented with damage progress as shown in Fig. 2, where the damage progress is assumed to be classified into four different levels: intact; almost intact; slightly damage; and heavily damage. Due to crack occurrence, AE activity starts to be observed e.g., one in the first cycle. And in subsequent second load cycle, the AE activity starts at the load level being equivalent to maximum prior load. This coincidence between pre-stress and applying stress is referred to as Kaiser effect and have been studied in civil engineering to evaluate initial rock stress (e.g., Seto et al [5]). During the third load cycle in which the material exhibits slightly damage, the onset of AE appearance is at a smaller level than previously. Decrease of effective areas against external force or accumulation of microcracks within materials appears to play a significant role in this fact. Considering the relation of the stress showing the onset of AE activity to the stress experienced, such damage-indices as Felicity ratio (Fowler [6]), CBI ratio (Yuyama et al [7]), and Load ratio (JSNDI [8]) have already been proposed. With damage evolution, not only the AE activity during uploading, but that during unloading becomes more intense. Therefore, it is also important to focus on unloading processes (Shiotani et al [9]). Accumulation of shear type of cracks seems to be attributed to this phenomenon. The ratio of accumulated number of AE activity during uploading to that during a whole loading cycle is referred to as Calm ratio (JSNDI, [8]).

For the ratios mentioned previously, they may be difficult to apply for in-situ monitoring since evaluation of the maximum stress in which materials have experienced is not readily assumed. Thus, a RTRI ratio has been proposed instead (Luo et al [10]). The RTRI ratio can be

defined with regard to any measured mechanical parameters, such as stress/load, strain/deformation. Specifically it is the ratio of the value of the parameter when AE is initiated divided by the maximum value of this parameter during the inspection period, regardless of the maximum load in the whole loading history of structures.

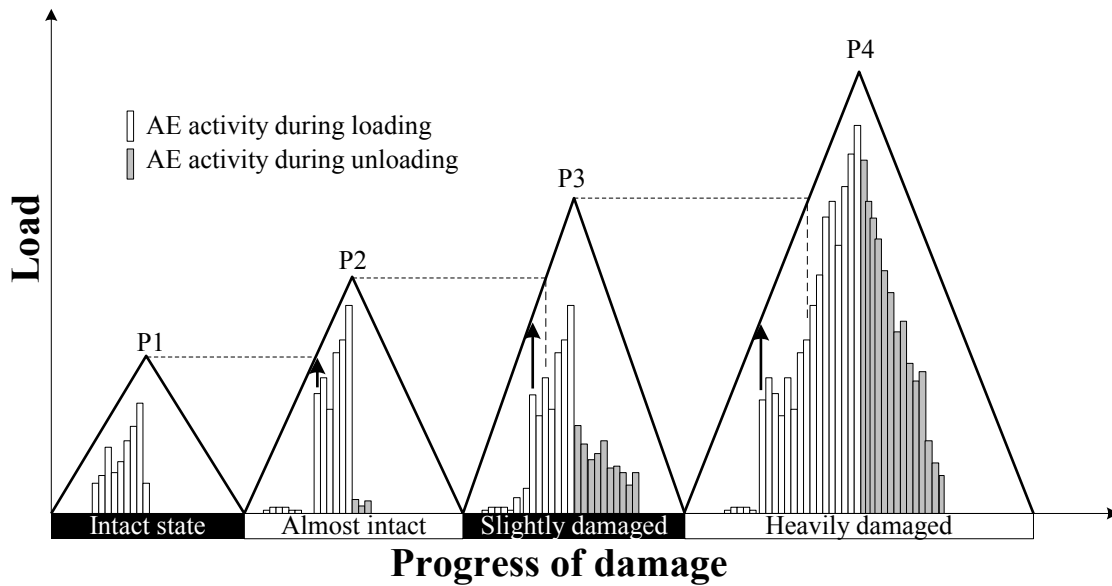


Fig. 2. AE activities with application of incremental cyclic loads.

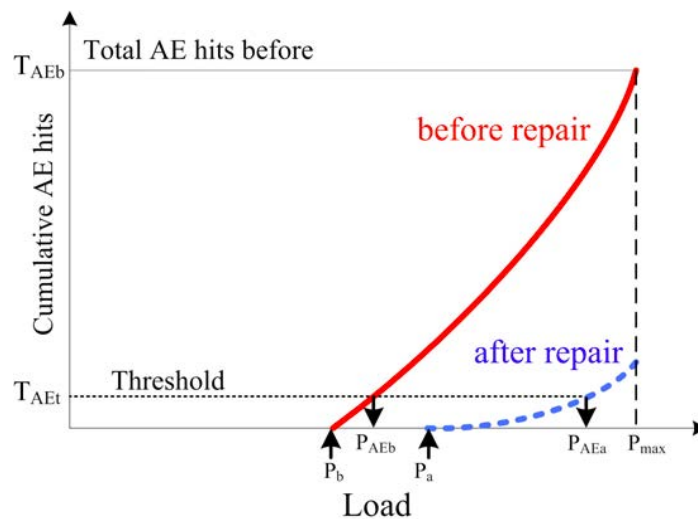


Fig. 3. Identification of the onset of AE activity in i-Load ratio.

Using these AE damage indices, current damage status of structures can be evaluated qualitatively; while recovery, suggesting how much degree the structures were repaired, could not be quantified. Since both Calm ratio and Load ratio are relative values, normalized by an accumulated number of AE activity during the whole loading cycle or by the maximum value of referred parameter like pressure, respectively, these indices do not take into account substantial differences in the obtained number of AE hits before and after repair. Therefore, the recovery rate has been proposed considering the numbers of AE hits obtained before and after repair [11]. Specifically to obtain the recovery rate, Load and Calm ratios are modified based on the AE activity observed as in demonstrated in Fig. 3 for the modification of Load ratio. Here, two typical AE hits

vs. load curves (before and after repair) are shown. Conventional “Load ratios” are defined by dividing P_b , or P_a values (before and after repair, respectively) with the previous maximum load, P_{max} . Instead, we introduce the threshold value (in percent a) to determine the onset of cumulative AE curve. Suppose total AE hits before repair, T_{AEb} , is 100 and we set a to be 10%. Thus, the threshold hit value or T_{AEt} is 10. This defines P_{AEb} for AE hits vs. load curve before repair. After the repair, we use the same threshold value as before, i.e., 10 in this case and we obtain P_{AEa} . By dividing P_{AEb} and P_{AEa} with the previous maximum load, P_{max} , we define improved Load ratios or “i-Load” ratios. As found we employ an identical condition for judging the onset of AE curves for before and after repair.

For modification of Calm ratio, we multiply a conventional Calm ratio with the ratio of cumulative AE activity after repair to that before repair. This allows us to factor in the variation of AE hits before and after. This new index is named improved Calm ratio or “i-Calm” ratio.

2.2 Grade providing fracture types

Figure 4 illustrates the variation of waveforms with fracture processes. In the process of progressing fracture within materials, tensile type of cracks would be mostly obtained in early stage, then mixed mode of tensile and shear type, followed by shear type of cracks (Yuyama et al [12]). It is known that tensile fracture velocity ranges from P-wave to 60-70% of S-wave velocity and shear fracture velocity would be 60-70% of S-wave velocity (Kanamori [13]). Corresponding to the variation of these crack types, it is expected that fracture velocity becomes smaller with progress of fracture although dislocation-scale becomes larger. This implies two important facts in AE waveforms: one is that gradients of ascending parts of waveforms become smaller with the progress of fracture; and the other suggests that low-frequency components would be dominant with progressing fracture. Therefore ‘grade’ is introduced [14], which is defined as the peak amplitude divided by the rise time. The large values of grade suggest the early stage of fracture where cracks of tensile type are dominantly generated, while smaller ones imply the approach to the final stage where cracks of shear type primarily occur (see Fig. 4). Indeed as shown in Fig. 5, the grade due to tensile type of failure exhibits the largest value followed by mixed type and the shear type of fracture. It is noted that applicability of the gradient has also been studied on the process of concrete materials (Iwanami et al. [16]) or on classification of crack types in combination with average frequency [17].

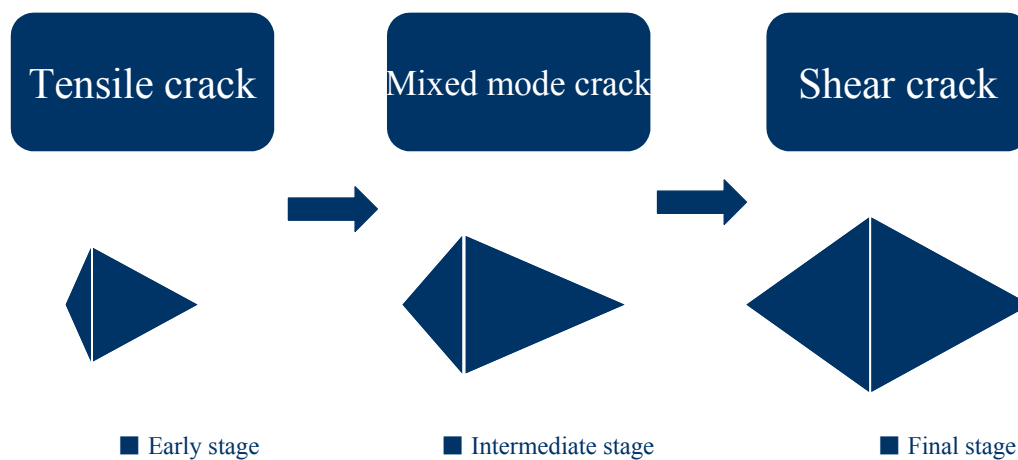


Fig. 4. Variation of AE waveforms with damage progress.

2.3 Improved b -value obtained from peak amplitude distributions

Because AE peak amplitude is associated with the scale of fracture, the b -value defined as a slope of the amplitude distribution is known as an effective index related to the states of fracture (Mogi [18], Scholz [19]). Larger b -values show the state of materials where microscopic fractures occur more predominantly than macroscopic fractures, whereas smaller b -values indicate that the occurrence of macro-fractures prevails. Since the b -value was originally defined in seismology i.e., obtained in a long time span with a lot of numbers of observatories, and therefore the precise evaluation was possible, being different from the AE applications where there existed issues to be addressed. Thus, instead of the seismic b -value, an improved b -value (Ib -value) has been proposed (Shiotani et al [1]), which is suitable for AE applications dealt with any kinds and scale of materials/ structures.

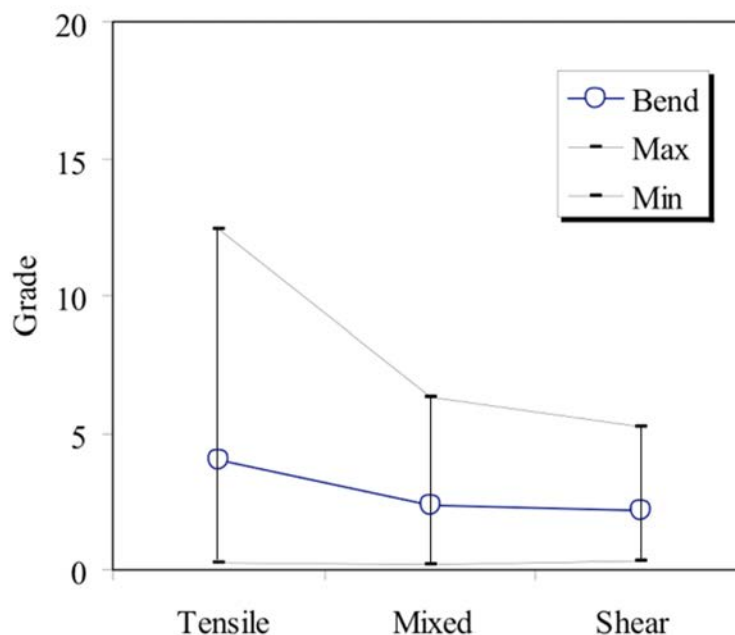


Fig. 5. Variation of grade ($\text{dB}/\mu\text{s}$) due to different types of fracture in four point bending test of RC. Fracture type characterization was implemented by SiGMA procedure ([15]).

In the improved b -value analysis, the number of AE data to be used should be first set. Roughly, two methods for determining the calculation number have conventionally been employed: a) accumulated numbers from the beginning data; and b) numbers per unit time. In the former case, the number of data used to determine the b -value is increasing with elapsed time. In the latter case, because the AE activity increases exponentially with approaching final failure, it is apparent that the number of AE data determining the b -value is differed in each unit time. Statistically it is so important to use the constant number of AE data when determining the b -value that the number of AE data: b , is introduced as in (1) to improve the calculation of the b -value:

$$\int_0^{\infty} n(a) da = \beta \quad (1)$$

where a is an amplitude, $n(a)$ is a number of AE at da and b is a number of AE data. Values of b between 50 and 100 are considered appropriate as suggested by other studies (Shiotani et al [20]). In actual, in the improved b -value calculation, a fixed number of b between 50 and 100 should be used throughout the whole experimental data.

The value of AE peak amplitude varies with monitoring conditions such as sensor installations, propagation media, and occurrence locations, resulting that the AE amplitude distribution is also dependent on these conditions. In order to obtain the b -value qualitatively, a method to determine the amplitude interval being independent on the distributed amplitude is necessary. In the improved b -value analysis, the range of AE amplitude is determined based on such statistical values as the mean m and standard deviation σ , where the upper amplitude w_2 and lower w_1 are formulated as $m+a_1\sigma$ and $m-a_2\sigma$, respectively. We define the accumulated numbers of amplitude over w_1 and w_2 , as $N(w_1)$ and $N(w_2)$, which is obtained by,

$$N(w_1) = N(\mu - \alpha_2\sigma) = \int_{\mu - \alpha_2\sigma}^{\infty} n(a)da \quad (2)$$

$$N(w_2) = N(\mu + \alpha_1\sigma) = \int_{\mu + \alpha_1\sigma}^{\infty} n(a)da \quad (3)$$

where the interval of amplitude analyzed would be $(a_1+a_2)s$. Then the Ib -value is given by,

$$Ib = \frac{\log_{10} N(w_1) / N(w_2)}{(\alpha_1 + \alpha_2)\sigma} \quad (4)$$

where a_1 and a_2 are empirical constants. It is noted that since Ib -value is calculated on the basis of decibel unit. When comparing with seismic b -value, the Ib -value shall be multiplied by a coefficient of 20. The Ib -value has successfully been applied to evaluate the developing process of fracture in such materials as soil (Shiotani et al. [2]), rock (Shiotani et al. [21]), and concrete (Shiotani et al. [20, 22, 23]). Several similar attempts have so far been found elsewhere [e.g., 24] but it is noted that improved b -value is the original employing constant numbers of AE data in combination with statistical values of amplitude distribution to the AEs' b -value analysis. Also it is very important to recognize when applying the AE technique to low attenuation materials with plural numbers of AE sensors or to the materials where numerous macroscopic failures happen over the area of interest that: for the former case, as the b -value analysis shall be carried out based on the AE source magnitude i.e., calculation based on a specified sensor shall be avoided and source magnitude, and AE source amplitude, average amplitude with all contributed sensor to the source location, or AE amplitude with first arrival sensor shall be employed; and for the latter case, in addition to the former consideration, the b -value shall be obtained individually with sectioning area of interest into several parts.

3. Acceleration of mobile traffic with train passage

When secondary AE monitoring is carried out utilizing such mobile loads as railway traffic [25, 26], it is worth understanding that what frequency components are directly generated due to the train passage. In order to know the frequency components, accelerometers were placed on the bottom of an elevated arch brick bridge. The acceleration due to the train passage was measured with two accelerometers (750WI, TEAC) of which the frequency response ranges from 3 Hz to 10 kHz. To study higher frequency spectrum, the acceleration signals were recorded in a signal recorder (GX-1, TEAC) with a sampling of 200 kHz.

As a result, the frequency spectrum showed a slightly difference with the direction of train movement, namely in-coming trains or out-going trains. The frequency due to the train passage ranged from 80 Hz to 130 Hz. Figure 6a shows a typical waveform detected and its FFT result due to train passage as shown in Fig. 6b.

It is generally recognized that this range of frequency, namely 50- 180 Hz, is far below the frequency response of AE monitoring system, suggesting no influence on AE monitoring. To verify this assumption the experimental study with a reaction type shaker were conducted.

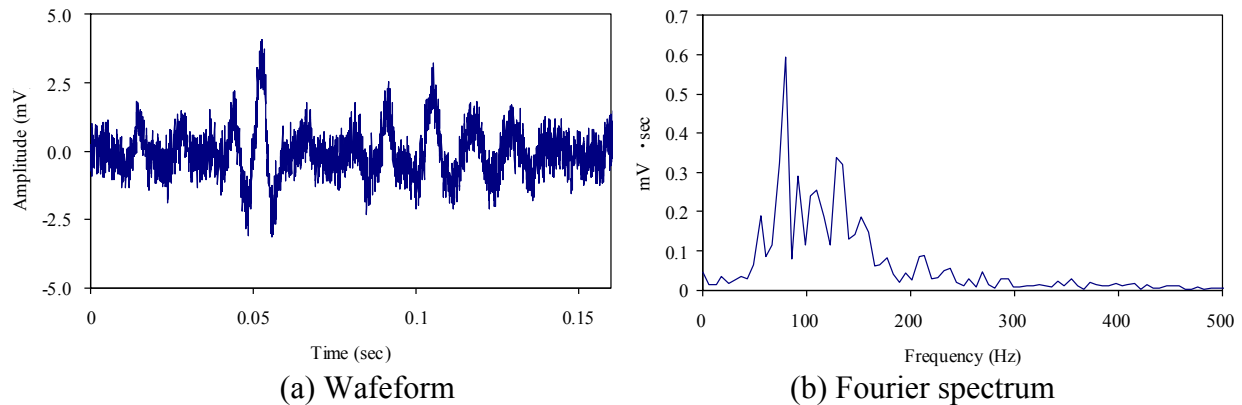


Fig. 6. Typical detected AE signal due to train-induced acceleration.

Three frequencies (with the force output in newtons), 30 Hz (300 N), 40 Hz (160 N) and 50 Hz (100 N), were excited by a reaction-type shaker (Model F4/Z820WA, Wilcoxon Research, Inc.). The shaker used has a reproducible frequency ranging from 10 Hz to 7.5 kHz. A brick wall was employed as a propagation medium, which has a height of 1,530 mm, a width of 1,530 mm and a thickness of 430 mm. The shaker was firmly stud-mounted on one side, and an AE sensor of 60 kHz resonance (R6, PAC) was set on the other side of the brick wall with wax, resulting in propagation distance of 430 mm. AE signals detected were recorded with Mistras AE system under the condition of 2 MHz sampling and a 1k words length. It is noted that the frequency response of the AE monitoring system ranges from 10 kHz to 10 MHz.

Surprisingly, although the accelerations were excited with a range of frequency between 30 Hz to 50 Hz, showing far below frequency range of that in in AE monitoring system, AE waveforms detected had frequency peaks ranged from 7.8 kHz to 9.8 kHz, suggesting increase of two orders of magnitude in the frequency of excitations. A typical waveform and its FFT result in case of 50 Hz excitation can be found in Fig. 7. A peak frequency was observed at 9.8 kHz in case of 50 Hz.

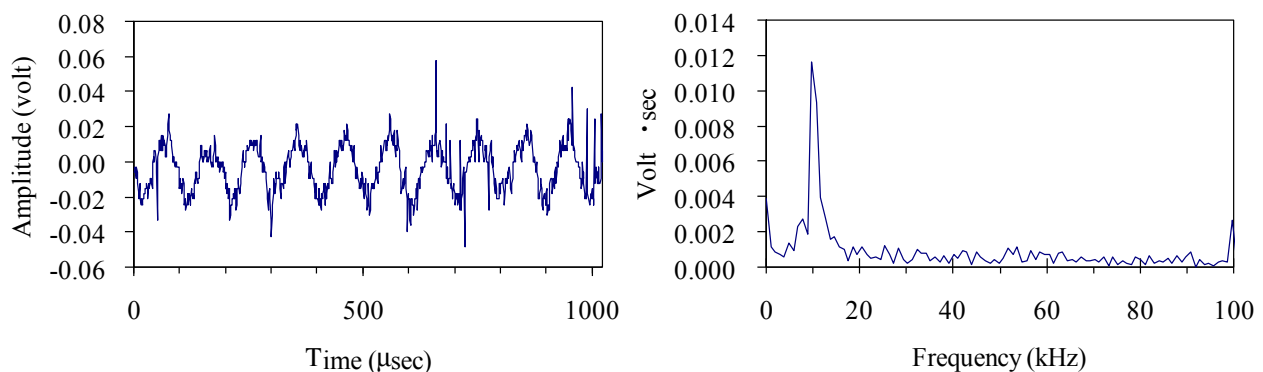


Fig. 7. Typical waveform and FFT result in acceleration of 50 Hz.

This suggests that even when the lower frequency accelerations than that of the response of AE system were generated, the AE sensors detected the induced accelerations as AE signals for

the case of large energy. From this discussion, it leads to a conclusion that train passage or compatible passage by vehicles has a potential to generate indirect AE signals that have a peak frequency around the lowest limit of the AE system, namely 10 kHz in our experimental condition. Thus, to avoid such indirect emissions due to passage-induced noise superimposed to AE signals due to crack behavior, spatial filter using AE source location might be crucial since the frequency of the secondary AE activity includes these lower range of AE frequencies.

4. Strategic phased AE monitoring

With sparsely arrayed AE sensors at low frequency, wide range monitoring for infrastructures is possible, suggesting most-likely deteriorated areas, while more precise investigation is possible when employing high-frequency resonant AE sensors with dense arraying. In this way an objective area and the resolution of monitoring can be arranged by using suitable type of AE sensors according to the demand. The following is an example when AE monitoring was applied to such large infrastructures as bridges, where the preliminary investigations showed little deterioration in a 45-m bridge span by both surface-crack observation and physical tests of excavated cores [27].

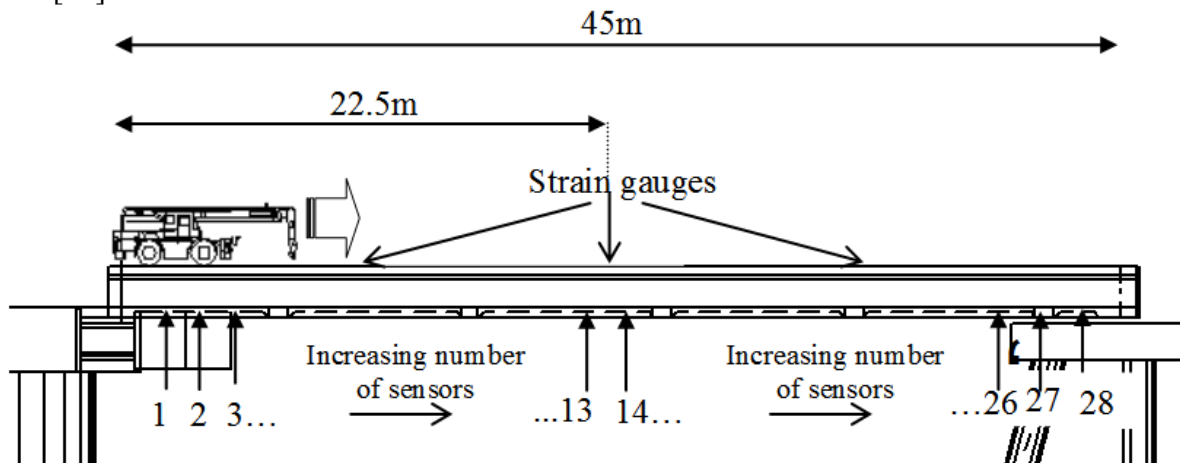


Fig. 8. AE monitoring details with crane mobile load. Positions both of AE sensors and strain gauges are shown.

In order to know the relatively damaged area for the longitudinal structure, a linear arrangement of AE sensors with a space of 1.5 m over 45 m in a longitudinal direction is carried out as shown in Fig. 8. A total of 28 sensors of 60-kHz resonance are placed on the bottom surface of the bridge with wax. The AE testing was performed while moving a heavy vehicle of 20 tons crane over the bridge. Based on the AE activity the part of structure being most likely to exhibit higher degree of damage than the other areas was followed to select the detail investigation, or end up in this first monitoring when no active parts of AE were found. In the former case, the selected area is again measured for AE activity with a denser sensor array in 2D. Using the 2D arrayed AE sensors, a surface ultrasonic examination is also conducted in order to investigate the P-wave velocity of concrete at the area of interest.

As stated already, in order to calculate the Calm ratio, the AE activity should be correlated with a mechanical parameter. In this case, it was conducted by the measured strain at the middle point of the bridge span and the AE activity recorded by the two sensors placed closest to the center (#13 and #14 of Fig. 8).

The number of hits for three different trips of the crane exhibited the resultant Calm ratios ranging from 0.3 to 0.45 for any individual passage of the crane, indicating serious damage according to past studies [26].

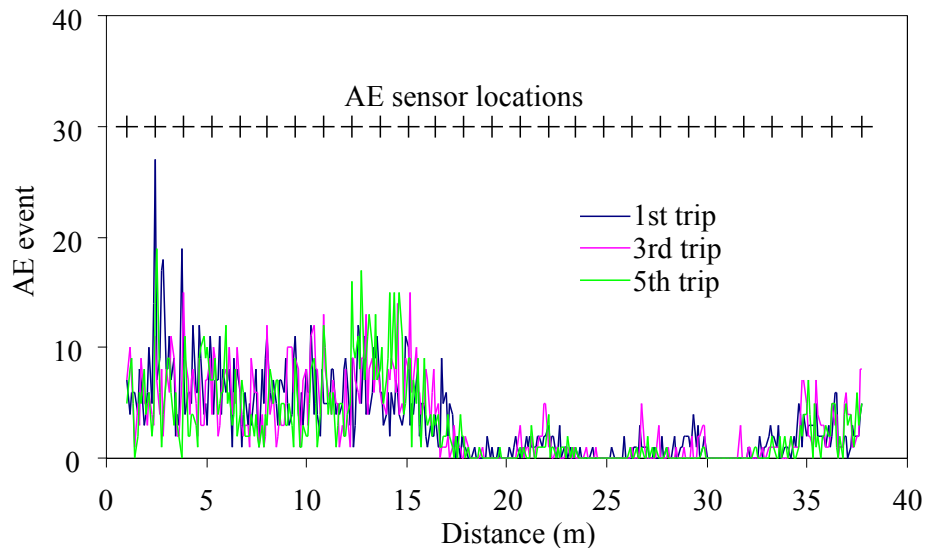


Fig. 9. 1D AE sources along with repeated mobile loads.

One-dimensional AE sources are determined by the 28 linearly placed sensors. The locations of AE sensors and resultant AE events activity within each 10-cm segment are shown in Fig. 9. Intensive AE activity was always emerged at about 3 m, irrespective to the trip, and therefore an area around 3 m in the figure was chosen for the subsequent detail monitoring, where the separation distance of sensor is 1.5 m, forming the examined area of 3 m by 3 m of three parallel arrays of three as shown in Fig. 10. Nine sensors were used for this detail test.

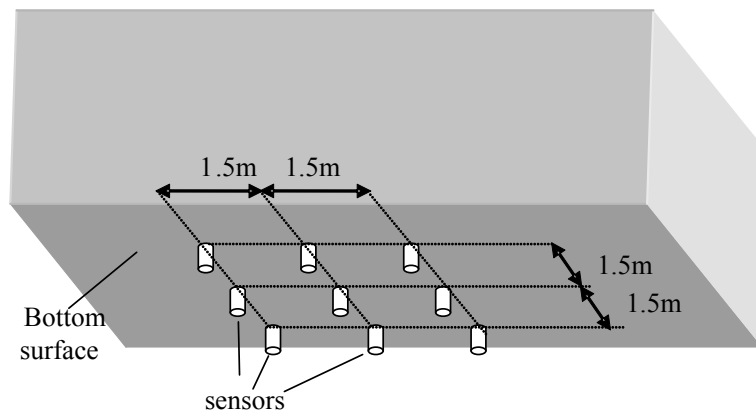


Fig. 10. Arrangement of AE sensors (60 kHz resonant) both for 2D AE monitoring and UT.

As shown in Fig. 11, remarkable numbers of AE events ranging from small to large scale were obtained. Specifically those appeared along the tires’ trace of the mobile vehicle employed. Velocity tomogram leads to a characteristic low velocity zone, developed diagonally in the area of interest. The low velocity zone might be attributed to a subsurface defect, although the depth cannot be easily determined. Considering the fact that the AE events were intensively generated on this low velocity zone, it can result from concrete cracks, delaminations of different layers (e.g. asphalt on concrete) or friction between the tendon ducts. Also matrix concrete would be possible origins to induce AE activity due to the loading. As found in this phased AE monitoring,

this sequential investigation, started with global AE monitoring then local AE monitoring, followed by detailed measurements of ultrasonic P-wave velocity are very useful in characterizing the quality of large-scale concrete structures.

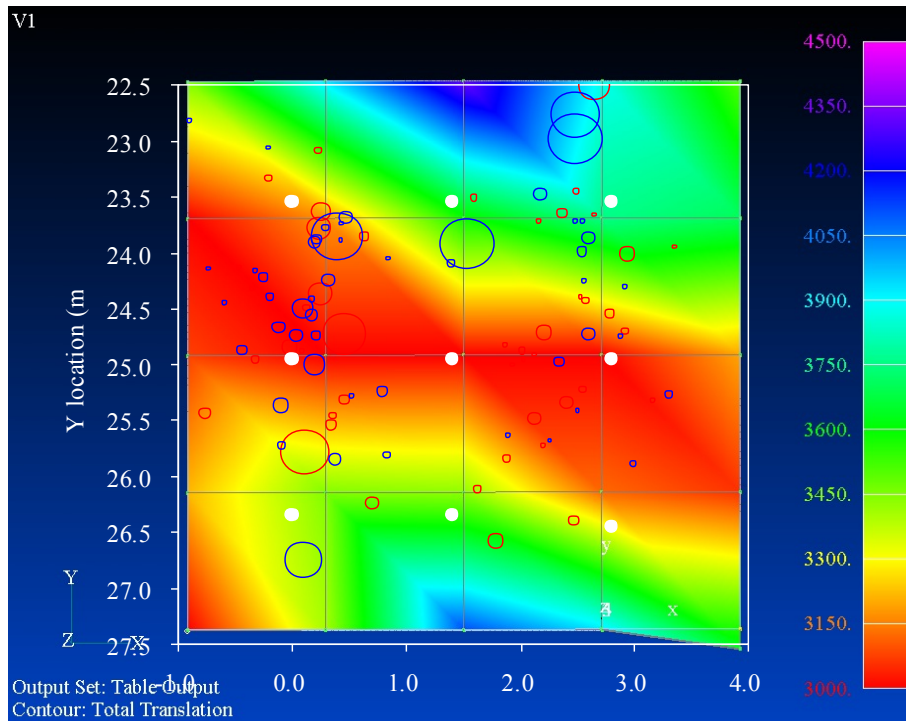


Fig. 11. Identified 2D AE sources along with mobile load (see circles) and velocity tomogram obtained from surface UT measurement. The vertical direction of the figure corresponds to the longitudinal direction of the bridge.

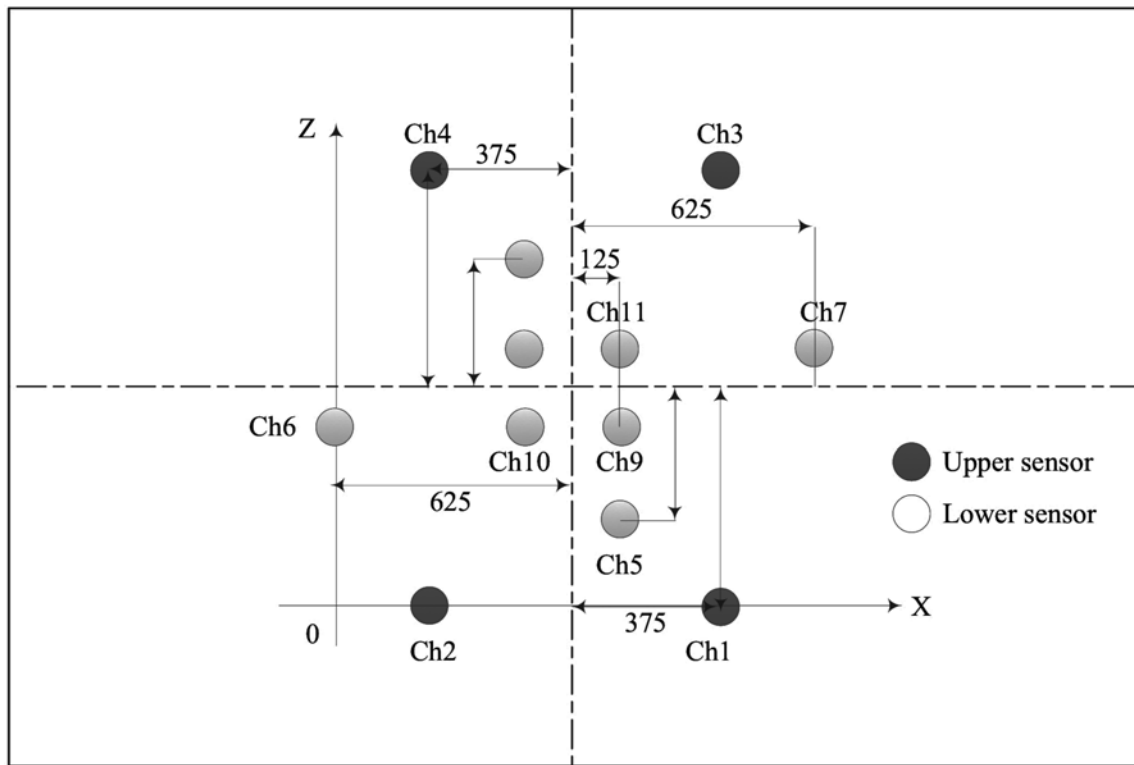
5. Evaluation of fatigue damage of concrete bridge deck

5.1 Experimental set up

Repeating wheel loading, particularly by heavy vehicles, is known to be the major accelerator to cause serious fatigue damage of reinforced concrete (RC) deck on road bridges [e.g., 28]. A visual investigation from the bottom surface of the deck so far assesses the integrity of the bridge deck; however, this visual evaluation is only possible after the emergence of surface crack i.e., internally evolving cracks due to rebar corrosion or delamination among layers are only recognized when they develop into the critical stage as to be observed on the surface. In addition this visual observation cannot be applied for the deck, of which the bottom surface has already covered with such reinforcing sheets as steel and FRP [e.g., 30]. In the following, AE testing is experimentally applied to the fatigue failure of RC deck with steel-wheel loading apparatus. Note that AE monitoring is conducted applying static loads when repeated wheel loading is suspended. Specifically the static loads are applied after the initial loading, 10,000 loading and 20,000 loading. In addition to the AE monitoring, internal conditions were also assessed by ultrasonic tomography. The experimental detail can be found in [29].

The RC test specimen being subject to the cyclic load, having dimensions of 3,000 x 2,200 x 180 mm was set on an experimental apparatus. To accelerate the subsequent fatigue damage,

initial load up to 150 kN was applied to the center of the specimen, followed by repeated wheel load of 100 kN. The wheel loading is applied to the central part in the longitudinal axis up to 20,000 times of passage. After each stage of initial state, 10,000 times and 20,000 times of passage, the test was stopped for elastic wave tomography tests to obtain the internal velocity distribution. Subsequently incremental cyclic loads by 20 kN up to 100 kN are applied at the center of the specimen to induce the secondary AE activity from existent defects. AE monitoring was conducted with 12 AE sensors of 60-kHz resonance, placing six on the top and six on the bottom as shown in Fig. 12. The signals detected by the sensor were amplified by 40 dB, and processed and recorded by AE monitoring system (SAMOS, PAC) with 1 MHz sampling and 2k samples. With regard to the tomography, totally four sections of 50 x 18 cm each avoiding the loading area was set for the measurement as shown in Fig. 13. In each section, elastic waves were generated by the pulser on both surfaces placing five-sensor with a space of 50 mm on the other surface in turn. The sensors and monitoring system used are the same as in the AE monitoring as shown previously. To input transit time of the entire ray paths into the tomography program [31], the first motion of the detected waves was extracted.



Unit: mm

Fig. 12. Arrangement of 12 AE sensors.

5.2 Ultrasonic tomography

As a typical case, velocity distributions in L1 section (see Fig. 13) are shown in Fig. 14. In general, concrete with the P-wave velocity of more than 3,500 m/s is evaluated as good, and in case of more than 4,500 m/s as excellent, while those of less than 3,000 m/s are considered as poor and as very poor when less than 2,000 m/s [32]. As seen in Fig. 14, the evolution of damage areas due to increase of wheel loadings could be identified with low velocity zones denoted by

yellow to red colors, corresponding to less than 3,000 m/s in the velocity. As in our past studies [e.g., 33], the damage areas could be identified with low velocity zones of elastic wave.

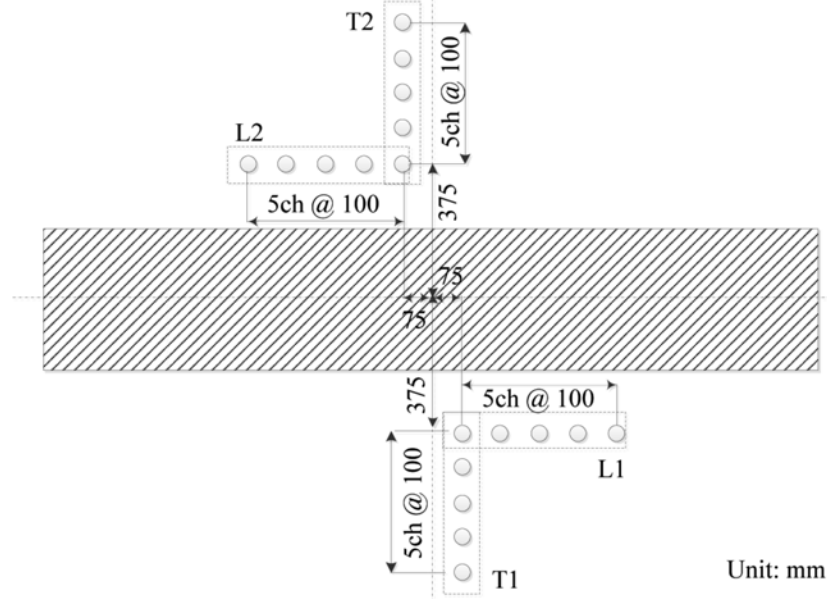


Fig. 13. Sensor array of elastic wave tomography.

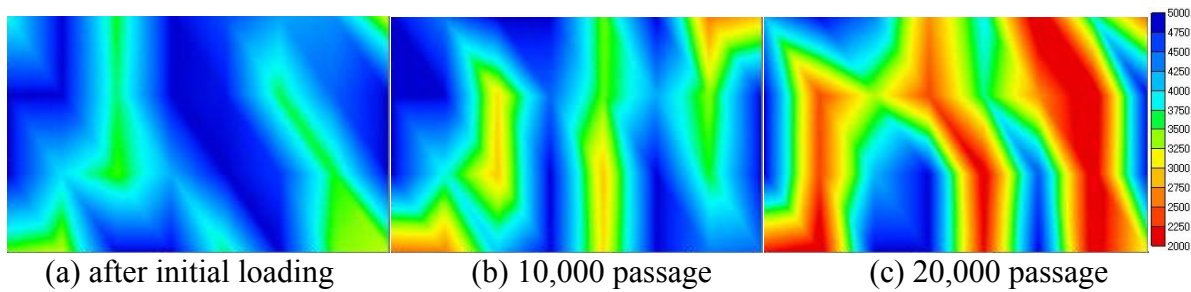


Fig. 14. Tomogram in L1 section. Legend shows the velocity in m/s.

5.3 Limitation of solely damage-evaluation with Calm ratio and RTRI ratio

The Calm and RTRI ratios both from incremental cyclic load tests can be found in Fig. 15 and Fig. 16, respectively. Again, AE measurement was conducted with incremental cyclic loads following the specified numbers of wheel loading. Therefore no mechanical noise due to wheel loading was included in these AE activities. In these figures, diamonds denoting the case of ‘after initial loading,’ exhibit the AE activity in the second loading after the initial wheel loading with 150 kN, i.e., the specimen had already experienced the load up to 150 kN. In the same way, squares indicate the result when 10,001st loading and 20,001st for triangles. It is noted that if damage degree could be obtained quantitatively based on the past stress-experience, the ratios in a certain situation, e.g., 10,000 passage in the figures, must stand as an intrinsic value, irrespective to the load applied; however contrary to this assumption, the ratios varied corresponding to the load applied. Specifically in the Calm ratio as shown in Fig. 15, a large applied load gives large Calm ratio, indicating the development of damage due to load increase. For the RTRI ratio shown in Fig. 16, large RTRI ratios, implying damage mitigation, were obtained as load increased. In either case, both ratios could not well quantify the damage by their values. These indices are plotted in Calm-RTRI ratios chart as shown in Fig. 17. In the window, provisional lines are drawn to classify the damage. As seen, the plots in the case of initial loading reveal in the bottom-right indicating intact/minor damage, and these plots shift to the top-left as passage

proceeds, implying the progress of failure. Combination plots of these two indices of Calm and RTRI ratios have a potential to quantify the fatigue damage.

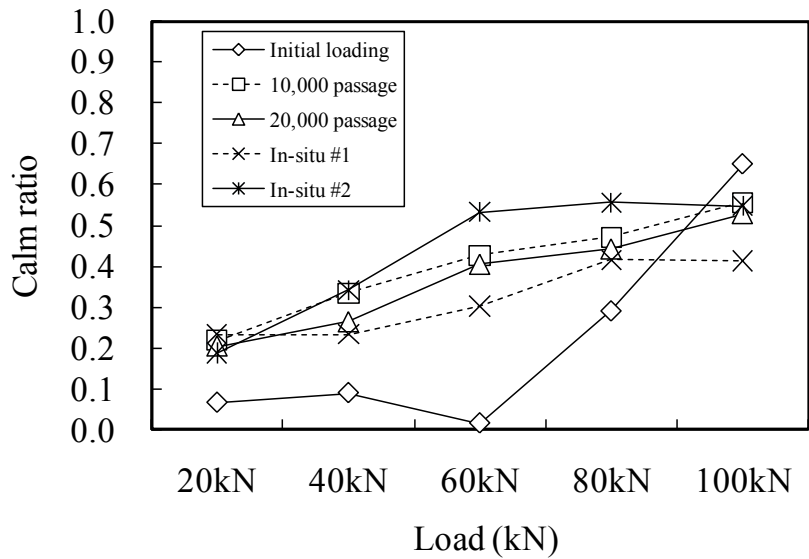


Fig. 15. Calm ratios in three damage cases.

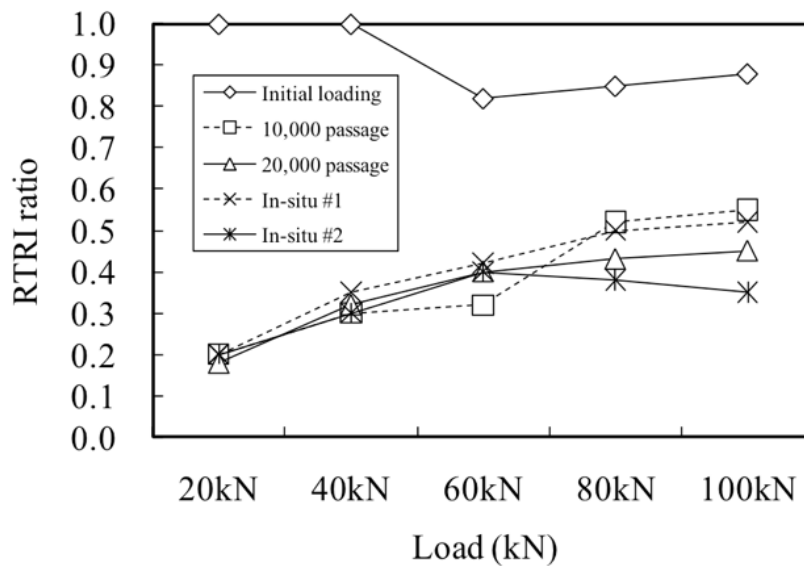


Fig. 16. RTRI ratios in three damage cases.

5.4 Peak frequency

The frequency features such as peak and centroid provide valuable information on materials' damage status [34]. This fact was readily confirmed when controlled artificial signals, of which the frequency components are known already, were excited. In this case unique variations of frequency component through travelling are only dependent on the materials properties. Ultrasonic waves lose their high frequency components when they travel through the media, influenced by the attenuation/scattering effect from defects, and as a result the lower frequency components of detected signals are enhanced for the severely damaged cases. As for AE waveforms, however, resultant frequency components are influenced also by the source types, namely fracture behavior causing various displacement-time function in addition to the materials properties, i.e., the frequency components of the measured AE signal do not always reflect the materials damage

condition alone. Fortunately in this study we are dealing with the secondary AE activity obtained mainly from identical types of source, namely, friction between existent crack interfaces, the frequency components of detected AE waveforms can be regarded as influenced principally by the quality of propagation media. Figure 18 shows the average of peak frequencies of detected AE waveforms in each case. Undoubtedly the peak frequency decreases with damage progress, and it was confirmed that the peak frequency of measured AE signals could be a clue to provide the degree of damage.

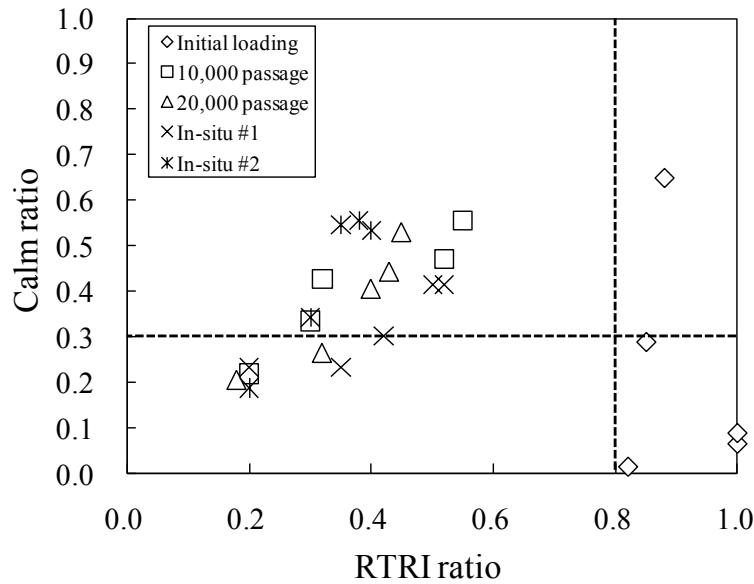


Fig. 17. Calm and RTRI ratios in three damage cases.

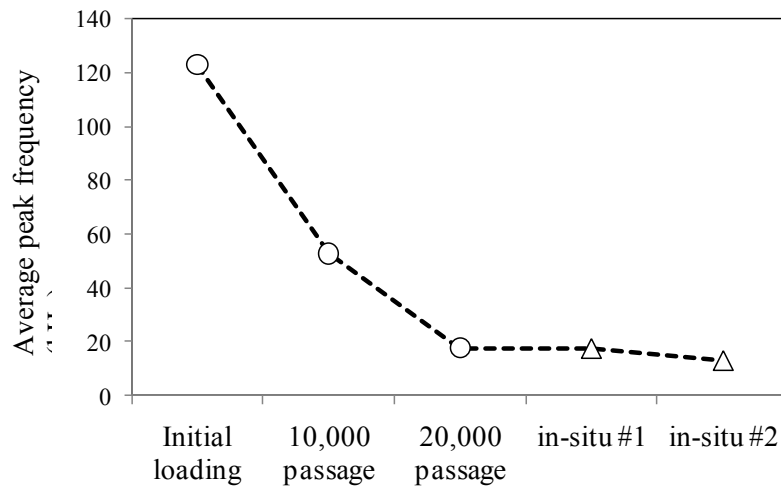


Fig. 18. Average peak frequencies of AE waveforms.

5.5 Specimens cut from actual bridge deck

Elastic wave excitations for tomography and AE measurement were both conducted for two specimens cut from in-situ concrete deck. In this particular case, one of the most complex deterioration patterns to investigate is taken. Specifically to reinforce the deck after severe deterioration, an additional concrete layer over the original deck was cast; however, invisible lateral cracks were also generated as shown in Fig. 19. The specimens are referred to as No. 1 for seriously damaged case and No. 2 for intermediately damaged case based on the sectional observa-

tion. For these in-situ specimens, Calm ratio and RTRI ratio are given in Figs. 15 and 16, respectively. With in-situ specimens, variations of both ratios due to applied load could be observed as before; it is noted that two results of in-situ specimen #1 & #2 enclose those of 10,000 and 20,000 passage damage, and those are quite different from that of initial loading.

As noted earlier, in-situ specimen #1 appeared to be more deteriorated than that of #2; however, the findings from Calm ratio, RTRI ratio and the combination of both ratios (see Figs. 15-17) could not separate the damage of the two specimens adequately. This might be caused by the heterogeneity of damage evolution. The damage condition observed from the side could not always reflect the internal damage.



Fig. 19. Side view of in-situ specimen #1 cut from actual concrete bridge deck.

The average peak frequencies from the in-situ specimens again show their similarity (Fig. 18). Low average frequencies were obtained from both of the in-situ specimens. Although the evolution pattern of the cracks were different from ones of the wheel loading test, the average peak frequencies in the in-situ cases is equal to or even less than the value of 20,000, suggesting the in-situ specimens were damaged as equivalent or more to the case of 20,000 passage.

As described above, using sparsely arrayed AE sensors, followed by extracting AE frequency features, global investigation of bridge decks' integrity can be carried out. Once the area of interest is determined, further detailed information as sectional damage can be visualized by ultrasonic tomography procedure.

6. New approach for assessing damage with transfer functions of AE waveforms [35]

The frequency characteristics of AE waves could imply the damage condition of infrastructures in comparison to other features of elastic waves. In this case, exact quantitative evaluation for the damage is only possible in case where every AE waves travelled in the compatible distance. As the frequency characteristics of AE waves are also known, which depend on the resultant propagation distance, obtained frequency does not always demonstrate the damage condition, providing the rough evaluation [36]. Thus as one of on-going studies, transfer functions of propagation media are briefly described here to quantify the damage with AE waveforms.

6.1 Conceptual configuration

AE waveforms are obtained as convolution of functions of source, propagation media, sensor and acquisition system in the time domain, and those frequency responses can be formulated by a simple multiple equation in the frequency domain:

$$X(f) = U(f)T(f)D(f)S(f) \quad (5)$$

Here $X(f)$, $S(f)$, $D(f)$, $T(f)$, $U(f)$ are Fourier transforms of detected AE waveforms, AE source, propagation media, sensor and acquisition system, respectively. $D(f)$ in Eq. 5 is the target to quantify the damage; however, as $S(f)$ is not readily obtained in AE technique, an approach to identify $D(f)$ irrespective to source time function is crucial. In AE application, plural numbers of sensors are employed to locate the AE source, and therefore the comparison of waveforms detected among different sensors for an AE source could suffice this requirement as in Eq. 6 assuming the frequency responses of all the sensors employed are compatible.

$$\frac{X_2(f)}{X_1(f)} = \frac{T_2(f)}{T_1(f)} \cdot \frac{D_2(f)}{D_1(f)} \equiv \frac{D_2(f)}{D_1(f)} \quad (6)$$

On the other hand, when $D(f)$ is dependent on propagation media attenuation, Eq. 7 can be defined as well, where f is a frequency (Hz), V is a P-wave velocity (m/s) and Q is a normalized value demonstrating attenuation rate.

$$D(f) = \exp\left(-\frac{\pi f}{VQ}d\right) \quad (7)$$

By combining Eq. 6 and Eq. 7, Eq. 8 is obtained.

$$\frac{X_i(f)}{X_1(f)} \equiv \frac{D_i(f)}{D_1(f)} = \exp\left(-\frac{\pi f}{VQ}\Delta d_i\right) \quad (8)$$

$$\Delta d_i = d_i - d_1 \quad (d_i \geq d), (i = 2, \dots, n)$$

Equation 8 shows that a function of frequency response can be expressed by an exponential function dependent on the difference of distance Δd and frequency f .

6.2 Preliminary examination

As shown in Fig. 20, concrete specimen of 500 x 500 x 100 mm was prepared placing four AE sensor of 60 kHz resonance at the four corners on the bottom surface. Ultrasonic wave excitation was made using the wideband AE sensor (1045S, Fuji Ceramics), where electric pulse was made by PUNDIT (-500 kHz, CNS Electronics).

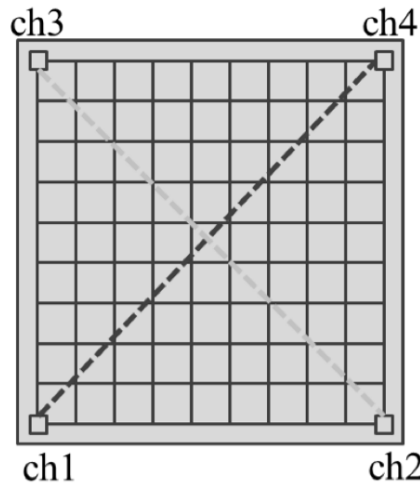


Fig. 20. Sensor arrangement and positions of pulse excitations.

To examine the potential influence of heterogeneity of the concrete specimen on the transfer function in the intact specimen, excitations at the intersectional points in the line between Ch1

and Ch4 sensors were conducted with Ch2 and Ch3 operated as receivers. Switching of sensor pairs was also used. Figure 21 shows the ratio of Ch1 to Ch4 in frequency response when the excitations were made along the line between Ch2 and Ch3. As many excitation points were employed, three lines for the mean value and mean \pm standard deviations σ were drawn. Two important facts can be found: even for intact condition the frequency response showed difference from the point measured, and the frequency response needs to be discussed in the range of effective frequency response, i.e., this case the range of 60 to 180 kHz.

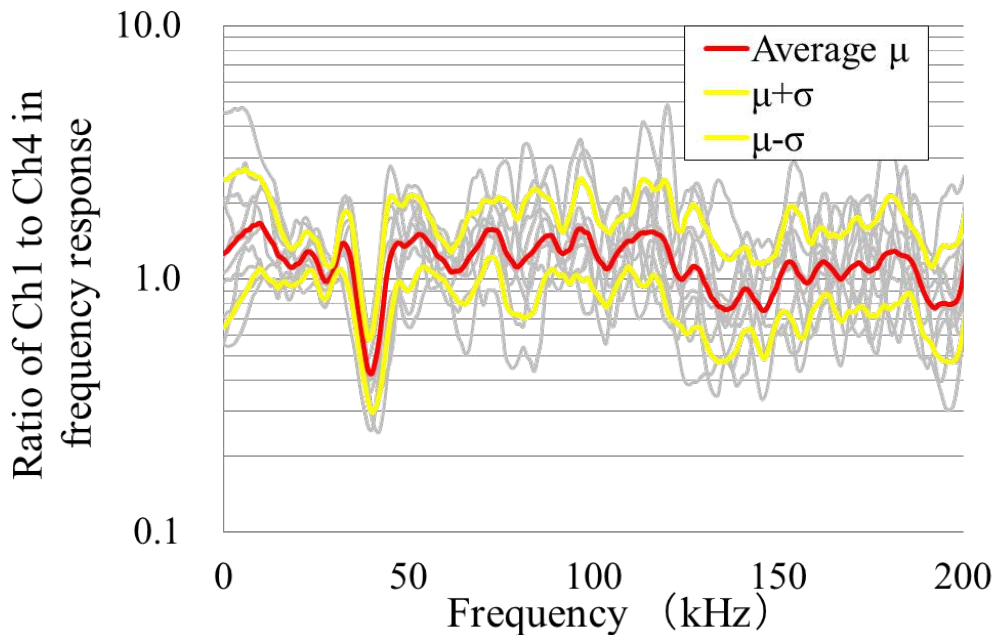


Fig. 21. Ratio of Ch1 to Ch4 in frequency response when the excitations were made along the line between Ch2 and Ch3.

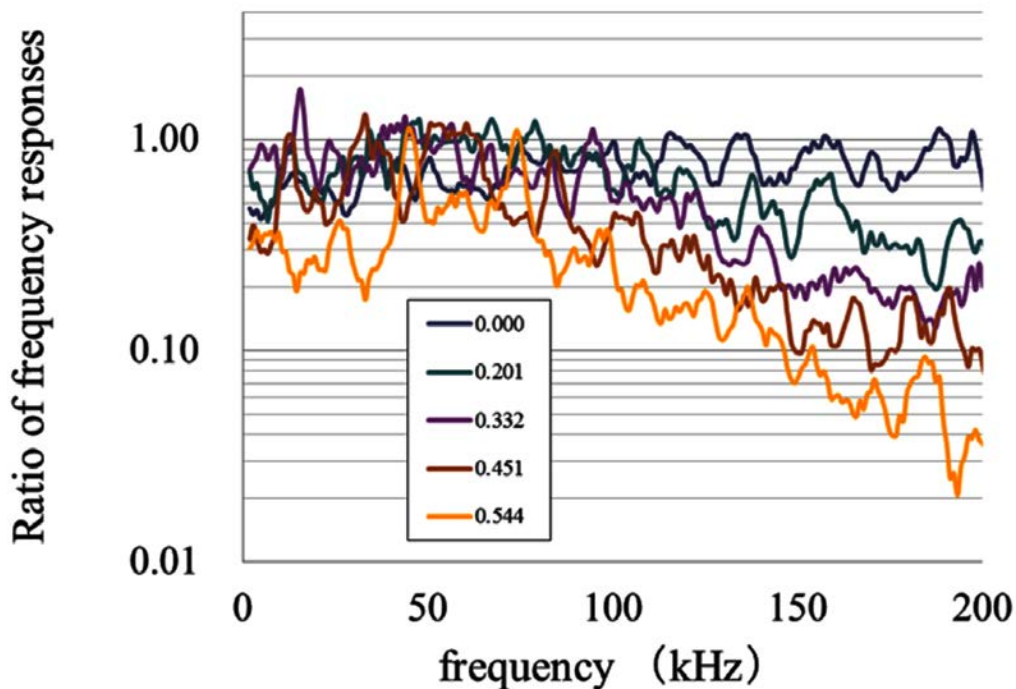


Fig. 22. Ratios of frequency responses for the differences of propagation distances.

To verify the frequency response corresponding to the propagation distance, other intersectional points than above were used to excite the signal. The ratios of frequency responses for the differences of propagation distances can be found in Fig. 22. The legends of the figure show the difference of propagation distances. The decrease rate for higher frequency above 100 kHz becomes more remarkable as the difference of propagation distances becomes larger. As this trend had a good accordance with Eq. 8, the slope of the ratios, α in Fig. 22 were calculated by the approximation, where the slope can be defined as Eq. 9.

$$\alpha = \frac{\pi \Delta d}{V Q} \quad (9)$$

Figure 23 shows the relation between the slope α and differences of propagation distances. Surprisingly the relation can be approximated by a linear equation, resulting in good agreement with Eq. 8. Of course this slope α correlates well to the difference of propagation distance, but more likely to demonstrate the properties of propagation media. This is the very concept to quantify the damage of the materials with transfer functions using AE waveforms.

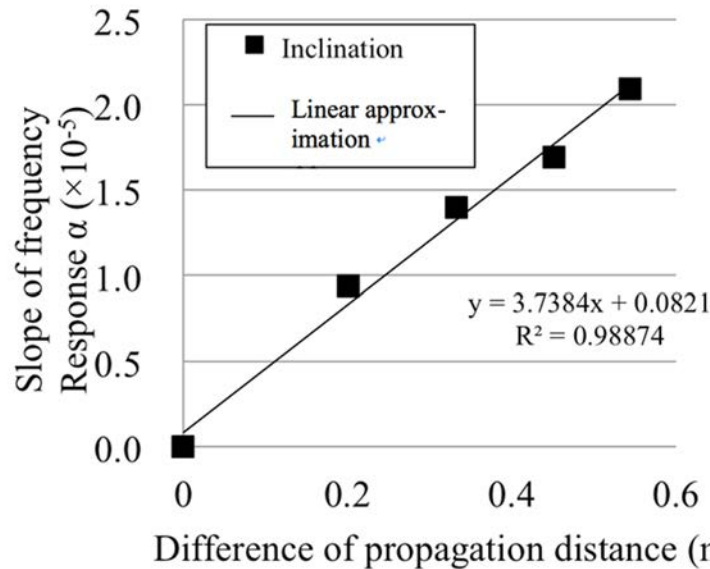


Fig. 23. Slopes of frequency response with the differences of propagation distances.

6.3 Application to the mortar specimens with several degrees of artificial damage

To verify whether the concept of the ratio of frequency responses is applicable to the damage assessment of concrete, homogeneous standard mortar with formed polystyrene spheres simulating damage was prepared as test specimens. As shown in Fig. 1, the prism mortar specimens have dimensions of 150 x 150 mm with different heights: about 100, 200, 300, 400 and 500 mm. In order to simulate the damage, spherical foamed styrene material (6 mm in diameter) was used as a false cavity, with four types of volumetric percentages as 0%, 1%, 5% and 10%. Two types of elastic wave excitation were made by pencil-lead break and electric pulser (PAC) with a wideband AE sensor (1045S, Fuji Ceramics). Piezoelectric sensors of 60 kHz resonant (R6, PAC) are employed for the receiver. The signals detected by the sensor were amplified by 40 dB at the amplifier, and processed and recorded by AE monitoring system (SAMOS, PAC) with 1 MHz rate and 1k words samples. The elastic wave was excited at the center on the top surface of the specimen, and received by the sensor installed in the bottom surface

As a typical case, the result of damage content of 5% is shown as in Fig. 25. Figure 25a shows the frequency distribution for the case of elastic wave excitation by electric pulser, and b shows that by pencil lead break. As can be found, the frequency spectra decrease with the increase of propagation distance, and the decrease rate is large as the frequency becomes high. It can be thus obvious that this result accords well to the theoretical formula as shown in Eq. 7 demonstrating the decay with the propagation distance. As for the difference of propagation distances, the attenuation trend as a function of frequency becomes remarkable when the propagation distance becomes longer even in the case of the same degree of damage (5% in this case), suggesting that it is not easy to evaluate degradation only by the frequency related parameters as the frequency centroid and the peak-frequency which are well used to relate damage with elastic waves' parameter.

The ratio of frequency spectrum response is determined based on the cases of at least 100-mm propagation distance. Specifically, the ratio of frequency response for the 96-mm propagation is obtained from the spectra of 196-mm and 100-mm propagation distances. Other ratios of the spectral difference of propagation distance for 208 mm, 320 mm and 444 mm are obtained in a similar manner from the frequency spectra of 200-500 mm in propagation distances (or the height of specimens). Calculated results (for 96 mm, 208 mm, 320 mm, and 444 mm) as a function of the frequency can be found in Fig. 26. Two straight lines in the figure show the linear approximation over the frequency between 0 to 200 kHz for the ratio of frequency responses of distance difference 96 mm and 444 mm. In this experiment, as the same type of receiving sensor were used for all the measurement, $T_2(f)/T_1(f)$ in Eq. 2 can be regarded as 1 in all the frequency bands. Because of the heterogeneity of the mortar specimen, the ratio of frequency responses does not form a straight line like a theoretical formula. Therefore, the regression line is used by carrying out linear approximation of the frequency response ratio.



Fig. 24. Mortar specimens with simulated damages (Damage content: 1%).

As found in Fig. 26, the larger the difference of propagation distance, the larger the slopes of the ratio of frequency responses. Here, it was verified experimentally that the theoretical formula, Eq. 8, simulates the practical behavior well. By using the slopes obtained from Fig. 26, the ratio of frequency responses and the relation of a distance difference to each mix rate of damage simulation are shown in Fig. 27. We find that correlations were uniquely acquired in all damage mixture rate and in both excitations. The frequency slope obviously becomes large with the increase of damage volume.

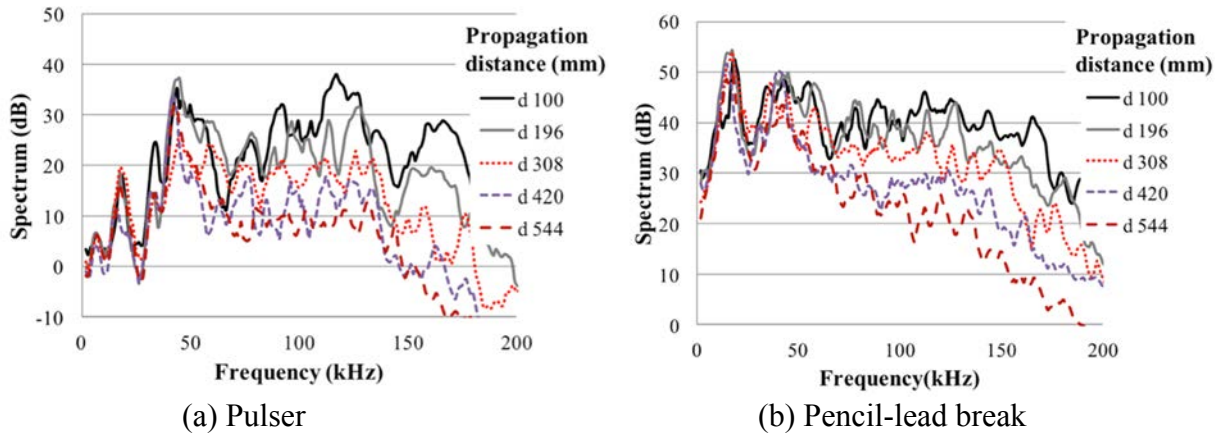


Fig. 25. Frequency distributions with different distances (damage content: 5%).

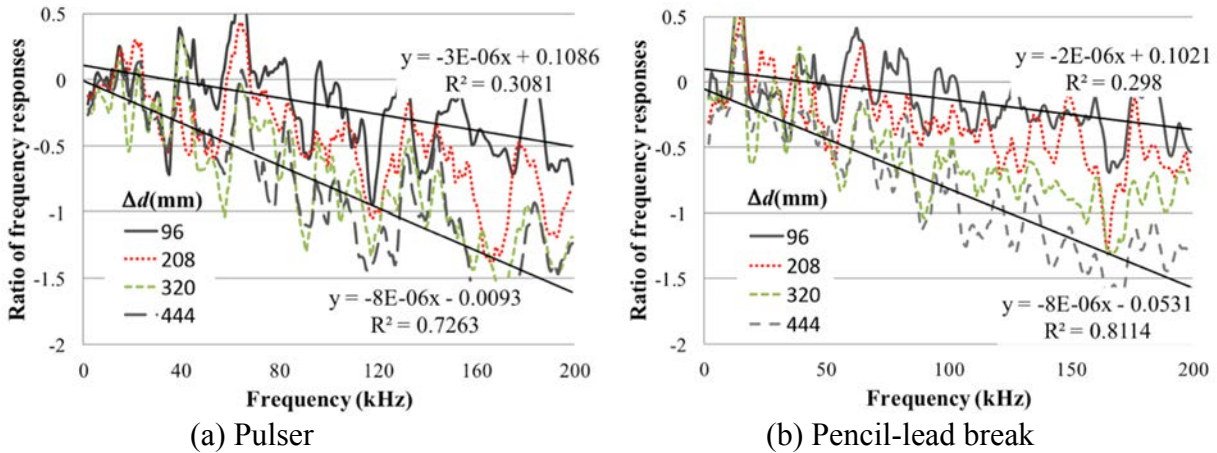


Fig. 26 Ratio of frequency responses with differences of propagations (damage content 5%).

Q-value is also determined by using Eq. 8, substituting P-wave velocity, V , which was obtained by another measurement, and it is shown in Fig. 28. As mentioned previously, the velocity of a P-wave shows the dispersion depending on the frequency, e.g., the velocity becomes large to a certain frequency then decreases, and this tendency appears more noticeable when more damage was included [37]. In addition, since Q-value also depends on the frequency, showing the dispersion [38], the value depends on frequency. Q values by two excitation methods (pencil-lead and pulser) were different as shown in Fig. 28; the damage could also be evaluated by Q-value, e.g., Q-value showing between 170-270 demonstrates intact condition of the material, 130 stands for 5%, and about 100 for 10% damage. The dependency of Q value on the frequency and allowable range of Q-value in regard to damage will be clarified in a subsequent paper.

7. Conclusions

In this paper, recent advances of AE technology for damage assessment in infrastructures were given mainly utilizing secondary AE activity. The phased AE measurement followed by ultrasonic tomography enables us to detail the damage; however, since it takes time and cost, an innovative study project being referred to as ‘AE tomography,’ which implement AE source location simultaneously with tomographic approach are on-going [37, 38]. The detail will be presented in follow-up papers.

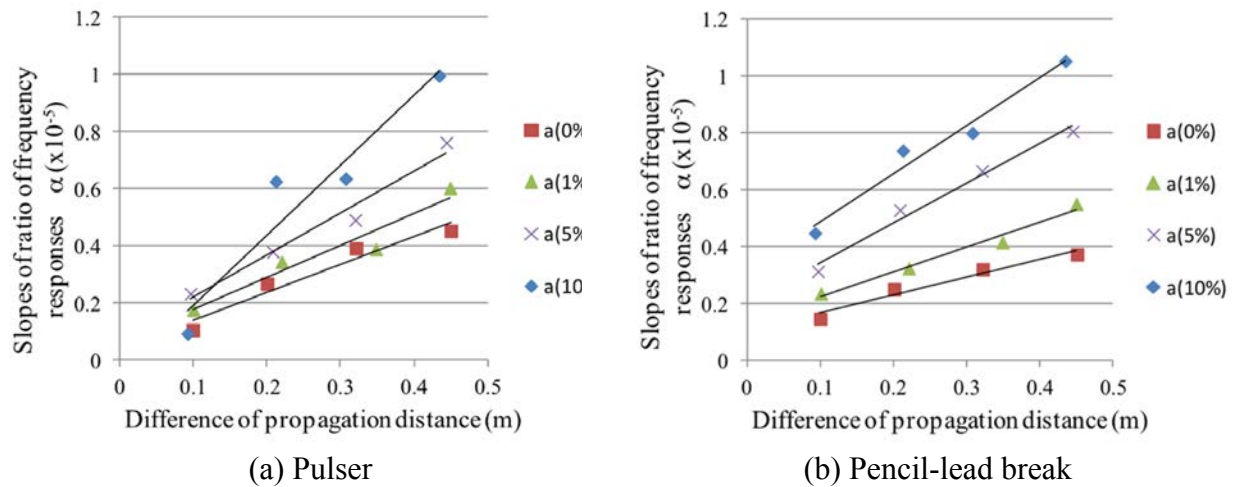


Fig. 27 Relation between slopes of the ratio of frequency responses and difference of propagation distances.

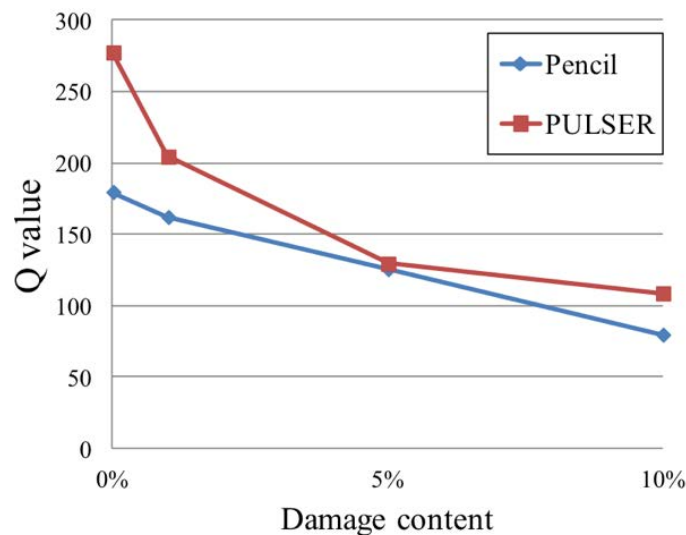


Fig. 28 Q -values with damages for pulser and pencil-lead break.

In infrastructural asset management, performance assessment of the structure with monitoring is regarded as a key subject and this will be incorporated in the coming ISO5500X series 'Asset Management' in 2014 [39]. AE technique could be a major contributor for the standards; however, without careful examinations and comprehension on the AE technique, especially the use of secondary AE activity and its application to in-situ facilities, it will come to naught. This paper concludes enumerating following must-issues to be studied from now on in consideration of ultrasonic technique:

- The relation of the damage scale and frequency employed;
- The relation of damage volume with elastic wave parameters;
- Exploration of elastic waveforms' parameter to represent the damage;
- Suitable frequency of sensors based on the present findings;
- Adequate sensor arrangement corresponding to the objective scale of damage; and
- In practice demonstration of the priority of AE measurement in comparison with other NDT in terms of adaptability and sensitivity for a various magnitude of damage.

It must be noted as well that all the above issues shall be implemented in conjunction with other subjects on design; definition of damage by engineer, on finance; estimation of life cycle cost when applying monitoring, and on risk: consideration of probability of failure together with consequent damage.

Acknowledgements

The works presented here were findings through the joint studies with other distinguished researchers: Prof. M. Ohtsu (Kumamoto University), Dr. X. Luo (Railway Research Institute), Dr. R. Kawase (Koken Engineering), Dr. D.G. Aggelis (Ioannina University), Mr. S. Momoki (Tobishima Corporation), Prof. T. Kamada (Osaka University), Graduates from Kyoto University, and others. Valuable contributions from them are extremely appreciated.

References

1. T Shiotani, K Fujii, T Aoki and K Amou, 'Evaluation of progressive failure using AE sources and improved b-value on slope model tests', *Progress in AE VII*, pp 529-534, 1994.
2. T Shiotani and M Ohtsu, 'Prediction of slope failure based on AE activity', *ASTM Acoustic Emission: Standards and Technology Update*, ASTM STP 1353, pp156-172, 1999.
3. T Shiotani, K Kumagai, K Matsumoto, K Kobayashi and H Chikahisa, 'Evaluation of excavation-induced microcracks during construction of an under-ground power plant using acoustic emission', *Contribution of Rock Mechanics to the New Century*, pp 573-57, 2004.
4. T Shiotani, 'Evaluation of long-term stability for rock slope by means of acoustic emission technique', *NDT & E International*, Vol. 39, Issue 3, pp 217-228, 2006.
5. M Seto, M. Utagawa and K. Katsuyama, 'The estimation of pre-stress from AE in cyclic loading of pre-stressed rock', *Progress in AE VII*, pp 159-166, 1992.
6. T J Fowler, 'Experience with acoustic emission monitoring of chemical process industry vessels', *Progress in AE III*, pp 150-162, 1986.
7. S Yuyama, T Okamoto, M Shigeishi, M Ohtsu and T Kishi, 'A proposed standard for evaluating structural integrity of reinforced concrete beams by AE, Acoustic Emission', *ASTM Standards and Technology Update*, ASTM STP1353, pp 25-40, 1998.
8. The Japanese Society for Non-Destructive Inspection, 'Recommended practice for in situ monitoring of concrete structures by acoustic emission', *NDIS2421*, p 24, 2000.
9. T Shiotani, M Shigeishi and M Ohtsu, 'Acoustic emission characteristics of concrete-piles', *Construction and Buildings Materials Vol. 13*, pp 73-85, 1999.
10. X Luo, H Haya, T Inaba, T Shiotani and Y Nakanishi, 'Experimental study on evaluation of breakage in foundations using train-induced acoustic emission', *Proc., Structural Engineering World Congress 2002*, Paper No. T9-1-e-3, 2002.
11. T Shiotani and D G Aggelis, 'Evaluation of repair effect for deteriorated concrete piers of intake dam using AE activity', *Journal of Acoustic Emission* 25, pp 69-79, 2007.
12. S Yuyama, T Okamoto, M Shigeishi and M Ohtsu, 'Quantitative evaluation and visualization of cracking process in reinforced concrete specimen by moment tensor analysis of acoustic emission', *Progress in AE VII*, pp 347-354, 1994.
13. H Kanamori, 'Physics of Earthquake', Iwanami Shoten Publishers, 1994 (in Japanese).
14. T Shiotani, M Ohtsu and K Ikeda, 'Detection and evaluation of AE waves due to rock deformation', *Construction and Building Materials*, 15, pp 235-246, 2001.

15. M Ohtsu, 'Simplified moment tensor analysis and unified decomposition of acoustic emission source: Application to in situ hydrofracturing test', *Journal of Geophysical Research*, Vol. 96, No. B4, pp 4211-4221, 1991.
16. M Iwanami, T Kamada and S Nagataki, 'Application of AE technique for crack monitoring in RC beams', *JCI Proceedings of Cement and Concrete*, 51, 1997.
17. Recommendation of RILEM TC-212-ACD: acoustic emission and related NDE techniques for crack detection and damage evaluation in concrete, 'The method for classification of active cracks in concrete structures by acoustic emission', Springer, *Materials and Structures*, 43, pp 1187-1189, 2010.
18. K Mogi, 'Magnitude frequency relation for elastic shocks accompanying fractures of various materials and some related problems in earthquakes', *Bull. Earthq. Res. Inst.*, 40, pp 831-853, 1962.
19. H Scholz, 'The frequency-magnitude relation of microfracturing in rock and its relation to earthquakes', *Bull. Seismo. So. America*, 58(1), pp 399-415, 1968.
20. T Shiotani, Z Li, S Yuyama and M Ohtsu, 'Application of the AE improved b-value to quantitative evaluation of fracture process in concrete materials', *Journal of Acoustic Emission*, 19, pp 118-133, 2001.
21. T Shiotani, M. Ohtsu and K. Monma, 'Rock failure evaluation by AE improved b-value', *JSNDI & ASNT, Proc. 2nd Japan-US Sym. on Advances in NDT*, pp 421-426, 1998.
22. T Shiotani, J. Bisschop and JGM van Mier, 'Temporal and spatial development of drying shrinkage cracking in cement-based materials', *Engineering Fracture Mechanics*, pp 1509-1525, 2003.
23. T Shiotani, Y. Nakanishi, K. Iwaki, X. Luo and H. Haya, 'Evaluation of reinforcement in damaged railway concrete piers by means of acoustic emission', *Journal of Acoustic Emission*, 23, pp 260-271, 2006.
24. S Colombo, I G Mai and M C Forde, 'Assessing damage of reinforced concrete beam using "b-value" analysis of acoustic emission signals', *Journal of Materials in Civil Engineering*, 15, pp 280-286, 2003.
25. T Shiotani, Y Nakanishi, X Luo, H Haya and T Inaba, 'Evaluation of structural integrity in railway structures using train-induced acoustic emission', *Structural Faults and Repair 2003*, CD-ROM, 2003.
26. T Shiotani, Y Nakanishi, X Luo, H Haya and T Inaba, 'Damage evaluation of railway structures by means of acoustic emission', *Key Engineering Materials*, 270-273, pp 1622-1630, 2004.
27. T Shiotani, D G Aggelis and O Makishima, 'Global monitoring of large concrete structures using acoustic emission and ultrasonic techniques: case study', *ASCE Journal of Bridge Engineering*, Vol. 14, No. 2, pp 188-192, 2009.
28. K Sonoda and T Horikawa, 'Fatigue strength of reinforced concrete slab under moving loads', *IABSE Rep.* 37, pp 455-462, 1982.
29. T Shiotani, H Ohtsu, S Momoki, HK Chai, H Onishi, T Kamada, 'Damage evaluation for concrete bridge deck by means of stress wave techniques', *ASCE, Journal of Bridge Engineering*, in print.
30. H Saadatmanesh, A Wei and M R Ebsnni, 'RC beams strengthened with GFRP plate I: experimental study', *Journal of Structural Engineering*, 117(11), pp 3417-3433. 1991.
31. Y Kobayashi, T Shiotani, DG Aggelis and H Shiojiri, 'Three-dimensional seismic tomography for existing concrete structures', *Proceedings of Second International Operational Analysis Conference*, Vol. 2, pp 595-600, 2007.
32. EA Whitehurst, 'Evaluation of concrete properties from sonic tests', *ACI Monograph No.* 2, 73, 1966.

33. T Shiotani and DG Aggelis, 'Damage quantification of aging concrete structures by means of NDT', Engineering Technics Press, Proceedings of Structural Faults and Repair 2006 (CD-ROM), 2006.
34. T Shiotani and DG Aggelis, 'Wave propagation in cementitious material containing artificial distributed damage', Materials and Structures, 42, pp 377-384, 2009.
35. T Shiotani and Y Takada, 'Damage assessment of civil engineering materials by means of transfer function of AE waveforms', Abstracts of AEWG54, S6-2, 2012
36. D Polyzos, A Papacharalampopoulos, T Shiotani and DG Aggelis, 'Dependence of AE parameters on the propagation distance', JSNDI, Progress in Acoustic Emission XV, pp 43-48, 2010.
37. DG Aggelis et al., "Stress wave scattering: Friend or enemy of non destructive testing of concrete?," Journal of Solid Mechanics and Materials Engineering, Vol. 2, No. 4, 2008.
38. K Yoshimura et al., "Experimental study on imaging hydraulic conductivity of rock masses based on elastic wave velocity dispersion," BUTSURI-TANSA, Vol. 62, No. 3, pp. 307-318, 2009.
39. T Shiotani, N Okude, S Momoki and Y Kobayashi, Proposal of AE tomography technique for the assessment of infrastructures, Proc. 2011 National Conference on Acoustic Emission, pp 39-42, 2011 (in Japanese).
40. Y Kobayashi and T Shiotani, Seismic tomography with estimation of source location for concrete structures, Engineering Technics Press, Structural Faults and Repair 2012, 14th International Conference and Exhibition, CD-ROM, 2012.
41. ISO 55000 International Standard for Asset Management, URL: www.iso55000.info, June 30, 2012.

Preliminary Investigations of Acoustics Emission Signal from Snow and its Wavelet Transform

Karmjeet Singh, Yogesh C. Nagar, Jagdish C. Kapil, Pramod K. Satyawali and Ashwagosh Ganju

Snow and Avalanche Study Establishment, Manali (H.P.), 175 103, India

Abstract

A new approach is presented for the detection of deformation of snow with the help of plate waveguide for avalanche warning. Avalanches are difficult to predict due to heterogeneity of the snow media and the uncertainties associated with triggering mechanisms. Monitoring of acoustic emission (AE) is a very effective non-destructive technique, which is applied to identify micro and macro-cracks and their temporal advancement in snow. The propagation of these elastic waves in attenuated media to long distance is helpful for extracting useful information for slope monitoring. Since the snow exhibits a high attenuation during wave propagation, a less attenuative media like plate sensors (solid steel and aluminium waveguide) is essential. Preliminary experiments towards the formation of Lamb waves in a plate coupled with snow was performed with the help of piezoelectric sensors. Different deformations (1-100 mm/min) were applied to various snow samples having different densities (300-450 kg/m³). The dependence of stress-strain with AE and visible crack is examined along with the wavelet transform. The wavelet transform (WT) was used and applied on the time-frequency of AE present in plate waveguide. Lamb waves are detected from a long distance, which help in understanding the physical condition of snow stability with the help of waveguide.

Keywords: Snow, waveguide, wavelet transform

1. Introduction

The effect of climate change has resulted in significant impact on catastrophic events such as snow avalanche in the cryospheric regions of Himalaya. Summer temperature rise, changes in snowfall pattern, fluctuation in mean seasonal temperature, heavy precipitations are few indications of global climate changes and these have adverse effect on the avalanche activity. Avalanches are difficult to predict due to heterogeneity of the snow media and the uncertainties associated with triggering mechanisms. In most cases, initially, there is a formation of crack at micro/macro scale inside the snow pack, which leads to the fracture initiation and finally the formation of an avalanche. During this crack formation acoustic emission (AE) are emitted. Acoustic emissions are elastic wave, which are formed when snow is under critical stress and give the information prior to any failure [1, 2]. Monitoring of AE is a very effective and non-destructive technique, which has been applied to recognize instability and their temporal advancement in snow [3]. Acoustic emission in porous media (like snow and soil) is difficult to measure because of the high attenuation of the source signal during propagation [4, 5]. High frequencies are more attenuated than lower frequencies due to small wavelength [6]. The prime challenge in this kind of study is to detect the behavior of such changes (AE signal) prior to large failure in snow. The phenomenon of propagation of acoustic wave inside the snow takes place through the solid skeleton of snow and pore structure. Mainly three types of waves travel through the snow; two are longitudinal and one is shear (transverse) waves. The shear wave travels through the solid snow and the longitudinal wave travel through the pore space as well as solid snow structure. As shear waves are not supported by air of pore space so they do not travel

through pores. Propagation of wave through pore is again depends on the pore structure of snow which might be opened or closed and the propagative wave is highly attenuated [7, 8]. If a solid media is in contact with snow the transmission of the acoustic wave can take place, which help us understand the behavior and physical status of snow. The propagation of these elastic waves in attenuative media up to a long distance is useful for extracting important information for slope monitoring. Since the snow exhibits a high attenuation during wave propagation [4, 5, 9, 10], a less attenuative medium like plate waveguide (solid steel and aluminum plate guide) is required [11]. The associated elastic waves travel through the snow medium and enter into the plate structure in the form of longitudinal, shear and Lamb waves [12]. Shear wave propagation depends upon the couplant used between snow and plate. Out of these three longitudinal and Lamb waves are dominated in plate. Lamb waves are formed inside the plate when the thickness is comparable to the wavelength of guiding plate media. These waves travel up to long distance due to multiple reflections from boundaries of plate or structure. The low attenuation feature of Lamb wave makes it a perfect choice for guiding wave, which can travel up to long distances [13]. Various kind of waveguide is developed for different length and shapes and the thickness of waveguide is a key parameter for good signal strength [11].

2. Approach

Preliminary studies towards the formation of Lamb waves in a plate coupled with snow were performed with the help of piezoceramic sensors. The dependence of AE and visible crack with stress-strain was examined along with the wavelet transform. Due to various types of deformations, AE activity develops in the snow sample. The associated elastic waves travel through the snow medium [7] and enter into the plate structure where these can be dominated in the form of Lamb waves [12]. The application of guided waves for evaluation of material properties involves modes of propagation in a material (plates), which are given by the well-known dispersion curves (dependence of velocity on frequency)[14]. The present work describes the AE response in snow as a function of stress and strain. The AE in snow indicates qualitative information of major crack, creep-glide rupture, inter-granular deformation and friction between various grains of snow [1]. Different deformation rates were applied to various snow samples having different densities. The wavelet transform (WT) was applied to Lamb wave, which is a potential technique to detect attenuation of source signal, presence of cracks, defects and different modes of Lamb waves in plates [15-20]. Wavelet transformations have been performed on different kind of AE signal. Results show that various types of Lamb wave modes and their dominance with time. The WT was applied to the time-frequency analysis of both symmetric and anti-symmetric Lamb wave modes. Experiments were performed using the artificial AE signal produced on the surface of waveguide plate to ensure sensors coupling and attenuation of source signal [21]. WT and frequency components of AE signal can give important information about energy carried by different frequency components.

3. Instrumentation

In order to see the structural deformation in snow, a compression test was performed with 2.5 kN load cell on various snow samples (with density 300-450 kg/m³) under Universal Testing Machine (UTM). All snow samples were cylindrical in shape having 65 mm in diameter and 150 mm in length and were loaded uniaxially under a constant strain rate from 10⁻² to 10⁻⁴ s⁻¹. Variable deformation rates of 1, 5, 10, 100 mm/min. were applied.

AE signals were detected by a set of seven piezoceramic sensors. The sensors were attached to the plate with the help of H210 high-vacuum compound grease in a circular pattern with a distance of 50.5 mm from the center of the circular plate waveguide (thickness 2 mm, diameter 130 mm) as shown in Fig. 1a and 1b. In order to have the proper contact, the air between the sensors and waveguide plate was removed. Similarly a thin ice layer was used for contact between snow sample and waveguide plate. In order to see the proper contact between the AE sensors, and waveguide plate, a standard procedure [Hsu-Nielson source] was followed, i.e. a pencil lead (0.5 mm, HB) was broken close to the contact. The AE instrumentation consists of Physical Acoustic Corporation (PAC) MISTRAS-2003 (SAMOS AE system), which has a frequency range from 1 kHz to 530 kHz. The analysis has been carried out on single wideband piezoceramic transducers (PAC R30I-AST transducers) with operating range 125–450 kHz (resonance frequency 300 kHz; dimensions, 29x31 mm). To avoid the chamber and other background noise the threshold level of the sensors was set to be 45-50 dB. The peak sensitivity of sensors was -22 dB ref. 1 V/ μ bar. Other parameters, viz. Peak Definition Time (PDT), Hit Definition Time (HDT), Hit Lockout Time (HLT), were set to be 200 μ s, 800 μ s and 1000 μ s, respectively.

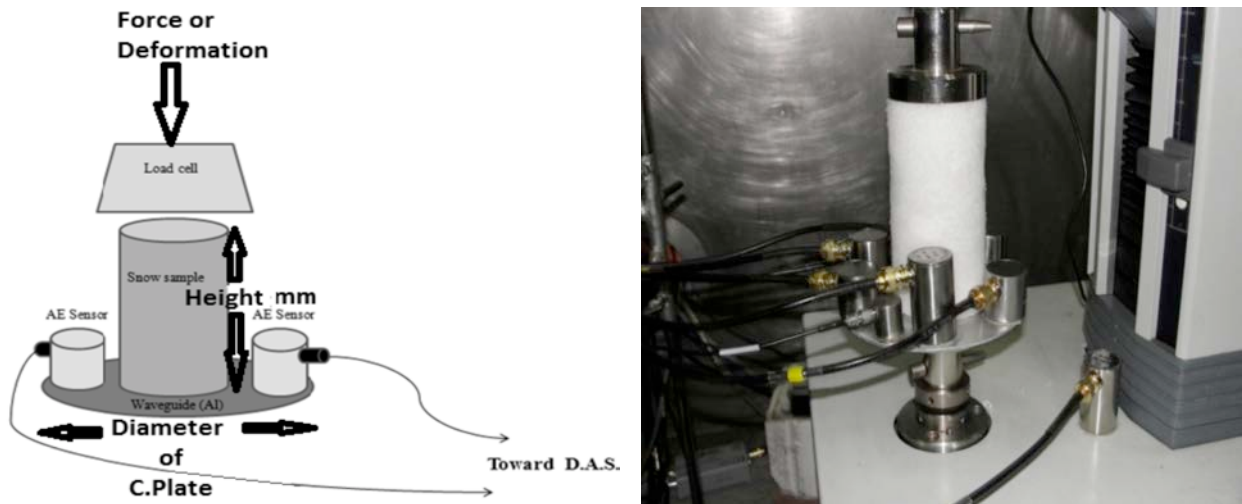


Fig. 1. a) Deployment scheme of deformation of snow sample. b) piezoceramic transducers on aluminium plate used for testing.

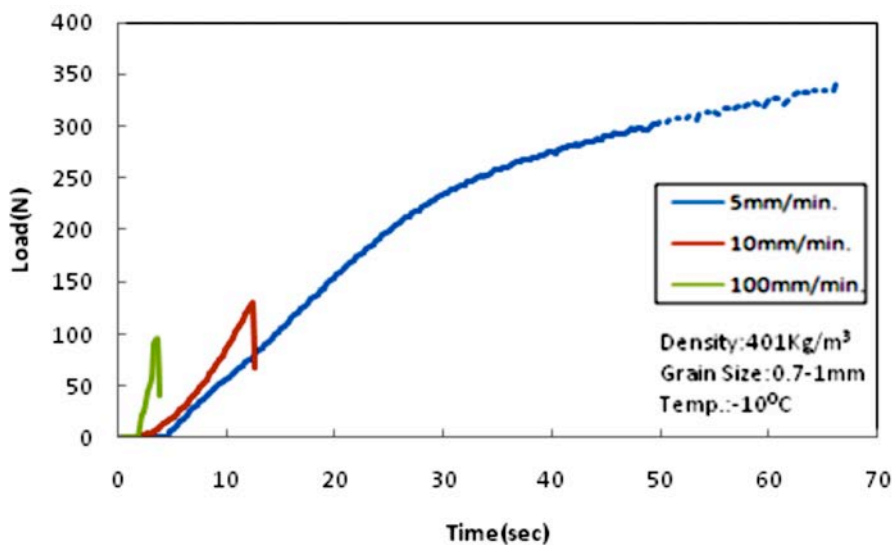


Fig. 2. Load-time curves of snow under three deformation rates.

4. Results and Discussion

4.1 Mechanical deformation of snow sample

It has been observed that snow behaves differently under different strain rates (Fig. 2). When the deformation rate is small (5 mm/min) snow starts to deform due to the basal slip inside the snow grains [23]. For higher deformation rates, brittle transition occurred, which corresponds to the complete breakage of snow grains inside the sample (disjointment) [23, 24]. Both the brittle transition at 10 and 100 mm/min took place below 5% strain level. The same behaviour was observed after repeating the experiment for multiple times with same parameters.

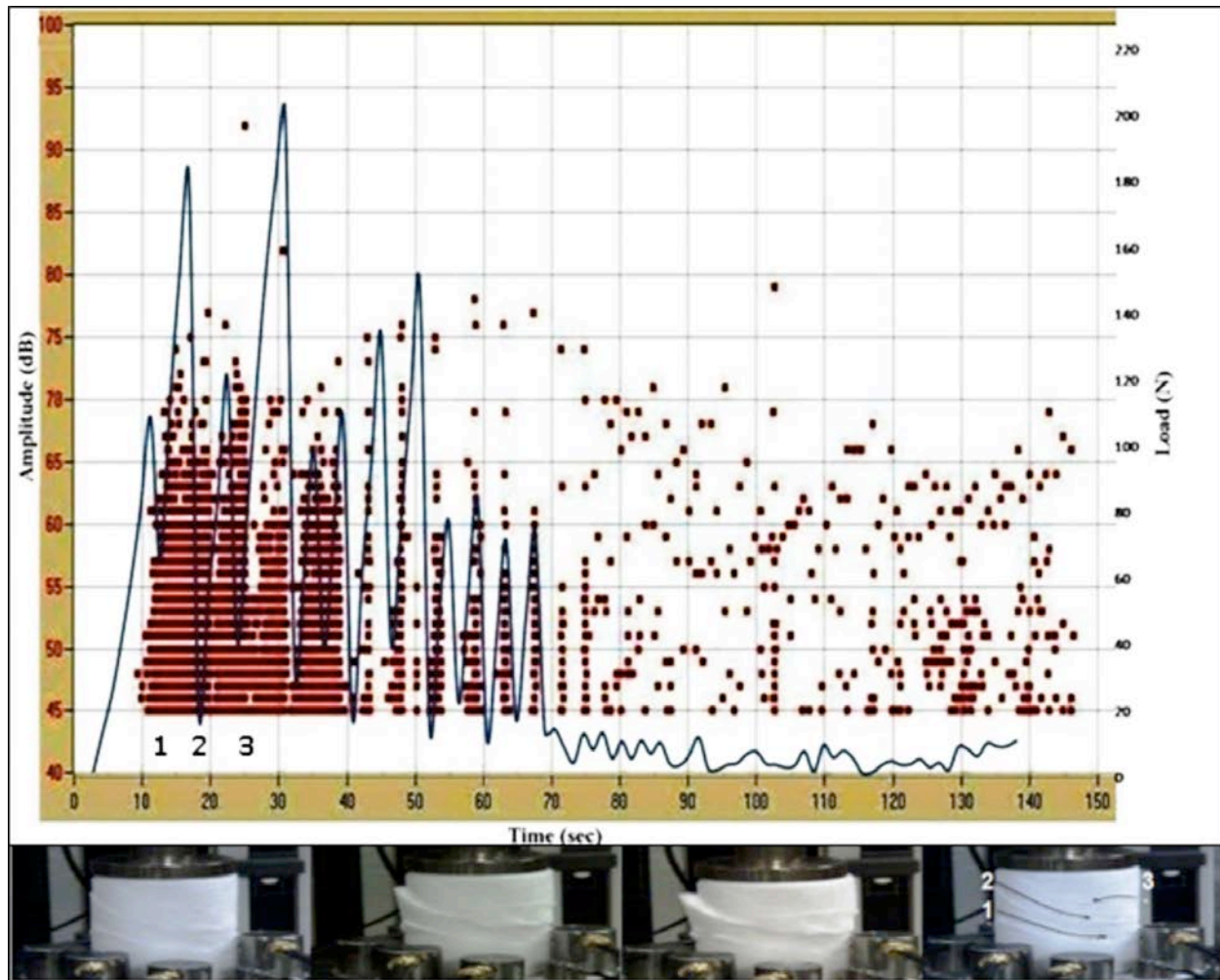


Fig. 3. Amplitude distributions of AE events with load applied to Snow having density 401 kg/m^3 (grain sizes 0.7-1.0 mm) with deformation rate 10 mm/min at -10°C under uniaxial compression tests. Photographs below show the progressive formation of major cracks, 1, 2, 3.

Figure 3 gives load versus time, along with AE activity and shows the typical nature of AE events, which were irregular for this snow sample. The amplitude of each AE event is also indicated. This was due to the heterogeneity of snow sample. From the load-time analysis it was found that sample was getting irregular deformation with applied stress before pre-failure stage [25]. Similar behavior could not be observe in others sample with density lower than 400 kg/m^3 . Therefore, it was speculated based on the observations that load behavior of snow is changed close to 400 kg/m^3 [26]. The AE increases with the applied stress and the reason for this may be

due to deformation of snow, crack, creep-glide rupture, inter-granular deformation and friction between various snow grains. When sample changes its behavior from less dense to more dense state, the AE activity lasts between 10–40 second. This directly corresponds to structural deformation of snow sample before complete failure. The AE growth developed prior to the first crack. This is at 12 sec and is marked as “1”. It was found that during the formation of second and third crack (marked 2 and 3 at 18 sec and at 24 sec), there was large increases in AE intensity (Fig. 3). Almost complete deformation of snow sample took place after the appearance of the third crack, and the next peak in load diagram corresponds to mixed effect of all three cracks. Afterwards small internal crack events took place, which contain mainly burst kind of AE signals. In other samples, changes of AE behavior was seen. The behavior was similar only in initial stage where they follow load curve before densification. No major visible crack was found in low deformation rates, i.e. 1 and 5 mm/min. It was found that after three main cracks, AE rate was quite scattered. A number of spikes of AE events were observed in later part, which corresponds to small sliding events in deformed snow and no visible crack were found during the rest of experiment. At last when the sample is released from the load a few relaxation events of inter-granular grain were observed at ~140 sec. During the process of major cracking, large continuous events were observed, which show the sliding friction, shearing and slip or intergranular breaking of snow grains.

4.2 Wavelet analysis of acoustic emissions

AE signals from snow samples consist of various frequency components. Two types of AE signal were captured. First was in continuous mode and second was in burst mode (Fig. 4a and 4b).

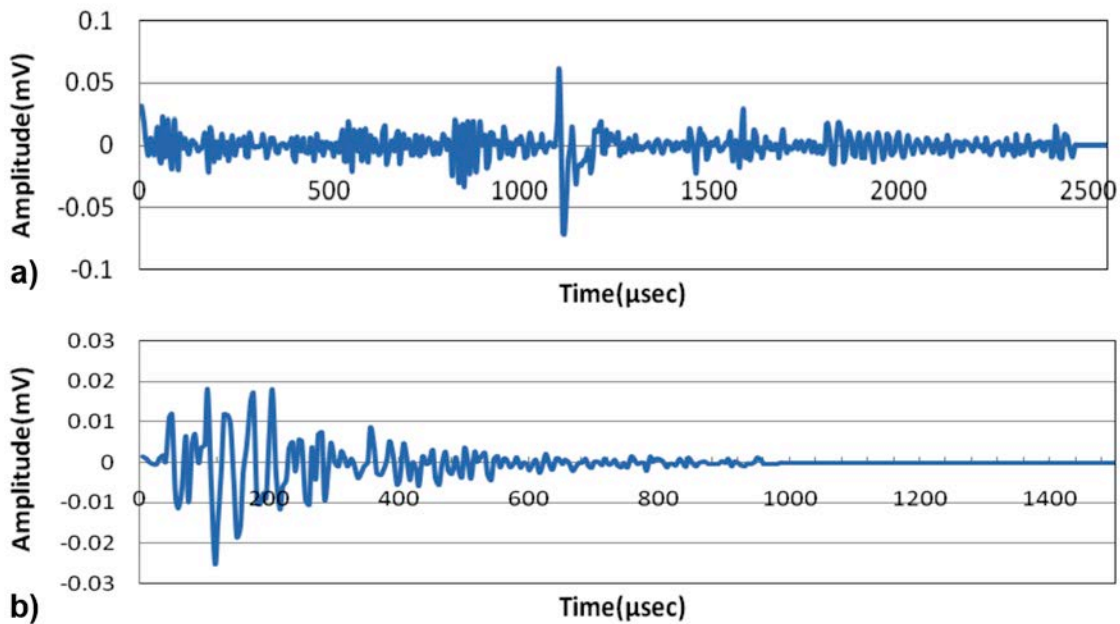


Fig. 4 Typical AE signals (a) in continuous mode. (b) in burst mode.

Wavelet analysis (WT) was done to decompose these emitted signals into different frequencies component to understand the composition of various frequency components and their temporal variation. Freeware software AGU-Vallen Wavelet from Vallen-Systeme GmbH, 2001 [27] was used for time-frequency and wavelet analysis. It uses Gabor (Gaussian form) wavelet as a mother function where correlation between frequency, time and amplitude can be easily achieved. It has been observed during the compression test of snow that continuous AE

signals have generally small amplitude, which occurred near the yield stress of the snow. The acoustic impulses of small amplitude are released close to each other, which reflect that all the events form a band [28]. This shows the continuum behavior of snow before any major failure inside the sample. The continuous emission was sensitive to strain rate, as the strain rates varied from $10^{-4} - 10^{-3} \text{ s}^{-1}$. These activities show that the snow deformation and failure were strain rate dependent. The strain rate dependencies were characterized as brittle behavior at higher strain rates and plastic deformation corresponding to low strain rates. The burst type signals are the isolated events during the failure of snow and can be characterized as crack growth and catastrophic failure. The burst type emissions were observed during the brittle transition, which is due to the disjointment of snow grain bond in the sample [23]. It was observed that burst signals were dominant during the crack formation. In all failure cases there were emissions of continuous signals, which were followed by burst signals. Therefore, acoustic emission spectra can be used to characterize the brittle and plastic behavior of snow.

For wavelet analysis burst signal was analysed and a typical of this is shown in Fig. 4b. It was found from the wavelet coefficient that it has maximum amplitude at $125 \mu\text{s}$. Wavelet coefficients with respect to frequency have been drawn for $125 \mu\text{s}$. It was found that signal mainly contains of two major frequencies of 32 kHz and 160 kHz as shown in Fig. 5. This shows that signal is dominant in lower frequency ranges. In the present case, most signals (both continuous and burst) were in the lower frequencies ranges below 200 kHz.

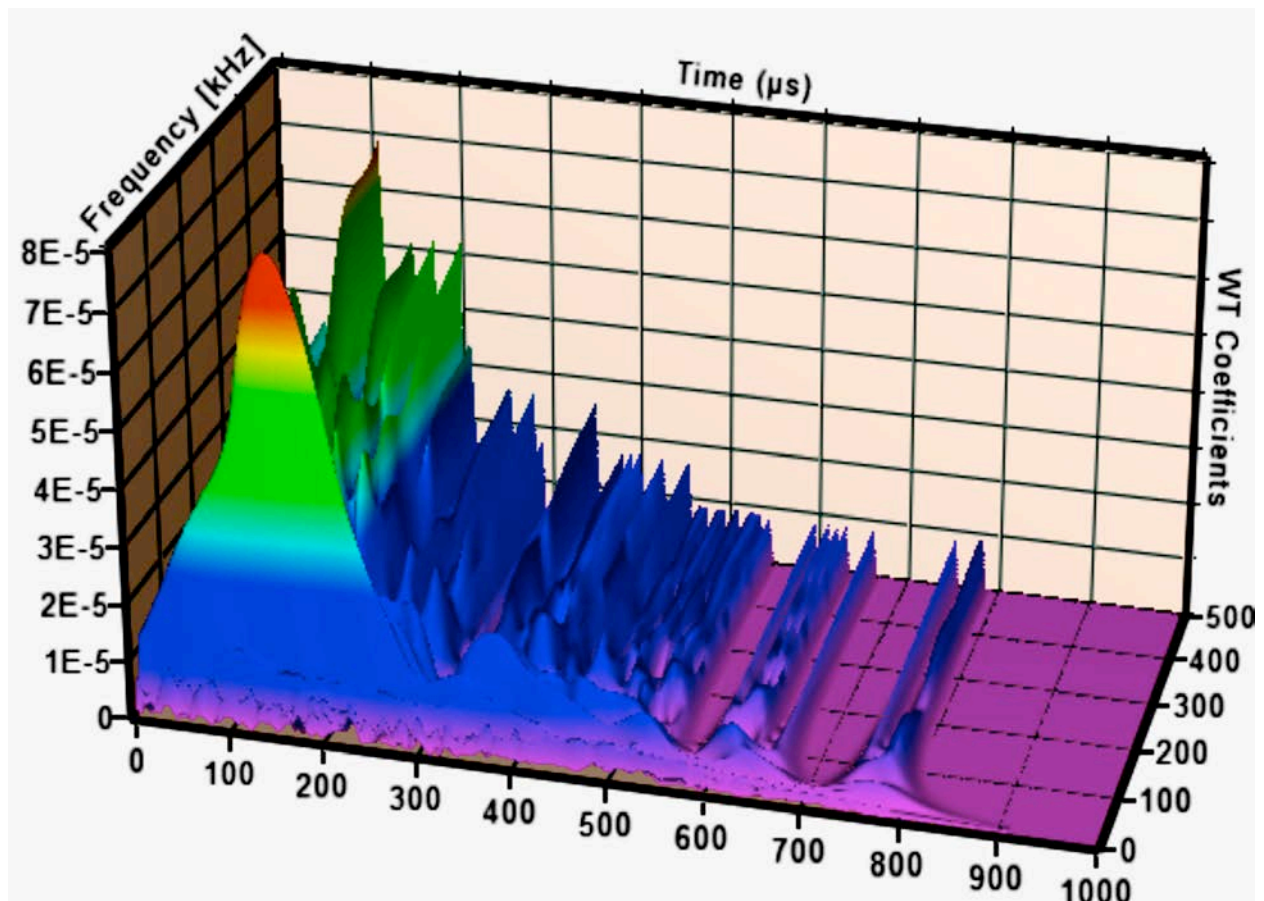


Fig. 5 Three-dimensional diagram of wavelet coefficient of a burst AE signal (Fig. 4b) against time and frequency.

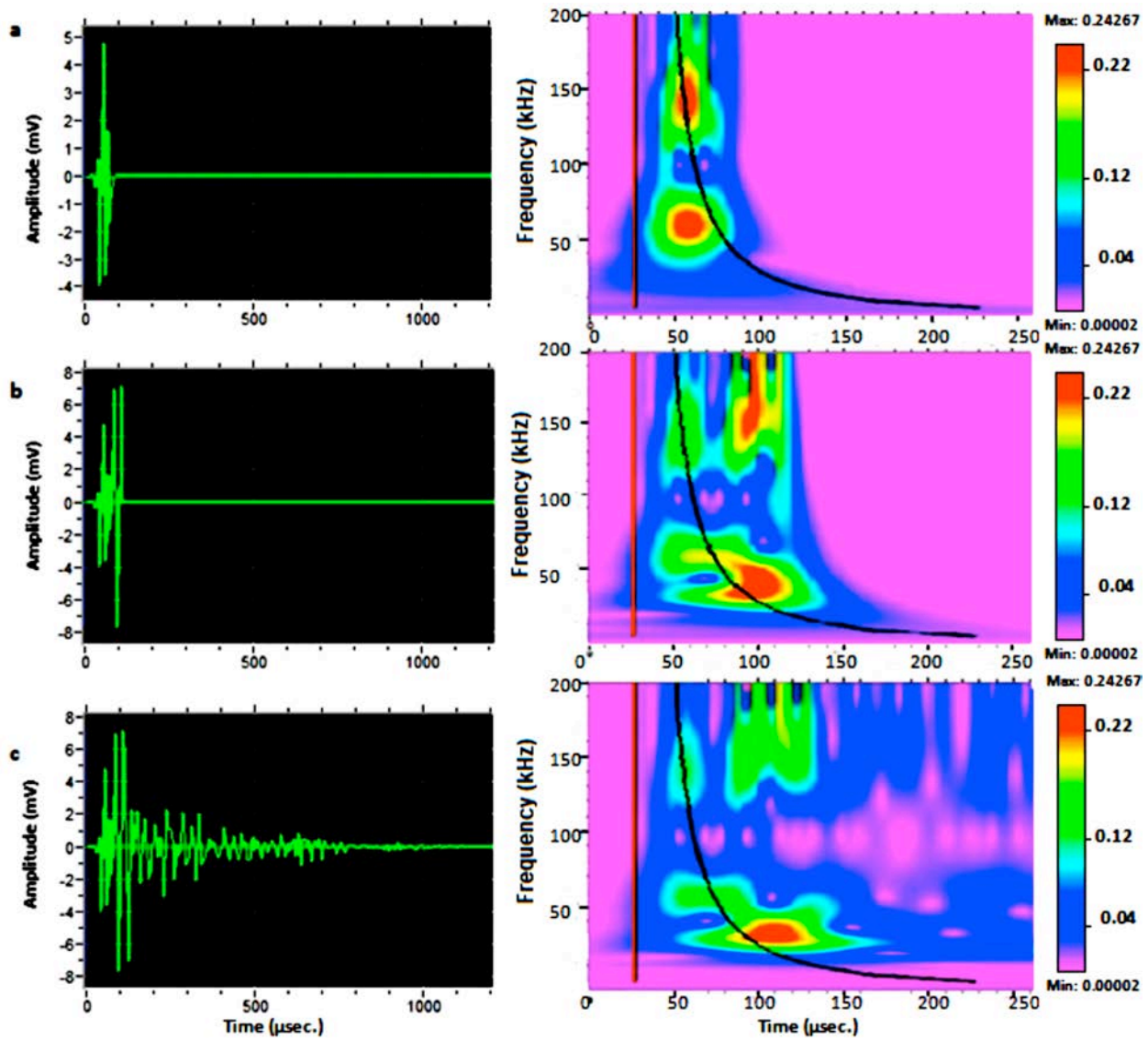


Fig. 6. Time- frequency plots of a signal between 0 to 200 kHz and time 0 to 250 μ s (for three segments of a burst signal).

Figure 6 shows the time-frequency plots of a single burst signal at different time segments. Color code scheme on the right-hand side shows the magnitude of WT coefficient. Symmetric (S_0) and anti-symmetric mode (A_0) dispersion curves were drawn for circular plate waveguide of thickness 2 mm and shown in Fig. 6. The anti-symmetric mode is dominant in the frequency ranges 20-70 kHz and 120-170 kHz. In the present experiment, disturbances comes through the snow sample, which is out of plane with respect to plate waveguide. Thus, anti-symmetric mode's domination should be expected, as found in the time-frequency diagrams. A_0 -mode domination is an important factor for analysis, helping to select suitable piezoceramic sensors for better avalanche forecasting.

5. Conclusion

An attempt was made to correlate AE with the various damage mechanisms occurring inside snow with varying parameters. The AE activity is a strong function of strain rate, density and grain size of snow sample. Snow shows continuous AE behavior throughout the deformation. AE increased near the yield point of snow in the stress-time curve. AE can be used to continuously

monitor the evolution of the damage in snow sample. Burst type AE signals were related to crack formation and failure of snow sample regardless of the others parameters. WT was used to identify the AE s during major crack formation.

Acknowledgement

We would like to thank Sh. Prem Datt, Sh. Paramvir Singh, Sh. Siddheshwar Kumar and Sh. Vinod Kumar for their help and support during this study.

References

- [1] Sinha, N.K., “Acoustic Emission and Micro cracking in Ice”, *Proceedings 1982 SESA/ Japan Society for Mechanical Engineers*, Honolulu/Maui, Hawaii. 1982, pp. 767-772.
- [2] Carlo Scapozza, Felix Bucher, Peter Amann, Walter J. Ammann, Perry Bartelet, “The temperature and density-dependent acoustic emission response of snow in monoaxial compression tests”, *Annals of Glaciology (International Glaciological Society)*, **38**, 2004, 291-298.
- [3] Masera, D., Bocca, P. and Grazzini, A., “Frequency Analysis of Acoustic Emission Signal to Monitor Damage Evolution in Masonry Structures”, *Journal of Physics (Conference series)* 305/012134, 2011.
- [4] Albert, D.G., “Reduction of blast noise by a snow cover”, *Noise Control Engineering Journal* **50**, 2002, 200-203.
- [5] Iwase, T., Sakuma, T. and Yoshihisa, K., “Measurements and simulations on sound propagation above snow field”, *The 2001 International Congress and Exhibition on Noise Control Engineering*, Hague, Netherlands, 27-30 August, 2001.
- [6] Biot, M.A., “Theory of Propagation of Elastic Waves in a Fluid-Saturated Porous Solid. II. Higher Frequency Range”, *Journal of the Acoustical Society of America*, **28** (2), 1956.
- [7] Zhekamukhov, M.K. and Malkandueva, L.M., “Propagation of elastics vibration in snow”, *Journal of Engineering Physics and Thermo physics*, **77**, (6), 2004, 1205.
- [8] Johnson, J.B., “On the application of Biot’s theory to acoustic wave propagation in snow”, *Cold Region Science and Technology*, **6**, 1982, 49-60.
- [9] Ishida, T., “Acoustic Properties of Snow”, *Contributions from the Institute of Low Temperature Science, (Bulletin)*, **A20**: 1965, 23-63.
- [10] Marco, O., Buser, O., Villemain, P., Touvier, F., Revol, H.P. “Acoustic impedance measurement of snow density”, *Annals of Glaciology (International Glaciological Society)*, **26**, 1998, 92-96.
- [11] Ono, Kanji and Cho, Hideo, “Rods and tubes as AE waveguide”, *Journal of Acoustic Emission*, **22**, 2004, 243-252.
- [12] Su, Z. and Ye. L., *Identification of damage using Lamb waves*, Springer, Berlin, 2009.
- [13] Greve, D.W., Oppenheim, I.J. and Zheng, Peng, “Lamb Waves and Nearly-Longitudinal Waves in Thick Plates”, *Dept. of Electrical and Computer Engineering, Carnegie Mellon University, Pittsburgh, PA*, 15213.
- [14] Rose, J.L., “Dispersions Curve in guided wave testing”, *Ultrasonic Laboratory, Department of Ultrasonic and Mechanics, Pennsylvania State University, PA 16802*, 2003.
- [15] Manthei, G., Eisenblatter, J. and Spies, T., “Determination of wave attenuation in rock salt in the frequency ranges 1-100kHz using located AE events”, *Journal of Acoustic Emission*, **24**, 2006.
- [16] Finkel, P., Miller, R.K., Friesel, M.A., Finlayson, R.D., Cole, P.T., Barsoum, M.W. and El-Raghy, T., “Characterization of the damage and fracture mechanisms in Ti_3SiC_2 using Acoustic emission”, *J. Acoustic Emission*, **18**, 2000, 61-67.

- [17] Surgeon, M., Buelens, C., Wevers, M. and Meester, P.D., “Waveform based analysis techniques for the reliable acoustic emission composite structures”, *Journal of Acoustic Emission*, **18**, 2000, 34-40.
- [18] Nakamura, H., Arakawa, T., Yamada, M., “Examination of AE wave propagation routes in small model tank”, *Journal of Acoustic Emission*, **23**, 2005, 243-248.
- [19] Nishino, H., Uchida, F., Takashina, S., Takemoto, M. and Ono, K., “A new method of AE source location in pipes using cylindrical guided waves”, *Journal of Acoustic Emission*, **18**, 2000, 102-110.
- [20] Bayray, M., “Investigation of acoustic emission waveform on pressure vessel”, Vienna University of Technology, Austria, *Journal of Acoustic Emission*, **19**, 2001, 241-257.
- [21] Yamada, H., Mizutani, Y., Nishino, H., Takemoto, M. and Ono, K., “Lamb wave source location of impact on anisotropic plates”, *Journal of Acoustic Emission*, Vol. **18**, 2000, 51-60.
- [22] Hamstad, M.A., Gallagher, A.O. and Gary, J.A., “Wavelet Transform Applied to Acoustic Emission Signals: Part 2:” *Journal of Acoustic Emission*, **20**, 2002, 39-61.
- [23] Kinoshita, Seiiti, “Compression of Snow at Constant Speed”, *Physics of Snow and Ice: proceedings*, **1**(2), 1967, 911-927.
- [24] Narita, H., “Mechanical behaviour and structure of snow under uniaxial tensile stress”, *Journal of Glaciology*, **26**(94), 275–282, 1980.
- [25] Sinha, N.K., Shkhinek, K. and Smirnov, V., “On borehole indenter (BHI) measurement and analysis”, *Cold Regions Science and Technology*, **76-77**, 2012, 109-120.
- [26] Abele, G., and Gow, A.J., “Compressibility characteristics of compacted snow (CRREL Report)”, Cold Regions Research and Engineering Laboratory, USA, 1976.
- [27] AGU-Vallen Wavelet, Vallen-Systeme GmbH, Munich, Germany, <http://www.vallen.de/wavelet/index.html>, 2001.
- [28] Ono, K., Cho, H. and Takuma, M., “The origin of continuous emissions”, *Journal of Acoustic Emission*, **23**, 2005, 206-214.
- [29] Hamstad, M.A., “Small diameter waveguide for wideband acoustic emission”, *Journal of Acoustic Emission*, **24**, 2006, 234.

Attenuation of Lamb Waves in CFRP Plates

Kanji Ono¹ and Antolino Gallego²

¹ Department of Materials Science and Engineering, University of California, Los Angeles (UCLA), Los Angeles, CA 90095

² Department of Applied Physics, University of Granada, Granada, Spain

Abstract

The paper presents the Lamb wave attenuation of Carbon Fiber Reinforced Plastic (CFRP) plates on the basis of an experimental transmitter-sensor scheme. We measured separately the S_0 and A_0 Lamb modes of CFRP plates with three different kind of laminate lay-ups; unidirectional $[0]_{8s}$ (and $[90]_{8s}$), cross-ply $[0, 90]_{4s}$, and quasi-isotropic $[0,45,-45,90]_{2s}$. Several ultrasound transmitters were used as actuator and short-duration high-voltage pulses were used for excitation. Two kinds of AE resonant sensors with resonance frequency around 260 and 500 kHz, respectively, were used to record the Lamb waveforms of the plates. By using sensors on both sides of the plate, the confirmation and separation of both modes, S_0 and A_0 , were successfully carried out. This result was also confirmed by using the wavelet transform of the recorded signals. The experiment was carried out at several transmitter-sensor distances, so both phase and group velocities and attenuation could be obtained. By means an appropriate fitting of a theoretical model of attenuation, including the geometrical attenuation, the damping factor of both modes was obtained for each laminate and sensing frequency. The experimental results for velocities and damping factors were compared with previously published and theoretical ones. Directivity results are also reported, showing complex behavior dependent on laminate layups as expected.

Keywords: Composites, CFRP, Lamb waves, attenuation, directivity

1. Introduction

In recent years, composite structures are increasingly used in strength-critical applications in aircraft, requiring more effective NDE methods. These materials, however, have high stress wave attenuation characteristics and AE has encountered stiff barriers against its uses in the aircraft industry [1,2]. Problems are mounted as typical composites are used in anisotropic sheets, requiring more elaborate Lamb-wave theories than usual ultrasonic body or surface waves. Some attenuation studies have been published [3,4], but only recently systematic works have appeared [5-12] on Lamb (or plate) waves in composite materials. However, mode-frequency specific attenuation data is scarce and we conducted an experimental study to fill the gap. Another motivation is to use such data as the basis for an improved NDE method based on the acousto-ultrasonics approach [13], which often disregarded the nature of the waves it is relying on. This trend seems to be inherited in many SHM methods as these often ignore real conditions of wave generation and detection using only idealized models.

In searching for the base attenuation data in isotropic materials, we found the scarcity of Lamb wave data even for Al. Kasama et al. [14] used a laser method (YAG laser generation, laser interferometer detection) to obtain S_0 -wave propagation data. The attenuation results are shown in Fig. 1 for PMMA and Al thin sheets (0.5 and 1 mm data shown; for Al, 0.3 and 0.7 mm

data also obtained). The data has eliminated the geometrical spreading effect of the inverse-square-root distance. For Al, the attenuation coefficient α (of the exponential decay with distance) is 0.25 to 2 Np/m (or 2.2 to 17 dB/m) at 0.5~5 MHz, whereas it is much higher for PMMA by a factor of 10~50. In Fig. 1, x marks represent corresponding P-wave attenuation values. Note there are significant frequency effects (higher for viscoelastic PMMA) and also a thickness effect. Aljets found 2 Np/m using pencil-lead break source and PAC μ 80 sensor [11].

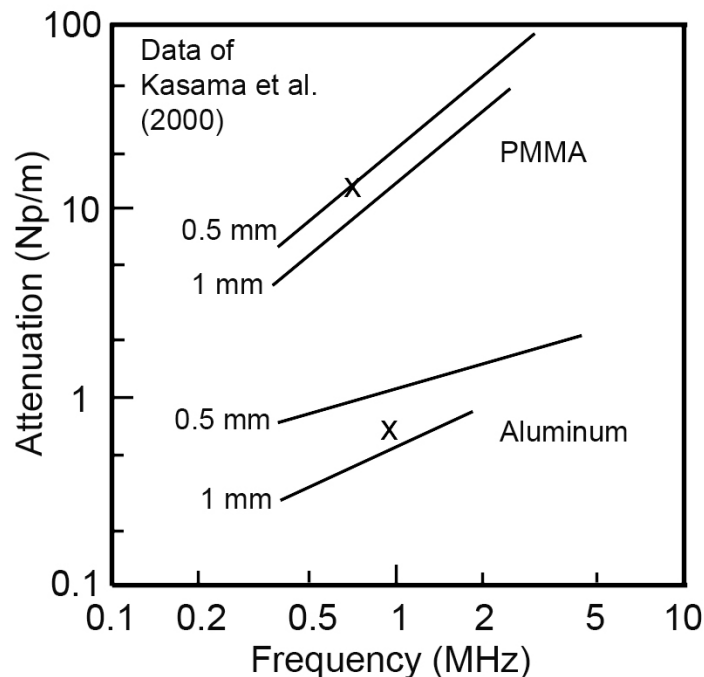


Fig. 1 Lamb wave attenuation in PMMA and Al sheets. Redrawn data of Kasama et al. [14].

Kasama's experimental setup is shown schematically in Fig. A1 (in Appendix) from his thesis [15]. YAG laser beam is focused on a plate edge in the in-plane orientation and a laser interferometer detected the surface displacement as a function of distance from the source. They used only the initial S_0 -mode segment as later segment includes both modes, as shown in Fig. A2. Wavelet amplitude at a selected frequency, P , is then determined and its peak (also see Fig. A2) and the integrated WT energy of $E = \int P^2 dt$ were plotted against the distance of propagation. Typical examples of the peak-amplitude fit and WT energy fit are shown in Figs. A3 and A4, respectively. The peak amplitude-distance curves were fitted to the inverse square-root-exponential attenuation that includes the geometrical spreading effect. The attenuation coefficient, α , is obtained from the best-fit equation. The integrated WT energy data was fitted to the square of the above expression, again yielding the attenuation coefficient, α . These are eqns. (1) and (2) below.

$$P = P_o \left[\frac{1}{\sqrt{x}} \right] \exp(-\alpha x) \quad (1)$$

$$E = E_o \left[\frac{1}{x} \right] \exp(-2\alpha x) \quad (2)$$

Both of these equations are based on the wave radiation pattern of a point source [16]. Kasama confirmed the predicted directivity of [16] by measuring the peak amplitude of S_0 waves at 50 mm from the source. The polar plot shows good agreement with theoretical shape of the P-wave radiation pattern [16, 17]. Note that the directivity of a point source can be approximated with the $\cos-\theta$ angular dependence (equivalent to the half of a dipole point source) [18].

In the present work, three CFRP plates were used to determine their wave attenuation behavior. An aluminum alloy sheet was used to generate companion data. For this phase, we used the resonance nature of sensors to define the frequency ranges of waves. Orientation effects were also evaluated and results given, but this part is complex and requires more extensive investigation with modeling calculations.

2. Experiment: methods and results

Attenuation: Carbon Fiber Reinforced Plastic (CFRP) plates with three different kind of laminate lay-ups were obtained from Dr. W. Prosser of NASA Langley Research Center; AS4 fibers, 3502 epoxy; unidirectional $[0]_{8s}$ (and $[90]_{8s}$) [UD], cross-ply $[0, 90]_{4s}$ [XP], and quasi-isotropic $[0, 45, -45, 90]_{2s}$ [QI]. Their dimensions were 508x382 mm and 2.2 mm thick (16 plies). For comparison, 7475 Al plate (in cold-worked condition, 610x370 mm) of 3.1 mm thickness was used. S_0 and A_0 Lamb mode waves were generated on the CFRP plates by using an actuator of one edge. For A_0 component, an wedge (7°) was used so that only one edge is in contact with the actuator surface (Fig. 2). Several ultrasound sensors were used as actuator and fast high-voltage step-down pulses were used for excitation. Panametrics V101 (0.5 MHz, 25 mm), PAC Pico (0.5 MHz, 3.2-mm element, 5-mm case diameter), PAC $\mu 30$ (0.3 MHz) and DECI SH225 shear sensor (details not known) were used. As receivers, PAC Pico and PAC $\mu 30$ were mainly used. These were coupled directly to digital scope board inputs (Gage Applied, 1450, $1M\Omega$ input impedance) using its signal averaging function. The receivers have the resonance frequency around 260 and 500 kHz, respectively, and recorded Lamb waveforms have approximately the same values. However, the actual frequency varied systematically and we need analysis by wavelet transform to get a single frequency attenuation data. This part is not finished and will be reported later. By using sensors on both sides of the plate, the confirmation and separation of both modes, S_0 and A_0 , were successfully carried out. However, placing sensors on both sides simultaneously, amplitude was reduced. Thus, experiments were done on one side at a time. Distance was defined as that from plate edge to the center of receiver, though attenuation was measured starting from the sensor closest to the transmitter to minimize distance error.

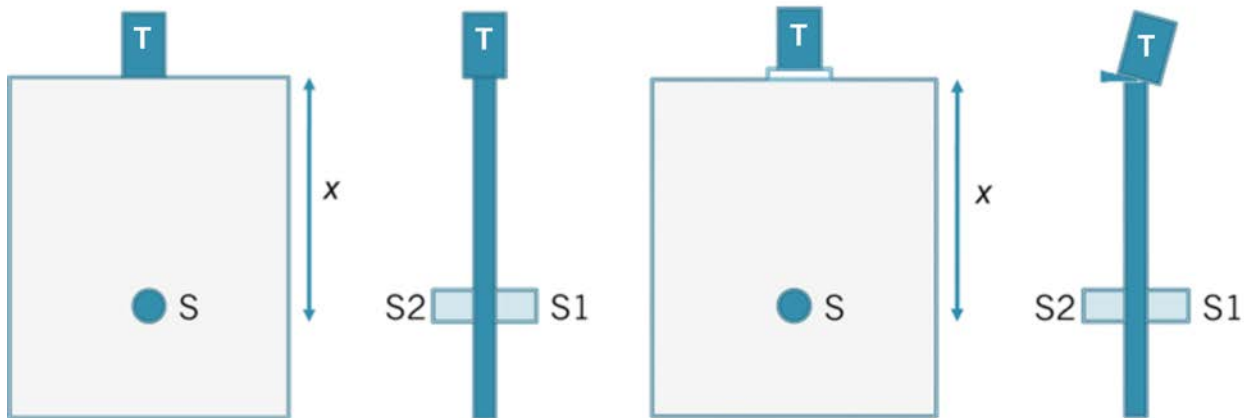


Fig. 2 Sensor placement for S_0 (left) and A_0 (right) wave generation. Transmitter (T). Sensor (S).

Figure 3 shows waveforms for Al case using V101 actuator at propagation distance $x = 100$ - 400 mm. Receiver was Pico sensor showing ~ 500 kHz frequency. Figure 4a shows the sum of two sensor signals from two sides, while Fig. 4b shows the difference of two side signals. These give S_0 and A_0 propagation characteristics. Figure 5 illustrates the wavelet transform coefficients

with color showing the amplitude (used AGU-Vallen WT). The maximum energy frequency was 475 kHz for S_0 and 430 kHz for A_0 propagation mode, respectively. Note that dispersion effect is shown for the S_0 mode, but it is absent for A_0 mode.

The peak amplitude (ignoring the dispersion effect) and the usual attenuation model with the inverse-square-root distance relation, eqn. 1, were used. For V101 transmitter, using Pico or $\mu 30$ receiver, we found the attenuation coefficient (damping factor), α , to be as below in Np/m:

S_0	1.397 (Pico)	0.676 ($\mu 30$)
A_0	0.560 (Pico)	1.112 ($\mu 30$)

Using Pico as a receiver and changing transmitter between V101 and Pico, we found α for S_0 to be as follow:

$$\text{V101 (transmitter)} \rightarrow \text{Pico (sensor)} \quad 1.397; \quad \text{Pico (transmitter)} \rightarrow \text{Pico (sensor)} \quad 1.625$$

All the α values for S_0 mode are much higher than Kasama's values (even though Al plate here was at least 3 times thicker). This must be due to the dispersion effect. In fact, for V101-Pico case, A_0 value was less than a half S_0 value of α .

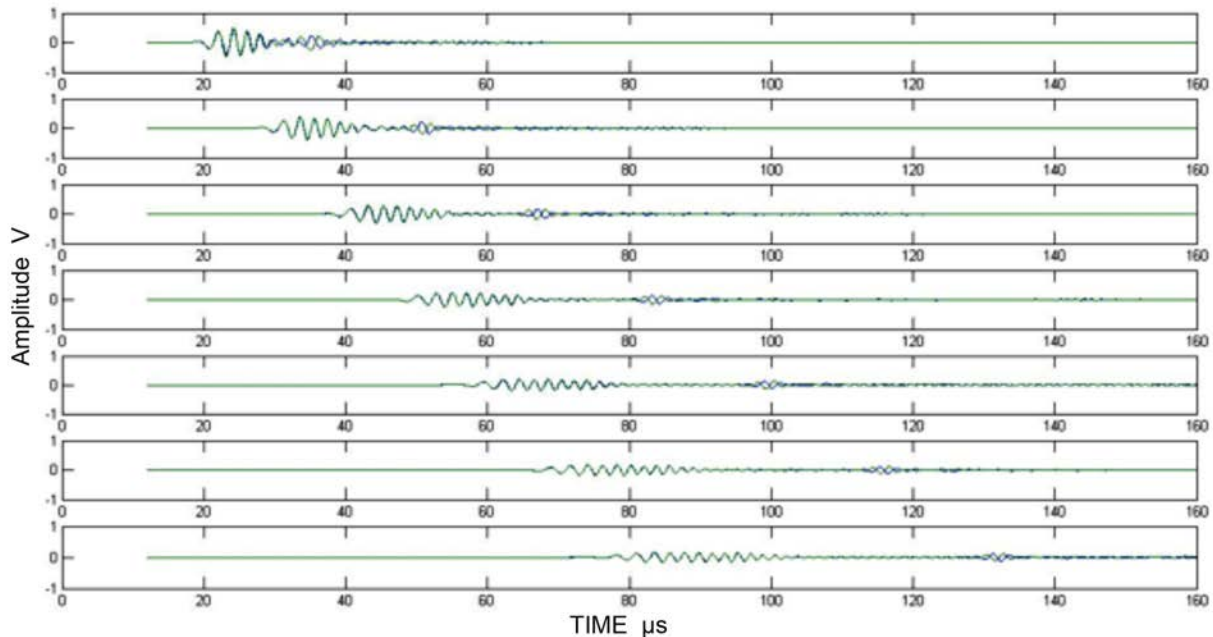


Fig. 3 Waveforms for Al case using V101 transmitter at propagation distance $d = 100\text{-}400$ mm.

Similar experiments were conducted using the identical setup, but with CFRP plates. For the UD plate, measurements were taken along the fiber direction (0°) and at the transverse direction (90°). Waveforms similar to Fig. 4a and 4b are given in Fig. 6. On the right side, reflected waves are seen (these were cut out for S_0 waves for clarity). The UD- S_0 case turns out to be a special case because of the near-field effect of the large aperture actuator (25-mm diameter). Peak amplitude actually increased up to 250 mm. Fit to the attenuation expression is shown in Fig. 7 for UD- S_0 case with V101-Pico combination and using reflected large distance data as well. For A_0 mode in the same plate, results are shown in Fig. 8. Again the initial part does not fit the attenuation expression well, but shows the attenuation coefficient over ten times that of S_0 case is found.

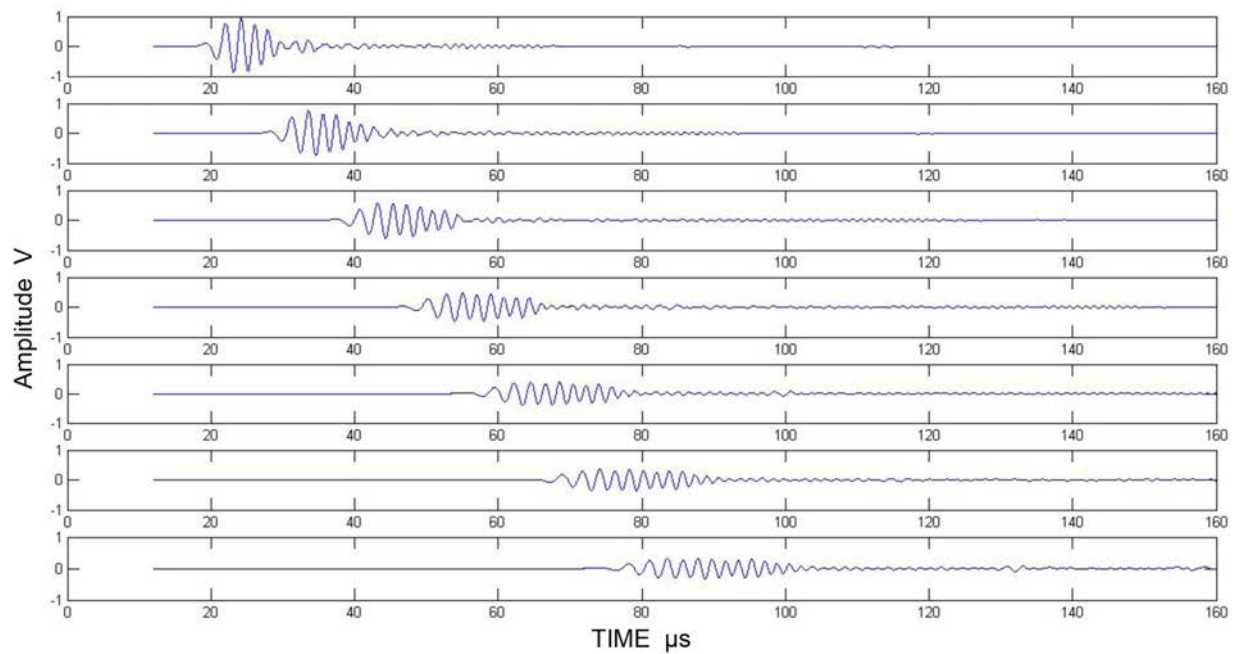


Fig. 4a The sum of two sensor signals from two sides, giving S_0 mode.

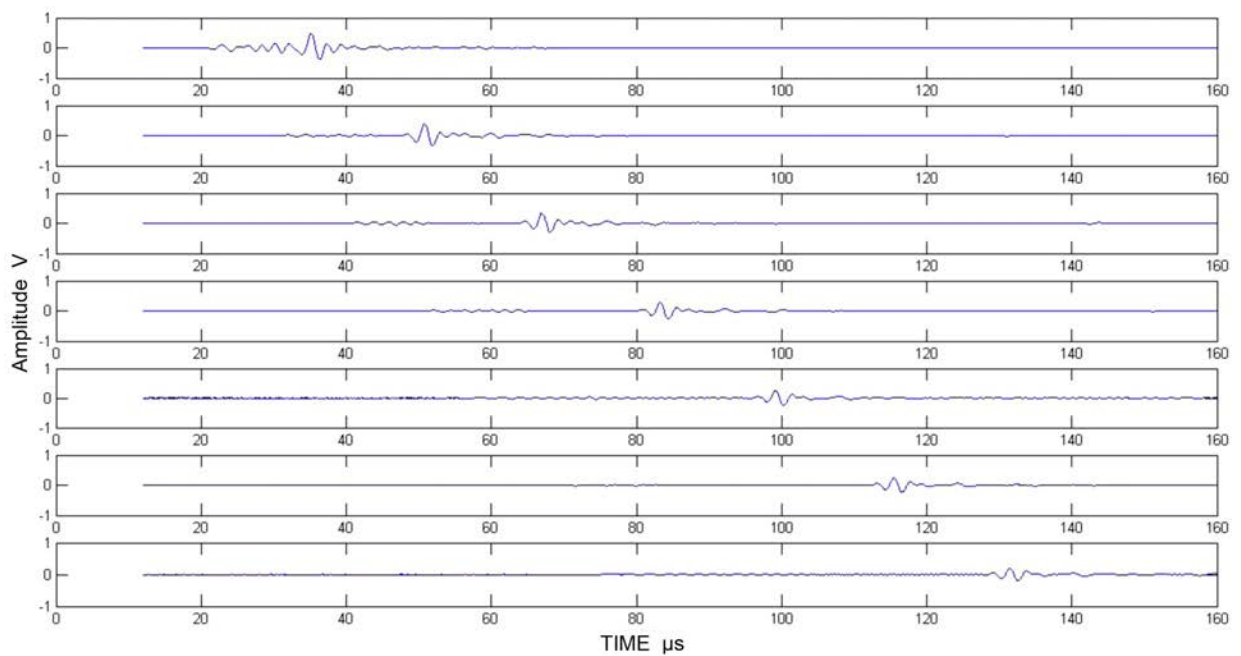


Fig. 4b The difference of two sensor signals from two sides, giving A_0 mode.

Table 1. Attenuation coefficients of Lamb waves (in Np/m) with V101 transmitter.

Plate	S_0 (Pico)	S_0 ($\mu 30$)	A_0 (Pico)	A_0 ($\mu 30$)
Aluminum 7475	1.397	0.676	0.560	1.112
C1-[0] _{8s}	0.560	0.552	6.123	6.935
C1-[90] _{8s}	12.21	9.471	-	9.535
C2-[0,90] _{4s}	1.082	0.237	-	9.105
C3-[0,45,45,90] _{2s}	4.254	1.455	-	10.577

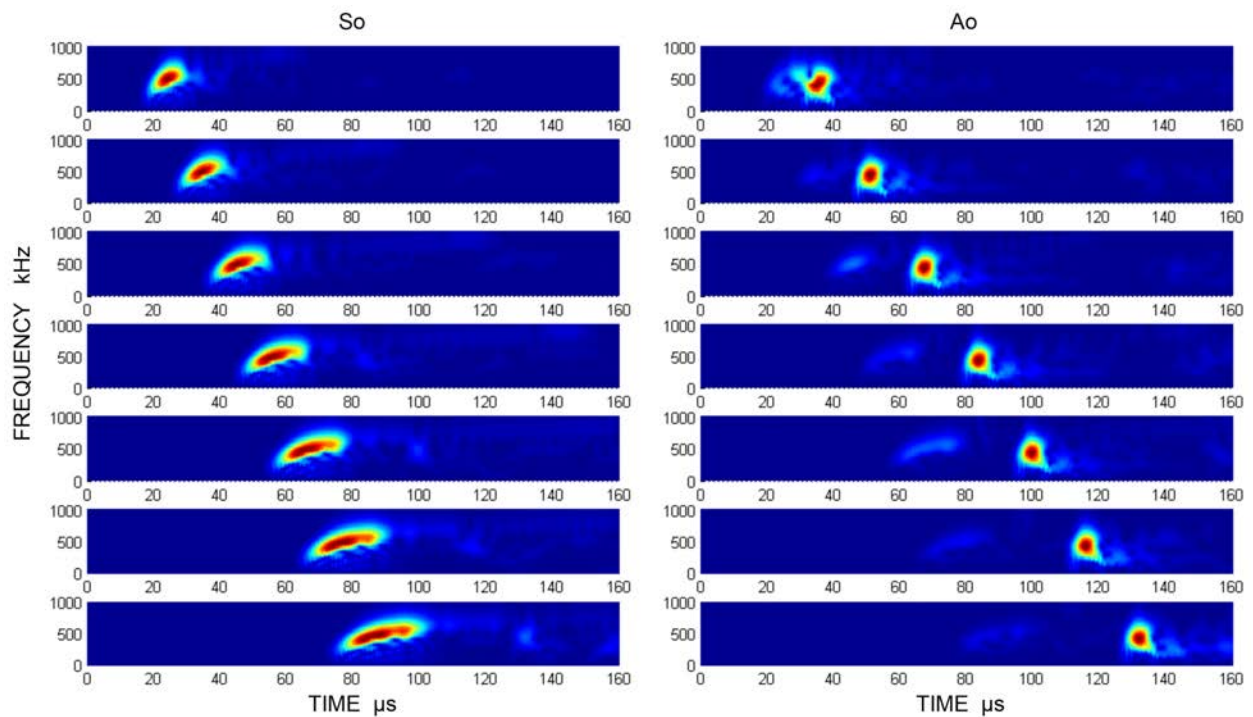


Fig. 5 AGU-Vallen wavelet transform coefficients with color showing the amplitude for S_0 and A_0 propagation. Al V101—Pico. Left used Fig. 4a waveforms. Right used Fig. 4b waveforms.

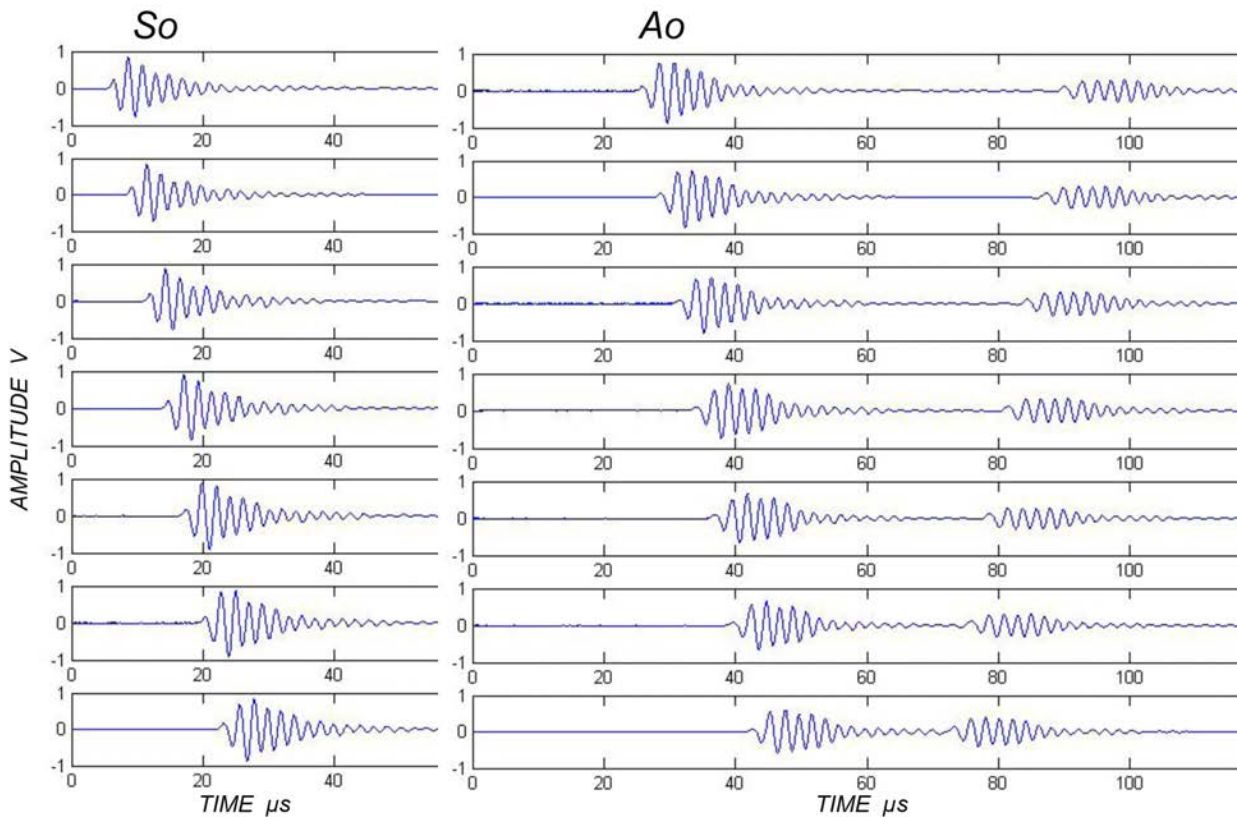


Fig. 6 Waveforms for S_0 and A_0 propagation. UD CFRP in the fiber direction. V101—Pico. Left: sum of two side waveforms. Right: difference of two side waveforms. Reflections are visible for the right figure.

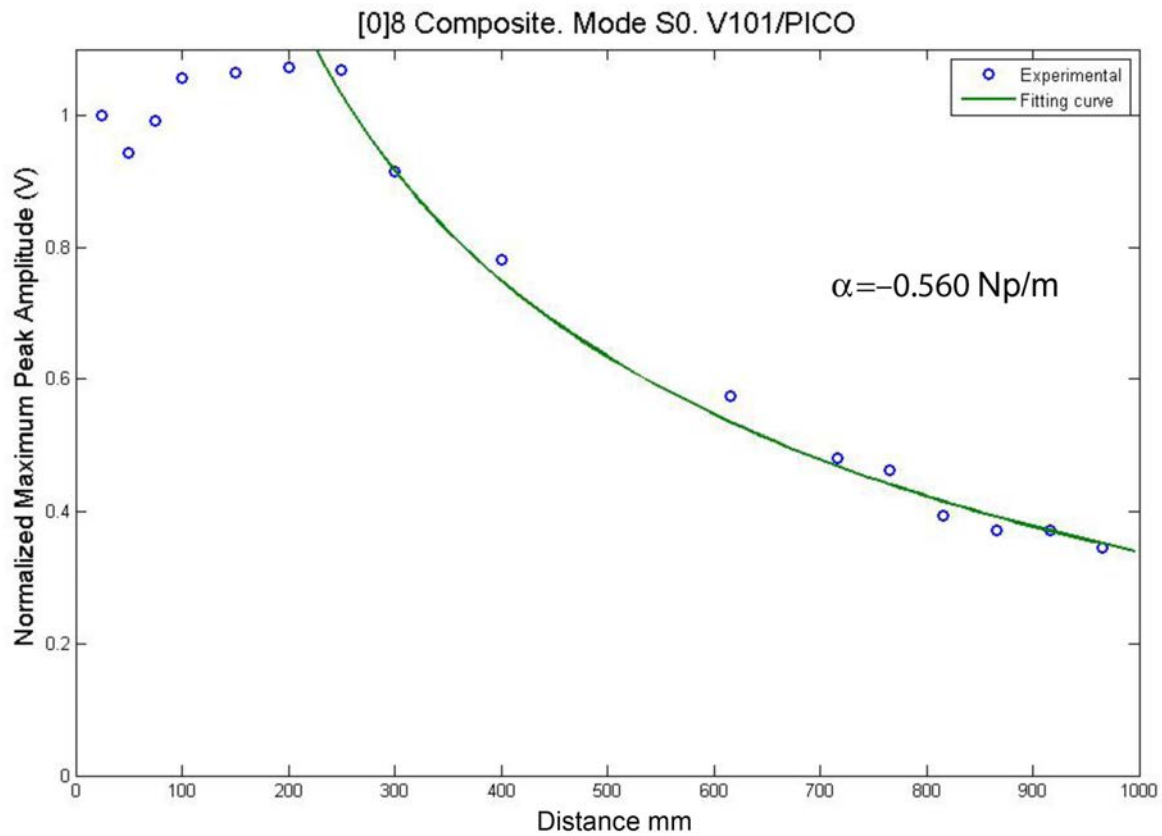


Fig. 7 Fit to the attenuation expression using peak amplitude beyond 200 mm. UD- S_0 case with V101-Pico combination.

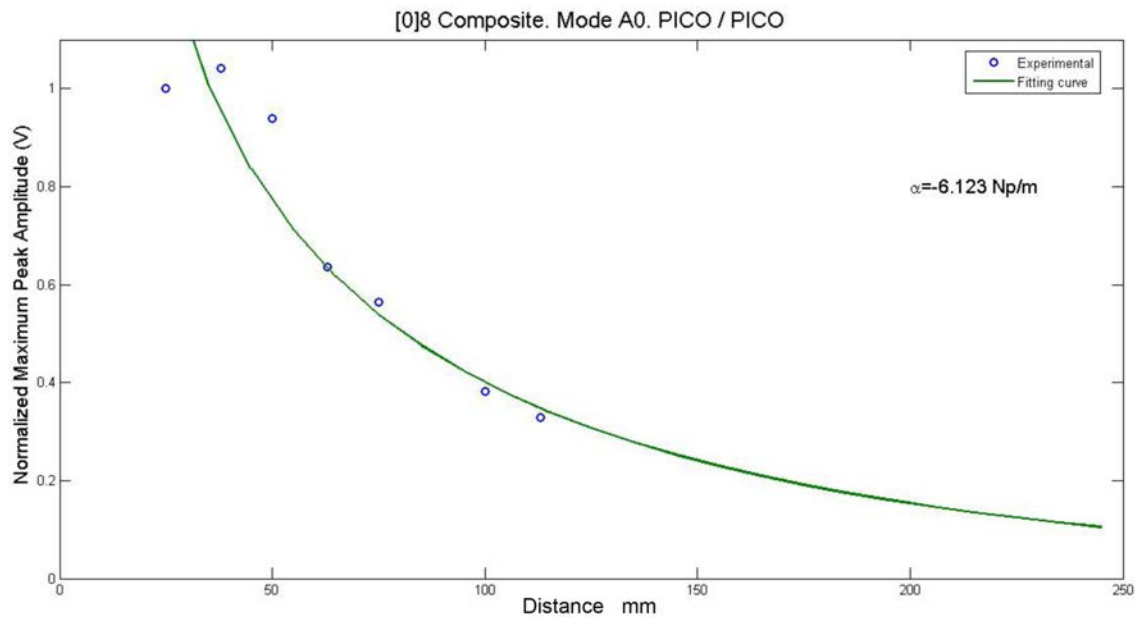


Fig. 8 Fit to the attenuation expression using peak amplitude. UD- A_0 case with Pico-Pico combination.

Curve fittings for other CFRP cases are better than those for UD- 0° cases. Results for the attenuation coefficients are summarized in Table 1. For S_0 mode, attenuation was lower for $\mu 30$ data in all cases, reflecting the lower nominal frequency of 260 kHz. For A_0 mode in Al plate, attenuation was lower for $\mu 30$ in the two cases we can compare, indicating that the dispersion

effect is higher at 260 kHz for this mode. On the other hand, attenuation was very high for A_0 mode using Pico sensor (nominally at 500 kHz) for 90°-orientation of UD, XP and QI plates and could not be measured.

Directivity: The directivity of Lamb wave propagation was explored. First, we examined the directional behavior in an isotropic Al plate as shown in Fig. 9. Data points for Al are given with squares. It follows the usual piston source directivity, matching well to the case of $ka = 2.9$, where k is the wave number. For both transmitter and receiver, we used Pico sensors, giving the nominal frequency of 500 kHz. The sensor case diameter is 5 mm and the PZT element diameter is 3.2 mm. Using $a = 2.5$ mm, ka value is equal to 1.75 at the S_0 -mode velocity of 4.5 mm/ μ s. This indicates that the directivity of S_0 -mode waves is narrower than that of P-waves.

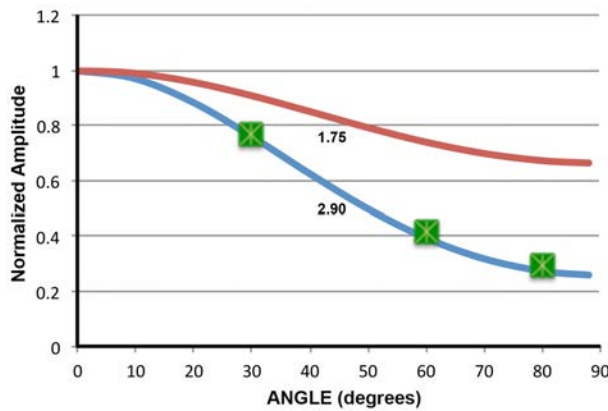


Fig. 9 The directivity of S_0 waves, Al, 500 kHz. P-wave directivity is plotted for ka of 1.75 and 2.9. Propagation distance = 50 mm.

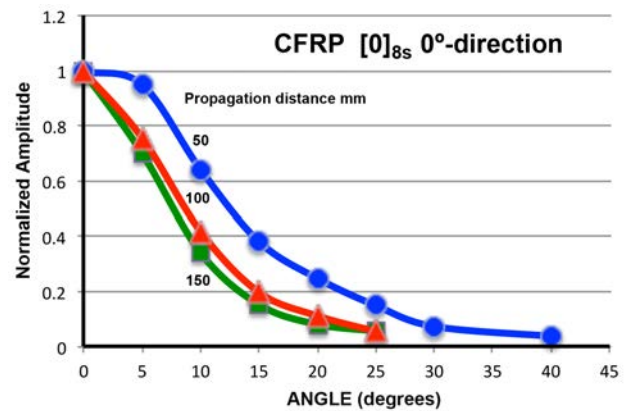


Fig. 10 The directivity of S_0 waves, CFRP-UD. 0° angle = fiber direction. Propagation distances of 50, 100 and 150 mm used.

The directivity in unidirectional CFRP is much sharper than in Al as shown in Fig. 10. The 0°-propagation angle corresponds to the fiber direction in the UD composite plate. Again, two Pico sensors were used as transmitter and receiver. Half-value angle was 12.5° at 50-mm distance of propagation, decreasing further to 8° at 150 mm. The latter case is comparable to P-wave directivity at $ka \approx 15$. The observed dependence on the propagation distance originates from attenuation effects that increase with the angle away from the fiber direction. Suzuki showed that P-wave attenuation doubled from 0° to 30° in UD-GFRP [19].

The directivity in a quasi-isotropic CFRP (QI) plate is much more complex. When the 0°-fiber direction (located at the top and bottom plies) coincides with the 0° propagation angle, observed amplitude changes were moderate at 50-mm distance, as shown in Fig. 11. The variation became larger with larger distance with the normalized amplitude increasing to a peak at ~10°. This is followed by a gradual decrease. The angular dependence varied with the propagation distance, which raised the relative peak height to 1.74 times the 0° value at 150 mm. This angular dependence suggests that the 45° ply immediately below the 0° ply causes this effect. Here, positive values were arbitrarily taken for angles measured counter-clockwise. We refer this as QI-0 configuration.

When the QI plate is rotated 90° and the 0° propagation angle is oriented along the 90°-fiber plies (at the mid-thickness), the directivity characteristics were different as shown in Fig. 12. That is, waves at 0° angle is propagating along the fiber direction in the 90° plies. In this case, the

orientation dependence was nearly absent ($\leq \pm 20\%$). Effects of propagation distance between 50 and 100 mm were also small. These are marked as 90-50 and 90-100 in the figure [this is referred to as QI-90.] and two curves from Fig. 11 are re-plotted for comparison (as 0-50 and 0-100). This finding shows that the positions of various plies have large effects on radiation and propagation patterns. Here, 45°-direction (on QI-90) is perpendicular to the 45°-direction (on QI-0) in Fig. 11.

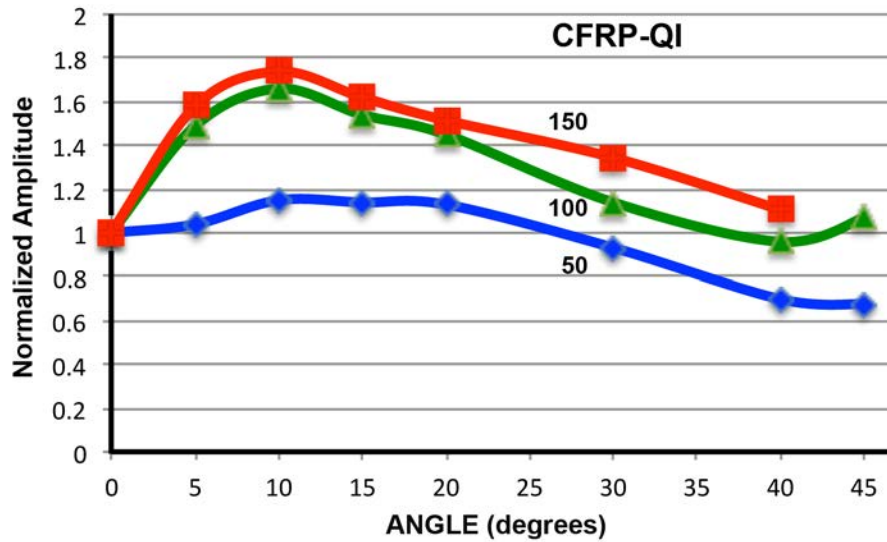


Fig. 11 The directivity of S₀ waves in CFRP-QI plate. T/R: Pico sensors; 0° propagation angle is parallel to the 0°-ply orientation on the outside. Propagation distance = 50, 100 and 150 mm.

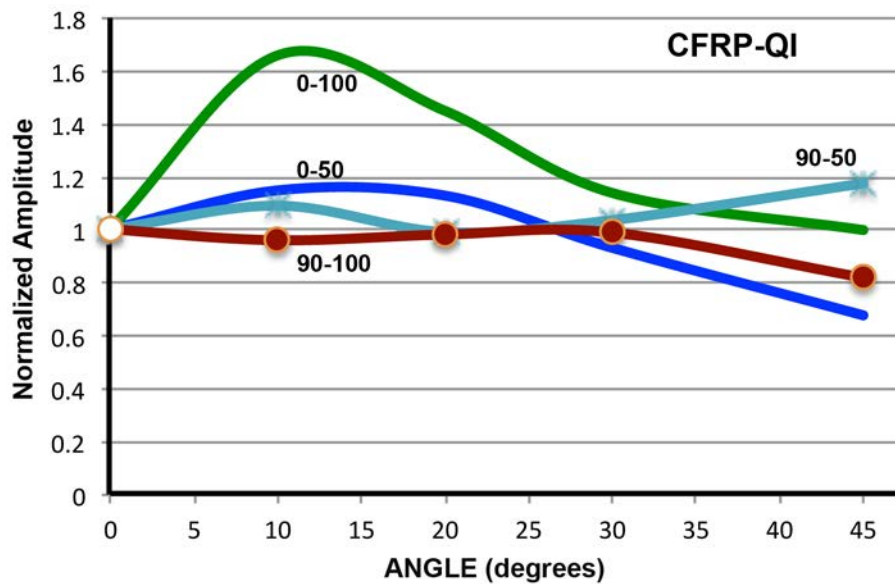


Fig. 12 The directivity of S₀ waves in CFRP-QI plate. T/R: Pico sensors; 0° propagation angle is parallel to the 90°-ply orientation at mid-thickness. Propagation distance = 50 and 100 mm. Two curves from Fig. 11 are also shown for comparison (marked 0-50 and 0-100).

Another series of directivity measurement was repeated with the range of angle into the negative side. Figure 13 shows the results. The positive side is essentially the same as in Fig. 11 (amplitude for 100-mm propagation is lower, however). On the negative side, the normalized amplitude is relatively unchanged; to be precise, it dips to ~0.8 at 5-10°, then slowly rises to ~1.2 at

-30°. The directivity of this QI plate is asymmetric even though the wave velocity is orientation-independent. It appears that subsurface plies are responsible for this asymmetric behavior.

When this experiment is run using a larger transmitter, Panametrics V101 (500 kHz, 25-mm element size), with Pico as a receiver, the directivity is strongly affected as shown in Fig. 14. In comparison to Pico transmitter, the ka value is eight times larger for V101. The amplitude was reduced to 0.2~0.3 at 30-40° on both sides and the peak height at $\theta = 10^\circ$ reached only 1.2. Obviously, this behavior is due to narrower beam generated by a larger transmitter, accentuating the asymmetric behavior.

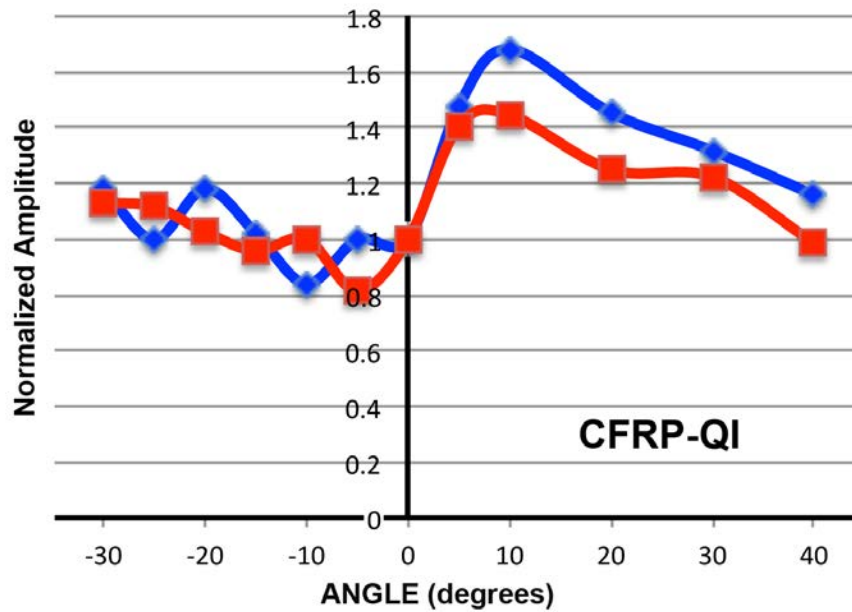


Fig. 13 Asymmetric directivity in CFRP-QI plate. 0° orientation. 100 mm (■) and 150 mm (◆) propagation distance. Transmitter: Pico, Receiver: Pico.

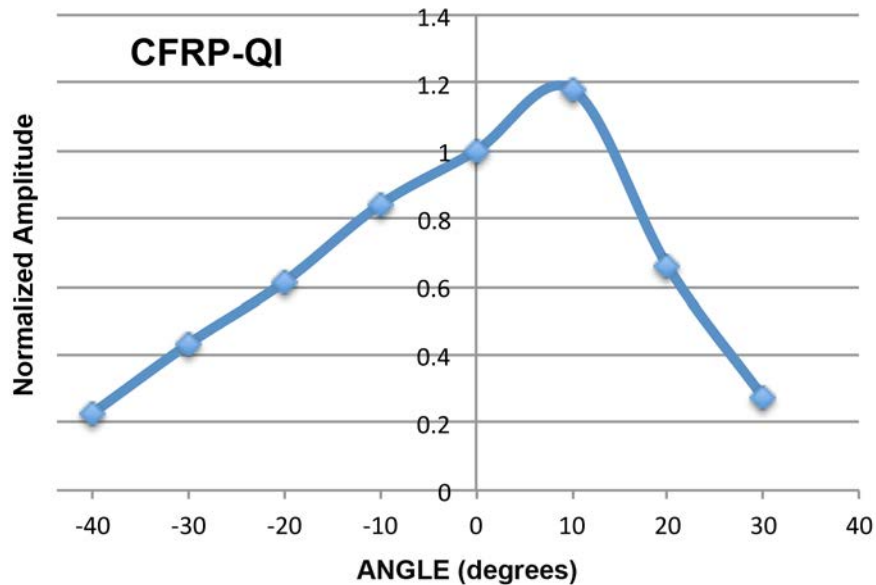


Fig. 14 Asymmetric directivity in CFRP-QI plate. 0° orientation. 150 mm propagation distance. Transmitter: V101, Receiver: Pico.

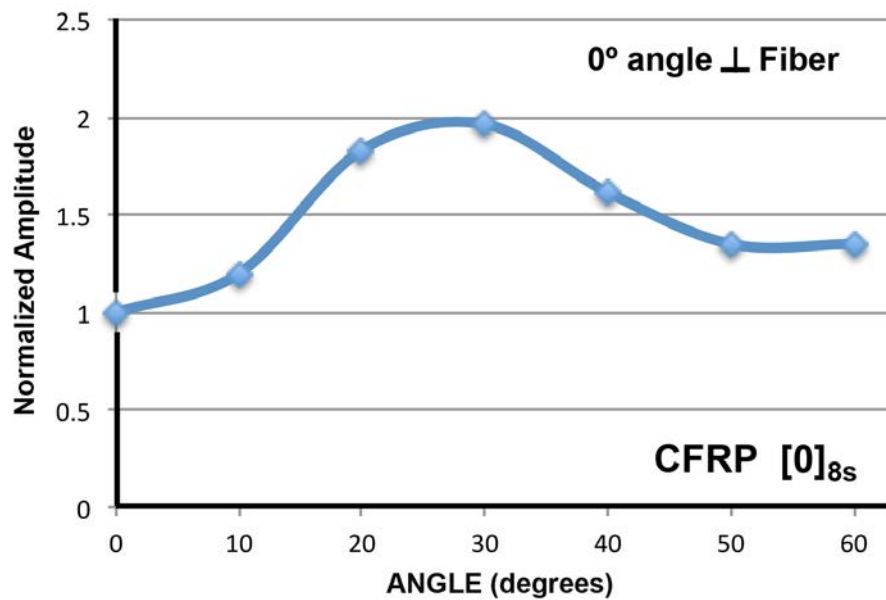


Fig. 15 The directivity of S_0 waves in CFRP-UD plate. T/R: Pico sensors; 0° propagation angle is perpendicular to the fiber orientation. Propagation distance = 100 mm.

Yet another unexpected behavior was found in the CFRP-UD plate. Here, the 0° angle corresponds to the normal direction of the fiber. Observed amplitude increased with angle, reaching a peak at $\sim 30^\circ$, as shown in Fig. 15. This is in sharp contrast to Fig. 10, where the directivity of wave showed a narrow focus around the 0° orientation. Obviously, initial wave entry to the broadside of fibers produces substantial differences from the case where wave propagation starts from the ends of the fibers in the 0° -fiber direction. Still, no apparent explanation is available.

Discussion

Attenuation: The data in Table 1 are apparent attenuation coefficients since specific frequency components are not compared by the use of wavelet transform. On the other hand, in dealing with practical attenuation case, these values are representative of observed attenuation (with dispersion effect, but without the geometrical spreading effects). We will in the near future conduct such analysis and report the frequency dependent attenuation data removing the dispersion induced amplitude loss. The above data are still interesting:

1. Attenuation of A_0 or flexural mode is much higher than S_0 or extensional mode. Exception is when waves propagate along the transverse direction to the fiber in the UD plate.
2. Pico data are higher than $\mu 30$ data most of the time. The difference in frequency is from 260 to 430-500 kHz, which is about twice and not really that large.
3. In the UD- 90° direction, both S_0 and A_0 propagation modes attenuate greatly.
4. While QI plates are useful in design, stress wave inspection is difficult due to high attenuation of both Lamb modes.
5. XP plates can be a good compromise in inspectability and design freedom.

Some of these values can be compared to theoretical studies, and are comparable in cases of similar materials/layups within a factor of two to three. However, theory is for plane waves and at a fixed frequency. Thus, we must first eliminate dispersion effect in our data. Thickness effect found in [14] was noted in Prosser's work [3] as well. So this may make a comparison difficult.

We attempted to use lower frequency sensors at 30-150 kHz, but mode mixing prevented us from getting meaningful data. Larger plates are also necessary for such experiments.

For the case of XP plate, we can compare with Aljets' data for twill-weave CFRP of 2.5-mm thick [11]. Along the fiber direction, he obtained 1.78 Np/m for S_0 waves at 250-300 kHz, and 6.17 Np/m for A_0 waves at 150-200 kHz, respectively. These values were recalculated from his Fig. 56. Signal source was pencil-lead breaks. At the direction 45° to the fibers, attenuation coefficients were slightly higher at 2.67 and 6.49 Np/m for S_0 and A_0 waves, respectively. The attenuation coefficients for S_0 waves were significantly higher than our XP results. A possible origin is their use of twill-weave, which produces undulations of fibers and higher resin contents. The differences for A_0 waves were smaller; our $\mu 30$ data is only 50% higher than Aljets data.

What this work shows is that it is indeed difficult to conduct AE or acousto-ultrasonic experiments at frequency above 250 kHz due to high attenuation. As CARP's procedures for FRP tank inspection used under 100-kHz range, aerospace composite NDE should look for the lower frequency range to provide workable and practical solutions. In acousto-ultrasonic methods, typical excitation mode is surface-driven sensor. This generates mainly flexural mode, which attenuates highly. We need to devise a means to excite extensional mode with good efficiency and movability.

Directivity: Preliminary examination of directivity in CFRP has revealed a complex behavior. In UD-composite along the fiber direction, waves travel along the fibers with narrow beam spread. In most other cases, ready understanding is unavailable except that the transmitter radiation pattern and the directional attenuation of CFRP plates jointly produced the observed characteristics. It is necessary to accumulate more experimental results before consistent interpretations can be developed. It will be helpful if we can separate radiation pattern and orientation dependent attenuation as a function of frequency and propagation modes. Obviously, high-level modeling is needed to explain these findings. However, understanding these characteristics will benefit future AE applications on composite materials.

Conclusion

Apparent attenuation of Lamb wave propagation was measured for specific modes on CFRP plates of three different layups. Generally, attenuation is high limiting the reach of stress-wave based NDE methods. It is essential to utilize a lower frequency range for practical NDE methods. Directivity of wave propagation revealed complex behavior, requiring further studies.

Acknowledgement

Assistance of Zhiyuan Wu in experiment and of Elisabet Suárez Vargas in analysis is highly appreciated.

References

1. U. Schnars, R. Henrich, "Applications of NDT methods on composite structures in aerospace industry", Online-Proc. Conf. on Damage in Composite Materials – CDCM2006, Vol. 12, No. 12 (2006). <http://www.ndt.net/article/cdcm2006/>
2. T. Ullmann, T. Schmidt, S. Hofmann, R. Jemmali, "In-line quality assurance for the manufacturing of carbon fiber reinforced aircraft structures", *2nd Intl Symp. on NDT in Aerospace 2010* -

- Tu.1.A.4. <http://www.ndt.net/article/aero2010/papers/tu1a4.pdf>
3. W.H. Prosser, "Advanced AE techniques in composite materials research", *J. Acoustic Emission*, vol. 14, 1996, pp. S1-S11.
 4. A.K. Mal, Y. Bar-Cohen and S.S. Lih, "Wave attenuation in fiber-reinforced composites," *M3D: Mechanics and Mechanisms of Material Damping*, ASTM STP 1169, American Society for Testing and Materials, 1992, pp. 245-261.
 5. M. Castaings, B. Hosten, "Air-coupled measurement of plane wave, ultrasonic plate transmission for characterising anisotropic, viscoelastic materials", *Ultrasonics*, vol. 38, 2000, pp. 781-786.
 6. M. Castaings, B. Hosten, T. Kundu, "Inversion of ultrasonic, plane-wave transmission data in composite plates to infer viscoelastic material properties. *NDT & E International*, vol. 33, no.6, 2000, pp. 377-92.
 7. B. Hosten, "Heterogeneous structure of modes and Kramers-Kronig relationship in anisotropic viscoelastic materials", *J. Acoust. Soc. Am.* vol. 104 (3), September 1998, pp. 1382-1388.
 8. M. Castaings, M.V. Predoi, B. Hosten, "Ultrasound propagation in viscoelastic material guides", *Proceedings of the COMSOL Multiphysics User's Conference 2005 Paris*, 6 p.
 9. M. Calomfirescu, "Lamb Waves for Structural Health Monitoring in Viscoelastic Composite Materials", Logos Verlag, Berlin, Germany, 2008. 119 p.
 10. M. Sause, Identification of failure mechanisms in hybrid materials utilizing pattern recognition techniques applied to acoustic emission signals, Augsburg Univ. doctoral dissertation, Mensch und Buch Verlag, 2010, 305 p.
 11. D. Aljets, "*Acoustic Emission Source Location in Composite Aircraft Structures using Modal Analysis*", Ph.D. Thesis, Faculty of Advanced Technology, University of Glamorgan, June 2011, 163 p. <http://dspace1.isd.glam.ac.uk/dspace/bitstream/10265/575/1/PhD%20Thesis%20Dirk%20Aljets.pdf>
 12. M.A. Torres-Arredondo, C.-P. Fritzen, "A viscoelastic plate theory for the fast modelling of Lamb wave solutions in NDT/SHM applications", *Ultragarsas (Ultrasound)*, vol. 66, No. 2, 2011, pp. 7-13.
 13. Acousto-Ultrasonics, Special Issue, *J. Acoustic Emission*, vol. 12, nos. 1/2, pp. 1-103.
 14. H. Kasama, M. Takemoto, K. Ono, "Attenuation measurement of Laser excited So-Lamb wave by the wavelet transform and porosity estimation in superplastic Al-Mg plate", *Hihakaisensa (Nondestructive Testing)*, vol. 49, no. 4, 2000, pp. 269-276.
 15. H. Kasama, MS Thesis, Dept. Mechanical Engineering, Aoyama Gakuin Univ., Sagamihara, Kanagawa, Japan, 1999, 102 p.
 16. D.A. Hutchins, R.J. Dewhurst, and S.B. Palmer, "Directivity patterns of laser-generated ultrasound in aluminum", *J. Acoust. Soc. Am.* vol. 70, 1981, pp. 1362-1369.
 17. S.J. Davies, C. Edwards, G.S. Taylor and S.B. Palmer, "Laser-generated ultrasound: its properties, mechanisms and multifarious applications", *J. Phys. D: Appl. Phys.* vol. 26 (1993) 329-348.
 18. X.M. Tang, Zhenya Zhu, and M.N. Töksöz, "Radiation patterns of compressional and shear transducers at the surface of an elastic half-space", *J. Acoust. Soc. Am.* 95 (1), 1994, 71-76.
 19. H. Suzuki, "Fracture dynamics via inverse analysis of viscoelastic waves", doctoral thesis, Tokyo Inst. Technology, 2000, 176 p.

Appendix

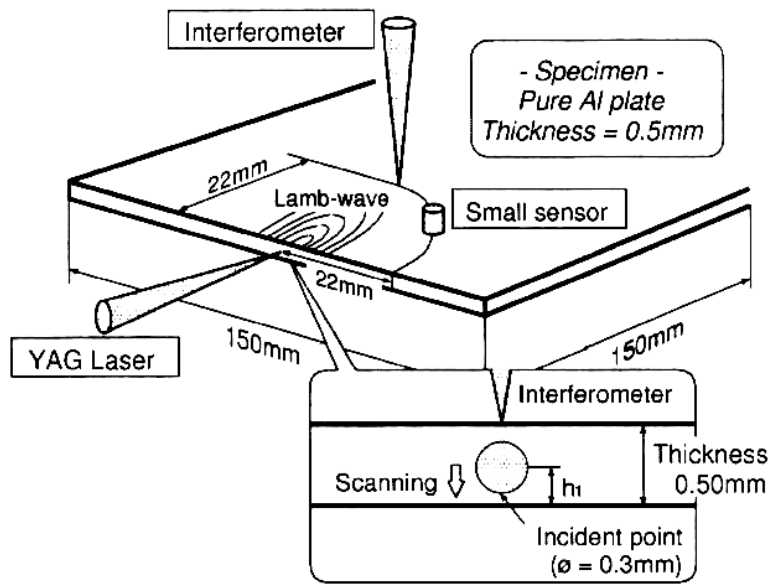


Fig. A1 Laser generation and detection of Lamb waves in Al sheet. [15]

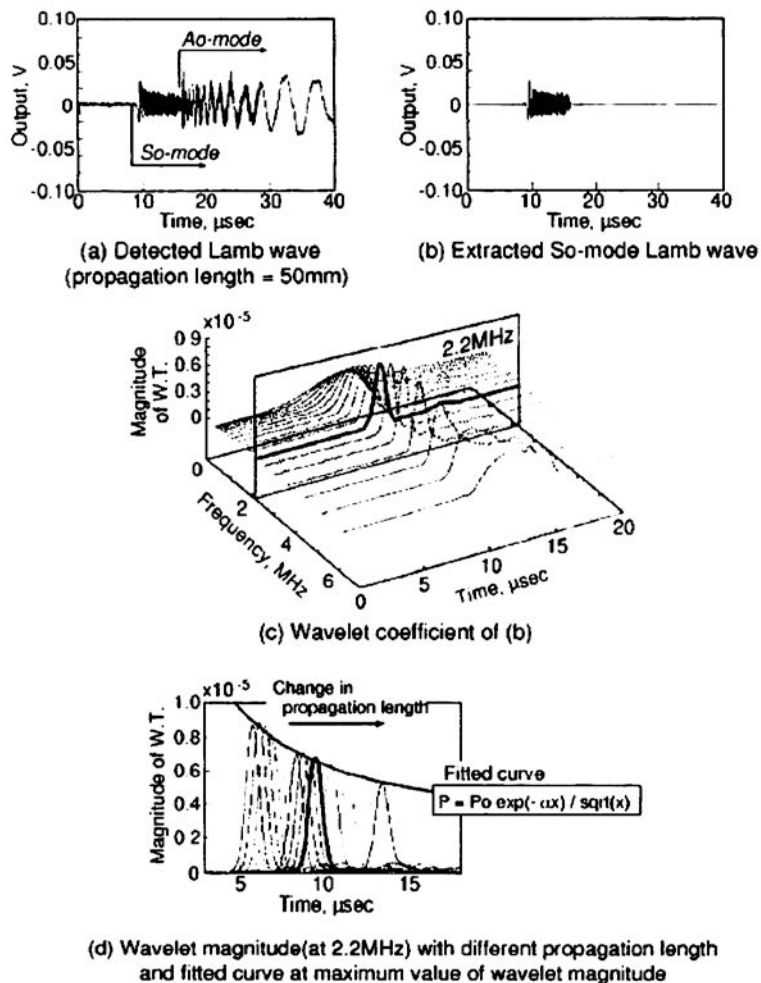


Fig. A2 Extraction of S_0 component, WT analysis and fitting to geometrical spread-attenuation curve (eqn. 1)[15].

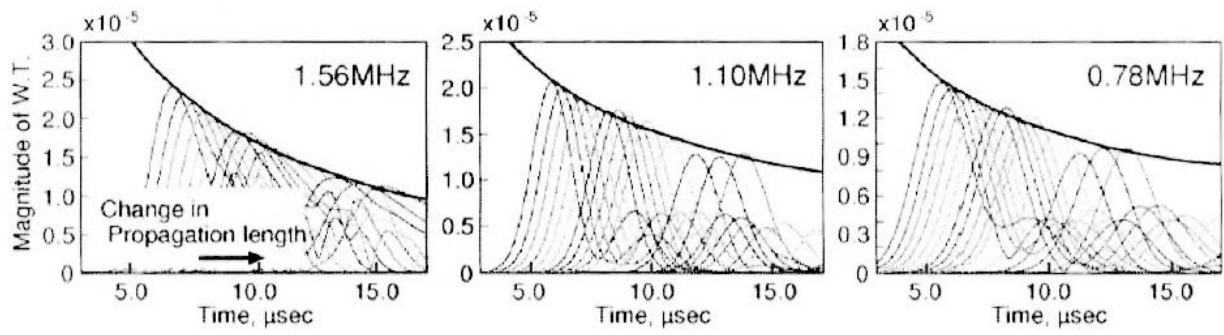


Fig. A3 Curve fitting of WT peak amplitude to eqn. 1. Three examples for 1.0-mm thick Al [15]

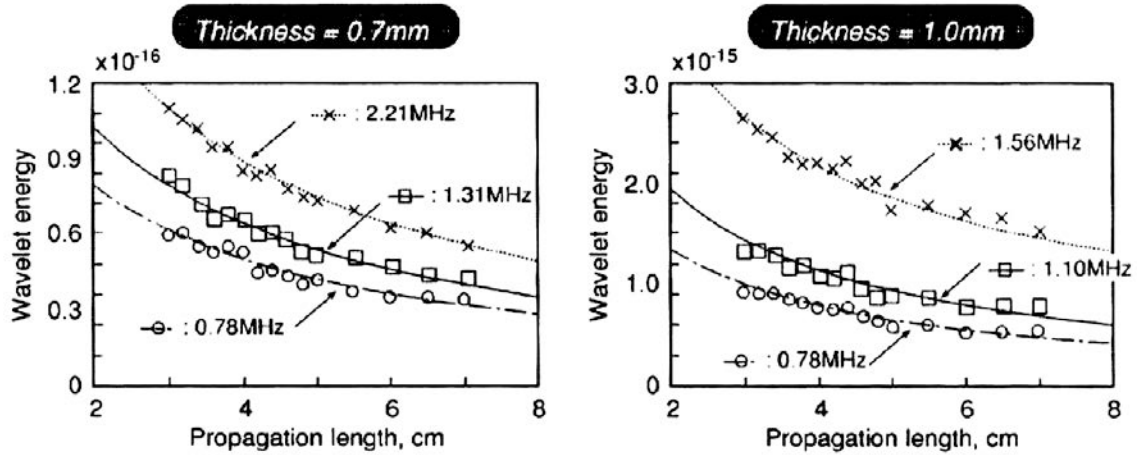


Fig. A4 Curve fitting of WT energy to eqn. 2. Three examples each for 0.7- and 1.0-mm thick Al [15].

Application of ICI Principle for AE Data Processing

Vera Barat¹, Sergey Elizarov¹, Irina Bolokhova² and Evgeniy Bolokhov²

¹ Interunis Ltd., Moscow, Russia

² National Research University "Moscow Power Engineering Institute", Moscow, Russia

Abstract

During AE data processing, it is often necessary to determine the change points of parameters. The most important problems are arrival time detection and AE data segmentation. The first-arrival time of acoustic emission (AE) signal is very important parameter, which is used for event location and identification. At present there are many advanced arrival time determination methods, which significantly increase accuracy of estimation in comparison with traditional threshold crossing method. However, advanced methods have several disadvantages connected with algorithm parameters selection. Arrival time estimation algorithms are based on a calculation of several statistical parameters within a sliding time window. The time-window length is often chosen empirically by the operator. When criteria for window length selection are undefined an incorrect length selection is possible, as well as incorrect AE signal arrival time definition. This paper describes the method based on intersection of confidence interval (ICI) principle. This method allows one to select time parameters optimally and in automatic mode. Application of ICI principle increases the accuracy and reliability of first-arrival time estimation. The problem of segmentation data arises in connection with the necessity to identify the data. Specifically the definition in the data stream of time intervals corresponding to different stages of the observed processes.

Keywords: Signal processing, AE source location, intersection of confidence interval (ICI)

1. Introduction

The signal processing holds a significant place in theory and practice of nondestructive testing, since the accuracy of estimation of the tested equipment depends on the correctness of processing and analysis of diagnostic information. Such problems of signal processing like signal detection, filtering and parameters estimation are urgent for any type of nondestructive testing. The AE testing has many distinctive features as compared with other types of testing. The distinctive characteristics of AE testing generate specific problems of the AE data processing. Among such problems we can mention the necessity of separation of AE signal components, which correspond to different wave modes, clustering of AE signals and impulses and determination of the signal arrival time.

The necessity of determination of the signal arrival time stems from the fact that the AE testing is remote. It allows for detecting defects at the distance up to several tens meters from the place of sensor location. The defect location can be determined by location, which is based, as a rule, on the time-of-arrival technique wherein the defect coordinates are determined from the difference of arrival times for signals at different sensors and from the speed of AE wave propagation. With such techniques, the accuracy of location, and as consequence, the reliable results of AE testing as a whole are governed by the accuracy of determination of the signal arrival time.

The conventional method of signal arrival time definition is the threshold method based on the first threshold crossing. The threshold method is very simple in implementation but has low

accuracy. The error in signal arrival time determination by the threshold method can reach hundreds of microseconds, and the error in determination of defect coordinates can be several meters.

Most modern AE systems, in addition to the conventional threshold processing of AE data, are supplied with an advanced floating threshold method. The floating threshold varies according to a noise level registered by the AE system. The signal start point will be detected, when the signal samples exceed an averaged value of noise amount by a preset number of times. An adaptive change of the threshold value allows for defining more precisely the arrival time of a signal through reducing an influence of the noise level. A limitation of the floating threshold method is the low accuracy during determination of the arrival time for far-field signals, which are emitted by the AE sources far removed from the sensors [1].

At present, a number of advanced time arrival determination methods [2] based on different principles of digital signal processing (wave modes isolation filtering, wavelet thresholding, cross-correlation analysis) and statistical time-series analysis (auto-regressive analysis, STA/LTA methods, high order statistics approach) have been developed. This paper is devoted to the comparative analysis of existing statistical methods and the description of the signal arrival time determination algorithm by using the ICI principle.

2. Review of advanced statistical methods

During the statistical analysis of time series, the waveform of AE signal can be considered as a stochastic, as a rule, stationary noise process, against which impulses of acoustic emission are observed. Since the AE impulses create a short-term variability in the properties of noise process, the problem of signal arrival time determination can be considered as change point detection. Among a great number of change point detection methods, we selected those, such as Likelihood-ratio procedure, Akaike information criteria [3], and high order statistics (HOS) approach [4], of which application in AE signals processing has been successfully tested.

2.1 Maximum likelihood estimation method

The maximum likelihood estimation (MLE) method is a parametrical method of statistical analysis [5] used for estimation and check of statistical hypotheses. Advantage of MLE method is the possibility to construct optimum statistical criteria. The basis for this method is the likelihood function, eqn. (1) expressing the joint probability in a signal of samples x_1, x_2, \dots, x_n . The likelihood function is equal to the product of probability of each value of sample:

$$L(x_1, x_2, \dots, x_n, \theta) = \varphi(x_1, \theta) \cdot \varphi(x_2, \theta) \dots \varphi(x_n, \theta), \quad (1)$$

where $\varphi(x)$ = probability density function, and θ = a set of parameters of time series distribution. To construct statistical conclusions, in regard to parameters of the analyzed time series θ , a maximum of likelihood function or a maximum of its logarithm should be determined.

To determine the AE signal arrival time, MLE can be used as a criterion for testing hypothesis that the AE signal parameters do not change over the period of observation. The alternative hypothesis is the hypothesis according to which there exists a change point of the signal k properties, corresponding to the moment of AE signal arrival, eqn. (2). As a parameter changing with the AE signal arrival it is reasonable to select the dispersion.

$$\begin{aligned}
H_0 : \sigma_1^2 &= \sigma_2^2 = \dots = \sigma_n^2 = \sigma^2 \\
H_1 : \sigma_1^2 &= \dots = \sigma_k^2 \neq \sigma_{k+1}^2 = \dots = \sigma_2^2
\end{aligned} \tag{2}$$

The logarithm of maximum likelihood function L is defined by eqn. (3). The argument k at which $\log L$ function reaches a maximum, determines the moment of AE signal arrival [6]. As the MLE method is parametrical, σ_1 and σ_2 should be preliminarily estimated.

$$\log L(k, \sigma_1^2, \sigma_2^2) = -\frac{n}{2} \log 2\pi - \frac{k}{2} \log \sigma_1^2 - \frac{n-k}{2} \log \sigma_2^2 - \frac{\sum_{i=1}^k (x_i - \bar{x})^2}{2\sigma_1^2} - \frac{\sum_{i=k+1}^n (x_i - \bar{x})^2}{2\sigma_2^2} \tag{3}$$

2.2 Akaike information criteria

Many researchers have proved that the AE signal can be considered as an autoregressive (AR) process, whose current values depend on previous values; see eqn. (4). The process structure is represented by the coefficients of autoregressive equation, which form an autoregressive model.

$$X_t = c + \sum_{i=1}^p a_i X_{t-i} + \varepsilon_t, \tag{4}$$

To check the signal conformance to the model, different criteria are used. The most popular is the Akaike information criterion (AIC). The application of the Akaike information criterion for defining the signal arrival time lies in the fact that the noise and the AE signal correspond to different autoregressive models, and the moment of signal origin corresponds to the maximum change point of the autoregressive equation coefficients. Therefore, the extreme of Akaike information criterion will correspond to the signal arrival time. As a classic case, values of AIC criterion are calculated through the autoregressive equation coefficients. In contrast, Maeda [4] calculated the AIC function directly from the signal without using the AR coefficients. For time series x of length N , the AIC is defined as:

$$AIC(k) = k \cdot \log(\text{var}(x[1, k])) + (N - k - 1) \cdot \log(\text{var}(x[k + 1, N])) \tag{5}$$

The signal time-of-arrival determination algorithm has been well studied and actively engaged in practice. Sedlak et al. [3] developed a two-stage AIC based approach for determining the arrival times of AE signals, in which the AIC function is applied to a characteristic function that represents the raw signal, instead of directly to the raw signal.

2.3 HOS approach

The HOS approach belongs to statistical methods using a sliding time window. The signal arrival time is determined with the help of the HOS approach as the change point of signal distribution nature. Noise has a normal distribution with zero high-order moments. At the moment of signal arrival the distribution character is changed, as demonstrated by a sharp increase of any of high-order statistic parameters. Lokajicek and Klima [4] analyze the possibility of applying the different order moments. The most exact results of the time-of-arrival determination can be obtained when using the sixth order derivative of the moment is used.

2.4 Comparative analysis of time determination estimation (TDE) methods

Notwithstanding the fact that time determination methods of the signal origin described in 2.1-2.3 are based on different approaches, all of them fall in the same class, namely, the change point detection methods. In the MLE method a variance change is determined, a minimum value of AIC criterion corresponds to the change point of autoregressive equation coefficients, while using the HOS approach, a change point of the process probability distribution law is determined.

Let us consider application of the above methods for definition. The AIC and MLE methods are applied to the total length of a signal, and the signal time-of-arrival is determined by an extremum of the corresponding function. The higher order moments are calculated inside the sliding time window, and to the origin of AE signal there corresponds a sharp increase of the statistical parameter. By way of illustration, Fig. 1 shows application of the above methods for determination of the time-of-arrival of a model signal (Fig. 1a). The times of signal arrival are marked with red point.

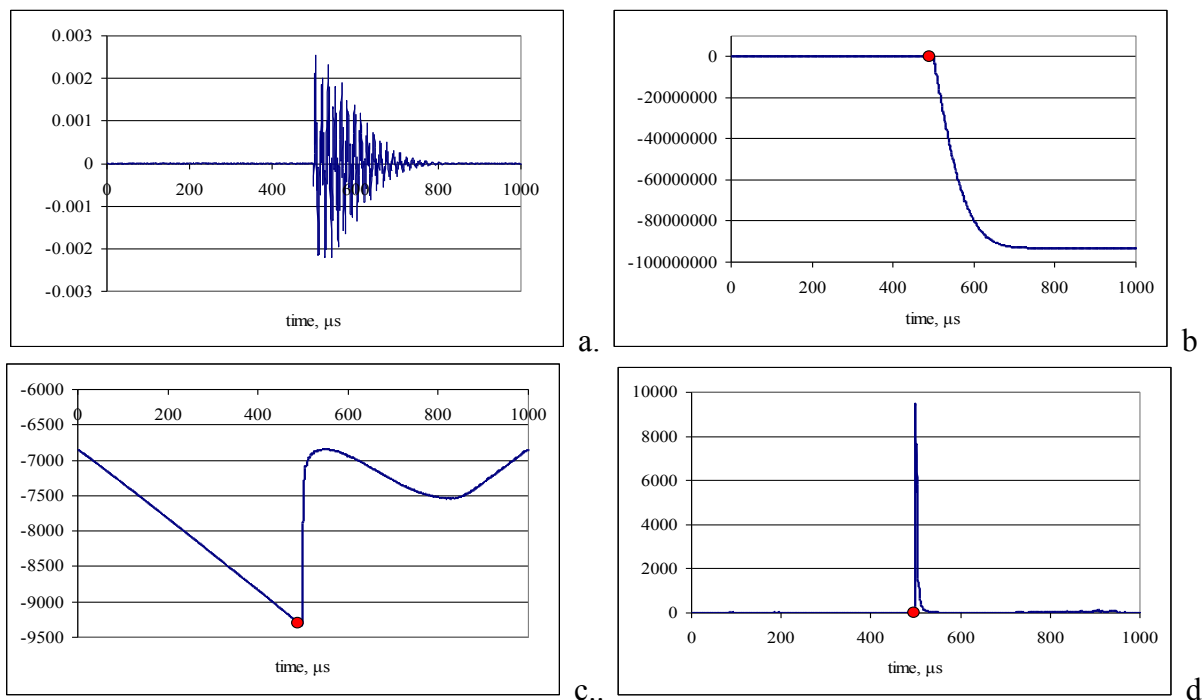


Fig. 1 a. Initial AE signal, b. MLE function (eq.3), c. AIC criterion, d. sixth order moment

3. ICI change point detection method

The ICI principle has been widely and successfully used in recent years for solving the most diverse problems from the field of data processing; for filtering [8-10], classification [7], and estimation of various signal parameters. In essence, the ICI principle is a universal method of change point determination, wherein the decision of changing any signal parameter is made by the absence of the intersection of confidence intervals constructed for this parameter at different sections of the considered signal.

The ICI method can be successfully used for determination of the signal arrival time, since the AE signal parameters, such as dispersion, high order moments, and frequency characteristics,

differ from the noise parameters. Therefore, the confidence intervals constructed for these parameters to the right and to the left of the point of signal origin will not intersect (Fig. 2).

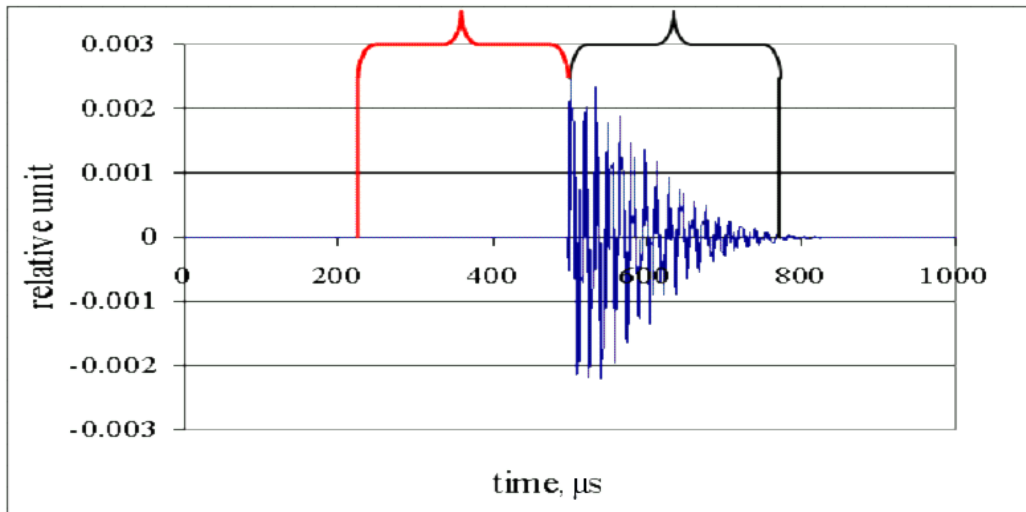


Fig. 2 Confidence intervals of informative parameters of the AE signal and the noise should not intersect.

The simplest usage of ICI method is the calculation of confidence intervals for the selected informative parameter in two sliding windows, and determination of the signal time-of-arrival from the absence of the intersection of intervals. The more complicated algorithm of ICI method consists in application of the cascade of nested windows with the different length (Fig. 3). For each fragment of the signal under study, the window with the optimal length is selected. The optimum window length is selected as follows. The informative parameter confidence intervals are calculated for all nested windows. Further, the windows of which the confidence interval doesn't intersect with the confidence interval of minimal window are excluded from consideration. In accordance with ICI principle the optimal window length is equal to the maximal length of other windows with the intersected confidence intervals. Thus, in the ICI method the sliding window with the variable length is realized. The length of window adapts for the change in signal properties.

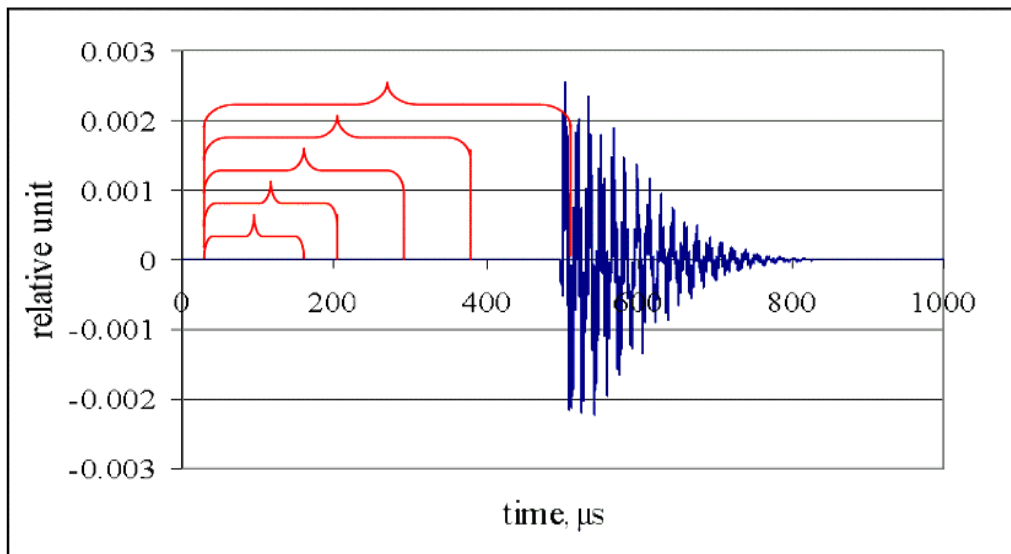


Fig. 3 The nested windows used in the ICI method.

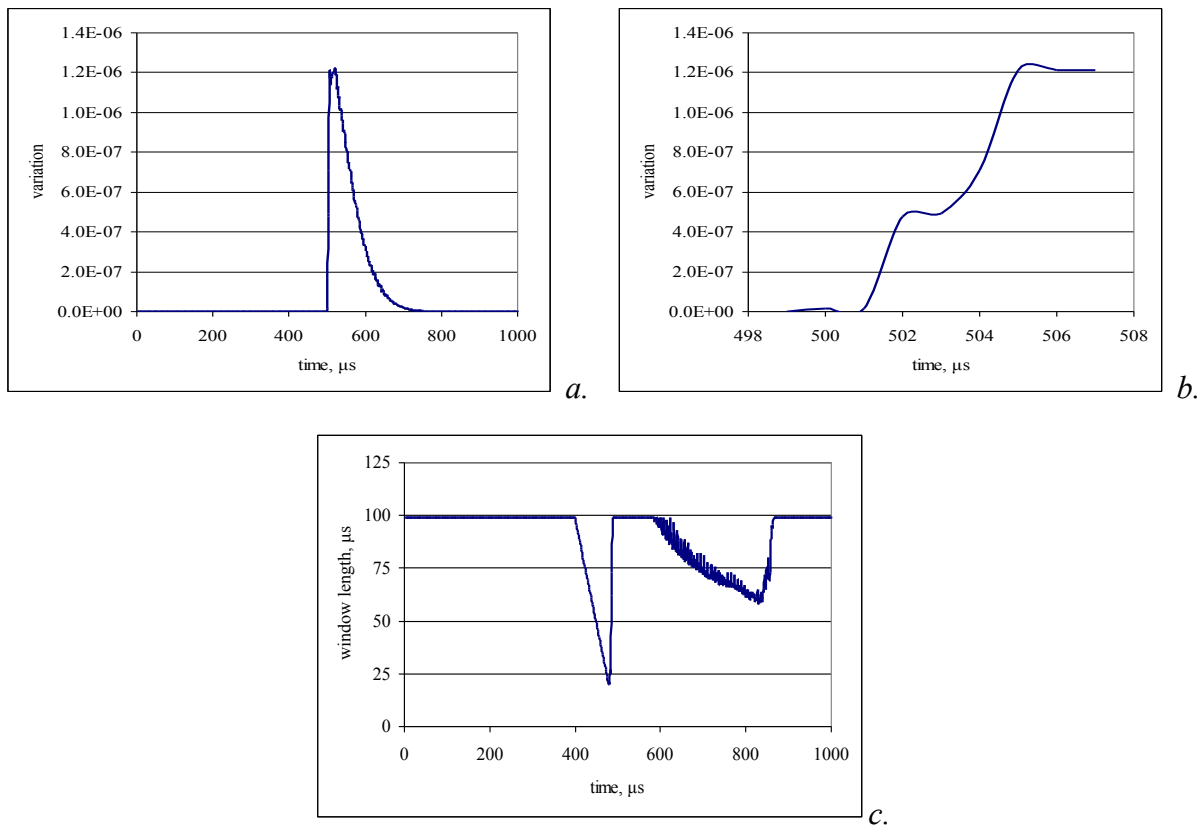


Fig. 4 a. AE signal variance calculated using sliding window with variable length, b. Initial part of variance rising, c. length of the sliding window.

If the signal part under consideration represents a stationary process, all confidence intervals, from the minimum window to the maximum one, will intersect, and according to the ICI principle the window optimum length will be equal to the maximum value. No intersection of the confidence intervals indicates that the signal fragment under study contains the change point, that is, in the case concerned, the start point of acoustic emission impulse. The optimum window length defines the distance to the change point, as the change point becomes closer, the window length decreases reaching the minimum value.

As described above, the ICI principle can be realized in combination with any signal processing algorithm, which requires that the informative parameter be calculated within the sliding window. As the most evident parameter distinguishing the noise and the impulse of acoustic emission is the dispersion, we will consider the ICI principle application for determination of the signal time-of-arrival from the change of dispersion in the cascade of nested windows of different length. Figure 4 shows that the values of the local variance of the AE signal are calculated using a sliding window of variable length. As seen in fig. 4c, in the neighborhood of the signal start point the length of sliding window starts to decrease, reaching its minimum value at the point corresponding to the arrival time of AE signal. Due to the adaptive changes in the size of the window, there is a sharp increase in the local value of dispersion. Duration of growth from zero to its maximum value is about 3 μs.

The ICI-based method is rested on various statistical approaches to determine the time-of-arrival of AE signal. It uses calculation of informative parameters in a sliding time window. In

addition, the ICI method uses elements of LTA/STA technique by comparing properties of signals in different time scales, and a comparison is made between values of informative parameters calculated using windows with the different lengths.

The disadvantage of this method is more calculations in comparison with the other methods for the signal arrival time determination. Its main advantages are adaptability, reducing an error in the signal time-of-arrival determination, and information redundancy. When using the ICI principle, the signal arrival time can be determined from the sharp increase of values of informative parameters in the concerned case of dispersion, and from the moment when the optimum size of window reaches a minimum value.

3.1 Selection of window length

Adequacy of results received when employing the ICI principle depends on a correct selection of its parameters – lengths of nested windows. The window length is an important parameter, since the maximum and minimum lengths of windows define accordingly the maximum and minimum scale of signal observation. Under selection of the observation scale, the error leads to the uncertainty of results.

With numerical experiments, within the limits of this paper, principles for selection of the maximum and minimum window length have been defined. The minimum length is selected with the help of a stationary noisy signal. As the stationary signal parameters do not vary with time, the minimum length of window should provide the intersection of confidence intervals with the window of any arbitrary large length. Otherwise, “false detections” of AE impulses are possible. The maximum length of window should not exceed the characteristic length of the AE signal. Alternatively, the significant errors in determination of the signal time-of-arrival or the AE signal omission can occur.

3.2 Application of ICI method in combination with HOS approach

The ICI method can be used in combination with any informative parameter, such as an average value, a variance, a median, and other statistical characteristics of signal. If an informative parameter of the high-order moments is used, application of the ICI principle can be considered as the improved HOS method, which allows for making an adaptive selection of the sliding window length. Since the result of HOS calculation depends on the time window length, the method of adaptive change of its length will allow for increasing the accuracy and validity of the HOS approach in determining the signal origin time.

In implementing the ICI principle, the calculation of confidence intervals of high-order moments presents a certain difficulty. In default of analytical formulas for the confidence intervals of the above fourth-order moments, we offer to use the bootstrap processing technique [11]. According to the bootstrap technique, a set of samples is formed on the basis of the main analyzed sample of signal values by eliminating some elements from it in a random manner. On the set of samples, a sampling empirical distribution of an informative parameter (for example, the sixth or eighth order moment) is constructed, while on the basis of the empirical distribution constructed is a sampling confidence interval.

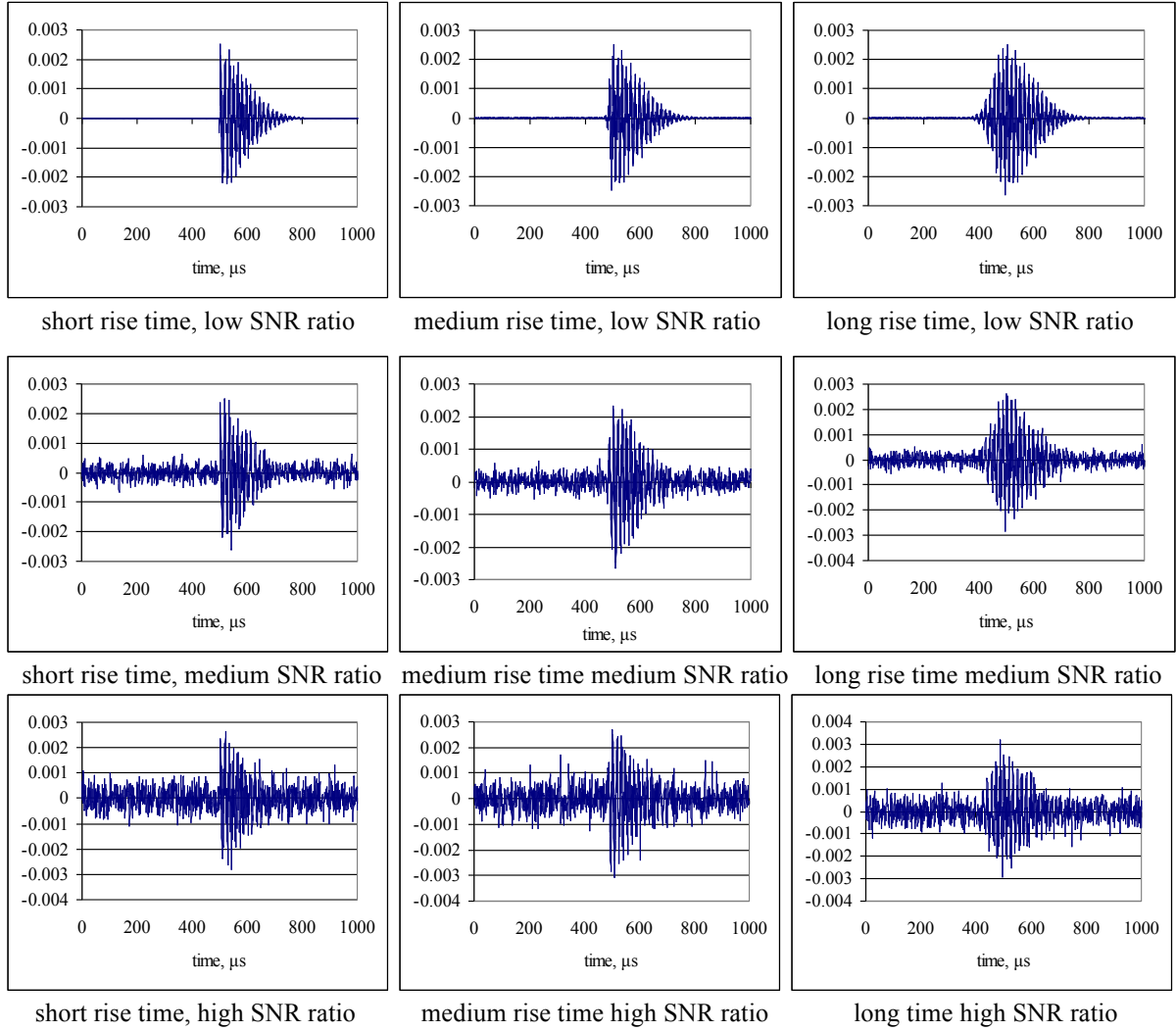


Fig. 5. Examples of model AE signals.

4. Arrival time estimation results

To compare the accuracy of signal time-of-arrival determination using different methods, a numerical experiment has been carried out wherein models of AE signals are presented by analytical formula (6),

$$s(t) = A(t-t_0) \sum_{i=1}^N \sin(\omega_i t + \varphi_i) + noise(t) \quad (6)$$

where $A(t)$ = nonsymmetrical envelope of harmonic process, and $noise(t)$ = Gaussian noise.

In model signals the parameters varied and had an effect on the accuracy of signal arrival time determination, such as signal rise time and SNR ratio. It is obvious that the high level of noise and long rise time interfere with the exact definition of rise time of AE signals. Figure 5 shows examples of the model signals. In total, about 500 signals were analyzed with the rise time from 1 to 100 readings and with SNR ratio from 50 to 2.

The arrival time for each of the signals was estimated by three methods: by a derivative of 6th order statistical function with the constant length of time window equal to 100 μ s (HOS approach), by a derivative of variation function with the variable length of time window (ICI

approach) and by means of the Akaike criterion. Figure 6 illustrates the error in determination of the signal time of origin by different methods.

Figure 6a illustrates the error in the method based on calculation of the sixth-order moment. As is obvious from the figure, the value of error depends on the signal rise time. The less is the rise time, the more exact is the determination of signal origin. The delay of estimated time-of-arrival as compared with the true value follows from the final length of time window that reduces the method sensitivity. However, it should be noted, that decrease in the time window length will not lead to increase in the method accuracy, since at the small window length "false extrema" appear, making the interpretation of result difficult and reducing the validity of this method.

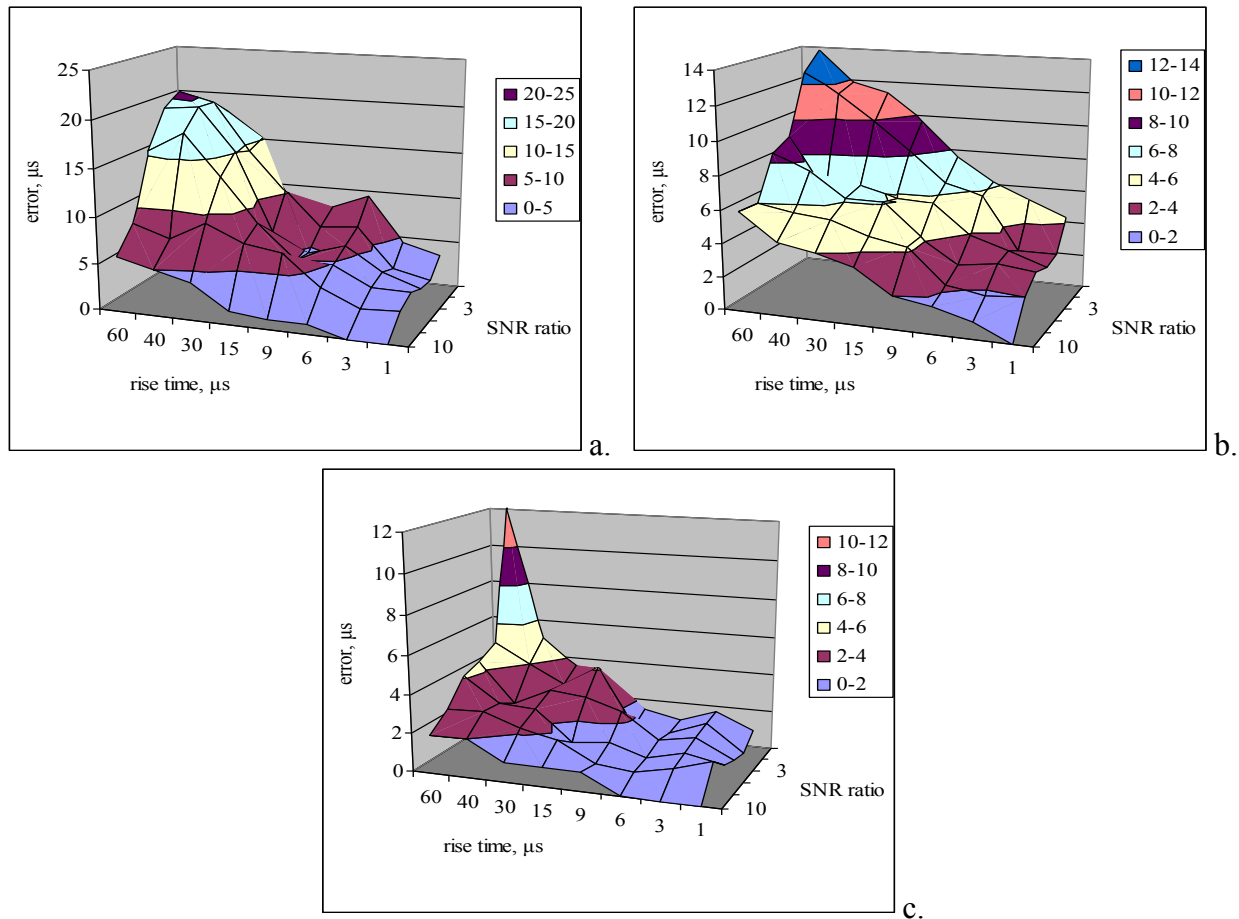


Fig. 6 Error in time-of-arrival determination by different methods depending on signal rise time and SNR ratio. a. HOS approach, b. ICI method on the basis of signal variance, c. AIC criterion.

If a variable-size sliding window is used in accordance with the ICI principle (Fig. 6b), the error in time-of-arrival determination decreases for signals with the long rise time at the cost of the window size adaptation to the shape of the signal analyzed. However, this case shows the SNR ratio dependence of the method accuracy not observed in the previous method.

The best results for signals of any shape can be obtained by using the Akaike criterion (Fig. 6c). The method accuracy is defined by the fact that the Akaike criterion reflects changes in spectral characteristics of the signal not associated directly with increase of signal values. Therefore, the errors in the signal time-of-arrival estimation, which are received by means of AIC do not depend directly on the shape of signals under analysis and on the level of noise containing in

them. In spite of the fact, that Akaike criterion shows the minimal error level, this method has disadvantages, which are not apparent from this study. The main disadvantage is that this method requires a preliminary choice of the region of interest, the signal part that contains the starting point of AE signal. The two-stage method implementation scheme makes on-line use difficult.

Table 1 shows the typical values of error of different methods.

Table 1. Arrival time error values

Arrival time error values, μs	HOS approach	ICI method	AIC criteria
for signals with a long rise time	13.7	8.1	3.6
for signal with a low SNR ratio	10.3	8.1	3.0
average error	7.8	4.7	2.1

5. ICI-based acoustic emission data classification.

5.1 Supervised and unsupervised classification.

A convenient way of AE event identification is clustering, that is a self-organized data structuring method. While being clustered, AE pulses are joined into groups on the ground of the distance measure, provided by some metric in feature space. If the clustering parameters are chosen successfully, AE events are clustered in such way, that each cluster corresponds to the particular certain process in testing structure, or to the certain process stage, that differs from other stages by its quantitative adjectives. After AE impulses are clustered, AE source that generated events in certain cluster could be identified by expert review.

Nevertheless, clustering is an out-of-control process, and even advanced methods could not guarantee data grouping correctness in line with physical model of ongoing processes. Clustering does not involve usage of information given, *a priori*, that is, on one hand, an advantage of method, because it can be implemented without such information, and, on the other hand, a disadvantage, as a priori information could not be taken into account even if it is available to the researcher.

Modern stage of AE testing development is confined to its possibilities enhancing, foremost by identification of testing structure internal processes. These processes could be material lapsing or destruction, or technological processes. Many investigations are being established in order to reveal the nature of AE as a result the dependence between AE parameters and mechanical properties of material is being stated. This dependence is a diagnostic model, used to estimate the state of testing structure, and this model might be taken into account as a priori information while classifying AE events.

Availability of a priori information involves usage of supervised classification methods. The distinction between supervised classification and clustering is a preliminary definition of all classes for supervised classification, while this stage is not performed during clustering. A priori information could be represented as a learning sample, consisting of typical for each class AE

events, or as a knowledge base with testing structure internal processes, which generate certain AE events.

AE data identification and classification special feature is a particular AE events ensemble (not single event or single quantitative criteria) characterizing each testing structure internal process. That is why classification objects are ensembles of AE events, detected during certain period, not single events. Such time sequence of events could characterize some process, or its stage, in testing structure. For each process stage AE events parameters are spaced under the particular distribution law that could be stated empirically in experimental research.

5.2 ICI – based classification algorithm.

Aforesaid allows to suggest an algorithm of AE data supervised classification that implements two main functions [1]: the first is detaching of time periods in AE events flow with certain empirical distribution laws of informative AE parameters, and the second is AE events classification within detached time windows.

Results of laboratory experiments on corrosion process are shown on Fig. 7. Due to shortness of experiment duration, this results are not of diagnostic concern, but it allows to present application of supervised classification algorithm introduced above.

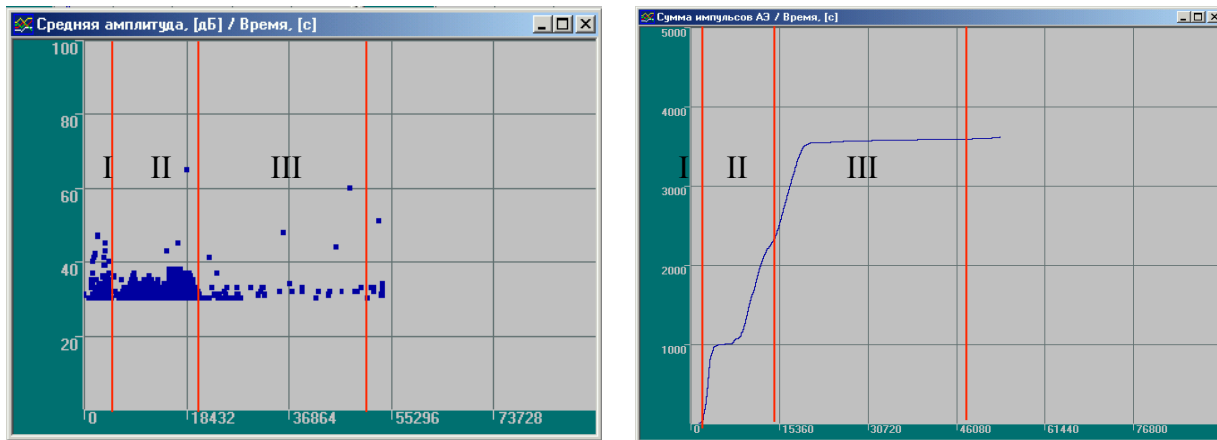


Fig. 7 AE data obtained during corrosion growth. a. AE amplitude, dB; b. AE event run-on.

For illustration purpose one channel data is chosen. Figure 7a contains amplitude vs. time, and Fig. 7b, AE events run-on vs. time during experiment. It is possible to detach three stages of corrosion process development; those are going along with quality changes of anode and cathode reactions behavior. Certain process stage is typified by amplitude and AE activity distribution (Fig. 8). Empiric two-dimensional distribution of this features $\varphi(A, Ev)$ could be used as a priori information for Bayesian classification [13].

5.2.1 ICI segmentation.

Supervised stage classification algorithm could be implemented in corrosion monitoring system. It contains two main stages: the first one is detaching of process stages while registering AE data, the second one is detached stages identification by Bayesian classification with properties statistical distributions typical for each stage as a priori information. Stages detaching by ICI method allows to effectively get stages of various continuance, from order of milliseconds to order of

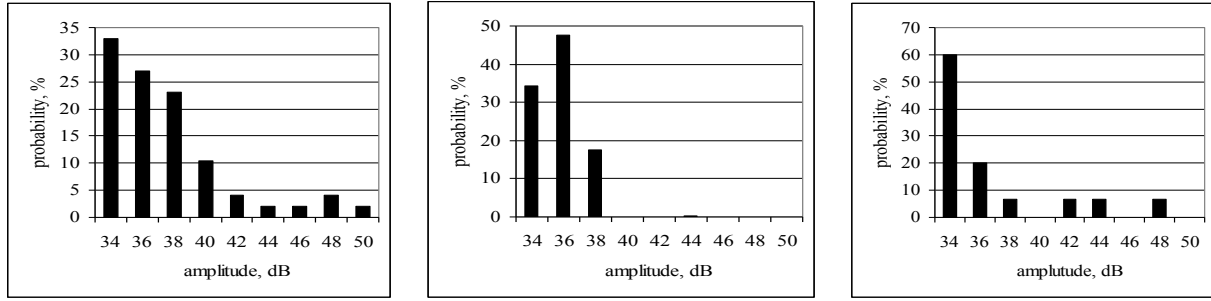


Fig. 8 AE impulse amplitude distribution for I, II and III stage of corrosion process.

hours. Several observation intervals of different scale should be chosen in accordance with ICI method [12]. The shortest interval duration is determined by expected shortest stage of the process. For segmentation purposes mean values and confidence intervals of informative features are calculated in each interval of specified durations. If all of get confidence intervals intersect, the whole observed interval corresponds to one process stage. On the contrary, if some confidence intervals do not intersect, it reveals existence of change point, corresponding to second stage start, within AE data.

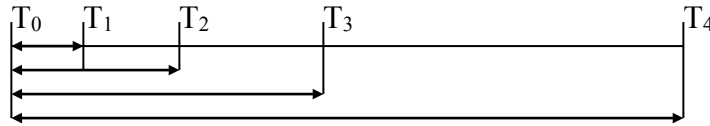


Fig. 9 Embedded time windows for ICI segmentation.

Four embedded time windows are shown on Fig. 9. Confidence intervals $\{A_{AE_T1}\}$, $\{A_{AE_T2}\}$, $\{A_{AE_T3}\}$, $\{A_{AE_T4}\}$ for informative AE data feature – amplitude A_{AE} – are calculated within each time interval. If intersection of minimal and maximal duration windows confidence intervals is not null $\{A_{AE_T1}\} \cap \{A_{AE_T4}\} \neq \emptyset$, then process stage has not changed within this time interval. If intersection of all windows confidence intervals does not occur, it means that time period from T_0 to T_4 contains more then one process stage. Change point is located in interval between end point of maximal window where confidence intervals do intersect and end point of first window, where they do not. For instance, if $\{A_{AE_T1}\} \cap \{A_{AE_T3}\} \neq \emptyset$ and $\{A_{AE_T1}\} \cap \{A_{AE_T4}\} = \emptyset$, then change point occurs in $[T_3, T_4]$. To find its location more preciously the procedure with time windows (obviously with smaller time scale) and confidence intervals should be repeated within found interval $[T_3, T_4]$.

5.2.2 Bayesian classification

After stage separation it is possible to perform data identification. In accordance with suggested algorithm stage identification could be implemented by Bayesian classification. By Bayes theorem, on account of empiric informative properties distributions the object belongs to one class $\{w_i\}$ with probability $p(w_i)$, where q_i = priory probability for each class, and $\varphi_i(A, Ev)$ = two-dimensional empirical distribution of informative features for i^{th} stage of investigated process:

$$p(w_i) = \frac{q_i \varphi_i(A, Ev)}{\sum_{j=1}^k q_j \varphi_j(A, Ev)}. \quad (7)$$

6. Conclusion

In this paper different methods for change point detection in AE data have been considered, and a comparative analysis of accuracy of different methods has been made. Furthermore, a new algorithm of signal arrival time determination and AE data classification based on ICI principle is offered. These methods allow for increasing the estimation and classification accuracy.

References

1. J.M. Rodgers, The “Use of a Floating Threshold for Online Acoustic Emission Monitoring of Fossil High Energy Piping”, AE Consulting, 1994
2. Karen M Holford and Mark Eaton, “Recent Advances in Acoustic Emission”, Proceedings of World Conference of Acoustic Emission, 2011, Beijing, pp. 58-66
3. P. Sedlak, Y. Hirose, S.A. Khan, M. Enoki and J. Sikula, “New Automatic Localization Technique of Acoustic Emission Signals in Thin Plates”. *Ultrasonics*, **49**, 2009, 254-62.
4. T. Lokajicek and K. Klima, “A First Arrival Identification System of Acoustic Emission (AE) Signals by Means of a Higher-Order Statistics Approach”. *Measurement Science and Technology*. **17**, 2006, 2461-66.
5. J. Chen, A.K. Gupta, Parametric statistical change point analysis. Birkhaeuser, 2000, 184p.
6. S.K. Yung and L.T. Ikelle, An Example of Seismic Time Picking by 3rd Order Bicoherence. *Geophysics*, **62**, 1997, 1947-1952
7. C. Alippi, G. Boracchi, M. Roveri, A just-in-time adaptive classification system based on the intersection of confidence intervals rule. *Neural Networks*, **24** (2011), pp. 791-800.
8. Vladimir Katkovnik, Karen Egiazarian, Ilya Shmulevich, “Adaptive varying window size selection based on intersection of confidence intervals rule ”, Signal Processing Laboratory, Tampere University of Technology, Tampere, Finland
9. P. Stachel, R. Zivanovic and P. Schegner, Enhanced Segmentation of Disturbance Records by Adaptive Thresholding, *Proceedings of Power Systems Computation Conference (PSCC'08)*, Glasgow, Scotland, July 2008.
10. V. Barat, D. Grishin, M. Rostovtsev, Detection of AE signals against background friction noise, *Journal of Acoustic Emission*, **29**, 2011, pp. 133-141
11. B. Efron and R.J. Tibshirani, An introduction to the bootstrap. Chapman and Hall, London, 1993.
12. Cesare Alippi, Giacomo Boracchi, Manuel Roveri: A just-in-time adaptive classification system based on the intersection of confidence intervals rule. *Journal Neural Networks*, **24**, Issue 8, October, 2011 Pages 791-800
13. A. Afifi, S. P. Azen. Statistical analysis: a computer oriented approach. Academic Press, 1972

Modeling of the Far-field Acoustic Emission from a Crack under Stress

Warida Ben Khalifa¹, Karim Jezzine¹, Sébastien Grondel², Gaëtan Hello³
and Alain Lhémercy¹

¹CEA, LIST, centre de Saclay, bât. 611, point courrier 120, 91191 Gif-sur-Yvette cedex, France

²Département OAE, IEMN, UMR CNRS 8520, Université de Valenciennes et du Hainaut Cambrésis, Le Mont Houy, 59313 Valenciennes Cedex 9, France

³IUP GSI-GEII-GM, LMEE, 40 rue du Pelvoux, CE1455 Courcouronnes, 91020 Evry Cedex, France

Abstract

Models for predicting the received time-domain waveform by a transducer as a result of an acoustic emission (AE) event are proposed. They aim at simulating AE examinations of large structures subjected to various stresses (e.g. mechanical loadings) in different domains (aerospace, pressure-vessel industries, etc.). The energy released by a crack under stress can propagate as guided waves in thin structures. In thick ones, the acoustic far field radiated by a crack under stress is dominated by the presence of Rayleigh wave. 2D models for guided waves in plate-like structures are proposed as well as 3D models for Rayleigh wave. A piston-like model is used to obtain the delivered voltage at the transducer output, whereas a formulation is proposed coupling models for the AE sources and for the propagation of guided or Rayleigh waves. Specifically, the coupling of the expression of the crack-opening displacement and Green's functions for Rayleigh wave is achieved through an integral formulation relying on the elastodynamic reciprocity principle. For the AE source model, a constant crack propagation velocity is considered. The exact analytical solution from a fracture-mechanics based model is used to obtain the crack opening displacement. Green's functions for Rayleigh wave are calculated using reciprocity considerations without the use of integral transform techniques. Predictions computed with this 3D model are compared to results from the literature for validation purpose on simple geometries and for a penny-shaped tensile crack. For thin structures, a similar coupling formulation based on the elastodynamic reciprocity principle has been derived, allowing the amplitudes of the possibly propagating guided modes at a given frequency to be predicted.

Keywords: Rayleigh wave, guided waves, AE sensor, crack propagation.

1. Introduction

Acoustic emission (AE) in a thick structure is dominated by the presence of Rayleigh wave in the far field. Indeed, Rayleigh wave decays as $1/\sqrt{r}$ whereas bulk waves decay as $1/r$. In a thin structure, the energy released by a defect under stress propagates as guided waves.

Different models have been developed to simulate AE from buried crack under stress. For instance, Harris and Pott [1] developed a Rayleigh wave AE model from a buried crack that predicts Rayleigh waves excited by the starting of a faulting event. The surface wave is expressed by an integral formulation relying on the elastodynamic reciprocity theorem. This formulation combines bulk waves emitted by the starting event and the Rayleigh wave components of the Green's tensor, calculated in [2] from the coupling between the P-wave and S-wave component (SV) polarized in the plane of incidence. The Rayleigh wave is then evaluated by means of the stationary phase technique and the particle velocity of the emitted wave is approximated near the Rayleigh wave arrival time.

A method using a seismic moment tensor approach [3] has been also adopted in the AE field to describe the damage processes since micro-damage and seismic rupture share the same source mechanism, at different time and length scales. The moment tensor method was used for describing different types of point sources and equivalent body forces for displacement discontinuities. Aki and Richards [3] summarized studies of elastic waves generated by seismic sources, where surface wave terms of Green's tensor have been calculated in cylindrical coordinates in the case of a vertically heterogeneous half space.

In the case of a thin structure, the prediction of guided waves emitted by a crack under stress was calculated by reciprocity considerations [7], a moment tensor method [4] or a finite element method [5]. Bogert [4] calculated the AE in plates using a seismic moment tensor method and Green's function. He compared different crack types and different propagation models. In addition, he studied the effect of the use of first and third order plate theory solutions on the AE signal. Achenbach [7] calculated the AE from a surface-breaking crack in a plate. The amplitudes of symmetric and antisymmetric modes were calculated separately by an integral formulation as a function of the crack opening displacement.

In this paper, AE from a crack under stress is obtained by applying the elastodynamic reciprocity principle. In the first part, we present a 3D AE model of Rayleigh wave emitted by a defect under stress. This model couples a fracture-mechanics source model and a Rayleigh-wave Green's function. Green's functions are obtained by applying the elastodynamic reciprocity principle following a method presented by Achenbach in [6]. The AE source model used in the coupling formulation is determined from the exact solution of the crack opening displacement as a function of the initial and final crack length and the crack propagation velocity.

In the second part we present a model for the AE of guided waves using an integral formulation method proposed by Achenbach [7]. This formulation combines a guided wave propagation model and a fracture mechanics source model. The modal solution is calculated by the SAFE method (semi analytical finite elements method).

The originality of the method lies in the fact that this formulation combines a propagation model and a fracture-mechanics source model with an arbitrary crack orientation. The work presented in this paper will be integrated in CIVA, a commercial NDE simulation package developed at CEA-LIST.

2. Rayleigh wave AE from buried crack in a thick structure

2.1 Application of the reciprocity theorem for computing the emitted Rayleigh wave

In a 3D geometry, the particle displacement associated to the Rayleigh wave emitted by a growing crack under stress can be calculated by applying the elastodynamic reciprocity principle. In the frequency domain, the elastodynamic reciprocity theorem for a body of volume V and surface S is written as:

$$\int_V [f_j^A u_j^B - f_j^B u_j^A] dV = \int_S [\tau_{ij}^B u_j^A - \tau_{ij}^A u_j^B] n_i dS \quad (1)$$

where n_i are the components of the outward normal to S , f_j , u_j and τ_{ij} are the components of body forces, displacements and stresses.

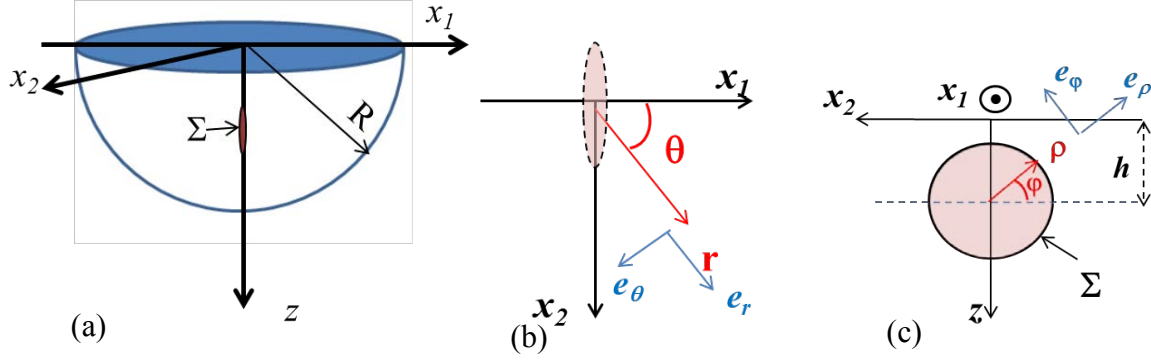


Fig. 1: (a) Geometry of the AE problem, (b) definition of the global cylindrical coordinate system (r, θ, z) and (c) geometry of the crack and definition of the local cylindrical coordinate system (ρ, φ, z)

We define state A as the solution of the acoustic emission problem and state B as the Rayleigh wave emitted by a point source applied in the x_k direction ($x_k = x_1, x_2$ or z). We apply the reciprocity equation to the region of the half space defined in Fig. 1 where Σ is the surface of the crack located in the (x_2, z) plane. The integrals over the free surface and the hemisphere of radius R as $R \rightarrow \infty$ vanish and the reciprocity equation leads to:

$$u_k^A(\xi) = \int_{\Sigma} [u_{i,k}^G(X, \xi) \tau_{ij}^A - u_i^A \tau_{ij,k}^G(X, \xi)] n_j(X) d\Sigma(X) \quad (2)$$

where $u_{i,k}^G$ and $\tau_{ij,k}^G$ denote the displacement and stress components of the Rayleigh Green's tensor, respectively. $X = (r, \theta, z)$ and $\xi = (r_0, \theta_0, z_0)$ are the positions of the observation point and of the source, respectively.

2.1.1 Rayleigh Green's function

The particle displacement of the Rayleigh wave generated by a point load in a cylindrical coordinate system can be calculated by applying the elastodynamic reciprocity theorem [6].

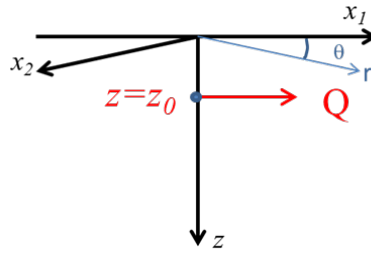


Fig. 2: Half space subjected to a point load at $z=z_0$.

The displacement components of Rayleigh wave generated by a point load of magnitude Q (Figure 2) applied at $z=z_0$ in the x_1 direction are:

$$u_{r,1} = \frac{k_R}{4i} \frac{Q V^R(z_0)}{I} V^R(z) \Phi'(k_R r) \cos \theta \quad (3)$$

$$u_{\theta,1} = \frac{k_R}{4i} \frac{Q V^R(z_0)}{I} V^R(z) \left(\frac{-1}{r k_R} \right) \Phi(k_R r) \sin \theta \quad (4)$$

$$u_{z,1} = \frac{k_R}{4i} \frac{QV^R(z_0)}{I} W^R(z) \Phi(k_R r) \cos \theta \quad (5)$$

where $\Phi'(x) = \frac{d\Phi}{dx}$. In the case of a point load of magnitude M in the x_2 direction, we have:

$$u_{r,2} = -\frac{k_R}{4i} \frac{MV^R(z_0)}{I} V^R(z) \Phi'(k_R r) \sin \theta \quad (6)$$

$$u_{\theta,2} = \frac{k_R}{4i} \frac{MV^R(z_0)}{I} V^R(z) \left(\frac{-1}{rk_R} \right) \Phi(k_R r) \cos \theta \quad (7)$$

$$u_{z,2} = -\frac{k_R}{4i} \frac{MV^R(z_0)}{I} W^R(z) \Phi(k_R r) \sin \theta \quad (8)$$

In the case of a point load of magnitude P in the z direction, we have:

$$u_{r,z} = -\frac{k_R}{4i} \frac{PW^R(z_0)}{I} V^R(z) \Phi_0'(k_R r) \quad (9)$$

$$u_{\theta,z} = 0 \quad (10)$$

$$u_{z,z} = -\frac{k_R}{4i} \frac{PW^R(z_0)}{I} W^R(z) \Phi_0(k_R r) \quad (11)$$

where

$$I = \int_0^\infty \left[T_{rr}^R(z) V^R(z) - T_{rz}^R(z) W^R(z) \right] dz. \quad (12)$$

Expressions of V^R , W^R , T_{rr}^R and T_{rz}^R are available in [6] and

$$\Phi(k_R r) = H_1^{(1)}(k_R r) \quad (13)$$

$$\Phi_0(k_R r) = H_0^{(1)}(k_R r) \quad (14)$$

$H_n^{(1)}$ is the first kind Hankel function of order n . The Rayleigh wave number is defined as:

$$k_R = \frac{k_t}{\eta_R} \quad (15)$$

where η_R is given using a standard approximate formula for the Rayleigh wave velocity by

$$\eta_R = \frac{0.87 + 1.12\nu}{1 + \nu} \quad (16)$$

where k_t is the shear wave number:

$$k_t = \omega \left(\frac{\rho}{\mu} \right)^{\frac{1}{2}} \quad (17)$$

ρ , ν , λ and μ denote the density of the medium, the Poisson ratio and the elastic Lamé constants

defined by: $\lambda = \frac{E\nu}{(1+\nu)(1-2\nu)}$ and $\mu = \frac{E}{2(1+\nu)}$, where E is the Young's modulus.

We express the Green tensor in cylindrical coordinates using the superposition principle:

$$G^R = \begin{pmatrix} u_{r,r} & u_{r,\theta} & u_{r,z} \\ u_{\theta,r} & u_{\theta,\theta} & u_{\theta,z} \\ u_{z,r} & u_{z,\theta} & u_{z,z} \end{pmatrix} \quad (18)$$

where

$$u_{r,r} = \frac{k_R}{4i} \frac{V^R(z_0)}{I} V^R(z) \Phi'(k_R r), \quad (19)$$

$$u_{\theta,r} = 0, \quad (20)$$

$$u_{z,r} = \frac{k_R}{4i} \frac{V^R(z_0)}{I} W(z) \Phi(k_R r), \quad (21)$$

$$u_{r,\theta} = 0, \quad (22)$$

$$u_{\theta,\theta} = \frac{k_R}{4i} \frac{V^R(z_0)}{I} V(z) \left(\frac{-1}{rk_R} \right) \Phi(k_R r) (1 - 2(\sin \theta)^2) \quad (23)$$

$$u_{z,\theta} = 0. \quad (24)$$

We neglect terms attenuating with distance more rapidly than $1/\sqrt{r}$ and we use the asymptotic expansion for Hankel functions in the next calculations. These approximations were used by Aki and Richards in [3].

2.1.2 Acoustic emission source

We assume that the crack is a surface of displacement discontinuity. In the case of tensile circular crack of radius a loaded by uniform pressure σ on its faces, the crack opening displacement (COD), expressed from the complex solution issued from fracture mechanics in the local cylindrical coordinate system (ρ, φ, x_1) can be looked up in text books. One has:

$$\Delta u_1(\rho) = 2 \frac{4(1-\nu^2)\sigma}{\pi E} \sqrt{a^2 - \rho^2} \quad (25)$$

2.1.3 AE from tensile crack

Equation (2) can be written as:

$$\begin{aligned} u_k^A(\xi) &= \int_{\Sigma^+} \left[u_{i,k}^G(X, \xi) \tau_{ij}^A - u_i^A \tau_{ij,k}^G(X, \xi) \right] n_j(X) d\Sigma^+(X) \\ &+ \int_{\Sigma^-} \left[u_{i,k}^G(X, \xi) \tau_{ij}^A - u_i^A \tau_{ij,k}^G(X, \xi) \right] n_j(X) d\Sigma^-(X) \end{aligned} \quad (26)$$

Σ^+ and Σ^- are respectively the crack surface on $x_1 = 0^+$ and $x_1 = 0^-$.

In the case of a tensile stress (mode I), the displacement at the surface of the crack in the global cylindrical coordinate system is:

$$u_\theta^A = u_1^A \quad (3)$$

Eq. (26) can be written as:

$$u_k^A(\xi) = \int_{\Sigma^+} \left[-\Delta u_\theta^A \tau_{\theta\theta,k}^G(X, \xi) \right] n_\theta(X) d\Sigma^+(X) \quad (4)$$

where $\Delta u_\theta^A = u_\theta^A \Big|_{x_1=0^+} - u_\theta^A \Big|_{x_1=0^-}$ (5)

The integral over the surface Σ^+ can be written as:

$$u_k^A(\xi) = \int_{\Sigma^+} -\Delta u_\theta^A \left(\lambda \frac{\partial u_{r,k}^G(X, \xi)}{\partial r} + (\lambda + 2\mu) \frac{1}{r} \left(\frac{\partial u_{\theta,k}^G(X, \xi)}{\partial \theta} + u_{r,k}^G(X, \xi) \right) + \lambda \frac{\partial u_{z,k}^G(X, \xi)}{\partial z} \right) d\Sigma^+(X) \quad (30)$$

As $u_{i,k}^G(X, \xi) = u_{k,i}^G(\xi, X)$,

$$u_k^A(\xi) = \int_{\Sigma^+} -\Delta u_\theta^A \left(\lambda \frac{\partial u_{k,r}^G(\xi, X)}{\partial r} + (\lambda + 2\mu) \frac{1}{r} \left(\frac{\partial u_{k,\theta}^G(\xi, X)}{\partial \theta} + u_{k,r}^G(\xi, X) \right) + \lambda \frac{\partial u_{k,z}^G(\xi, X)}{\partial z} \right) d\Sigma^+(X) \quad (31)$$

We simplify the expression by considering a single dipole acting at the center of the crack, *i.e.* at $X = (0, 0, h)$ (see Fig. 1):

$$u_k^A(\xi) = \left(\lambda \frac{\partial u_{k,r}^G(\xi, h)}{\partial r} + (\lambda + 2\mu) \frac{1}{r} \left(\frac{\partial u_{k,\theta}^G(\xi, h)}{\partial \theta} + u_{k,r}^G(\xi, h) \right) + \lambda \frac{\partial u_{k,z}^G(\xi, h)}{\partial z} \right) \times \int_0^a \int_0^{2\pi} -\Delta u_1^A \rho d\rho d\varphi. \quad (6)$$

2.2 Simulation and comparison with literature

We assume that the crack diameter evolves from $l_0 = 1$ mm to $l = 5$ mm at a velocity $V = 2000$ m/s during $T = 0.8$ μ s, and we consider a sampling frequency $F_e = 50$ MHz. We define r_j and t_n as:

$$r_j = jV\Delta t \quad (33)$$

$$t_n = t_0 + n \frac{1}{F_e} \quad (34)$$

j varies from 0 to $J/2$, and n varies from 0 to N where:

$$\Delta t = 1/F_e \quad (35)$$

$$N = \frac{T}{\Delta t} \quad (36)$$

$$J = \frac{l}{V\Delta t} \quad (37)$$

Eq. (25) can be discretized as follows:

$$\Delta u_1(r_j, t_n) = 2\sigma \frac{4(1-\nu^2)}{\pi E} \sqrt{((l_0 + nV\Delta t)/2)^2 - r_j^2}, \text{ for } r_j \leq (l_0 + nV\Delta t)/2 \quad (38)$$

and

$$\Delta u_1(r_j, t_n) = 0, \text{ for } (l_0 + nV\Delta t)/2 \leq r_j \leq l/2 \quad (7)$$

We take the Fourier transform of the COD given by eq. (38) to obtain the displacement field of the emitted Rayleigh wave in the frequency domain given by eq. (32). The displacement field in the time domain is then obtained using the inverse Fourier transform of eq. (32).

We have simulated the displacement field of the Rayleigh wave emitted by a defect evolving at different velocities V . Figure 3 presents the particle velocity of the emitted wave in the time domain obtained by deriving eq. (32) in the time domain.

The amplitude of the emitted wave increases and the arrival time decreases when the crack propagation velocity increases. This observation can be explained by analyzing eq. (40). The displacement of the emitted wave in the time domain is obtained from the convolution of the spatial derivative of the Green's function with the integral of the COD over the crack faces, as

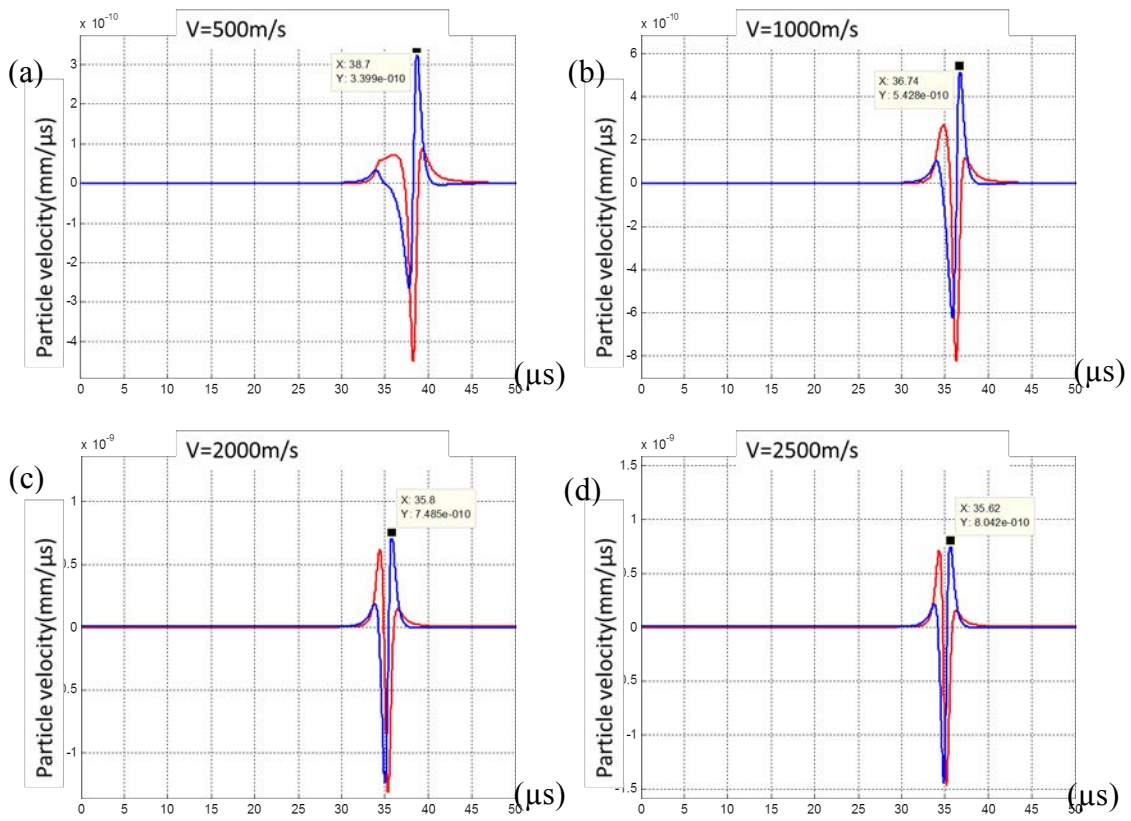


Fig. 3: Rayleigh wave particle velocity emitted by a crack under 200 MPa, normal component in red and radial component in blue. (a) $V= 500$ m/s, (b) $V= 1000$ m/s, (c) $V= 2000$ m/s and (d) $V= 2500$ m/s.

$$S = \int_0^a \int_0^{2\pi} -\Delta u_1^A \rho d\rho d\varphi \quad (40)$$

Figure 4 presents the quantity S in the time domain. The main contribution arises at a time corresponding to the end of the emitting process, which is inversely proportional to V .

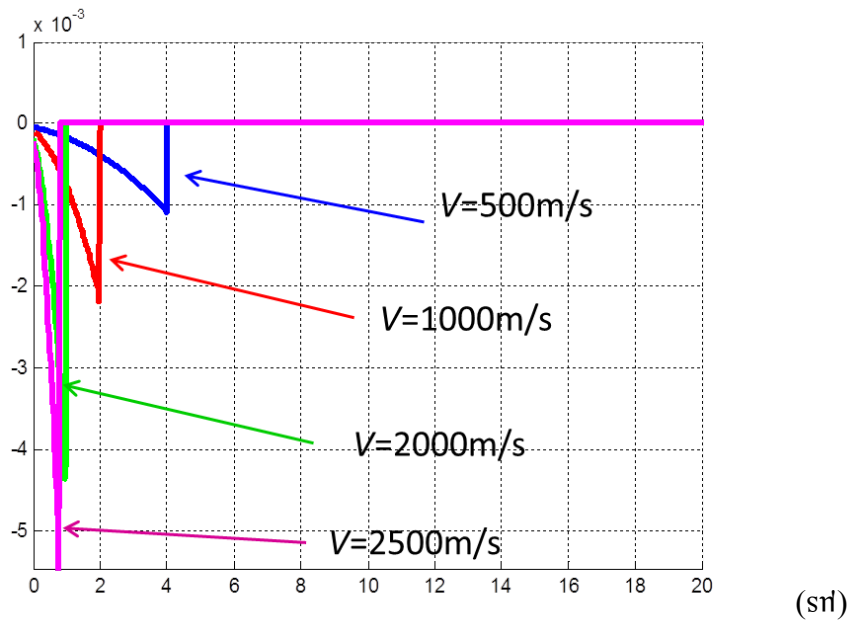


Fig. 4: Integral of the COD over the crack faces for $V= 500$, 1000 , 2000 and 2500 m/s.

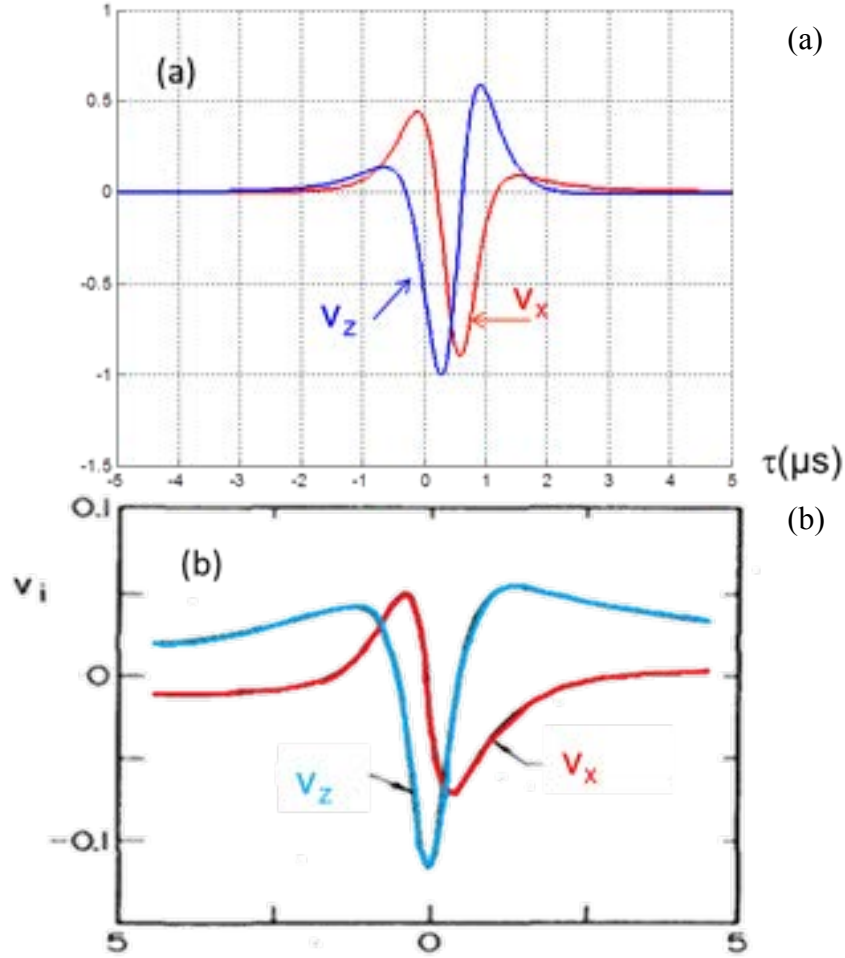


Fig. 5: Comparison of the Rayleigh wave acoustic emission normalized particle velocity obtained by our method (a) with a result from [1] (b).

We have compared our results with a result from literature [1] on Fig. 5. There is a good agreement between the two results. Differences can be explained by the assumptions used in the two models. Our integral formulation combines directly the COD and the Rayleigh wave Green's functions. This is not the case for Harris and Pott model [1]. Their integral formulation combines the body waves emitted from the crack approximated at the Rayleigh wave arrival time and Rayleigh wave Green's functions.

Our results presented in Fig. 5(a) are obtained by using the crack opening displacement at all points of the crack obtained from a fracture-mechanics exact model whereas results from the literature [1] in Fig. 5(b) present the velocity of the emitted wave from the starting of faulting event considering only the crack tip velocity.

3. Simulation of the reception by a piston-like transducer model

We have simulated the delivered voltage by an AE sensor using a piston-like model. In fact, only the sensitivity to the normal component of the particle velocity of the emitted wave has been considered. In this case, the delivered voltage can be written as [8]:

$$E = 2\pi \int_S m(r_0) v_z(r_0) dr_0. \quad (8)$$

We consider a crack propagating at a velocity $V = 2500$ m/s. The crack diameter is evolving from 1 mm to 5 mm under 200 MPa. The receiver is an AE sensor of radius $R=5$ mm and a constant sensitivity $m(r_0) = m_0 = 600$ V/m/s. The AE sensor is positioned at a distance $r = 100$ mm away from the epicenter of the crack. Figure 6 illustrates the geometry of the AE problem and the reception by an AE sensor.

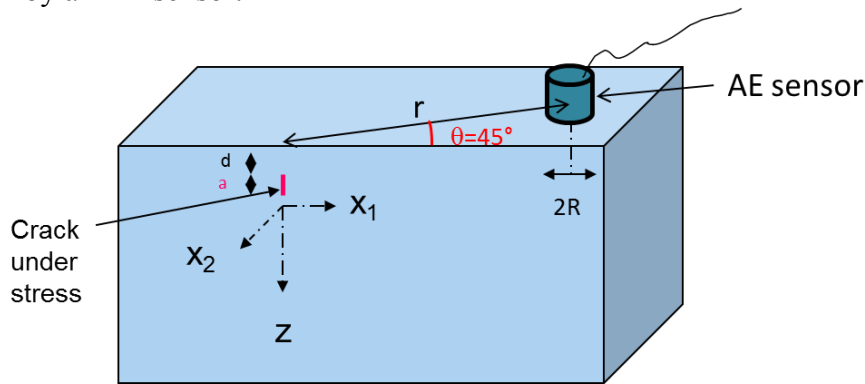


Fig. 6: Reception by an AE sensor.

The delivered voltage has been simulated using the method described in Sec. 2 and integrating the particle velocity over the sensor surface. Figure 7 presents the received waveform by the sensor, which results from the integration of the Rayleigh normal particle velocity over the sensor area.

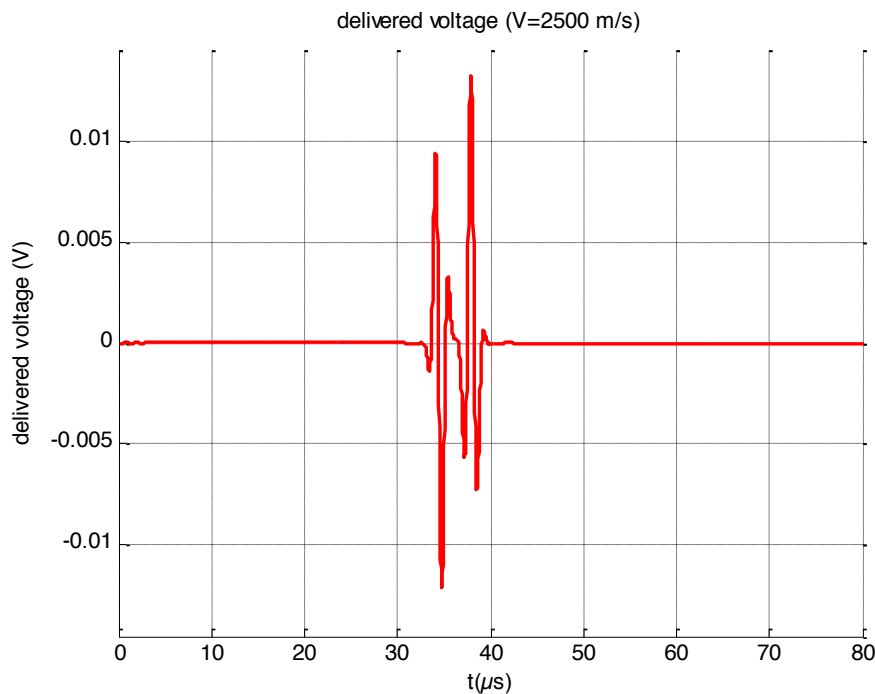


Fig. 7: Delivered voltage by an AE sensor.

4. Guided waves AE from buried crack in thin structure

This paragraph describes the AE in a plate by a crack of arbitrary orientation. The geometry of the problem is shown on Fig. 8. Guided modes generated by a crack under stress are calculated again by applying the elastodynamic reciprocity theorem following a method presented by Achenbach [7]. The acoustic field emitted by a crack under stress is now composed of both

symmetric and antisymmetric modes [7], whose displacement and stress fields can be written as follows:

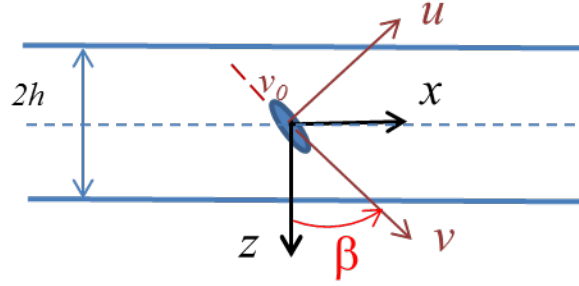


Fig. 8: Geometry of the acoustic emission problem in thin structure.

$$u_x^A = \pm i \left[\sum_{m=0}^{\infty} A_m^a V_a^m(z) e^{\pm i k_m x} + \sum_{m=0}^{\infty} A_m^s V_s^m(z) e^{\pm i k_m x} \right] \quad (9)$$

$$u_z^A = \left[\sum_{m=0}^{\infty} A_m^a W_a^m(z) e^{\pm i k_m x} + \sum_{m=0}^{\infty} A_m^s W_s^m(z) e^{\pm i k_m x} \right] \quad (10)$$

$$\tau_{xx}^A = \pm i \left[\sum_{m=0}^{\infty} A_m^s T_{xx}^{sm}(z) e^{\pm i k_m x} + \sum_{m=0}^{\infty} A_m^a T_{xx}^{am}(z) e^{\pm i k_m x} \right] \quad (11)$$

$$\tau_{xz}^A = \left[\sum_{m=0}^{\infty} A_m^a T_{xz}^{am}(z) e^{\pm i k_m x} + \sum_{m=0}^{\infty} A_m^s T_{xz}^{sm}(z) e^{\pm i k_m x} \right] \quad (12)$$

where k_m is the wave number of the m^{th} guided mode. Expressions of V_a^m , V_s^m , W_a^m , W_s^m , T_{xx}^{am} , T_{xx}^{sm} , T_{xz}^{am} and T_{xz}^{sm} are available in [7].

4.1 Application of the reciprocity theorem for the calculation of the emitted guided waves

We select state A as the solution of the acoustic emission problem presented by equations (42) to (45) and state B, as a virtual symmetric or antisymmetric wave.

4.1.1 Amplitude of symmetric modes:

We select state B as the n^{th} symmetric mode propagating in the positive x_1 direction. Displacement and stress components can be written as:

$$u_x^B = i V_s^n(z) e^{-i k_n x} \quad (13)$$

$$u_z^B = W_s^n(z) e^{-i k_n x} \quad (14)$$

$$\tau_{xx}^B = T_{xx}^{sn}(z) e^{-i k_n x} \quad (15)$$

$$\tau_{xz}^B = i T_{xz}^{sn}(z) e^{-i k_n x} \quad (16)$$

$$\tau_{zz}^B = T_{zz}^{sn}(z) e^{-i k_n x} \quad (17)$$

We apply the reciprocity relation to the region surrounding the crack defined in Fig. 9. In the absence of body forces, equation (1) may be written as:

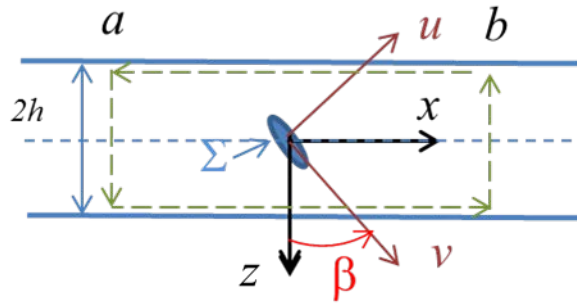


Fig. 9: Contours of integration used in the integral formulation.

$$\int_S [\tau_{ij}^B u_j^A - \tau_{ij}^A u_j^B] n_j dS = 0. \quad (18)$$

We define J_1 as the integral along the line $-h \leq z \leq h$, $x = a$, J_2 along $-h \leq z \leq h$, $x = b$ and J_3 , over Σ . Integrals along the free surfaces $z = \pm h$ vanish. J_1 may be written as:

$$J_1 = -\int_{-h}^h [\tau_{xx}^B u_x^A + \tau_{xz}^B u_z^A - \tau_{xx}^A u_x^B - \tau_{xz}^A u_z^B] dz \quad (19)$$

We replace displacement and stress components by their expressions from equations (42) to (45) and (46) to (50), so that integral J_1 can be expressed as follows:

$$J_1 = \sum_{m=0}^{\infty} i A_m^s [I_{mn}^s + I_{nm}^s] + \sum_{m=0}^{\infty} i A_m^A [I_{mn}^{as} + I_{nm}^{as}] e^{i(k_m - k_n)a} \quad (20)$$

where:

$$I_{mn}^{as} = \int_{-h}^h [T_{xx}^{sm}(z) V_s^n(z) - T_{xz}^{am}(z) W_s^n(z)] dz = 0 \quad (21)$$

and

$$I_{mn}^s = \int_{-h}^h [T_{xx}^{sm}(z) V_s^n(z) - T_{xz}^{sm}(z) W_s^n(z)] dz \quad (22)$$

As the summation produces non zero result only for $n = m$, the integral can be simplified as follows:

$$J_1 = 2i A_n^s I_{nn}^s \quad (23)$$

The contribution from $x = b$ leads to:

$$J_2 = 0 \quad (24)$$

Integration over the crack surface can be written as:

$$J_3 = \int_{\Sigma} [\tau_{uu}^A u_u^B + \tau_{uv}^A u_v^B - \tau_{uu}^B u_u^A - \tau_{uv}^B u_v^A] d\Sigma \quad (25)$$

J_3 is calculated from the contribution of the two line elements that define Σ , as follows:

$$J_3 = \int_{v_0}^{v_0+l} [\tau_{uu}^A u_u^B + \tau_{uv}^A u_v^B - \tau_{uu}^B u_u^A - \tau_{uv}^B u_v^A] \Big|_{u=0^+} dv + \int_{v_0+l}^{v_0} [\tau_{uu}^A u_u^B + \tau_{uv}^A u_v^B - \tau_{uu}^B u_u^A - \tau_{uv}^B u_v^A] \Big|_{u=0^-} dv \quad (26)$$

We express the integral over the crack faces as a function of the displacement and stress discontinuities:

$$J_3 = \int_{v_0}^{v_0+l} [\Delta \tau_{uu}^A \tilde{V}_s^n(0, v) + \Delta \tau_{uv}^A \tilde{W}_s^n(0, v) - \tilde{T}_{uu}^{sn}(0, v) \Delta u_u^A - \tilde{T}_{uv}^{sn}(0, v) \Delta u_v^A] dv \quad (27)$$

where

$$\tilde{V}_s^n(0, v) = u_u^B(0, v) \quad (28)$$

$$\tilde{W}_s^n(0, \nu) = u_\nu^B(0, \nu) \quad (29)$$

$$\tilde{T}_{uu}^{sn}(0, \nu) = \tau_{uu}^B(0, \nu) \quad (30)$$

$$\tilde{T}_{uv}^{sn}(0, \nu) = \tau_{uv}^B(0, \nu) \quad (31)$$

The amplitude of symmetric waves can be obtained from the condition that the total contour integral must vanish [eq. (51)]. One gets:

$$A_m^S = \frac{-i}{2I_{mm}^S} \int_{\nu_0}^{\nu_0+l} \left[\Delta\tau_{uu}^A \tilde{V}_s^n(0, \nu) + \Delta\tau_{uv}^A \tilde{W}_s^n(0, \nu) - \tilde{T}_{uu}^{sn}(0, \nu) \Delta u_u^A - \tilde{T}_{uv}^{sn}(0, \nu) \Delta u_\nu^A \right] d\nu \quad (32)$$

4.1.2 Amplitude of antisymmetric modes:

Similarly, the amplitude of antisymmetric modes can be obtained by selecting the n^{th} antisymmetric mode as a virtual wave for state B.

$$A_m^A = \frac{-i}{2I_{mm}^A} \int_{\nu_0}^{\nu_0+l} \left[\Delta\tau_{uu}^A \tilde{V}_a^n(0, \nu) + \Delta\tau_{uv}^A \tilde{W}_a^n(0, \nu) - \tilde{T}_{uu}^{an}(0, \nu) \Delta u_u^A - \tilde{T}_{uv}^{an}(0, \nu) \Delta u_\nu^A \right] d\nu \quad (66)$$

where

$$I_{mm}^A = \int_{-h}^h \left[T_{xx}^{am}(z) V_a^n(z) - T_{xz}^{am}(z) W_a^n(z) \right] dz \quad (33)$$

$$\tilde{V}_a^n(0, \nu) = u_u^B(0, \nu) \quad (34)$$

$$\tilde{W}_a^n(0, \nu) = u_\nu^B(0, \nu) \quad (35)$$

$$\tilde{T}_{uu}^{an}(0, \nu) = \tau_{uu}^B(0, \nu) \quad (36)$$

$$\tilde{T}_{uv}^{an}(0, \nu) = \tau_{uv}^B(0, \nu) \quad (37)$$

4.2 Simulation and comparison with literature

We consider an isotropic plate of 3 mm thickness and Poisson's ratio $\nu = 0.33$. We have simulated the surface strain of the first symmetric (S_0) and antisymmetric mode (A_0) emitted by a vertical surface-breaking tensile crack as shown in Fig. 10 and compared our simulation with a result from literature [5] obtained from a finite element method (FEM). We assume that the time dependence of the crack opening displacement is a unit Heaviside step function.

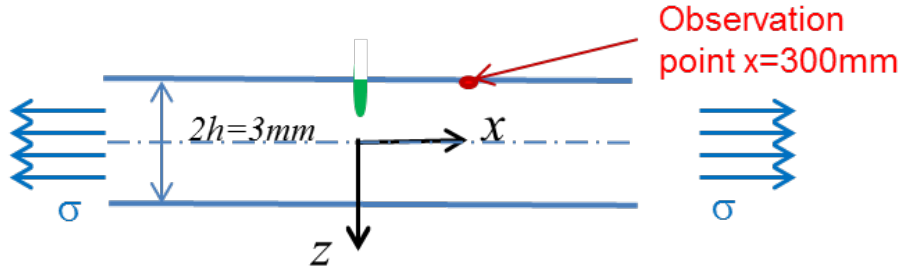


Fig. 10: Surface-breaking tensile crack.

The modal solutions were calculated by the semi-analytical finite element method (SAFE) [9]. Figure 11(a) presents the filtered surface strain for modes S_0 and A_0 generated by the surface-breaking tensile crack using a Gaussian window with 250 kHz center frequency and band-

width of 350 kHz (measured at -40dB points). The comparison of our model with the finite element results [5] shows a good agreement.

We have also performed a parametric study giving the mode amplitudes as a function of the crack depth. Results obtained with our model have also been compared with finite element results taken from [5]. A qualitative agreement between both models is observed as A_0 shows the highest amplitude for the most of the considered crack depths and S_0 amplitude increases slowly with the crack depth. Nevertheless, our results seem to underestimate the amplitude of the S_0 mode in comparison to finite element ones.

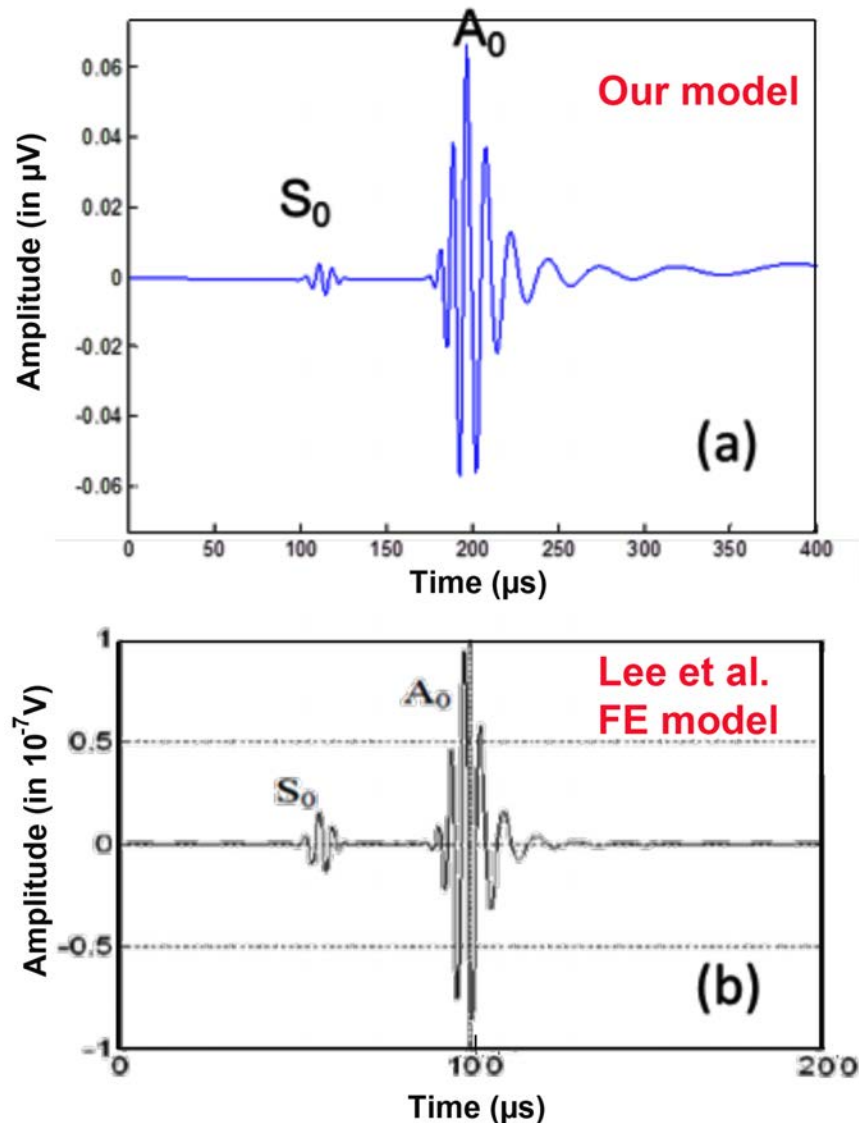


Fig. 11: Surface strain transient response from a surface-breaking crack of 1.5-mm depth at a distance $x=300\text{mm}$ from the plane of the crack (a) our result, (b) Result in [5] using a finite element model.

5. Conclusion

A formulation coupling an acoustic emission source model and a propagation model has been proposed in the case of thick structures in order to predict the acoustic emission from the propa-

gation of a crack under stress and to quantify the influence of the crack propagation velocity on the Rayleigh wave AE signals. Comparisons of our simulated results with results from the literature showed satisfying agreement even if the two models are different and not based on the same approximations and hypotheses. A similar formulation has been derived for guided wave and compared with results from the literature. In addition, the reception by an AE sensor has been simulated using a piston-like model considering only the sensitivity to the normal component of the emitted wave particle velocity.

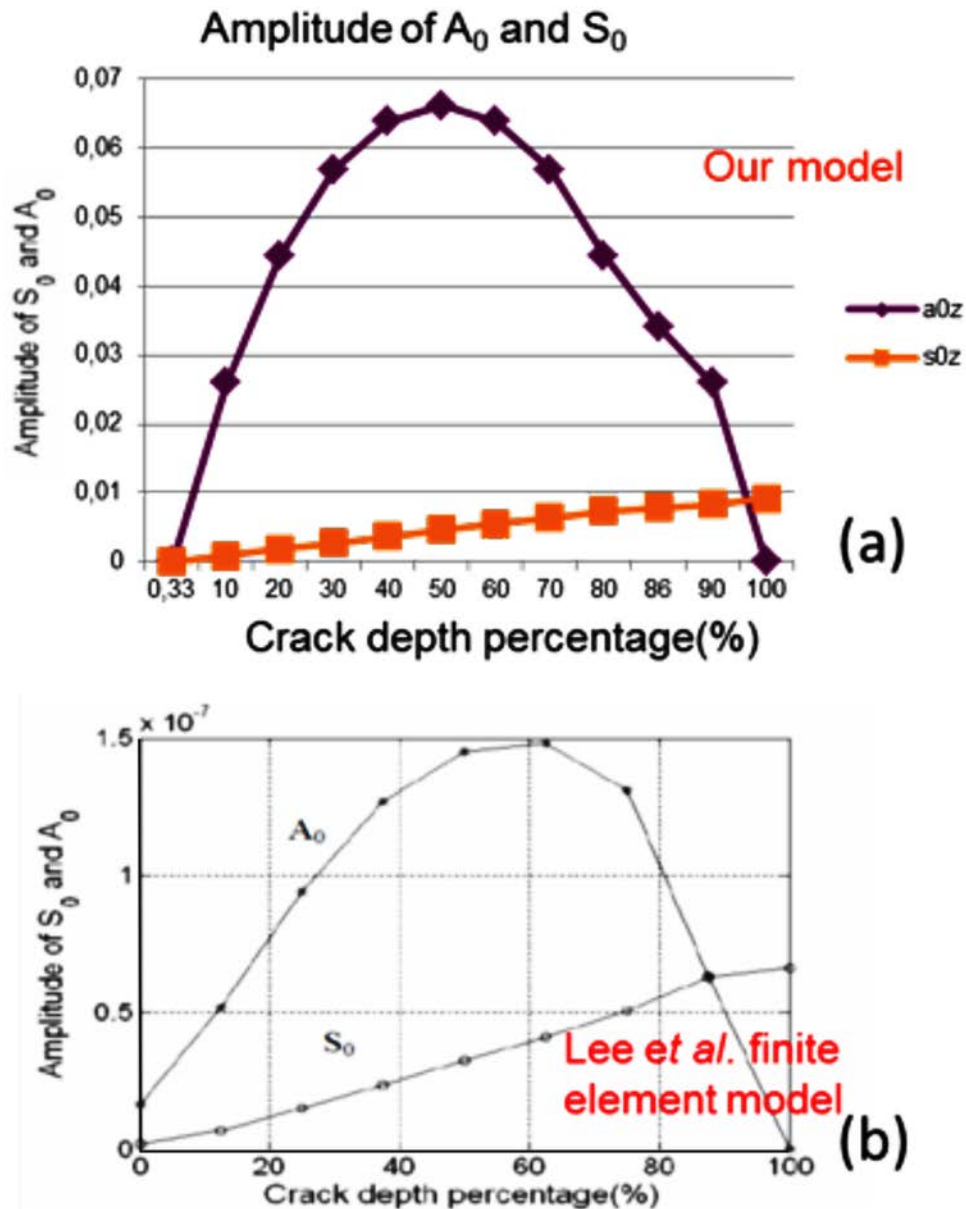


Fig. 12 : Amplitude of the first symmetric and antisymmetric emitted modes as a function of the surface-breaking crack depth at a distance $x= 300$ mm from the plane of the crack (a) our result, (b) Result in [5] using a finite element model.

Acknowledgements

The work presented in this paper was partly supported by ANR (French National Research Agency) for the project MACSIM - ANR-08-COSI-005-01.'

References

1. G P Harris and J Pott, 'Surface Motion Excited by Acoustic Emission from a Buried Crack', *J. Appl. Mech.* Vol 51, pp 77-83, March 1984.
2. J D Achenbach , A K Gautesen and H McMaken, 'Ray methods for waves in Elastic solids', Pitman publishing INC, 1982.
3. K Aki and P G Richards, 'Quantitative Seismology', University Science Books, 2002.
4. Ph B Bogert, 'Transient Waves from Acoustic Emission Sources in Isotropic Plates Using a Higher Order Extensional and Bending Theory', Doctoral Thesis, North Carolina State University, 2010.
5. C K Lee, J J Scholey, P D Wilcox, M R Wisnom, M I Friswell, B W Drinkwater, 'Guided Wave Acoustic Emission from Fatigue crack growth in Aluminium Plate', *Advanced Material Research.* Vol 13-14, pp 23-28, 2006.
6. J D Achenbach, 'Reciprocity in elastodynamics', Cambridge University Press, 2003.
7. J D Achenbach, 'Acoustic Emission from a Surface-breaking Crack in a Layer under Cyclic Loading', *J. Mech. Mat. and Struct.*, Vol 4, No 4, pp 649-657, 2009.
8. L Goujon and J C Baboux, 'Behaviour of acoustic emission sensors using broadband calibration techniques', *Meas. Sci. Technol.* Vol 14, pp 903-908, 2003.
9. K Jezzine, 'Approche modale pour la simulation de contrôle non destructifs par ondes élastiques guidées', doctoral thesis, Université de Bordeaux I, 2007.

Primary Calibration of Acoustic Emission Sensors by the Method of Reciprocity, Theoretical and Experimental Considerations

Thomas Monnier¹, Seydou Dia², Nathalie Godin² and Fan Zhang³

¹ Université de Lyon, INSA-Lyon, LVA EA 677, F-69621 Villeurbanne, France

² Université de Lyon, INSA-Lyon, MATEIS UMR 5510, F-69621 Villeurbanne, France

³ CETIM; Senlis, France

Abstract

This paper is focused on the calibration of acoustic emission (AE) sensors by means of the reciprocity method. Therefore, the problem of the reciprocity criterion in the case of ultrasonic waves in solid is addressed. This latter criterion is well established and widely used for the calibration of electro-acoustic transducer. However, and despite that the first papers have been published forty years ago, its application in the case of ultrasonic wave in solids now raises a number of discussions in the community of acoustic emission. To start with, we present a review of the concept of reciprocity since its origin in electromagnetism to its application to electro-acoustic transducers. We follow a critical analysis on the validity of the reciprocity theorem in the case of AE sensors. Next, a new aperture function will be presented, reconsidering the classical assumption of a constant sensitivity of the transducer's sole by achieving an experimental estimation of its actual vibration using contactless laser interferometry. Finally, an original method for shear wave calibration of AE sensors will be presented.

Keywords: AE sensors, calibration, reciprocity method, aperture effect.

1. Introduction

The reciprocity method is based upon the reciprocity theorem. In the field of electrical networks the following statement can translate the reciprocity theorem: "a given e.m.f. in the p -th branch will produce the same current in the q -th branch of a circuit as the same e.m.f. in the q -th branch would produce in the p -th branch" [1]. As a consequence of the principle of electro-mechanical equivalence, this theorem is applied to ultrasonic transducer.

McLean [2] was the first to propose a reciprocity-based technique for the calibration of electroacoustic transducers. The reciprocity technique has since then been developed and extended to carry out primary calibration of microphones, accelerometers and ultrasonic sonar transducers. It appears that this technique can be developed further to carry out calibration of transducers operating on an isotropic solid medium [3], and in particular for acoustic emission sensors as first proposed formally by Hatano [4].

The basic principle of the reciprocity calibration method is that three transducers, all of which are uncalibrated, are used as emitter and receiver successively. The basic experimental arrangement is shown in Fig. 1. The conditions of validity of this method are defined as follow:

1. AE sensors are assumed linear and reversible.
2. The coupling of the sensors must be reproducible (defined materials, constant thickness). [5]
3. The propagation medium is free of interference referred to the wave (attenuation, reflections, conversions, etc.).

As shown in Fig. 1, reciprocity calibration process consists of three steps. Each step involves two sensors: the emitter and the receiver. At each step current absorbed by the emitting sensor and voltage across the receiving sensor are measured. The sequence is repeated for the three AE sensors pairs.

Finally, computation performed on the measured voltages and currents yields the sensitivities of all three sensors. The reciprocity calibration process is relatively straightforward. The receiving sensitivity of sensor 2 can be written as:

$$M_2 = \sqrt{\frac{HE_{12}E_{23}I_{31}}{I_{12}I_{23}E_{31}}}$$

where H is the reciprocity parameter. H is frequency dependent and is defined as the ratio M/S for a given transducer. M is the receiving sensitivity of the transducer, and S the emitting sensitivity of the transducer. In this paper we review the theoretical basis of the reciprocity parameter and reciprocity calibration of AE sensors.

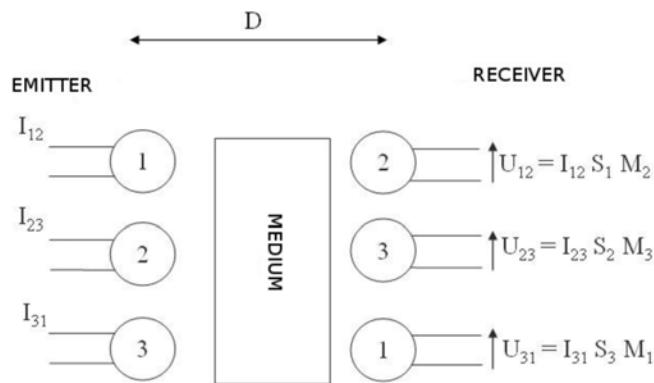


Fig. 1: Methodology of reciprocity calibration of AE sensors.

Using this methodology, we obtain the reception sensitivity curve of the sensor to be calibrated with reproducibility on the sensitivity to the resonant frequency of the order of 2dB, with some limitations:

- Only the surface wave response is available in the frequency band of 50 kHz to 1 MHz.
- Some difficulties remain to calibrate sensors low frequencies.

For what concerns Rayleigh waves calibration, our results are consistent with those obtained by the original work of Hatano [6] and those recently shown by other research teams [7-9].

This article is divided into three parts. The first section discusses the question of reciprocity criterion in the case of AE sensors. Then follows the introduction of a new aperture function. Finally, an original method for shear wave (S-wave) calibration of AE sensors will be presented.

2. The reciprocity parameter

To give a proper definition of the reciprocity parameter is not a simple task. Generally, the reciprocity parameter is defined by either quoting an equation or quoting a definition, neither of which gives any physical insight into the meaning of the parameter. The literature on acoustic reciprocity calibration is also confusing although the measurement procedure is relatively straightforward.

To our knowledge the only theoretical work on the reciprocity method in the case of acoustic transducer is owed to Bobber [10]. He showed that the reciprocity parameter can be expressed as the ratio of acoustic *volume velocity* to the *mean pressure* at the face of the transducer. He also proved that the reciprocity parameter is actually the transfer admittance of the medium. He deduced from that, reciprocity parameter for: (i) spherical wave, (ii) plane wave, (iii) acoustic couplers, (iv) diffused sound, (v) tubes.

Bobber's conclusions are relevant to the case of transducers totally immersed in fluid medium. Since in standard operation AE sensors are stuck to the external surface of solid medium, how reciprocity parameter can be derived?

Table 1: Expressions of reciprocity parameter

Medium	Geometrical arrangement	Reciprocity Parameter H
Fluid	Spherical wave	$\frac{2d}{\rho f}$
	Plane wave	$\frac{2A}{\rho C}$
Solid	Rayleigh wave (R-wave)	$\left[\frac{K2\pi f(1+\sigma)k}{E} \left(\frac{2}{\pi kd} \right)^{1/2} \right]^{-1}$ $k = 2\pi f \left[\frac{2(1+\sigma)\rho}{E} \right]^{1/2} Y$
	Longitudinal wave (L-wave)	$\frac{dE(1-\sigma)}{2f(1+\sigma)(1-2\sigma)}$
	Shear wave (S-wave)	$\frac{dE}{4f(1+\sigma)}$

d is the propagation path distance, ρ is the material density, f is the calibration frequency, C is the compliance of coupling medium, K and Y are numerical solutions to Lamb's equation for specific values of Poisson's ratio, σ is the material Poisson's ratio, E is Young's modulus.

Hill and Adams [5] gave the answer to that question, by defining AE measurement procedure in terms of transfer functions. Dimensional analysis of the equations obtained yields that the medium is excited by a *surface velocity*. Hill and Adams noted that this observation is consistent with the transformation of electrical to acoustical quantities. Most of the theories relating to the calibration of ultrasonic transducers in fluid use *volume velocity* for the source output and *acoustic pressure* as the received quantity. However, Hill and Adams have shown that other input and output quantities are possible. Among these possibilities, the ratio *Velocity/Force* is indicated for AE sensors. As a result R-wave reciprocity parameter is obtained from the basic theory of surface wave propagation on a semi-infinite half space – Lamb [11]. Hill and Adams showed that considering a point force driving the surface derives the reciprocity parameter, yielding vertical velocity a distance d away. This definition is the starting point for the finite element simulations we conducted in our laboratory. However, the results are not consistent with

the conclusions of Hill and Adams. Further investigations are currently conducted. Various expressions of the reciprocity parameter according to the type of wave and the propagation medium are summarized in Table 1, all coming from Hill [12] except for S-wave. In that particular case, we simply propose to adopt the same definition as for L-waves but replacing the expression of longitudinal wave velocity by the shear wave velocity.

So far we have pointed to the question of the definition of the reciprocity parameter. Now, it is necessary to make some special remarks about the fulfillment of the reciprocity criterion in the case of AE sensors.

The case of bulk waves (e.g. L-wave) is handled in Bobber's paper. In that case the reciprocity criterion is met for AE sensors. In the case of surface wave (R-wave), a phenomenon, called the aperture effect, makes possible the existence of frequencies, at which the sensor response is null. Thus, for these cut-off frequencies, the sensor can emit but cannot hear anything. Consequently reciprocity is not met.

Bobber defined a general reciprocity parameter for electro-acoustical transducer. Hill and Adams have defined the reciprocity parameter for AE sensors calibration. Although AE sensors in L-wave configuration met the reciprocity criterion, it is not the case for R-wave configuration due to aperture effect. In the next section we shall go into more details about the aperture function. First, a classical approach will be used to define it. Next, a new aperture function based on an original approach will be presented.

3. The aperture effect

Let us consider a wave, propagating on the surface of a propagation medium. An AE sensor is positioned on the propagation medium. When the sensor is submitted to the surface wave, the normal vibration velocity at each point of its face is not uniform. It can be derived that the voltage across the sensor is proportional to the average vibration velocity. Such average depends on the wavelength of the incident wave and the sensor diameter. This phenomenon, called the aperture effect, acts as a filter applied to the R-wave sensitivity of the sensor. The complex value of this filter in the frequency domain is called the aperture function. It has been shown that removing the aperture effect by combining the sensor's aperture function with its R-wave sensitivity yields its L-wave sensitivity.

To illustrate this phenomenon, Fig. 2 shows the displaced surface of a sine wave, for which the average movements gives zero values for the sensor's response at certain cut-off frequencies. For AE sensor larger than the wavelengths of interest, the classical recommendation to overcome this limitation simply consists in choosing sensing elements with a diameter as small as other constraints allow.

It has been shown [13, 14] that the voltage output of AE transducers is proportional to the normal surface velocity since these sensors have a dominant response to particle motion normal to the surface. Moreover, in Rayleigh wave-based reciprocity calibration, the sensor is mainly submitted to a normal vibration velocity because the fluid couplant strongly attenuates the in-plane component of the vibration [15]. A first approach to the calculation of the aperture function is provided by the ASTM [16], which consider that the sensor is hit by an ideal plane wavefront. Goujon et al. [17] refined the calculation of the aperture function by considering the case of a circular wavefront. In this paper, the size and shape of the sensor surface as well as the

inhomogeneity of its sensitivity will be taken into account to estimate the output voltage. The influence of the size and shape of the sensor on the output voltage is given by the following integral:

$$U = \frac{1}{S} \iint_S \omega(r) m(r) dS \quad (1)$$

where:

U is the open circuit voltage across the receiving sensor,

S the active surface of the sensor,

ω is the normal velocity of a point of the sensor surface,

m is the sensitivity of a point placed at the distance r from the center of the sensor's surface.

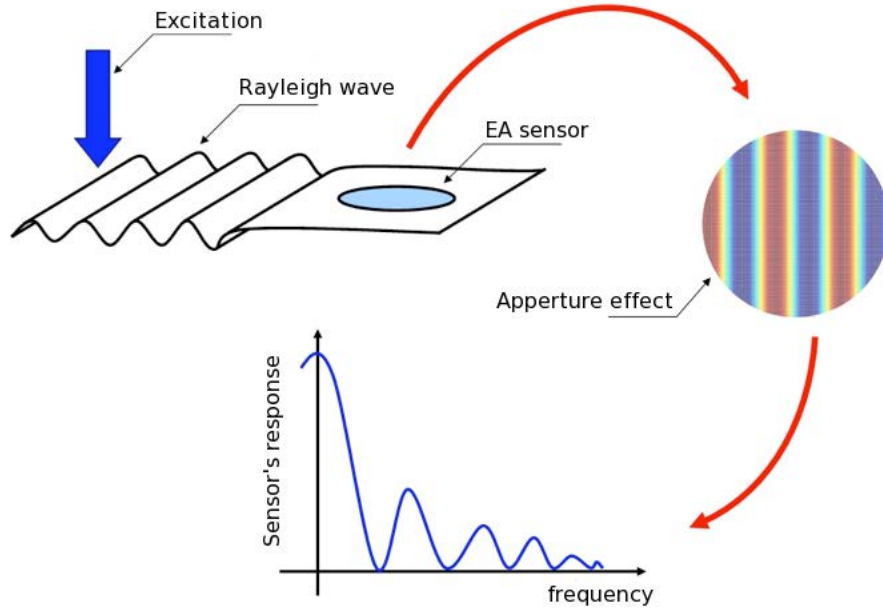


Fig. 2: Illustration of the aperture effect.

In the literature, a common assumption is to consider that $m(r)$ is uniform over the whole surface of the sensor. Consequently, in the case of cylindrical wave of amplitude A , the hypothesis $m(r) = m_0$ leads (1) to become:

$$U = \frac{m_0 A}{S} \iint_S \frac{e^{-jk_R r_0}}{\sqrt{r_0}} r dr d\theta \quad (2)$$

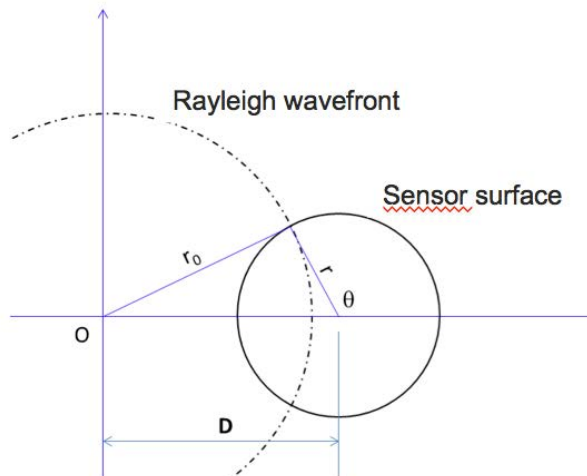


Fig. 3: Geometry used in the calculation of the aperture function of the AE sensor.

where r_0 , r and D are defined in Fig. 3, which shows the geometry used in the calculation of the aperture function.

The receiving sensitivity of a sensor in Rayleigh waves M_R is defined as the ratio between the open circuit voltage of the sensor U and the normal component of the Rayleigh-wave velocity at the center of the sensor ($r_0=D$), which can be written as:

$$\omega(D) = \frac{A}{\sqrt{D}} e^{-jk_R D} \quad (3)$$

Then, the expression of M_R is:

$$M_R = \frac{m_0}{S} \sqrt{D} e^{jk_R D} \iint_S \frac{e^{-jk_R r_0}}{\sqrt{r_0}} r dr d\theta \quad (4)$$

With $k_R = 2\pi f / c_R$ the Rayleigh wavenumber, c_R being the velocity of Rayleigh wave in steel, it follows immediately:

$$M_R = m_0 F(f, S) = m_0 \frac{\sqrt{D} e^{jk_R D}}{S} \iint_S \frac{e^{-jk_R r_0}}{\sqrt{r_0}} r dr d\theta \quad (5)$$

which defines the aperture function F of the sensor.

The aperture function depends not only on the geometry of the sensor as well as on the frequency and geometry of the incident wavefront, but also on spatial variations of the sensitivity of sensor surface. Indeed, one can find in [17] mentions of experimental deviations between the experimental and theoretical aperture function, which could be attributable to the false assumption of uniform sensitivity m_0 . Considering that the sensitivity of the sensor depends on the amplitude and phase of the free-end vibration of the sensor's surface, the new expression of the Rayleigh-wave sensitivity is thus:

$$M_R = \frac{\sqrt{D} e^{jk_R D}}{S} \iint_S m(r) \frac{e^{-jk_R r_0}}{\sqrt{r_0}} r dr d\theta \quad (6)$$

Here is made the assumption that the disc-shaped transducer exhibits an axisymmetric vibration profile, that is to say that $m(r)$ is only function of the distance r from the center of the sensor's surface. Thus the complex expression of $m(r)$ is:

$$m(r) = m_0 \psi(r) e^{-j\varphi(r)} \quad (7)$$

where m_0 is the maximum sensitivity to normal vibration of the sensor surface and φ the phase shift of this vibration. $\psi(r)$ is a real number comprised between 0 and 1 so that eqn. (5) holds with:

$$F(f, S) = \frac{\sqrt{D} e^{jk_R D}}{S} \iint_S \psi(r) \frac{e^{-j(\varphi(r)+k_R r_0)}}{\sqrt{r_0}} r dr \quad (8)$$

In the next section we present the approach that has been used to experimentally determine $\psi(r)$ and $\varphi(r)$, which are subsequently used in the computation of the new aperture function $F(f, S)$.

3.1 Experimental setup

A laser scanning velocimeter was setup in order to determine the vibration profiles of the AE transducer as well as the vibration of the surface of a steel block used for Rayleigh-wave sensor calibration. These measurements will allow combining the actual sensor sensitivity with the

theoretical diffraction effects due to the size of the transmitting and receiving areas, with regards to the wavelength of the Rayleigh waves.

As reminded in (1), the AE sensor voltage is the average of the normal velocity under its surface, weighted by its receiving sensitivity M_R defined in (4). M_R being referred to the Rayleigh wave vibration velocity at the center of the face of the sensor, it is independent from the amplitude A of the incoming wave. The sensitivity $m(r)$ has the same dimension as M_R as seen in (6) and the aperture function F is dimensionless. In comparison with the definition of (5), the dimensionless parameter $\psi(r)$ and $\varphi(r)$ are the only new parameters to be determined for the calculation of the new aperture function F defined in (8). Indeed, only the relative behavior of the sensor surface has to be determined in order to improve the representativeness of the aperture function since quantities such as the amplitude of the Rayleigh wave or the magnitude of the sensitivity m_0 do not appear in (8).

The laser interferometer detects the quasi-punctual normal velocity of the sensor, which is let to freely vibrate in air at atmospheric pressure. It is here assumed that the vibration behavior measured under free-boundary condition is representative enough of the one that could be expected when the transducer is coupled to the block with the fluid couplant. This question was addressed by measuring the vibration of the sensor when coupled to a glass block, which be more representative of the boundary conditions of the calibration method, but the laser measurement through the transparent block did not show a sufficient signal to noise ratio.

Thus, extrapolating the *relative* sensitivity of the sensor to be proportional to the experimentally determined normal velocity vibration profile allows recalculating the complex aperture function of the transducer with a non-uniform sensitivity $m(r)$.

3.1.1 Contactless measurement of the sensor's surface sensitivity

The acquisition of the velocity profile of the sensor surface was performed using a Polytec OFV 3001 laser velocimeter equipped with an OFV 303 head. The AE sensor used is a typical commercial PAC $\mu 80$ sensor from Euro Physical Acoustics driven by an Agilent 33250A arbitrary waveform generator. For each point of the surface, the time signal is digitized by a Tektronix TDS3012B oscilloscope and stored in a personal computer for post processing (Fig. 4).

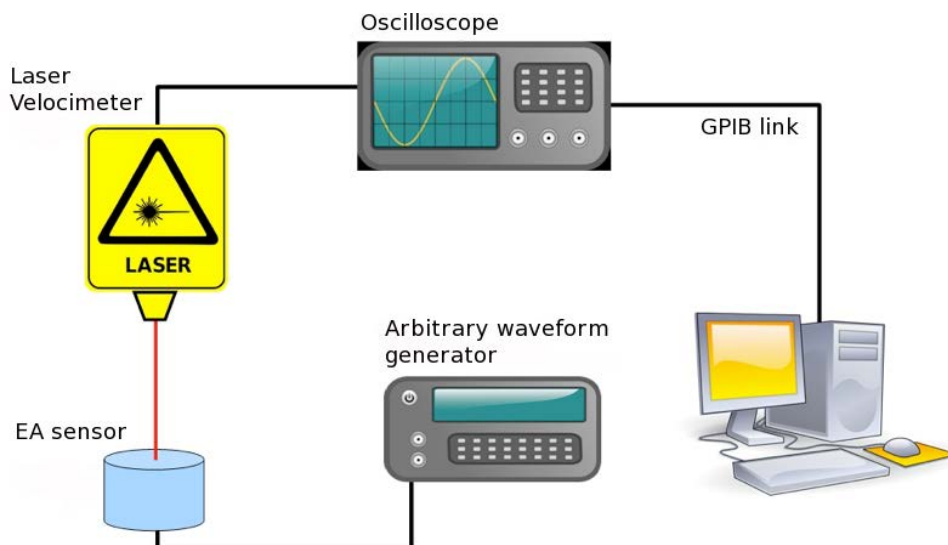


Fig. 4: Measurement of the AE sensor normal velocity.

The normal velocity of each point of the sensor surface is measured with 100- μm spacing, when the electrical input is a sinusoidal excitation at 300 kHz. Fig. 5a represents the peak-to-peak amplitude, in mm/s, of the velocity while Fig. 5b represents its phase relative to the one measured at the center of the sensor. The dashed pink line shows the outer circumference of the 9.5 mm diameter transducer. It can be seen that the local velocity at the sensor surface is far from being uniform, contrary to the classical assumption of a piston-like behavior. The center area vibrates out-of-phase and with much higher velocity than that the outer ring of the sensing surface. It has a diameter close to the 6.5 mm diameter of the piezoceramic, which is enclosed inside the transducer.

The magnitude and phase of the vibration of the surface being rather axisymmetric, it is decided to extract their profiles under this assumption, which meets the supposition made about the sensor being axisymmetric in (7).

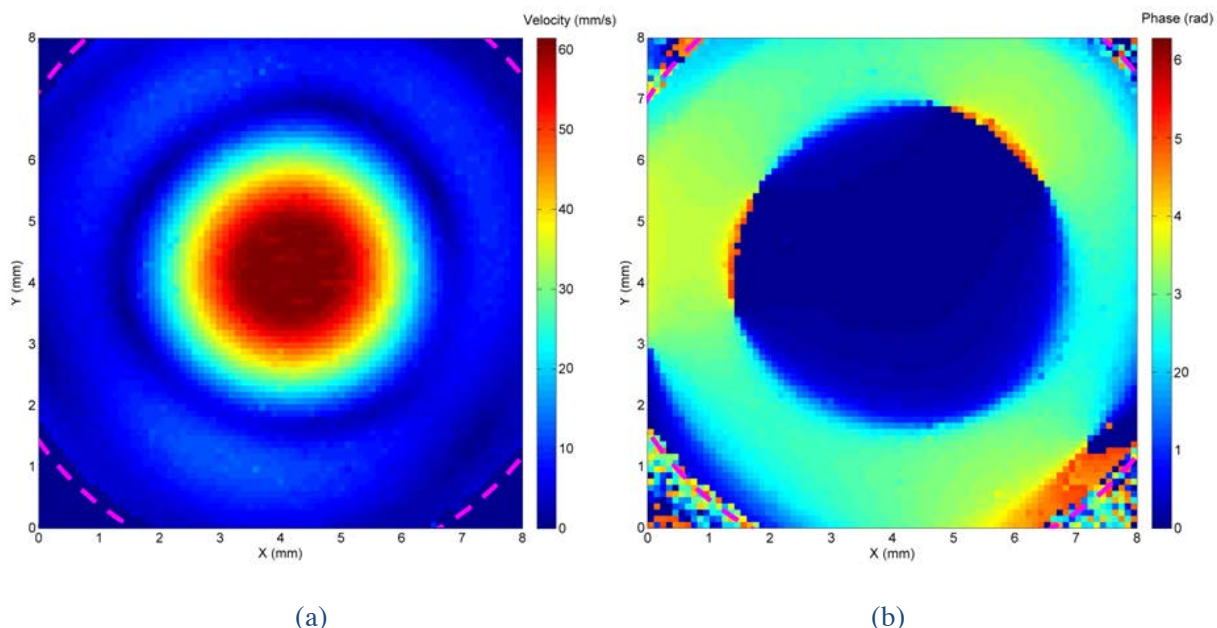


Fig. 5: Amplitude (a) and phase (b) of normal velocity of the sensor's surface in free condition.

Since the PAC $\mu 80$ sensor is fairly resonant, the local sensitivity $m(r)$ at the sensor face is derived from the local velocity measured at its central resonance frequency of 300 kHz. A proportionality relationship between those quantities is assumed. Fig. 6 shows the modulus of the Fourier spectrum profiles extracted at various frequencies in the case of a pulsed excitation of the sensor, and also that the sensitivity profile of the sensor is also a function of frequency. Consequently, the implementation of the proposed technique for a truly broadband sensor, which is quite rare in AE experiments, would require a procedure for extracting the complex sensitivity profile for each frequency component within the frequency band of the sensor.

In the present paper, it is decided to extrapolate the qualitative behavior of the sensor in the useful band as identical to the $\psi(r)$ and $\varphi(r)$ measured at 300 kHz. Indeed, by virtue of the particularly resonant behavior of this sensor, we assume that the qualitative effect of the difference between off-resonance velocity profiles is of the second order with regards to the quantitative effect of the variation of m_0 with the frequency, this later effect being actually taken into account.

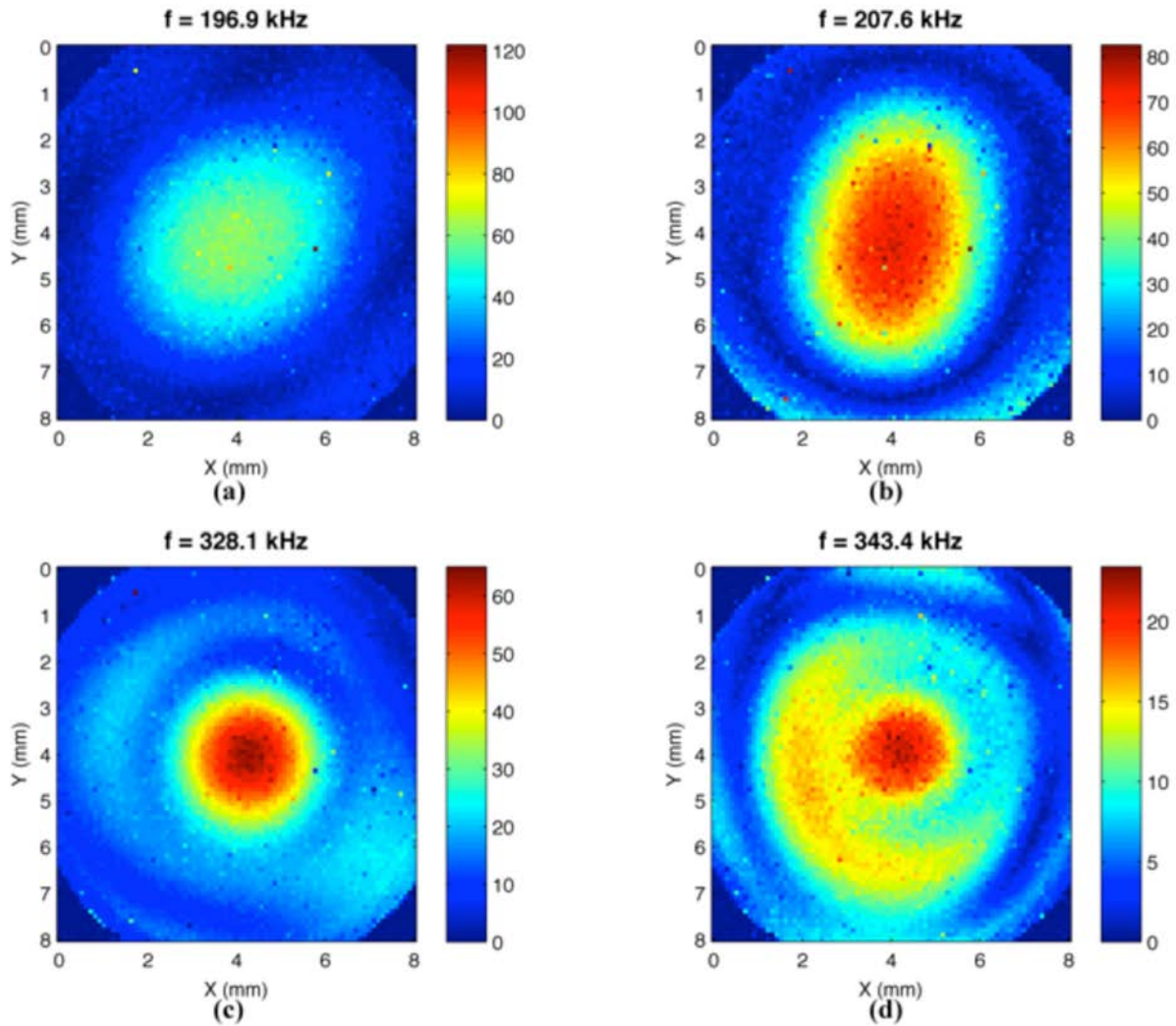


Fig. 6: Amplitude profiles of normal velocity at various frequencies.

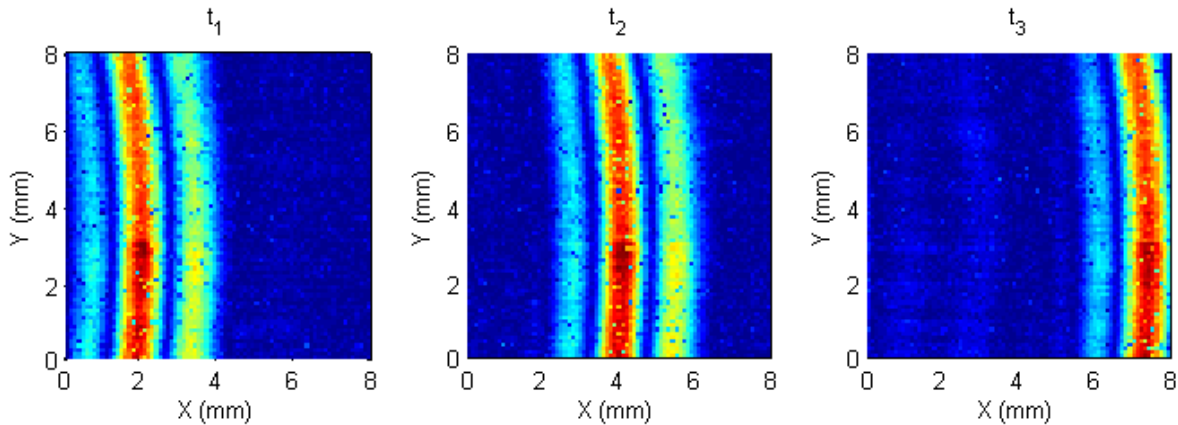


Fig. 7: Snapshots at consecutive instants showing the curvature of the wavefront.

3.1.2. Visualization of Rayleigh wavefront curvature in Rayleigh wave calibration

The Rayleigh wavefront that passes under the AE sensor is visualized using the same setup that the one described in [17], where a PAC $\mu 80$ sensor, coupled with glycerin on a $300 \times 300 \times 400$ mm steel transfer block, is used as an emitter and placed with its center at 30 mm from the center of the surface of interest. The transducer is driven with a short-pulse excitation provided by a

Panametrics 5052 pulser-receiver. The interrogated surface has the same area that the one of Fig. 5 and Fig. 6 and is also scanned with 100- μm spacing in both X and Y directions. Snapshots of Fig. 7 taken at close instants show that the wavefront propagating from left to right has a low curvature despite the relatively small distance between the transmitter and the reception area. This helps to understand the weak influence of the calculation proposed in [17] compared to the classical calculation involving a plane wavefront [16], as it will be shown in the next paragraph.

3.2 Application towards a better consideration of the actual aperture of AE sensor

Fig. 8 collects, in the 1 MHz frequency range, the results in terms of aperture function obtained for the two referenced models and for the present model, where the information of amplitude of vibration was first only added, then complemented by the information of phase. The solid line in Fig. 8 represents the aperture function proposed by the ASTM model [16] of a 300-kHz plane Rayleigh waves on stainless steel, by taking into account the actual active area of the sensor of about 6.5 mm in diameter instead of the 9.5-mm diameter of the sensor face. This function behaves like a squared cardinal sine, and exhibits one null value within the measured frequency range of 1 MHz, which is the upper frequency commonly used for the calibration of such kind of AE sensors. The dashed line in Fig. 8 represents the aperture function obtained by Goujon et al. model when the radius of curvature of the Rayleigh-wave beam from a remote transmitter is also taken into account. It is almost the same as the solid one because the wavefront of the cylindrical wave is here relatively flat, as one can observe in Fig. 7. So, the incoming wave from the actuator placed at a distance of 30 mm is quite close to the plane wave considered in the ASTM model.

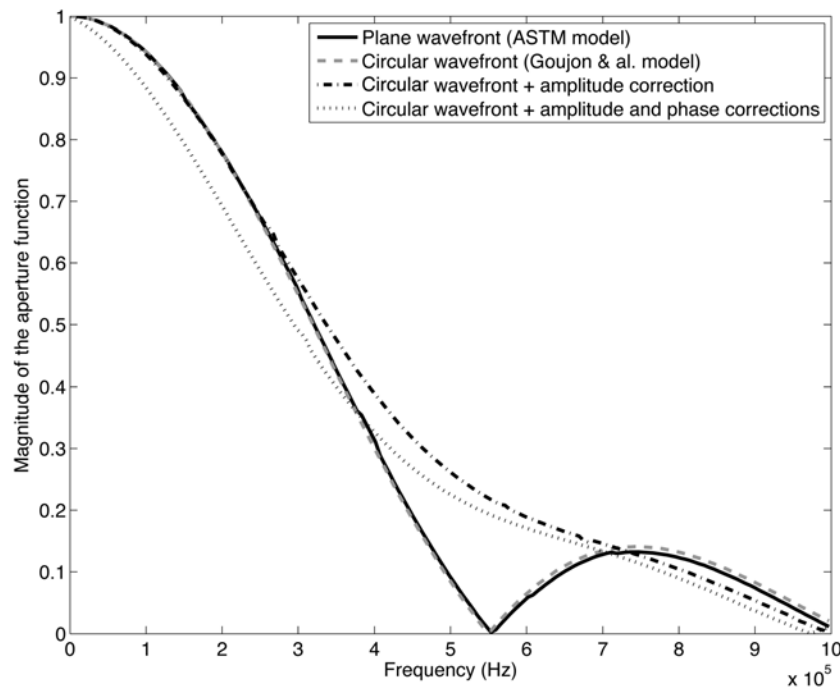


Fig. 8: Aperture function in the 0 to 1 MHz frequency range.

Taking into account the actual amplitude of vibration velocity sensor, the first cut-off frequency of the aperture function occurs at about 1.05 MHz. Moreover, if one also reflects the phase shift of vibrations of the surface, still under the assumption of axial symmetry, the widening of the first lobe of the aperture function is slightly less than when accounting for the

amplitude only. Knowing the difficulty to accurately measure the phase, it can be suggested that only considering the amplitude information may be sufficient to partially correct the aperture function without significant practical difficulty.

Aiming at performing a calibration of AE sensors on the surface of a block transfer (Rayleigh-wave calibration) instead of using the usual bulk-wave calibration method requires taking into account the aperture effect of the sensor.

In order to check the validity of the aperture effect correction in surface wave calibration, the PAC $\mu 80$ sensor sensitivity to Rayleigh waves is compared to the one obtained with longitudinal bulk waves. To produce the incident bulk wave, a longitudinal wave transducer was set to the opposite face of the block. The 300-mm thickness of the block is more than fifteen times the wavelength of longitudinal waves in steel and according to the relationship $d^2/(4\lambda)=1.25$ mm defining the near field limit of the sensor, the sensor is here in the far-field of the emitter. The radius of curvature of the wavefront travelling through the thickness of the propagating medium is large enough to consider it as a perfect plane wavefront. Since there is no aperture effect to be accounted for in the presence of such a plane wave of amplitude B hitting the sensor at normal incidence, the voltage across the sensor is:

$$U = \frac{B}{S} \iint_S m(r) r dr d\theta = \frac{B}{S} \cdot m_0 \iint_S \psi(r) e^{-j\varphi(r)} r dr d\theta \quad (9)$$

Under the hypotheses of the absence of geometrical influence of the frequency and axial symmetry of the d diameter sensor, (9) becomes:

$$U = m_0 \frac{B}{S} 2\pi \int_0^{d/2} \psi(r) e^{-j\varphi(r)} r dr = m_0 B K(d) \quad (10)$$

with $K(d)$ a constant value that is numerically computed. Hence the sensitivity to longitudinal bulk wave M_L versus frequency shows a flat curve with expression of:

$$M_L = m_0 K \quad (11)$$

Therefore, using (5) yields:

$$M_L = \frac{K}{F(f,S)} \cdot M_R \quad (12)$$

The aperture function $F(f,S)$ is the only quantity to be determined in order to validate the R-wave calibration method. The sensitivity to longitudinal bulk wave should thus be proportional to the ratio of the sensitivity to longitudinal bulk wave and the aperture function.

Fig. 9 shows various sensitivity spectra of the sensor PAC $\mu 80$. The curves represent the moduli of the complex sensitivities in the 1 MHz range. The solid curve shows the sensitivity obtained by bulk longitudinal-wave calibration whereas the dashed line represents the Rayleigh wave sensitivity, which we measured by applying the surface-wave reciprocity method proposed by Hatano [18]. According to (12), the bulk-wave sensitivity curve must be inferred from the Rayleigh-wave curve by simple division term by term.

In [17], Goujon *et al.* did not account for any geometrical variation of m , assuming $m=m_0$; e.g. $\psi(r)=1$ and $\varphi(r) = 0$, yielding $K = 1$. The dashed-dotted curve with cross markers is obtained according to the piston-like behavior model, which considers a uniform and in-phase displacement of every point of the surface of the sensor, e.g. considering $K = 1$ and substituting in (12) the aperture function F given by (5). The sensitivity curve thus obtained clearly does not fit the sensitivity measured with bulk longitudinal waves, invalidating the Goujon *et al.* model.

Without detracting from the quality of the work of these authors, their assumptions prevent to correctly account for the aperture effect outside the low-frequency range. Indeed, the too fast decay of the aperture function depicted in Fig. 8 makes the recalculated curve deviate from the experimental curve when the frequency exceeds about 400 kHz. In addition, the vanishing of the denominator for the cut-off frequency at $f = 550$ kHz causes the divergence of the recalculated M_L sensitivity. We believe that the presentation in [17] of results only for frequencies below this first cut-off frequency, combined with the fact that the approach was to calculate the sensitivity of Rayleigh waves from the sensitivity of bulk waves by multiplying the aperture function, thus avoiding the above mentioned problem of divergence, has overshadowed the limitations of the piston-like model.

The curve with black dot markers in Fig. 9 shows the bulk-wave sensitivity spectra obtained from the Rayleigh-wave sensitivity spectra divided by the new aperture function model (8). It shows a good agreement with the experimental curve for frequencies up to 450 kHz and a reasonable agreement for frequency above this value. As no normalization of the measured bulk-wave or Rayleigh-wave sensitivities were performed, one can deduce that the value of $K(d)$ is here close to 1. The good fit between the experimental curves and those derived through our aperture function, itself based on precise measurements of the vibrational behavior of the sensor, confirms our approach and validates the proposed model.

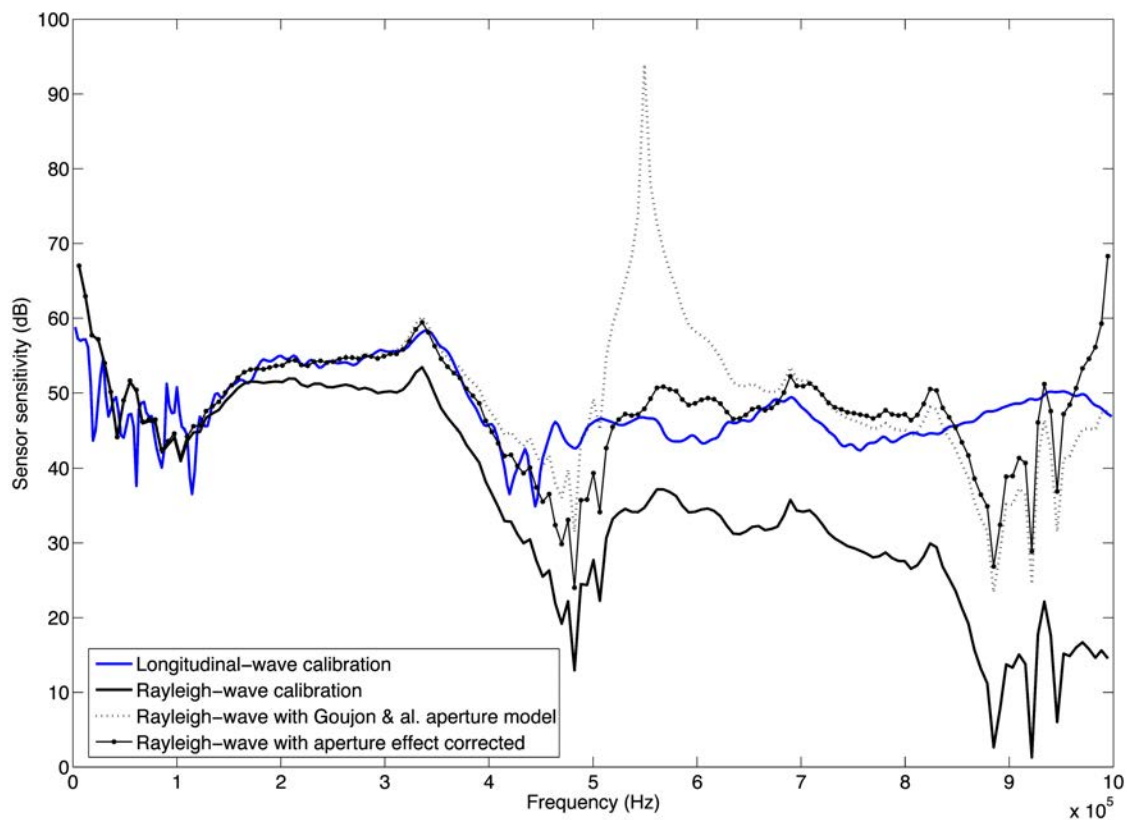


Fig. 9: Aperture effect correction of R-wave sensitivity and comparison with L-wave sensitivity in the 1 MHz range.

In the previous section we mentioned that aperture effect undermines the reciprocity criterion. With the new aperture function, we showed that L-wave sensitivity can be derived from R-wave sensitivity. In other words R-wave configuration for AE sensor meets reciprocity criterion.

4. Shear wave calibration of AE sensors

To our knowledge there are no previous attempts of S-wave calibration of AE sensors. Our first attempt was the classic arrangement for reciprocity calibration: three AE sensors and a propagating medium. The experimental arrangement is the same as the one Hatano used for L-wave calibration of AE sensors in [18]. With that method, it is possible to detect S-wave but it is not possible to isolate it from the whole signal. Indeed S-wave is partly buried in the preceding L-wave. To workaroud that issue, normal incidence S-wave transducers (Panametrics V151) have replaced two of the AE sensors. As S-wave calibration requires repeatable sensor coupling, a solid cement was used to validate the method. For practical reasons, namely to ease the sensor repositioning, a thick couplant was also used. This shear wave couplant from *Sofranel* showed good repeatability and produced comparable result to the one that was get from the use of the cement.

As shown in Fig. 10, the L-wave component became negligible compared to S-wave. Before computations the L-wave component is removed by proper windowing. Conventional hardware has been used for the calibration. Current is sent to the emitting sensor by means of the Agilent 33210A arbitrary waveform generator. Philips PM9355 current probe/amplifier is used to measure current absorbed by the emitting sensor. A Bruel & Kjaer 2638 amplifier is used to preamplify the voltage across the receiving transducer. Finally, a Tektronix Tds-340 oscilloscope records voltages with 512 averages.

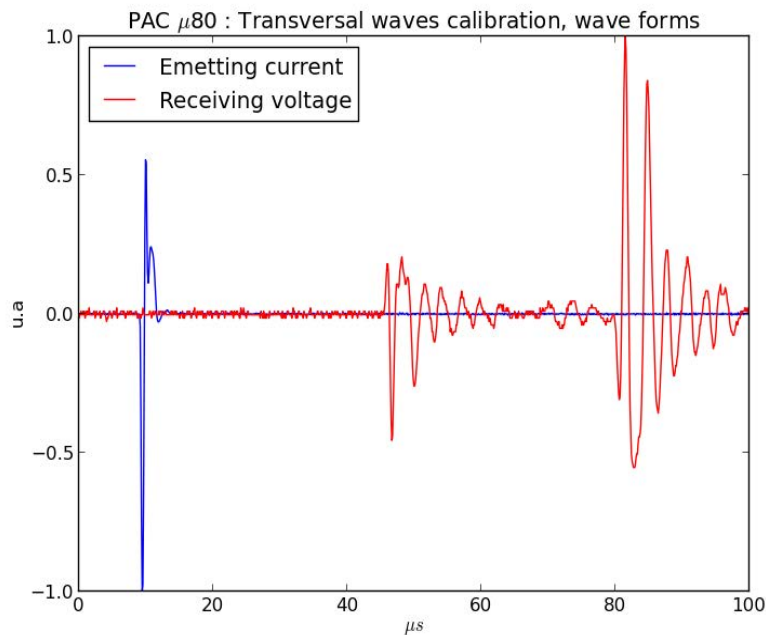


Fig. 10: Current absorbed by the emitter and voltage across the AE sensor in S-wave calibration.

What can be observed in Fig. 11 is the comparison between L-wave and S-wave sensitivities. It appears that the S-wave sensitivity is 15 dB below L-wave sensitivity. However both sensitivities have the same evolution. Tests conducted with other sensors, for instance with a PAC R-15alpha sensor, and different coupling fluids confirmed this trend.

S-wave AE calibration is a prime. We proposed a method with one AE sensor and two normal-incident S-wave transducers. Obtained results have demonstrated the technical feasibility

of that method. It is also important to note that S-wave sensitivity and L-wave sensitivity are linked. As a result, relying on R-wave sensitivity and the aperture function, one can derive L-wave sensitivity and finally S-wave sensitivity.

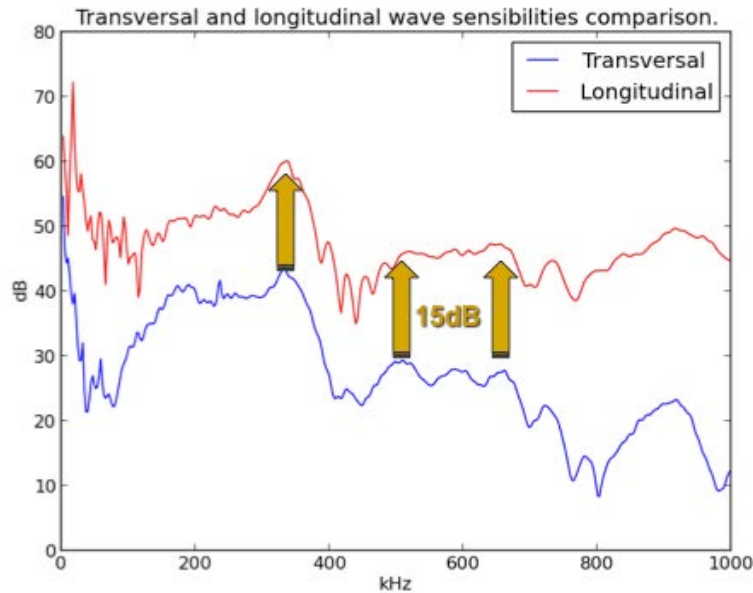


Fig. 11: S-wave calibration of a PAC μ 80 sensor: comparison with L-wave sensitivity.

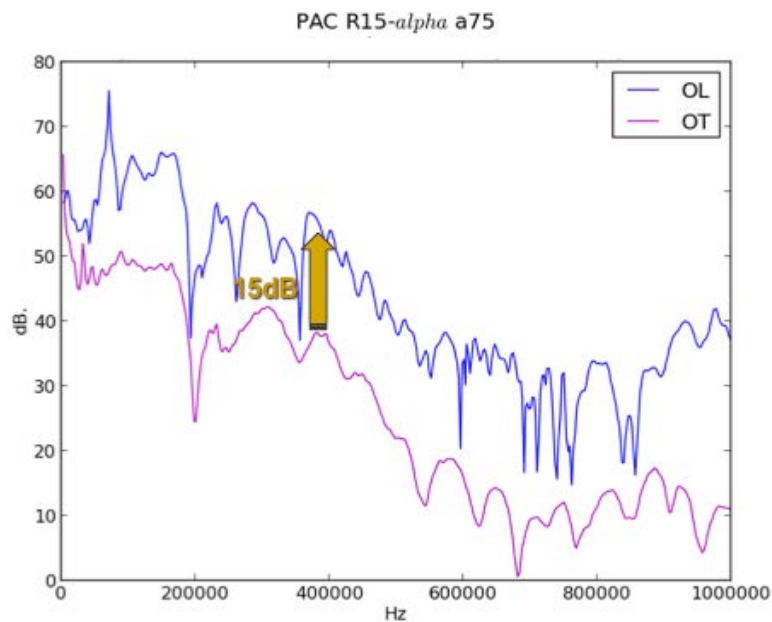


Fig. 12: S-wave calibration of a PAC R15alpha sensor: comparison with L-wave sensitivity.

5. Conclusion

Although proper definition of the reciprocity parameter is not a simple task, the objective of this paper was to present elements that are essential to a better understanding of the reciprocity parameter. First we have seen that Bobber's conclusions give physical insight to the definition of this parameter and that Hill and Adams extended it to AE sensors calibration. Next we presented a new aperture function. We have seen that aperture effect correction of R-wave sensitivity can be used to derive L-wave sensitivity. Finally, an original method for S-wave calibration of AE

sensors has been presented. The first results showed that it might be possible to derive S-wave sensitivity from L-wave sensitivity. As a result it can be inferred that knowledge of R-wave sensitivity is sufficient for the complete characterization of AE sensors.

Acknowledgements

This work was conducted as part of the MASCIM project, dealing with modeling of acoustic emission testing and funded by the French National Research Agency. The project partners are CEA LIST, CETIM, DCNS, EADS IW, and EXTEND UTC

References

- 1 Bleaney, B. I., Bleaney, B., Electricity and magnetism, 2nd édition. Oxford University Press, Oxford [1965].
- 2 McLean, W. R., Absolute measurement of sound without a primary standard. *J. Acoust. Soc. Amer.* **12** [1940], 140.
- 3 Breckenridge, F. R., Watanabe T., Hatano H., Calibration of acoustic emission transducers: comparison of two methods. *Progress in Acoustic Emission*, Vol. **1**, [1982], 448-458.
- 4 Hatano H., Mori E., Acoustic-emission transducer and its absolute calibration, *J. Acoust. Soc. Amer.* **59** [1976], 344.
- 5 Hill, R., Adams N. L., Reinterpretation of the reciprocity theorem for the calibration of acoustic emission transducers operating on a solid. *Acoustica* **43** [1979], 305-312.
- 6 Hatano H., Chaya T., Watanabe S., Jinbo K., Reciprocity Calibration of Impulse Responses of Acoustic Emission Transducers, *IEEE Transactions on ultrasonics, ferroelectrics and frequency control*, Vol. **45** (5) [1998], 1221-1228.
- 7 Keprt J., Benes P., Determination of Uncertainty in Calibration of Acoustic Emission Sensors, Hellenic Society for NDT, [2007], Chania, Crete-Greece
- 8 Keprt J., Benes P., Progress in Primary Calibration of Acoustic Emission Sensors, *Acoustic* [2008], Paris, 2217-2222.
- 9 Keprt J., Benes P., Primary calibration of acoustic emission sensors, *Fundamental and Applied Metrology*, [2009], Lisbon, Portugal
- 10 Bobber, R. J., General reciprocity parameter. *J. Acoust. Soc. Amer.* **39** [1966], 680.
- 11 Lamb H., On the propagation of tremors over the surface of an elastic solid., *Philos. Trans.* A203 [1904], 1.
- 12 Hill R., Reciprocity and other Acoustic Emission Transducer Calibration Techniques, *J. Acoustic Emission* **1** [1982], 73-80.
- 13 Gorman M.R., Ziola S. M., Plate waves produced by transverse matrix cracking, *Ultrasonics* **29** [1991] 251.
- 14 Gorman M.R., Plate Wave Acoustic Emission, *J. Acoust. Soc. Amer.* **90** [1991] 358-364.
- 15 Theobald P., Zeqiri B., Avison J. Couplants and their influence on AE sensor sensitivity, *J. Acoustic Emission* [2008] 26
- 16 ASTM Non destructive Testing Handbook: Acoustic Emission Testing 2nd ed. (Columbus, OH: American Society for Non Destructive Testing) [1987] 126-30
- 17 Goujon L., Baboux J. C., Behaviour of acoustic emission sensors using broadband calibration techniques, *Meas. Sci. Technol.* **14** [2003] 903-908.
- 18 Hatano, H. and Watanabe, T., Reciprocity Calibration of Acoustic Emission Transducers in Rayleigh-Wave and Longitudinal-Wave Sound Fields, *J. Acoust. Soc. Am.*, Vol. **101** [1997], 1450-1455.

Neural Network Burst Pressure Prediction In Tall Graphite-Epoxy Pressure Vessels From Acoustic Emission Data

Eric v. K. Hill¹, Christopher J. Foti², Ning Y. Leung² and Andrea E. Palacios²

¹ Aura Vector Consulting, 3041 Turnbull Bay Road, New Smyrna Beach, FL 32168

² Aerospace Engineering Department, Embry-Riddle Aeronautical University,
600 S. Clyde Morris Boulevard, Daytona Beach, FL 32114

Abstract

The goal of this research was to find an accurate and reliable method to predict the burst pressures of various undamaged tall graphite-epoxy pressure vessels at low proof pressures. A total of fifteen bottles were monitored with acoustic emission (AE) transducers while being pressurized to failure. The AE flaw growth data were then analyzed using artificial neural networks. A Kohonen self organizing map (SOM) was first used to classify the AE data into its various failure mechanisms, then a back-propagation neural network (BPNN) was used for burst pressure predictions. Both the unclassified AE data and the SOM classified AE data were input into two different software packages – NeuralWorks Professional II+ and MATLAB – yielding a total of four different predictions. Each prediction was tested using 12%, 25%, and 50% of the initial AE data. The final optimized predictions used the first 12% of the classified data, which resulted in essentially identical worst-case errors of about 6%. These lowest worst-case errors were produced using both the AE input data that were pre-classified into the four failure mechanisms using the Kohonen SOM plus categorical variables to identify the five different resin cure methods. The tall graphite-epoxy bottles tested had to be pressurized to almost 50% of their burst pressures to obtain sufficient AE data for accurate burst predictions. The use of low proof pressures ($\leq 25\%$) was inadequate in obtaining accurate burst pressure prediction.

Keywords: Back-propagation, self-organizing map, failure mechanisms, burst pressure prediction, composite pressure vessels, graphite/epoxy, neural networks, nondestructive evaluation

Introduction

In recent years, there have been many engineering applications that required the use of pressure vessels to store compressed gases and fluids. These applications range from the large storage tanks found on natural gas vehicles to the small, lightweight inert gas storage tanks used on modern spacecraft. For most purposes, a metallic pressure vessel is an effective and cost efficient solution. However, when dealing with aerospace applications it is very desirable to use lightweight structures. Even though the manufacture of a lightweight pressure vessel is expensive, the increased operational performance and decreased cost of operation due to a vehicle's lower mass make the use of lightweight pressure vessels advantageous, particularly in aerospace applications. For this reason composite overwrapped pressure vessels (COPVs) or fully composite pressure vessels are commonly used on modern aircraft and spacecraft. This includes extensive use on the Space Shuttle (see ref. 1). This project focuses on the evaluation of fully composite pressure vessels only. Composite pressure vessels have added weight savings over COPVs. However, they can be more difficult to manufacture and composite materials have a tendency to fail unpredictably due to variability in cure methods, layup techniques, and other manufacturing processes. Because of this variability in manufacturing quality, it is important to develop a practical method to nondestructively evaluate the ultimate strength or burst pressure of

each individual composite pressure vessel, and therefore, that is the primary focus of this research.

The data for this project were gathered in 1996 at the NASA Marshall Space Flight Center (Walker et al., 1995). Here, fifteen 146-mm diameter, tall IM7/977-2 graphite-epoxy pressure vessels were manufactured and tested. A tall pressure vessel is defined as a pressure vessel having a cylindrical section at least three times the length of vessel. In this case, the cylindrical portion of the bottles was 305 mm long, as opposed to the typical 100 mm long cylindrical region. The fifteen bottles were split into five groups of three bottles, in which each group was manufactured using a different resin cure method. These methods included autoclave cure, vacuum bag cure, low temperature cure with polyvinyl alcohol (PVA) removed, rotisserie cure at room temperature, and rotisserie cure at 177°C. Four acoustic emission transducers were affixed to each bottle as shown in Fig. 1. Transducer 1 was attached to the polar boss, while the three remaining transducers were attached around the periphery of the pressure vessel along the hoop fibers. The bottles were first pressurized at a rate of 68.95 kPa/sec up to 6.895 MPa, which is roughly 25% of the design or rated burst pressure. The bottles were held at this pressure for two minutes to allow them sufficient time for any creep to stop. The pressure was then brought back to zero and finally ramped up to failure, again at a rate of 68.95 kPa/sec. See Fig. 2. Acoustic emission data were gathered during the entire test using the AE transducers and a multi-channel AE analyzer. Finally, a portion of the AE data were input into a back-propagation neural network (BPNN) in order to predict the burst pressures of the graphite-epoxy pressure vessels. Although the BPNN successfully predicted the burst pressures for most of the bottles with less than a 20% error, the prediction on one bottle was in error by 37.8%. These errors are summarized in Table A1 in the Appendix.

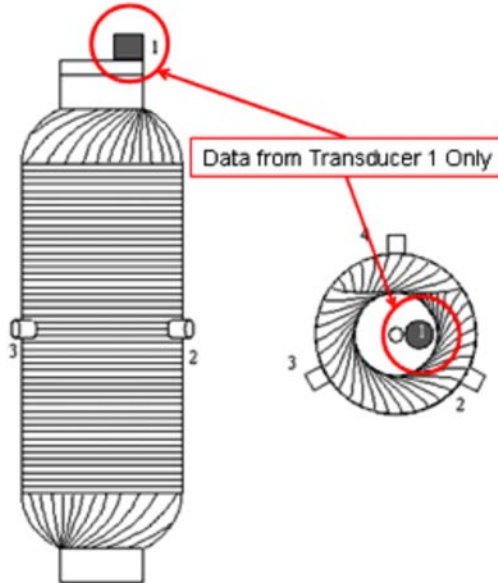


Fig. 1. AE transducer placement.

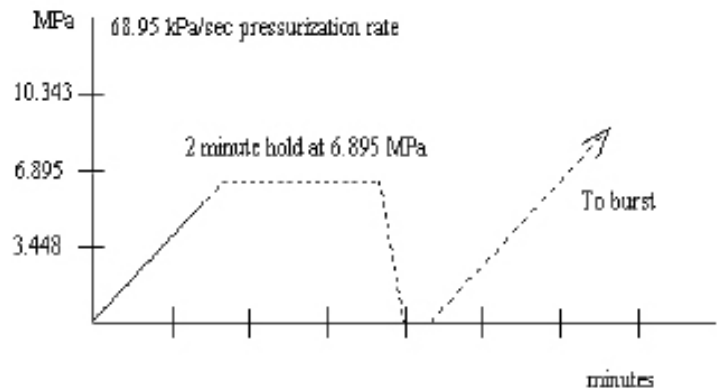


Fig. 2. Pressurization scheme.

The primary goal of this research was to use the data previously collected to devise a method of prediction yielding lower errors, with the specific goal of attaining a worst-case error of less than $\pm 10\%$. This was attempted by modifying the input to the artificial neural networks. Unlike the previous research, the AE data herein were first classified into the different failure mechanisms that occur during pressurization of composite pressure vessels using a Kohonen self organizing map (SOM) neural network. Both the original unclassified data and the classified

data generated by the SOM were then input into a back-propagation neural network, which predicted the burst pressures of the bottles. Two different neural network software packages were used – Neural Works Professional II+ and MATLAB – and the amount of AE data input into the neural networks was varied from the initial 12%, 0-25% and 0-50% of the AE data taken up to burst. The variability of the networks allowed for the testing of many different neural network configurations and helped to achieve a much improved burst pressure prediction. The secondary goal was to obtain accurate burst pressure predictions at low proof loads such that minimal damage is done to the composite pressure vessel. Details of the neural network analyses will be presented later.

Acoustic Emission Nondestructive Testing and Evaluation

Acoustic emission testing is a method to test and evaluate the integrity of a structure undergoing stress. In composites the matrix will begin to crack first, then the cracks will couple into micro-delaminations, following which the layers or plies of the composite will delaminate from one another on a macroscopic scale, then the fiber bundles within the composite will begin to break, and finally rupture will occur (Reifsnider et al. 1983). Each one of these failure mechanisms will release energy throughout the structure in the form of elastic mechanical waves that will have unique characteristics when compared to waves produced by other mechanisms. By measuring the acoustic emission hits using a piezoelectric transducer, the modes of failure occurring can be determined and the state of the structure can be inferred.

Two major aspects of AE data analysis that must be taken into account are noise and multiple hit data. Acoustic emission tests are highly prone to gathering noise from sources such as electromagnetic interference and mechanical rubbing. The noise must be filtered out by recognizing their characteristics such as very high or very low average frequencies. When AE hits occur in rapid succession, it is possible for the AE data acquisition system to mistake multiple independent hits as one long combined hit. This is referred to as multiple hit data (MHD). Multiple hit data tend to have high energies, long durations, and low average frequencies. In order to get accurate results, noise and MHD have to be removed from the data set prior to any analysis. Fortunately, the data used in this research had very little noise. However, there were some MHD that needed to be removed in order to attain more accurate predictions.

Artificial Neural Networks

In order to analyze the data gathered herein, artificial neural networks were employed. The method, by which an artificial neural network (ANN) analyzes data, is modeled after the biological neurons and synapses in the human brain. The ANN's interconnected neurons, or processing elements (PEs), are assigned random initial weights. Each PE sums together all of its weighted inputs and passes it through a transfer or activation function before it is output to the next neuron. The network optimizes the weights by going through iteration while trying to lower the error of the network's output. The main advantage of using neural networks is that very little needs to be known about the data to achieve good results. For example, if trying to curve fit data using statistics, the general shape of the curve must be known. It must be first determined if the curve should be linear, parabolic, exponential, or some other function. An artificial neural network will come up with its own way to fit the data and does not depend on the user's curve fitting intuition. Also, it is virtually impossible to employ statistics when there is noise present in the data. Noise will cause the analysis to "blow up" and result in unacceptably large prediction

errors. An ANN, on the other hand, can easily handle noisy data. Typically, the weights corresponding to the noisy data points will approach zero after many iterations, causing this data to have little effect on the output. Two kinds of ANN's were used to analyze the low pressure AE data. First, a Kohonen self organizing map was used to separate or classify the data into different failure mechanisms. Following classification, the AE data were input into a back-propagation neural network to predict burst pressures.

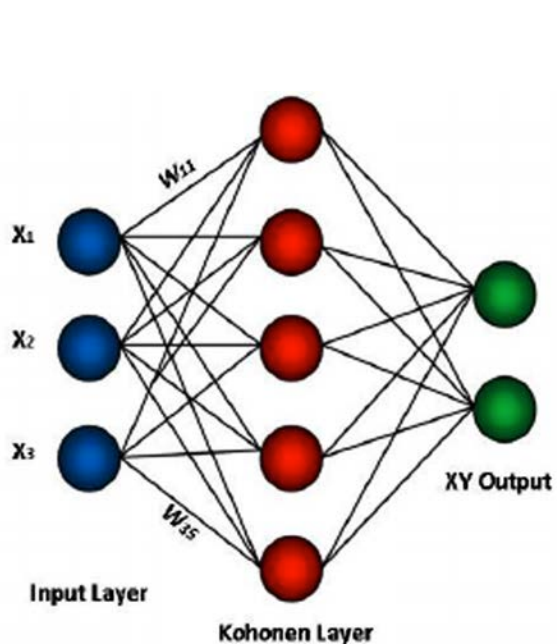


Fig. 3. Basic SOM architecture.

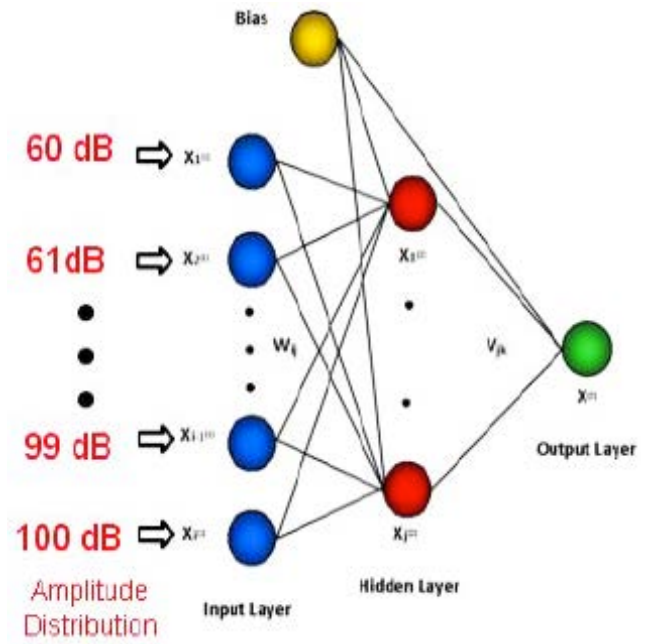


Fig. 4. BPNN architecture with amplitude histogram input.

Kohonen Self Organizing Maps

A Kohonen self organizing map (SOM) is a type of ANN which is used to categorize or classify data. The architecture of a SOM can be seen in Fig. 3. Data are first applied at the input layer of the SOM. There is one input neuron for each parameter of a data point. For example, here the AE data were categorized in the SOM by using amplitude, counts, duration, energy, and rise time; hence, there were 5 input neurons. The Kohonen layer, which in this case was one-dimensional, will then process and classify the data into a number of categories. The number of categories possible is defined by the size of the Kohonen layer. For example, four categories or failure mechanisms were expected for the graphite-epoxy bottles: matrix cracking, crack coupling, delaminations, and a mixture of fiber breaks with multiple hit data (Reifsnider et al., 1983). This resulted in the need to use a 4x1 Kohonen processing layer, which yielded four possible classifications. If the number of categories is unknown, it is best to use more categories than expected. The network will not necessarily use all of the categorizations possible, but the size of the processing layer should be optimized to yield the best classification. Finally, the output layer shown in Fig. 3 gives an x-y coordinate representing the categorization of each data point or AE hit.

Back-propagation Neural Networks

Unlike an SOM, a back-propagation neural network (BPNN) is used for prediction. A BPNN's architecture consists of an input layer, one or more hidden or processing layers, and a single neuron output layer as seen in Fig. 4. Data are first input to the BPNN through the input layer. When using AE data, typically an amplitude histogram is input into this layer with one neuron per each 1 decibel amplitude interval. For this application, the amplitude range of the

pressure vessel AE data ranged from 60-100 dB. With each decibel level requiring one input neuron, this yielded a total of 41 input neurons. The processing hidden layer then sums the weighted inputs from all the input neurons and passes them through the each hidden layer neuron transfer function; these outputs from the hidden layer then become the inputs to the single output layer neuron. In this case, the output from the single output layer neuron is the predicted burst pressure.

In order to produce a BPNN capable of accurately predicting burst pressures, the test data must be split into training and testing files. Since there were fifteen pressure vessels tested in this project, eight bottles were used to train the network, while the remaining seven were used to test it. The way the BPNN learns to predict is analogous to the method, in which a student learns to solve a problem. The student will first learn a subject and learn how to solve a set of problems relating to it. Later, the student will be tested on different, but similar, problems to determine or test how well the subject has been learned. Likewise, a portion of the AE data was used to train the network. This portion of data included the appropriate AE amplitude histograms for eight of the bottles along with their actual burst pressures. The network will predict the burst pressures by using randomly assigned initial neuron weights. In order to improve the prediction results, the output error is computed, and the BPNN will iterate until either a defined number of iterations occur or a specified RMS error is achieved between the training bottles' burst pressures and the BPNN's prediction results. The BPNN will finally be tested on the remaining bottles to check the prediction ability of the network. Here, the burst pressures are not supplied, but instead they must be predicted using only the untested bottles' amplitude distribution histograms as inputs.

Application of Artificial Neural Networks

Multiple approaches were taken to optimize the artificial neural network parameters to improve their burst pressure prediction ability. As stated earlier, the data were classified into four failure mechanisms using the SOM. Obtaining well categorized data proved to be a relatively simple task. However, determining the best way to input data into the BPNN was much more difficult. Two different neural network programs were used to determine which produced better results. NeuralWorks Professional II+, a program built solely for ANN's, and the neural networks application in MATLAB were both used. For each program, both categorized and uncategorized amplitude histograms were input into the BPNN's for burst pressure prediction. The hypothesis was that the classified data, which provided no data overlap and removed MHD, would result in lower errors when input into the BPNN. Additionally, the amount of amplitude data input into the SOM and BPNN was varied between the initial 12%, 25%, and 50% of the channel 1 AE hits up to burst. It was believed that more AE data would result in less prediction error; on the other hand, less data correlated to an earlier prediction, which meant less damage to the bottles. Finally, the method in which the input file was set up was varied. This included appending all four of the amplitude histograms to one another, removing the MHD and fiber breaks, using only the matrix cracking data, and using a categorical variable to specify cure type. All of these approaches will be discussed in further detail later.

NeuralWorks Professional II/PLUS Predictions

NeuralWorks Professional II/Plus is a software package that is specifically designed to generate artificial neural networks. For this project, this software was used to generate a series of BPNN's to predict burst pressures in tall graphite epoxy bottles using low-pressure acoustic

emission data. An SOM was also used to classify failure mechanisms within the AE data sets and thereby allow the BPNN to make more accurate predictions.

The SOM categorized the data using five different AE parameter inputs: rise time, duration, counts, energy and amplitude. This SOM classification process iterated 30 times through the total number of AE hits for each bottle, resulting in the four different classifications previously mentioned. Shown in Fig. 5 is an amplitude distribution histogram of the categorizations obtained from the SOM. Figure A1 in the Appendix is a three dimensional plot of amplitude, energy and duration of one of the bottles in the data set. It was expected that some of the data would overlap due to the fact that different failure mechanisms can appear similar when analyzing the various AE parameters. It is clearly seen that the largest group of the data from the amplitude histogram was categorized as matrix cracking.

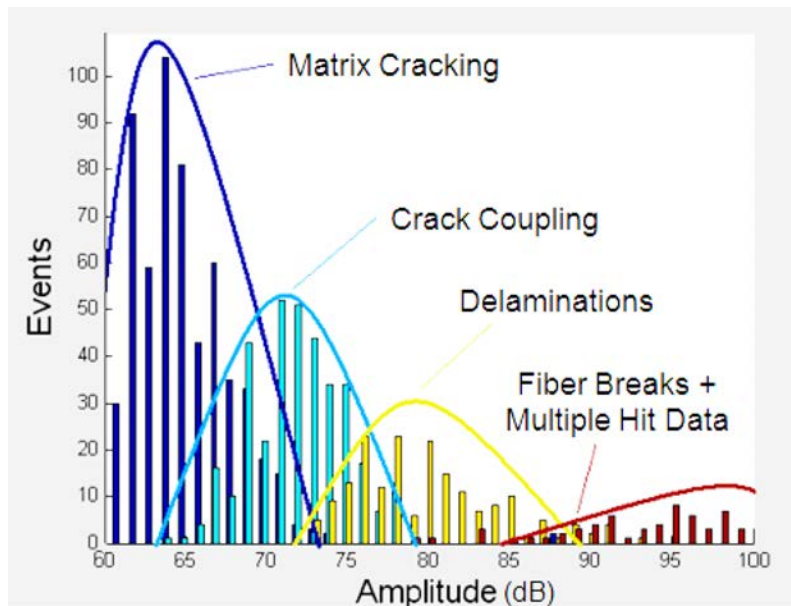


Fig. 5. Categorized amplitude distribution.

Once the SOM classified the data, it was necessary to determine the format in which the BPNN input files would be created. An input file for the uncategorized data would only have one amplitude histogram as an input. Because of this, the input file would have 41 columns: one for each amplitude level. On the other hand, the classified data had three appended amplitude histograms representing the first three failure mechanisms. This resulted in 123 columns. Further improvement of the input file resulted in the addition of three more columns, which used a binary categorical variable to indicate the cure type of the bottle. This variable can be seen in Table A2 of the Appendix. The additional columns made for a total of 126 columns to the categorized input file. An example of the format of the categorized file can be seen below in Fig. 6.

The BPNN was trained on seven of the fifteen bottles and tested on the remaining eight. To maximize the effectiveness of the training data, the bottle with the maximum burst pressure as well as the bottle with minimum burst pressure were used in the training file. Furthermore, one bottle of each of the cure types was included in the training files. The remaining bottles were chosen at random. By choosing these different types of bottles to train on, more accurate predictions were obtained. The bottles that were trained and tested on can be seen in Table A3 of the Appendix.

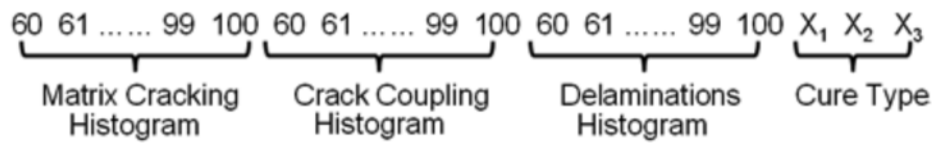


Fig. 6. BPNN categorized input file format.

The BPNN prediction was accomplished using two different methods. In the first method, uncategorized data were used as an input, while in the second, categorized data with MHD removed were used instead. Each method was tested with the initial 12%, 0-25% and 0-50% of the AE hits. Other parameters such as the number of neurons per layer, learning coefficients, and momentum were optimized in order to yield the best possible burst pressure predictions. An effort was made to train and test the network to predict failure using the least amount of data possible. It was expected that less data supplied to the BPNN would result in higher prediction errors but minimize damage done to the bottle during testing. To optimize the results for both methods, the number of neurons in the hidden layer of the BPNN was varied from 4 to 20 neurons. The learning coefficient value was optimized by varying it from 0.3 to 0.9, and the momentum was varied from 0.4 to 0.9. The root mean square (RMS) error for the seven training bottles was also varied from 0.1% to 5%. The normalized cumulative delta (norm-cum-delta) learning rule was used along with a hyperbolic tangent transfer function. The epoch size for the BPNN was set to seven, this being the number of files or bottles that the BPNN trained on.

The prediction accuracy for the uncategorized AE amplitude histogram data was better than expected. All of the cases resulted in less than a 20% error. This was unexpected, since the data were believed to include high amounts of multiple hit data. Here the optimum worst-case error occurred when 25% of the data were input to the BPNN. This resulted in an error of 7.94%. The errors and the neural network parameters that were used to achieve them can be seen in Table 1. Regarding the categorized data, the optimum worst-case error was 5.73%, which corresponded to 25% of the data input into the BPNN. This prediction was a 560% improvement over the original NASA Marshall Space Flight Center research predictions (Table A1, Appendix). The BPNN parameters used to attain these accuracies are summarized in Table 2.

Table 1: Uncategorized NeuralWorks prediction errors.

Input Data	RMS Criterion	Bottle ID	# of Hits	Hid. Lay. Neurons	Learn Coeff.	Momentum	BPNN Predicted Burst (Mpa)	Actual Burst (MPa)	% Error
12%	0.01	4C	111	7	0.5	0.5	17.18	15.79	8.13
25%	0.005	8C	1106	6	0.4	0.6	22.08	20.33	7.94
50%	0.005	8A	1623	4	0.45	0.4	18.02	20.92	16.1

Table 2: Categorized NeuralWorks prediction errors.

Input Data	RMS Criterion	Bottle ID	# of Hits	Hid. Lay. Neurons	Learn Coeff.	Momentum	BPNN Predicted Burst (Mpa)	Actual Burst (MPa)	% Error
12%	0.01	8A	390	10	0.42	0.47	19.13	20.92	9.31
25%	0.01	8C	1106	14	0.45	0.4	21.56	20.33	5.73
50%	0.01	8C	2211	10	0.42	0.47	21.76	20.33	6.57

MATLAB Neural Network Predictions

The primary purpose of using MATLAB in addition to NeuralWorks was to compare the burst-pressure prediction accuracies of both programs. The input data used for the MATLAB neural networks and the methodology of optimization were the same as those used previously for the NeuralWorks software. The only difference is that the neural network toolkit for SOMs in MATLAB was used to classify the data into their respective failure mechanisms. The classified data were subsequently input into MATLAB's BPNN toolkit for burst pressure prediction.

The SOMs for the different bottles were generated using the programming command called "newsom" in MATLAB. This program allowed the user to choose how MATLAB categorized the data. Since the tall bottles were made of graphite-epoxy, the SOMs were configured to have four failure mechanism classifications: matrix cracking, crack coupling, delaminations and fiber breaks with multiple hit data (Reifsnider et al., 1983). The different failure modes were color-coded and the data were manipulated into various plots using MATLAB. This software also allowed three-dimensional plots to be generated for the purpose of observing the energy, amplitude and duration of the bottles as they approach their burst pressures as shown in Fig. A2 of the Appendix. The classified AE hit data showed four different failure mechanisms in the amplitude histograms, but the classified data for the various failure mechanisms had considerable overlap as can be seen in Fig. 7.

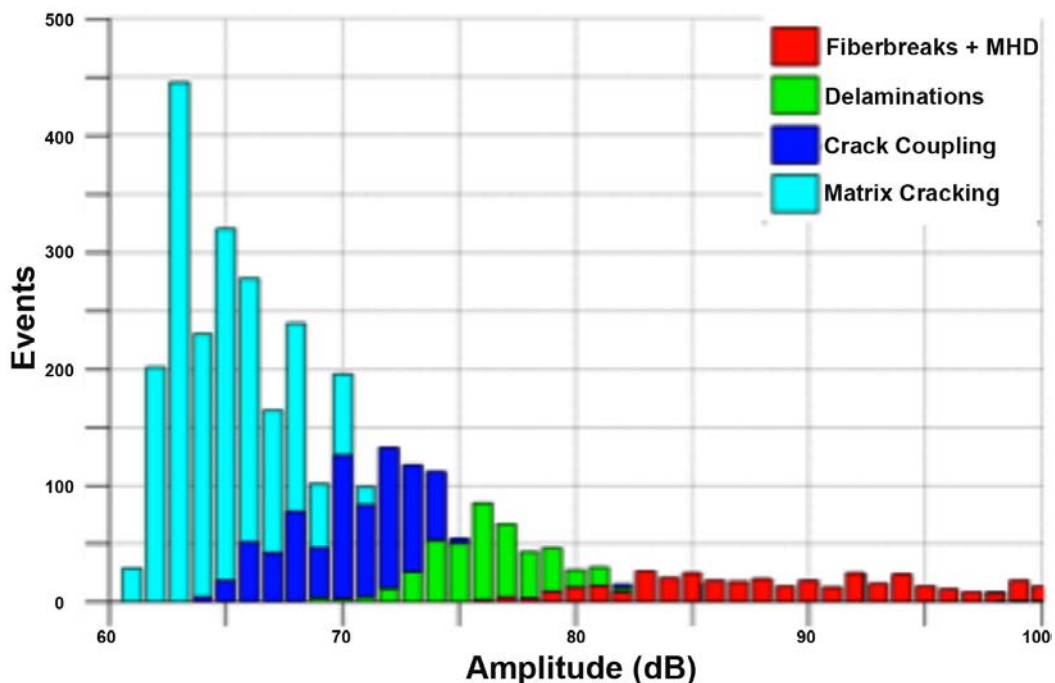


Fig. 7. MATLAB BPNN categorized amplitude distribution.

The BPNN in MATLAB runs the "newff" command from the neural network toolkit. This command required the input and target data sets for training and testing. The input for this particular case was the amplitude distributions acquired from the SOM, and the target was the burst pressure of the various bottles during AE recording. Again the number of hidden layer neurons was optimized for the BPNN. For burst-pressure prediction of the tall graphite-epoxy bottles, a loop was created to vary the number of hidden layer neurons from 1 to 20. The output of the BPNN was a matrix of errors in reference to the different number of hidden layer neurons. The optimum worst-case error was selected out of this group. It is important to note that the

MATLAB BPNN will randomly assign bottles to train, test and validate the network. To ensure that the network is set up properly, the bottles for the training, testing and validating can be chosen manually by splitting the bottles evenly according to the actual measured burst pressures (see Table A4 of the Appendix). This was done to ensure that high and low burst-pressure bottles were spread evenly among the test bottles. This prevented a scenario in which all the bottles chosen for training were those of high or low burst pressures, thus distorting the results.

As stated previously, the data were run in a similar fashion to that of NeuralWorks. Both categorized data and uncategorized data were input into the BPNN with various percentages of initial data used. However, the MATLAB BPNN experienced better results when predicting on matrix cracking only data. This is the only major difference in input data between the two methods of prediction. The results of the MATLAB uncategorized prediction can be seen in Table 3, and the results of the categorized prediction can be seen in Table 4.

Table 3: Uncategorized MATLAB prediction errors.

Input Data	Bottle ID	Hidden Layer Neurons	Learn Coeff.	Momentum	BPNN Predicted Burst Pressure (Mpa)	Actual Burst Pressure (Mpa)	% Error
12%	4B	4	0.5	0.8	19.27	17.74	8.63
25%	8A	11	0.6	0.6	18.63	20.92	-10.94
50%	7B	4	0.9	0.41	20.12	17.74	13.41

Table 4: Categorized MATLAB prediction errors.

Input Data	Bottle ID	Hidden Layer Neurons	Learn Coeff.	Momentum	BPNN Predicted Burst Pressure (Mpa)	Actual Burst Pressure (Mpa)	% Error
12%	8A	11	0.007	0.9	19.71	20.92	-5.79
25%	6B	6	0.007	0.9	20.63	22.34	-7.65
50%	4B	5	0.007	0.9	22.67	21.06	7.63

Conclusions and Recommendations

The low error achieved from the classified and the unclassified AE amplitude histogram data demonstrated that accurate pressure predictions can be obtained using both the NeuralWorks Professional II+ and MATLAB neural network software packages. NeuralWorks produced the lowest worst-case error of 5.73%, while MATLAB followed closely with a -5.79% error. Both SOMs effectively categorized the data into failure mechanisms, while the BPNNs used this categorized data to accurately predict burst pressures. After optimization of the network parameters, the BPNNs predicted burst pressures with less error when the AE data were categorized in almost every case. The two parameters that were not varied in this research were the hyperbolic tangent transfer or activation function and the normalized cumulative delta learning rule. It is possible that with a change in these two parameters that the prediction errors could be lowered even further. In general, it was found that NeuralWorks provided slightly

better, more refined results, while MATLAB was easier to use and produced results faster than NeuralWorks.

Besides the SOM classification of the failure mechanism data, the other factor that may have contributed even more significantly to the accuracy of the burst pressure predictions was the three digit categorical variables used to identify the five different cure types for the bottles. These can be seen in Table A2 of the Appendix. The addition of such categorical variables to the input data allows the BPNN to fit the data for each cure type separately rather than treating all the bottles as being from the same batch. This may explain a large part of the error obtained in the original analysis as can be seen in Table A1.

Another topic that was explored was the nondestructive testing of additional bottles. From Table A5 of the Appendix, it can be seen that the minimum burst pressure for any bottle in the data set was roughly 16 MPa. The highest pressure required to collect 12% of the total AE activity for any bottle was slightly below 13 MPa. It can be concluded from this that loading any future bottle of the types that were tested in this research to 13 MPa would result in at least 12% of the total AE activity being recorded. This should allow a burst pressure prediction within a $\pm 10\%$ worst-case error while preventing any bottle from failing during the hydroproof test. However, the data in Table A5 also indicate that the tall graphite-epoxy bottles tested herein, on average, had to be pressurized to almost 50% of their burst pressures to obtain sufficient AE data for accurate burst predictions. As such, the goal for obtaining accurate burst pressures at low proof pressures ($\leq 25\%$ of the average burst pressure (Hill et al., 1996)) was not met for this research.

For future tests, perhaps the best way to both lower proof pressures – and thereby minimize damage to the test article – plus ensure that there are sufficient AE data for burst pressure predictions would be to lower the threshold at which the AE data are taken from 60 dB down to 50 dB. This would substantially increase the amount of AE data available for processing and possibly allow AE data to be taken up to only 25% of the average burst pressure while generating worst-case prediction errors within $\pm 5\%$, values which are more typical for such tests.

Appendix

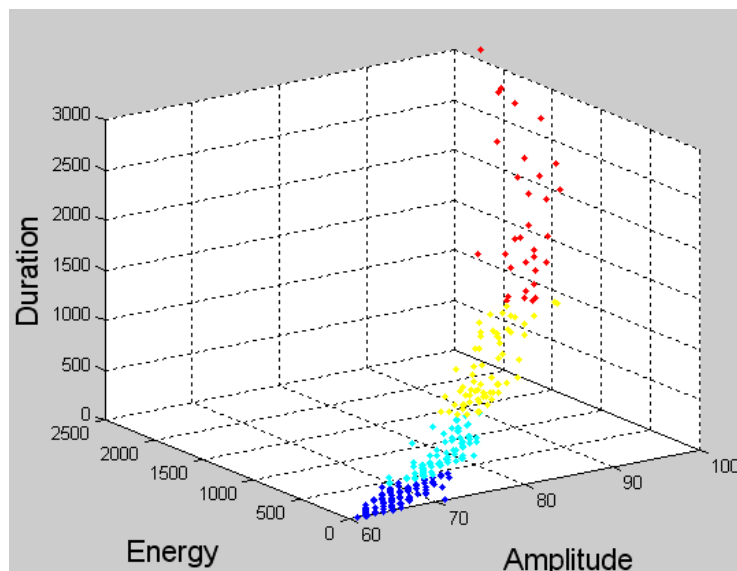


Figure A1: NeuralWorks SOM classification 3D plot.

Table A1: Original MSFC neural network burst pressure predictions [2].

Bottle Series (Cure Method)	AE Test Code	Actual Burst Pressure (MPa)	Predicted Burst Pressure (MPa)	Original Prediction Error
94PV0004 (Autoclave Cure)	GBT4A	20.61	19.84	-3.70%
	GBT4B	21.06	21.45	1.80%
	GBT4C	15.79	21.75	37.80%
94PV0005 (Vacuum Bag Oven Cure)	GBT5A	22.93	21.94	-4.30%
	GBT5B	22.53	20.16	-10.50%
	GBT5C	21.8	21.03	-3.50%
94PV0006* (Rotisserie Cure)	GBT6A	20.91	20.38	-2.60%
	GBT6B	22.34	20.32	-9.00%
	GBT6C	21.83	21.17	-3.00%
94PV0007 (Low Temp Cure- PVA Removed)	GBT7A	17.86	20.69	15.80%
	GBT7B	17.74	19.55	10.20%
	GBT7C	16.05	18.9	17.80%
94PV0008 (Rotisserie Cure at 350°F)	GBT8A	20.92	19.22	-8.10%
	GBT8B	21.4	22.8	6.50%
	GBT8C	20.33	19.27	-5.20%

Table A2: Cure type categorical variables.

Cure Type	Categorical Variable [X ₁ X ₂ X ₃]		
Autoclave	0	0	0
Vacuum Bag/Oven	0	0	1
Rotisserie	0	1	0
Low Temp	0	1	1
Rotisserie @ 350°F	1	0	0

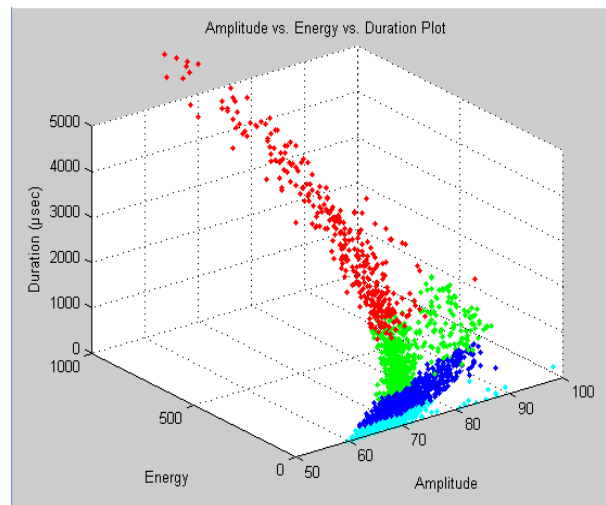


Fig. A2. MATLAB SOM classification 3D plot.

Table A3: NeuralWorks BPNN training and testing bottles.

Bottle ID	Cure Type Variable			Burst Pressure (Mpa)	Number of Hits	BPNN Input
4A	0	0	0	20.61	4,730	Test
4B	0	0	0	21.06	3,566	Test
4C	0	0	0	15.79 (Min)	1,000	Train
5A	0	0	1	22.93 (Max)	20,404	Train
5B	0	0	1	22.53	2,766	Test
5C	0	0	1	21.8	3,026	Train
6A	0	1	0	20.91	2,621	Test
6B	0	1	0	22.34	3,375	Train
6C	0	1	0	21.83	3,419	Test
7A	0	1	1	17.86	1,884	Train
7B	0	1	1	17.74	6,714	Test
7C	0	1	1	16.05	3,372	Train
8A	1	0	0	20.92	4,808	Test
8B	1	0	0	21.4	4,669	Train
8C	1	0	0	20.33	6,165	Test

Table A4: MATLAB BPNN training and testing bottles.

Burst Pressure (MPA)	Input Type	Bottle Name	Bottle Number
22.93	Train	GBT5A	4
22.53	Test	GBT5B	5
22.34	Validate	GBT6B	8
21.83	Train	GBT6C	9
21.8	Train	GBT5C	6
21.4	Train	GBT8B	14
21.06	Test	GBT4B	2
20.92	Validate	GBT8A	13
20.91	Train	GBT6A	7
20.61	Train	GBT4A	1
20.33	Train	GBT8C	15
17.86	Train	GBT7A	10
17.74	Validate	GBT7B	11
16.05	Test	GBT7C	12
15.79	Train	GBT4C	3

Table A5: Pressurization requirements with critical values highlighted.

Bottle ID	Bottle Failure	Initial 12% of Data	Initial 25% of Data	Initial 50% of Data
	Pressure (Mpa)	Pressure (Mpa)	Pressure (Mpa)	Pressure (Mpa)
GBT4A	20.61	11.42	14.34	17.41
GBT4B	21.06	11.56	14.06	17.41
GBT4C	15.79	10.58	11.42	13.09
GBT5A	22.93	11.14	11.42	12.25
GBT5B	22.53	12.81	15.04	18.66
GBT5C	21.80	11.56	13.93	16.99
GBT6A	20.91	10.17	12.67	16.15
GBT6B	22.34	11.56	14.34	18.10
GBT6C	21.83	9.61	12.39	16.43
GBT7A	17.86	10.58	12.53	14.76
GBT7B	17.74	6.96	9.33	12.53
GBT7C	16.05	5.84	7.30	9.48
GBT8A	20.92	9.75	12.25	15.74
GBT8B	21.40	9.05	11.98	15.46
GBT8C	20.33	7.66	11.28	15.04

Acknowledgements

The authors would like to thank James L. Walker II, NASA Marshall Space Flight Center for performing the hydrostatic testing on the 15 bottles, taking the original acoustic emission data, and making it available for this research effort.

References

1. "Orbiter Tank Locations" *NASA Operations Project Office* [online database], URL: <http://microgravity.grc.nasa.gov/SpaceOps/Shuttle/COPV/> [cited 10 December 2010].
2. J.L. Walker, G.L. Workman and S.S. Russell, "An Acoustic Emission and Acousto-Ultrasonic Analysis of Impact Damaged Composite Pressure Vessels," National Aeronautics and Space Administration, Marshall Space Flight Center, AL 35812, May 1996.
3. K.L. Reifsnider, E.G. Henneke, W.W. Stinchcomb and J.C. Duke, "Damage Mechanics and NDE of Composite Laminates," *Mechanics of Composite Materials: Recent Advances*, Z. Hashin and C.T. Herakovich, Editors, Pergamon Press, NY, 1983, pp. 399-420.
4. E.v.K. Hill, J.L. Walker II and G.H. Rowell, "Burst Pressure Prediction in Graphite/Epoxy Pressure Vessels Using Neural Networks and Acoustic Emission Amplitude Data," *Materials Evaluation*, Vol. 54, No. 6, 1996, pp. 744-748, 754.

Research and Applications of AE on Advanced Composites

Kanji Ono¹ and Antolino Gallego²

¹ Department of Materials Science and Engineering, University of California,
Los Angeles, CA 90095, USA

² University of Granada, 18071 Granada, Spain

Abstract

This paper reviews progress in acoustic emission (AE) research and its applications to high performance composite materials and structures. The achievement and inadequacy in understanding of AE from composites are examined along with cases of successful usage in commercial and aerospace fields, taking into account limitations due to high attenuation and anisotropy. New goals for the future are also discussed in view of new analytical tools and vastly advanced instrumentation.

Keywords: attenuation, localization of damage, inspection, Lamb waves, wave propagation, finite element method (FEM), frequency analysis, modeling and simulation, pattern recognition, signal processing, aerospace, chemical and petrochemical, advanced composites, fiber reinforced materials, pressure vessel, structural health monitoring, composite structural evaluation, composite materials NDT.

1. Introduction

Acoustic emission (AE) played an important role in the development of glass-fiber reinforced composite (GFRP) rocket motor cases for Polaris A3 circa 1962 [1]. It was the beginning of AE applications that have expanded greatly over the last 50 years. AE was next deployed in testing propellant tanks for the Apollo lunar module and other aerospace applications [2]. Aerojet engineers recognized the variation in AE to originate from resin, interlaminar and fiber failures [1, 2] and modified manufacturing processes, e.g., by eliminating the geometrical inflection points in design to reduce the interlaminar shear stresses [3]. They used the summation of AE amplitude to successfully predict the burst pressure and developed practical AE source location equipment [1]. Continued work on rocket motor cases at Thiokol introduced Kaiser effect and load-hold emissions to the burst pressure prediction [4]. These pioneering accomplishments still form the backbone of AE pressure vessel inspection technology today.

Research on fiber-reinforced composites started in early 1970s [5-7]. Results verified correlations of AE to micro-fracture mechanisms. In one of the earliest AE papers on composite materials research, Liptai [5] showed the breakdown of Kaiser effect (this is now known as Felicity effect) and gradual reduction of Felicity ratio (aka Load ratio per JSNDI for concrete applications) in cyclically loaded fiberglass reinforced plastic (FRP) NOL rings. The latter was recognized as static fatigue (or stress rupture, a well-known glass failure mode due to load hold) of glass fibers, but no follow-up AE study was apparently published. Significance of these findings was initially unnoticed, however. Kim et al. [6a] clearly observed Felicity effect in carbon fiber reinforced plastic (CFRP) as well, but dismissed this effect while Kimpara [6b] also found Felicity effect, but treated it as error. The first peer-reviewed paper on composite research seems to be from UCLA's Tetelman group on boron-epoxy composite [7]. They correlated fiber fracture to AE, electrical resistance and compliance changes.

A breakthrough came in 1977 when Fowler recognized that AE activities found before reaching prior maximum load indicate the degradation of FRPs [8, 9]; for this behavior, he coined a new term, Felicity effect, and defined Felicity ratio as (load at AE re-start during reloading)/(prior maximum load)[see also the follow-up work, 10-12]. Subsequently, the Committee on Acoustic Emission from Reinforced Plastics (CARP) was organized, including Fowler, Teti, Crump, Hagemeyer among others [13, 14]. Through extensive collaborative field tests, CARP developed FRP inspection technology and published method documents through Society of the Plastics Industry, then through ASME/ASTM [15, 16]. This Recommended Practice spelled out loading scheme, AE analysis and interpretation methods and evaluation guideline, enabling widespread AE applications of FRP vessel examination, in chemical industry in particular. Fowler [12] documented success achieved in reducing major accidents via this AE method. In a revised document published in 1995 [17], intensity analysis method is used, relying on severity and historic index, along with emission during load hold, total counts, high amplitude emission, Felicity effect as key elements of evaluation. Dr. Fowler states (e-mail, 2012) "In the absence of CARP, the revised procedure became an open document. A number of organizations modified it for their own in-house needs. Some equipment vendors programmed it for use with their proprietary equipment. Even though not a public document, the technique has widespread use." His students extended its uses in FRP design and analysis [18, 19]. Fowler [20] and Davies [21] gave details of the intensity analysis method, which has also been used in MONPAC system for examining metal chemical processing equipment [22].

With improved FRP technology combined with the advances in AE instrumentation, numerous studies on research and applications followed and have been documented in AE Testing volumes of ASNT Nondestructive Testing Handbooks [23], where one can find many AE uses, such as for testing bucket-truck FRP booms. Also available are six-volume conference proceedings of AECM [24a-f], ASTM and ASME codes and standards, and many journal/conference articles that reach into thousands. Hamstad contributed important reviews [25, 26] along with his many papers with his extensive composite research since early 1970s. See also other notable reviews [12, 20, 27, 28]. Gorman [29] and Wevers [30] reviewed AE methods for structural health monitoring (SHM) field. See [31] for a review of newer AE analysis techniques. Drouillard and Hamstad indexed early AE papers in [32].

We must realize first that AE has not provided an effective NDT tool for some parts of composite industry. Such a tool is sensitive to existing defects, and is globally applicable to a large component in real time monitoring condition. While many success stories exist in FRP industry, as noted above by Dr. Fowler, AE has only played limited roles in many aerospace sites. We know AE can do better. In this paper, selected aspects of research and applications will be reviewed to highlight the progress achieved and to point to areas in need of more work. The main focus will be on development from the last 10-15 years since references cited above [23-30] have provided adequate coverage for the earlier period. Hopefully, we can go to the next level of understanding to give better solutions. Applications of advanced composites are expanding beyond aerospace and chemical industries into transportation industry and utilities. Such expansion presents renewed challenges for AE to be a worthy NDT method. We do have to overcome problems due to high signal attenuation in composites and need to explore the causes of Felicity effect and stress rupture, just listing a few. Collectively, we should resolve these obstacles, and make AE into a truly indispensable NDT method.

Research

Fiber fracture

From the early days of AE, glass fiber (GF) fracture has been recognized as energetic AE source detected close to the fracture load. AE from single fibers, tows (or strand) and unidirectional (UD) composites was initially characterized with amplitude distribution in order to compare with other failure mechanisms. By now, the difficulty of using AE amplitude by itself in signal discrimination is well recognized. However, a misconception that fiber fracture always produces high-energy event still persists to this day and this section is intended to clarify the situation.

For typical 10- μm diameter UD GFRP, peak amplitude ranges from 60-80 dB (ref. 1 μV =0 dB; literature in the 80s often used 1 μV =20 dB and one needs to reduce amplitude values by 20 dB) [33-35]. This range depends on the fiber diameters and sensors used, but GF results are fairly consistent over the years when sensor difference is accounted for. Wolters [33] used sensitive resonant sensors with less than 10-mm propagation distance and found 40-60 dB for 6 μm , 65-85 dB for 13 μm and 80-100 dB for 24 μm fibers, while another reported 50-70 dB for 13.5 μm GF [34]. In our test of woven GFRP [36], high amplitude AE signals of 60 dB mean level were found at above 90% of the failure load, verified as fiber fracture microscopically. Woven GFRP failure mechanisms are the subject of a detailed study [37], and complementary AE study should allow better understanding of woven composites, which are increasingly used in aircraft fuselage with carbon fibers, such as Boeing 787 (A.K. Mal, July 2012, private communication). Recent studies [38-40] reexamined single fiber composite (or SFC, with epoxy matrix) tests. Nordstrom [38] used 18- μm glass fibers and found peak amplitude of fiber fracture at 80 dB (150 kHz sensor). He also obtained Weibull moduli of 7-9 and correlated the shape of stress-strain curves to progressing fiber fracture (see also [41]). Bohse [39] used 20- μm glass fibers with peak amplitude of fiber fracture to be 58-81 dB (PAC-WD sensor used). More recently, de Oliveira [40] conducted careful SFC tests determining the amplitude of fiber breaks along with source location data. Such amplitude correction with source location was introduced earlier [42], but has seldom been used since. Carey [43] also introduced distance correction in his AE signature analysis work on CFRP. Using 21- μm GF, SFC showed 20-dB attenuation over 45 mm and fiber-break AE mean amplitude of 73 (53-79) dB (58 dB for 11- μm GF); the lower values are due to the use of a wideband sensor (DWC B1025). In single tow 9- μm GF composite experiment, Nanjyo et al. [44] obtained lower amplitude values ranging from 46-56 dB (Pico sensor). Diameter and sensor differences are responsible for the observed variation in amplitude ranges since GF strength and modulus are essentially unchanged. Berthelot obtained comparable amplitude range for 13-15 μm GF and for 7- μm T300 CF [45, 46].

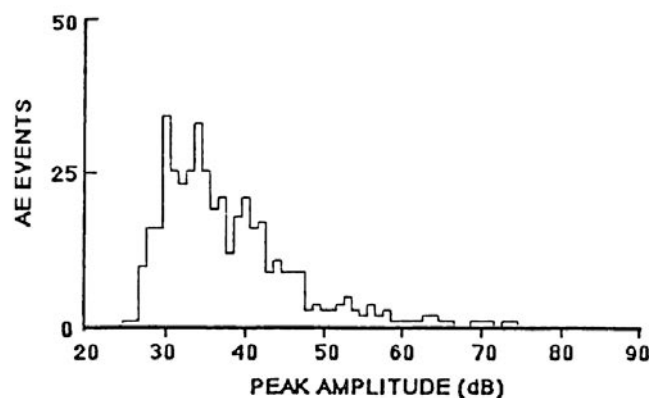


Fig. 1 Peak amplitude distribution of fiber fracture at 40-60% of the fracture load from 9-ply UD sample with pre-cut mid-ply [48]. Celion G50 fiber.

When carbon fibers (CF) were tested initially, peak amplitude of AE signals for T300 CF was 30 dB less than glass fiber [34, 47]. In part, this is because most carbon fibers have 7- μm diameter, and earlier CF strength was lower (T300 tensile strength = 2.65 GPa circa 1982). In our study [48, 49], the peak amplitude range was 30-50 dB for Celion G50 UD composites of various cut-ply arrangements (MAC175 sensor). This is 10+ dB lower than our GF results [36]. These AE signals from CF started to occur at 25-33% of the composite strength and also had short duration (mostly <50 μs) [34, 47, 48]. Figure 1 shows the peak amplitude distribution due to fiber fracture at 350-530 MPa, corresponding to 40-60% of the fracture stress from 9-ply UD sample with the middle 3 plies pre-cut [48]. Berthelot [46, 75] and Awerbuch [50] observed similar amplitude range (30-50 dB) during tensile and fatigue tests of CFRP coupons (CF not specified in [50], but probably T-300). Nanjyo's tow composite tests in 1992 [44] were also conducted for PAN (M50, 5- μm diameter) and pitch (XN50, 10 μm diameter) CF as well, giving comparable amplitude as GF data cited above; 44-56 dB for M50 and 38-58 dB for XN50. These CF were stronger than T300 or G50; 4.2 GPa for M50 and 3.7 GPa for XN50, accounting for the higher amplitude by nearly 20 dB (Fig. 2). In this study [44], the Weibull analysis of CF fracture strength and AE hits-strength distributions was reported. For three lots of CF, Weibull moduli of 5.7 to 13 were found for the fracture strength, while AE hits had higher Weibull moduli, $m = 7$ to 35, indicating multiple CF fracture in the tow tests [44]. A recent statistical analysis of AE signals from non-bonded GF bundles showed m to be 2.8-4.0 for 15- μm diameter fibers [41], which are about a half of $m = 5.6$ to 9 in tow tests [38, 40].

Recently, a new method for composite fracture study appeared [51, 52]; this is "High resolution Synchrotron Radiation Computed Tomography (SRCT)" and was used to capture fiber damage progression in a cross-ply CFRP laminate. Wright [51] showed that transverse-ply cracks initiate at 20% of the failure load, whilst 0°-splitting initiates at ~40% and large delaminations at ~60%. It is important to note that these cracking events occur in advance of significant fiber breaks that start after 60%. In Scott [52], fiber fracture was analyzed and compared with other studies, including AE. AE results for fiber fracture accumulation showed the same trend as SRCT and Weibull moduli are similar (also similar to [38, 40, 44]). The number of fiber breaks (N_f) was found to follow

$$N_f = C (\sigma/\sigma_o)^m, \quad (1)$$

where σ is stress and σ_o is characteristic stress and m is Weibull modulus. See also [38]. It is hoped this method can be used widely leading to more definitive AE mechanistic studies.

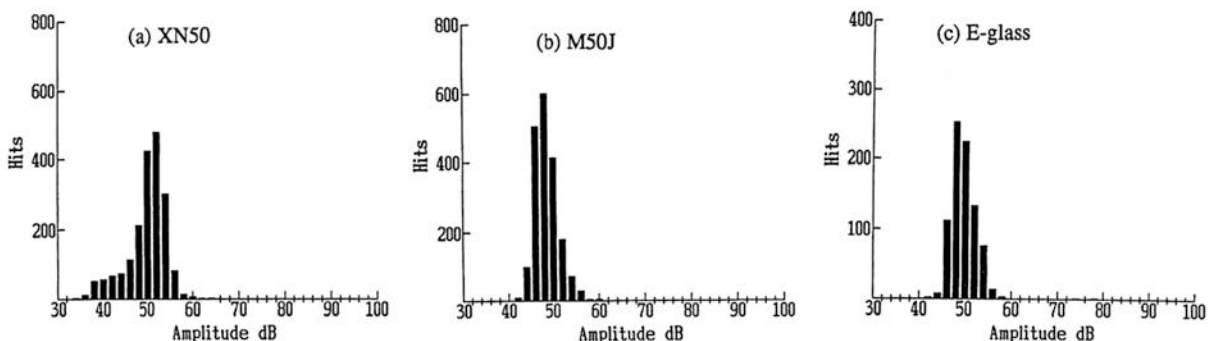


Fig. 2 Peak amplitude distribution of fiber fracture of a) XN50 pitch CF, b) M50 PAN CF, c) E-glass fiber tow-composite samples. Pico sensor. [44]

SFC tests with 7- μm carbon fibers, Bohse [39] showed amplitude of fiber fracture at 45-75 dB with the median value of 65 dB (WD sensor used; fiber unidentified, but ~late-90s vintage), comparable to usual GF fracture amplitude. In this work, CF diameter is ~1/3 of GF (~18 dB in

area) and less than 10 dB amplitude difference implies that higher CF modulus (by a factor of 3.5) accounted for the comparatively stronger AE in CF fracture (assuming comparable fracture strains). This CF SFC fracture result is 20-30 dB higher than previous studies from the 1980s [34]. This higher range of AE amplitude for CF fracture seems to reflect higher CF strength (2.5 GPa for G50 to 6.3 GPa for Toray T1000) and higher fracture strain values (0.7% for G50 to 2.2% for T1000). This is obviously due to dramatic improvements of CF properties in the last three decades. Thus, if one uses newer CF fracturing at 3-5 GPa (50-80% of T1000 fiber strength) in lieu of the G50 CF fractured at 350-530 MPa in 1988, 40 dB stronger AE signals are expected. Thus, we should observe CF fracture amplitude of similar or higher magnitude as 10- μ m GF. In fact, Sause et al. [53] showed this recently. Comparing E-GF (6.5 μ m) and T800-CF (5.2 μ m), he obtained fiber fracture energy of 12.6 and 13.1 mNm^3/s^2 . Assuming similar signal durations, the amplitude is expected to be comparable for comparable fiber diameters. It should be clear that AE amplitude from fiber fracture can vary widely. Small diameter, low strength CF produces AE amplitude comparable to the matrix sources (in 30-40 dB), while larger diameter fibers lead to higher amplitude to 80 dB. For thicker filaments, it can be even higher; AE signals from 150- μ m boron filaments produced 95+ dB signals [54]. Fiber optic samples also give similar strong AE.

Recent tow composite tests using T1000 CF indicates the number of CF fracture at stresses below 60% of the fracture strength is grossly reduced with improved CF quality (no amplitude data was reported unfortunately) [55]. Figure 3 shows this behavior in tensile testing with intermittent load hold (ILH) for characterizing Felicity ratio, but cumulative hits start to rise rapidly after the fifth load hold or at 213 lbs (failed at 352 lbs) or 60.5% of 6.77 GPa fracture strength. The same NASA group examined Kevlar tow composites as well. In this case, fibers start to fail at ~90% of the fracture strength [56]. This behavior is in common with GF composites. Detailed analysis of these experiments of UD composites should clarify this situation on amplitude levels.

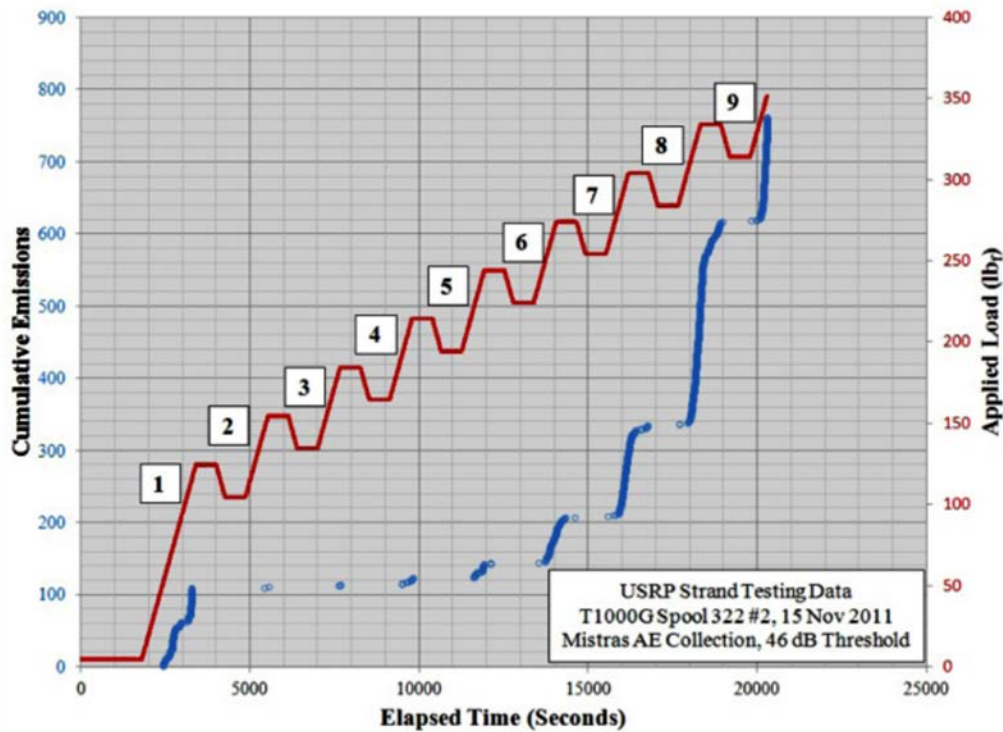


Fig. 3 AE of T1000 CF tow-composite test using ILH schedule at NASA. Red: Applied load (in lbs), Blue: AE. [55] (1 lbs = 4.54 N)

When a carbon or glass fiber fractures, it does so in brittle manner. Typical crack velocity in brittle fracture is several tenths of mm/ μ s or higher (e.g., 0.52 mm/ μ s for PMMA [57] and 1.6 mm/ μ s for glass [58]). Actual cracking velocity is expected to be much smaller as a static crack needs to accelerate under stress. For GF and CF, fracture time is expected to be 0.7~2 μ s assuming crack velocity of 5~10 m/s (or μ m/ μ s). The lower velocity limit is for GF [58], while CF crack velocity is expected to be twice that since CF moduli are ~4 times that of GF (crack velocity scaling with the Rayleigh velocity [57]). This translates to the center frequency of 0.5~1.4 MHz for AE signals from fiber fracture, which is partially within the high frequency range of common AE sensors, such as PAC WD, Pico and DWC B1025/B1080. Indeed, Gorman [59] reported such fiber-break signals from a COPV cover the entire range of flat sensor response (20-400 kHz), in contrast to matrix cracks (splitting), for which detected signals had frequency contents confined below 50 kHz. He also observed that, in hundreds of pressure vessel tests, including both CFRP and FRP vessels, waves with the highest frequencies appeared when the load or pressure level exceeds above 80% of ultimate stress. Thus, tow composite behavior extends to the windings of COPV. SFC samples in de Oliveira's study also showed high-frequency components [40]. His signals contained strong 300-1050 kHz components (using DWC B1025), especially when debonding accompanies a fiber break or when 7- μ m CF SFC has a fiber break. He attributes the effect of debonding to the higher freedom of the fiber ends at fracture. In contrast, GF fiber break signals without simultaneous debonding (11 and 21 μ m GF) have the highest peak at ~170 kHz with gradually decreasing high-frequency components. Gorman [59] observed similar vibration-induced AE from broken ends of tows and further clarification of debonding may be worthwhile in providing new inspection scheme. It should be noted here that Kim and Nairn [60] showed that fiber-matrix debonding always accompanies a fiber fracture in GF and CF SFC. Their epoxy resin (Epon 828) did not exhibit flat or conical fracture envisioned by earlier work [34]. We must have independent proof before assigning to an AE cluster a mechanism of fiber fracture with or without debonding.

When using broadband sensors, the observed peaks in the frequency spectra have to be treated with caution. Unless one has broadband flat-in-frequency sensor and propagation path, the peak frequency differs from the source-defined frequency. Most available sensors today have limited frequency range and have resonance peaks. Sheet or plate geometry has preferential frequency ranges of wave propagation. For example, Bohse [39] correlated fiber fracture to 500-kHz peak using WD sensor while matrix fracture contains lower frequency peaks only. This work and many others clearly demonstrated that one can often identify AE mechanisms via the frequency domain information. In fact, it is an important part of our pattern recognition analysis studies on composite AE [61a-c]. On the other hand, one cannot conclude fiber fracture has such a frequency peak because the WD sensor used is the origin of this peak (WD has three main resonances including one at 500 kHz [62]). Such arguments assigning frequency peaks to some specific AE sources have shown up too often in the past [63-65], yet most such claims revert to specific sensor or sample resonances and sensor-source path has significant effects. For example, de Groot et al. [64] examined a variety of CFRP and assigned frequency ranges to specific mechanisms. Such correlation is valid for the test condition they utilized, but the particular peaks originated from the use of WD sensor again, which was also the sensor used in Giordano et al. [65]. Eaton et al. [66] warned that "the overriding effects of specimen geometry and sensor response can produce misleading results" in their study to use frequency for separating source mechanisms having the differing relaxation time. One should not expect specific frequency peaks in other test arrangements, except for the general concept of faster source events to have higher frequency contents. It is instructive to refer to the most broadband AE study reported to date by Scruby and Battle, extending the limit to 3 MHz (-6 dB point) [67]. They did find two peaks for

the signal from fatigue crack propagation, the main one at 600 kHz. However, these peaks are due to the normal modes of the sample. Even more broadband system is needed to identify the key frequency of fiber fracture via the frequency spectrum analysis since fracture time is quite short, on the order of 0.1-1 μ s.

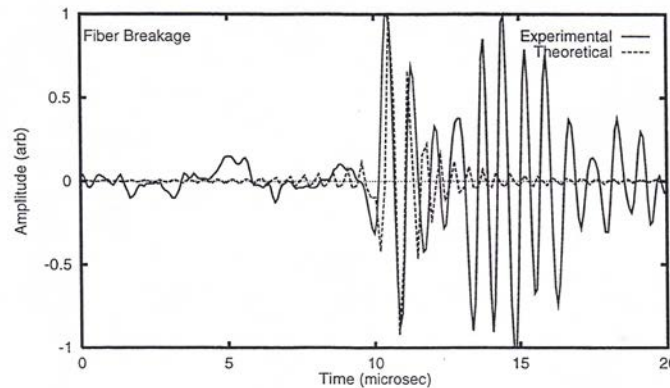


Fig. 4 Waveforms of fiber fracture (theory-broken line; experiment-solid line). [68]

This situation regarding the frequency peaks also arises in theoretical studies. For example, Guo et al. [68] obtained the solution of the wave motion produced by a general source in a composite plate using laminate theory with transverse shear correction. He identified the distinguishing features of the wave motion produced by various micro-fracture events (e.g., matrix cracking, delamination, fiber break, etc.) in thin composite laminates. Guo represented fiber fracture with 0.125- μ s cracking time in a model CFRP plate among others. Using the experimental transfer function of a broadband sensor (B1025) showing 200-2000 kHz bandwidth (within 3 dB of the peak at 1 MHz), the calculated waveform for CF fracture shows dominant \sim 1 MHz oscillations. See Fig. 4. The apparent frequency in this waveform is much lower than the expected center frequency of the original crack model, or 8 MHz. Note that Guo did not claim fiber fracture AE to have 1 MHz peak frequency. Recently, Sause [69] used finite-element modeling of laminated composites and crack models for CF fracture (in-plane) and resin fracture (out-of-plane) with 0.1- μ s cracking time. The CF crack produced displacement signals dominated by \sim 1-MHz S_0 waves (where S_0 velocity starts to decrease sharply), whereas the resin crack produced 100-300 kHz A_0 waves. His model included Lamb wave propagation of 50 mm from the source. Here, the Lamb-wave dispersion effects play the central role in limiting the upper frequency limit of the simulated AE signal and deciding the centroid frequency. Sause has presented more extensive analysis of related modeling in his thesis work [70]. His results point to the additional factor we must consider in trying to assess the source function when AE moves through thin sheets/plates. [It is noted that Ichikawa et al. [A1] reported theoretical calculations for the intensity of Lamb wave modes and dispersion effects as a function of frequency-thickness product. They used steel as the medium, but confirmed the Lamb-wave behavior observed by others. See Appendix 1.]

In considering the frequency contents of AE signals, one must not forget that high frequency components are attenuated rapidly as the signals travel from the source to sensors. Unless the sensors are almost over the source, the high frequency components above 200-300 kHz are reduced to background beyond 0.5-1 m distance. This has been known for 30 years and was incorporated in the CARP procedures, but we have no effective remedy applicable to typical applications. In laboratory, sensors are close to sources and we can try to understand the basic behavior.

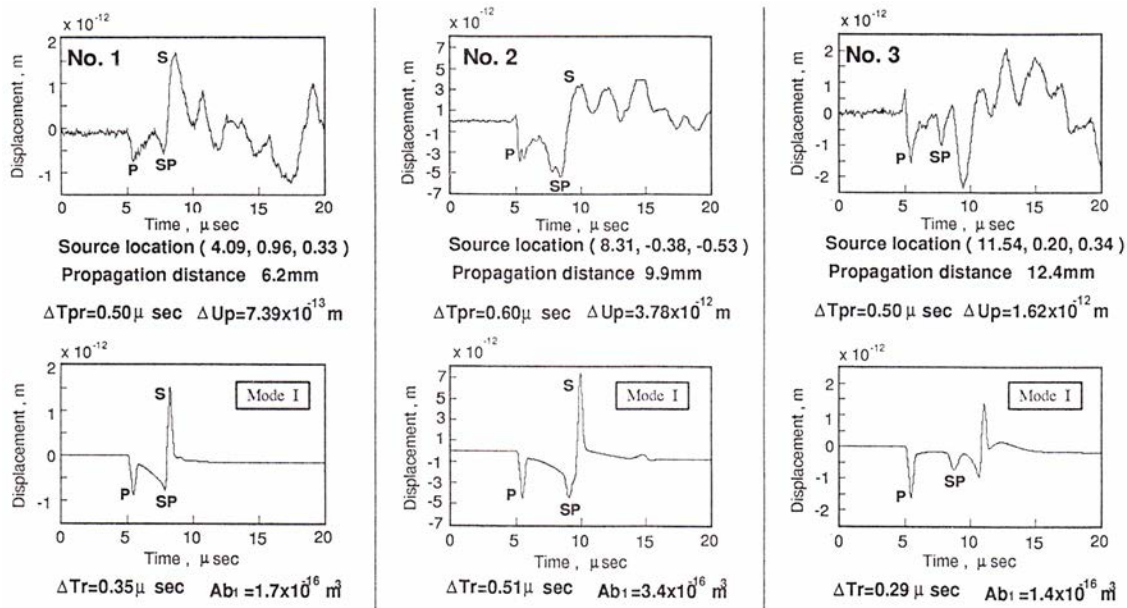


Fig. 5 Observed and matched calculated waveforms with source parameters. UD GFRP test. [71]

Another approach to the study of fiber-AE originated from Takemoto group at Aoyama Gakuin University. Suzuki et al. [71] conducted elaborate experimental analysis of GF fracture, deducing the source function for detected AE signals during tensile testing of UD FRP. The goal of getting the force-time function of an AE source is similar to the deconvolution approach from the 1980s, but waveform simulation and matching of source parameters distinguish this method from the past attempts [72]. Suzuki [71] incorporated the viscoelastic nature of FRP by introducing a frequency independent relaxation function, $R(t)$, after Weaver [73] and extended the Green's function approach of Ohtsu and Ono [74]. Suzuki [71] used a NIST-type displacement sensor, as well as an 8-channel source location system that identified the source position (using 8 Pico sensors). Both displacement waveform and location data were fed as input to waveform simulation algorithm. Adjusting the source rise time and crack volume, theoretical and experimental waveforms were matched. Here, the latter waveform was obtained by a conical displacement sensor of NIST design derivative (PAC S9208). Examples of such pair are shown in Fig. 5 for fiber-break cases. A cross plot of source parameters, crack volume vs. rise time, in Fig. 6, indicates the crack velocity limits of 2-22 m/s. The median crack velocity is 6.5 m/s in a good agreement with the measured crack velocity in glass of 5 m/s [58].

Note that, in elastodynamic theory [73, 74], the source parameter representing its magnitude is given by the product of the source area (A) and displacement (b_i), or crack volume. In fiber fracture, fiber opening equals b_i , not the released elastic energy. Thus, the energy analysis given in the past, such as by Lorenzo [70] and Berthelot [75] needs to be modified. Another overlooked aspect of AE signal analysis is the modeling of sensor input. For example, Berthelot [75] used a rectangular pulse to represent a crack signal, which is a sensible first-order approximation for surface displacement due to an opening crack detected at the epicenter. Note that the source displacement function is step-wise, but with a slope (Fig. 4 in [75]). Because Green's function is convolved with the source [74], surface displacement becomes a Gaussian-type mono-pole pulse (left: Fig. 5, [75]). It was simplified to a rectangular one (right: Fig. 5, [75]). AE sensors, however, typically respond to the velocity component. Thus, the sensor responds to two sharp pulses of opposite polarity separated by the duration of the rectangular pulse (T_f). In this case, the FFT of the velocity response has the center frequency of $1/2T_f$, instead of the displacement response that

peaks at zero and vanishes at $1/T_f$. When one uses a Gaussian shaped displacement pulse (a half-width of $0.22 \mu\text{s}$; Appendix 2, Fig. A2a), its FFT gradually vanishes without multiple zero points as can be seen in Fig. A2b. Note the half-width is 2 MHz, equaling the inverse of the base width of $\sim 0.5 \mu\text{s}$ in Fig. A2a. The derivative of the Gaussian pulse is known as a Gaussian mono-pulse and is shown in Fig. A2c. The FFT pairs of Gaussian mono-pulses of 0.2 to 2 MHz are shown in Fig. A3. It is evident that these pulses are broad and one can hardly use the spectra for source discrimination. Even recent AE modeling efforts have not taken these points raised here and reevaluation is called for.

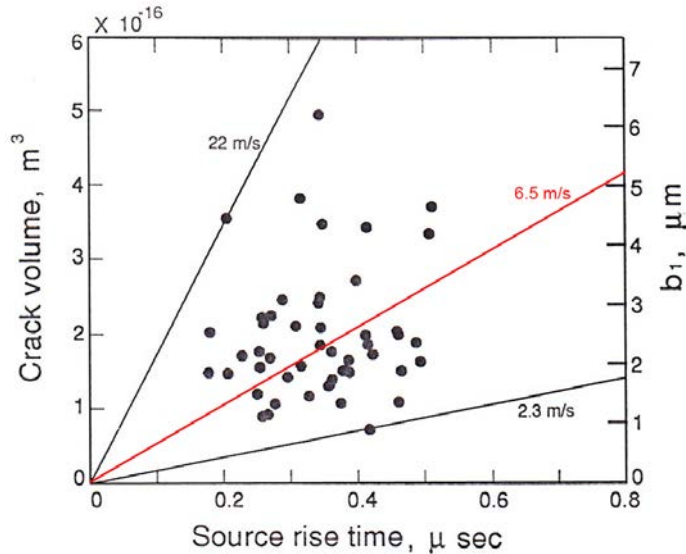


Fig. 6 Crack volume vs. source rise time. Data points are within the zone between crack velocities of 2.3 and 22 m/s. [71]

Still another issue evolves from the examination of Fig. 5. Note the three waveforms originated from fiber fracture, but with different propagation paths and distances (6.2 to 12.2 mm). These differences resulted in P, SP and S waves arriving at variable timing. Typical argument for the frequency contents relies on the P-wave arrival. However, a sensor detects all arrivals and time differences dictate the frequency spectra of the received AE signals. This aspect must be accounted for as well in discussing the frequency content of an AE signal when it consists of bulk waves.

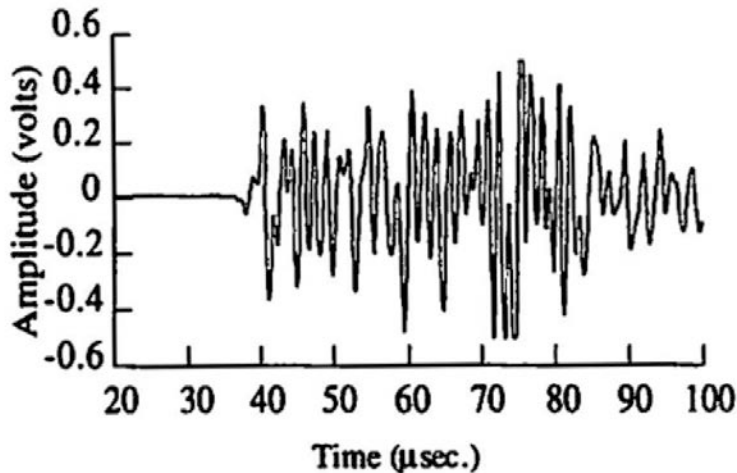


Fig. 7 Typical waveform from a transverse matrix crack in $[0/90_n/0]$ CFRP. [77a]

Matrix and interfaces

AE signals originating from the matrix and interfaces are varied and range from weak to strong, making unambiguous characterization difficult in practical composite structures. Several different mechanisms are expected to overlap as well. In model composites, however, clear distinction is possible.

Transverse matrix cracks: In 1979, as a part of an extensive investigation on composite failure mechanisms, Bailey et al. [76] first reported using AE for detecting transverse crack initiation in GFRP, while CFRP produced no AE due to pre-failure degradation. Prosser [77a] reported one-to-one correlation between observed S_0 Lamb wave signals and transverse matrix cracks in cross-ply composites (Fig. 7) when 90° -ply thickness exceeds 0.4 mm (3 plies). Notice that this signal is of high-frequency type (~ 700 kHz) and in thick cases (>6 plies) of very high amplitude (>80 dB). Gorman and Ziola [77b] showed even stronger events in $(0/90)_s$ CFRP, ranging up to 98 dB, but with >100 μ s duration. [Note this work is the first to exploit the plate wave characteristics of AE signals in typically thin composite samples.] Some of these signals with short duration are hard to differentiate from fiber-break signals. When transverse matrix cracks occur, three possible micro-mechanisms exist; i) matrix (resin) cracking, ii) debonding of fiber-resin boundaries and iii) fracture of bridging fibers. Matrix is low strength and slower fracture produces only low energy (amplitude) AE. See [39] for epoxy cracks having ~ 55 dB AE even for large area cracks. Matrix cracks are present in notched woven-roving fracture surfaces in [36, 37] as resin-rich areas of the size of roving diameter exist throughout the composite. In laminates made from UD prepregs, only the interlaminar layers have contiguous resin constituent and the contribution of mechanism (i) is limited. Debonding is expected to be the main mechanism for the transverse matrix cracking in laminates with straight fibers and as the source of first ply failure. Mechanisms i) and ii) typically coexist in woven composites [36, 37]. Woo and Choi [78] characterized debonding AE to have low amplitude (under 70 dB) and low frequency (lower frequency peaks than the sensor resonance of 265 kHz for PAC μ 30) using *in situ* microscopical observation of the notch-tip zone. They showed, however, that once macro-cracking begins, higher amplitude/frequency (>70 dB, 430-450 kHz) peaks are dominant, implying bridging fiber failures contribute substantially. Fracture surface showed both of these (ii and iii) mechanisms. Elevated temperature exposure (wet or dry) affects the matrix-bonding behavior, which was detected with AE. Schoßig et al. [79] used environmental SEM to assess damage mechanisms of short-fiber GFRP and identified 14 different mechanisms and recorded AE simultaneously. However, too many processes occur together. No clear correlation to AE signal characteristics is established so far. Bussiba et al. [80] exposed CFRP (0/10 layup) to 100°C for 2 weeks and saw accelerated debonding with the knee strain down from 1.5% to 0.6%. Wet exposure of GFRP was reported in [61c, see also 81].

Godin et al. [82-85] made a series of well-designed studies using UD, angle-ply and cross-ply composites with advanced pattern recognition analysis. Using Kohonen map and k-means methods, they identified four distinct signal types and attributed them to matrix cracking, interfacial debonding, fiber fracture and delamination. Waveforms of the 2nd and 3rd types are visually indistinguishable, however. The use of Kohonen maps appears effective in identifying clusters of AE signals and will be examined in a later section. In de Oliveira's thesis [40], he summarized nearly 20 other AE works on transverse matrix cracking and also reported own cross-ply GFRP testing [see also 60]. He developed artificial neural networks based on self-organizing maps with waveform and wavelet-transform data as input. Among six clusters identified, transverse matrix cracking produced two types of AE signals having characteristic S_0 waves centering at 350-400 kHz lasting 30-60 μ s. The low frequency part arrived first as expected for S_0 waves. Shorter

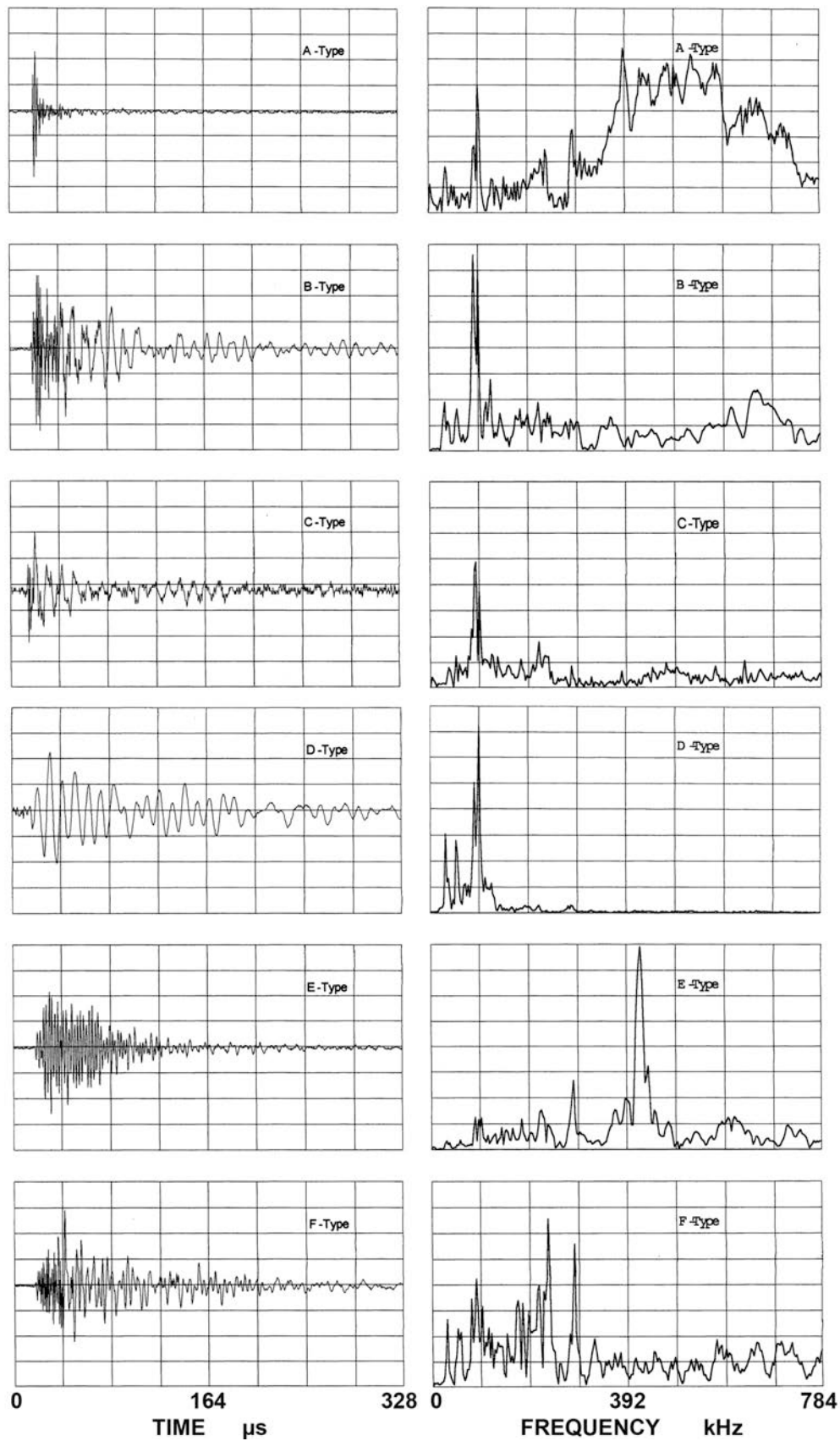


Fig. 8 Waveforms and frequency spectra of 6 different types, classified by pattern recognition analysis of AE signals from QI CFRP laminate. Time scale: 41.0 $\mu\text{s}/\text{div}$, Frequency: 97.7 kHz/div, Amplitude scale varies. WD sensor at the sample center. Huang [61b]

duration signals (type II) are attributed to the initiation, while longer ones (type I) to the propagation of transverse matrix cracks [60].

Delamination-Shear: Ono [48] reported AE from the delamination of UD CFRP with pre-cut plies with several different shearing zones. Shear strength level was 5 – 24 MPa. Overlap length ranged from 25 to 75 mm (13 mm width). Tensile loading produced initially medium amplitude signals (50 - 70 dB) with an average event duration of $\sim 120 \mu\text{s}$ from the initiation of Mode II delamination. At higher loads, high amplitude events (70-130 dB) of long ($> 200 \mu\text{s}$) event duration were found. These are caused by rapid advances of delamination under mainly Mode II loading with out-of-plane stress near cut edges. Lagunegrand et al. [86] examined free-edge delamination on $\pm 30^\circ$ angle ply CFRP and identified 90-100 dB signals as Mode-III delamination induced AE. This delamination occurred between $+30^\circ$ and -30° plies in shear, while mixed mode shear was reported in $[15_n/90_m/-15_n]_s$ laminates. Scholey [87] examined delamination in large-sized QI CFRP samples with cut plies, getting 10-50 pm A_0 -wave amplitude as the area of delamination reaches $\sim 30 \times 50$ mm after loading. Surprisingly, duration is only $\sim 100 \mu\text{s}$, implying delamination expands in small steps. Huang [61b,c] examined waveforms of various AE origins of CFRP tensile samples (UD, cross-ply, quasi-isotropic) in conjunction with pattern recognition analysis. One of six types identified is due to delamination, which becomes active just prior to sample failures. As shown in Fig. 8, type-D delamination signal has the lowest frequency content (~ 100 kHz) and long duration, while fiber-break AE (types A and B, latter with larger matrix debonding) has highest frequency content and short duration. (Type C is from transverse matrix crack with ~ 100 kHz peak, type E from splitting with ~ 400 kHz peak and type F from shear crack in $\pm 45^\circ$ plies at medium frequency.) Corresponding power spectra show features originating from WD sensor resonances (esp. at ~ 100 , ~ 230 , ~ 300 and ~ 400 kHz) as the sensor primarily detected signals under its face in the middle of a narrow sheet sample. Effects of Lamb wave types may be present for types A and D, in particular.

De Oliveira [40, 42] identified two types (IV and V) of delamination-induced AE signals in cross-ply GFRP tests. Both are A_0 -mode waves with low frequency contents under 400 kHz (down to 20 kHz in type V) and strongest contents at 150-230 kHz. Type IV was observed at lower loads, attributed to matrix-fiber decohesion as well as delamination. Type V appeared near final fracture when delamination activity was high.

Delamination-Opening: Bohse and coworkers [88, 89] studied Mode I (crack-opening type) delamination using DCB specimens and correlated AE energy with strain energy release rate (G_{Ic}), supporting the concept of damage zone concept ahead of the crack tip. They consider the presence of matrix cracking and matrix-fiber interfacial debonding, the latter in stronger interface condition. Some bridging fiber fracture is possible as well as in [78]. This also has more high frequency component, allowing the discrimination of the two mechanisms. In both, however, the main frequency feature is the dominant low frequency components below 200 kHz. Amplitude of these AE is mostly ($\sim 90\%$) in 60-80 dB range. Another CFRP DCB tests [64] reported essentially same results with a comparable low frequency peak (120 kHz with minor one ~ 300 kHz, both characteristic of WD sensor). This low frequency peak was also seen in epoxy resin crack and in lap-shear AE.

Recently, Sause et al. [53] published a comprehensive study of DCB tests with AE analysis examining interlaminar crack propagation in GFRP and CFRP. They conducted pattern recognition analysis to identify three clusters, corresponding to matrix cracking, interfacial failure and fiber breakage, using mostly frequency-based features, such as average, centroid, initiation, peak,

weighted peak frequency, six partial powers, etc. Cross plot of partial power at 450-600 kHz vs. weighted peak frequency easily separated the 3 clusters. Figure 4 in [53] compares observed and FEM-simulated signals and wavelet spectrograms, showing good agreement. Interfacial failure dominates cumulative signal amplitude, followed by matrix cracks. Fiber breaks contribution is low as this comes from bridging failure. This theory-test-model hybrid approach holds great promise in assessing complex structural composite design under various loading conditions, integrating AE as a part of health-monitoring scheme.

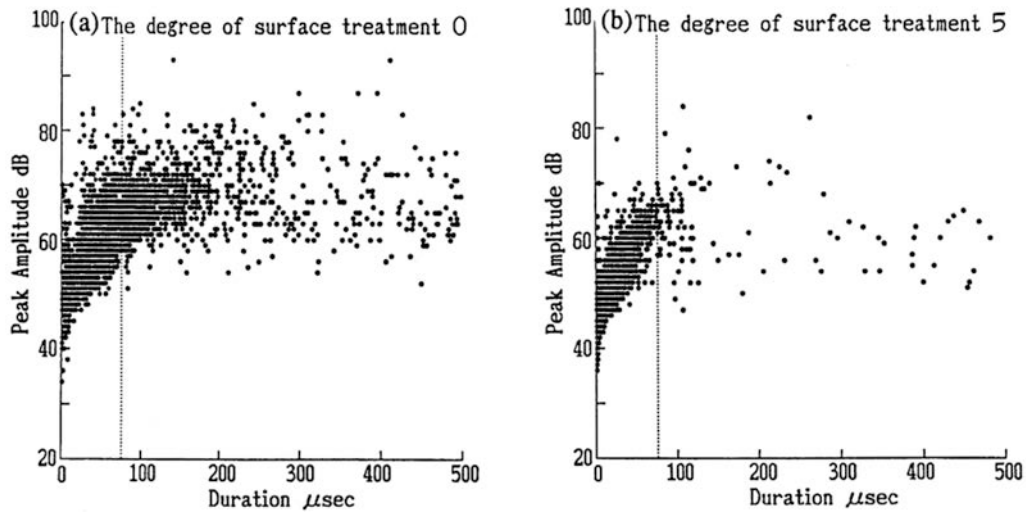


Fig. 9 Amplitude vs. duration of tow-composite samples with (a) no and (b) maximum surface treatment. [44]

Fiber-pullout: In tow composite tests, Nanjyo [44] used 4 different levels of (pitch-)CF surface treatment. Without treatment (level 0), many fiber pull-outs of up to 100 μm were observed after failure. With maximum treatment (level 5), fiber-matrix bonding improved and few fiber pull-outs were found producing flat fracture surface. Comparison of these two conditions on amplitude-duration plots indicates events with 60-80 dB amplitude, longer than 80 μs duration increased more than ten-folds in the level-0 sample. These long duration signals are due to fiber pull-outs. This means pull-out AE amplitude is 9 dB higher to fiber fracture (Fig. 9) on average. However, differentiation must rely on duration. Single glass-fiber pull-out experiment by Mielke [90] produced similar results regarding amplitude, though fiber diameters of 20-25 μm were used and fiber-break amplitude was ~ 10 dB higher than pull-out signals while another study examined pull-out of SiC fiber from glass matrix [91]. A more recent work used AE in single Kevlar-fiber pull-out tests, and showed energetic signals of 50-90 dB (Pico sensor). However, AE part is difficult to evaluate lacking key details [92].

Mixed mode cases: Mizutani et al. [93] examined fracture of cross-ply CFRP under central point loading and observed four separate types of AE signals. Signal simulation using laser sources allowed him to establish source mechanisms of fiber fracture, transverse crack, delamination (shear) and matrix crack, designated as type-A, -B, -C and -D. These 4 signal types are shown in Fig. 10 together with wavelet spectrograms. Two sensors placed at 90° angle from the loading point (along 0° and 90° relative to the surface fiber axis) showed vastly different waveforms, helping the identification process. Of 327 total, initial 70 events showed the following: Mode-I type fiber fracture in the front layer (the first event + 3), followed by transverse matrix cracks in the mid-lamina (27), from the middle part on, delamination (15) and splitting-type matrix cracks (11), (13 unidentified). They also studied the same experiment, but under dynamic loading

condition. Details can be seen in JAE [94]. Four types of cross-ply CFRP plates were impacted. Lamb-wave AE signals were detected by small AE sensors on both surfaces to separate S_0 and A_0 modes. Only Impact-AE is obtained when the impact energy is below a fracture threshold. When internal fracture occurs, both Impact-AE and fracture-induced AE (or Fracture-AE) were detected. Most of strong AE signals were correlated with splitting matrix fracture source (type D in Fig. 10).

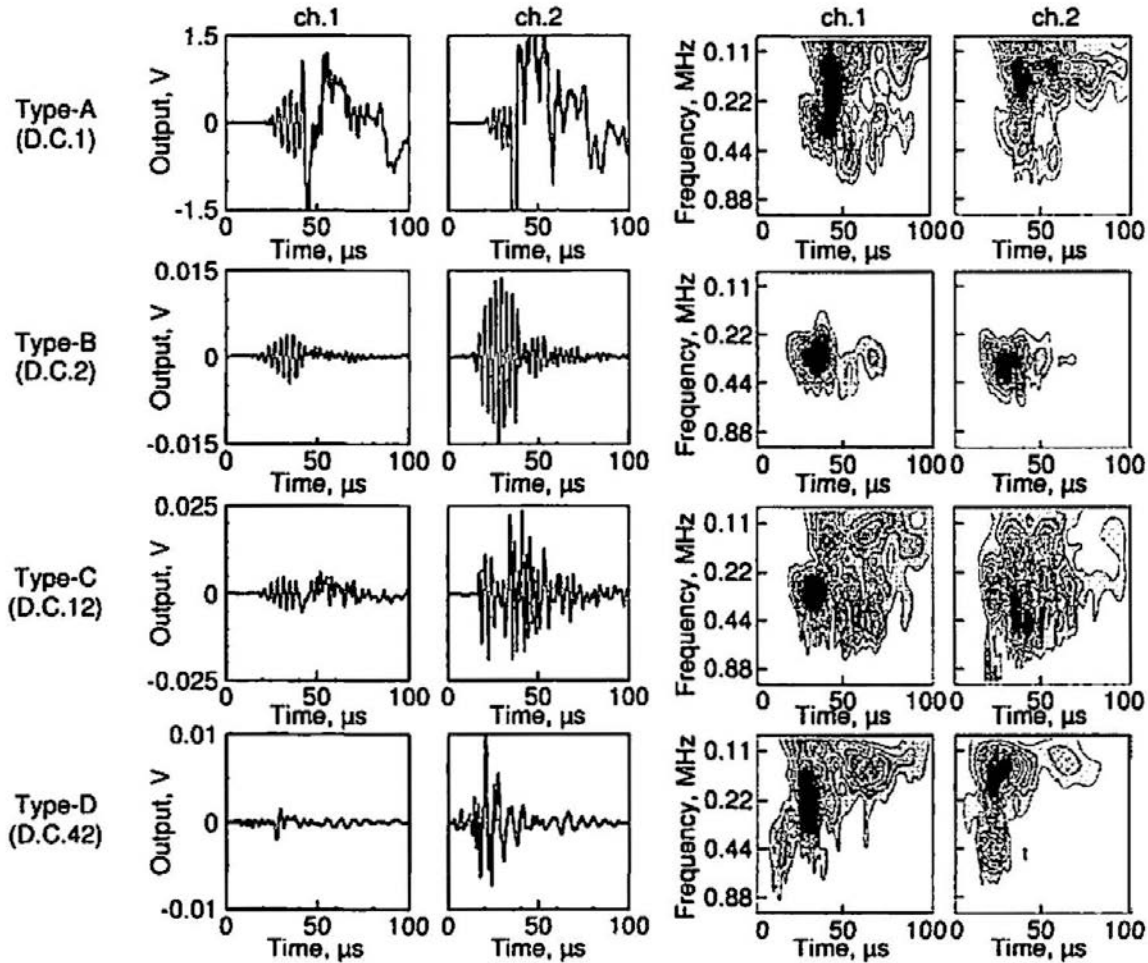


Figure 10 Waveforms and wavelet spectrograms of 4 types of signals from point-loaded cross-ply CFRP. [87]

There are other types of matrix fracture. For example, matrix fracture similar to the transverse matrix crack, but fibers oriented along the loading direction, also occurs. This is usually called splitting and corresponding waveform is that of type E in Fig. 8 [61b,c] (also type III in [40, 42]). Another type of matrix fracture occurs under shear stress along the fiber-matrix interfaces in angle plies, such as those $\pm 45^\circ$ plies in quasi-isotropic laminates. This has a characteristic waveform of type F in Fig. 8. Both E and F types have slowly rise time, reflecting slower growth of such cracking (WD sensor was on top of these sources 0.5 mm away, so no propagation induced slow rise time). The characterization of signal types relied on the laminate types and when these signal types were emitted during loading. (Note these features are dependent of test conditions: these tests used thin (~ 1 mm thick), narrow (13 mm wide) CFRP samples with WD sensor attached at mid-section. See also [95].)

Felicity effects

When damage accumulates in materials, Kaiser effect breaks down. This is usually characterized by Felicity ratio; the stress of AE restart/prior maximum stress. Felicity ratio has been linked to the residual strength of composites, and has been studied over many years: see Hamstad's thorough discussion in 1986 [96]. Changes in Felicity ratio on laminates are shown in Fig. 11a and b. In Fig. 11a, Hamstad [96] shows a schematic plot of GFRP data by Fowler and Gray [10], where it drops with applied load. Awerbuch's data on a multi-ply CFRP decreased with increasing prior stress above 1/3 of the tensile strength of 272 MPa [97]. Felicity ratio was down to 0.7 with prior stress of 220 MPa or 80% of the maximum. These are data from tensile coupons. On bend testing, GFRP also exhibited Felicity effect, but stress level at the start of decreasing Felicity ratio is higher (75-80%) instead of 45-60% in Fig. 11a, as shown in Fig. 12 [98]. Obviously, the difference arises from different failure mechanisms between tension and bend tests, but exact cause is unknown. AE monitoring in compression-after-impact or bending tests with damages showed the reduction of FR values [e.g., 99, 100]. Various AE parameters including FR were combined with neural networks for burst pressure prediction [e.g., Hill, [23], pp. 382-387].

The origins of Felicity effects need to be explored further as we find few articles beyond Hamstad [96]. It is obvious that the stiffness of fiber-damaged zone is reduced and stress/strain differentials develop against the surrounding sound zones upon reloading. This is realized during any unload-reload step [cf. 41], since the stiffness is proportional to the fraction of intact fibers. A damaged zone has a lower stiffness and deforms more. The stress/strain differentials, in turn, produce additional interlaminar stresses, leading to premature delamination. This can be the source of Felicity effect in impact-damaged vessels. In the absence of fiber damage, delamination itself should give rise to frictional AE during an unload-reload step. At any interlaminar, resin-rich layer between plies of different fiber orientations, interlaminar shear stresses are always present. While the shear fracture strain is of the order of 1% in most resins used today, it is common to use longitudinal-hoop fiber angles of 60-70° and substantial interlaminar shear stresses result upon loading. With our current AE methods, separating delamination and frictional AE signals is feasible. With the above scenarios for Felicity effect, we should expect strong FR dependence on lay-up sequence.

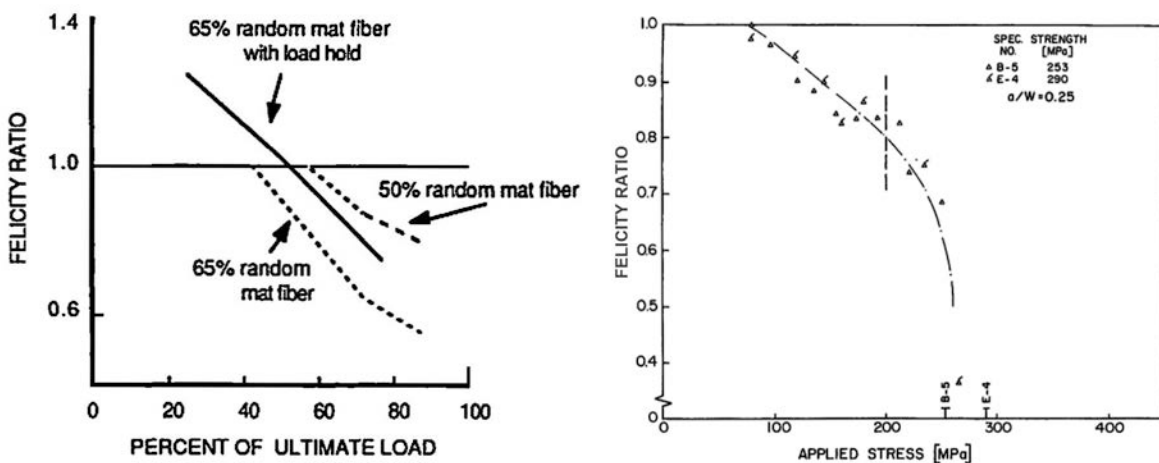


Fig. 11 a) FR vs. applied load of GFRP [96]. b) FR vs. applied stress of multiply CFRP [97].

Felicity ratio (FR) provided sensitive measure of developing damage under compressive tests [101]. CFRP laminates with 914 or PEEK resin matrix having a seeded defect were cyclically loaded and $f = 1 - FR$ was used as damage indicator (of internal delamination). Applied load P

and f are related with laminate specific manner with high R^2 -values >0.98 . See Fig. 13. As the marks for visible crack indicates, f -value gives the warning of internal damage.

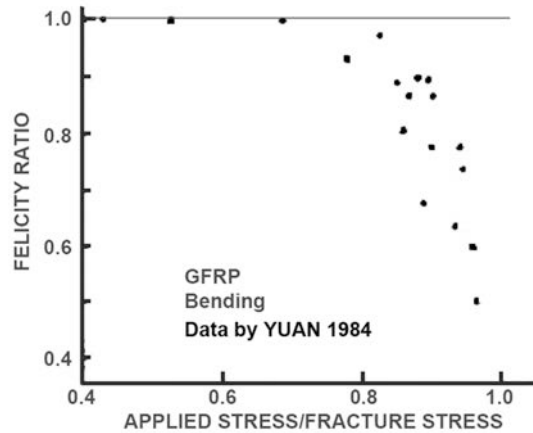


Fig. 12 FR vs. stress ratio of a GFRP under bending load [98].

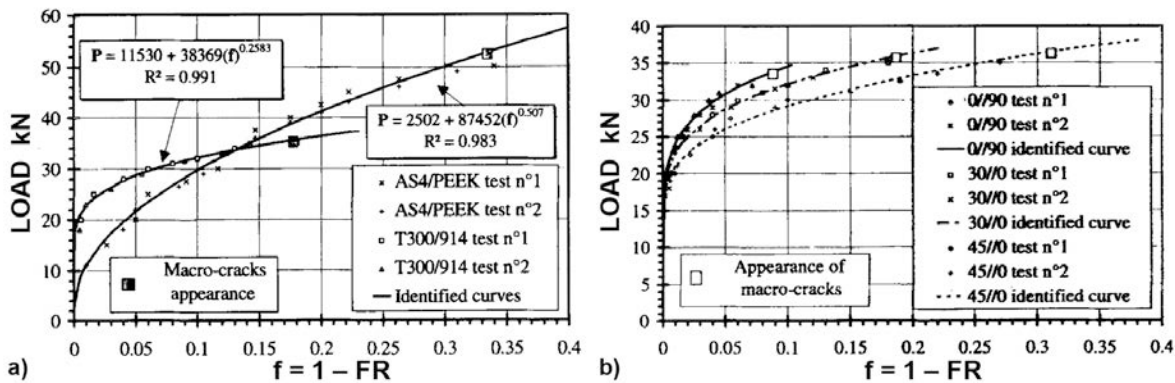


Fig. 13 Cyclically applied peak load vs. $f = 1 - FR$ for CFRP. a) with different resin, b) different orientation [101] Loading is compressive and CFRP has an internal defect to initiate delamination. Appearance of macro-cracks is marked by squares.

Several stressing sequences are used in obtaining FR. The usual one is to unload from the previous maximum as in [101], whereas incomplete unload sequences are more convenient to perform. One such example is shown in Fig. 3, called intermittent load hold (ILH), while CARP procedure calls for 10% unload with stepped loading (Fig. 4, [15]). The origin of Felicity effects is most likely from frictional (secondary) AE [97], but the link between Felicity effects and residual strength is empirical. Toward clarifying this link, NASA has embarked on extensive basic study of FR as they view this as one key element in the prediction of composite over-wrapped pressure vessel (COPV) performance. Specifically, it was found that some COPV failed in accelerated stress rupture testing; that is, COPV is pressurized and held for extended periods. They cannot afford such a failure in space [102]. Two composite tests using Kevlar 49 and IM7 and T1000 carbon fibers were initiated with 4 sensors mounted on 250 mm long samples [55, 103-105]. AE results for a T1000 tow test was seen in Fig. 3. FR from this and similar tests showed quite different behavior compared what we have observed previously. Figure 14 shows the new findings. Data for an IM7 COPV is also included for comparison. Felicity ratios given here were determined using the first AE event for Kevlar-epoxy tow, and the mean of the first 15 events for T1000 tow, IM7 tow, and the single IM7 COPV. FR values are in all 4 cases higher than 0.9 even very close to the failure load. FR is above 1.0 up to load ratio of 0.6-0.7 for CF and 0.85 for Kevlar fiber. For COPV, FR stays above 1.05 to load ratio of 0.78. First, these finding again

imply that fibers remain intact to much higher stress levels than older CFs like G50 used in [48] (IM7 is relatively old, however) as discussed earlier in conjunction with Fig. 3. A recent study [106] of T1000 Weibull modulus indicates that m-value at lower strength range exceeds 30 (overall $m = 5.9$), thus virtually eliminating fiber fracture below 80% of the average strength. Second, frictional mechanisms are not as active as in old CFRP, reflective of better interfacial bonding. Interlaminar shear strength has doubled from previously common AS4/3501 (76 MPa) to newer T1000 CFRP (150 MPa). This condition is true even in COPV, in which windings of various orientations are expected to lead to interlaminar shearing and friction (it is unclear if this particular COPV was subjected to autofrettage* (*an over-pressurization step to put the metal liner in compression), which can suppress AE at lower loads.) Third, flaws like splitting or delamination are not expected in tow composites, although this is not the case for COPV. As higher FR values are linked to low damage state and higher failure strength, more extensive studies on composite Felicity effects seem to be highly advisable. These should point to improved materials and manufacturing processes. FR on pressure vessels will be discussed later.

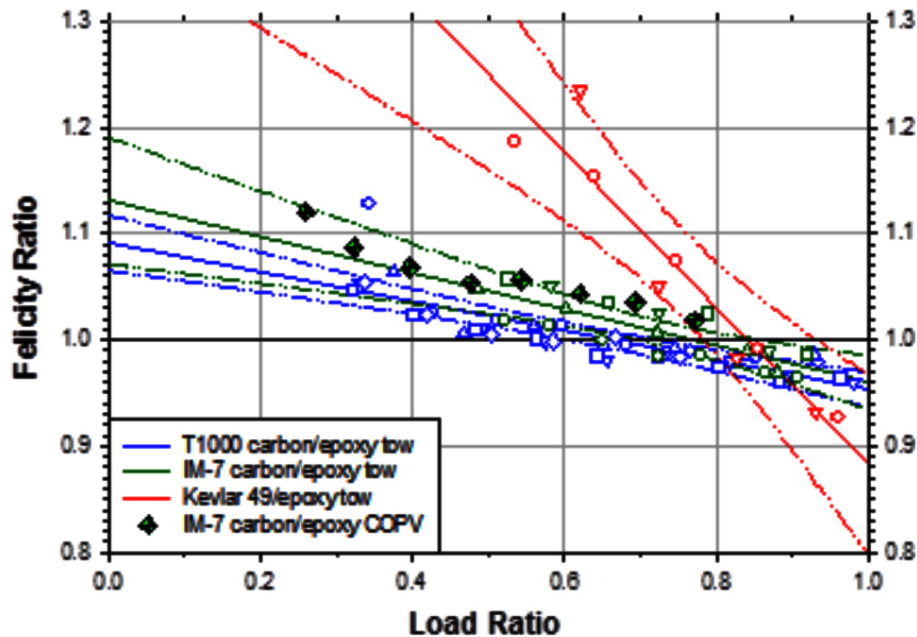


Fig. 14 FR vs. load ratio for T1000 carbon-epoxy tow (black-dotted), IM7 carbon-epoxy tow (grey-dashed), Kevlar 49 -epoxy tow (white-solid lines), and an IM7 composite overwrapped pressure vessel (large crossed hexagonal symbols). 95 % confidence intervals also shown. [105]

Wave propagation

Typical composite structures comprise thin members and AE signals are transmitted as Lamb or plate waves of extensional (or symmetric) and flexural (asymmetric) modes. Many composite members are anisotropic as well. Basic aspects on plate waves have been covered well in [12] and standard textbook [107]. In composite AE field, work by Gorman and coworkers [108-110] brought the focus on the peculiar wave propagation behavior of AE signals in thin composites, especially on the aspect of source orientation producing different wave modes. Hamstad and his NIST colleagues enhanced our understanding with extensive finite element modeling studies to shed light on the source types and resultant plate waves [111-114]. Large wave attenuation in composites has been accounted for in CARP methods [8-17, 20, 21]. Downs and Hamstad [115] showed the sharp amplitude drop (20 dB in 6 mm) due to geometrical spreading in CFRP vessels of inverse-square-root distance dependence. More recently, the anisotropic nature of composite plates has been included in analysis. Mal et al. [116] used a classical damping factor approach to

anisotropic wave analysis and found satisfactory results between theory and experiment (though this work is difficult to transfer to AE study). Sause incorporated suitable source models and wave propagation analysis on such CFRP model sheets [53, 69, 70]. Using complex elastic modulus obtained by air-ultrasonic technique [117, 118], some wave propagation analysis included attenuation factors as well [119-122]. Anisotropic velocity calculations are also reported for common CFRP layups [123-126].

Actual measurements of attenuation are limited. Suzuki [71b] measured P-wave attenuation in 60% UD-GFRP as a function of propagation direction and frequency. Along the fibers (at 0°), attenuation was 60 dB/m for 0 – 1 MHz and 180 dB/m normal to fibers (at 90°), 0 – 1 MHz. See Appendix 3. Suzuki also showed the relaxation function model of Weaver [73] fits the data above 1 MHz, but measured attenuation did not diminish at low frequencies contradicting model prediction. Prosser [76a] obtained apparent attenuation of S_0 and A_0 waves in IM7/977-2 CFRP of 1.2 and 3.7 mm thick quasi-isotropic laminates. For S_0 mode in the thinner plate, attenuation was 42 dB/m (410 kHz) and for A_0 mode it was 83 dB/m (85 kHz). For the thick plate, corresponding values were 35 dB/m (230 kHz) and 51 dB/m (90 kHz), indicating the effect of thickness and frequency. Attenuation observed on a CFRP pressure vessel [115] was higher. These values change when geometrical spread of inverse-square-root (Lamb waves) is accounted for. Gallego and Ono [127] reported attenuation measurements on CFRP plates of three types of layups (UD, XP, QI). S_0 and A_0 wave modes are separately evaluated and frequency effects are examined. Attenuation is also high. It is evident that any AE analysis must consider frequency-dependent signal loss through the transmission. It must be pointed out that some of theoretical papers on Lamb wave attenuation [117-126] state that guided waves propagate long distances. This is contrary to their results, many showing 100+ dB/m, and without experimental support.

Applications

Pressure vessels and tanks - 1

When AE applications mature, we find few reports in publications especially after these are compiled in reference books, like NDT Handbook [23] and codes and standards established. Applications to chemical tanks and vessels fall into this category after the first three AERC/AECM conferences [24a-c]. Rocket motor case applications are at a similar state [see [23], pp. 377-381]; actually, few reports had appeared from the beginning due to their sensitive nature. In this connection, it is interesting to find a review on the burst pressure prediction; Joselin [128] covers the subject quite comprehensively, introducing each paper adequately without inserting own interpretation. Thus, a reader must judge which approach is successful/unsuccessful on his/her own. Also many papers from AECM series conference proceedings are missing, as access to them may be difficult outside the US. Still this review is a recommended reading on this topic.

There are two important issues at this time. One is the evaluation of impact damage and the other is estimating the residual life of COPV. The first topic is not limited to pressure vessels, but it is one of the critical problems in aerospace circle. This has been studied with AE for more than 20 years [e.g., 129-135]. It is known that impact energy links to the burst pressure. Many AE parameters have been “successful” in predicting the burst pressure [23, 128]. An example of burst pressure-Felicity ratio correlation is shown in Fig. 15 [130]. While the sample size of this study is small, it is believed a larger database has been prepared to show the same trend within the aerospace circle. Yet industrial practice still uses AE as a supplementary method. As a tool for space COPV inspection, Chang [136] in 2003 assessed AE to be *better* on “inspection time” and “field use”, as *average* on “flaw characterization”, “simplicity” and “COPV preparation” and

as *weak* on “whole field”, “data evaluation” and “sensitivity”. In the AE field, we think “whole field”, and “sensitivity” as AE’s major strong points, but actual judgment by the practicing engineers is much more critical.

As mentioned in *Felicity effect* section, NASA is attempting to use AE for COPV burst pressure prediction [102-105]. This is now based on the higher levels of newly measured FR values of near unity. Figure 16 shows Felicity ratio with increasing previous highest pressure for an IM7 COPV during two separate pressurizations to 6800 psi (circles) and to burst (crosses). A linear fit is made to both pressurization data. Once the FR value at burst is established with confidence, this will allow burst pressure prediction from lower pressure ILH loading schedule. As noted before, this FR-pressure relation is comparable to tow composite behavior. This surprising similarity is promising in a sense that newer COPV manufacturing is eliminating many sources of flaws that previously decreased FR values, and also reduced COPV strength. It is hoped to see even better correlation develops in the case of newer T1000 fibers.

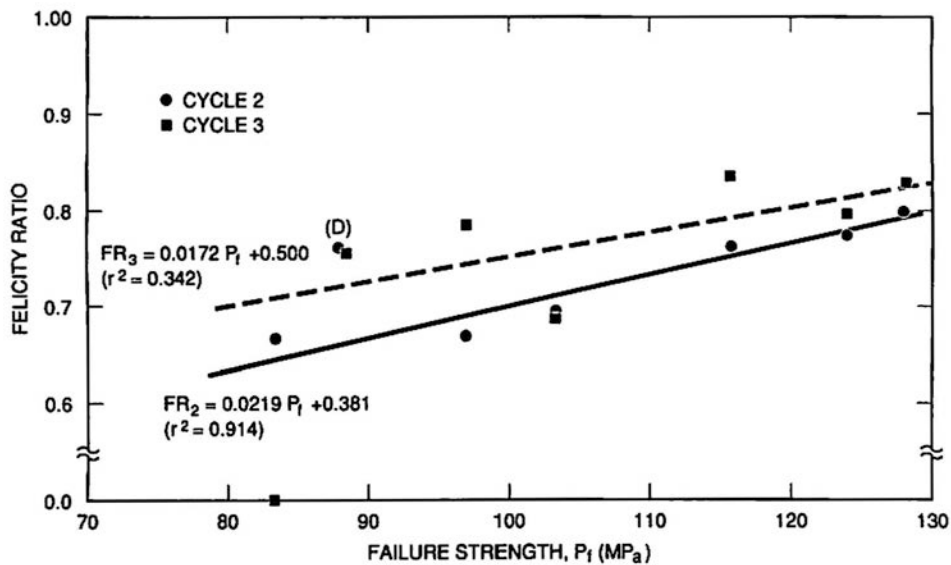


Fig. 15 FR values are almost linearly related to failure strength of spherical Kevlar COPV [130].

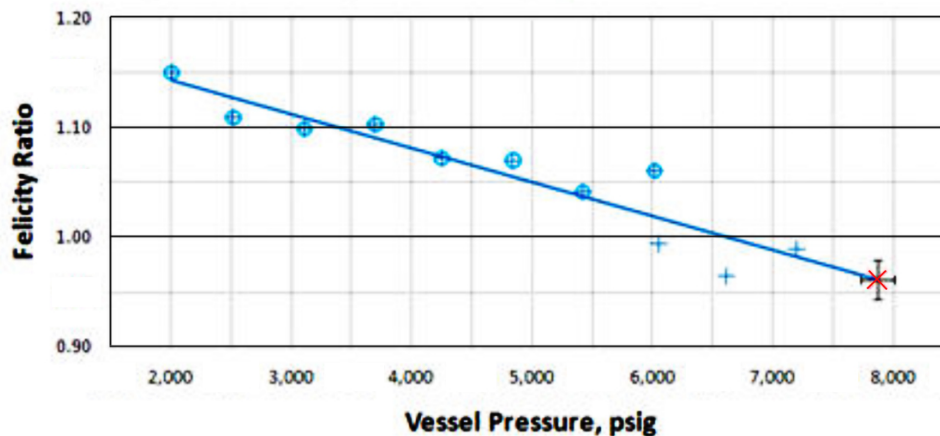


Fig. 16 Felicity ratio vs. increasing previous highest pressure for an IM7 COPV. Data from [105].

In connection to the use of FR values, it should be noted that another parameter is useful in some cases. Downs and Hamstad [133] defined Shelby (countdown) ratio, which is (the load

during unload when a predefined AE activity level is reached) divided by (the previous maximum load). This ratio was used much like FR values in correlating to the burst strength of CFRP pressure vessels. This ratio is being used in the NASA study discussed above [102-105].

The second problem of estimating the residual life of COPV comes from stress rupture behavior of high strength fibers. It is well known that silicate glass suffers from static fatigue, i.e., time dependent fracture due to the presence of moisture, aka. stress corrosion cracking. Similar effects exist in COPV made with Kevlar and carbon fibers. Figure 17 shows sustained load design curves for three types of COPV. These are used for determining the allowable sustained-load operating stress for a specified time at load using a probability of survival of 0.999. The time at pressure represents the sum of the time that the COPV is pressurized at or above 60% of mean expected operating pressure [136]. Over a long period of service, allowable applied stresses are quite low relative to the static strength. Of the three fibers, carbon fibers give the best performance at longer times (>100 hrs).

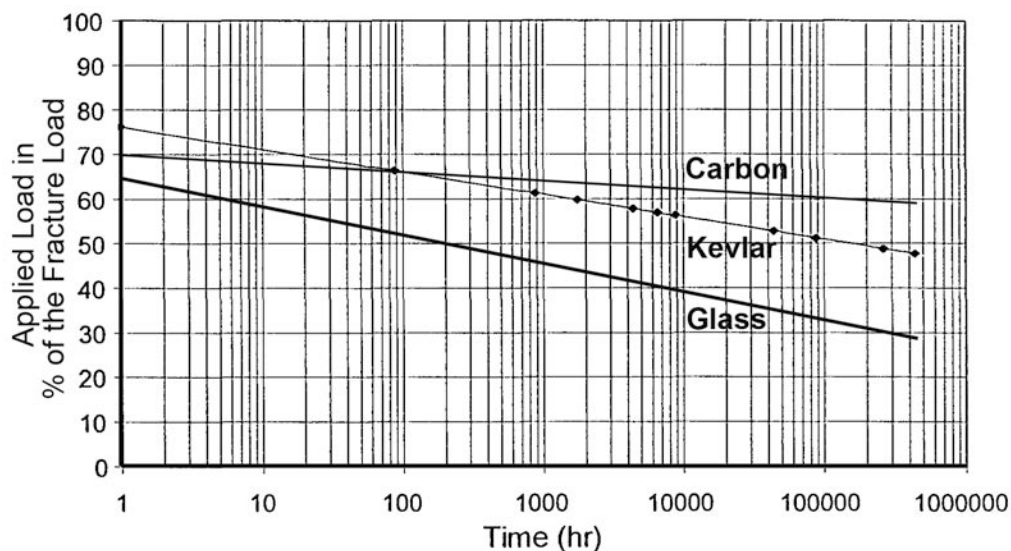


Fig. 17 Sustained load design curves for three types of COPV. Data from [136].

Since fiber fracture is the root cause, AE can play a significant role in resolving this problem of estimating the residual life. From the earliest days of AE, the stress rupture issue was recognized and Liptai [5] reported the process of stress rupture of a GFRP NOL ring. See Fig. 18a, which follows two hrs of loading before fracture with rising AE counts. This sample was loaded to 80% of the expected fracture load. Another NOL ring was loaded in fatigue at 50% of the ultimate load. At each 2000 cycles, it was loaded to 75% with AE monitoring, shown in Fig. 18b. As listed in the figure, estimated FR values decreased with loading cycles, quickly dropping to ~0.5 (as noted earlier in Introduction). Since then, however, only a few reports of AE monitoring of stress rupture of FRP appeared in the last 40 years [136-140]. There are reports of FRP stress rupture studies [e.g., 141-143]. NASA conducted wide-ranging study of Kevlar COPV used in Space Shuttles (24 used in each orbiter vehicle) after the Columbia accident and reestablished the reliability to be 0.998 relying mainly on accelerated pressurization testing. Raman spectroscopy was used to evaluate the residual stress state of Kevlar [144]. No mention of AE appeared in the report. However, another program is in progress [55,102-105,140] at NASA. On stress rupture tests, only a glimpse of data can be viewed so far [145], showing the usual increase in AE just prior to failure. In some cases, other data appear inconsistent [140] and we need to wait for the completion of the program. Still the location data on a successful test of a COPV shows several

concentrations of energetic AE events within 24 hrs of final failure (slide 19, [145]). Two views are given in Fig. 19. Such data point to the availability of information that warns incipient failure if continuous AE monitoring is used. Without monitoring, projecting 0.999-level reliability will probably require a new strategy yet to be formulated.

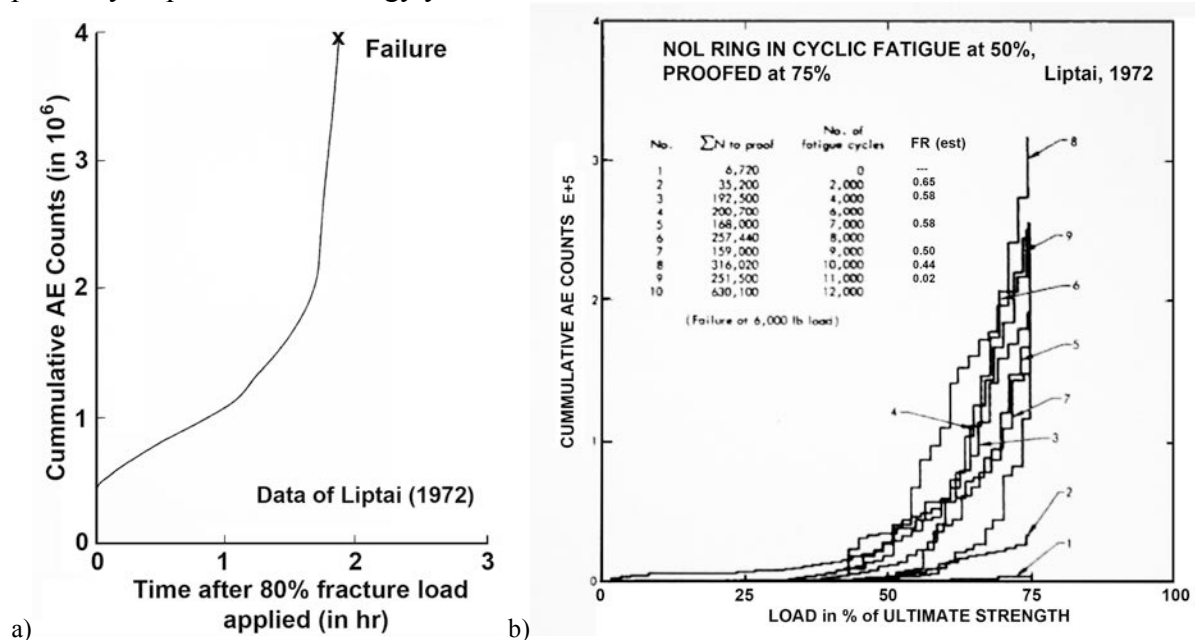


Fig. 18 a) Cumulative AE counts vs. time at 80% of fracture load applied. b) AE counts vs. load under fatigue load with intermittent proofing. Data from [5].

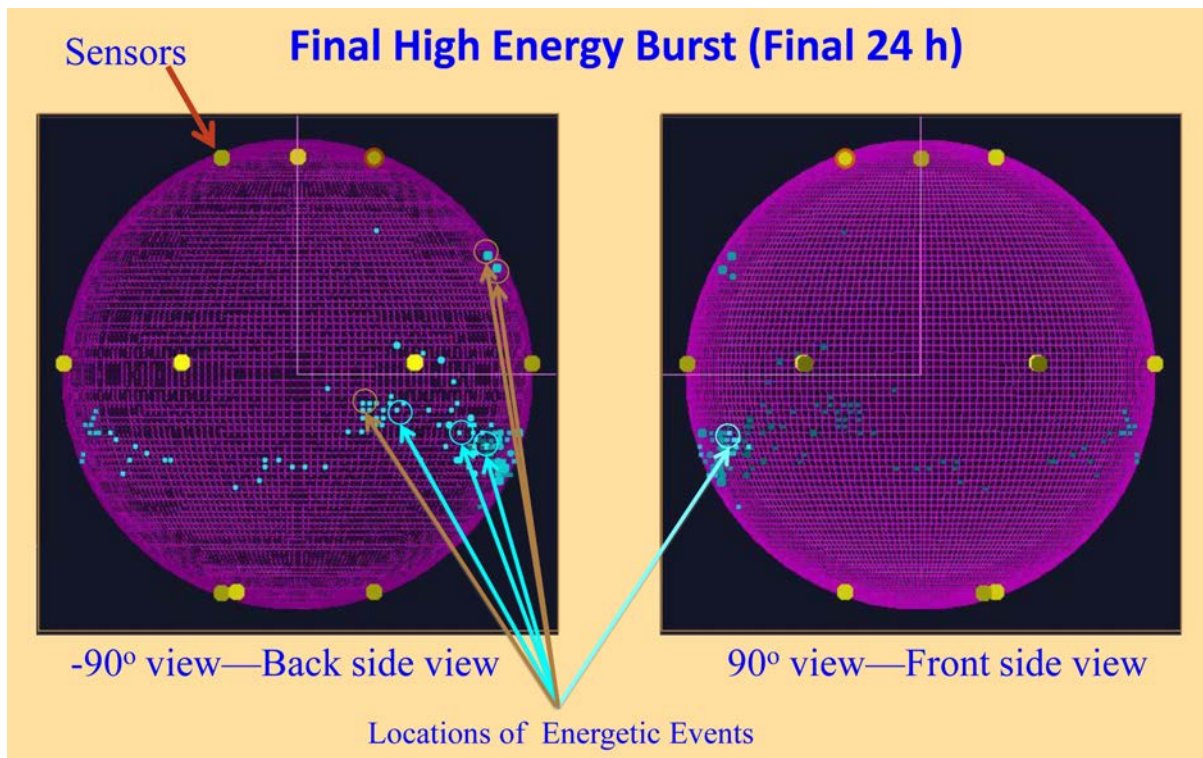


Fig. 19 Distribution of energetic AE events in 24-hrs period before the final fracture. Kevlar COPV. Data from [145] with color inverted for easier viewing.

Pressure vessels and tanks – 2

AE tests of smaller tanks have occupied some European AE groups of late. These have to be

done at low cost and rapidly. See [146-148]. A similar effort was undertaken by Propane Education & Research Council in the US, using ISO11119-3 as the basis. They chose to use only visual inspection, relying instead on the safety factor [149]. They stated in their Exemption request to the US Dept. of Transportation (prepared by Battelle) that “Electronic methods which have been examined to some level of detail in the laboratory include acoustic emission and acousto-ultrasonics (sic). Other potential inspection methods include holography, shearography, and thermography. These methods are used by highly trained staff in controlled laboratory and manufacturing plant conditions for quality control and special purpose applications. However, available data indicate the quality of damage detection in composite cylinders by these methods is inconsistent and varies significantly with the material selection, design, and manufacturing techniques. Consequently, unique NDI test criteria will be necessary for each different cylinder design, even though they may be from the same manufacturer. Practical application of these methods will be erratic and inconsistent for operations which inspect more than one cylinder type at one time, as is typically done in cylinder and propane industries.” Their products, LPG/CNG cylinders, are inexpensive, requiring the lowest cost inspection method. Yet, this seems to be the state of general NDT community that is so ignorant of the state-of-the-art in AE technology. The safety factors they incorporated are still of interest; This value, minimum stress ratio, is defined as the ratio of the fiber stress at calculated design minimum burst pressure divided by the fiber stress at 2/3 times test pressure (i.e. working pressure). For cylinders without liners or with non-load-sharing liners, the stress ratios are:

- Glass fibers – 3.4
- Aramid fibers – 3.1
- Carbon fibers – 2.4

These cylinders are designed to last 15 to 50 years and the minimum stress ratio is to assure against failure due to stress rupture. Note CF can be stressed the highest. It is not known if this has received DOT approval.

On the side of chemical vessels, AE is well accepted thanks to the efforts of Dr. Fowler and the CARP, as mentioned in the Introduction. A manufacturer of FRP vessels [150] recommends AE testing of their product as follow: “Acoustic emission tests on used equipment are most effective when there is baseline information available. It is therefore recommended that all critical FRP equipment be baseline AE tested soon after start-up. Once in service, the amount of AE testing that is done is the owner’s prerogative. Often, equipment is tested at a point in time approximately halfway through the estimated life span of the equipment. Ongoing testing will depend on the results of this test. When critical equipment is nearing the end of its service life, regular AE testing can provide a meaningful structural evaluation that may prolong equipment use and prevent unexpected failure. Acoustic emission testing identifies and locates active defects in laminates by detecting minute acoustic impulses that are generated as a defect propagates under load. A major advantage of this procedure is its ability to monitor an entire piece of equipment quickly.” This is a welcome testimony for the validity of AE testing.

Small, but extremely high-pressure cylinders also present technical challenge, as in the case of 100-MPa hydrogen cylinders [151]. Also see Gorman [152] for AE specific discussion. A new ASME Code case was developed based on AE to provide the accept-or-reject criteria. These are based on the curvatures of cumulative events and energy curves that quantitatively measure pressure vessel stability. These are COPV, but the liners do not carry load, unlike the space counterpart discussed in the previous section (these carry 20-30% load [144]). An example of AE cumulative event (ΣAE during load hold) analysis is shown in Fig. 20. Left curves are AE events curves for 4 channels. At 320-570 s, load is held and event rates started to decline, which are fitted with exponential functions of the form

$$\Sigma AE = A \exp(B t) + C, \quad (2)$$

t = time and A , B , C constants. For the curve on the right, shape factor B is -0.0183 and goodness of fit is $R^2 = 0.91$. When B is negative, AE event rates decay and the vessel is accepted as stable. Other factors used include the number of fiber breaks, fiber break energy, background

energy oscillation effect (which begins at 60-75% of burst pressure) and frictional AE. This Code is now published from ASME (Section X, Appendix 8, 2010) [151b] and being applied in the field. This Code requires for vessel acceptance that the value of B falls between -0.1 and -0.001 and $R^2 \geq 0.80$. Alternately, it is possible to use time required for the structure to emit 99% of AE events on a dwell, namely, $t_{99\%}$. Here, $t_{99\%} = \ln(0.01)/B$ and takes values between 25 and 40 min. For various non-AE requirements, see [151a and b].

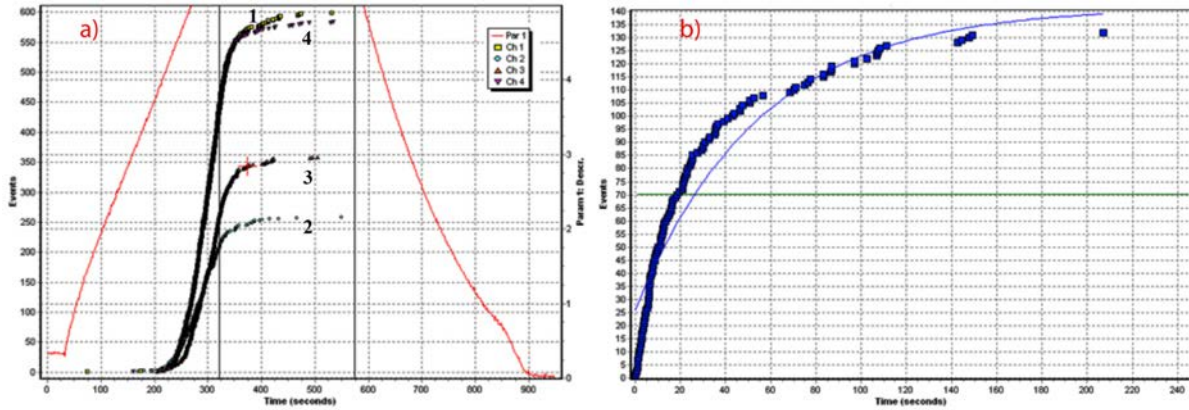


Fig. 20 a) Cumulative events and pressure vs. time. Load is held between two vertical lines. b) Exponential fitting of the cumulative events vs. time for channel 1 during pressure hold period. [152]

Wind turbines

Increasing size of wind turbine power generators demands constant monitoring and maintenance. Articles of applicable NDT methods and of AE methods have appeared [153-157]. Ciang et al. [153] reviewed various SHM methods, with a broad discussion on AE with a dozen references. Some new approaches are suggested. Reference [154] suggests somewhat limitedly “AE is considered more robust for low-speed operation of wind turbine compared to the classic vibration based methods. This approach is also more ideal for identifying early faults in gearbox bearings.” Reference [155] is a brief summary, while [156] reported on an AE test of 25-m long blade with a static step loading schedule and noted locations of AE events at 77% of the fracture load. Sensor placements tightly (20-50 cm spacing) surrounded the eventual failure site.



Fig. 21 Surface damage above the spar-cap skin interface with 3 R6I AE sensors (#18-20). [100]

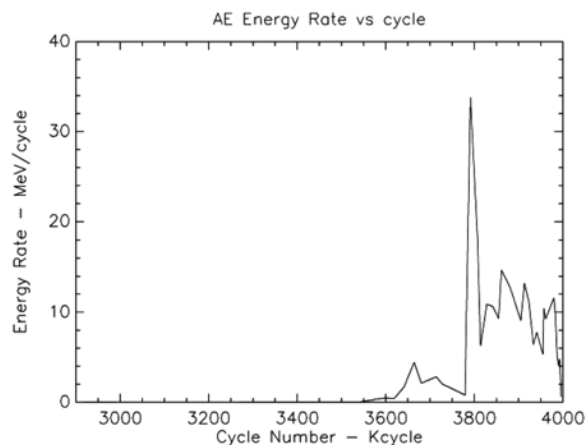


Fig. 22 AE energy rate vs. fatigue cycles. [157]

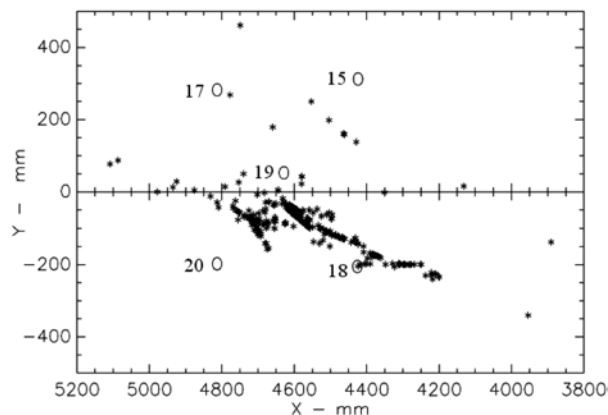


Fig. 23 AE event locations near the spar cap end. [157]

Rumsey et al. [157] conducted high-cycle fatigue loading of TX-100 blade of 9-m length to over 4 million cycles. Dr. Beattie performed AE testing portion. This blade has 6-mm balsa wood at center, a glass cloth supporting a single ply of UD carbon fibers at 20° , then the top mat layer on both sides. At mid-length, spar cap is joined to the base side, where eventual failure was predicted and AE monitored. At ~ 2.5 million fatigue cycles, a large visible crack developed parallel to the chord axis on the high-pressure side at ~ 4.5 m. The crack then grew along the 20° off-pitch-axis carbon fiber direction until the test was stopped at 4 million cycles. Figure 21 shows the surface damage above the spar cap skin interface with 3 AE sensors (PAC R6I) nearby. Almost immediately with test start, AE detected AE events and followed the evolution of blade failure around the end of the spar cap at 4.5 m, but no significant damage in any other monitored areas (24-channel system used). Significant AE appeared at 3.55 million cycles and extreme damage indications started at 3.78 million cycles (see AE energy rate in Fig. 22). The locations of the AE events (Fig. 23) matched the visual damage shown in Fig. 21. The most significant result of this test was that only AE was able to predict and identify the damage location and severity while a few other SHM sensors failed to see the damage.

Another approach for AE characterization, i.e., pattern recognition/neural network, has been used for AE signals from turbine blade tests. [158-160] This approach provided damage grade assessment, relatable to the state of cracks and other flaws developed in fatigue loadings [158]. Load-hold emissions were useful in setting up the classifiers. Other methods evaluated different aspects of blade state assessment [159, 160]. This application is still developing and new methods are expected in this Conference.

Space Shuttle

NASA tried to develop and implement on-board impact detection technologies after the loss of the Space Shuttle Columbia. Prosser [161, 162] described a system called Shuttle Wing Leading Edge Impact Detection System (WLEIDS). It had been installed on all Space Shuttle missions till recent retirement of the fleet. The system tested accelerometers and AE sensors for detecting the impact of launch foam debris on the leading edge made of reinforced carbon-carbon and on thermal protection tiles. Even though a foam block tested was ~ 0.8 kg, its speed is 240-290 m/s and produced detectable damages with the sensors. Some hypervelocity (6.8 km/s) tests were done, indicating different waveforms from the slow impacts. Implementation on shuttle fleet relied on flight-qualified accelerometers that proved to function at lower frequency range than AE sensors, while reducing the signal acquisition frequency down to 20 kHz, beneficial in data

storage and transmission to the Mission Control on earth. For each Space Shuttle, 66 sensors were on board and 22 battery-powered data acquisition/wireless transmission units were mounted in each wing cavity. The system recorded data from all sensors continuously during launch and ascent to orbit. The data was transmitted wirelessly to a laptop computer in the crew compartment and then downlinked to ground. The monitored data consists of rms values of g-force. A summary file of the largest peaks is also stored and used for preliminary analysis. When warranted, detailed analysis follows. For all flights since Columbia, the WLEIDS has performed exceptionally well. None of probable impact events have been of amplitude consistent with critical damage to the RCC leading edge and in-flight inspection at the suspected impact locations using the Orbital Boom Sensing System has not revealed damage. Post-analysis of the entire records evaluated the system performance on flight for future deployment. Some of the waveform records in the ground tests can be seen in [161] and key components of the Shuttle Wing Leading Edge Impact Detection System are shown in Fig. 24.

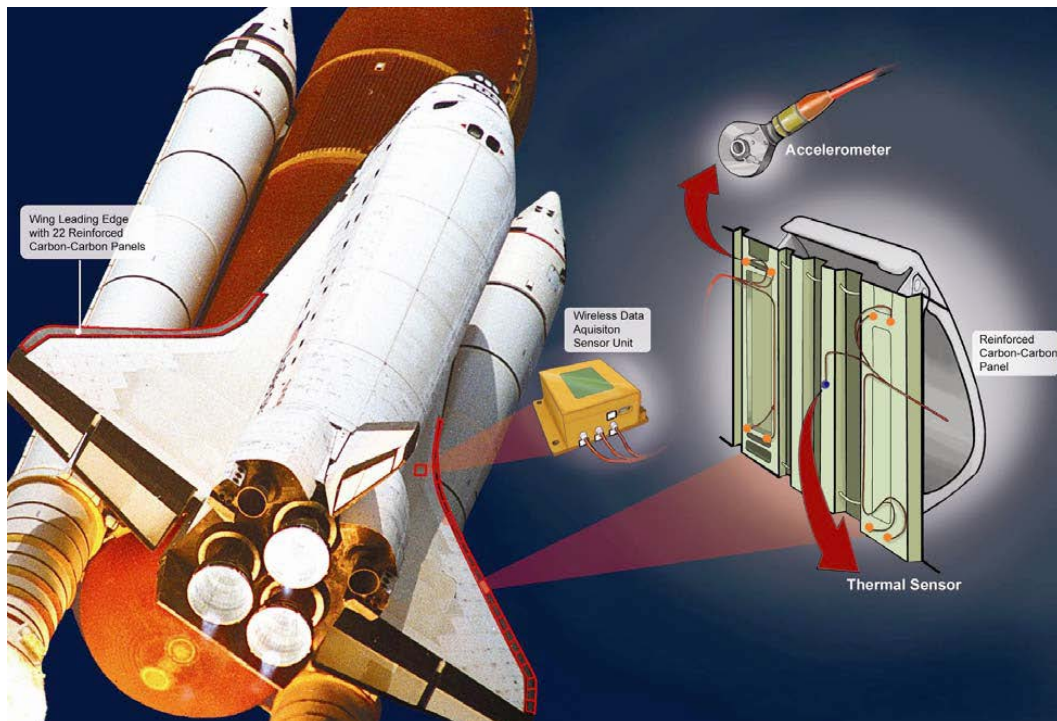


Fig. 24 Key components of the Shuttle Wing Leading Edge Impact Detection System. [161]

Sandwich structures

In practical composite design, sandwich structures are widely used [163]. Aluminum or Nomax honeycomb core is widely used in aerospace applications and foam core is common in less demanding design. AE studies of such structures are not many. Burman [164] conducted an extensive study of sandwich composites under static and fatigue loading conditions and used AE for monitoring crack initiation and growth in the core. AE location aided failure process study on invisible subsurface damages. AE behavior is typical one with rising AE near fracture, and amplitude reaching into >80-dB range. Sandwich composite panels are finding new applications in rehabilitating aging infrastructures [165, 166]. Reference [165] used a small AE system and obtained some AE results on tensile samples, but only rough data outline is given. Larger samples with cyclic loading are also tested, but results are not clearly analyzed or presented. [166] used 16-channel AE system and obtained some AE results during stepwise loading and signal attenuation on the panel, but definitive results are yet to come. In these ambitious projects, it is hoped that past AE experience in the literature is used to better outcomes.

In similar composites with 30+% GFRP skin and balsa-wood core, Hoa [167] studied their AE behavior extensively, producing an ASTM document (ASTM E1888-12). It is worth noting that, starting from FR concept, Hoa defined a trend number $Z = A_2/A_1$, where

A_1 is AE parameter (counts, hits) upon loading to P_1 .

A_2 is AE parameter (counts, hits) upon reloading to P_1 .

Under cyclic loads, Z tends to vanish in a good vessel (or a zone), while Z in damaged one starts to rise. This parameter is useful in judging this type of sandwich composite and may be applicable for other types.

Aircraft applications

In 1984, we were invited to monitor the testing of a prototype all Kevlar composite aircraft (Avtek) using AE. See Fig. 25, which shows an 8-channel AET-5000 system. The Avtek plane was supported at the main wings and canard wing tips while the mid-fuselage was pulled down. 30- and 175-kHz sensors were distributed, especially at the canard attachments. This position turned out to be much weaker than design load, producing significant AE and stopping the test before damage. This demonstrated the AE test's worth, but the Kevlar plane project did not continue long unfortunately.



Figure 25 AE monitoring of prototype Avtek aircraft in 1984. Dr. I. Roman, on leave from Hebrew University of Jerusalem, operated AET-5000 system. [The original of the cover photo shown in JAE vol. 3]

AE applications in aircraft industry appear to have advanced according to the anecdotes from AE equipment makers, but little is known in the open literature for obvious reason. Only about a dozen papers appeared in JAE in the past 30 years with direct connection to airframe, but only metallic. Composite structural components are increasing their importance even in commercial aircraft, but the role of AE is apparently limited. Pfeiffer and Wevers [168] detailed AE and Lamb wave methods for aircraft SHM applications as a part of AISHA project under European Research Area. For critical damages, appropriate Lamb modes are being identified for such parts as helicopter tailbooms and Airbus slat tracks. Takeda [169] reviewed small-diameter optical fiber sensors for damage monitoring and structural health monitoring (SHM) of composite structures. They also reported on results from ACS-SIDE project in Japan with optical SHM. Fiber-Bragg grating (FBG) sensors are combined with PZT actuators for Lamb wave inspection of CFRP structures. Several articles on NDT in aircraft manufacturing appeared recently [170-174], but only one briefly mentioned AE's use in predevelopment-design phase [170]. Our concerted efforts to change the perception of key people in this industry are needed. For example, an improved activation method of impact/delamination damage for AE diagnosis will be needed to provide a better technique to aircraft people. On composite panels, the benefit of global

inspection with AE often evaporates from high wave attenuation behavior. An innovative method is required also.

Figure 26 shows expanding uses of composite in modern commercial and military aircrafts. This poses a formidable challenge for NDE/NDT of composite components during manufacturing, service inspections, flight conditions and SHM. Numerous laboratory tests have been carried out during last decades on large composite components for aircraft structures. At the beginning of the 1990s, Boeing designed and built a 64-channels AE system, called AE Pre-failure Warning System (AEPWS), which was used on a prototype of a low tail horizontal stabilizer (LTHS) box [175]. AEPWS, based on calculation of the AE energy (MARSE), was used to monitor selected flights for the first lifetime (50,000 flights) of fatigue cycling of the LTHS. At the end of the 1990s, Saab Aerospace (Sweden) monitored by AE two full-scale test on the JAS 39 Gripen combat aircraft, partially manufactured from CFRP [176]. In the first one, the wings and the vertical stabilizer (which are primarily manufactured from CFRP) were monitored by a 72-channels PAC AE system in order to localize damage in the early stage. It was possible even without any false alarms and no more damage was detected by other NDT techniques. During the more than 100 real-time tests FR index was checked.

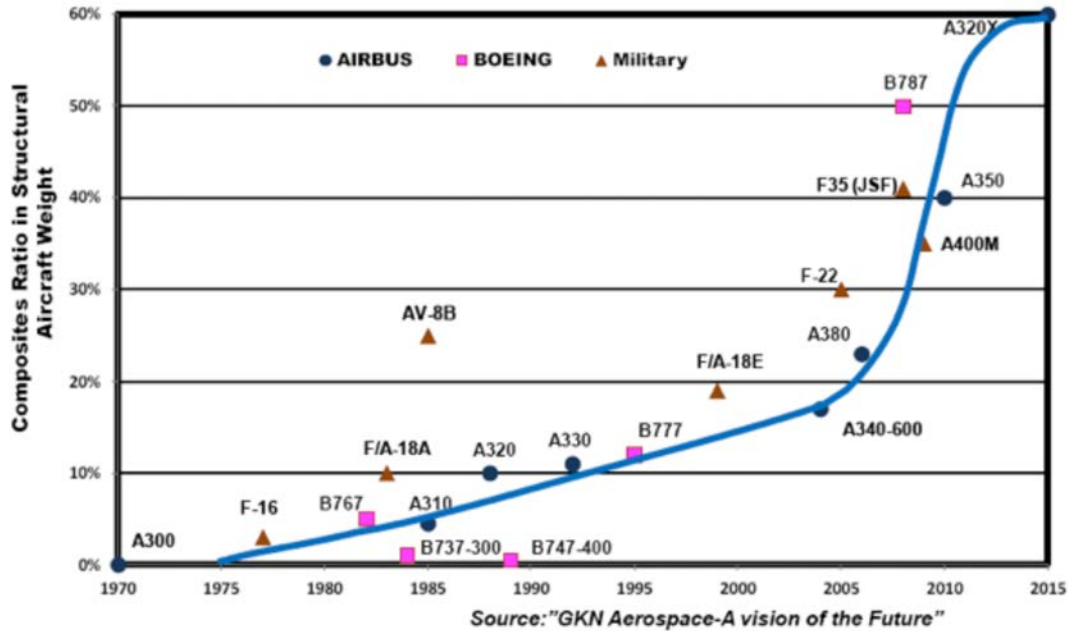


Fig. 26 Composites ratio in structural aircraft weight during last decades in commercial and military aircrafts.

Toward the goal of more active AE utilization in composite aircraft area, some papers are of interest [177-179]. Leone et al. [177] monitored AE in several honeycomb sandwich composites curved fuselage panes, each containing a different scenario of damage, using the Full Scale Aircraft Structure Test Evaluation and Research (FASTER) placed in Atlantic City (US). In particular, the evolution of particular notches artificially made on the full-scale T700-CFRP sandwich panels was monitored by AE using an 8-channel 150 kHz resonant sensor configuration located in circle (see Fig. 27). A good correlation was found between the notch progression (see Fig. 28) and AE accumulated and during loading of the panels (see Fig. 29). The most of the events recorded were below 70 dB (between 85-97 %). Figure 29 shows that the percentage of high-amplitude events, normally associated with fiber breakage, was less than 5% of the total AE events recorded.



Fig. 27 Left: Honeycomb sandwich composite panel. Right: A segment of the panel showing the AE sensors arrangement, a photogrammetry system and an artificial notch. [177]



Fig. 28 Notch-tip damage after complete final fracture in two sandwich panels. [177]

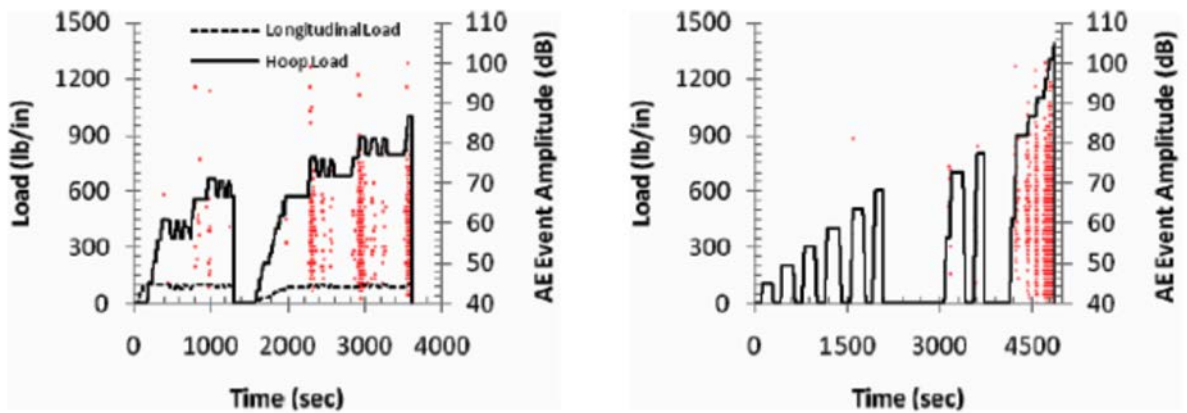


Fig. 29 Load-time history and accumulation of AE events and amplitudes recorded during loading two panels. Each dot signifies a three-hit event. [177]

Sensors and Sensing

Aljets [178, 179] completed a thesis with new approach to source location methods and validated them on large CFRP plates. One is to use an array of 3 closely positioned (45 mm) sensors. Using this sensor array, wave modes and source locations are obtained with two different methods. The array sensor approach is similar to Sachse's patent of 4-sensor array, but the latter was for source location purpose [180]. As we saw earlier in this review, the knowledge of wave modes is

very important information today. More such work on large samples must be pursued to make AE acceptable to industry engineers. In this connection, a new method of Lamb-wave detection should be of interest. Yeum et al. [181] used a sensor of two coaxial PZT elements, a center disc and a surrounding ring. This sensor needs to be placed only on one surface. The mode decomposition can be performed at any selected frequency without changing the PZT size and/or spacing configuration, aided by solving 3D Lamb-wave propagation equations with the PZT size and shape as input. This technique was demonstrated for Lamb waves in an aluminum plate, but should be applicable to composite plates as well.

Optical sensing of AE signals relied on bulky components initially, but the size of sensors and associated equipment started to shrink. Wevers et al. [182] introduced an intensity modulated optical sensor based on the microbending into a CFRP plate and evaluated AE from developing damage, though S/N ratio needed improvements. Surgeon and Wevers [183] evaluated effects of adding optical sensors into CFRP plates. When optical fibers are near the stress-carrying plies, degradation was detectable. Subsequent reports from this group [184, 185] examined signal processing aspect for S/N improvements and a different sensing principle, using polarimetric single-mode optical fiber sensors. Other approaches also appeared more recently [186-188] with interferometric techniques. FBG sensors are from a different principle and is amenable to source localization. See Tsuda's article [189] on its use in SHM applications along with [169]. For embedded usage, see [190]. The main obstacle for wider uses of optical sensing is still the cost of equipment.

Pattern recognition – Clustering

When we initiated using pattern recognition analysis (PRA) software, called ILS, in the early 1980s [61a, 191, 192], we relied on autoregressive modeling to obtain the signal feature vectors and utilized principal component analysis. It was cumbersome, but the promise of signal discrimination was encouraging. We next used Icepak software from TISEC in the 1990s, which vastly ran faster and reported CFRP signal classification results discussed earlier [61b,c, 95]. With Icepak, several algorithms including artificial neural network were available, but we primarily used k-NN. In these studies, we had to supply the likely clustering scheme based on separate aspects, such as special specimen geometry, loading range, microscopy, etc. Unsupervised PRA algorithm started to appear [193] and Noesis software improved the coordination with PAC's data acquisition hardware in an integrated operation. This approach basically uses the standard AE parameters along with partial power spectral density, chosen to represent different AE source features. A different approach is taken in Vallen's VisualClass that relies on time-staggered power spectral features. In the past decade, PRA has become a common tool in AE examination [194, 195; see also Hill, [23], pp. 382-387].

Kohonen introduced a new concept in classifying a large body of diverse data [196]. This is known as the Self-organizing Map (SOM). It has been incorporated into PRA scheme for AE data analysis [40, 82-85, 197-199]. For non-specialists, it is easiest to start with [40, 84]. In the simplest term, SOM helps achieve "Birds of a feather flock together" phenomenon by directing a data vector (characterized by multiple features) into an area of a map where other data vectors of similar characteristics are already present. Godin [84] combined SOM with k-means method to improve further AE data classification. [200, 201] are recent studies that take advantage of the new PRA method with SOM. SOM Toolbox for MATLAB is available from Prof. Kohonen's group [<http://www.cis.hut.fi/somtoolbox/links/somsoftware.shtml>] and can be incorporated into own data analysis package. With the SOM, robust unsupervised PRA is possible and this should become a practical AE analysis tool shortly.

Concluding Remarks

During the past ~50 years, we have expanded the knowledge base on AE. Still, further advances are critically needed to make AE an indispensable tool for composite industry. This article has attempted to review “composite AE” from materials researchers’ perspectives and to survey how AE has contributed to various applications. The first part was reasonably achieved but the second part was only partially fulfilled, as it has been difficult to gain information of AE technology practiced in various industries. We have also identified a few crucial problems that have to be resolved to reach our goal of making AE a useful tool for industry. These include displacement-velocity sensor response, high wave attenuation in composites and the lack of understanding of Felicity effect and stress rupture. Promising developments include new methods for high-pressure vessel monitoring sanctioned by ASME, SOM-based unsupervised PRA, and tackling of issues with wave attenuation and stress rupture. We trust this article presents a fresh summary of what has been discovered and utilized, points out obstacles to surmount and gives some suggestions to future work, hopefully serving as inspiration for developing a new technology.

Acknowledgment: The author (K.O.) wishes to thank Drs. Timothy Fowler and Michael Gorman for critically reviewing this manuscript.

References

1. a) A.T. Green, C.S. Lockman, R.K. Steele, Acoustic verification of structural integrity of Polaris chambers, *Modern Plastics*, vol. 41, July 1964, pp. 137-139, 178, 180.
- b) A.T. Green, C.S. Lockman, H.K. Haines, Acoustical analysis of filament-wound Polaris chambers, Report 0672-01F. Aerojet-General Corporation, Sacramento, CA. [NTIS: AD418330] 1963.
2. a) A.T. Green, C.S. Lockman, S.J. Brown, R.K. Steele, "Feasibility study of acoustic repressurization system," NASA CR55472, March 1966.
- b) A.T. Green, Proc. 27th European Conference on Acoustic Emission Testing (EWGAE27), Cardiff, Wales, UK, Sep. 2006, pp. 3-16.
3. T. Asakawa and C.F. Peregoy, "Manufacturing technology for large monolithic fiberglass reinforced plastic rocket motor case", Volume I, II. Appendixes. DTIC AD0483226, Nov. 1965.
4. E.C. Jenssen, H. Spanheimer, A.J. De Herrera, "Prediction of composite pressure vessel performance by application of the Kaiser effect in acoustic emissions", Presented at the American Society of Mechanical Engineers, Paper No. H300-12-2-037, June 1975.
5. R.G. Liptai, "Acoustic emission from composite materials," *Composite Materials: Testing and Design*, ASTM-STP-497, 1972, pp. 285-298.
6. a) H.C. Kim, A.P. Ripper Neto and R.W.B. Stephens, "Some observations on acoustic emission during continuous tensile cycling of a carbon fibre/epoxy composite," *Nature, Physical Science*, vol. 237, 1972, pp. 78-80.
- b) M. Takehana and I. Kimpara, "AE from FRP fracture processes," *Proc. US-Japan Symposium on Acoustic Emission, Japanese volume*, 1972, Sec. 4, pp. 1-22.
7. J. Fitz-Randolph, D.C. Phillips, P.W.R. Beaumont and A.S. Tetelman, "Acoustic emission studies of a boron-epoxy composite", *J. Comp. Matls*, vol. 5, 1971, pp. 542-548.
8. T.J. Fowler, "Acoustic Emission Testing of Fiber Reinforced Plastics" American Society of Civil Engineers (ASCE) Fall Convention and Exhibit, Preprint 3092, ASCE, New York, 1977.
9. T.J. Fowler (1979), "Acoustic Emission Testing of Fiber Reinforced Plastics," *Proceedings Paper 15021*, J. Technical Council, ASCE, vol. 105 (TC2): 281-289.

10. T.J. Fowler and E. Gray (1979), "Development of an Acoustic Emission Test for FRP Equipment." Preprint 3583, American Society of Civil Engineers, New York, 1979.
11. T.J. Fowler and R.S. Scarpellini (1980), "Acoustic Emission Testing of FRP Equipment - I," *Chemical Engineering*, CHEEA, vol. 87, no. 21: 145-148.
12. T.J. Fowler, "Acoustic emission testing of chemical process industry vessels," *Progress in Acoustic Emission II* (Proc. IAES-7), JSNDI, Tokyo, 1984, pp. 421-449.
13. T.N. Crump and M.A. Droge, "The Characterization of Fiberglass Reinforced Plastics Using Acoustic Emission", *Managing Corrosion with Plastics, Volume IV*, National Association of Corrosion Engineers, 1979, Houston.
14. T.G. Hagemeyer, "Monitoring of an FRP Pressure Vessel During Pressure Testing", *Managing Corrosion with Plastics, Volume IV*, National Association of Corrosion Engineers, 1979, Houston.
15. CARP, "Recommended Practice For Acoustic Emission Testing of Fiberglass Reinforced Plastic Resin (RP) Tanks/Vessels", The Society of the Plastics Industry, Inc., New York, 1982, 13 p. Revised and republished, 1987.
16. a) ASME, "Acoustic emission examination of fiber reinforced plastic vessels", *Boiler and Pressure Vessel Code, Section V, Article 11, Nondestructive Examination*, American Society of Mechanical Engineers, New York, 1985, 2010.
b) ASTM E1067/E1067M-11 Standard Practice for Acoustic Emission Examination of Fiberglass Reinforced Plastic Resin (FRP) Tanks/Vessels, 2011.
17. T.F. Fowler, "Revisions to the CARP Recommended Practice for Tanks and Vessels", *Proc. AECM-5*, 1995, pp. 263-272.
18. P.H. Ziehl, "Development of a damage based design criterion for fiber reinforced vessels", PhD Thesis, The University of Texas at Austin, 2000, 317 p.
19. N. Ativitavas, "Acoustic emission signature analysis of failure mechanisms in fiber reinforced plastic structures", PhD Thesis, The University of Texas at Austin, 2002, 444 p.
20. T.J. Fowler, "Experience with acoustic emission monitoring of chemical process industry vessels," *Progress in Acoustic Emission III* (Proc. IAES-8), JSNDI, Tokyo, 1986, pp. 150-162.
21. R. Davies, "Acoustic emission as a basis for plant integrity monitoring", *Progress in Acoustic Emission III* (Proc. IAES-8), JSNDI, Tokyo, 1986, pp. 9-25.
22. T.J. Fowler, J.A. Blessing, P.J. Conlisk and T.L. Swanson, The MONPAC system, *J. Acoustic Emission*, vol. 8, no. 3, 1989, 1-10.
23. *Acoustic Emission Testing, Nondestructive Testing Handbook*, 3rd edition, Vol. 6, American Society for Nondestructive Testing, Columbus, OH, 2005. (2nd edition, Vol. 5, 1987).
24. a)-f) *Proceedings of 1st to 6th International Symp. on AE from Reinforced Plastics/Composite Materials*, SPI/ASNT, 1983, 1986, 1989, 1992, 1995, 1998.
25. M.A. Hamstad, "A review: acoustic emission as a tool for composite materials studies," *Experimental Mechanics*, vol. 26, no. 1, March 1986, pp. 7-13.
26. M. A. Hamstad, "Thirty years of advances and some remaining challenges in the application of acoustic emission to composite materials," *Acoustic Emission Beyond the Millennium*, eds. T. Kishi et al., Elsevier, Oxford, UK, 2000, pp. 77-91.
27. CARP Aerospace/Advanced composites subcommittee. "Guidance for development of AE applications on composites", *J. Acoustic Emission*, vol. 11, 1993, pp. C1-C24.
28. J. Bohse, "Acoustic emission examination of polymer-matrix composites", *J. Acoustic Emission*, vol. 22, 2004, pp. 208-23.
29. M.R. Gorman, "Acoustic emission in structural health monitoring (SHM)", *Encyclopedia of Structural Health Monitoring*, ch. 4, eds. C. Boller et al., J. Wiley, 2009, pp. 79-100.
30. K. Lambrihs, M. Wevers, "Applications of acoustic emission for SHM: A review", *Encyclopedia of Structural Health Monitoring*, ch. 13, eds. C. Boller et al., J. Wiley, 2009, pp. 289-

301.

31. K. Ono, "Acoustic Emission in Materials Research – A Review", *J. Acoust Emission*, vol. 29, 2011, pp. 284–308.
32. T.F. Drouillard, M.A. Hamstad, ref. 24a, sec. 6, pp. 1-60; 24b, pp. 60-71, 24c, pp. 391-413.
33. J. Wolters, "Acoustic emission monitoring of fracture mechanisms in short fiber reinforced thermoplastics: basic studies on model compounds", ref. 24b, pp. 29-36, 1986.
34. L. Lorenzo and H.T. Hahn, "Acoustic emission study of fracture of fibers embedded in epoxy matrix", ref. 24a, session 2, pp. 1-13, 1983.
35. T. Imafuku, M. Shiwa, N. Koizumi, S. Yuyama, and T. Kishi, "Acoustic emission testing of FRP panel tank", ref. 24b, pp. 180-183, 1986.
36. I. Roman and K. Ono, "Acoustic emission characterization of fracture mechanisms in woven roving glass-epoxy composites," *Progress in Acoustic Emission, II*, eds. M. Onoe et al., JSNDI, Tokyo, 1984, pp. 496-503.
37. N.V. De Carvalho, S.T. Pinho, P. Robinson, "An experimental study of failure initiation and propagation in 2D woven composites under compression", *Composites Science and Technology*, vol. 71, 2011, pp. 1316–1325.
38. R.A. Nordstrom, "Acoustic emission characterization of microstructural failure in the single fiber fragmentation test", PhD. Thesis, Swiss Federal Institute of Technology, Diss. No. 11402, Zurich, Switzerland, 1996.
39. J. Bohse, "Acoustic emission characteristics of micro-failure process in polymer blends and composites, *Compos Sci Technol.* vol. 60, 2000, 1213–1226.
40. R. de Oliveira (R.F.da C. Oliveira), "*Health Monitoring of FRP using Acoustic Emission and Fibre Optic Techniques*", PhD Thesis, University of Porto, 2004, 237 p.
41. M. R'Mili, M. Moevus, N. Godin, "Statistical fracture of E-glass fibres using a bundle tensile test and acoustic emission monitoring", *Compos Sci Technol.* vol. 68, 2008, 1800–1808.
42. L. Lorenzo, H.T. Hahn, "On the applicability of amplitude distribution analysis to the fracture process of composite materials", *J. Acoustic Emission*, vol. 5, 1986, pp. 15-24.
43. S.A. Carey, "Acoustic emission and acousto-ultrasonic signature analysis of failure mechanisms in carbon fiber reinforced polymer materials", PhD Thesis, 2008, College of Engineering and Computing, University of South Carolina, Columbia, SC.
44. A. Nanjyo, M. Mohri, K. Ono, "Acoustic emission behavior during tensile fracture of resin-impregnated strands of pitch-based carbon fiber", ref. 24d, pp. 44-54, 1992.
45. J.M. Berthelot, J. Rhazi, "Different types of amplitude distributions in composite materials", ref. 24b, 1986, pp. 96-103.
46. J.M. Berthelot, J. Rhazi, "Acoustic emission in carbon fibre composites", *Composites Science and Technology*, vol. 37, 1990, 411-428.
47. D. Valentin, Ph. Bonniau, A.R. Bunsell, "Failure mechanism discrimination in carbon fibre-reinforced epoxy composites", *Composites*, vol. 14, 1983, pp. 345-351.
48. K. Ono, "Acoustic emission behavior of flawed unidirectional carbon fiber-epoxy composites", *J. of Reinforced Plastics and Composites*, Vol. 7, January 1988, pp. 90-105.
49. See also ref. 24b, pp. 22-28. Table 2 was not printed correctly in ref. 48a above.
50. J. Awerbuch, M. R. Gorman and M. Madhukar, "Monitoring damage accumulation in filament-wound graphite/epoxy laminate coupons during fatigue loading through acoustic emission", ref. 24a, 1983, pp. 73-102.
51. a) P. Wright, M. Mavrogordato, A.J. Moffat, I. Sinclair, S.M. Spearing, "High resolution computed tomography for modelling laminate damage", *Proc 17th Int Conf Compos Mater., ICCM-17*, Edinburgh, 2009, paper T1.4, 10 p.
<http://www.iccm-central.org/Proceedings/ICCM17proceedings/Themes/TSAI/T1.4%20Wright.pdf>
52. A.E. Scott, M. Mavrogordato, P. Wright, I. Sinclair, S.M. Spearing, "In situ fibre fracture

measurement in carbon–epoxy laminates using high resolution computed tomography”, *Compos Sci Technol.* vol. 71, 2011, pp. 1471–1477.

53. M.G.R. Sause, T. Müller, A. Horoschenkoff and S. Horn, “Quantification of failure mechanisms in mode-I loading of fiber reinforced plastics utilizing acoustic emission analysis”, *Composites Science and Technology*, vol. 72, 2012, pp. 167–174

54. K. Ono, “Acoustic emission behavior of metal-fiber laminates”, *Progress in Acoustic Emission XIV*, IAES19, JSNDI, 2008, pp. 201-208.

55. A.R.A. Abraham, K.L. Johnson, C.T. Nichols, R.L. Saulsberry, J.M. Waller, “Use of statistical analysis of acoustic emission data on carbon-epoxy COPV materials-of-construction for enhanced felicity ratio onset determination”, NASA report JSC-CN-26080, pp. 1-15, 2012.

56. J.M. Waller, R.L. Saulsberry and E. Andrade, “Use of acoustic emission to monitor progressive damage accumulation in Kevlar®-49 composites,” *QNDE Conference vol. 29*. AIP Conf. 1211, 2010, pp. 1111-1118.

57. P.D. Washabaugh, W.G. Knauss, “A reconciliation of dynamic crack velocity and Rayleigh wave speed in isotropic brittle solids”, *Intl J. of Fracture*, vol. 65, 1994, pp. 97-114.

58. T. Cramer, A. Wanner, and P. Gumbsch, “Crack velocities during dynamic fracture of glass and single crystalline silicon, *phys. stat. sol. (a)*, vol. 164, 1997, pp. R5-R6.

59. M.R. Gorman, “Modal AE analysis of fracture and failure in composite materials, and the quality and life of high pressure composite pressure vessels”, *J. Acoustic Emission*, vol. 29, 2011, pp. 1-28.

60. B.W. Kim, J.A. Nairn, “Observations of fiber fracture and interfacial debonding phenomena using the fragmentation test in single fiber composites”, *J. Composite Mat.*, vol. 36, no. 15, 2002, pp. 1825-1858.

61. a) M. Ohtsu and K. Ono, "Pattern recognition analysis of acoustic emission from unidirectional carbon fiber-epoxy composites by using autoregressive modeling," *J. Acoustic Emission*, vol. 6, 1987, pp. 61-72.

b) Q. Huang, Characterization of acoustic emission from failure processes of carbon fiber/epoxy composites by pattern recognition”, PhD thesis, University of California, Los Angeles, 1993, 172 p.

c) K. Ono and Q. Huang, "Pattern recognition analysis of acoustic emission signals", *Progress in Acoustic Emission VII*, eds. T. Kishi et al., JSNDI, Tokyo, 1994, pp. 69-78.

62. K. Ono, H. Cho and T. Matsuo, “Experimental transfer functions of acoustic emission sensors”, *J. of Acoustic Emission*, vol. 26, 2008, pp. 72-90.

63. A. Maslouhi, C. Roy and D. Proulx, “Characterization of acoustic emission signals generated in carbon-epoxy composites”, ref 24b, pp. 112-116, 1986.

64. P.J. de Groot, P.A.M. Wijnen, R.B.F. Janssen, “Real-time frequency determination of acoustic emission for different fracture mechanisms in carbon/epoxy composites”, *Composites Science and Technology*, vol. 55, 1995, pp. 405-412.

65. M. Giordano, A. Calabro, C. Esposito, A. Lizza, A. D'Amore, L. Nicolais, “An acoustic emission characterization of the failure modes in polymer-composite materials”, *Composite Science and Technology*, vol. 58, 1997, pp. 1923-1928

66. M. Eaton, K. Holford, C. Featherston, R. Pullin, “Damage in carbon fibre composites: the discrimination of acoustic emission signals using frequency”, *J Acoust Emission* vol. 25, 2007, pp. 140–8.

67. a) C.B. Scruby, “Acoustic emission measurements using point-contact transducers,” *J. of Acoustic Emission*, vol. 4, 1985, pp. 9-18.

b) D.J. Buttle, C.B. Scruby, “Characterization of fatigue of aluminum alloys by acoustic emission, Part I and II, *J. Acoustic Emission*, vol. 9, 1990, pp. 243-254, 255-270.

68. D. Guo, A. Mal and K. Ono, “Wave theory of acoustic emission in composite laminates”, *J. of Acoustic Emission*, vol. 14, 1996, pp. S19-S46.

69. M.G.R. Sause and S. Horn, "Simulation of lamb wave excitation for different elastic properties and acoustic emission source geometries", *J. Acoustic Emission*, vol. 28, 2010, pp. 142-154.
70. M. Sause, "Identification of failure mechanisms in hybrid materials utilizing pattern recognition techniques applied to acoustic emission signals", Augsburg Univ. doctoral dissertation, Mensch und Buch Verlag, 2010, 305 p.
71. a) H. Suzuki, M. Takemoto and K. Ono, "The fracture dynamics in a dissipative glass-fiber/epoxy model composite with AE source simulation analysis", *J. Acoustic Emission*, vol. 14, 1996, pp. 35-50.
- b) H. Suzuki, "Fracture dynamics via inverse analysis of viscoelastic waves", doctoral thesis, Tokyo Inst. Technology, 2000, 176 p.
72. e.g., M. Enoki, T. Kishi, "Acoustic emission source characterization in materials", *Acoustic Emission – Beyond the Millenium*, 2000, Elsevier, pp. 1-17.
73. R.L. Weaver, W. Sachse and L. Niu, "Transient ultrasonic waves in a viscoelastic plate: Theory", *J. Acoust. Soc. Am.*, vol. 85, no. 6, 1989, pp. 2255-2261.
74. M. Ohtsu and K. Ono, "A generalized theory of acoustic emission and Green's function in a half space", *J. Acoustic Emission*, vol. 3, no. 1, 1984, pp. 27-40.
75. J.M. Berthelot, "Relation between amplitudes and rupture mechanisms in composite materials", ref. 24b, 1986, pp. 126-133.
76. J.E. Bailey, P.T. Curtis and A. Parvizi, "On the Transverse Cracking and Longitudinal Splitting Behaviour of Glass and Carbon Fibre Reinforced Epoxy Cross Ply Laminates and the Effect of Poisson and Thermally Generated Strain", *Proc. R. Soc. Lond. A* vol. 366, 1979, pp. 599-623.
77. a) W.H. Prosser, "Advanced AE techniques in composite materials research", *J. Acoustic Emission*, vol. 14, 1996, pp. S1-S11.
- b) M.R. Gorman and S. M. Ziola, "Plate waves produced by transverse matrix cracking," *Ultrasonics*, vol. 29, 1991, pp. 245-251.
78. S.-C. Woo, N.-S. Choi, "Analysis of fracture process in single-edge-notched laminated composites based on the high amplitude acoustic emission events", *Composites Science and Technology*, vol. 67, 2007, pp. 1451-1458.
79. M. Schoßig, A. Zankel, C. Bierögel, P. Pölt, W. Grellmann, "ESEM investigations for assessment of damage kinetics of short glass fibre reinforced thermoplastics – Results of in situ tensile tests coupled with acoustic emission analysis", *Composites Science and Technology*, vol. 71, 2011, pp. 257-265.
80. A. Bussiba, M. Kupiec, S. Ifergane, R. Piat, T. Böhlke, "Damage evolution and fracture events sequence in various composites by acoustic emission", *Science and Technology*, vol. 68, 2008, pp. 1144-1155.
81. P.L. Chiou, W.L. Bradley, "Moisture-induced degradation of glass/epoxy filament-wound composite tubes", *J. of Thermoplastic Composite Materials*, vol. 9, no. 2, 1996, p. 118.
82. S. Huguet, N. Godin, R. Gaertner, L. Salmon, D. Villard, "Use of acoustic emission to identify damage modes in glass fibre reinforced polyester", *Composites Science and Technology*, vol. 62, 2002, pp. 1433-1444.
83. N. Godin, S. Huguet, R. Gaertner, L. Salmon, "Clustering of acoustic emission signals collected during tensile tests on unidirectional glass/polyester composite using supervised and unsupervised classifiers", *NDT&E International*, vol. 37, 2004, pp. 253-264.
84. N. Godin, S. Huguet, R. Gaertner, "Integration of the Kohonen's self-organising map and k-means algorithm for the segmentation of the AE data collected during tensile tests on cross-ply composites", *NDT&E International*, vol. 38, 2005, pp. 299-309
85. N. Godin, S. Huguet, R. Gaertner, "Influence of hydrolytic ageing on the acoustic emission signatures of damage mechanisms occurring during tensile tests on a polyester composite: Application of a Kohonen's map", *Composite Structures*, vol. 72, 2006, pp. 79-85.

86. L. Lagunegrand, T. Lorriot, R. Harry, H. Wargnier, J.M. Quenisset, "Initiation of free-edge delamination in composite laminates", *Composites Science and Technology*, vol. 66, 2006, pp. 1315–1327.
87. J.J. Scholey, P.D. Wilcox, M.R. Wisnom and M.I. Friswell "Quantitative experimental measurements of matrix cracking and delamination using acoustic emission," *Composites: Part A*, vol. 41, 2010, pp. 612-623.
88. J. Bohse, T. Krietsch, J.H. Chen, A.J. Brunner, "Acoustic emission analysis and micro-mechanical interpretation of mode I fracture toughness test on composite materials", *Fracture of polymers, composites and adhesives*, eds. J.G. Williams and A. Pavan, ESIS publication 27, 2000, pp. 15 – 26.
89. J. Bohse, J. Chen, Acoustic emission examination of mode I, mode II and mixed mode I/II interlaminar fracture of unidirectional fiber-reinforced polymers. *J. Acoust Emission*, vol. 19, 2001, pp. 1–10.
90. W. Mielke, A. Hampe, O. Hoyer, K. Schumacher, "Analysis of AE-events from single fibre pull-out experiments, ref. 24c, 1989, pp. 323-331; see also *J. Acoust Emission*, vol. 9, 1990, pp. 103-108.
91. M. Enoki, D. Valentin, H. Tsuda & T. Kishi, "Characterization of debonding process of fiber reinforced composites by acoustic emission", *Nondestructive Testing and Evaluation*, vol. 8-9, 1992, pp. 857-868.
92. K. Tanaka, K. Minoshima, W. Grela, K. Komai, "Characterization of the aramid/epoxy interfacial properties by means of pull-out test and influence of water absorption", *Composites Science and Technology*, vol. 62, 2002, pp. 2169–2177.
93. Y. Mizutani, K. Nagashima, M. Takemoto, K. Ono, "Fracture mechanism characterization of cross-ply carbon-fiber composites using acoustic emission analysis", *NDT&E International*, vol. 33, 2000, pp. 101-110.
94. K. Ono, Y. Mizutani, M. Takemoto, "Analysis of acoustic emission from impact and fracture of CFRP laminates," *J. Acoustic Emission*, vol. 25, 2007, pp. 179-186.
95. K. Ono, Q. Huang, J.Y. Wu, "AE pattern recognition analysis of the fracture of glass fiber composites exposed to hot-wet conditions", ref. 24e, 1995, pp. 197-204.
96. M.A. Hamstad, "A discussion of the basic understanding of the Felicity effect in fiber composites", *J. Acoustic Emission*, vol. 5, 1986, pp. 95-102.
97. J. Awerbuch, M. R. Gorman and M. Madhukar, "Monitoring acoustic emission during quasi-static loading/unloading cycles of filament-wound graphite/epoxy laminate coupons", ref. 24a, 1983, pp. 139-157.
98. Z. Yuan, "Acoustic emission characterizations of internal damage for GFRP", *Progress in Acoustic Emission II* (Proc. IAES-7), JSNDI, Tokyo, 1984, pp. 458-463.
99. O.-Y. Kwon and D.-H. Hong, Acoustic emission monitoring of impact-damaged CFRP laminates during flexural tests", *Progress In Acoustic Emission VIII*, JSNDI, 1996, pp. 163-168.
100. J.-H. Shin, O.-Y. Kwon , "Acoustic emission monitoring of lightning-damaged CFRP laminates during compression-after-impact test", *J. Korean Society for Nondestructive Testing*, vol. 32, no. 3, 2012, pp. 269-275.
101. F. Lachaud, B. Lorrain, L. Michel, R. Barriol, "Experimental and numerical study of delamination caused by local buckling of thermoplastic and thermoset composites", *Composites Science and Technology*, vol. 58, 1998, pp. 721-733
102. R.L. Saulsberry, N.J. Greene, L. Hernandez, "Stress rupture nondestructive evaluation of composite overwrapped pressure vessels".
- <http://research.jsc.nasa.gov/BiennialResearchReport/2011/287-2011-Biennial.pdf>

103. J.M. Waller, C.T. Nichols, D.J. Wentzel, and R.L. Saulsberry, "Use of modal acoustic emission to monitor damage progression in carbon fiber/epoxy composites", QNDE Conference, vol. 30, AIP Conf. 1335, 919-926, 2011.
104. J.M. Waller, R.L. Saulsberry, E. Andrade, "Use of acoustic emission to monitor progressive damage accumulation in Kevlar 49 composites", QNDE Conference, vol. 29, AIP Conf. 1211, 2010, pp. 1111-1118.
105. NASA - NNWG NDE Working Group Homepage, updated April 10, 2012.
[http://www.nnwg.org/current/WSTF/In-Situ NDE.html](http://www.nnwg.org/current/WSTF/In-Situ%20NDE.html)
106. K. Naito, Y. Tanaka, J.-M. Yang, Y. Kagawa, "Tensile properties of ultrahigh strength PAN-based, ultrahigh modulus pitch-based and high ductility pitch-based carbon fibers", Carbon, vol. 46, 2008, pp. 189-195.
107. K.F. Graff, *Wave Motion in Elastic Solids*, Oxford, 1975, 649 p.
108. M.R. Gorman and W.H. Prosser, "AE source orientation by plate wave analysis," J. Acoustic Emission, vol. 9, no. 4, 1990, pp. 283-288.
109. M.R. Gorman and S. M. Ziola (1991), "Plate waves produced by transverse matrix cracking," Ultrasonics, vol. 29, 1991, pp. 245-251.
110. M.R. Gorman (1991), "Plate wave acoustic emission," J. Acoustical Society of America, vol. 90, no. 1, 1991, pp. 358-364.
111. J. Gary and M. Hamstad, "On the far-field structure of waves generated by a pencil break on a thin plate," J. Acoustic Emission, vol. 12, no. 3-4, 1994, pp. 157-170.
112. M.A. Hamstad, J. Gary, A. O'Gallagher, "Far-field acoustic emission waves by three-dimensional finite element modeling of pencil breaks on a thick plate," J. Acoustic Emission, vol. 14, no. 2, 1996, pp. 103-114.
113. M.A. Hamstad, J. Gary, A. O'Gallagher, "Wideband acoustic emission signals as a function of source rise-time and plate thickness," J. Acoustic Emission, vol. 16, 1998, pp. S251-S259.
114. W.H. Prosser, M.A. Hamstad, J. Gary, A. O'Gallagher, "Comparison of finite element and plate theory methods for modeling acoustic emission waveforms," J. of Nondestructive Evaluation, vol. 18, no. 3, 1999, pp. 83-90.
115. K.S. Downs and M.A. Hamstad, "Correlation of regions of acoustic emission activity with burst locations for spherical graphite/epoxy pressure vessels," J. Acoustic Emission, vol. 13, nos. 3-4, 1995, pp. 56-66.
116. A.K. Mal, Y. Bar-Cohen and S.S. Lih, "Wave attenuation in fiber-reinforced composites," M3D: *Mechanics and Mechanisms of Material Damping*, ASTM STP 1169, American Society for Testing and Materials, 1992, pp. 245-261.
117. M. Castaings, B. Hosten, "Air-coupled measurement of plane wave, ultrasonic plate transmission for characterising anisotropic, viscoelastic materials", Ultrasonics, vol. 38, 2000, pp. 781-786.
118. M. Castaings, B. Hosten, T. Kundu, "Inversion of ultrasonic, plane-wave transmission data in composite plates to infer viscoelastic material properties. NDT & E International, vol. 33, no.6, 2000, pp. 377-92.
119. B. Hosten, "Heterogeneous structure of modes and Kramers-Kronig relationship in anisotropic viscoelastic materials", J. Acoust. Soc. Am. vol. 104, no. 3, September 1998, pp. 1382-1388.
120. M. Castaings, M.V. Predoi, B. Hosten, "Ultrasound propagation in viscoelastic material guides", *Proceedings of the COMSOL Multiphysics User's Conference 2005 Paris*, 6 p.
121. M. Calomfirescu, "Lamb Waves for Structural Health Monitoring in Viscoelastic Composite Materials", Logos Verlag, Berlin, Germany, 2008. 119 p.
122. M.A. Torres-Arredondo, C.-P. Fritzen, "A viscoelastic plate theory for the fast modelling of Lamb wave solutions in NDT/SHM applications", Ultragarsas (Ultrasound), vol. 66, no. 2, 2011,

pp. 7-13.

123. L. Wang, F.G. Yuan, "Group velocity and characteristic wave curves of Lamb waves in composites: Modeling and experiments", *Composites Science and Technology*, vol. 67, 2007, pp. 1370–1384.

124. M.D. Seale and B.T. Smith, "Lamb wave propagation in thermally damaged composites", *Review of Progress in QNDE*, eds. D.O. Thompson and D.E. Chimenti, vol. 15A, Plenum Press, New York, 1996, pp. 261-266.

125. G. Caprino, V. Lopresto, C. Leone, I. Papa, "Acoustic emission source location in unidirectional carbon-fiber-reinforced plastic plates with virtually trained artificial neural networks", *J. of Applied Polymer Science*, vol. 122, 2011, pp. 3506–3513.

126. L. Taupin, A. Lhémy and G. Inquiété, "A detailed study of guided wave propagation in a viscoelastic multilayered anisotropic plate", *J. Phys.: Conf. Ser.* vol. 269, 2011, 012002, 14 p.

127. A. Gallego and K. Ono, "An improved acousto-ultrasonic scheme with lamb wave mode separation and damping factor in CFRP plates", *Proc. EWGAE30-ICAE7*, Granada, Spain, 2012, pp. 573-580.

128. R. Joselin, T. Chelladurai, "Burst pressure prediction of composite pressure chambers using acoustic emission technique: a review", *J. Fail. Anal. and Preven.* vol. 11, 2011, pp. 344–356.

129. J.W. Whittaker, W.D. Brosey and M.A. Hamstad, "Felicity ratio behavior of pneumatically and hydraulically loaded spherical composite test specimens", *J. Acoustic Emission*, vol. 9, 1990, pp. 75-83

130. J.W. Whittaker, W.D. Brosey and M.A. Hamstad, "Correlation of Felicity ratio and strength behavior of impact-damaged spherical composite test specimens", *J. Acoustic Emission*, vol. 9, 1990, pp. 84-90

131. M.R. Gorman, "Burst prediction by acoustic emission in filament wound pressure vessels", *J. Acoustic Emission*, vol. 9, 1990, 131-139.

132. K.S. Downs and M.A. Hamstad, "Correlation of acoustic emission Felicity ratios and hold-based rate movement and burst strength," *J. Acoustic Emission*, vol. 13, nos. 3-4, 1995, pp. 45-55.

133. K.S. Downs and M.A. Hamstad, "Acoustic emission from depressurization to detect/ evaluate significance of impact damage to graphite/epoxy pressure vessels," *J. Composite Materials*, vol. 32, no. 3, 1998, pp. 258-307.

134. Y. Mizutani, K. Saiga, H. Nakamura, N. Takizawa, T. Arakawa and A. Todoroki, "Integrity evaluation of COPVs by means of acoustic emission testing", *J. Acoustic Emission*, vol. 26, 2008, pp. 109-119.

135. Y. Mizutani, S. Sugimoto, R. Matsuzaki, A. Todoroki, "Fundamental study on integrity evaluation method for COPVs by means of acoustic emission testing", *J. Acoustic Emission*, vol. 27, 2009, pp. 89-97.

136. J.B. Chang, "Implementation guidelines for ANSI/AIAA S-081: Space systems composite overwrapped pressure vessels", *Aerospace Report No. TR-2003(8504)-1*, AD A413531, 2003, 83 p.

137. M.A. Hamstad and T.T. Chiao, "Acoustic emission from stress rupture and fatigue on an organic fiber composite," *Composite Reliability*, ASTM STP 580, 1975, pp. 191-201, UCRL-74745.

138. C. Le Floc, "Acoustic emission applied to observe damage in composite material high-pressure fluid storage tanks", *Societe Nationale Industrielle Aerospatiale Paris (France)*, ESA-86-97173, AD-D440906, 1986.

139. P.L. Chiou, W.L. Bradley, "Moisture-induced degradation of glass/epoxy filament-wound composite tubes", *J. of Thermoplastic Composite Materials*, vol. 9, no. 2, 1996, p. 118.

140. M.R. Horne, E.I. Madaras, "Evaluation of acoustic emission NDE of Kevlar composite over

wrapped pressure vessels”, NASA/TM-2008-215558, Langley Research Center, Hampton, Virginia, 2008.

141. W.W. Schmidt, G.M. Ecord, “Static fatigue life of Kevlar aramid/epoxy pressure vessels at room and elevated temperatures”, NASA Johnson Space Center, AD-D437607, AIAA PAPER 83-1328, 1983.

142. E.Y. Robinson, “Design prediction for long term stress rupture service of composite pressure vessels”, NASA_Techdoc_19950021870, Accession-ID: 95N28291, 1995.

143. G.M. Fallatah, N. Dodds and A.G. Gibson, “Long term creep and stress rupture of aramid fibre”, *Plastics, Rubber and Composites*, vol. 36, no. 9, 2007, pp. 403-412.

144. M.T. Kezirian, K.L. Johnson, S.L. Phoenix, “Composite overwrapped pressure vessels (COPV): Flight rationale for the Space Shuttle Program”, AIAA Paper, 2011.

http://ntrs.nasa.gov/archive/nasa/casi.ntrs.../20110015972_2011016890.pdf

145. D. McColskey, M. Hamstad, R. Saulsberry, J. Waller, “Production/performance monitoring of composite tanks and methods for certification and production/performance monitoring of composite tanks”, NIST-NASA presentation.

http://www1.eere.energy.gov/hydrogenandfuelcells/pdfs/ihfpv_mccloseky.pdf

146. J. Bohse, G.W. Mair and P. Novak, “Acoustic emission testing of high-pressure composite cylinders”, EWGAE27, 2006, 267-272.

147. P. Tscheliesnig, “More than a quarter century of acoustic emission testing (AT) at TÜV Austria”, EWGAE27, 2006, pp. 365-376.

148. G. Lackner, R. Dusek, “A case study for crack detection within a gas cylinder using acoustic emission testing”, EWGAE29, 2010, pp. 224-230.

149. D.R. Stephens and R.L. Osborne (Battelle), “Composite propane cylinder regulatory approval request”, Docket 10662, Propane Education & Research Council, Washington DC, 2004.

150. Anon. *FRP Inspection Guide*, Reichhold, Inc., Research Triangle Park, NC 27709. 2009.

151. a) N.L. Newhouse, G.B. Rawls, M.D. Rana, B.F. Shelley, M.R. Gorman, “Development of ASME section X code rules for high pressure composite hydrogen pressure vessels with non-load sharing liners”, Proceedings of the 2010 ASME Pressure Vessels and Piping Conference, PVP 2010, Paper No. PVP2010-25349, 2010, 10 p.

b) ASME Boiler and Pressure Vessel Code, Sec. X, Fiber-reinforced Plastic Pressure Vessels, Mandatory Appendix 8-620 and NB10-0601, Supplement 9.

152. M.R. Gorman, “Modal AE analysis of fracture and failure in composite materials, and the quality and life of high pressure composite pressure vessels”, *J. Acoustic Emission*, vol. 29, 2011, pp. 1-28.

153. C.C. Ciang, J.R. Lee and H.J. Bang, “Structural health monitoring for a wind turbine system: a review of damage detection methods”, *Meas. Sci. Technol.* vol. 19, 2008, 122001 (20 pp) doi:10.1088/0957-0233/19/12/122001

154. B. Lu, Y. Li, X. Wu and Z. Yang, “A review of recent advances in wind turbine condition monitoring and fault diagnosis”, *Proc. IEEE conference on power electronics and machines in wind applications*. 2009. pp. 1-7.

155. M A Drewry and G A Georgiou, “A review of NDT techniques for wind turbines”, *Insight*, vol. 49 no. 3 March 2007, pp. 137-141. www.ndt.net/search/docs.php3?id=4550

156. K.K. Borum, M. McGugan and P. Brøndsted, “Condition monitoring of wind turbine blades”, *Polymer Composite Materials for Wind Power Turbines*, eds: H. Lilholt et al., Risø National Laboratory, Roskilde, Denmark, 2006, pp. 139-145.

157. M.A. Rumsey, J. Paquette, J.R. White, R.J. Werlink, A.G. Beattie, C.W. Pitchford, J. van Dam, “Experimental Results of Structural Health Monitoring of Wind Turbine Blades”, AIAA paper AIAA-2008-1348, 2008. sandia.gov/wind/asme/AIAA-2008-1348.pdf

158. A.A. Anastassopoulos, D.A. Kouroussis, V.N. Nikolaidis, A. Proust, A.G. Dutton, M.J.

- Blanch, L.E. Jones, P. Vionis, D.J. Lekou, D.R.V. van Delft, P.A. Joosse, T.P. Philippidis, T. Kossivas, G. Fernando, “Structural integrity evaluation of wind turbine blades using pattern recognition analysis on acoustic emission data”, EWGAE22, vol. I, 2002, pp. 21-28.
159. P.A. Joosse, M.J. Blanch, A.G. Dutton, D.A. Kouroussis, T.P. Philippidis, P. Vionis, “Acoustic emission monitoring of small wind turbine blades”, *Proc. 21st ASME Wind Energy Symp.*, 2002, AIAA-2002-0063 pp. 1–11.
160. G.R. Kirikera, V. Shinde, M.J. Schulz, A. Ghoshal, M. Sundaresan and R. Allemang, 2007 “Damage localization in composite and metallic structures using a structural neural system and simulated acoustic emissions”, *Mech. Syst. Signal Process.* vol. 21, 2007, pp. 280–297.
161. W. Prosser, E. Madaras, G. Studor, and M. Gorman, “Acoustic emission detection of impact damage on space shuttle structures”, *J. Acoustic Emission.* vol. 23, 2005, pp. 37-46.
162. W. Prosser, E. Madaras, G. Studor, and M. Gorman, “Thermal protection system monitoring of space structures”, *Encyclopedia of Structural Health Monitoring*, eds. C. Boller et al., J. Wiley, 2009, pp. 289-298.
163. A. Marshall, “Sandwich construction”, *Handbook of Composites*, ed. G. Lubin, Van Nostrand Reinhold, 1982, pp. 557-601.
164. M. Burman, “Fatigue crack initiation and propagation in sandwich structures”, PhD thesis, Department of Aeronautics, Kungliga Tekniska Högskolan, (Royal Institute of Technology), S-100 44 Stockholm, Sweden, Report No. 98-29, 1998, 171 p.
165. R.E. Rodriguez-Vera, N.J. Lombardi, M.A.S. Machado, J. Liu, E.D. Sotelino, “Fiber reinforced polymer bridge decks”, FHWA/IN/JTRP-2011/04, 2011, Purdue Univ., W. Lafayette, IN, 99 p.
166. J.C. Flannigan, “Acoustic emission monitoring on fiber reinforced bridge panels”, MS thesis, Kansas State University, Manhattan, Kansas, 2008, 68 p.
167. P. Ouellette and S.V. Hoa, “Acoustic emission signal trends during high cycle fatigue of FRP/balsa wood core vessels”, *J. Acoustic Emission.* vol. 11, no. 2, 1993, pp. 65-70.
168. H. Pfeiffer, M. Wevers, “Aircraft integrated structural health assessment – structural health monitoring and its implementation within the European project AISHA”, EU Project Meeting on Aircraft Integrated Structural Health Assessment (AISHA), Leuven, Belgium, June 2007. www.ndt.net/search/docs.php3?MainSource=69
169. N. Takeda and S. Minakuchi, “Recent development of structural health monitoring technologies for aircraft composite structures in Japan”, *Proc. 17th Int. Conf. on Composite Materials (ICCM-17)*, Edinburgh, UK, 27-31 July 2009.
170. G. Tober, D. Schiller, “NDT in aerospace - state of art”, WCNDT paper, 2000. <http://www.ndt.net/article/wcndt00/papers/idn904/idn904.htm>
171. H. Speckmann, R. Henrich, “Structural Health Monitoring (SHM) - Overview on Airbus activities”, *Proc. 16th World Conf. NDT*, Montreal 2004, paper 536.
172. U. Schnars, R. Henrich, “Applications of NDT methods on composite structures in aerospace industry”, *Online-Proc. Conf. on Damage in Composite Materials – CDCM2006*, vol. 12, no. 12 (2006). <http://www.ndt.net/article/cdcm2006/>
173. D. Roach, “Assessing conventional and advanced NDI for composite aircraft”, *High Performance Composites*, June 2008, 3 p. <http://www.compositesworld.com/articles/assessing-conventional-and-advanced-ndi-for-composite-aircraft>
174. a) T. Ullmann, T. Schmidt, S. Hofmann, R. Jemmali, “In-line quality assurance for the manufacturing of carbon fiber reinforced aircraft structures”, *2nd Intl Symp. on NDT in Aerospace 2010 - Tu.1.A.4.* <http://www.ndt.net/article/aero2010/papers/tu1a4.pdf>
 b) V. Giurgiutiu, A. Zagrai, J.J. Bao, J.M. Redmond, D. Roach, K. Rackow, “Active sensors for health monitoring of aging aerospace structures”, *Intl J. of COMADEM*, vol. 6(1) January 2003, pp. 3-21.

175. B.C. Dykes and W.T. Hardrath, "An acoustic emission pre-failure warning system for composite structural tests", ref. 24d, 1992, pp. 175-180.
176. D. Lindahl and M. Knuuttila, "Acoustic emission monitoring of the Jas 39 Gripen Combat Aircraft", *Progress in AE, X*, (IAES15), Japanese Society for NDI, 2000, pp. 219-224.
177. F.A. Leone, Jr., D. Ozevin, V. Godinez, B. Mosinyi, J.G. Bakuckas, Jr., J. Awerbuch, A. Lau, T.-M. Tan, "Acoustic emission analysis of full-scale honeycomb sandwich composite curved fuselage panels", *Proc. of SPIE*, vol. 6934, 2008, pp. 1-16.
178. D. Aljets, "*Acoustic Emission Source Location in Composite Aircraft Structures using Modal Analysis*", Ph.D. Thesis, Faculty of Advanced Technology, University of Glamorgan, June 2011, 163 p. <http://dSPACE1.isd.glam.ac.uk/dSPACE/bitstream/10265/575/1/PhD%20Thesis%20Dirk%20Aljets.pdf>
179. D. Aljets, A. Chong, S. Wilcox, K. Holford, "Acoustic emission source location in plate-like structures using a closely arranged triangular sensor array" *J. Acoustic Emission*, vol. 28, 2011, pp. 85-98.
180. W.H. Sachse, S. Sancar, "Acoustic emission source location on plate-like structures using a small array of transducers", US Patent 4,592,034, May 27, 1986.
181. C.M. Yeum, H. Sohn, J.B. Ihn, "Lamb wave mode decomposition using concentric ring and circular piezoelectric transducers", *Wave Motion*, vol. 48, 2011, pp. 358-370.
182. M. Wevers, L. Rippert, and S. Van Huffel, "Optical fibres for in situ monitoring the damage development in composites and the relation with acoustic emission measurements", *J. Acoustic Emission*, vol. 18, 2000, pp. 41-50.
183. M. Surgeon, M. Wevers, "The influence of embedded optical fibres on the fatigue damage progress in quasi-isotropic CFRP laminates", *J. Composite Materials*, vol. 35, 2001, pp. 931-940.
184. S. Vandenplas, J.-M. Papy, M. Wevers, S. Van Huffel and D. Inaudi, "Acoustic emission monitoring using a polarimetric single mode optical fiber sensor", *Proc. SPIE 5855*, 17th Intl. Conf. on Optical Fiber Sensors, 2005, p. 1064.
185. M. Wevers, L. Rippert, J.-M. Papy, and S. Van Huffel, "Processing of transient signals from damage in CFRP composite materials monitored with embedded intensity-modulated fiber optic sensors", *NDT&E Int.*, vol. 39, 2006, pp. 229-235,
186. I. Ohsawa, K. Kageyama, Y. Tsuchida, M. Kanai, "Development of a novel optical fiber sensor for AE detection in composites", *J. Acoustic Emission*, vol. 21, 2003, pp. 176-186.
187. H. Cho, R. Arai, M. Takemoto, "Development of stabilized and high sensitive optical fiber acoustic emission system and its application", *J. Acoustic Emission*, vol. 23, 2005, pp. 72-80.
188. T. Matsuo, H. Cho, M. Takemoto, "Utilization of cascade optical fiber ae system for source location of Lamb waves through a cross-ply CFRP plate", *J. Acoustic Emission*, vol. 24, 2006, pp. 84-96.
189. H. Tsuda, "A Bragg wavelength-insensitive fiber Bragg grating ultrasound sensing system that uses a broadband light and no optical filter", *Sensors*, vol. 11, 2011, pp. 6954-6966.
190. P.M. Lam, K.T. Lau, H.Y. Ling, Z.Q. Su, H.Y. Tam, "Acousto-ultrasonic sensing for delaminated GFRP composites using an embedded FBG sensor" *Opt. Laser Eng.* vol. 47, 2009, pp. 1049-1055.
191. M. Ohtsu and K. Ono, "Pattern Recognition Analysis of Magneto mechanical Acoustic Emission Signals," *J. Acoustic Emission*, vol. 3(2), 1984, pp. 69-80.
192. K. Ono, K. Kawamoto, "Digital signal analysis of acoustic emission from carbon fiber/epoxy composites," *J. Acoustic Emission*, vol. 9, 1990, pp. 109-116.
193. A.A. Anastassopoulos and T.P. Philippidis, "Clustering methodology for the evaluation of acoustic emission from composites", *J. Acoustic Emission*, vol. 13, 1995, pp. 11-22.

194. E.v.K. Hill, S.-A.T. Dion, J.O. Karl, N.S. Spivey and J.L. Walker II, "Neural network burst pressure prediction in composite overwrapped pressure vessels," *J. Acoustic Emission*, vol. 25, 2008, pp. 187-193.
195. F.F. Barsoum, J. Suleman, A. Korcak E.v.K. Hill, "Acoustic emission monitoring and fatigue life prediction in axially loaded notched steel specimens," *J. Acoustic Emission*, vol. 27, 2009, pp. 40-63.
196. T. Kohonen, "The self-organizing map", *Proc. IEEE*, vol. 78, no. 9, 1990, pp. 1464-1480.
197. V. Emamian, M. Kaveh, and A.H. Tewfik, "Robust clustering of acoustic emission signals using the Kohonen network," in *Proc. IEEE Int. Conf. Acoustics, Speech, Signal Processing*, vol. 6, Istanbul, Turkey, June 2000, pp. 3891-3894.
198. M.L. Marsden and E.v.K. Hill, "Classification of Fatigue Cracking Data in a Simulated Aircraft Fuselage Using a Self Organizing Map," *First International Conference on Nonlinear Problems in Aviation and Aerospace*, S. Sivasundaram, editor, Embry-Riddle Aeronautical University Press, Daytona Beach, FL, 1997, pp. 405-410.
199. E.v.K. Hill, J. Iizuka, I.K. Kaba, H.L. Surber, Y.P. Poon, "Neural network burst pressure prediction in composite overwrapped pressure vessels using mathematically modeled acoustic emission failure mechanism data", *Research in Nondestructive Evaluation*, vol. 23, 2012, pp. 89-103.
200. R. Gutkin, C.J. Green, S. Vangrattanachai, S.T. Pinho, P. Robinson, P.T. Curtis, "On acoustic emission for failure investigation in CFRP: Pattern recognition and peak frequency analyses", *Mechanical Systems and Signal Processing*, vol. 25, 2011, pp. 1393-1407.
201. R. de Oliveira, A.T. Marques, "Health monitoring of FRP using acoustic emission and artificial neural networks", *Computers and Structures*, vol. 86, 2008, pp. 367-373.

Appendix 1: Lamb wave propagation

In 1986, Ichikawa et al. [A1] investigated the optimum conditions for using Lamb waves for inspection of steel sheets, which fail from nonmetallic inclusions under heavy deformation. Using theoretical results, they developed an improved inspection system for use in steel production lines. From the basic Lamb wave behavior, they noted complexity, such as 1) some modes are difficult to excite or detect depending on frequency-thickness product, or fd values, 2) the sharpness of flaw reflection varies strongly with fd values, and 3) flaw reflection pulse has a different frequency from that of the excitation pulse.

Pulse excitation and detection typically uses piezoelectric sensors that respond to normal displacement; on the plate surfaces, one needs vertical particle displacements from Lamb waves. For a plate of thickness, d , scalar and vector potentials are introduced to represent displacement and stress within the plate using free boundary conditions on the surfaces. The components of a displacement vector (U , W) for the wave propagation direction, x , and for the normal (thickness) direction, z , are given by:

For symmetric modes:

$$\left. \begin{aligned} U &= \alpha k_s \left(\frac{\cosh q_s z}{\sinh q_s \delta} - \frac{2q_s s_s}{k_s^2 + s_s^2} \times \frac{\cosh s_s z}{\sinh s_s \delta} \right) \\ &\quad \times \exp \left[i \left(k_s x - \omega t - \frac{\pi}{2} \right) \right] \\ W &= -\alpha q_s \left(\frac{\sinh q_s z}{\sinh q_s \delta} - \frac{2k_s^2}{k_s^2 + s_s^2} \times \frac{\sinh s_s z}{\sinh s_s \delta} \right) \\ &\quad \times \exp [i(k_s x - \omega t)] \end{aligned} \right\} \quad (3a)$$

For asymmetric modes

$$\left. \begin{aligned} U &= \beta k_a \left(\frac{\sinh q_a z}{\cosh q_a \delta} - \frac{2q_a s_a}{k_a^2 + s_a^2} \times \frac{\sinh s_a z}{\cosh s_a \delta} \right) \\ &\quad \times \exp \left[i \left(k_a x - \omega t - \frac{\pi}{2} \right) \right] \\ W &= -\beta q_a \left(\frac{\cosh q_a z}{\cosh q_a \delta} - \frac{2k_a^2}{k_a^2 + s_a^2} \times \frac{\cosh s_a z}{\cosh s_a \delta} \right) \\ &\quad \times \exp [i(k_a x - \omega t)] \end{aligned} \right\} \quad (3b)$$

where $d = 2\delta$, $q_s^2 = k_s^2 - k_l^2$, $q_a^2 = k_a^2 - k_l^2$, $s_s^2 = k_s^2 - k_t^2$, $s_a^2 = k_a^2 - k_t^2$, $\omega = 2\pi f$: angular frequency, $k_{s(a,l,t)}$: wave number for symmetric (asymmetric, longitudinal, transverse) wave, $\alpha, \beta = \text{constant}$. W_δ is defined as an index to express the magnitude of the surface normal displacement, W , relative to the integrated mean-square displacement as:

$$W_\delta = \frac{[W]_{z=d}}{\sqrt{\int_{-d}^d (U^2 + W^2) dz}} \quad (4)$$

Using equations 3 and 4 with the shear modulus of steel = 80.3 GPa, density = 7.8 Mg/m³, Poisson's ratio = 0.28, the phase velocity and W_δ in dB scale are shown against fd in Fig. A1 (a) and (b). These are reproduced from Figs. 4 and 5 in [A1]. It is evident that W_δ varies widely depending on the wave mode and fd values. It is significant that the surface normal displacement

of S_0 mode is less than -17 dB for $fd \leq 1$ MHz·mm, while that for A_0 is always above -6 dB. This explains why S_0 mode is usually not observed at low frequencies, especially for thin structures.

The wave dispersion also affects the pulse amplitude. The group velocity C_g is given by

$$\frac{C}{C_g} = 1 - \frac{f}{c} \left(\frac{\partial C}{\partial f} \right), \quad (5)$$

where C is the phase velocity. When a pulse with the center frequency f_0 and its spread in the frequency domain Δf (in half-value width) travels time t over distance l , resulting in pulse spread in time of Δt (in half-value pulse width) of:

$$\begin{aligned} \Delta t &= A_0 \left[\frac{\partial t}{\partial f} \right]_{f=f_0} \times \Delta f \\ &= A_0 \Delta f \left[\frac{\partial C_g}{\partial f} / C_g^2 \right]_{f=f_0} \end{aligned} \quad (6)$$

where A_0 is a constant. A parameter D_g defined below indicates the sharpness of a pulse affected by the velocity dispersion. With the transverse velocity C_t , we have:

$$D_g = \frac{\partial}{\partial (fd)} \left(\frac{C_g}{C_t} \right) / \left(\frac{C_g}{C_t} \right)^2 \quad (7)$$

Results of calculation are shown in Fig. A1(c) (which is Fig. 6 in [A1]). When the value of D_g vanishes, the dispersion effect is minimal. Again, D_g varies strongly with fd values, depending on the wave mode. Open circles marked P_1 to P_8 (in Fig. A1 (b) and (c)) indicate the points where $D_g = 0$. Table 1 in [A1] gives the fd values (along with C/C_L , C_g/C_L and W_d (in dB)) corresponding to P_1 to P_8 :

P_i	P_1	P_2	P_3	P_4	P_5	P_6	P_7	P_8
fd value	1.42	2.52	2.80	4.81	6.97	7.26	7.41	9.09
wave mode	A_0	S_0	A_1	A_1	S_1	A_3	A_3	A_2
C/C_L	0.79	1.23	2.00	1.33	1.38	2.80	2.60	1.40
C_g/C_L	1.01	0.54	1.18	0.69	0.70	0.78	0.78	0.71
W_d (in dB)	-6.0	-4.0	-8.5	-5.1	-5.2	-3.8	-3.9	-5.1

There seems another vanishing D_g point at $fd = 4.12$ for S_1 mode, but W_δ is low here. Judging from various wave propagation data, both theoretical and experimental, it appears that when $D_g \leq \pm 0.3 \sim 0.5$, pulse propagation is possible without suffering excessive dispersion effects.

Considering both W_δ and D_g , this work leads to approximate ranges where good pulse detection with low dispersion loss can be expected:

S_0 mode	$fd = 1 \sim 2, > 3.5$
A_0 mode	> 0.5
S_1 mode	~ 2.7
A_1 mode	$2 \sim 4$
S_2 mode	$3.5 \sim 7$
A_2 mode	> 5.8

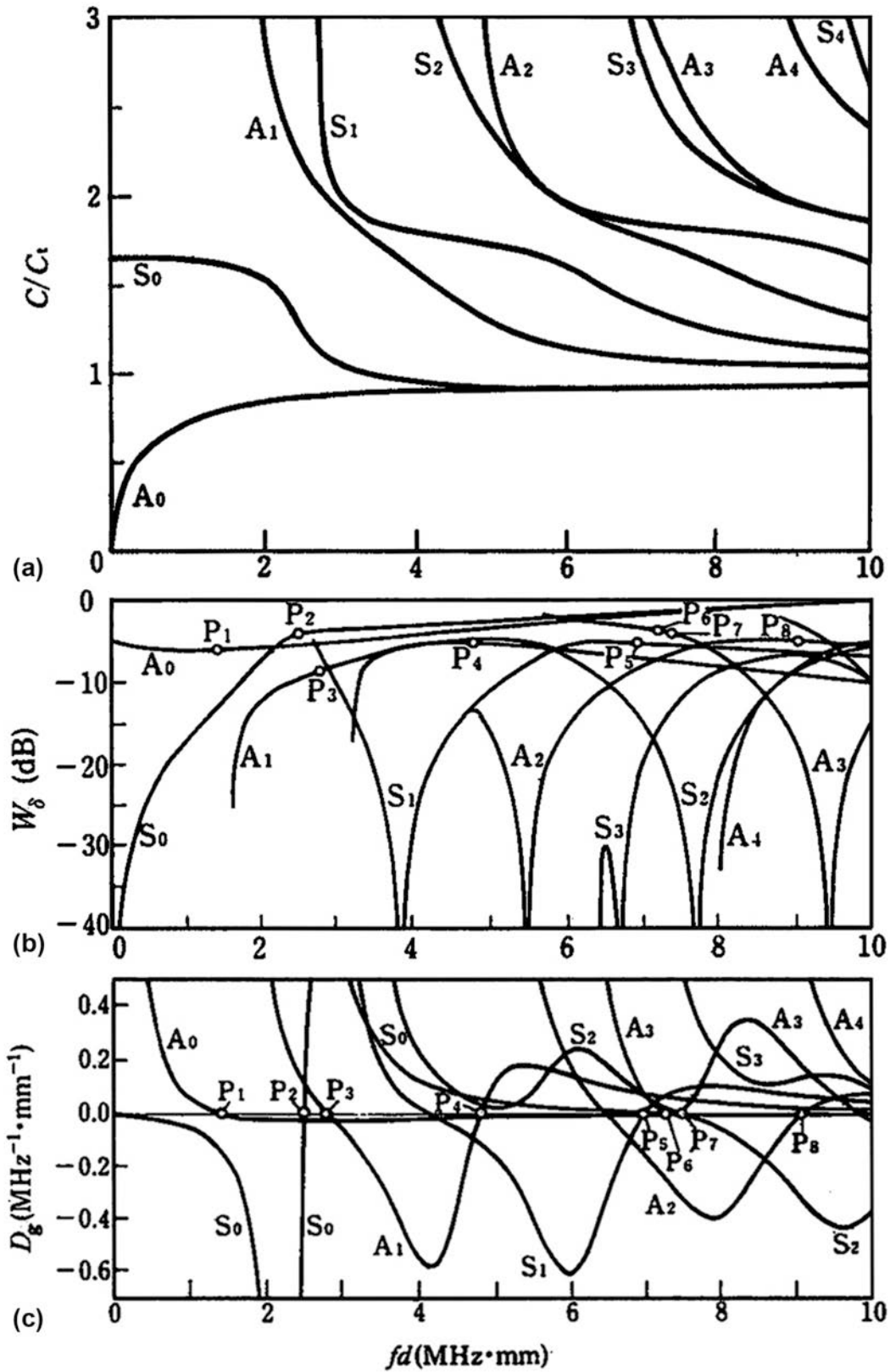


Fig. A1. a) Phase velocity of Lamb waves vs. fd values. b) Index for surface normal displacement W_δ in dB scale vs. fd values. c) Parameter for dispersion effect D_g vs. fd values. These figures were assembled from Figs. 4-6 in Ichikawa et al. [A1], matching the abscissa.

Since W_δ is in dB scale, it should dictate the outcome, while effects of D_g parameter needs to be explored experimentally.

This result of Ichikawa et al. [A1] is for isotropic medium and not directly applicable to fiber composite materials. However, this gives for the first time explanations for oft-peculiar Lamb-wave propagation behavior. In practical inspection setups, one also needs to consider frequency-dependent attenuation effects.

Appendix 2: Gaussian Pulses

A Gaussian pulse is defined as a function of time t

$$G(t) = \exp[-t^2/2\sigma^2] \quad (8)$$

where σ is a pulse width parameter [A2]. The pulse width at one-half of the peak height, $t_{1/2}$, (also called the full width at half-maximum or FWHM) is given by

$$t_{1/2} = \sqrt{8 \ln(8)} \sigma = 2.35482 \sigma. \quad (9)$$

Figure A2 (a) shows a Gaussian pulse with $t_{1/2} = 0.22 \mu\text{s}$ [A3]. The power spectral density of this pulse is given in Fig. A2 (b). It peaks at $f = 0$ and the spectral width at one-half of the peak height, $f_{1/2}$, is equal to 2.0 MHz. The half-height widths are related to each other by [A4]

$$t_{1/2} \times f_{1/2} = 0.44. \quad (10)$$

The time derivative of a Gaussian pulse defines a Gaussian mono-pulse (aka monocycle). Using the center frequency, f_c , it is given by [A5]

$$V(t, f_c, A) = 2\sqrt{e} A \pi t f_c \exp[-2(\pi t f_c)^2], \quad (11)$$

where A is the peak height. A Gaussian mono-pulse at 2 MHz is shown in Fig. A2 (c) [A6]. In the frequency domain, this is given by

$$V(f, f_c, A) = \frac{A}{2} \sqrt{\frac{2e}{\pi}} \frac{f}{f_c} \exp\left[-\frac{1}{2} \left(\frac{f}{f_c}\right)^2\right]. \quad (12)$$

The inverse of the center frequency is essentially pulse duration, τ . That is,

$$\tau \times f_c \sim 1. \quad (13)$$

A pair of waveform and its frequency spectrum from [A5] was scaled to 2 MHz to 200 kHz center frequencies. Four such pairs are illustrated in Fig. A3, (a) to (d).

The most striking feature of Fig. A3 is the broadness of the spectra. For a 2 MHz pulse (of 0.5- μs duration), -3 dB half-power points are at 1 and 3.2 MHz. At 200 kHz (5- μs long pulse), the corresponding frequency range is from 100 to 320 kHz. Thus, a variation in source duration has to be quite large to be noticeable in the detected frequency spectra. Since most sensors and structures have natural frequencies, their dominance will be difficult to overcome.

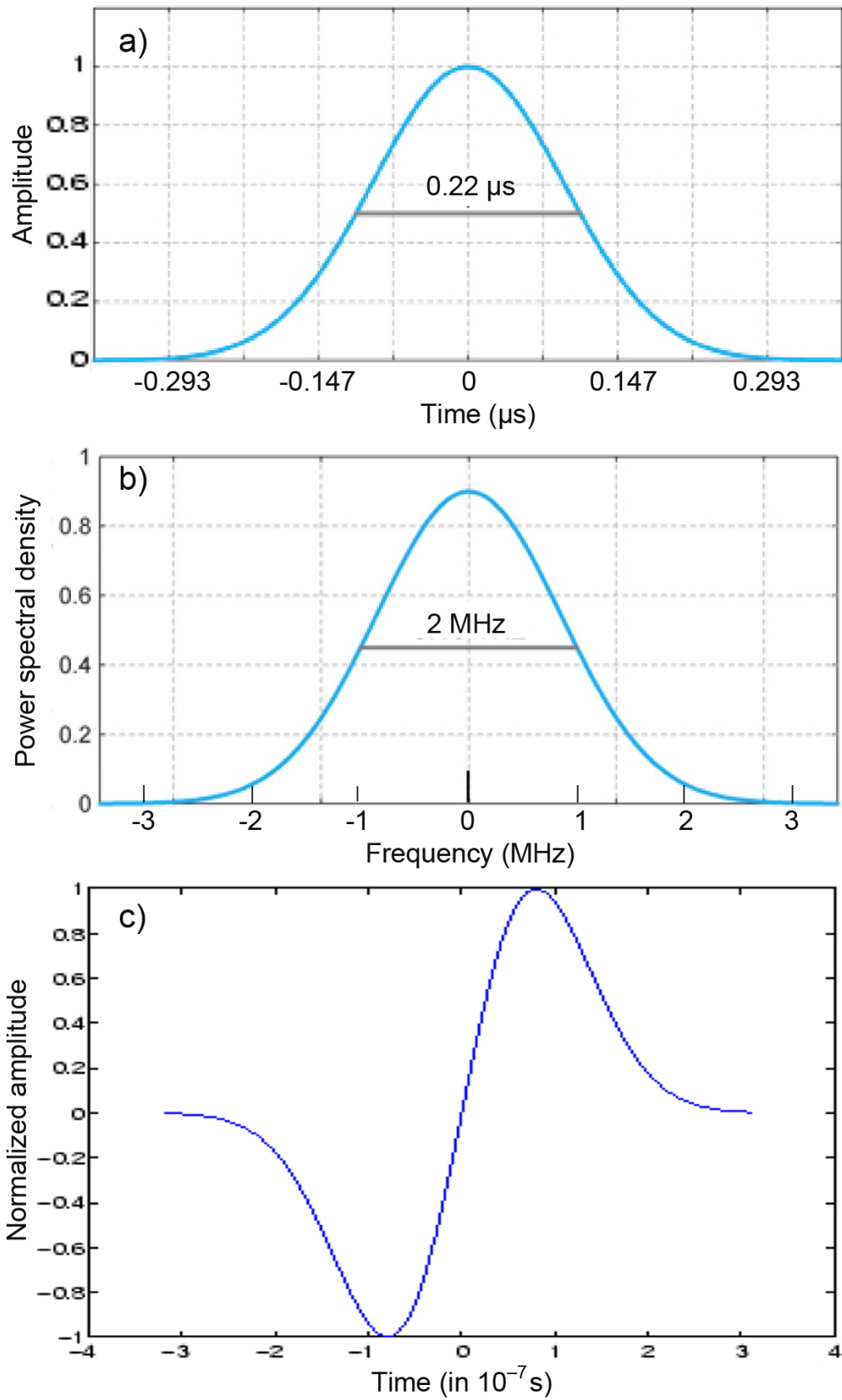


Fig. A2. a) 2-MHz Gaussian pulse. b) Its power spectral density. [A3] c) 2-MHz Gaussian monopulse. [A6]

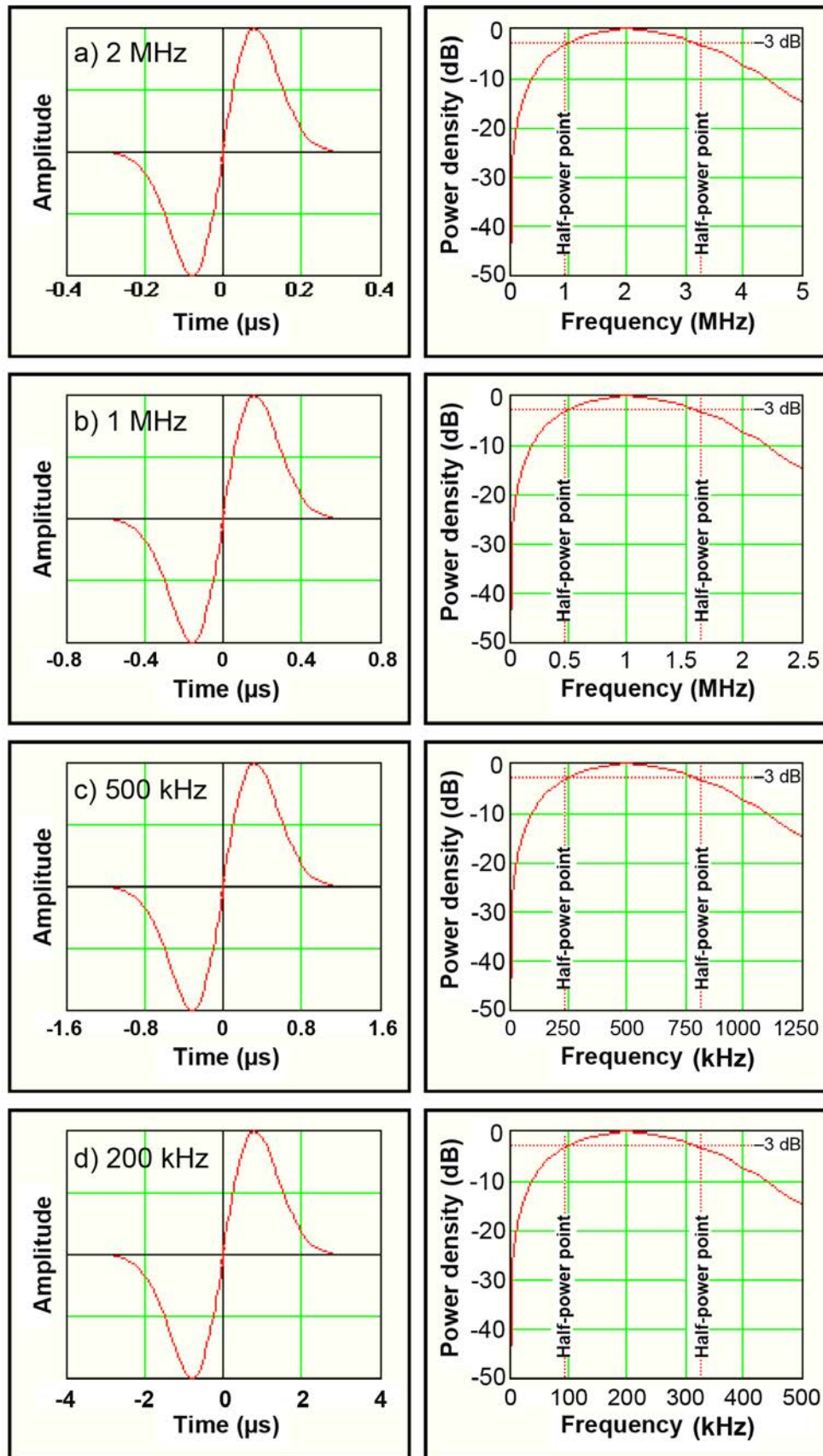


Fig. A3. a) 2-MHz Gaussian monopulse and its power spectral density. b) Same for 1 MHz. c) Same for 500 kHz. d) Same for 200 kHz. [A5]

Appendix 3: Directionality of Attenuation and Source Types

Suzuki [71b] measured P-wave attenuation in UD-GFRP with 60% fiber content using a laser technique. Figures 4.15(g), 4.16 and 4.17 from his thesis are shown in Fig. A4 below. These show high attenuation especially for 90° orientation at 160-180 dB/m, but even for the orientation along fibers (0°) it is 60~80 dB/m. These are still 2 to 5 times less than in epoxy.

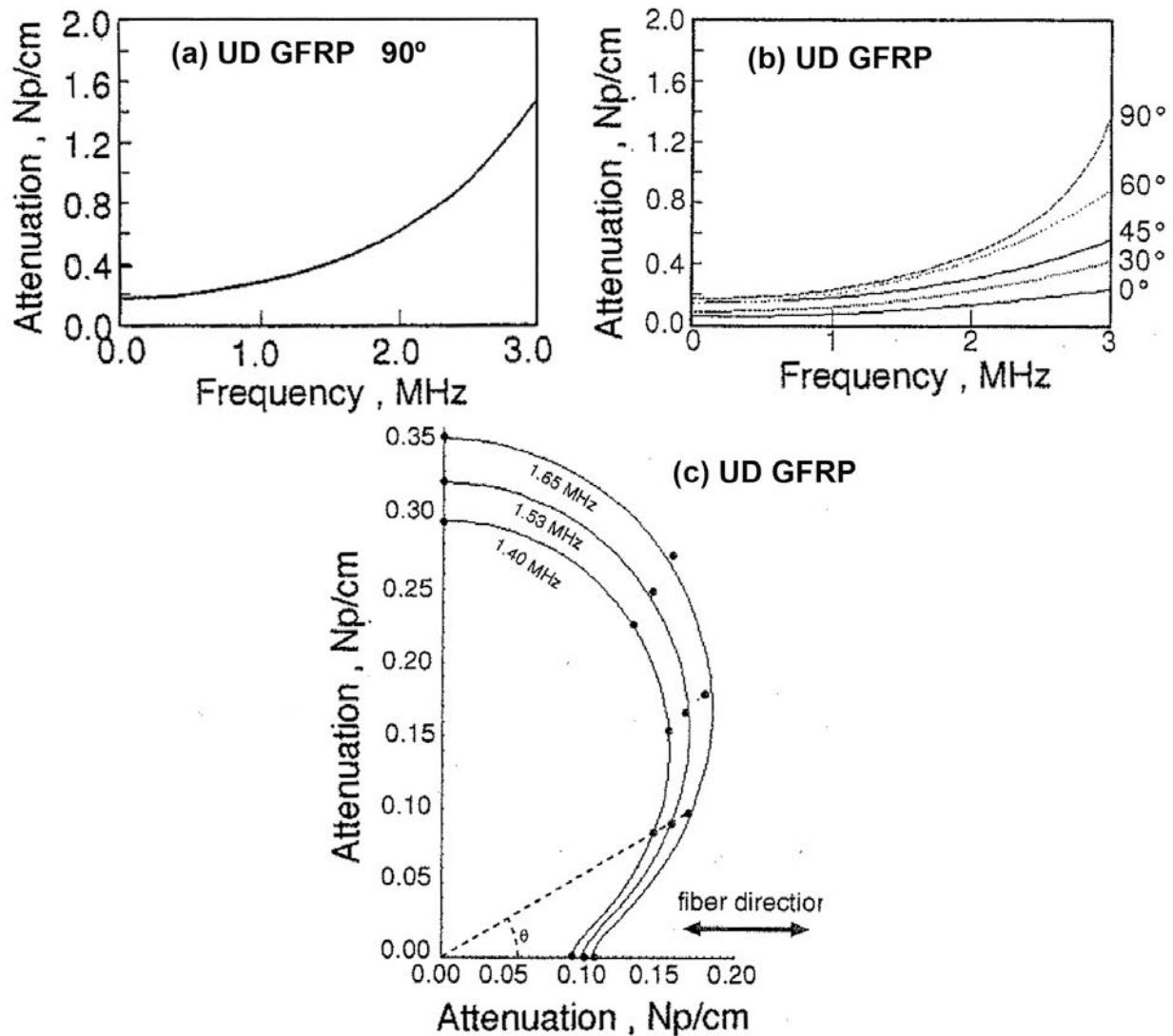


Fig. A4. a), b) Frequency dependence of P-wave attenuation in GFRP. c) Orientation dependence at 1.4~1.65 MHz. [71b]

Downs et al. [A7] examined the directionality of AE sources in an Al plate, that is, the orientation dependence of FEM-generated AE signals due to three types of sources, i.e., in-plane dipole, microcrack initiation, and shear at 45° about the y-axis without a moment. They used wavelet transform to characterize the absolute WT peak magnitude as a function of radiation angle and source depth. The fall-off with increasing angle is dramatic for the in-plane dipole (nearly 100%), as shown in Fig. A5. It is least for the microcrack initiation, except for a source at the mid-plane, where the 45° shear has the least fall-off. The results also demonstrated that the WT absolute peak magnitudes have their greatest values when the source is close to the surface and have their lowest values when the source is located at or near the mid-plane.

The directionality WT magnitude of microcrack sources is shown in Fig. A6, where 0°-amplitude was used to normalize other radiation angles. Here, frequency: 270 kHz, propagation distance: 180 mm, plate thickness: 4.7 mm. S_0 and A_0 data behaved differently; Source depth effect was present for the A_0 mode, but not for the S_0 mode. In both modes, the magnitude did not vanish at 90°.

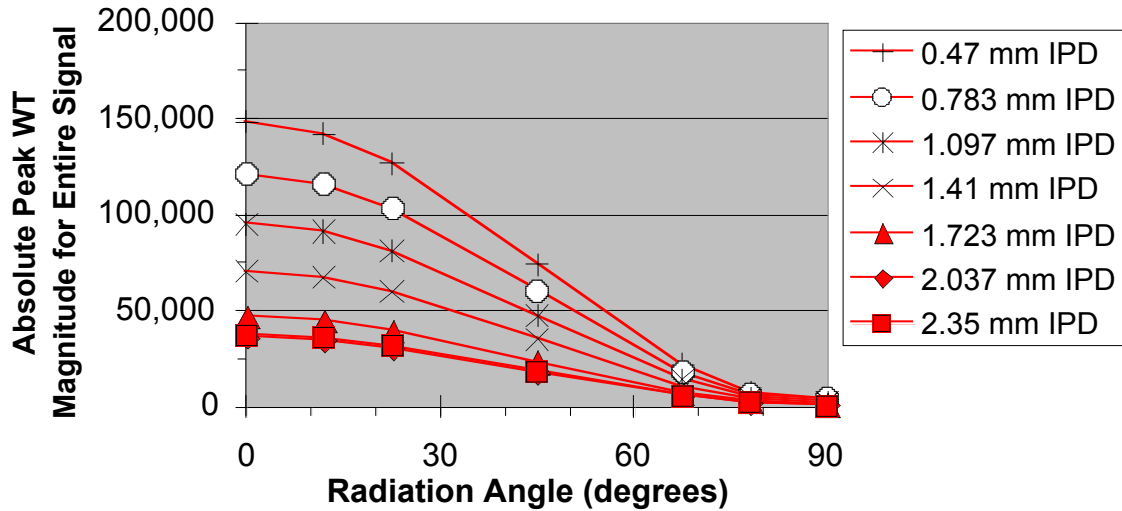


Fig. A5. Absolute peak WT magnitudes for various source depths for in-plane dipole source at 180 mm propagation distance [A7].

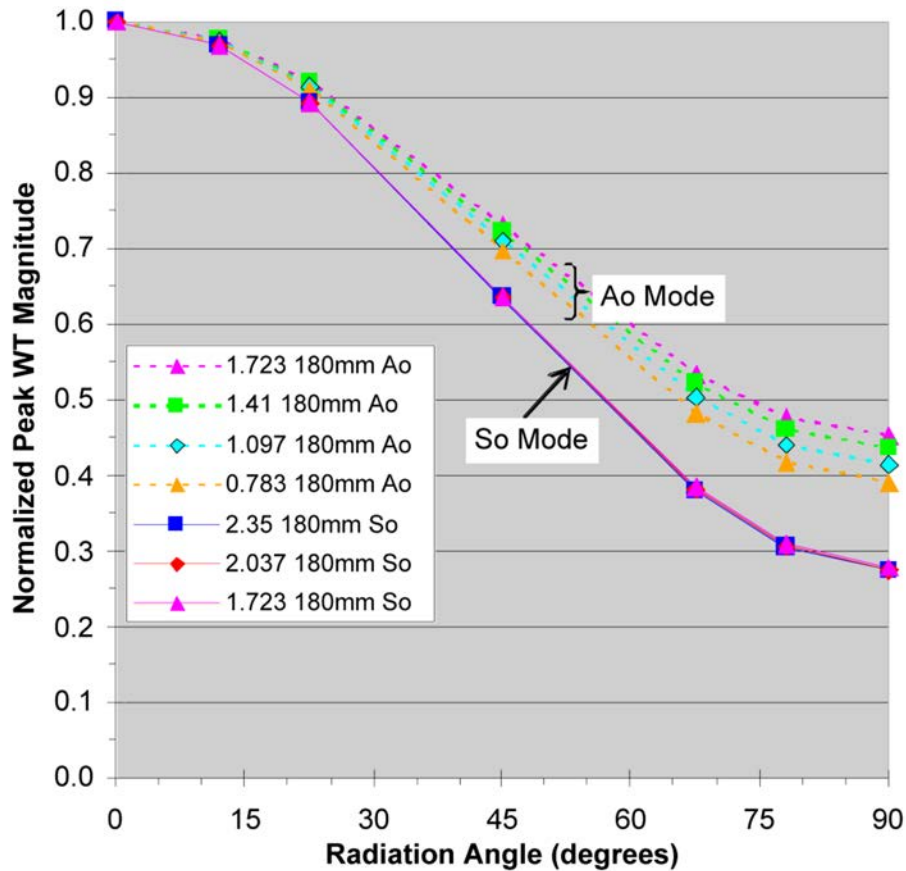


Fig. A6. Normalized peak WT magnitudes for microcrack source at 270 kHz; legend lists source depth (mm), propagation distance (mm), and mode [A7].

References for Appendices

- A1. F. Ichikawa, K. Kurita, H. Maruyama, S. Takahashi, “Study on optimum conditions for Lamb wave ultrasonic testing and its application to product line”, Kawasaki Steel Tech. Report, vol. 18, 1986, pp. 192-198.
- A2. S. Smith, Gaussian Pulses. <http://gamma.ethz.ch/download/pdf/pulses/gaussian.pdf>
- A3. Introduction to Optical Pulses, Optipedia, Free optics information SPIE. Excerpt from R. Paschotta, Field Guide to Laser Pulse Generation, SPIE Press, Bellingham, WA (2008).
spie.org/x32442/xml?pf=true
- A4. Gaussian pulses, Encyclopedia of Laser Physics and Technology.
www.rp-photonics.com/gaussian_pulses.html
- A5. P. Withington, Impulse Radio Overview, Time Domain Corp.
user.it.uu.se/~carle/Notes/UWB.pdf
- A6. Gaussian monopulse – Matlab: www.mathworks.com/help/toolbox/signal/ref/gmonopuls.html
- A7. K.S. Downs, M.A. Hamstad and A. O’Gallagher, “Practical aspects of acoustic emission source location by a wavelet transform”, J. Acoustic Emission, vol. 21, 2003, pp. 52-69.